Physics Reference Manual

Version: geant4 10.0 (6 December 2013)

Contents

Part I

Introduction

Chapter 1

Introduction

1.1 Scope of This Manual

The Physics Reference Manual provides detailed explanations of the physics implemented in the Geant4 toolkit. The manual's purpose is threefold:

- to present the theoretical formulation, model, or parameterization of the physics interactions included in Geant4,
- to describe the probability of the occurrence of an interaction and the sampling mechanisms required to simulate it, and
- to serve as a reference for toolkit users and developers who wish to consult the underlying physics of an interaction.

This manual does not discuss code implementation or how to use the implemented physics interactions in a simulation. These topics are discussed in the User's Guide for Application Developers. Details of the object-oriented design and functionality of the Geant4 toolkit are given in the User's Guide for Toolkit Developers. The Installation Guide for Setting up Geant4 in Your Computing Environment describes how to get the Geant4 code, install it, and run it.

1.2 Definition of Terms

Several terms used throughout the Physics Reference Manual have specific meaning within Geant4, but are not well-defined in general usage. The definitions of these terms are given here.

- **process** - a C++ class which describes how and when a specific kind of physical interaction takes place along a particle track. A given particle type typically has several processes assigned to it. Occaisionally "process" refers to the interaction which the process class describes.
- **model** - a C++ class whose methods implement the details of an interaction, such as its kinematics. One or more models may be assigned to each process. In sections discussing the theory of an interaction, "model" may refer to the formulae or parameterization on which the model class is based.
- **Geant3** - a physics simulation tool written in Fortran, and the predecessor of Geant4. Although many references are made to Geant3, no knowledge of it is required to understand this manual.

1.3 Status of this document

4.12.01 created by D.H. Wright

Chapter 2

Monte Carlo Methods

The Geant4 toolkit uses a combination of the composition and rejection Monte Carlo methods. Only the basic formalism of these methods is outlined here. For a complete account of the Monte Carlo methods, the interested user is referred to the publications of Butcher and Messel, Messel and Crawford, or Ford and Nelson [1, 2, 3].
Suppose we wish to sample x in the interval $[x_1,\ x_2]$ from the distribution $f(x)$ and the *normalised* probability density function can be written as :

$$f(x) = \sum_{i=1}^{n} N_i f_i(x) g_i(x) \tag{2.1}$$

where $N_i > 0$, $f_i(x)$ are *normalised* density functions on $[x_1,\ x_2]$, and $0 \leq g_i(x) \leq 1$.
According to this method, x can sampled in the following way:

1. select a random integer $i \in \{1, 2, \cdots n\}$ with probability proportional to N_i
2. select a value x_0 from the distribution $f_i(x)$
3. calculate $g_i(x_0)$ and accept $x = x_0$ with probability $g_i(x_0)$;
4. if x_0 is rejected restart from step 1.

It can be shown that this scheme is correct and the mean number of tries to accept a value is $\sum_i N_i$.
In practice, a good method of sampling from the distribution $f(x)$ has the following properties:

- all the subdistributions $f_i(x)$ can be sampled easily;

- the rejection functions $g_i(x)$ can be evaluated easily/quickly;
- the mean number of tries is not too large.

Thus the different possible decompositions of the distribution $f(x)$ are not equivalent from the practical point of view (e.g. they can be very different in computational speed) and it can be useful to optimise the decomposition. A remark of practical importance : if our distribution is not normalised

$$\int_{x_1}^{x_2} f(x)dx = C > 0$$

the method can be used in the same manner; the mean number of tries in this case is $\sum_i N_i/C$.

2.1 Status of this document

18.01.02 created by M.Maire.

Bibliography

[1] J.C. Butcher and H. Messel. *Nucl. Phys. 20* 15 (1960)

[2] H. Messel and D. Crawford. *Electron-Photon shower distribution, Pergamon Press* (1970)

[3] R. Ford and W. Nelson. *SLAC-265, UC-32* (1985)

[4] Particle Data Group. Rev. of Particle Properties. *Eur. Phys. J. C15. (2000) 1.* http://pdg.lbl.gov

Chapter 3

Particle Transport

3.1 Transportation

The transportation process is responsible for determining the geometrical limits of a step. It calculates the length of step with which a track will cross into another volume. When the track actually arrives at a boundary, the transportation process locates the next volume that it enters.

If the particle is charged and there is an electromagnetic (or potentially other) field, it is responsible for propagating the particle in this field. It does this according to an equation of motion. This equation can be provided by Geant4, for the case a magnetic or EM field, or can be provided by the user for other fields.

The transportation updates the time of flight of a particle, utilising its initial velocity.

Some additional details on motion in fields:

In order to intersect the model Geant4 geometry of a detector or setup, the curved trajectory followed by a charged particle is split into 'chords segments'. A chord is a straight line segment between two trajectory points. Chords are created utilizing a criterion for the maximum estimated distance between a curve point and the chord. This distance is also known as the sagitta.

The equations of motions are solved utilising Runge Kutta methods. Runge Kutta methods of different can be utilised for fields depending on the numerical method utilised for approximating the field. Specialised methods for near-constant magnetic fields are under development.

3.1.1 Status of This Document

17.11.11 minor revisions by V. Ivanchenko

3.2 True Step Length

Geant4 simulation of particle transport is performed step by step [1]. A *true step length* for a next physics interaction is randomly sampled using the *mean free path* of the interaction or by various *step limitations* established by different Geant4 components. The smallest step limit defines the new true step length.

3.2.1 The Interaction Length or Mean Free Path

Computation of mean free path of a particle in a media is performed in Geant4 using cross section of a particular physics process and density of atoms. In a simple material the number of atoms per volume is:

$$n = \frac{\mathcal{N}\rho}{A}$$

where:

$\mathcal{N}$	Avogadro's number
ρ	density of the medium
A	mass of a mole

In a compound material the number of atoms per volume of the i^{th} element is:

$$n_i = \frac{\mathcal{N}\rho w_i}{A_i}$$

where:

w_i	proportion by mass of the i^{th} element
A_i	mass of a mole of the i^{th} element

The **mean free path** of a process, λ, also called the **interaction length**, can be given in terms of the total cross section :

$$\lambda(E) = \left(\sum_i [n_i \cdot \sigma(Z_i, E)] \right)^{-1}$$

where $\sigma(Z, E)$ is the total cross section per atom of the process and $\sum_i$ runs over all elements composing the material.

$\sum_i [n_i \sigma(Z_i, E)]$ is also called the *macroscopic cross section*. The mean free path is the inverse of the macroscopic cross section.
Cross sections per atom and mean free path values may be tabulated during initialisation.

3.2.2 Determination of the Interaction Point

The mean free path, λ, of a particle for a given process depends on the medium and cannot be used directly to sample the probability of an interaction in a heterogeneous detector. The number of mean free paths which a particle travels is:

$$n_\lambda = \int_{x_1}^{x_2} \frac{dx}{\lambda(x)}, \tag{3.1}$$

which is independent of the material traversed. If n_r is a random variable denoting the number of mean free paths from a given point to the point of interaction, it can be shown that n_r has the distribution function:

$$P(n_r < n_\lambda) = 1 - e^{-n_\lambda} \tag{3.2}$$

The total number of mean free paths the particle travels before reaching the interaction point, n_λ, is sampled at the beginning of the trajectory as:

$$n_\lambda = -\log(\eta) \tag{3.3}$$

where η is a random number uniformly distributed in the range $(0, 1)$. n_λ is updated after each step Δx according the formula:

$$n'_\lambda = n_\lambda - \frac{\Delta x}{\lambda(x)} \tag{3.4}$$

until the step originating from $s(x) = n_\lambda \cdot \lambda(x)$ is the shortest and this triggers the specific process.

3.2.3 Step Limitations

The short description given above is the *differential approach* to particle transport, which is used in the most popular simulation codes EGS and Geant3. In this approach besides the other (*discrete*) processes the continuous energy loss imposes a limit on the step-size too [2], because the cross section of different processes depend of the energy of the particle. Then it is assumed that the step is small enough so that the particle cross sections remain approximately constant during the step. In principle one must use very small steps in order to insure an accurate simulation, but computing time increases as the step-size decreases. A good compromise depends on required accuracy of a concrete simulation. For electromagnetic physics the

problem is reduced using integral approach, which is described below in sub-chapter 7.3. However, this only provides effectively correct cross sections but step limitation is needed also for more precise tracking. Thus, in Geant4 any process may establish additional step limitation, the most important limits see below in sub-chapters 7.1.3 and 6.1.6).

3.2.4 Updating the Particle Time

The laboratory time of a particle should be updated after each step:

$$\Delta t_{lab} = 0.5\Delta x(\frac{1}{v_1} + \frac{1}{v_2}), \tag{3.5}$$

where Δx is a true step length traveled by the particle, v_1 and v_2 are particle velocities at the beginning and at the end of the step correspondingly.

3.2.5 Status of This Document

09.10.98 created by L. Urbán.
27.07.01 minor revisions by M. Maire
01.12.03 integral method subsection added by V. Ivanchenko
12.08.04 splitted and partly moved in introduction by M. Maire
25.12.06 minor revision by V. Ivanchenko
15.12.08 minor revision by J. Apostolakis
08.12.10 revisions by V. Ivanchenko
17.11.11 moved to transportation chapter by V. Ivanchenko

Bibliography

[1] S. Agostinelli et al., Geant4 – a simulation toolkit *Nucl. Instr. Meth. A506 (2003) 250.*

[2] J. Apostolakis et al., Geometry and physics of the Geant4 toolkit for high and medium energy applications. *Rad. Phys. Chem. 78 (2009) 859.*

Part II

Particle Decay

Chapter 4

Decay

The decay of particles in flight and at rest is simulated by the *G4Decay* class.

4.1 Mean Free Path for Decay in Flight

The mean free path λ is calculated for each step using

$$\lambda = \gamma\beta c\tau$$

where τ is the lifetime of the particle and

$$\gamma = \frac{1}{\sqrt{1-\beta^2}}.$$

β and γ are calculated using the momentum at the beginning of the step. The decay time in the rest frame of the particle (proper time) is then sampled and converted to a decay length using β.

4.2 Branching Ratios and Decay Channels

G4Decay selects a decay mode for the particle according to branching ratios defined in the *G4DecayTable* class, which is a member of the *G4ParticleDefinition* class. Each mode is implemented as a class derived from *G4VDecayChannel* and is responsible for generating the secondaries and the kinematics of the decay. In a given decay channel the daughter particle momenta are calculated in the rest frame of the parent and then boosted into the laboratory frame. Polarization is not currently taken into account for either the parent or its daughters.

A large number of specific decay channels may be required to simulate an experiment, ranging from two-body to many-body decays and $V - A$ to semi-leptonic decays. Most of these are covered by the five decay channel classes provided by Geant4:

G4PhaseSpaceDecayChannel	: phase space decay
G4DalitzDecayChannel	: dalitz decay
G4MuonDecayChannel	: muon decay
G4TauLeptonicDecayChannel	: tau leptonic decay
G4KL3DecayChannel	: semi-leptonic decays of kaon .

4.2.1 G4PhaseSpaceDecayChannel

The majority of decays in Geant4 are implemented using the *G4PhaseSpaceDecayChannel* class. It simulates phase space decays with isotropic angular distributions in the center-of-mass system. Three private methods of *G4PhaseSpaceDecayChannel* are provided to handle two-, three- and N-body decays:

TwoBodyDecayIt()
ThreeBodyDecayIt()
ManyBodyDecayIt()

Some examples of decays handled by this class are:

$$\pi^0 \rightarrow \gamma\gamma,$$

$$\Lambda \rightarrow p\pi^-$$

and

$$K^0{}_L \rightarrow \pi^0\pi^+\pi^-.$$

4.2.2 G4DalitzDecayChannel

The Dalitz decay

$$\pi^0 \rightarrow \gamma + e^+ + e^-$$

and other Dalitz-like decays, such as

$$K^0{}_L \rightarrow \gamma + e^+ + e^-$$

and

$$K^0{}_L \rightarrow \gamma + \mu^+ + \mu^-$$

are simulated by the *G4DalitzDecayChannel* class. In general, it handles any decay of the form

$$P^0 \rightarrow \gamma + l^+ + l^-,$$

where P^0 is a spin-0 meson of mass M and $l^{\pm}$ are leptons of mass m. The angular distribution of the γ is isotropic in the center-of-mass system of the parent particle and the leptons are generated isotropically and back-to-back in their center-of-mass frame. The magnitude of the leptons' momentum is sampled from the distribution function

$$f(t) = (1 - \frac{t}{M^2})^3 (1 + \frac{2m^2}{t})\sqrt{1 - \frac{4m^2}{t}},$$

where t is the square of the sum of the leptons' energy in their center-of-mass frame.

4.2.3 Muon Decay

G4MuonDecayChannel simulates muon decay according to $V-A$ theory. The electron energy is sampled from the following distribution:

$$d\Gamma = \frac{{G_F}^2 {m_\mu}^5}{192\pi^3} 2\epsilon^2(3 - 2\epsilon)$$

where:

Γ	:	decay rate
ϵ	:	$= E_e/E_{max}$
E_e	:	electron energy
E_{max}	:	maximum electron energy $= m_\mu/2$

The magnitudes of the two neutrino momenta are also sampled from the $V-A$ distribution and constrained by energy conservation. The direction of the electron neutrino is sampled using

$$cos(\theta) = 1 - 2/E_e - 2/E_{\nu e} + 2/E_e/E_{\nu e}$$

and the muon anti-neutrino momentum is chosen to conserve momentum. Currently, neither the polarization of the muon nor the electron is considered in this class.

4.2.4 Leptonic Tau Decay

G4TauLeptonicDecayChannel simulates leptonic tau decays according to $V-A$ theory. This class is valid for both

$$\tau^{\pm} \rightarrow e^{\pm} + \nu_{\tau} + \nu_{e}$$

and

$$\tau^{\pm} \rightarrow \mu^{\pm} + \nu_{\tau} + \nu_{\mu}$$

modes.

The energy spectrum is calculated without neglecting lepton mass as follows:

$$d\Gamma = \frac{{G_F}^2 {m_\tau}^3}{24\pi^3} p_l E_l (3E_l {m_\tau}^2 - 4{E_l}^2 m_\tau - 2m_\tau {m_l}^2)$$

where:
Γ : decay rate
E_l : daughter lepton energy (total energy)
p_l : daughter lepton momentum
m_l : daughter lepton mass

As in the case of muon decay, the energies of the two neutrinos are not sampled from their $V-A$ spectra, but are calculated so that energy and momentum are conserved. Polarization of the τ and final state leptons is not taken into account in this class.

4.2.5 Kaon Decay

The class *G4KL3DecayChannel* simulates the following four semi-leptonic decay modes of the kaon:

$${K^{\pm}}_{e3} : K^{\pm} \rightarrow \pi^0 + e^{\pm} + \nu$$
$${K^{\pm}}_{\mu 3} : K^{\pm} \rightarrow \pi^0 + \mu^{\pm} + \nu$$
$${K^0}_{e3} : K^0_L \rightarrow \pi^{\pm} + e^{\mp} + \nu$$
$${K^0}_{\mu 3} : K^0_L \rightarrow \pi^{\pm} + \mu^{\mp} + \nu$$

Assuming that only the vector current contributes to $K \rightarrow l\pi\nu$ decays, the matrix element can be described by using two dimensionless form factors, f_+ and f_-, which depend only on the momentum transfer $t = (P_K - P_\pi)^2$.
The Dalitz plot density used in this class is as follows [1]:

$$\rho\left(E_\pi, E_\mu\right) \propto f_+^2\left(t\right)[A + B\xi\left(t\right) + C\xi\left(t\right)^2]$$

where: $A = m_K(2E_\mu E_\nu - m_K E'_\pi) + {m_\mu}^2(\frac{1}{4}E'_\pi - E_\nu)$
$B = {m_\mu}^2(E_\nu - \frac{1}{2}E'_\pi)$
$C = \frac{1}{4}{m_\mu}^2 E'_\pi$
$E'_\pi = {E_\pi}^{max} - E_\pi$

Here $\xi(t)$ is the ratio of the two form factors

$$\xi(t) = f_-(t)/f_+(t).$$

$f_+(t)$ is assumed to depend linearly on t, i.e.

$$f_+(t) = f_+(0)[1 + \lambda_+(t/{m_\pi}^2)]$$

and $f_-(t)$ is assumed to be constant due to time reversal invariance.

Two parameters, λ_+ and $\xi(0)$ are then used for describing the Dalitz plot density in this class. The values of these parameters are taken to be the world average values given by the Particle Data Group [2].

4.3 Status of this document

05.07.12 updated muon decay section - D.H. Wright
10.04.02 re-written by D.H. Wright
02.04.02 editing by Hisaya Kurashige
14.11.01 editing by Hisaya Kurashige

Bibliography

[1] L.M. Chounet, J.M. Gaillard, and M.K. Gaillard, Phys. Reports 4C, 199 (1972).

[2] *Review of Particle Physics* The European Physical Journal C, 15 (2000).

Part III

Electromagnetic Interactions

Chapter 5

Gamma Incident

5.1 Introduction

All processes of gamma interaction with media in Geant4 are happen at the end of the step, so these interactions are *discrete* and corresponding processes are following $G4VDiscreteProcess$ interface.

5.1.1 General Interfaces

There are a number of similar functions for discrete electromagnetic processes and for electromagnetic (EM) packages an additional base classes were designed to provide common computations [1]. Common calculations for discrete EM processes are performed in the class $G4VEmProcess$. Derived classes (5.1) are concrete processes providing initialisation. The physics models are implemented using the $G4VEmModel$ interface. Each process may have one or many models defined to be active over a given energy range and set of $G4Regions$. Models are implementing computation of energy loss, cross section and sampling of final state. The list of EM processes and models for gamma incident is shown in Table 5.1.

5.1.2 Status of This Document

06.12.07 created by V. Ivanchenko
11.12.08 extended list of models by V. Ivanchenko
08.12.10 cleaned up by V. Ivanchenko
20.11.11 updated list of processes/models by V. Ivanchenko
29.11.13 updated list of processes/models by V. Ivanchenko

Bibliography

[1] J. Apostolakis et al., Geometry and physics of the Geant4 toolkit for high an dmedium energy applications. *Rad. Phys. Chem. 78 (2009) 859.*

Table 5.1: List of process and model classes for gamma.

EM process	EM model	Ref.
G4PhotoElectricEffect	G4PEEffectFluoModel	5.2
	G4LivermorePhotoElectricModel	9.7
	G4LivermorePolarizedPhotoElectricModel	
	G4PenelopePhotoElectricModel	10.1.5
G4PolarizedPhotoElectricEffect	G4PolarizedPEEffectModel	17.1
G4ComptonScattering	G4KleinNishinaCompton	5.3
	G4KleinNishinaModel	5.3
	G4LivermoreComptonModel	9.2
	G4LivermoreComptonModelRC	
	G4LivermorePolarizedComptonModel	9.3
	G4LowEPComptonModel	11.1
	G4PenelopeComptonModel	10.1.2
G4PolarizedCompton	G4PolarizedComptonModel	17.1
G4GammaConversion	G4BetheHeitlerModel	5.4
	G4PairProductionRelModel	
	G4LivermoreGammaConversionModel	9.5
	G4BoldyshevTripletModel	9.6
	G4LivermoreNuclearGammaConversionModel	
	G4LivermorePolarizedGammaConversionModel	
	G4PenelopeGammaConvertion	10.1.4
G4PolarizedGammaConversion	G4PolarizedGammaConversionModel	17.1
G4RayleighScattering	G4LivermoreRayleighModel	9.4
	G4LivermorePolarizedRayleighModel	
	G4PenelopeRayleighModel	10.1.3
G4GammaConversionToMuons		5.5

5.2 PhotoElectric effect

The photoelectric effect is the ejection of an electron from a material after a photon has been absorbed by that material. In the standard model *G4PEEffectFluoModel* it is simulated by using a parameterized photon absorption cross section to determine the mean free path, atomic shell data to determine the energy of the ejected electron, and the K-shell angular distribution to sample the direction of the electron.

5.2.1 Cross Section

The parameterization of the photoabsorption cross section proposed by Biggs et al. [1] was used :

$$\sigma(Z, E_\gamma) = \frac{a(Z, E_\gamma)}{E_\gamma} + \frac{b(Z, E_\gamma)}{E_\gamma^2} + \frac{c(Z, E_\gamma)}{E_\gamma^3} + \frac{d(Z, E_\gamma)}{E_\gamma^4} \tag{5.1}$$

Using the least-squares method, a separate fit of each of the coefficients a, b, c, d to the experimental data was performed in several energy intervals [2]. As a rule, the boundaries of these intervals were equal to the corresponding photoabsorption edges. The cross section (and correspondingly mean free path) are discontinuous and must be computed 'on the fly' from the formula 5.1.

5.2.2 Final State

Choosing an Element

The binding energies of the shells depend on the atomic number Z of the material. In compound materials the i^{th} element is chosen randomly according to the probability:

$$Prob(Z_i, E_\gamma) = \frac{n_{ati}\sigma(Z_i, E_\gamma)}{\sum_i [n_{ati} \cdot \sigma_i(E_\gamma)]}.$$

Shell

A quantum can be absorbed if $E_\gamma > B_{shell}$ where the shell energies are taken from `G4AtomicShells` data: the closest available atomic shell is chosen. The photoelectron is emitted with kinetic energy :

$$T_{photoelectron} = E_\gamma - B_{shell}(Z_i) \tag{5.2}$$

Theta Distribution of the Photoelectron

The polar angle of the photoelectron is sampled from the Sauter-Gavrila distribution (for K-shell) [3], which is correct only to zero order in αZ :

$$\frac{d\sigma}{d(\cos\theta)} \sim \frac{\sin^2\theta}{(1-\beta\cos\theta)^4}\left\{1+\frac{1}{2}\gamma(\gamma-1)(\gamma-2)(1-\beta\cos\theta)\right\} \tag{5.3}$$

where β and γ are the Lorentz factors of the photoelectron.
$\cos\theta$ is sampled from the probability density function :

$$f(\cos\theta) = \frac{1-\beta^2}{2\beta}\frac{1}{(1-\beta\cos\theta)^2} \quad \Longrightarrow \quad \cos\theta = \frac{(1-2r)+\beta}{(1-2r)\beta+1} \tag{5.4}$$

The rejection function is :

$$g(\cos\theta) = \frac{1-\cos^2\theta}{(1-\beta\cos\theta)^2}\left[1+b(1-\beta\cos\theta)\right] \tag{5.5}$$

with $b = \gamma(\gamma-1)(\gamma-2)/2$
It can be shown that $g(\cos\theta)$ is positive $\forall \cos\theta \in [-1,\ +1]$, and can be majored by :

$$\begin{aligned} gsup &= \gamma^2\ [1+b(1-\beta)] \text{ if } \gamma \in\ ]1,2] \\ &= \gamma^2\ [1+b(1+\beta)] \text{ if } \gamma > 2 \end{aligned} \tag{5.6}$$

The efficiency of this method is $\sim 50\%$ if $\gamma < 2$, $\sim 25\%$ if $\gamma \in [2,\ 3]$.

5.2.3 Relaxation

Atomic relaxations can be sampled using the de-excitation module of the low-energy sub-package 14.1. For that atomic de-excitation option should be activated. In the *physics_list* sub-library this activation is done automatically for *G4EmLivermorePhysics*, *G4EmPenelopePhysics*, *G4EmStandardPhysics_option3* and *G4EmStandardPhysics_option4*. For other standard physics constructors the de-excitation module is already added but is disabled. The simulation of fluorescence and Auger electron emmision may be enabled for all geometry via UI commands:

/process/em/fluo true
/process/em/auger true

There is a possiblity to enable atomic deexcitation only for *G4Region* by

its name:

/process/em/deexcitation myregion true true false

where three boolean arguments enable/disable fluorescence, Auger electron production and PIXE (deexcitation induced by ionisation).

5.2.4 Status of this document

09.10.98 created by M. Maire
08.01.02 updated by M. Maire
22.04.02 re-worded by D.H. Wright
02.05.02 modifs in total cross section and final state (M. Maire)
15.11.02 introduction added by D.H. Wright
08.12.10 revision by V. Ivanchenko
20.11.11 revision by V. Ivanchenko
20.12.12 revision by V. Ivanchenko

Bibliography

[1] Biggs F., and Lighthill R., Preprint Sandia Laboratory, SAND 87-0070 (1990)

[2] Grichine V.M., Kostin A.P., Kotelnikov S.K. et al., Bulletin of the Lebedev Institute no. 2-3, 34 (1994).

[3] Gavrila M. Phys.Rev. 113, 514 (1959).

5.3 Compton scattering

The Compton scattering is an inelastic gamma scattering on atom with the ejection of an electron. In the standard sub-package two model *G4KleinNishinaCompton* and *G4KleinNishinaModel* are available. The first model is the fastest, in the second model atomic shell effects are taken into account.

5.3.1 Cross Section

When simulating the Compton scattering of a photon from an atomic electron, an empirical cross section formula is used, which reproduces the cross section data down to 10 keV:

$$\sigma(Z, E_\gamma) = \left[P_1(Z)\ \frac{\log(1+2X)}{X} + \frac{P_2(Z) + P_3(Z)X + P_4(Z)X^2}{1 + aX + bX^2 + cX^3} \right]. \quad (5.7)$$

$$\begin{aligned} Z &= \text{atomic number of the medium} \\ E_\gamma &= \text{energy of the photon} \\ X &= E_\gamma / mc^2 \\ m &= \text{electron mass} \\ P_i(Z) &= Z(d_i + e_i Z + f_i Z^2). \end{aligned}$$

The values of the parameters can be found within the method which computes the cross section per atom. A fit of the parameters was made to over 511 data points [1, 2] chosen from the intervals

$$1 \le Z \le 100$$

$$E_\gamma \in [10\ \text{keV}, 100\ \text{GeV}].$$

The accuracy of the fit was estimated to be

$$\frac{\Delta\sigma}{\sigma} = \begin{cases} \approx 10\% & \text{for } E_\gamma \simeq 10\ \text{keV} - 20\ \text{keV} \\ \le 5 - 6\% & \text{for } E_\gamma > 20\ \text{keV} \end{cases}$$

5.3.2 Sampling the Final State

The Klein-Nishina differential cross section per atom is [3]:

$$\frac{d\sigma}{d\epsilon} = \pi r_e^2\ \frac{m_e c^2}{E_0}\ Z \left[\frac{1}{\epsilon} + \epsilon \right] \left[1 - \frac{\epsilon \sin^2\theta}{1+\epsilon^2} \right] \quad (5.8)$$

where r_e = classical electron radius
$m_e c^2$ = electron mass
E_0 = energy of the incident photon
E_1 = energy of the scattered photon
ϵ = E_1/E_0 .

Assuming an elastic collision, the scattering angle θ is defined by the Compton formula:

$$E_1 = E_0 \, \frac{m_e c^2}{m_e c^2 + E_0(1 - \cos\theta)}. \tag{5.9}$$

Sampling the Photon Energy

The value of ϵ corresponding to the minimum photon energy (backward scattering) is given by

$$\epsilon_0 = \frac{m_e c^2}{m_e c^2 + 2E_0}, \tag{5.10}$$

hence $\epsilon \in [\epsilon_0, 1]$. Using the combined composition and rejection Monte Carlo methods described in [4, 5, 6] one may set

$$\Phi(\epsilon) \simeq \left[\frac{1}{\epsilon} + \epsilon\right]\left[1 - \frac{\epsilon \sin^2\theta}{1+\epsilon^2}\right] = f(\epsilon)\cdot g(\epsilon) = [\alpha_1 f_1(\epsilon) + \alpha_2 f_2(\epsilon)]\cdot g(\epsilon), \tag{5.11}$$

$$\begin{array}{lll} \alpha_1 = \ln(1/\epsilon_0) & ; & f_1(\epsilon) = 1/(\alpha_1 \epsilon) \\ \alpha_2 = (1-\epsilon_0^2)/2 & ; & f_2(\epsilon) = \epsilon/\alpha_2. \end{array}$$

f_1 and f_2 are probability density functions defined on the interval $[\epsilon_0, 1]$, and

$$g(\epsilon) = \left[1 - \frac{\epsilon}{1+\epsilon^2}\sin^2\theta\right]$$

is the rejection function $\forall \epsilon \in [\epsilon_0, 1] \Longrightarrow 0 < g(\epsilon) \leq 1$. Given a set of 3 random numbers r, r', r'' uniformly distributed on the interval [0,1], the sampling procedure for ϵ is the following:

1. decide whether to sample from $f_1(\epsilon)$ or $f_2(\epsilon)$:
   if $r < \alpha_1/(\alpha_1 + \alpha_2)$ select $f_1(\epsilon)$, otherwise select $f_2(\epsilon)$

2. sample ϵ from the distributions corresponding to f_1 or f_2:
   for $f_1 : \epsilon = \epsilon_0^{r'} \qquad (\equiv \exp(-r'\alpha_1))$
   for $f_2 : \epsilon^2 = \epsilon_0^2 + (1-\epsilon_0^2)r'$

3. calculate $\sin^2\theta = t(2-t)$ where $t \equiv (1 - \cos\theta) = m_e c^2(1-\epsilon)/(E_0\epsilon)$

4. test the rejection function:
   if $g(\epsilon) \geq r''$ accept ϵ, otherwise go to step 1.

Compute the Final State Kinematics

After the successful sampling of ϵ, the polar angles of the scattered photon with respect to the direction of the parent photon are generated. The azimuthal angle, ϕ, is generated isotropically and θ is as defined in the previous section. The momentum vector of the scattered photon, $\overrightarrow{P_{\gamma 1}}$, is then transformed into the `World` coordinate system. The kinetic energy and momentum of the recoil electron are then

$$\begin{aligned} T_{el} &= E_0 - E_1 \\ \overrightarrow{P_{el}} &= \overrightarrow{P_{\gamma 0}} - \overrightarrow{P_{\gamma 1}}. \end{aligned}$$

Doppler broading of final electron momentum due to electron motion is implemented only in *G4KleinNishinaModel*. For that emphirical electron density profile function is used.

5.3.3 Atomic shell effects

The differential cross-section described above is valid only for those collisions in which the energy of the recoil electron is large compared to its binding energy (which is ignored). In the alternative model (*G4KleinNishinaModel*) atomic shell effects are taken into account. For that a sampling of a shell is performed with the weight proportional to number of shell electrons. Electron energy distribution function is approximated via simplified form

$$F(T) = \exp\left(-T/E_b\right)/E_b, \tag{5.12}$$

where E_b is shell bound energy, T - kinetic energy of the electron.

The value T is sampled and scattering is sampled in the rest frame of the electron according the algorithm described in the previous sub-chapter. After sampling an inverse Lorentz transformation to the laboratory frame is performed. Potential energy $(E_b + T)$ is subtracted from the scattered electron kinetic energy. If final electron energy become negative then sampling is repeated. Atomic relaxation are sampled if deexcitation module is enabled. Enabling of atomic relaxation for Compton scattering is performed in the same way as for photoelectric effect 5.2.3.

5.3.4 Status of This Document

09.10.98 created by M. Maire
14.01.02 minor revision by M. Maire
22.04.02 reworded by D.H. Wright

18.03.04 include references for total cross section (M. Maire)
10.12.10 revised by V. Ivanchenko
20.11.12 revised by V. Ivanchenko
29.11.13 revised by V. Ivanchenko

Bibliography

[1] Hubbell, Gimm and Overbo. *J. Phys. Chem. Ref. Data 9 (1980) 1023.*

[2] H. Storm and H.I. Israel *Nucl. Data Tables A7 (1970) 565.*

[3] O. Klein and Y. Nishina. *Z. Physik 52 (1929) 853.*

[4] J.C. Butcher and H. Messel. *Nucl. Phys. 20 (1960) 15.*

[5] H. Messel and D. Crawford. *Electron-Photon shower distribution, Pergamon Press* (1970)

[6] R. Ford and W. Nelson. *SLAC-265, UC-32 (1985).*

[7] B. Rossi. *High energy particles, Prentice-Hall* 77-79 (1952)

5.4 Gamma Conversion into e^+e^- Pair

In the standard sub-package two models are available. The first model is implemented in the class *G4BetheHeitlerModel*, it is derived from Geant3 and is applicable below $100GeV$. In the second (*G4PairProductionRelModel*) Landau-Pomenrachuk-Migdal (LPM) effect is taken into account and this model can be applied for very high energy gammas.

5.4.1 Cross Section

The total cross-section per atom for the conversion of a gamma into an (e^+, e^-) pair has been parameterized as

$$\sigma(Z, E_\gamma) = Z(Z+1)\ \left[F_1(X) + F_2(X)\ Z + \frac{F_3(X)}{Z}\right], \tag{5.13}$$

where E_γ is the incident gamma energy and $X = \ln(E_\gamma/m_e c^2)$. The functions F_n are given by

$$\begin{aligned} F_1(X) &= a_0 + a_1 X + a_2 X^2 + a_3 X^3 + a_4 X^4 + a_5 X^5 \\ F_2(X) &= b_0 + b_1 X + b_2 X^2 + b_3 X^3 + b_4 X^4 + b_5 X^5 \\ F_3(X) &= c_0 + c_1 X + c_2 X^2 + c_3 X^3 + c_4 X^4 + c_5 X^5, \end{aligned} \tag{5.14}$$

with the parameters a_i, b_i, c_i taken from a least-squares fit to the data [1]. Their values can be found in the function which computes formula 5.13. This parameterization describes the data in the range

$$1 \leq Z \leq 100$$

and

$$E_\gamma \in [1.5\ \text{MeV}, 100\ \text{GeV}].$$

The accuracy of the fit was estimated to be $\frac{\Delta\ \sigma}{\sigma} \leq 5\%$ with a mean value of $\approx 2.2\%$. Above 100 GeV the cross section is constant. Below $E_{low} = 1.5$ MeV the extrapolation

$$\sigma(E) = \sigma(E_{low}) \cdot \left(\frac{E - 2m_e c^2}{E_{low} - 2m_e c^2}\right)^2 \tag{5.15}$$

is used.

In a given material the mean free path, λ, for a photon to convert into an (e^+, e^-) pair is

$$\lambda(E_\gamma) = \left(\sum_i n_{ati} \cdot \sigma(Z_i, E_\gamma) \right)^{-1} \tag{5.16}$$

where n_{ati} is the number of atoms per volume of the i^{th} element of the material.

Corrected Bethe-Heitler Cross Section

As written in [2], the Bethe-Heitler formula corrected for various effects is

$$\begin{aligned} \frac{d\sigma(Z,\epsilon)}{d\epsilon} &= \alpha r_e^2 Z[Z + \xi(Z)] \left\{ [\epsilon^2 + (1-\epsilon)^2] \left[\Phi_1(\delta(\epsilon)) - \frac{F(Z)}{2} \right] \right. \\ &\left. + \frac{2}{3}\epsilon(1-\epsilon) \left[\Phi_2(\delta(\epsilon)) - \frac{F(Z)}{2} \right] \right\} \end{aligned} \tag{5.17}$$

where α is the fine-structure constant and r_e the classical electron radius. Here $\epsilon = E/E_\gamma$, E_γ is the energy of the photon and E is the total energy carried by one particle of the (e^+, e^-) pair. The kinematical limits of ϵ are therefore

$$\frac{m_e c^2}{E_\gamma} = \epsilon_0 \leq \epsilon \leq 1 - \epsilon_0. \tag{5.18}$$

Screening Effect The *screening variable*, δ, is a function of ϵ

$$\delta(\epsilon) = \frac{136}{Z^{1/3}} \frac{\epsilon_0}{\epsilon(1-\epsilon)}, \tag{5.19}$$

and measures the 'impact parameter' of the projectile. Two screening functions are introduced in the Bethe-Heitler formula :

$$\begin{aligned} \text{for } \delta \leq 1 \quad \Phi_1(\delta) &= 20.867 - 3.242\delta + 0.625\delta^2 \\ \Phi_2(\delta) &= 20.209 - 1.930\delta - 0.086\delta^2 \\ \text{for } \delta > 1 \quad \Phi_1(\delta) &= \Phi_2(\delta) = 21.12 - 4.184\ln(\delta + 0.952). \end{aligned} \tag{5.20}$$

Because the formula 5.17 is symmetric under the exchange $\epsilon \leftrightarrow (1-\epsilon)$, the range of ϵ can be restricted to

$$\epsilon \in [\epsilon_0, 1/2]. \tag{5.21}$$

Born Approximation The Bethe-Heitler formula is calculated with plane waves, but Coulomb waves should be used instead. To correct for this, a *Coulomb correction function* is introduced in the Bethe-Heitler formula :

$$\begin{aligned} \text{for } E_\gamma &< 50 \text{ MeV}: \quad F(z) = 8/3 \ln Z \\ \text{for } E_\gamma &\geq 50 \text{ MeV}: \quad F(z) = 8/3 \ln Z + 8 f_c(Z) \end{aligned} \tag{5.22}$$

with

$$\begin{aligned} f_c(Z) &= (\alpha Z)^2 \left[\frac{1}{1+(\alpha Z)^2} \right. \\ &\left. +0.20206 - 0.0369(\alpha Z)^2 + 0.0083(\alpha Z)^4 - 0.0020(\alpha Z)^6 + \cdots \right]. \end{aligned} \tag{5.23}$$

It should be mentioned that, after these additions, the cross section becomes negative if

$$\delta > \delta_{max}(\epsilon_1) = \exp\left[\frac{42.24 - F(Z)}{8.368} \right] - 0.952. \tag{5.24}$$

This gives an additional constraint on ϵ :

$$\delta \leq \delta_{max} \Longrightarrow \epsilon \geq \epsilon_1 = \frac{1}{2} - \frac{1}{2}\sqrt{1 - \frac{\delta_{min}}{\delta_{max}}} \tag{5.25}$$

where

$$\delta_{min} = \delta\left(\epsilon = \frac{1}{2}\right) = \frac{136}{Z^{1/3}}\ 4\epsilon_0 \tag{5.26}$$

has been introduced. Finally the range of ϵ becomes

$$\epsilon \in [\epsilon_{min} = \max(\epsilon_0, \epsilon_1),\ 1/2]. \tag{5.27}$$

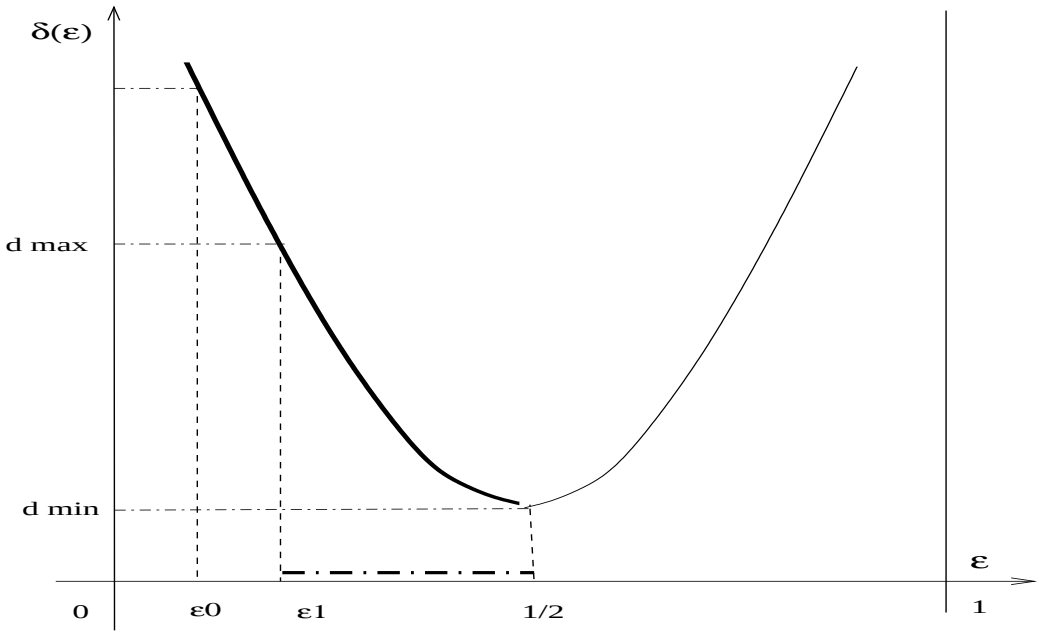

Gamma Conversion in the Electron Field The electron cloud gives an additional contribution to pair creation, proportional to Z (instead of Z^2). This is taken into account through the expression

$$\xi(Z) = \frac{\ln(1440/Z^{2/3})}{\ln(183/Z^{1/3}) - f_c(Z)}. \tag{5.28}$$

Factorization of the Cross Section ϵ is sampled using the techniques of 'composition+rejection', as treated in [3, 4, 5]. First, two auxiliary screening functions should be introduced:

$$\begin{aligned} F_1(\delta) &= 3\Phi_1(\delta) - \Phi_2(\delta) - F(Z) \\ F_2(\delta) &= \frac{3}{2}\Phi_1(\delta) - \frac{1}{2}\Phi_2(\delta) - F(Z) \end{aligned} \tag{5.29}$$

It can be seen that $F_1(\delta)$ and $F_2(\delta)$ are decreasing functions of δ, $\forall\delta \in [\delta_{min}, \delta_{max}]$. They reach their maximum for $\delta_{min} = \delta(\epsilon = 1/2)$:

$$\begin{aligned} F_{10} &= \max F_1(\delta) = F_1(\delta_{min}) \\ F_{20} &= \max F_2(\delta) = F_2(\delta_{min}). \end{aligned} \tag{5.30}$$

After some algebraic manipulations the formula 5.17 can be written :

$$\begin{aligned} \frac{d\sigma(Z,\epsilon)}{d\epsilon} &= \alpha r_e^2 Z[Z + \xi(Z)]\frac{2}{9}\left[\frac{1}{2} - \epsilon_{min}\right] \\ &\quad \times \left[N_1\ f_1(\epsilon)\ g_1(\epsilon) + N_2\ f_2(\epsilon)\ g_2(\epsilon)\right], \end{aligned} \tag{5.31}$$

where

$$N_1 = \left[\frac{1}{2} - \epsilon_{min}\right]^2 F_{10} \qquad f_1(\epsilon) = \frac{3}{\left[\frac{1}{2}-\epsilon_{min}\right]^3}\left[\frac{1}{2} - \epsilon\right]^2 \qquad g_1(\epsilon) = \frac{F_1(\epsilon)}{F_{10}}$$

$$N_2 = \frac{3}{2}F_{20} \qquad f_2(\epsilon) = \text{const} = \frac{1}{\left[\frac{1}{2}-\epsilon_{min}\right]} \qquad g_2(\epsilon) = \frac{F_2(\epsilon)}{F_{20}}.$$

$f_1(\epsilon)$ and $f_2(\epsilon)$ are probability density functions on the interval $\epsilon \in [\epsilon_{min}, 1/2]$ such that

$$\int_{\epsilon_{min}}^{1/2} f_i(\epsilon)\, d\epsilon = 1$$

, and $g_1(\epsilon)$ and $g_2(\epsilon)$ are valid rejection functions: $0 < g_i(\epsilon) \leq 1$.

5.4.2 Final State

The differential cross section depends on the atomic number Z of the material in which the interaction occurs. In a compound material the element i in which the interaction occurs is chosen randomly according to the probability

$$Prob(Z_i, E_\gamma) = \frac{n_{ati}\sigma(Z_i, E_\gamma)}{\sum_i [n_{ati} \cdot \sigma_i(E_\gamma)]}. \tag{5.32}$$

Sampling the Energy Given a triplet of uniformly distributed random numbers (r_a, r_b, r_c) :

1. use r_a to choose which decomposition term in 5.31 to use:

$$\text{if } r_a < N_1/(N_1 + N_2) \rightarrow f_1(\epsilon)\ g_1(\epsilon) \text{ otherwise } \rightarrow f_2(\epsilon)\ g_2(\epsilon) \tag{5.33}$$

2. sample ϵ from $f_1(\epsilon)$ or $f_2(\epsilon)$ with r_b :

$$\epsilon = \frac{1}{2} - \left(\frac{1}{2} - \epsilon_{min}\right) r_b^{1/3} \quad \text{or} \quad \epsilon = \epsilon_{min} + \left(\frac{1}{2} - \epsilon_{min}\right) r_b \tag{5.34}$$

3. reject ϵ if $g_1(\epsilon)$or $g_2(\epsilon) < r_c$

NOTE : below $E_\gamma = 2$ MeV it is enough to sample ϵ uniformly on $[\epsilon_0,\ 1/2]$, without rejection.

Charge The charge of each particle of the pair is fixed randomly.

Polar Angle of the Electron or Positron

The polar angle of the electron (or positron) is defined with respect to the direction of the parent photon. The energy-angle distribution given by Tsai [6] is quite complicated to sample and can be approximated by a density function suggested by Urban [7] :

$$\forall u \in [0,\ \infty[\quad f(u) = \frac{9a^2}{9+d}\left[u\exp(-au) + d\ u\exp(-3au)\right] \tag{5.35}$$

with

$$a = \frac{5}{8} \quad d = 27 \qquad \text{and } \theta_{\pm} = \frac{mc^2}{E_{\pm}}\ u. \tag{5.36}$$

A sampling of the distribution 5.35 requires a triplet of random numbers such that

$$\text{if } r_1 < \frac{9}{9+d} \rightarrow u = \frac{-\ln(r_2 r_3)}{a} \quad \text{otherwise } u = \frac{-\ln(r_2 r_3)}{3a}. \tag{5.37}$$

The azimuthal angle ϕ is generated isotropically. The e^+ and e^- momenta are assumed to be coplanar with the parent photon. This information, together with energy conservation, is used to calculate the momentum vectors of the (e^+, e^-) pair and to rotate them to the global reference system.

5.4.3 Ultra-Relativistic Model

It is implemented in the class *G4PairProductionRelModel* and is configured above $80GeV$ in all reference Physics lists. The cross section is computed using direct integration of differential cross section [6] and not its parameterisation described in 5.4.1. LPM effect is taken into account in the same way as for bremsstrahlung 8.2.2. Secondary generation algorithm is the same as in the standard Bethe-Haitler model.

5.4.4 Status of This Document

12.01.02 created by M.Maire.
21.03.02 corrections in angular distribution (mma)
22.04.02 re-worded by D.H. Wright
10.12.10 revision by V. Ivanchenko
20.11.12 revision by V. Ivanchenko

Bibliography

[1] J.H.Hubbell, H.A.Gimm, I.Overbo *Jou. Phys. Chem. Ref. Data 9:1023* (1980)

[2] W. Heitler *The Quantum Theory of Radiation, Oxford University Press* (1957)

[3] R. Ford and W. Nelson. *SLAC-210, UC-32* (1978)

[4] J.C. Butcher and H. Messel. *Nucl. Phys. 20* 15 (1960)

[5] H. Messel and D. Crawford. *Electron-Photon shower distribution, Pergamon Press* (1970)

[6] Y. S. Tsai, *Rev. Mod. Phys. 46* 815 (1974), Y. S. Tsai, *Rev. Mod. Phys. 49* 421 (1977)

[7] L.Urban in GEANT3 writeup, section PHYS-211. *Cern Program Library* (1993)

5.5 Gamma Conversion into $\mu^+\mu^-$ Pair

The class *G4GammaConversionToMuons* simulates the process of gamma conversion into muon pairs. Given the photon energy and Z and A of the material in which the photon converts, the probability for the conversions to take place is calculated according to a parameterized total cross section. Next, the sharing of the photon energy between the μ^+ and μ^- is determined. Finally, the directions of the muons are generated. Details of the implementation are given below and can be also found in [1].

5.5.1 Cross Section and Energy Sharing

In the field of the nucleus, muon pair production on atomic electrons, $\gamma + e \to e + \mu^+ + \mu^-$, has a threshold of $2m_\mu(m_\mu + m_e)/m_e \approx 43.9$ GeV . Up to several hundred GeV this process has a much lower cross section than the corresponding process on the nucleus. At higher energies, the cross section on atomic electrons represents a correction of $\sim 1/Z$ to the total cross section.

For the approximately elastic scattering considered here, momentum, but no energy, is transferred to the nucleon. The photon energy is fully shared by the two muons according to

$$E_\gamma = E_\mu^+ + E_\mu^- \tag{5.38}$$

or in terms of energy fractions

$$x_+ = \frac{E_\mu^+}{E_\gamma}, \qquad x_- = \frac{E_\mu^-}{E_\gamma}, \qquad x_+ + x_- = 1 \; .$$

The differential cross section for electromagnetic pair creation of muons in terms of the energy fractions of the muons is

$$\frac{d\sigma}{dx_+} = 4\,\alpha\,Z^2\,r_c^2\left(1 - \frac{4}{3}\,x_+x_-\right)\log(W)\;, \tag{5.39}$$

where Z is the charge of the nucleus, r_c is the classical radius of the particles which are pair produced (here muons) and

$$W = W_\infty\,\frac{1 + (D_n\sqrt{e} - 2)\,\delta\,/m_\mu}{1 + B\,Z^{-1/3}\,\sqrt{e}\,\delta\,/m_e} \tag{5.40}$$

where

$$W_\infty = \frac{B\,Z^{-1/3}}{D_n}\,\frac{m_\mu}{m_e} \qquad \delta = \frac{m_\mu^2}{2\,E_\gamma\,x_+x_-} \qquad \sqrt{e} = 1.6487\ldots.$$

$$\begin{aligned} \text{For hydrogen} \qquad & B = 202.4 \qquad D_n = \quad 1.49 \\ \text{and for all other nuclei} \qquad & B = 183 \qquad D_n = \quad 1.54\, A^{0.27}. \end{aligned} \tag{5.41}$$

These formulae are obtained from the differential cross section for muon bremsstrahlung [2] by means of crossing relations. The formulae take into account the screening of the field of the nucleus by the atomic electrons in the Thomas-Fermi model, as well as the finite size of the nucleus, which is essential for the problem under consideration. The above parameterization gives good results for $E_\gamma \gg m_\mu$. The fact that it is approximate close to threshold is of little practical importance. Close to threshold, the cross section is small and the few low energy muons produced will not travel very far. The cross section calculated from Eq. (5.39) is positive for $E_\gamma > 4m_\mu$ and

$$x_{\min} \le x \le x_{\max} \quad \text{with} \quad x_{\min} = \frac{1}{2} - \sqrt{\frac{1}{4} - \frac{m_\mu}{E_\gamma}} \qquad x_{\max} = \frac{1}{2} + \sqrt{\frac{1}{4} - \frac{m_\mu}{E_\gamma}}\,, \tag{5.42}$$

except for very asymmetric pair-production, close to threshold, which can easily be taken care of by explicitly setting $\sigma = 0$ whenever $\sigma < 0$.

Note that the differential cross section is symmetric in x_+ and x_- and that

$$x_+ x_- = x - x^2$$

where x stands for either x_+ or x_-. By defining a constant

$$\sigma_0 = 4\,\alpha\, Z^2\, r_c^2 \log(W_\infty) \tag{5.43}$$

the differential cross section Eq. (5.39) can be rewritten as a normalized and symmetric as function of x:

$$\frac{1}{\sigma_0}\,\frac{d\sigma}{dx} = \left[1 - \frac{4}{3}\,(x - x^2)\right]\,\frac{\log W}{\log W_\infty}\,. \tag{5.44}$$

This is shown in Fig. 5.1 for several elements and a wide range of photon energies. The asymptotic differential cross section for $E_\gamma \to \infty$

$$\frac{1}{\sigma_0}\,\frac{d\sigma_\infty}{dx} = 1 - \frac{4}{3}\,(x - x^2)$$

is also shown.

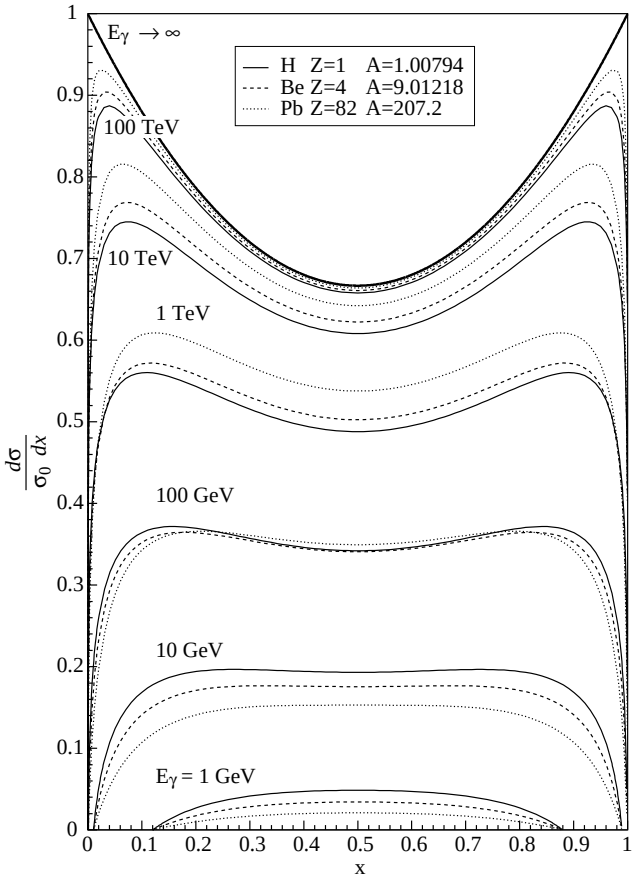

Figure 5.1: Normalized differential cross section for pair production as a function of x, the energy fraction of the photon energy carried by one of the leptons in the pair. The function is shown for three different elements, hydrogen, beryllium and lead, and for a wide range of photon energies.

5.5.2 Parameterization of the Total Cross Section

The total cross section is obtained by integration of the differential cross section Eq. (5.39), that is

$$\sigma_{\rm tot}(E_\gamma) = \int_{x_{\rm min}}^{x_{\rm max}} \frac{d\sigma}{dx_+}\, dx_+ = 4\,\alpha\, Z^2\, r_c^2 \int_{x_{\rm min}}^{x_{\rm max}} \left(1 - \frac{4}{3}\, x_+ x_-\right) \log(W)\, dx_+ \,. \tag{5.45}$$

W is a function of (x_+, E_γ) and (Z, A) of the element (see Eq. (5.40)). Numerical values of W are given in Table 5.2.

Table 5.2: Numerical values of W for $x_+ = 0.5$ for different elements.

E_γ GeV	W for H	W for Be	W for Cu	W for Pb
1	2.11	1.594	1.3505	5.212
10	19.4	10.85	6.803	43.53
100	191.5	102.3	60.10	332.7
1000	1803	919.3	493.3	1476.1
10000	11427	4671	1824	1028.1
∞	28087	8549	2607	1339.8

Values of the total cross section obtained by numerical integration are listed in Table 5.3 for four different elements. Units are in μbarn , where $1\,\mu\text{barn} = 10^{-34}\,\text{m}^2$.

Table 5.3: Numerical values for the total cross section

E_γ GeV	$\sigma_{\rm tot}$, H μbarn	$\sigma_{\rm tot}$, Be μbarn	$\sigma_{\rm tot}$, Cu μbarn	$\sigma_{\rm tot}$, Pb μbarn
1	0.01559	0.1515	5.047	30.22
10	0.09720	1.209	49.56	334.6
100	0.1921	2.660	121.7	886.4
1000	0.2873	4.155	197.6	1476
10000	0.3715	5.392	253.7	1880
∞	0.4319	6.108	279.0	2042

Well above threshold, the total cross section rises about linearly in $\log(E_\gamma)$ with the slope

$$W_M = \frac{1}{4\, D_n \sqrt{e}\, m_\mu} \tag{5.46}$$

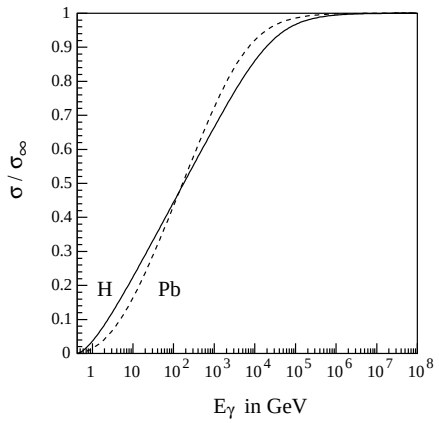

Figure 5.2: Total cross section for the Bethe-Heitler process $\gamma \to \mu^+\mu^-$ as a function of the photon energy E_γ in hydrogen and lead, normalized to the asymptotic cross section σ_∞.

until it saturates due to screening at σ_∞. Fig. 5.2 shows the normalized cross section where

$$\sigma_\infty = \frac{7}{9}\,\sigma_0 \qquad \text{and} \qquad \sigma_0 = 4\,\alpha\,Z^2\,r_c^2\,\log(W_\infty)\;. \tag{5.47}$$

Numerical values of W_M are listed in Table 5.4.

Table 5.4: Numerical values of W_M.

Element	W_M 1/GeV
H	0.963169
Be	0.514712
Cu	0.303763
Pb	0.220771

The total cross section can be parameterized as

$$\sigma_{\text{par}} = \frac{28\,\alpha\,Z^2\,r_c^2}{9}\;\log(1 + W_M C_f E_g)\;, \tag{5.48}$$

with

$$E_g = \left(1 - \frac{4m_\mu}{E_\gamma}\right)^t \left(W_{\text{sat}}^s + E_\gamma^s\right)^{1/s}\;. \tag{5.49}$$

and

$$W_{\text{sat}} = \frac{W_\infty}{W_M} = B\,Z^{-1/3}\,\frac{4\sqrt{e}\,m_\mu^2}{m_e}\;.$$

The threshold behavior in the cross section was found to be well approximated by $t = 1.479 + 0.00799 D_n$ and the saturation by $s = -0.88$. The agreement at lower energies is improved using an empirical correction factor, applied to the slope W_M, of the form

$$C_f = \left[1 + 0.04 \log\left(1 + \frac{E_c}{E_\gamma}\right)\right] \ ,$$

where

$$E_c = \left[-18. + \frac{4347.}{B\, Z^{-1/3}}\right] \text{ GeV} \ .$$

A comparison of the parameterized cross section with the numerical integration of the exact cross section shows that the accuracy of the parametrization is better than 2%, as seen in Fig. 5.3.

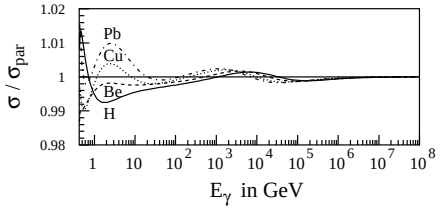

Figure 5.3: Ratio of numerically integrated and parametrized total cross sections as a function of E_γ for hydrogen, beryllium, copper and lead.

5.5.3 Multi-differential Cross Section and Angular Variables

The angular distributions are based on the multi-differential cross section for lepton pair production in the field of the Coulomb center

$$\frac{d\sigma}{dx_+\, du_+\, du_-\, d\varphi} = \frac{4\, Z^2 \alpha^3}{\pi}\, \frac{m_\mu^2}{q^4}\, u_+\, u_-$$

$$\left\{ \frac{u_+^2 + u_-^2}{(1+u_+^2)\,(1+u_-^2)} - 2x_+x_- \right.$$

$$\left[\frac{u_+^2}{(1+u_+^2)^2} + \frac{u_-^2}{(1+u_-^2)^2}\right] - \left. \frac{2u_+u_-(1-2x_+x_-)\,\cos\varphi}{(1+u_+^2)\,(1+u_-^2)} \right\} \ . \qquad (5.50)$$

Here

$$u_\pm = \gamma_\pm \theta_\pm \quad , \qquad \gamma_\pm = \frac{E_\mu^\pm}{m_\mu} \quad , \qquad q^2 = q_\parallel^2 + q_\perp^2 \quad , \qquad (5.51)$$

where

$$q_\parallel^2 = q_{\min}^2\,(1 + x_- u_+^2 + x_+ u_-^2)^2\,,$$
$$q_\perp^2 = m_\mu^2\left[(u_+ - u_-)^2 + 2\,u_+ u_-(1-\cos\varphi)\right]\,. \tag{5.52}$$

q^2 is the square of the momentum $\mathbf{q}$ transferred to the target and $q_\parallel^2$ and $q_\perp^2$ are the squares of the components of the vector $\mathbf{q}$, which are parallel and perpendicular to the initial photon momentum, respectively. The minimum momentum transfer is $q_{\min} = m_\mu^2/(2E_\gamma\, x_+ x_-)$.

The muon vectors have the components

$$\begin{aligned}\mathbf{p}_+ &= p_+\,(\ \ \sin\theta_+\cos(\varphi_0+\varphi/2)\,,\quad \sin\theta_+\sin(\varphi_0+\varphi/2)\,,\cos\theta_+)\,,\\ \mathbf{p}_- &= p_-\,(-\sin\theta_-\cos(\varphi_0-\varphi/2)\,,-\sin\theta_-\sin(\varphi_0-\varphi/2)\,,\cos\theta_-)\,,\end{aligned} \tag{5.53}$$

where $p_\pm = \sqrt{E_\pm^2 - m_\mu^2}$. The initial photon direction is taken as the z-axis. The cross section of Eq. (5.50) does not depend on φ_0. Because of azimuthal symmetry, φ_0 can simply be sampled at random in the interval $(0,\,2\,\pi)$.

Eq. (5.50) is too complicated for efficient Monte Carlo generation. To simplify, the cross section is rewritten to be symmetric in u_+, u_- using a new variable u and small parameters ξ, β, where $u_\pm = u \pm \xi/2$ and $\beta = u\,\varphi$. When higher powers in small parameters are dropped, the differential cross section in terms of u, ξ, β becomes

$$\begin{aligned}\frac{d\sigma}{dx_+\,d\xi\,d\beta\,u du} &= \frac{4\,Z^2\alpha^3}{\pi}\,\frac{m_\mu^2}{\left(q_\parallel^2 + m_\mu^2(\xi^2+\beta^2)\right)^2}\\ &\quad\left\{\xi^2\left[\frac{1}{(1+u^2)^2} - 2\,x_+x_-\,\frac{(1-u^2)^2}{(1+u^2)^4}\right] + \frac{\beta^2(1-2x_+x_-)}{(1+u^2)^2}\right\}\,,\end{aligned} \tag{5.54}$$

where, in this approximation,

$$q_\parallel^2 = q_{\min}^2\,(1+u^2)^2\,.$$

For Monte Carlo generation, it is convenient to replace (ξ, β) by the polar coordinates (ρ, ψ) with $\xi = \rho\cos\psi$ and $\beta = \rho\sin\psi$. Integrating Eq. 5.54 over ψ and using symbolically du^2 where $du^2 = 2u\,du$ yields

$$\frac{d\sigma}{dx_+\,d\rho\,du^2} = \frac{4Z^2\alpha^3}{m_\mu^2}\,\frac{\rho^3}{(q_\parallel^2/m_\mu^2+\rho^2)^2}\,\left\{\frac{1-x_+x_-}{(1+u^2)^2} - \frac{x_+x_-(1-u^2)^2}{(1+u^2)^4}\right\}. \tag{5.55}$$

Integration with logarithmic accuracy over ρ gives

$$\int \frac{\rho^3\, d\rho}{(q_\parallel^2/m_\mu^2+\rho^2)^2} \approx \int\limits_{q_\parallel/m_\mu}^{1} \frac{d\rho}{\rho} = \log\left(\frac{m_\mu}{q_\parallel}\right) . \tag{5.56}$$

Within the logarithmic accuracy, $\log(m_\mu/q_\parallel)$ can be replaced by $\log(m_\mu/q_{\min})$, so that

$$\frac{d\sigma}{dx_+\, du^2} = \frac{4\, Z^2\alpha^3}{m_\mu^2} \left\{ \frac{1-x_+x_-}{(1+u^2)^2} - \frac{x_+x_-(1-u^2)^2}{(1+u^2)^4} \right\} \log\left(\frac{m_\mu}{q_{\min}}\right) . \tag{5.57}$$

Making the substitution $u^2 = 1/t - 1$, $du^2 = -dt\,/t^2$ gives

$$\frac{d\sigma}{dx_+\, dt} = \frac{4\, Z^2\alpha^3}{m_\mu^2} \left[1 - 2\, x_+x_- + 4\, x_+x_-t\,(1-t)\right] \log\left(\frac{m_\mu}{q_{\min}}\right). \tag{5.58}$$

Atomic screening and the finite nuclear radius may be taken into account by multiplying the differential cross section determined by Eq. (5.55) with the factor

$$\left(F_a(q) - F_n(q)\right)^2 , \tag{5.59}$$

where F_a and F_n are atomic and nuclear form factors. Please note that after integrating Eq. 5.55 over ρ, the q-dependence is lost.

5.5.4 Procedure for the Generation of $\mu^+\mu^-$ Pairs

Given the photon energy E_γ and Z and A of the material in which the γ converts, the probability for the conversions to take place is calculated according to the parametrized total cross section Eq. (5.48). The next step, determining how the photon energy is shared between the μ^+ and μ^-, is done by generating x_+ according to Eq. (5.39). The directions of the muons are then generated via the auxilliary variables t, ρ, ψ. In more detail, the final state is generated by the following five steps, in which $R_{1,2,3,4,\ldots}$ are random numbers with a flat distribution in the interval [0,1]. The generation proceeds as follows.

1) Sampling of the positive muon energy $E_\mu^+ = x_+\, E_\gamma$.
This is done using the rejection technique. x_+ is first sampled from a flat distribution within kinematic limits using

$$x_+ = x_{\min} + R_1(x_{\max} - x_{\min})$$

and then brought to the shape of Eq. (5.39) by keeping all x_+ which satisfy

$$\left(1 - \frac{4}{3}\, x_+ x_-\right) \frac{\log(W)}{\log(W_{\max})} < R_2\,.$$

Here $W_{\max} = W(x_+ = 1/2)$ is the maximum value of W, obtained for symmetric pair production at $x_+ = 1/2$. About 60% of the events are kept in this step. Results of a Monte Carlo generation of x_+ are illustrated in Fig. 5.4. The shape of the histograms agrees with the differential cross section illustrated in Fig. 5.1.

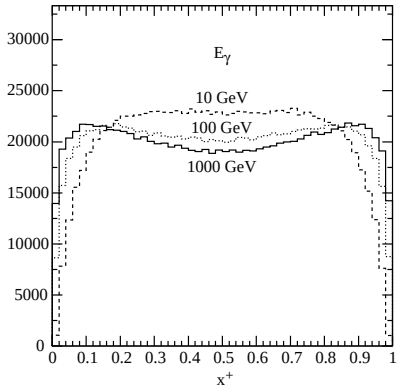

Figure 5.4: Histogram of generated x_+ distributions for beryllium at three different photon energies. The total number of entries at each energy is 10^6.

2) Generate $t(= \frac{1}{\gamma^2\theta^2+1})$.
The distribution in t is obtained from Eq.(5.58) as

$$f_1(t)\, dt = \frac{1 - 2\, x_+ x_- + 4\, x_+ x_- t\,(1-t)}{1 + C_1/t^2}\, dt\,, \quad 0 < t \leq 1\,. \tag{5.60}$$

with form factors taken into account by

$$C_1 = \frac{(0.35\, A^{0.27})^2}{x_+ x_-\, E_\gamma/m_\mu}\,. \tag{5.61}$$

In the interval considered, the function $f_1(t)$ will always be bounded from above by

$$\max[f_1(t)] = \frac{1 - x_+ x_-}{1 + C_1}\,.$$

For small x_+ and large E_γ, $f_1(t)$ approaches unity, as shown in Fig. 5.5.

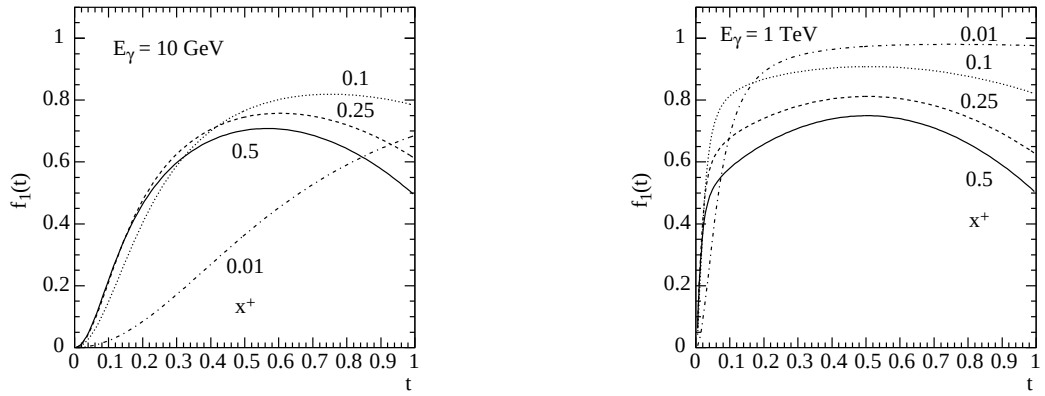

Figure 5.5: The function $f_1(t)$ at $E_\gamma = 10\,\mathrm{GeV}$ (left) and $E_\gamma = 1\,\mathrm{TeV}$ (right) in beryllium for different values of x_+.

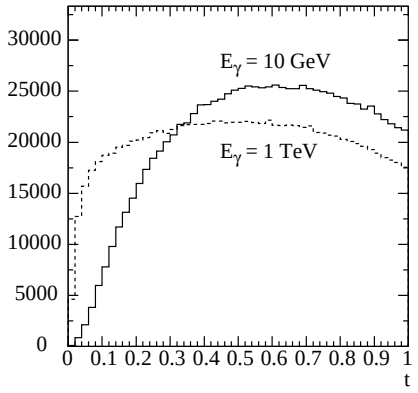

Figure 5.6: Histograms of generated t distributions for $E_\gamma = 10\,\mathrm{GeV}$ (solid line) and $E_\gamma = 100\,\mathrm{GeV}$ (dashed line) with 10^6 events each.

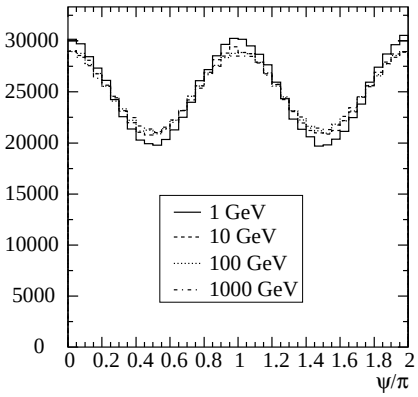

Figure 5.7: Histograms of generated ψ distributions for beryllium at four different photon energies.

The Monte Carlo generation is done using the rejection technique. About 70% of the generated numbers are kept in this step. Generated t-distributions are shown in Fig. 5.6.

3) Generate ψ by the rejection technique using t generated in the previous step for the frequency distribution

$$f_2(\psi) = \Big[1{-}2\,x_+x_-{+}4\,x_+x_-t\,(1{-}t)\,(1{+}\cos(2\psi))\Big]\,, \qquad 0 \le \psi \le 2\pi\,. \quad (5.62)$$

The maximum of $f_2(\psi)$ is

$$\max[f_2(\psi)] = 1 - 2\,x_+x_-\,[1 - 4\,t\,(1-t)]\,. \quad (5.63)$$

Generated distributions in ψ are shown in Fig. 5.7.

4) Generate ρ.
The distribution in ρ has the form

$$f_3(\rho)\,d\rho = \frac{\rho^3\,d\rho}{\rho^4 + C_2}\,, \quad 0 \le \rho \le \rho_{\max}\,, \quad (5.64)$$

where

$$\rho^2_{\max} = \frac{1.9}{A^{0.27}}\,\left(\frac{1}{t} - 1\right), \quad (5.65)$$

and

$$C_2 = \frac{4}{\sqrt{x_+x_-}}\left[\left(\frac{m_\mu}{2E_\gamma x_+x_-\,t}\right)^2 + \left(\frac{m_e}{183\,Z^{-1/3}\,m_\mu}\right)^2\right]^2\,. \quad (5.66)$$

The ρ distribution is obtained by a direct transformation applied to uniform random numbers R_i according to

$$\rho = [C_2(\exp(\beta\,R_i) - 1)]^{1/4}\,, \quad (5.67)$$

where

$$\beta = \log\left(\frac{C_2 + \rho^4_{\max}}{C_2}\right)\,. \quad (5.68)$$

Generated distributions of ρ are shown in Fig. 5.8
5) Calculate θ_+, θ_- and φ from t, ρ, ψ with

$$\gamma_\pm = \frac{E^\pm_\mu}{m_\mu} \qquad \text{and} \qquad u = \sqrt{\frac{1}{t} - 1}\,. \quad (5.69)$$

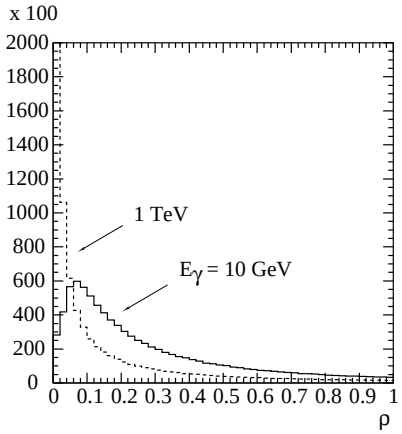

Figure 5.8: Histograms of generated ρ distributions for beryllium at two different photon energies. The total number of entries at each energy is 10^6.

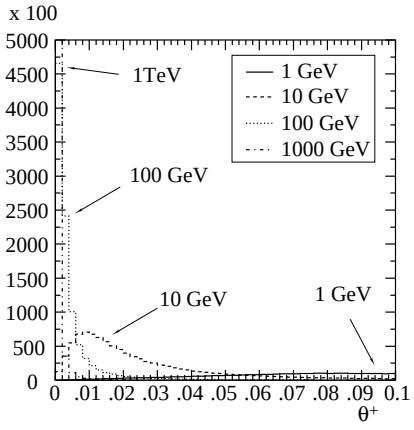

Figure 5.9: Histograms of generated θ_+ distributions at different photon energies.

according to

$$\theta_+ = \frac{1}{\gamma_+}\left(u + \frac{\rho}{2}\cos\psi\right), \quad \theta_- = \frac{1}{\gamma_-}\left(u - \frac{\rho}{2}\cos\psi\right) \quad \text{and} \quad \varphi = \frac{\rho}{u}\sin\psi\,. \tag{5.70}$$

The muon vectors can now be constructed from Eq. (5.53), where φ_0 is chosen randomly between 0 and 2π. Fig. 5.9 shows distributions of θ_+ at different photon energies (in beryllium). The spectra peak around $1/\gamma$ as expected.

The most probable values are $\theta_+ \sim m_\mu/E_\mu^+ = 1/\gamma_+$. In the small angle approximation used here, the values of θ_+ and θ_- can in principle be any positive value from 0 to ∞. In the simulation, this may lead (with a very small probability, of the order of m_μ/E_γ) to unphysical events in which θ_+ or θ_- is greater than π. To avoid this, a limiting angle $\theta_{\rm cut} = \pi$ is introduced, and the angular sampling repeated, whenever $\max(\theta_+, \theta_-) > \theta_{\rm cut}$.

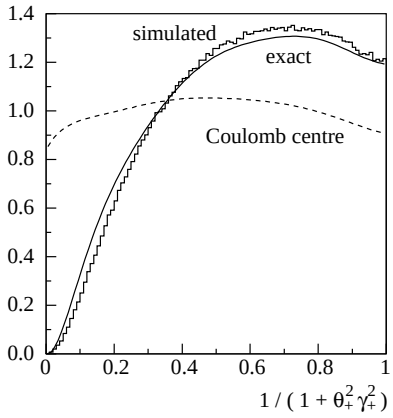

Figure 5.10: Angular distribution of positive (or negative) muons. The solid curve represents the results of the exact calculations. The histogram is the simulated distribution. The angular distribution for pairs created in the field of the Coulomb centre (point-like target) is shown by the dashed curve for comparison.

Figs. 5.10,5.11 and 5.12 show distributions of the simulated angular characteristics of muon pairs in comparison with results of exact calculations. The latter were obtained by means of numerical integration of the squared matrix elements with respective nuclear and atomic form factors. All these calculations were made for iron, with $E_\gamma = 10\,\text{GeV}$ and $x_+ = 0.3$. As seen from Fig. 5.10, wide angle pairs (at low values of the argument in the figure) are suppressed in comparison with the Coulomb center approximation. This is due to the influence of the finite nuclear size which is comparable to the inverse mass of the muon. Typical angles of particle emission are of

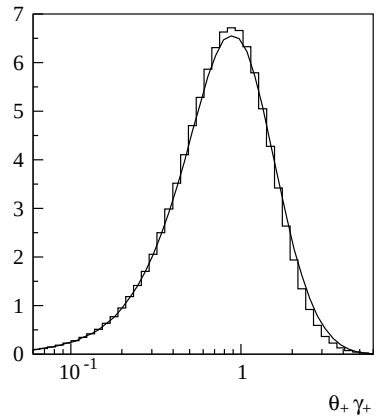

Figure 5.11: Angular distribution in logarithmic scale. The curve corresponds to the exact calculations and the histogram is the simulated distribution.

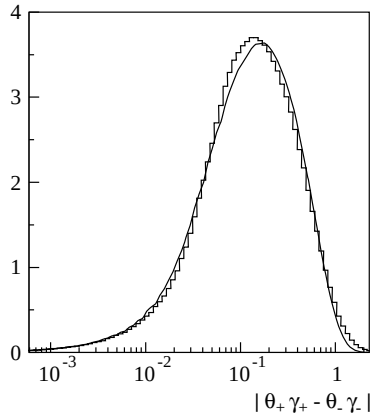

Figure 5.12: Distribution of the difference of transverse momenta of positive and negative muons (with logarithmic x-scale).

the order of $1/\gamma_{\pm} = m_{\mu}/E_{\mu}^{\pm}$ (Fig. 5.11). Fig. 5.12 illustrates the influence of the momentum transferred to the target on the angular characteristics of the produced pair. In the frame of the often used model which neglects target recoil, the pair particles would be symmetric in transverse momenta, and coplanar with the initial photon.

5.5.5 Status of this document

28.05.02 created by H. Burkhardt.
01.12.02 re-worded by D.H. Wright

Bibliography

[1] H. Burkhardt, S. Kelner, and R. Kokoulin, Monte Carlo Generator for Muon Pair Production. *CERN-SL-2002-016 (AP) and CLIC Note 511, May 2002.*

[2] S.R. Kelner, R.P. Kokoulin, and A.A. Petrukhin, About cross section for high energy muon bremsstrahlung. *Moscow Phys. Eng. Inst. 024-95, 1995. 31pp.*

Chapter 6

Elastic scattering

6.1 Multiple Scattering

Elastic scattering of electrons and other charged particles is an important component of any transport code. Elastic cross section is huge when particle energy decreases, so multiple scattering (MSC) approach should be introduced in order to have acceptable CPU performance of the simulation. A universal interface *G4VMultipleScattering* is used by all Geant4 MSC processes [1]:

- *G4eMultipleScattering;*
- *G4hMultipleScattering;*
- *G4MuMultipleScattering.*

For concrete simulation the *G4VMscModel* interface is used, which is an extension of the base *G4VEmModel* interface. The following models are available:

- *G4UrbanMscModel* - since Geant4 10.0 only one *Urban* model is available and it is applicable to all types of particles;
- *G4GoudsmitSaundersonModel* - for electrons and positrons [2];
- *G4WentzelVIModel* - for muons and hadrons, for muons should be included in Physics List together with *G4CoulombScattering* process, for hadrons large angle scattering is simulated by hadron elastic process.

The discussion on Geant4 MSC models is available in Ref.[3]. Below we will describe models developed by L. Urban [4], because these models are used in many Geant4 applications and have general components reused by other models.

6.1.1 Introduction

MSC simulation algorithms can be classified as either *detailed* or *condensed*. In the detailed algorithms, all the collisions/interactions experienced by the particle are simulated. This simulation can be considered as exact, it gives the same results as the solution of the transport equation. However, it can be used only if the number of collisions is not too large, a condition fulfilled only for special geometries (such as thin foils, or low density gas). In solid or liquid media the average number of collisions is very large and the detailed simulation becomes very inefficient. High energy simulation codes use condensed simulation algorithms, in which the global effects of the collisions

are simulated at the end of a track segment. The global effects generally computed in these codes are the net energy loss, displacement, and change of direction of the charged particle. The last two quantities are computed from MSC theories used in the codes and the accuracy of the condensed simulations is limited by accuracy of MSC approximation.

Most particle physics simulation codes use the multiple scattering theories of Molière [5], Goudsmit and Saunderson [6] and Lewis [7]. The theories of Molière and Goudsmit-Saunderson give only the angular distribution after a step, while the Lewis theory computes the moments of the spatial distribution as well. None of these MSC theories gives the probability distribution of the spatial displacement. Each of the MSC simulation codes incorporates its own algorithm to determine the angular deflection, true path length correction, and spatial displacement of the charged particle after a given step. These algorithms are not exact, of course, and are responsible for most of the uncertainties of the transport codes. Also due to inaccuracy of MSC the simulation results can depend on the value of the step length and generally user has to select the value of the step length carefully.

A new class of MSC simulation, the *mixed* simulation algorithms (see e.g.[8]), appeared in the literature recently. The mixed algorithm simulates the *hard* collisions one by one and uses a MSC theory to treat the effects of the *soft* collisions at the end of a given step. Such algorithms can prevent the number of steps from becoming too large and also reduce the dependence on the step length. Geant4 original implementation of a similar approach is realized in *G4WentzelVIModel* [3].

The Urban MSC models used in Geant4 belongs to the class of condensed simulations. Urban uses model functions to determine the angular and spatial distributions after a step. The functions have been chosen in such a way as to give the same moments of the (angular and spatial) distributions as are given by the Lewis theory [7].

6.1.2 Definition of Terms

In simulation, a particle is transported by steps through the detector geometry. The shortest distance between the endpoints of a step is called the *geometrical path length*, z. In the absence of a magnetic field, this is a straight line. For non-zero fields, z is the length along a curved trajectory. Constraints on z are imposed when particle tracks cross volume boundaries. The path length of an actual particle, however, is usually longer than the *geometrical path length*, due to multiple scattering. This distance is called the *true path length*, t. Constraints on t are imposed by the physical processes acting on the particle.

The properties of the MSC process are determined by the *transport mean free paths*, λ_k, which are functions of the energy in a given material. The k-th transport mean free path is defined as

$$\frac{1}{\lambda_k} = 2\pi n_a \int_{-1}^{1} [1 - P_k(cos\chi)] \frac{d\sigma(\chi)}{d\Omega} d(cos\chi) \tag{6.1}$$

where $d\sigma(\chi)/d\Omega$ is the differential cross section of the scattering, $P_k(cos\chi)$ is the k-th Legendre polynomial, and n_a is the number of atoms per volume.

Most of the mean properties of MSC computed in the simulation codes depend only on the first and second transport mean free paths. The mean value of the geometrical path length (first moment) corresponding to a given true path length t is given by

$$\langle z \rangle = \lambda_1 \left[1 - \exp\left(-\frac{t}{\lambda_1} \right) \right] \tag{6.2}$$

Eq. 6.2 is an exact result for the mean value of z if the differential cross section has axial symmetry and the energy loss can be neglected. The transformation between true and geometrical path lengths is called the *path length correction*. This formula and other expressions for the first moments of the spatial distribution were taken from either [8] or [9], but were originally calculated by Goudsmit and Saunderson [6] and Lewis [7].

At the end of the true step length, t, the scattering angle is θ. The mean value of $cos\theta$ is

$$\langle cos\theta \rangle = \exp\left[-\frac{t}{\lambda_1} \right] \tag{6.3}$$

The variance of $cos\theta$ can be written as

$$\sigma^2 = \langle cos^2\theta \rangle - \langle cos\theta \rangle^2 = \frac{1 + 2e^{-2\kappa\tau}}{3} - e^{-2\tau} \tag{6.4}$$

where $\tau = t/\lambda_1$ and $\kappa = \lambda_1/\lambda_2$. The mean lateral displacement is given by a more complicated formula [8], but this quantity can also be calculated relatively easily and accurately. The square of the *mean lateral displacement* is

$$\langle x^2 + y^2 \rangle = \frac{4\lambda_1^2}{3} \left[\tau - \frac{\kappa + 1}{\kappa} + \frac{\kappa}{\kappa - 1} e^{-\tau} - \frac{1}{\kappa(\kappa - 1)} e^{-\kappa\tau} \right] \tag{6.5}$$

Here it is assumed that the initial particle direction is parallel to the the z axis. The lateral correlation is determined by the equation

$$\langle x v_x + y v_y \rangle = \frac{2\lambda_1}{3} \left[1 - \frac{\kappa}{\kappa - 1} e^{-\tau} + \frac{1}{\kappa - 1} e^{-\kappa\tau} \right] \tag{6.6}$$

where v_x and v_y are the x and y components of the direction unit vector. This equation gives the correlation strength between the final lateral position and final direction.

The transport mean free path values have been calculated in Refs.[10],[11] for electrons and positrons in the kinetic energy range 100 eV - 20 MeV in 15 materials. The Urban MSC model in Geant4 uses these values for kinetic energies below 10 MeV. For high energy particles (above 10 MeV) the transport mean free path values have been taken from a paper of R. Mayol and F. Salvat [12]. When necessary, the model linearly interpolates or extrapolates the transport cross section, $\sigma_1 = 1/\lambda_1$, in atomic number Z and in the square of the particle velocity, β^2. The ratio κ is a very slowly varying function of the energy: $\kappa > 2$ for $T >$ a few keV, and $\kappa \to 3$ for very high energies (see [9]). Hence, a constant value of 2.5 is used in the model.

Nuclear size effects are negligible for low energy particles and they are accounted for in the Born approximation in [12], so there is no need for extra corrections of this kind in the Urban model.

6.1.3 Path Length Correction

As mentioned above, the path length correction refers to the transformation $t \longrightarrow g$ and its inverse. The $t \longrightarrow g$ transformation is given by Eq. 6.2 if the step is small and the energy loss can be neglected. If the step is not small the energy dependence makes the transformation more complicated. For this case Eqs. 6.3,6.2 should be modified as

$$\langle cos\theta \rangle = \exp\left[- \int_0^t \frac{du}{\lambda_1(u)} \right] \tag{6.7}$$

$$\langle z \rangle = \int_0^t \langle cos\theta \rangle_u \, du \tag{6.8}$$

where θ is the scattering angle, t and z are the true and geometrical path lengths, and λ_1 is the transport mean free path.

In order to compute Eqs. 6.7,6.8 the t dependence of the transport mean free path must be known. λ_1 depends on the kinetic energy of the particle which decreases along the step. All computations in the model use a linear approximation for this t dependence:

$$\lambda_1(t) = \lambda_{10}(1 - \alpha t) \tag{6.9}$$

Here λ_{10} denotes the value of λ_1 at the start of the step, and α is a constant. It is worth noting that Eq. 6.9 is *not* a crude approximation. It is rather

good at low (< 1 MeV) energy. At higher energies the step is generally much smaller than the range of the particle, so the change in energy is small and so is the change in λ_1. Using Eqs. 6.7 - 6.9 the explicit formula for $\langle cos\theta \rangle$ and $\langle z \rangle$ are:

$$\langle cos\theta \rangle = (1 - \alpha t)^{\frac{1}{\alpha \lambda_{10}}} \tag{6.10}$$

$$\langle z \rangle = \frac{1}{\alpha(1 + \frac{1}{\alpha \lambda_{10}})} \left[1 - (1 - \alpha t)^{1 + \frac{1}{\alpha \lambda_{10}}} \right] \tag{6.11}$$

The value of the constant α can be expressed using λ_{10} and λ_{11} where λ_{11} is the value of the transport mean free path at the end of the step

$$\alpha = \frac{\lambda_{10} - \lambda_{11}}{t \lambda_{10}} \tag{6.12}$$

At low energies ($T_{kin} < M$, M - particle mass) α has a simpler form:

$$\alpha = \frac{1}{r_0} \tag{6.13}$$

where r_0 denotes the range of the particle at the start of the step. It can easily be seen that for a small step (i.e. for a step with small relative energy loss) the formula of $\langle z \rangle$ is

$$\langle z \rangle = \lambda_{10} \left[1 - \exp\left(-\frac{t}{\lambda_{10}} \right) \right] \tag{6.14}$$

Eq. 6.11 or 6.14 gives the mean value of the geometrical step length for a given true step length. The actual geometrical path length is sampled in the model according to the simple probability density function defined for $v = z/t \in [0, 1]$:

$$f(v) = (k + 1)(k + 2)v^k(1 - v) \tag{6.15}$$

The value of the exponent k is computed from the requirement that $f(v)$ must give the same mean value for $z = vt$ as Eq. 6.11 or 6.14. Hence

$$k = \frac{3\langle z \rangle - t}{t - \langle z \rangle} \tag{6.16}$$

The value of $z = vt$ is sampled using $f(v)$ if $k > 0$, otherwise $z = \langle z \rangle$ is used. The $g \longrightarrow t$ transformation is performed using the mean values. The transformation can be written as

$$t(z) = \langle t \rangle = -\lambda_1 \log\left(1 - \frac{z}{\lambda_1} \right) \tag{6.17}$$

if the geometrical step is small and

$$t(z) = \frac{1}{\alpha}\left[1 - (1 - \alpha w z)^{\frac{1}{w}}\right] \tag{6.18}$$

where

$$w = 1 + \frac{1}{\alpha \lambda_{10}}$$

if the step is not small, i.e. the energy loss should be taken into account.

6.1.4 Angular Distribution

The quantity $u = cos\theta$ is sampled according to a model function $g(u)$. The shape of this function has been chosen such that Eqs. 6.3 and 6.4 are satisfied. The functional form of g is

$$g(u) = q[pg_1(u) + (1-p)g_2(u)] + (1-q)g_3(u) \tag{6.19}$$

where $0 \leq p, q \leq 1$, and the g_i are simple functions of $u = cos\theta$, normalized over the range $u \in [-1,\ 1]$. The functions g_i have been chosen as

$$g_1(u) = C_1 \quad e^{-a(1-u)} \qquad -1 \leq u_0 \leq u \leq 1 \tag{6.20}$$

$$g_2(u) = C_2 \quad \frac{1}{(b-u)^d} \qquad -1 \leq u \leq u_0 \leq 1 \tag{6.21}$$

$$g_3(u) = C_3 \qquad -1 \leq u \leq 1 \tag{6.22}$$

where $a > 0$, $b > 0$, $d > 0$ and u_0 are model parameters, and the C_i are normalization constants. It is worth noting that for small scattering angles, θ, $g_1(u)$ is nearly Gaussian ($exp(-\theta^2/2\theta_0^2)$) if $\theta_0^2 \approx 1/a$, while $g_2(u)$ has a Rutherford-like tail for large θ, if $b \approx 1$ and d is not far from 2 .

6.1.5 Determination of the Model Parameters

The parameters a, b, d, u_0 and p, q are not independent. The requirement that the angular distribution function $g(u)$ and its first derivative be continuous at $u = u_0$ imposes two constraints on the parameters:

$$p\ g_1(u_0) = (1-p)\ g_2(u_0) \tag{6.23}$$

$$p\ a\ g_1(u_0) = (1-p)\ \frac{d}{b-u_0}\ g_2(u_0) \tag{6.24}$$

A third constraint comes from Eq. 6.7 : $g(u)$ must give the same mean value for u as the theory. It follows from Eqs. 6.10 and 6.19 that

$$q\{p\langle u\rangle_1 + (1-p)\langle u\rangle_2\} = [1 - \alpha\ t]^{\ \frac{1}{\alpha\lambda_{10}}} \tag{6.25}$$

where $\langle u\rangle_i$ denotes the mean value of u computed from the distribution $g_i(u)$. The parameter a was chosen according to a modified Highland-Lynch-Dahl formula for the width of the angular distribution [13], [14].

$$a = \frac{0.5}{1 - cos(\theta_0)} \tag{6.26}$$

where θ_0 is

$$\theta_0 = \frac{13.6MeV}{\beta cp} z_{ch}\sqrt{\frac{t}{X_0}}\ \left[1 + h_c \ln\left(\frac{t}{X_0}\right)\ \right] \tag{6.27}$$

when the original Highland-Lynch-Dahl formula is used. Here $\theta_0 = \theta_{plane}^{rms}$ is the width of the approximate Gaussian projected angle distribution, p, βc and z_{ch} are the momentum, velocity and charge number of the incident particle, and t/X_0 is the true path length in radiation length unit. The correction term $h_c = 0.038$ in the formula. This value of θ_0 is from a fit to the Molière distribution for singly charged particles with $\beta = 1$ for all Z, and is accurate to 11 % or better for $10^{-3} \leq t/X_0 \leq 100$ (see e.g. Rev. of Particle Properties, section 23.3).

The model uses a slightly modified Highland-Lynch-Dahl formula to compute θ_0. For electrons/positrons the modified θ_0 formula is

$$\theta_0 = \frac{13.6MeV}{\beta cp} z_{ch}\sqrt{y}c \tag{6.28}$$

where

$$y = \ln\left(\frac{t}{X_0}\right) \tag{6.29}$$

The correction term c and coeffitients c_i are

$$c = c_0\dot{(}c_1 + c_2 y), \tag{6.30}$$

$$c_0 = 0.990395 - 0.168386Z^{1/6} + 0.093286Z^{1/3}, \tag{6.31}$$

$$c_1 = 1 - \frac{0.08778}{Z}, \tag{6.32}$$

$$c_2 = 0.04078 + 0.00017315Z. \tag{6.33}$$

This formula gives a much smaller step dependence in the angular distribution than the Highland form. The value of the parameter u_0 has been chosen as

$$u_0 \quad = \quad 1 - \frac{\xi}{a} \tag{6.34}$$

where

$$\xi = d_1 + d_2 v + d_3 v^2 + d_4 v^3 \tag{6.35}$$

with

$$v = \ln\left(\frac{t}{\lambda_1}\right) \tag{6.36}$$

The parameters d_i-s have the form

$$d_i = d_{i0} + d_{i1} Z^{\frac{1}{3}} + d_{i2} Z^{\frac{2}{3}} \tag{6.37}$$

The numerical values of the d_{ij} constants can be found in the code.

The tail parameter d is the same as the parameter ξ .

This (empirical) expression is obtained comparing the simulation results to the data of the MuScat experiment [16]. The remaining three parameters can be computed from Eqs. 6.23 - 6.25. The numerical value of the parameters can be found in the code.

In the case of heavy charged particles (μ, π, p, etc.) the mean transport free path is calculated from the electron or positron λ_1 values with a 'scaling' applied. This is possible because the transport mean free path λ_1 depends only on the variable $P\beta c$, where P is the momentum, and βc is the velocity of the particle.

In its present form the model samples the path length correction and angular distribution from model functions, while for the lateral displacement and the lateral correlation only the mean values are used and all the other correlations are neglected. However, the model is general enough to incorporate other random quantities and correlations in the future.

6.1.6 Step Limitation Algorithm

In Geant4 the boundary crossing is treated by the transportation process. The transportation ensures that the particle does not penetrate in a new volume without stopping at the boundary, it restricts the step size when the particle leaves a volume. However, this step restriction can be rather weak in big volumes and this fact can result a not very good angular distribution after the volume. At the same time, there is no similar step limitation when a particle enters a volume and this fact does not allow a good backscattering simulation for low energy particles. Low energy particles penetrate too deeply

into the volume in the first step and then - because of energy loss - they are not able to reach again the boundary in backward direction.

MSC step limitation algorithm has been developed [4] in order to achieve optimal balance between simulation precision and CPU performance of simulation for different applications. At the start of a track or after entering in a new volume, the algorithm restricts the step size to a value

$$f_r \cdot max\{r, \lambda_1\} \tag{6.38}$$

where r is the range of the particle, f_r is a parameter $\in [0, 1]$, taking the max of r and λ_1 is an empirical choice.The value of f_r is constant for low energy particles while for particles with $\lambda_1 > \lambda_{lim}$ an effective value is used given by the scaling equation

$$f_{reff} = f_r \cdot \left[1 - sc + sc * \frac{\lambda_1}{\lambda_{lim}}\right] \tag{6.39}$$

(The numerical values $sc = 0.25$ and $\lambda_{lim} = 1\ mm$ are used in the equation.) In order not to use very small - unphysical - step sizes a lower limit is given for the step size as

$$tlimitmin = max\left[\frac{\lambda_1}{nstepmax}, \lambda_{elastic}\right] \tag{6.40}$$

with $nstepmax = 25$ and $\lambda_{elastic}$ is the elastic mean free path of the particle (see later).

It can be easily seen that this kind of step limitation poses a real constraint only for low energy particles. In order to prevent a particle from crossing a volume in just one step, an additional limitation is imposed: after entering a volume the step size cannot be bigger than

$$\frac{d_{geom}}{f_g} \tag{6.41}$$

where d_{geom} is the distance to the next boundary (in the direction of the particle) and f_g is a constant parameter. A similar restriction at the start of a track is

$$\frac{2d_{geom}}{f_g} \tag{6.42}$$

At this point the program also checks whether the particle has entered a new volume. If it has, the particle steps cannot be bigger than $t_{lim} = f_r\ max(r, \lambda)$. This step limitation is governed by the physics, because t_{lim} depends on the particle energy and the material.

The choice of the parameters f_r and f_g is also related to performance. By default $f_r = 0.02$ and $f_g = 2.5$ are used, but these may be set to any other value in a simple way. One can get an approximate simulation of the backscattering with the default value, while if a better backscattering simulation is needed it is possible to get it using a smaller value for f_r. However, this model is very simple and it can only approximately reproduce the backscattering data.

6.1.7 Boundary Crossing Algorithm

A special stepping algorithm has been implemented in order to improve the simulation around interfaces. This algorithm does not allow 'big' last steps in a volume and 'big' first steps in the next volume. The step length of these steps around a boundary crossing can not be bigger than the mean free path of the elastic scattering of the particle in the given volume (material). After these small steps the particle scattered according to a single scattering law (i.e. there is no multiple scattering very close to the boundary or at the boundary).

The key parameter of the algorithm is the variable called *skin*. The algorithm is not active for $skin \leq 0$, while for $skin > 0$ it is active in layers of thickness $skin \cdot \lambda_{elastic}$ before boundary crossing and of thickness $(skin-1)\cdot\lambda_{elastic}$ after boundary crossing (for $skin = 1$ there is only one small step just before the boundary). In this active area the particle performs steps of length $\lambda_{elastic}$ (or smaller if the particle reaches the boundary traversing a smaller distance than this value).

The scattering at the end of a small step is single or plural and for these small steps there are no path length correction and lateral displacement computation. In other words the program works in this thin layer in 'microscopic mode'. The elastic mean free path can be estimated as

$$\lambda_{elastic} = \lambda_1 \cdot rat\,(T_{kin}) \tag{6.43}$$

where $rat(T_{kin})$ a simple empirical function computed from the elastic and first transport cross section values of Mayol and Salvat [12]

$$rat\,(T_{kin}) = \frac{0.001(MeV)^2}{T_{kin}\,(T_{kin} + 10MeV)} \tag{6.44}$$

T_{kin} is the kinetic energy of the particle.

At the end of a small step the number of scatterings is sampled according to the Poisson's distribution with a mean value $t/\lambda_{elastic}$ and in the case of

plural scattering the final scattering angle is computed by summing the contributions of the individual scatterings. The single scattering is determined by the distribution

$$g(u) = C\frac{1}{(2a+1-u)^2} \tag{6.45}$$

where $u = \cos(\theta)$, a is the screening parameter, C is a normalization constant. The form of the screening parameter is the same as in the single scattering (see there).

6.1.8 Implementation Details

The step length of a particles is determined by the physics processes or the geometry of the detectors. The tracking/stepping algorithm checks all the step lengths demanded by the (continuous or discrete) physics processes and determines the minimum of these step lengths (see 3.2). The MSC model should be called to compute step limit after all processes except the transportation process. The following sequence of computations are performed to make the step:

- the minimum of all processes *true step length* limit t including one of the MSC process is selected;
- The conversion $t \longrightarrow g$ (*geometrical step limit*) is performed;
- the minimum of obtained value g and the transportation step limit is selected;
- The final conversion $g \longrightarrow t$ is performed.

The reason for this ordering is that the physics processes 'feel' the true path length t traveled by the particle, while the transportation process (geometry) uses the z step length.

After the actual step of the particle is done, the MSC model is responsible for sampling of scattering angle and relocation of the end-point of the step. The scattering angle θ of the particle after the step of length 't' is sampled according to the model function given in Eq. 6.19 . The azimuthal angle ϕ is generated uniformly in the range $[0, 2\pi]$.

After the simulation of the scattering angle, the lateral displacement is computed using Eq. 6.5. Then the correlation given by Eq. 6.6 is used to determine the direction of the lateral displacement. Before 'moving' the particle according to the displacement a check is performed to ensure that the relocation of the particle with the lateral displacement does not take the particle beyond the volume boundary.

Default MSC parameter values optimized per particle type are shown in Table 6.1. Note, that there is three types of step limitation by multiple scattering process:

- `Minimal` - only f_r parameter is used, was used for g4 7.1 release;
- `UseSafety` or $skin = 0$ - uses particle range and geometrical safety;
- `UseDistanceToBoundary` - uses particle range, geometrical safety and linear distance to geometrical boundary.

particle	e^+, e^-	*muons, hadrons*	*ions*
StepLimitType	*fUseSafety*	*fMinimal*	*fMinimal*
skin	0	0	0
f_r	0.04	0.2	0.2
f_g	2.5	0.1	0.1
LateralDisplacement	*true*	*true*	*false*

Table 6.1: The default values of parameters for different particle type.

The parameters of the model can be changed via public functions of the base class *G4VMultipleSacttering*. They can be changed for all multiple scattering processes simultaneously via *G4EmProcessOptions* class or via Geant4 UI commands. The following commands are available:

/process/msc/StepLimit UseDistanceToBoundary
/process/msc/LateralDisplacement false
/process/msc/RangeFactor 0.02
/process/msc/GeomFactor 2.5
/process/msc/Skin 2

6.1.9 Status of this document

09.10.98 created by L. Urbán.
15.11.01 major revision by L. Urbán.
18.04.02 updated by L. Urbán.
25.04.02 re-worded by D.H. Wright
07.06.02 major revision by L. Urbán.
18.11.02 updated by L. Urbán, now it describes the new angle distribution.
05.12.02 grammar check and parts re-written by D.H. Wright
13.11.03 revision by L. Urbán.

01.12.03 revision by V. Ivanchenko.
17.05.04 revision by L. Urbán.
01.12.04 updated by L. Urbán.
18.03.05 sampling z + mistyping corrections (M. Maire)
22.06.05 grammar, spelling check by D.H. Wright
12.12.05 revised by L. Urbán, according to Geant4 8.0
14.12.05 updated implementation Details (M. Maire)
08.06.06 revised by L. Urbán, according to Geant4 8.1
25.11.06 revised by L. Urbán, according to Geant4 8.2
29.03.07 revised by L. Urbán, for Geant4 8.3
13.06.07 modified introduction (M. Maire)
17.06.07 explain effective F_R (L. Urbán)
25.06.07 update description of options by V. Ivanchenko
05.12.07 revised by L. Urbán, for Geant4 9.1
08.12.08 revised by L. Urbán, for Geant4 9.2
11.12.08 minor revision by V. Ivanchenko
11.12.09 minor revision by V. Ivanchenko, for Geant4 9.3
09.12.09 revision by V. Ivanchenko, for Geant4 9.4
25.11.11 minor revision by V. Ivanchenko, for Geant4 9.5
03.12.13 minor revision by L. Urban, for Geant4 10.0

Bibliography

[1] J. Apostolakis et al., Geometry and physics of the Geant4 toolkit for high and medium energy applications. *Rad. Phys. Chem. 78 (2009) 859.*

[2] O. Kadri, V. Ivanchenko, F. Gharbi, A. Trabelsi, Incorporation of the Goudsmit-Saunderson electron transport theory in the Geant4 Monte Carlo code, *Nucl. Instrum. and Meth. B 267 (2009) 3624.*

[3] V.N. Ivanchenko et al., Geant4 models for simulation of multiple scattering, *J. Phys.: Conf. Ser. 219 (2010) 032045.*

[4] L. Urban, A multiple scattering model, *CERN-OPEN-2006-077, Dec 2006. 18 pp.*

[5] G.Z. Molière *Z. Naturforsch. 3a (1948) 78.*

[6] S. Goudsmit and J.L. Saunderson. *Phys. Rev. 57 (1940) 24.*

[7] H.W. Lewis. *Phys. Rev. 78 (1950) 526.*

[8] J.M. Fernandez-Varea et al. *NIM B73 (1993) 447.*

[9] I. Kawrakow and A.F. Bielajew *NIM B 142 (1998) 253.*

[10] D. Liljequist and M. Ismail. *J.Appl.Phys. 62 (1987) 342.*

[11] D. Liljequist et al. *J.Appl.Phys. 68 (1990) 3061.*

[12] R. Mayol and F. Salvat *At.Data and Nucl.Data Tables 65 (1997) 55.*.

[13] V.L. Highland *NIM 129 (1975) 497.*

[14] G.R. Lynch and O.I. Dahl *NIM B58 (1991) 6.*

[15] G. Shen et al. *Phys. Rev. D 20 (1979) 1584.*

[16] D. Attwood et al. *NIM B 251 (2006) 41.*

6.2 Discrete Processes for Charged Particles

Some processes for charged particles following the same interface $G4VEmProcess$ as gamma processes described in section 5.1:

- G4CoulombScattering;
- G4eplusAnnihilation (with additional AtRest methods);
- G4eplusPolarizedAnnihilation (with additional AtRest methods);
- G4eeToHadrons;
- G4NuclearStopping;
- G4MicroElecElastic;
- G4MicroElecInelastic.

Corresponding model classes follow the $G4VEmModel$ interface:

- G4DummyModel (zero cross section, no secondaries);
- G4eCoulombScatteringModel;
- G4eSingleCoulombScatteringModel;
- G4IonCoulombScatteringModel;
- G4eeToHadronsModel;
- G4PenelopeAnnihilationModel;
- G4PolarizedAnnihilationModel;
- G4ICRU49NuclearStoppingModel;
- G4MicroElecElasticModel;
- G4MicroElecInelasticModel.

Some processes from do not follow described EM interfaces but provide direct implementations of the basic $G4VDiscreteProcess$ process:

- G4AnnihiToMuPair;
- G4ScreenedNuclearRecoil;
- G4Cerenkov;
- G4Scintillation;
- G4SynchrotronRadiation;

6.2.1 Status of This Document

10.12.10 created by V. Ivanchenko
29.11.13 updated by V. Ivanchenko

6.3 Single Scattering

Single elastic scattering process is an alternative to the multiple scattering process. The advantage of the single scattering process is in possibility of usage of theory based cross sections, in contrary to the Geant4 multiple scattering model [1], which uses a number of phenomenological approximations on top of Lewis theory. The process *G4CoulombScattering* was created for simulation of single scattering of muons, it also applicable with some physical limitations to electrons, muons and ions. Because each of elastic collisions are simulated the number of steps of charged particles significantly increasing in comparison with the multiple scattering approach, correspondingly its CPU performance is pure. However, in low-density media (vacuum, low-density gas) multiple scattering may provide wrong results and single scattering processes is more adequate.

6.3.1 Coulomb Scattering

The single scattering model of Wentzel [2] is used in many of multiple scattering models including Penelope code [4]. The Wentzel for describing elastic scattering of particles with charge ze ($z = -1$ for electron) by atomic nucleus with atomic number Z based on simplified scattering potential

$$V(r) = \frac{zZe^2}{r} exp(-r/R), \tag{6.46}$$

where the exponential factor tries to reproduce the effect of screening. The parameter R is a screening radius [3]

$$R = 0.885 Z^{-1/3} r_B, \tag{6.47}$$

where r_B is the Bohr radius. In the first Born approximation the elastic scattering cross section $\sigma^(W)$ can be obtained as

$$\frac{d\sigma^{(W)}(\theta)}{d\Omega} = \frac{(ze^2)^2}{(p\beta c)^2} \frac{Z(Z+1)}{(2A+1-cos\theta)^2}, \tag{6.48}$$

where p is the momentum and β is the velocity of the projectile particle. The screening parameter A according to Moliere and Bethe [3]

$$A = \left(\frac{\hbar}{2pR}\right)^2 (1.13 + 3.76(\alpha Z/\beta)^2), \tag{6.49}$$

where α is a fine structure constant and the factor in brackets is used to take into account second order corrections to the first Born approximation.

The total elastic cross section σ can be expressed via Wentzel cross section (6.48)

$$\frac{d\sigma(\theta)}{d\Omega} = \frac{d\sigma^{(W)}(\theta)}{d\Omega}\left(\frac{Z}{(1+\frac{(qR_N)^2}{12})^2}+1\right)\frac{1}{Z+1}, \tag{6.50}$$

where q is momentum transfer to the nucleus, R_N is nuclear radius. This term takes into account nuclear size effect [5], the second term takes into account scattering off electrons. The results of simulation with the single scattering model (Fig.6.1) are competitive with the results of the multiple scattering.

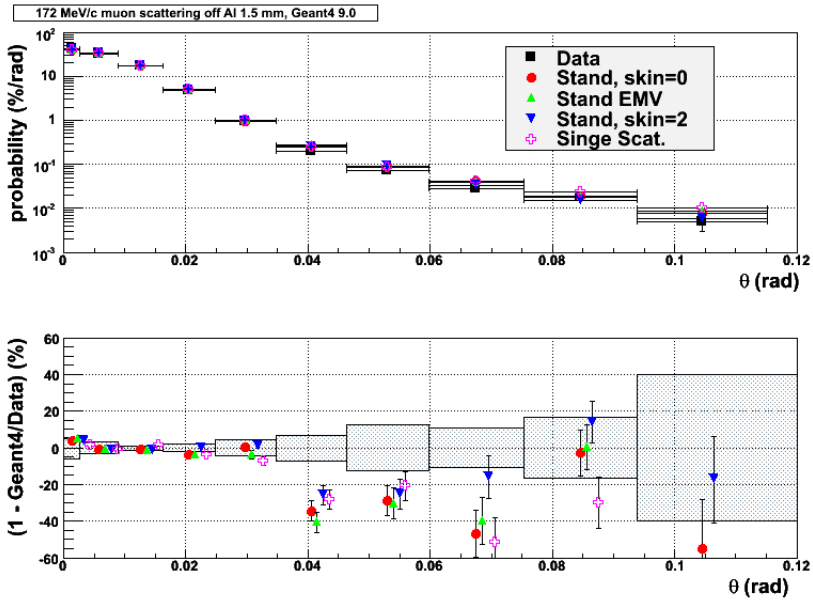

Figure 6.1: Scattering of muons off 1.5 mm aluminum foil: data [6] - black squares; simulation - colored markers corresponding different options of multiple scattering and single scattering model; in the bottom plot - relative difference between the simulation and the data in percents; hashed area demonstrates one standard deviation of the data.

6.3.2 Implementation Details

The total cross section of the process is obtained as a result of integration of the differential cross section (6.50). The first term of this cross section is integrated in the interval $(0, \pi)$. The second term in the smaller interval $(0, \theta_m)$, where θ_m is the maximum scattering angle off electrons, which is determined using the cut value for the delta electron production. Before

sampling of angular distribution the random choice is performed between scattering off the nucleus and off electrons.

6.3.3 Status of This Document

06.12.07 created by V. Ivanchenko
08.12.10 added chapter on discrete processes by V.Ivanchenko

Bibliography

[1] L. Urban, A multiple scattering model, *CERN-OPEN-2006-077, Dec 2006. 18 pp.*

[2] G. Wentzel, *Z. Phys. 40 (1927) 590.*

[3] H.A. Bethe, *Phys. Rev. 89 (1953) 1256.*

[4] J.M. Fernandez-Varea et al. *NIM B 73 (1993) 447.*

[5] A.V. Butkevich et al., *NIM A 488 (2002) 282.*

[6] D. Attwood et al. *NIM B 251 (2006) 41.*

6.4 Ion Scattering

The necessity of accurately computing the characteristics of interatomic scattering arises in many disciplines in which energetic ions pass through materials. Traditionally, solutions to this problem not involving hadronic interactions have been dominated by the multiple scattering, which is reasonably successful, but not very flexible. In particular, it is relatively difficult to introduce into such a system a particular screening function which has been measured for a specific atomic pair, rather than the universal functions which are applied. In many problems of current interest, such as the behavior of semiconductor device physics in a space environment, nuclear reactions, particle showers, and other effects are critically important in modeling the full details of ion transport. The process *G4ScreenedNuclearRecoil* provides simulation of ion elastic scattering [1]. This process is available with extended electromagnetic example *TestEm7*.

6.4.1 Method

The method used in this computation is a variant of a subset of the method described in Ref.[2]. A very short recap of the basic material is included here. The scattering of two atoms from each other is assumed to be a completely classical process, subject to an interatomic potential described by a potential function

$$V(r) = \frac{Z_1 Z_2 e^2}{r} \phi\left(\frac{r}{a}\right) \tag{6.51}$$

where Z_1 and Z_2 are the nuclear proton numbers, e^2 is the electromagnetic coupling constant ($q_e^2/4\pi\epsilon_0$ in SI units), r is the inter-nuclear separation, ϕ is the screening function describing the effect of electronic screening of the bare nuclear charges, and a is a characteristic length scale for this screening. In most cases, ϕ is a universal function used for all ion pairs, and the value of a is an appropriately adjusted length to give reasonably accurate scattering behavior. In the method described here, there is no particular need for a universal function ϕ, since the method is capable of directly solving the problem for most physically plausible screening functions. It is still useful to define a typical screening length a in the calculation described below, to keep the equations in a form directly comparable with our previous work even though, in the end, the actual value is irrelevant as long as the final function $\phi(r)$ is correct. From this potential $V(r)$ one can then compute the classical scattering angle from the reduced center-of-mass energy $\varepsilon \equiv E_c a/Z_1 Z_2 e^2$ (where E_c is the kinetic energy in the center-of-mass frame) and reduced

impact parameter $\beta \equiv b/a$

$$\theta_c = \pi - 2\beta \int_{x_0}^{\infty} f(z)\, dz/z^2 \tag{6.52}$$

where

$$f(z) = \left(1 - \frac{\phi(z)}{z\,\varepsilon} - \frac{\beta^2}{z^2}\right)^{-1/2} \tag{6.53}$$

and x_0 is the reduced classical turning radius for the given ε and β.

The problem, then, is reduced to the efficient computation of this scattering integral. In our previous work, a great deal of analytical effort was included to proceed from the scattering integral to a full differential cross section calculation, but for application in a Monte-Carlo code, the scattering integral $\theta_c(Z_1,\, Z_2,\, E_c,\, b)$ and an estimated total cross section $\sigma_0(Z_1,\, Z_2,\, E_c)$ are all that is needed. Thus, we can skip algorithmically forward in the original paper to equations 15-18 and the surrounding discussion to compute the reduced distance of closest approach x_0. This computation follows that in the previous work exactly, and will not be reintroduced here.

For the sake of ultimate accuracy in this algorithm, and due to the relatively low computational cost of so doing, we compute the actual scattering integral (as described in equations 19-21 of [2]) using a Lobatto quadrature of order 6, instead of the 4th order method previously described. This results in the integration accuracy exceeding that of any available interatomic potentials in the range of energies above those at which molecular structure effects dominate, and should allow for future improvements in that area. The integral α then becomes (following the notation of the previous paper)

$$\alpha \approx \frac{1 + \lambda_0}{30} + \sum_{i=1}^{4} w_i'\, f\left(\frac{x_0}{q_i}\right) \tag{6.54}$$

where

$$\lambda_0 = \left(\frac{1}{2} + \frac{\beta^2}{2\,x_0^2} - \frac{\phi'(x_0)}{2\,\varepsilon}\right)^{-1/2} \tag{6.55}$$

$w_i' \in$[0.03472124, 0.1476903, 0.23485003, 0.1860249]
$q_i \in$[0.9830235, 0.8465224, 0.5323531, 0.18347974]
Then

$$\theta_c = \pi - \frac{\pi\beta\alpha}{x_0} \tag{6.56}$$

The other quantity required to implement a scattering process is the total scattering cross section σ_0 for a given incident ion and a material through

which the ion is propagating. This value requires special consideration for a process such as screened scattering. In the limiting case that the screening function is unity, which corresponds to Rutherford scattering, the total cross section is infinite. For various screening functions, the total cross section may or may not be finite. However, one must ask what the intent of defining a total cross section is, and determine from that how to define it.

In Geant4, the total cross section is used to determine a mean-free-path l_μ which is used in turn to generate random transport distances between discrete scattering events for a particle. In reality, where an ion is propagating through, for example, a solid material, scattering is not a discrete process but is continuous. However, it is a useful, and highly accurate, simplification to reduce such scattering to a series of discrete events, by defining some minimum energy transfer of interest, and setting the mean free path to be the path over which statistically one such minimal transfer has occurred. This approach is identical to the approach developed for the original TRIM code [3]. As long as the minimal interesting energy transfer is set small enough that the cumulative effect of all transfers smaller than that is negligible, the approximation is valid. As long as the impact parameter selection is adjusted to be consistent with the selected value of l_μ, the physical result isn't particularly sensitive to the value chosen.

Noting, then, that the actual physical result isn't very sensitive to the selection of l_μ, one can be relatively free about defining the cross section σ_0 from which l_μ is computed. The choice used for this implementation is fairly simple. Define a physical cutoff energy E_{min} which is the smallest energy transfer to be included in the calculation. Then, for a given incident particle with atomic number Z_1, mass m_1, and lab energy E_{inc}, and a target atom with atomic number Z_2 and mass m_2, compute the scattering angle θ_c which will transfer this much energy to the target from the solution of

$$E_{min} = E_{inc} \frac{4\, m_1\, m_2}{(m_1 + m_2)^2} \sin^2 \frac{\theta_c}{2} \tag{6.57}$$

. Then, noting that α from eq. 6.54 is a number very close to unity, one can solve for an approximate impact parameter b with a single root-finding operation to find the classical turning point. Then, define the total cross section to be $\sigma_0 = \pi b^2$, the area of the disk inside of which the passage of an ion will cause at least the minimum interesting energy transfer. Because this process is relatively expensive, and the result is needed extremely frequently, the values of $\sigma_0(E_{inc})$ are precomputed for each pairing of incident ion and target atom, and the results cached in a cubic-spline interpolation table. However, since the actual result isn't very critical, the cached results can be stored in a very coarsely sampled table without degrading the calculation at

all, as long as the values of the l_μ used in the impact parameter selection are rigorously consistent with this table.

The final necessary piece of the scattering integral calculation is the statistical selection of the impact parameter b to be used in each scattering event. This selection is done following the original algorithm from TRIM, where the cumulative probability distribution for impact parameters is

$$P(b) = 1 - \exp\left(\frac{-\pi\, b^2}{\sigma_0}\right) \tag{6.58}$$

where $N\,\sigma_0 \equiv 1/l_\mu$ where N is the total number density of scattering centers in the target material and l_μ is the mean free path computed in the conventional way. To produce this distribution from a uniform random variate r on (0,1], the necessary function is

$$b = \sqrt{\frac{-\log r}{\pi\, N\, l_\mu}} \tag{6.59}$$

This choice of sampling function does have the one peculiarity that it can produce values of the impact parameter which are larger than the impact parameter which results in the cutoff energy transfer, as discussed above in the section on the total cross section, with probability $1/e$. When this occurs, the scattering event is not processed further, since the energy transfer is below threshold. For this reason, impact parameter selection is carried out very early in the algorithm, so the effort spent on uninteresting events is minimized.

The above choice of impact sampling is modified when the mean-free-path is very short. If $\sigma_0 > \pi\left(\frac{l}{2}\right)^2$ where l is the approximate lattice constant of the material, as defined by $l = N^{-1/3}$, the sampling is replaced by uniform sampling on a disk of radius $l/2$, so that

$$b = \frac{l}{2}\sqrt{r} \tag{6.60}$$

This takes into account that impact parameters larger than half the lattice spacing do not occur, since then one is closer to the adjacent atom. This also derives from TRIM.

One extra feature is included in our model, to accelerate the production of relatively rare events such as high-angle scattering. This feature is a cross-section scaling algorithm, which allows the user access to an unphysical control of the algorithm which arbitrarily scales the cross-sections for a selected fraction of interactions. This is implemented as a two-parameter

adjustment to the central algorithm. The first parameter is a selection frequency f_h which sets what fraction of the interactions will be modified. The second parameter is the scaling factor for the cross-section. This is implemented by, for a fraction f_h of interactions, scaling the impact parameter by $b' = b/\sqrt{scale}$. This feature, if used with care so that it does not provide excess multiple-scattering, can provide between 10 and 100-fold improvements to event rates. If used without checking the validity by comparing to un-adjusted scattering computations, it can also provide utter nonsense.

6.4.2 Implementation Details

The coefficients for the summation to approximate the integral for α in eq.(6.54) are derived from the values in Abramowitz & Stegun [4], altered to make the change-of-variable used for this integral. There are two basic steps to the transformation. First, since the provided abscissas x_i and weights w_i are for integration on [-1,1], with only one half of the values provided, and in this work the integration is being carried out on [0,1], the abscissas are transformed as:

$$y_i \in \left\{ \frac{1 \mp x_i}{2} \right\} \tag{6.61}$$

Then, the primary change-of-variable is applied resulting in:

$$q_i = \cos \frac{\pi\, y_i}{2} \tag{6.62}$$

$$w'_i = \frac{w_i}{2} \sin \frac{\pi\, y_i}{2} \tag{6.63}$$

except for the first coefficient $w'_1$where the sin() part of the weight is taken into the limit of λ_0 as described in eq.(6.55). This value is just $w'_1 = w_1/2$.

6.4.3 Status of this document

06.12.07 created by V. Ivanchenko from paper of M.H. Mendenhall and R.A. Weller
06.12.07 further edited by M. Mendenhall to bring contents of paper up-to-date with current implementation.

Bibliography

[1] M.H. Mendenhall, R.A. Weller, An algorithm for computing screened Coulomb scattering in Geant4, *Nucl. Instr. Meth. B 227 (2005) 420.*

[2] M.H. Mendenhall, R.A. Weller, Algorithms for the rapid computation of classical cross sections for screened coulomb collisions, *Nucl. Instr. Meth. in Physics Res. B58 (1991) 11.*

[3] J.P. Biersack, L.G. Haggmark, A Monte Carlo computer program for the transport of energetic ions in amorphous targets, *Nucl. Instr. Meth. in Physics Res. 174 (1980) 257.*

[4] M. Abramowitz, I. Stegun (Eds.), Handbook of Mathematical Functions, *Dover, New York, 1965, pp. 888, 920.*

6.5 Single Scattering, Screened Coulomb Potential and NIEL

Alternative model of Coulomb scattering of ions have been developed based on [1] and references therein. The advantage of this model is the wide applicability range in energy from 50 keV to 100 TeV per nucleon.

6.5.1 Nucleus–Nucleus Interactions

As discussed in Ref. [1], at small distances from the nucleus, the potential energy is a Coulomb potential, while - at distances larger than the Bohr radius - the nuclear field is screened by the fields of atomic electrons. The interaction between two nuclei is usually described in terms of an interatomic Coulomb potential (e.g., see Section 2.1.4.1 of Ref. [2] and Section 4.1 of Ref. [3]), which is a function of the radial distance r between the two nuclei

$$V(r) = \frac{zZe^2}{r}\ \Psi_{\rm I}(r_{\rm r}), \tag{6.64}$$

where ez (projectile) and eZ (target) are the charges of the bare nuclei and $\Psi_{\rm I}$ is the *interatomic screening function* and $r_{\rm r}$ is given by

$$r_{\rm r} = \frac{r}{{\rm a}_{\rm I}}, \tag{6.65}$$

with ${\rm a}_{\rm I}$ the so-called *screening length* (also termed *screening radius*). In the framework of the Thomas–Fermi model of the atom (e.g., see Ref. [1] and references therein) - thus, following the approach of ICRU Report 49 (1993) -, a commonly used screening length for $z = 1$ incoming particles is that from Thomas–Fermi

$${\rm a}_{\rm TF} = \frac{C_{\rm TF}\,{\rm a}_0}{Z^{1/3}}, \tag{6.66}$$

and - for incoming particles with $z \geq 2$ - that introduced by Ziegler, Biersack and Littmark (1985) (and termed *universal screening length*):

$${\rm a}_{\rm U} = \frac{C_{\rm TF}\,{\rm a}_0}{z^{0.23} + Z^{0.23}}, \tag{6.67}$$

where

$${\rm a}_0 = \frac{\hbar^2}{me^2}$$

is the Bohr radius, m is the electron rest mass and

$$C_{\rm TF} = \frac{1}{2}\left(\frac{3\,\pi}{4}\right)^{2/3} \simeq 0.88534$$

is a constant introduced in the Thomas–Fermi model.

The simple scattering model due to Wentzel [5] - with a single exponential screening-function $\Psi_{\rm I}(r_{\rm r})$ {e.g., see Ref. [1] and references therein} - was repeatedly employed in treating single and multiple Coulomb-scattering with screened potentials. The resulting elastic differential cross section differs from the Rutherford differential cross section by an additional term - the so-called *screening parameter* - which prevents the divergence of the cross section when the angle θ of scattered particles approaches 0°. The screening parameter $A_{\rm s}$ [e.g., see Equation (21) of Bethe (1953)] - as derived by Molière (1947, 1948) for the single Coulomb scattering using a Thomas–Fermi potential - is expressed as

$$A_{\rm s} = \left(\frac{\hbar}{2\,p\;a_{\rm I}}\right)^2 \left[1.13 + 3.76 \times \left(\frac{\alpha z Z}{\beta}\right)^2\right] \tag{6.68}$$

where $a_{\rm I}$ is the screening length - from Eqs. (6.66, 6.67) for particles with $z = 1$ and $z \geq 2$, respectively; α is the fine-structure constant; p (βc) is the momentum (velocity) of the incoming particle undergoing the scattering onto a target supposed to be initially at rest; c and $\hbar$ are the speed of light and the reduced Planck constant, respectively. When the (relativistic) mass - with corresponding rest mass m - of the incoming particle is much lower than the rest mass (M) of the target nucleus, the differential cross section - obtained from the Wentzel–Molière treatment of the single scattering - is:

$$\frac{d\sigma^{\rm WM}(\theta)}{d\Omega} = \left(\frac{zZe^2}{2\,p\,\beta c}\right)^2 \frac{1}{\left[A_{\rm s} + \sin^2(\theta/2)\right]^2}. \tag{6.69}$$

Equation (6.69) differs from Rutherford's formula - as already mentioned - for the additional term $A_{\rm s}$ to $\sin^2(\theta/2)$. As discussed in Ref. [1], for $\beta \simeq 1$ (i.e., at very large p) and with $A_{\rm s} \ll 1$, one finds that the cross section approaches a constant:

$$\sigma_{\rm c}^{\rm WM} \simeq \left(\frac{2\,zZe^2 a_{\rm I}}{\hbar c}\right)^2 \frac{\pi}{1.13 + 3.76 \times (\alpha z Z)^2}. \tag{6.70}$$

As discussed in Ref. [1] and references therein, for a scattering under the action of a central potential (for instance that due to a screened Coulomb field), when the rest mass of the target particle is no longer much larger than the relativistic mass of the incoming particle, the expression of the differential cross section must properly be re-written - in the center of mass system - in terms of an "effective particle" with momentum equal to that of the incoming particle (p'_{in}) and rest mass equal to the relativistic reduced mass

$$\mu_{\rm rel} = \frac{mM}{M_{1,2}}, \tag{6.71}$$

where $M_{1,2}$ is the invariant mass; m and M are the rest masses of the incoming and target particles, respectively. The "effective particle" velocity is given by:

$$\beta_{\rm r} c = c \sqrt{\left[1 + \left(\frac{\mu_{\rm rel} c}{p'_{in}}\right)^2\right]^{-1}}.$$

Thus, one finds (e.g, see Ref. [1]):

$$\frac{d\sigma^{\rm WM}(\theta')}{d\Omega'} = \left(\frac{zZe^2}{2\,p'_{in}\,\beta_{\rm r} c}\right)^2 \frac{1}{\left[A_{\rm s} + \sin^2(\theta'/2)\right]^2}, \tag{6.72}$$

with

$$A_{\rm s} = \left(\frac{\hbar}{2\,p'_{in}\;a_{\rm I}}\right)^2 \left[1.13 + 3.76 \times \left(\frac{\alpha z Z}{\beta_{\rm r}}\right)^2\right] \tag{6.73}$$

and θ' the scattering angle in the center of mass system.

The energy T transferred to the recoil target is related to the scattering angle as $T = T_{max} \sin^2(\theta'/2)$ - where T_{max} is the maximum energy which can be transferred in the scattering (e.g., see Section 1.5 of Ref. [2]) -, thus, assuming an isotropic azimuthal distribution one can re-write Eq. (6.72) in terms of the kinetic recoil energy T of the target

$$\frac{d\sigma^{\rm WM}(T)}{dT} = \pi \left(\frac{zZe^2}{p'_{in}\,\beta_{\rm r} c}\right)^2 \frac{T_{max}}{\left[T_{max}\,A_{\rm s} + T\right]^2}. \tag{6.74}$$

Furthermore, one can demonstrates that Eq. (6.74) can be re-written as (e.g, see Ref. [1]);

$$\frac{d\sigma^{\rm WM}(T)}{dT} = 2\,\pi \left(zZe^2\right)^2 \frac{E^2}{p^2 M c^4} \frac{1}{\left[T_{max}\,A_{\rm s} + T\right]^2} \tag{6.75}$$

with p and E the momentum and total energy of the incoming particle in the laboratory. Equation (6.75) expresses - as already mentioned - the differential cross section as a function of the (kinetic) energy T achieved by the recoil target.

6.5.2 Nuclear Stopping Power

Using Eq. (6.75) the nuclear stopping power - in $\mathrm{MeV\,cm^{-1}}$ - is obtained as

$$-\left(\frac{dE}{dx}\right)_{\rm nucl} = 2\,n_A \pi \left(zZe^2\right)^2 \frac{E^2}{p^2 M c^4} \left[\frac{A_{\rm s}}{A_{\rm s}+1} - 1 + \ln\left(\frac{A_{\rm s}+1}{A_{\rm s}}\right)\right] \tag{6.76}$$

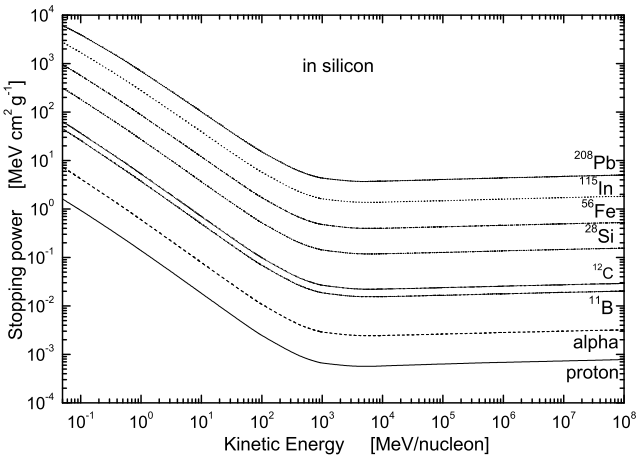

Figure 6.2: Nuclear stopping power from Ref. [1] - in MeV cm^2 g^{-1} - calculated using Eq. (6.76) in silicon is shown as a function of the kinetic energy per nucleon - from 50 keV/nucleon up 100 TeV/nucleon - for protons, α-particle and ^{11}B-, ^{12}C-, ^{28}Si-, ^{56}Fe-, ^{115}In-, ^{208}Pb-nuclei.

with n_A the number of nuclei (atoms) per unit of volume and, finally, the negative sign indicates that the energy is lost by the incoming particle (thus, achieved by recoil targets). As discussed in Ref. [1], a slight increase of the nuclear stopping power with energy is expected because of the decrease of the screening parameter with energy.

For instance, in Fig. 6.2 the nuclear stopping power in silicon - in MeV cm^2 g^{-1} - is shown as a function of the kinetic energy per nucleon - from 50 keV/nucleon up 100 TeV/nucleon - for protons, α-particles and ^{11}B-, ^{12}C-, ^{28}Si-, ^{56}Fe-, ^{115}In-, ^{208}Pb-nuclei.

A comparison of the present treatment with that obtained from Ziegler, Biersack and Littmark (1985) - available in SRIM (2008) [8] - using the so-called *universal screening potential* (see also Ref. [9]) is discussed in Ref. [1]: a good agreement is achieved down to about 150 keV/nucleon. At large energies, the non-relativistic approach due to Ziegler, Biersack and Littmark (1985) becomes less appropriate and deviations from stopping powers calculated by means of the universal screening potential are expected and observed.

The non-relativistic approach - based on the universal screening potential - of Ziegler, Biersack and Littmark (1985) was also used by ICRU (1993) to calculate nuclear stopping powers due to protons and α-particles in materials. ICRU (1993) used as screening lengths those from Eqs. (6.66, 6.67) for protons and α-particles, respectively. As discussed in Ref. [1], the stopping powers for protons (α-particles) from Eq. (6.76) are less than $\approx 5\%$ larger

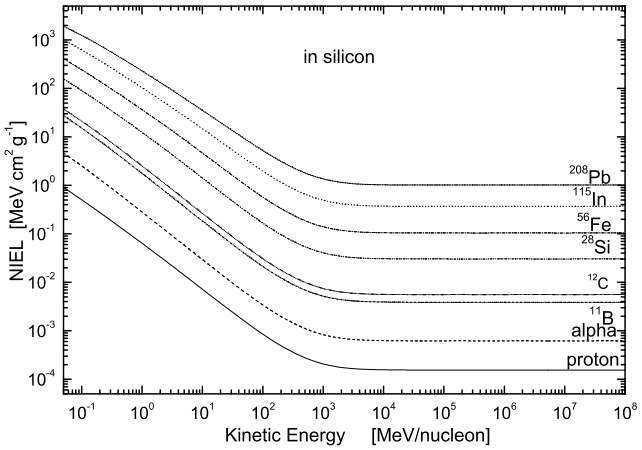

Figure 6.3: Non-ionizing stopping power from Ref. [1] - in $\mathrm{MeV\,cm^2\,g^{-1}}$ - calculated using Eq. (6.79) in silicon is shown as a function of the kinetic energy per nucleon - from 50 keV/nucleon up 100 TeV/nucleon - for protons, α-particles and ^{11}B-, ^{12}C-, ^{28}Si-, ^{56}Fe-, ^{115}In-, ^{208}Pb-nuclei. The threshold energy for displacement is 21 eV in silicon.

than those reported by ICRU (1993) from 50 keV/nucleon up to $\approx$ 8 MeV (19 MeV/nucleon). At larger energies the stopping powers from Eq. (6.76) differ from those from ICRU - as expected - due to the complete relativistic treatment of the present approach (see Ref. [1]).

The simple screening parameter used so far [Eq. (6.73)] - derived by Molière (1947) - can be modified by means of a *practical correction*, i.e.,

$$A'_{\mathrm{s}} = \left(\frac{\hbar}{2\,p'_{in}\;a_{\mathrm{I}}}\right)^2 \left[1.13 + 3.76 \times C \left(\frac{\alpha z Z}{\beta_{\mathrm{r}}}\right)^2\right], \tag{6.77}$$

to achieve a better agreement with low energy calculations of Ziegler, Biersack and Littmark (1985). For instance - as discussed in Ref. [1] -, for α-particles and heavier ions, with

$$C = (10\pi z Z \alpha)^{0.12} \tag{6.78}$$

the stopping powers obtained from Eq. (6.76) - in which A'_{s} replaces A_{s} - differ from the values of SRIM (2008) by less than $\approx$ 4.7 (3.6) % for α-particles (lead ions) in silicon down to about 50 keV/nucleon. With respect to the tabulated values of ICRU (1993), the agreement for α-particles is usually better than 4% at low energy down to 50 keV/nucleon - a 5% agreement is achieved at about 50 keV/nucleon in case of a lead medium. At very high energy, the stopping power is slightly affected when A'_{s} replaces A_{s} (a further disvussion is found in Ref. [1]).

6.5.3 Non-Ionizing Energy Loss due to Coulomb Scattering

A relevant process - which causes permanent damage to the silicon bulk structure - is the so-called *displacement damage* (e.g., see Chapter 4 of Ref. [2], Ref. [10] and references therein). Displacement damage may be inflicted when a *primary knocked-on atom* (PKA) is generated. The interstitial atom and relative vacancy are termed Frenkel-pair (FP). In turn, the displaced atom may have sufficient energy to migrate inside the lattice and - by further collisions - can displace other atoms as in a collision cascade. This displacement process modifies the bulk characteristics of the device and causes its degradation. The total number of FPs can be estimated calculating the energy density deposited from displacement processes. In turn, this energy density is related to the *Non-Ionizing Energy Loss* (NIEL), i.e., the energy per unit path lost by the incident particle due to displacement processes.

In case of Coulomb scattering on nuclei, the non-ionizing energy-loss can be calculated using the Wentzel–Molière differential cross section [Eq. (6.75)] discussed in Sect. 6.5.1, i.e.,

$$-\left(\frac{dE}{dx}\right)^{\mathrm{NIEL}}_{\mathrm{nucl}} = n_A \int_{T_d}^{T_{max}} T\, L(T)\, \frac{d\sigma^{\mathrm{WM}}(T)}{dT}\, dT \ , \tag{6.79}$$

where E is the kinetic energy of the incoming particle, T is the kinetic energy transferred to the target atom, $L(T)$ is the fraction of T deposited by means of displacement processes. The expression of $L(T)$ - the so-called *Lindhard partition function* - can be found, for instance, in Equations (4.94, 4.96) of Section 4.2.1.1 in Ref. [2] (see also references therein). $T_{\mathrm{de}} = T\, L(T)$ is the so-called *damage energy*, i.e., the energy deposited by a recoil nucleus with kinetic energy T via displacement damages inside the medium. The integral in Eq. (6.79) is computed from the minimum energy T_d - the so-called *threshold energy for displacement*, i.e., that energy necessary to displace the atom from its lattice position - up to the maximum energy T_{max} that can be transferred during a single collision process. T_d is about 21 eV in silicon. For instance, in Fig. 6.3 the non-ionizing energy loss - in $\mathrm{MeV\,cm^2\,g^{-1}}$ - in silicon is shown as a function of the kinetic energy per nucleon - from 50 keV/nucleon up 100 TeV/nucleon - for protons, α-particles and ^{11}B-, ^{12}C-, ^{28}Si-, ^{56}Fe-, ^{115}In-, ^{208}Pb-nuclei.

A further discussion on the agreement with the results obtained by Jun and collaborators (2003) - using a relativistic treatment of Coulomb scattering of protons with kinetic energies above 50 MeV and up to 1 GeV upon silicon - can be found in Ref. [1].

6.5.4 G4IonCoulombScatteringModel

As discussed sofar, high energetic particles may inflict permanent damage to the electronic devices employed in a radiation environment. In particular the *nuclear energy loss* is important for the formation of defects in semiconductor devices. Nuclear energy loss is also responsible for the displacement damage which is the typical cause of degradation for silicon devices. The electromagnetic model *G4IonCoulombScatteringModel* was created in order to simulate the single scattering of protons, alpha particles and all heavier nuclei incident on all target materials in the energy range from 50–100 keV/nucleon to 10 TeV.

6.5.5 The Method

The differential cross section previously described is calculated by means of the class *G4IonCoulombCrossSection* where a modified version of the Wentzel's cross section is used. To solve the scattering problem of heavy ions it is necessary to introduce an effective particle whose mass is equal to the relativistic reduced mass of the system defined as

$$\mu_r \equiv \frac{m_1 m_2 c^2}{E_{cm}}. \tag{6.80}$$

where m_1 and m_2 are incident and target rest masses respectively and E_{cm} (in Eq. (6.71) $M_{1,2} = E_{cm}/c^2$) is the total center of mass energy of the two particles system. The effective particle interacts with a fixed scattering center with interacting potential expressed by Eq. (6.64) . The momentum of the effective particle is equal to the momentum of the incoming particle calculated in the center of mass system ($\mathbf{p}_r \equiv \mathbf{p}_{1cm}$). Since the target particle is inside the material it can be considered at rest in the laboratory as a consequence the magnitude of $\mathbf{p}_r$ is calculated as

$$p_r \equiv p_{1cm} = p_{1lab}\frac{m_2 c^2}{E_{cm}}, \tag{6.81}$$

with E_{cm} given by

$$E_{cm} = \sqrt{(m_1 c^2)^2 + (m_2 c^2)^2 + 2E_{1lab} m_2 c^2}, \tag{6.82}$$

where p_{1lab} and E_{1lab} are the momentum and the total energy of the incoming particle in the laboratory system respectively. The velocity (β_r) of the effective particle is obtained by the relation

$$\frac{1}{\beta_r^2} = 1 + \left(\frac{\mu_r c^2}{p_r c}\right)^2. \tag{6.83}$$

The modified Wentzel's cross section is then equal to:

$$\frac{d\sigma(\theta_r)}{d\Omega} = \left(\frac{Z_1 Z_2 e^2}{p_r c\ \beta_r}\right)^2 \frac{1}{(2A_s + 1 - \cos\theta_r)^2} \tag{6.84}$$

(in Eq. (6.72) $p'_{in} \equiv p_r$) where Z_1 and Z_2 are the nuclear proton numbers of projectile and of target respectively; A_s is the screening coefficient [see Eq. (6.73)] and θ_r is the scattering angle of the effective particle which is equal the one in the center of mass system ($\theta_r \equiv \theta_{1cm}$). Knowing the scattering angle the recoil kinetic energy of the target particle after scattering is calculated by

$$T = m_2 c^2 \left(\frac{p_{1lab} c}{E_{cm}}\right)^2 (1 - \cos\theta_r). \tag{6.85}$$

The momentum and the total energy of the incident particle after scattering in the laboratory system are obtained by the usual Lorentz's transformations.

6.5.6 Implementation Details

In the *G4IonCoulombScatteringModel* the scattering off electrons is not considered: only scattering off nuclei is simulated. Secondary particles are generated when T [Eq. (6.85)] is greater then a given threshold for displacement T_d; it is not cut in range. The user can set this energy threshold T_d by the method *SetRecoilThreshold(G4double T_d)*. The default screening coefficient A_s is given by Eq. (6.73). If the user wants to use the one given by Eq. (6.77) the condition *SetHeavyIonCorr(1)* must be set. When $Z_1 = 1$ the Thomas-Fermi screening length [a_{TF} see Eq. (6.66)] is used in the calculation of A_s. For $Z_1 \geq 2$ the screening length is the universal one [a_U see Eq. (6.67)].
In the *G4IonCoulombCrossSection* the total differential cross section is obtained by the method *NuclearCrossSection()* where the Eq. (6.84) is integrated in the interval (0, π):

$$\sigma = \pi \left(\frac{Z_1 Z_2 e^2}{p_r c\ \beta_r}\right)^2 \frac{1}{A_s(A_s + 1)} \tag{6.86}$$

The cosine of the scattering angle is chosen randomly in the interval (-1, 1) according to the distribution of the total cross section and it is given by the method *SampleCosineTheta()* which returns $(1 - \cos\theta_r)$.

6.5.7 Status of This Document

02.12.10 created by C. Consolandi and P.G. Rancoita
10.12.10 minor edition by V. Ivanchenko

Bibliography

[1] M. Boschini et al., Nuclear and Non-Ionizing Energy-Loss for Coulomb Scattered Particles from Low Energy up to Relativistic Regime in Space Radiation Environment, *Proc. of the ICATPP Conference on Cosmic Rays for Particle and Astroparticle Physics, October 7–8 2010, Villa Olmo, Como, Italy, World Scientific, Singapore (2011);* arXiv:1011.4822v3 [physics.space-ph], available at the web site: *http://arxiv.org/abs/1011.4822*

[2] C. Leroy and P.G. Rancoita, Principles of Radiation Interaction in Matter and Detection, *2nd Edition, World Scientific (Singapore) 2009.*

[3] ICRU, Stopping Powers and Ranges for Protons and Alpha Particles. *ICRU Report 49, 1993.*

[4] J.F. Ziegler, J.P. Biersack, U. Littmark, The Stopping Range of Ions in Solids, *Vol. 1, Pergamon Press (New York) 1985.*

[5] G. Wentzel, *Z. Phys. 40 (1926), 590–593.*

[6] von G. Molière, *Z. Naturforsh. A2 (1947), 133–145; A3 (1948), 78.*

[7] H.A. Bethe, *Phys. Rev. 98 (1953), 1256–1266.*

[8] J.F. Ziegler, M.D. Ziegler, J.P. Biersack, The Stopping and Range of Ions in Matter, *SRIM version 2008.03 (2008)*, available at: *http://www.srim.org/*

[9] J.F. Ziegler, M.D. Ziegler, J.P. Biersack, The Stopping and Range of Ions in Matter, *SRIM Co. (Chester.) 2008.*

[10] C. Leroy and P.G. Rancoita, *Reports on Progress in Physics 70, 4 (2007) 493–625.*

[11] S.R. Messenger et al., *IEEE Trans. on Nucl. Sci. 50 (2003), 1919–1923.*

[12] I. Jun et al., *IEEE Trans. on Nucl. Sci. 50 (2003) 1924–1928.*

6.6 Electron Screened Single Scattering and NIEL

The present treatment[1] of electron–nucleus interaction is based on numerical and analytical approximations of the Mott differential cross section. It accounts for effects due to screened Coulomb potentials, finite sizes and finite rest masses of nuclei for electron with kinetic energies above 200 keV and up to ultra high. This treatment allows one to determine both the total and differential cross sections, thus, to calculate the resulting nuclear and non-ionizing stopping powers (NIEL). Above a few hundreds of MeV, neglecting the effects of finite sizes and rest masses of recoil nuclei the stopping power and NIEL result to be largely underestimated, while, above a few tens of MeV prevents a further large increase, thus, resulting in approaching almost constant values at high energies.

The non-ionizing energy-loss (NIEL) is the energy lost from a particle traversing a unit length of a medium through physical process resulting in permanent displacement damages (e.g. see Ref.[2]). The nuclear stopping power and NIEL deposition - due to elastic Coulomb scatterings - from protons, light- and heavy-ions traversing an absorber were previously dealt[3] and is available in Geant4 (6.5) (see also Sections 1.6, 1.6.1, 2.1.4–2.1.4.2, 4.2.1.6 of Ref.[4]). In the present model included in GEANT4, the nuclear stopping power and NIEL deposition due to elastic Coulomb scatterings of electrons are treated up to ultra relativistic energies.

6.6.1 Scattering Cross Section of Electrons on Nuclei

The scattering of electrons by unscreened atomic nuclei was treated by Mott extending a method - dealing with incident and scattered waves on point-like nuclei - of Wentzel and including effects related to the spin of electrons. The differential cross section (DCS) - the so-called *Mott differential cross section* (MDCS) - was expressed by Mott as two conditionally convergent infinite series in terms of Legendre expansions. In Mott–Wentzel treatment, the scattering occurs on a field of force generating a radially dependent Coulomb - unscreened (screened) in Mott (Wentzel) - potential. Furthermore, the MDCS was derived in the laboratory reference system for infinitely heavy nuclei initially at rest with negligible spin effects and must be numerically evaluated for any specific nuclear target. Effects related to the recoil and finite rest mass of the target nucleus (M) were neglected. Thus, in this framework the total energy of electrons has to be smaller or much smaller than Mc^2.

The MDCS is usually expressed as:

$$\frac{d\sigma^{\rm Mott}(\theta)}{d\Omega} = \frac{d\sigma^{\rm Rut}}{d\Omega}\ \mathcal{R}^{\rm Mott}, \tag{6.87}$$

where $\mathcal{R}^{\rm Mott}$ is the ratio between the MDCS and Rutherford's formula [RDCS, see Equation (1) of Ref.[1]]. For electrons with kinetic energies from several keV up to 900 MeV and target nuclei with $1 \leqslant Z \leqslant 90$, Lijian, Quing and Zhengming[5] provided a practical interpolated expression [Eq. (6.99)] for $\mathcal{R}^{\rm Mott}$ with an average error less than 1%; in the present treatment, that expression - discussed in Sect. 6.6.1 - is the one assumed for $\mathcal{R}^{\rm Mott}$ in Eq. (6.87) hereafter. The analytical expression derived by McKinley and Feshbach[6] for the ratio with respect to Rutherford's formula [Equation (7) of Ref.[6]] is given by:

$$\mathcal{R}^{\rm McF} = 1 - \beta^2 \sin^2(\theta/2) + Z\,\alpha\beta\pi \sin(\theta/2)\,[1 - \sin(\theta/2)] \tag{6.88}$$

with the corresponding differential cross section (McFDCS)

$$\frac{d\sigma^{\rm McF}}{d\Omega} = \frac{d\sigma^{\rm Rut}}{d\Omega}\ \mathcal{R}^{\rm McF}. \tag{6.89}$$

Furthermore, for Mc^2 much larger than the total energy of incoming electron energies the distinction between laboratory (i.e., the system in which the target particle is initially at rest) and center-of-mass (CoM) systems disappears (e.g., see discussion in Section 1.6.1 of Ref.[4]). Furthermore, in the CoM of the reaction the energy transferred from an electron to a nucleus initially at rest in the laboratory system (i.e., its recoil kinetic energy T) is related with the maximum energy transferable $T_{\rm max}$ as

$$T = T_{\rm max}\ \sin^2(\theta'/2) \tag{6.90}$$

[e.g., see Equations (1.27, 1.95) at page 11 and 31, respectively, of Ref.[4]], where θ' is the scattering angle in the CoM system. In addition, one obtains

$$dT = \frac{T_{\rm max}}{4\pi}\, d\Omega'. \tag{6.91}$$

Since for Mc^2 much larger than the electron energy θ is $\approx \theta'$, one finds that Eq. (6.90) can be approximated as

$$T \simeq T_{\rm max} \sin^2(\theta/2)\,, \tag{6.92}$$

$$\Longrightarrow \sin^2(\theta/2) = \frac{T}{T_{\rm max}} \tag{6.93}$$

and

$$dT \simeq \frac{T_{\max}}{4\pi}\, d\Omega. \tag{6.94}$$

Using Eqs. (6.88, 6.93, 6.94), Rutherford's formula and Eq. (6.89) can be respectively rewritten as:

$$\begin{aligned}
\Longrightarrow \frac{d\sigma^{\rm Rut}}{dT} &= \left(\frac{Ze^2}{p\beta c}\right)^2 \frac{\pi T_{\max}}{T^2}, &(6.95)\\
\Longrightarrow \frac{d\sigma^{\rm McF}}{T} &= \left(\frac{Ze^2}{p\beta c}\right)^2 \frac{\pi T_{\max}}{T^2}\left[1-\beta\frac{T}{T_{\max}}(\beta+Z\alpha\pi)+Z\alpha\beta\pi\sqrt{\frac{T}{T_{\max}}}\right] &(6.96)\\
&= \left(\frac{Ze^2}{p\beta c}\right)^2 \frac{\pi T_{\max}}{T^2}\ \mathcal{R}^{\rm McF}(T)
\end{aligned}$$

with

$$\mathcal{R}^{\rm McF}(T) = \left[1-\beta\frac{T}{T_{\max}}(\beta+Z\alpha\pi)+Z\alpha\beta\pi\sqrt{\frac{T}{T_{\max}}}\right]. \tag{6.97}$$

Finally, in a similar way the MDCS [Eq. (6.87)] is

$$\begin{aligned}
\frac{d\sigma^{\rm Mott}(T)}{dT} &= \frac{d\sigma^{\rm Rut}}{dT}\ \mathcal{R}^{\rm Mott}(T)\\
&= \left(\frac{Ze^2}{p\beta c}\right)^2 \frac{\pi T_{\max}}{T^2}\ \mathcal{R}^{\rm Mott}(T) &(6.98)
\end{aligned}$$

with $\mathcal{R}^{\rm Mott}(T)$ from Eq. (6.101).

Interpolated Expression for $\mathcal{R}^{\rm Mott}$

Recently, Lijian, Quing and Zhengming[5] provided a practical interpolated expression [Eq. (6.99)] which is a function of both θ and β for electron energies from several keV up to 900 MeV, i.e.,

$$\mathcal{R}^{\rm Mott} = \sum_{\rm j=0}^{4} a_{\rm j}(Z,\beta)(1-\cos\theta)^{\rm j/2}, \tag{6.99}$$

where

$$a_{\rm j}(Z,\beta) = \sum_{\rm k=1}^{6} b_{\rm k,j}(Z)(\beta-\overline{\beta})^{\rm k-1}, \tag{6.100}$$

and $\overline{\beta}\,c = 0.7181287\,c$ is the mean velocity of electrons within the above mentioned energy range. The coefficients $b_{\rm k,j}(Z)$ are listed in Table 1 of

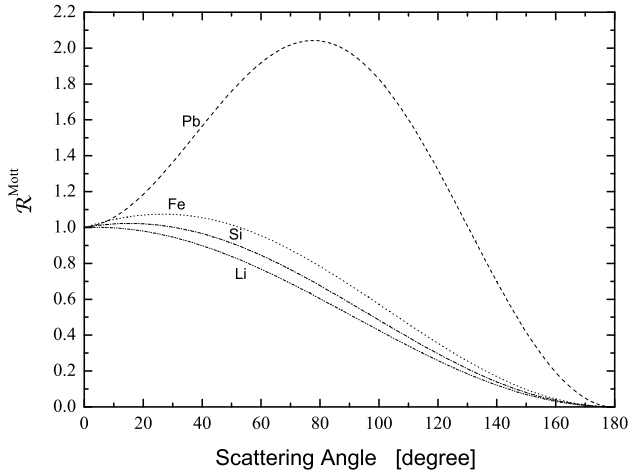

Figure 6.4: $\mathcal{R}^{\mathrm{Mott}}$ obtained from Eq. (6.99) at 100 MeV for Li, Si, Fe and Pb nuclei as a function of scattering angle.

Ref.[5] for $1 \leqslant Z \leqslant 90$. $\mathcal{R}^{\mathrm{Mott}}$ obtained from Eq. (6.99) at 100 MeV is shown in Fig. 6.4 for Li, Si, Fe and Pb nuclei as a function of scattering angle. Furthermore, it has to be remarked that the energy dependence of $\mathcal{R}^{\mathrm{Mott}}$ from Eq. (6.99) was studied and observed to be negligible above ≈ 10 MeV [for instance, see Eq. (6.100)].

Finally, from Eqs.(6.90, 6.99) [e.g., see also Equation (1.93) at page 31 of Ref.[4]], one finds that $\mathcal{R}^{\mathrm{Mott}}$ can be expressed in terms of the transferred energy T as

$$\mathcal{R}^{\mathrm{Mott}}(T) = \sum_{\mathrm{j}=0}^{4} a_{\mathrm{j}}(Z,\beta) \left(\frac{2T}{T_{\mathrm{max}}}\right)^{\mathrm{j}/2} . \tag{6.101}$$

Screened Coulomb Potentials

The simple scattering model due to Wentzel - with a single exponential screening function [e.g., see Equation (2.71) at page 95 of Ref.[4]] - was repeatedly employed in treating single and multiple Coulomb scattering with screened potentials. Neglecting effects like those related to spin and finite size of nuclei, for proton and nucleus interactions on nuclei it was shown that the resulting elastic differential cross section of a projectile with bare nuclear-charge ez on a target with bare nuclear-charge eZ differs from the Rutherford differential cross section (RDCS) by an additional term - the so-called *screening parameter* - which prevents the divergence of the cross section when the angle θ of scattered particles approaches 0° [e.g., see Section 1.6.1 of Ref.[4]]. For $z = 1$ particles the *screening parameter* $A_{\mathrm{s,M}}$ is

expressed as

$$A_{\rm s,M} = \left(\frac{\hbar}{2\,p\;a_{\rm TF}}\right)^2 \left[1.13 + 3.76 \times \left(\frac{\alpha Z}{\beta}\right)^2\right] \tag{6.102}$$

where α, c and $\hbar$ are the fine-structure constant, speed of light and reduced Planck constant, respectively; p (βc) is the momentum (velocity) of the incoming particle undergoing the scattering onto a target supposed to be initially at rest - i.e., in the laboratory system -; $a_{\rm TF}$ is the screening length suggested by Thomas–Fermi

$$\mathrm{a_{TF}} = \frac{C_{\rm TF}\,\mathrm{a_0}}{Z^{1/3}} \tag{6.103}$$

with

$$\mathrm{a_0} = \frac{\hbar^2}{me^2}$$

the Bohr radius, m the electron rest mass and

$$C_{\rm TF} = \frac{1}{2}\left(\frac{3\,\pi}{4}\right)^{2/3} \simeq 0.88534$$

a constant introduced in the Thomas–Fermi model [e.g., see Ref.[3] , Equations (2.73, 2,82) - at page 95 and 99, respectively - of Ref.[4], see also references therein]. The modified Rutherford's formula $[d\sigma^{\rm WM}(\theta)/d\Omega]$, i.e., the *differential cross section - obtained from the Wentzel–Molière treatment of the single scattering* on screened nuclear potential - is given by [e.g., see Equation (2.84) of Ref.[4] and Ref.[3], see also references therein]:

$$\frac{d\sigma^{\rm WM}(\theta)}{d\Omega} = \left(\frac{zZe^2}{2\,p\,\beta c}\right)^2 \frac{1}{\left[A_{\rm s,M} + \sin^2(\theta/2)\right]^2} \tag{6.104}$$

$$= \frac{d\sigma^{\rm Rut}}{d\Omega}\;\mathfrak{F}^2(\theta). \tag{6.105}$$

with

$$\mathfrak{F}(\theta) = \frac{\sin^2(\theta/2)}{A_{\rm s,M} + \sin^2(\theta/2)}. \tag{6.106}$$

$\mathfrak{F}(\theta)$ - the so-called *screening factor* - depends on the scattering angle θ and the screening parameter $A_{\rm s,M}$. As discussed in Sect. 6.6.1, the term $A_{\rm s,M}$ (the screening parameter) cannot be neglected in the DCS [Eq. (6.105)] for scattering angles (θ) within a forward (with respect to the electron direction) angular region narrowing with increasing energy from several degrees (for

high-Z material) at 200 keV down to less than or much less than a mrad above 200 MeV.

An approximated description of elastic interactions of electrons with screened Coulomb fields of nuclei can be obtained by the factorization of the MDCS, i.e., involving Rutherford's formula $[d\sigma^{\rm Rut}/d\Omega]$ for particle with $z = 1$, the screening factor $[\mathfrak{F}(\theta)]$ and the ratio $\mathcal{R}^{\rm Mott}$ between the RDCS and MDCS:

$$\frac{d\sigma_{\rm sc}^{\rm Mott}(\theta)}{d\Omega} \simeq \frac{d\sigma^{\rm Rut}}{d\Omega}\ \mathfrak{F}^2(\theta)\ \mathcal{R}^{\rm Mott}. \tag{6.107}$$

Thus, the corresponding screened differential cross section derived using the analytical expression from McKinley and Feshbach[6] can be approximated with

$$\frac{d\sigma_{\rm sc}^{\rm McF}(\theta)}{d\Omega} \simeq \frac{d\sigma^{\rm Rut}}{d\Omega}\ \mathfrak{F}^2(\theta)\ \mathcal{R}^{\rm McF}. \tag{6.108}$$

Zeitler and Olsen[7] suggested that for electron energies above 200 keV the overlap of spin and screening effects is small for all elements and for all energies; for lower energies the overlapping of the spin and screening effects may be appreciable for heavy elements and large angles.

Finite Nuclear Size

The ratio between the actual measured and that expected from the point-like differential cross section expresses the square of *nuclear form factor* ($|F|$) which, in turn, depends on the momentum transfer q, i.e., that acquired by the target initially at rest:

$$q = \frac{\sqrt{T(T + 2Mc^2)}}{c}, \tag{6.109}$$

with T from Eq. (6.90) or for Mc^2 larger or much larger than the electron energy from its approximate expression Eq. (6.92).

The approximated (factorized) differential cross section for elastic interactions of electrons with screened Coulomb fields of nuclei [Eq. (6.107)] accounting for the effects due to the finite nuclear size is given by:

$$\frac{d\sigma_{{\rm sc},F}^{\rm Mott}(\theta)}{d\Omega} \simeq \frac{d\sigma^{\rm Rut}}{d\Omega}\ \mathfrak{F}^2(\theta)\ \mathcal{R}^{\rm Mott}\,|F(q)|^2\,. \tag{6.110}$$

Thus, using the analytical expression derived by McKinley and Feshbach[6] [Eq. (6.88)] one obtains that the corresponding screened differential cross

section [Eq. (6.108)] accounting for the finite nuclear size effects

$$\frac{d\sigma^{\rm McF}_{{\rm sc},F}(\theta)}{d\Omega} \simeq \frac{d\sigma^{\rm Rut}}{d\Omega}\,\mathfrak{F}^2(\theta)\,\mathcal{R}^{\rm McF}\,|F(q)|^2 \tag{6.111}$$

$$= \frac{d\sigma^{\rm Rut}}{d\Omega}\,\mathfrak{F}^2(\theta)\,|F(q)|^2 \times\left\{1-\beta^2\sin^2(\theta/2)+Z\,\alpha\beta\pi\sin(\theta/2)\,[1-\sin(\theta/2)]\right\} \tag{6.112}$$

In terms of kinetic energy, one can respectively rewrite Eqs. (6.110, 6.111) as

$$\frac{d\sigma^{\rm Mott}_{{\rm sc},F}(T)}{dT} = \frac{d\sigma^{\rm Rut}}{dT}\,\mathfrak{F}^2(T)\,\mathcal{R}^{\rm Mott}(T)\;|F(q)|^2 \tag{6.113}$$

$$\frac{d\sigma^{\rm McF}_{{\rm sc},F}(T)}{dT} \simeq \frac{d\sigma^{\rm Rut}(T)}{dT}\,\mathfrak{F}^2(T)\;\mathcal{R}^{\rm McF}(T)\;|F(q)|^2 \tag{6.114}$$

with $d\sigma^{\rm Rut}/dT$ from Eq. (6.95), $\mathcal{R}^{\rm Mott}(T)$ from Eq. (6.101), $\mathcal{R}^{\rm McF}(T)$ from Eq. (6.97) and, using Eqs. (6.90, 6.92, 6.106),

$$\mathfrak{F}(T) = \frac{T}{T_{\rm max}A_{\rm s,M}+T}.$$

For instance, the form factor $F_{\rm exp}$ is

$$F_{\rm exp}(q) = \left[1+\frac{1}{12}\left(\frac{qr_{\rm n}}{\hbar}\right)^2\right]^{-2}, \tag{6.115}$$

where $r_{\rm n}$ is the nuclear radius, $r_{\rm n}$ can be parameterized by

$$r_{\rm n} = 1.27A^{0.27}\ {\rm fm} \tag{6.116}$$

with A the atomic weight. Equation (6.116) provides values of $r_{\rm n}$ in agreement up to heavy nuclei (like Pb and U) with those available, for instance, in Table 1 of Ref.[8] .

Finite Rest Mass of Target Nucleus

The DCS treated in Sects. 6.6.1–6.6.1 is based on the extension of MDCS to include effects due to interactions on screened Coulomb potentials of nuclei and their finite size. However, the electron energies were considered small (or much smaller) with respect to that (Mc^2) corresponding to rest mass (M) target nuclei.

The Rutherford scattering on screened Coulomb fields - i.e., under the action of a central forces - by massive charged particles at energies large or

much larger than Mc^2 was treated by Boschini et al.[3] in the CoM system (e.g., see also Sections 1.6, 1.6.1, 2.1.4.2 of Ref.[4] and references therein). It was shown that the differential cross section [$d\sigma^{\rm WM}(\theta')/d\Omega'$ with θ' the scattering angle in the CoM system] is that one derived for describing the interaction on a fixed scattering center of a particle with i) momentum $p'_{\rm r}$ equal to the momentum of the incoming particle (i.e., the electron in the present treatment) in the CoM system and ii) rest mass equal to the *relativistic reduced mass* $\mu_{\rm rel}$ [e.g., see Equations (1.80, 1.81) at page 28 of Ref.[4]]. $\mu_{\rm rel}$ is given by

$$\mu_{\rm rel} = \frac{mM}{M_{1,2}} \tag{6.117}$$

$$= \frac{mMc}{\sqrt{m^2c^2 + M^2c^2 + 2\,M\sqrt{m^2c^4 + p^2c^2}}}, \tag{6.118}$$

where p is the momentum of the incoming particle (the electron in the present treatment) in the laboratory system: m is the rest mass of the incoming particle (i.e., the electron rest mass); finally, $M_{1,2}$ is the invariant mass - e.g., Section 1.3.2 of Ref.[4] - of the two-particle system. Thus, the velocity of the interacting particle is [e.g., see Equation (1.82) at page 29 of Ref.[4]]

$$\beta'_{\rm r}c = c\sqrt{\left[1 + \left(\frac{\mu_{\rm rel}c}{p'_{\rm r}}\right)^2\right]^{-1}}. \tag{6.119}$$

For an incoming particle with $z = 1$, $d\sigma^{\rm WM}(\theta')/d\Omega'$ is given by

$$\frac{d\sigma^{\rm WM'}(\theta')}{d\Omega'} = \left(\frac{Ze^2}{2\,p'_{\rm r}\,\beta'_{\rm r}c}\right)^2 \frac{1}{\left[A_{\rm s} + \sin^2(\theta'/2)\right]^2}, \tag{6.120}$$

with

$$A_{\rm s} = \left(\frac{\hbar}{2\,p'_{\rm r}\,a_{\rm TF}}\right)^2 \left[1.13 + 3.76 \times \left(\frac{\alpha Z}{\beta'_{\rm r}}\right)^2\right] \tag{6.121}$$

the screening factor [e.g., see Equations (2.87, 2.88) at page 103 of Ref.[4]]. Equation (6.120) can be rewritten as

$$\frac{d\sigma^{\rm WM'}(\theta')}{d\Omega'} = \frac{d\sigma^{\rm Rut'}(\theta')}{d\Omega'}\,\mathfrak{F}^2_{\rm CoM}(\theta') \tag{6.122}$$

with

$$\frac{d\sigma^{\rm Rut'}(\theta')}{d\Omega'} = \left(\frac{Ze^2}{2p'_{\rm r}\beta'_{\rm r}c}\right)^2 \frac{1}{\sin^4(\theta'/2)} \tag{6.123}$$

the corresponding RDCS for the reaction in the CoM system [e.g., see Equation (1.79) at page 28 of Ref.[4]] and

$$\mathfrak{F}_{\rm CoM}(\theta') = \frac{\sin^2(\theta'/2)}{A_{\rm s} + \sin^2(\theta'/2)} \tag{6.124}$$

the screening factor. Using, Eqs. (6.90, 6.91), one can respectively rewrite Eqs. (6.123, 6.124, 6.122, 6.120) as

$$\frac{d\sigma^{\rm Rut'}}{dT} = \pi \left(\frac{Ze^2}{p'_{\rm r}\beta'_{\rm r}c}\right)^2 \frac{T_{\rm max}}{T^2} \tag{6.125}$$

$$\mathfrak{F}_{\rm CoM}(T) = \frac{T}{T_{\rm max}A_{\rm s} + T} \tag{6.126}$$

$$\frac{d\sigma^{\rm WM'}(T)}{dT} = \frac{d\sigma^{\rm Rut'}}{dT}\ \mathfrak{F}_{\rm CoM}(T) \tag{6.127}$$

$$\frac{d\sigma^{\rm WM'}(T)}{dT} = \pi \left(\frac{Ze^2}{p'_{\rm r}\beta'_{\rm r}c}\right)^2 \frac{T_{\rm max}}{(T_{\rm max}A_{\rm s} + T)^2}. \tag{6.128}$$

[e.g., see Equation (2.90) at page 103 of Ref.[4] or Equation (13) of Ref.[3]].

To account for the finite rest mass of target nucleus the factorized MDCS [Eq. (6.110)] has to be re-expressed in the CoM system using as:

$$\frac{d\sigma^{\rm Mott}_{{\rm sc},F,{\rm CoM}}(\theta')}{d\Omega'} \simeq \frac{d\sigma^{\rm Rut'}(\theta')}{d\Omega'}\ \mathfrak{F}^2_{\rm CoM}(\theta')\ \mathcal{R}^{\rm Mott}_{\rm CoM}(\theta')\ \ |F(q)|^2, \tag{6.129}$$

where $F(q)$ is the nuclear form factor (Sect. 6.6.1) with q the momentum transfer to the recoil nucleus [Eq. (6.109)]; finally, as discussed in Sect. 6.6.1, $\mathcal{R}^{\rm Mott}$ exhibits almost no dependence on electron energy above $\approx 10\,{\rm MeV}$, thus, since at low energies $\theta \backsimeq \theta'$ and $\beta \backsimeq \beta'_{\rm r}$, $\mathcal{R}^{\rm Mott}_{\rm CoM}(\theta')$ is obtained replacing θ and $\beta'_{\rm r}$ with θ' and $\beta'_{\rm r}$, respectively, in Eq. (6.99).

Using the analytical expression derived by McKinley and Feshbach[6] , one finds that the corresponding screened differential cross section accounting for the finite nuclear size effects [Eqs. (6.111, 6.112)] can be re-expressed as

$$\frac{d\sigma^{\rm McF}_{{\rm sc},F,{\rm CoM}}(\theta')}{d\Omega'} \simeq \frac{d\sigma^{\rm Rut'}(\theta')}{d\Omega'}\ \mathfrak{F}^2_{\rm CoM}(\theta')\ \ \mathcal{R}^{\rm McF}_{\rm CoM}(\theta')\ \ |F(q)|^2 \tag{6.130}$$

with

$$\mathcal{R}^{\rm McF}_{\rm CoM}(\theta') = \left\{1 - \beta_{\rm r}^2 \sin^2(\theta'/2) + Z\,\alpha\beta'_{\rm r}\pi \sin(\theta'/2)\,[1 - \sin(\theta'/2)]\right\}. \tag{6.131}$$

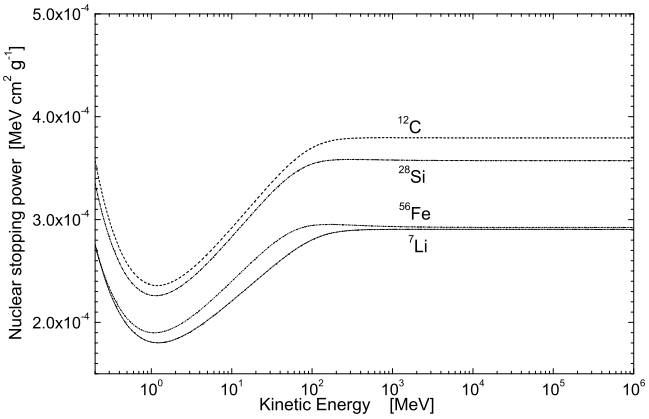

Figure 6.5: In MeV cm^2/g, nuclear stopping powers in ^{7}Li, ^{12}C, ^{28}Si and ^{56}Fe - calculated from Eq. (6.136) - and divided by the density of the material as a function of the kinetic energy of electrons from 200 keV up to 1 TeV.

In terms of kinetic energy T, from Eqs. (6.90, 6.91) one can respectively rewrite Eqs. (6.129, 6.130) as

$$\frac{d\sigma^{\rm Mott}_{{\rm sc},F,{\rm CoM}}(T)}{dT} = \frac{d\sigma^{\rm Rut'}}{dT}\,\mathfrak{F}^2_{\rm CoM}(T)\,\mathcal{R}^{\rm Mott}_{\rm CoM}(T)\,\left|F(q)\right|^2 \qquad (6.132)$$

$$\frac{d\sigma^{\rm McF}_{{\rm sc},F,{\rm CoM}}(T)}{dT} \simeq \frac{d\sigma^{\rm Rut'}(T)}{dT}\,\mathfrak{F}^2_{\rm CoM}(T)\,\mathcal{R}^{\rm McF}_{\rm CoM}(T)\,\left|F(q)\right|^2 \qquad (6.133)$$

with $d\sigma^{\rm Rut'}/dT$ from Eq. (6.125), $\mathfrak{F}_{\rm CoM}(T)$ from Eq. (6.126) and $\mathcal{R}^{\rm McF}_{\rm CoM}(T)$ replacing β with $\beta'_{\rm r}$ in Eq. (6.97), i.e.,

$$\mathcal{R}^{\rm McF}_{\rm CoM}(T) = \left[1-\beta'_{\rm r}\frac{T}{T_{\rm max}}(\beta'_{\rm r}+Z\alpha\pi)+Z\alpha\beta'_{\rm r}\pi\sqrt{\frac{T}{T_{\rm max}}}\right]. \qquad (6.134)$$

Finally, as discussed in Sect. 6.6.1, $\mathcal{R}^{\rm Mott}(T)$ exhibits almost no dependence on electron energy above ≈ 10 MeV, thus, since at low energies $\theta \backsimeq \theta'$ and $\beta \backsimeq \beta'_{\rm r}$, $\mathcal{R}^{\rm Mott}_{\rm CoM}(T)$ is obtained replacing β with $\beta'_{\rm r}$ in Eq. (6.101).

6.6.2 Nuclear Stopping Power of Electrons

Using Eq. (6.132), the nuclear stopping power - in MeV cm^{-1} - of Coulomb electron–nucleus interaction can be obtained as

$$-\left(\frac{dE}{dx}\right)^{\rm Mott}_{\rm nucl} = n_A\int_0^{T_{max}}\frac{d\sigma^{\rm Mott}_{{\rm sc},F,{\rm CoM}}(T)}{dT}\,T\,dT \qquad (6.135)$$

with n_A the number of nuclei (atoms) per unit of volume [e.g., see Equation (1.71) of Ref.[4]] and, finally, the negative sign indicates that the energy

is lost by the electron (thus, achieved by recoil targets). Using the analytical approximation derived by McKinley and Feshbach[6], i.e., Eq. (6.133), for the nuclear stopping power one finds

$$-\left(\frac{dE}{dx}\right)^{\mathrm{McF}}_{\mathrm{nucl}} = n_A \int_0^{T_{max}} \frac{d\sigma^{\mathrm{McF}}_{\mathrm{sc},F,\mathrm{CoM}}(T)}{dT}\, T\, dT. \tag{6.136}$$

As already mentioned in Sect. 6.6.1, the large momentum transfers - corresponding to large scattering angles - are disfavored by effects due to the finite nuclear size accounted for by means of the nuclear form factor (Sect.6.6.1). For instance, the ratios of nuclear stopping powers of electrons in silicon are shown in Ref.[1] as a function of the kinetic energies of electrons from 200 keV up to 1 TeV. These ratios are the nuclear stopping powers calculated neglecting i) nuclear size effects (i.e., for $|F_{\mathrm{exp}}|^2 = 1$) and ii) effects due to the finite rest mass of the target nucleus [i.e., in Eq. (6.136) replacing $d\sigma^{\mathrm{McF}}_{\mathrm{sc},F,\mathrm{CoM}}(T)/dT$ with $d\sigma^{\mathrm{McF}}_{\mathrm{sc},F}(T)/dT$ from Eq. (6.114)] both divided by that one obtained using Eq. (6.136). Above a few tens of MeV, a larger stopping power is found assuming $|F_{\mathrm{exp}}|^2 = 1$ and, in addition, above a few hundreds of MeV the stopping power largely decreases when the effects of nuclear rest mass are not accounted for.

In Fig. 6.5 , the nuclear stopping powers in ^{7}Li, ^{12}C, ^{28}Si and ^{56}Fe are shown as a function of the kinetic energy of electrons from 200 keV up to 1 TeV. These nuclear stopping powers in MeV cm^2/g are calculated from Eq. (6.136) and divided by the density of the medium.

6.6.3 Non-Ionizing Energy-Loss of Electrons

In case of Coulomb scattering of electrons on nuclei, the non-ionizing energy-loss can be calculated using (as discussed in Sect. 6.6.1–6.6.2) the MDCRS or its approximate expression McFDCS [e.g., Eqs. (6.132, 6.133), respectively], once the screened Coulomb fields, finite sizes and rest masses of nuclei are accounted for, i.e., in Mev/cm

$$-\left(\frac{dE}{dx}\right)^{\mathrm{NIEL}}_{\mathrm{n,Mott}} = n_A \int_{T_d}^{T_{max}} T\, L(T)\, \frac{d\sigma^{\mathrm{Mott}}_{\mathrm{sc},F,\mathrm{CoM}}(T)}{dT}\, dT \tag{6.137}$$

or

$$-\left(\frac{dE}{dx}\right)^{\mathrm{NIEL}}_{\mathrm{n,McF}} = n_A \int_{T_d}^{T_{max}} T\, L(T)\, \frac{d\sigma^{\mathrm{McF}}_{\mathrm{sc},F,\mathrm{CoM}}(T)}{dT}\, dT \tag{6.138}$$

[e.g., see Equation (4.113) at page 402 and, in addition, Sections 4.2.1–4.2.1.2 of Ref.[4]], where T is the kinetic energy transferred to the target nucleus,

$L(T)$ is the fraction of T deposited by means of displacement processes. The *Lindhard partition function*, $L(T)$, can be approximated using the so-called *Norgett–Robintson–Torrens expression* [e.g., see Equations (4.121, 4.123) at pages 404 and 405, respectively, of Ref.[4] (see also references therein)]. $T_{\rm de} = T\,L(T)$ is the so-called *damage energy*, i.e., the energy deposited by a recoil nucleus with kinetic energy T via displacement damages inside the medium. In Eqs. (6.137, 6.138) the integral is computed from the minimum energy T_d - the so-called *threshold energy for displacement*, i.e., that energy necessary to displace the atom from its lattice position - up to the maximum energy T_{max} that can be transferred during a single collision process. For instance, T_d is about 21 eV in silicon requiring electrons with kinetic energies above ≈ 220 kev.

As already discussed with respect to nuclear stopping powers in Sect. 6.6.2, the large momentum transfers (corresponding to large scattering angles) are disfavored by effects due to the finite nuclear size accounted for by the nuclear form factor. For instance, the ratios of NIELs for electrons in silicon are shown in Ref.[1] as a function of the kinetic energy of electrons from 220 keV up to 1 TeV. These ratios are the NIELs calculated neglecting i) nuclear size effects (i.e., for $|F_{\rm exp}|^2 = 1$) and ii) effects due to the finite rest mass of the target nucleus [i.e., in Eq. (6.138) replacing $d\sigma^{\rm McF}_{{\rm sc},F,{\rm CoM}}(T)/dT$ with $d\sigma^{\rm McF}_{{\rm sc},F}(T)/dT$ from Eq. (6.114)] both divided by that one obtained using Eq. (6.138). Above ≈ 10 MeV, the NIEL is $\approx 20\%$ larger assuming $|F_{\rm exp}|^2 = 1$ and, in addition, above (100–200) MeV the calculated NIEL largely decreases when the effects of nuclear rest mass are not accounted for.

6.7 *G4eSingleScatteringModel*

The *G4eSingleScatteringModel* performs the single scattering interaction of electrons on nuclei. The differential cross section (DCS) for the energy transferred is define in the *G4ScreeningMottCrossSection* class. In this class the analytical McKinley and Feshbach [6] Mott differential cross Section approximation is implemented. This CDS is modified by the introduction of the Moliere's [9] screening coefficient. In addition the exponential charge distribution Nuclear Form Factor is applied [10]. This treatment is fully performed in the center of mass system and the usual Lorentz transformations are applied to obtained the energy and momentum quantities in the laboratory system after scattering. This model well simulates the interacting process for low scattering angles and it is suitable for high energy electrons (from 200 keV) incident on medium light target nuclei. The nuclear energy loss (i.e. nuclear stopping power) is calculated for every single interaction. In

addition the production of secondary scattered nuclei is simulated from a threshold kinetic energy which can be decided by the user (threshold energy for displacement).

6.7.1 The method

In the *G4eSingleScatteringModel* the method *ComputeCrossSectionPerAtom()* performs the total cross section computation. The *SetupParticle()* and the *DefineMaterial()* methods are called to defined the incident and target particles. Before the total cross section computation, the *SetupKinematic()* method of the *G4ScreeningMottCrossSection* class calculates all the physical quantities in the center of mass system (CM). The scattering in the CM system is equivalent to the one of an effective particle which interacts with a fixed scattering center. The effective particle rest mass is equal to the relativistic reduced mass of the system μ whose expression is calculated by:

$$\mu = m\frac{Mc^2}{E_{cm}} \tag{6.139}$$

where m and M are rest masses of the electron and of the target nuclei respectively. E_{cm} is the total center of mass energy and, since the target is at rest before scattering, its expression is calculated by:

$$E_{cm} = \sqrt{(mc^2)^2 + (Mc^2)^2 + 2E'Mc^2} \tag{6.140}$$

where $E = \gamma' mc^2$ is the total energy of the electron before scattering in the laboratory system. The momentum and the scattering angle of the effective particle are equal to the corresponding quantities calculated in the center of mass system ($p \equiv p_{cm}$, $\theta \equiv \theta_{cm}$) of the incident electron:

$$pc = p'c\frac{Mc^2}{E_{cm}} \tag{6.141}$$

where p' is the momentum of the incident electron calculated in the laboratory system. The velocity of the effective particle is related with its momentum by the following expression:

$$\frac{1}{\beta^2} = 1 + \left(\frac{\mu c^2}{pc}\right)^2 \tag{6.142}$$

The integration of the DCS is performed by the *NuclearCrossSection()* method of the *G4ScreeningMottCrossSection*:

$$\sigma_{tot} = 2\pi \int_{\theta_{min}}^{\theta_{max}} \frac{d\sigma(\theta)}{d\Omega} \sin\theta d\theta \tag{6.143}$$

The integration is performed in the scattering range [0 ;π] but the user can decide to vary the minimum (θ_{min}) and the maximum (θ_{max}) scattering angles. The DCS is then given by:

$$\frac{d\sigma(\theta)}{d\Omega} = \left(\frac{Ze^2}{\mu c^2\ \beta^2\gamma}\right)^2 \frac{R_{McF}|F_N(q)|^2}{\big(2A_s + 2\sin^2(\theta/2)\big)^2} \tag{6.144}$$

where Z is the atomic number of the nucleus, A_s is the screening coefficient whose expression has been given by Moliere[9] :

$$A_s = \left(\frac{\hbar}{2p\ a_{TF}}\right)^2 \left[1.13 + 3.76\left(\frac{\alpha Z}{\beta}\right)^2\right] \tag{6.145}$$

where a_{TF} is the Thomas-Fermi screening length given by:

$$a_{TF} = \frac{0.88534\ a_0}{Z^{1/3}} \tag{6.146}$$

and a_0 is the Bhor radius. R_{McF} is the ratio of the Mott to the Rutherfor DCS given by McKinley and Feshbach approximation [6]:

$$R_{McF} = \left[1 - \beta^2\sin^2(\theta/2) + Z\alpha\beta\pi\sin(\theta/2)\big(1 - \sin(\theta/2)\big)\right] \tag{6.147}$$

The nuclear form factor for the exponential charge distribution is given by [10]:

$$F_N(q) = \left[1 + \frac{(qR_N)^2}{12\hbar^2}\right]^{-2} \tag{6.148}$$

where R_N is the nuclear radius that is parameterized by:

$$R_N = 1.27A^{0.27}\ \text{fm}. \tag{6.149}$$

q is the momentum transferred to the nucleus and it is calculated as:

$$qc = \sqrt{T(T + 2Mc^2)} \tag{6.150}$$

where T is the kinetic energy transferred to the nucleus. This kinetic energy is calculated in the *GetNewDirection()* method as:

$$T = \frac{2Mc^2(p'c)^2}{E_{cm}^2}\sin^2\theta/2. \tag{6.151}$$

The scattering angle θ calculation is performed in the *GetScatteringAngle()* method of *G4ScreeningMottCrossSection* class. By means of *AngleDistribution()* function the scattering angle is chosen randomly according to the total

cross section distribution (p.d.f. probability density function) by means of the inverse transform method.

In the *SampleSecondary()* method of *G4eSingleScatteringModel* the kinetic energy of the incident particle after scattering is then calculated as $E'_{new} = E' - T$ where E' is the electron incident kinetic energy (in lab.); in addition the new particle direction and momentum are obtained from the scattering angle information.

6.7.2 Implementation Details

The scattering angle probability density function $f(\theta)$ (p.d.f.) is performed by the *AngleDistribution()* of *G4ScreeningMottCrossSection* class where the inverse transform method is applied. The normalized cumulative function of the cross section is calculated as a function of the scattering angle in this way:

$$\sigma_n(\theta) \equiv \int f(\theta)d\theta = \frac{2\pi}{\sigma_{tot}} \int_0^\theta \frac{d\sigma(t)}{d\Omega} \sin t dt \tag{6.152}$$

The normalized cumulative function $\sigma_n(\theta)$ depends on the DCS and its values range in the interval [0;1]. After this calculation a random number r, uniformly distributed in the same interval [0;1], is chosen in order to fix the cumulative function value (i.e. $r \equiv \sigma_n(\theta)$). This number is the probability to find the scattering angle in the interval $[\theta;\ \theta + d\theta]$. The scattering angle θ is then given by the inverse function of $\sigma_n(\theta)$.

The threshold energy for displacement `Th` can by set by the user in her/his own *Physic* class by adding the electromagnetic model:

```
G4eSingleCoulombScatteringModel* mod=
new G4eSingleCoulombScatteringModel();
mod->SetRecoilThreshold(Th);
```

If the energy lost by the incident particle is grater then this threshold value a new secondary particle is created for transportation processes. The energy lost is added to *ProposeNonIonizingEnergyDeposit()* of the *G4ParticleChangeForGamma* class.

In next patches the NIEL and the Lijian's et al. Mott's approximations[5] calculations will be included in the *G4eSingleCoulombScatteringModel*.

6.8 Status of this Document

17.11.11 created by C. Consolandi and P.G. Rancoita

Bibliography

[1] M. Boschini et al., Nuclear and Non-Ionizing Energy-Loss of Electrons with Low and Relativistic Energies in Materials and Space Environment,Proc. of the ICATPP Conference on Cosmic Rays for Particle and Astroparticle Physics, October 3–7 (2011), Villa Olmo, Como, Italy, S. Giani, C. Leroy, L. Price, P.G. Rancoita and R. Ruchri, Editors, World Scientific, Singapore (2012); arXiv 1111.4042.

[2] C. Leroy and P.G. Rancoita, Particle Interaction and Displacement Damage in Silicon Devices operated in Radiation Environments, *Rep. Prog. in Phys.* 70 (no. 4)(2007), 403–625, doi: 10.1088/0034-4885/70/4/R01.

[3] M. Boschini et al., Nuclear and Non-Ionizing Energy-Loss for Coulomb Scattered Particles from Low Energy up to Relativistic Regime in Space Radiation Environment, Proc. of the ICATPP Conference on Cosmic Rays for Particle and Astroparticle Physics, October 7–8 (2010), Villa Olmo, Como, Italy, S. Giani, C. Leroy and P.G. Rancoita, Editors, World Scientific, Singapore (2011), 9–23, IBSN: 978-981-4329-02-6; arXiv 1011.4822.

[4] C. Leroy and P.G. Rancoita, *Principles of Radiation Interaction in Matter and Detection*, 3rd Edition, World Scientific (Singapore) 2011.

[5] T. Lijian, H. Quing and L. Zhengming, *Radiat. Phys. Chem.* 45 (1995), 235–245.

[6] A.Jr. McKinley and H. Feshbach, *Phys. Rev.* 74 (1948), 1759–1763.

[7] E. Zeitler and A. Olsen, *Phys. Rev.* 136 (1956), A1546-A1552.

[8] H. De Vries, C.W. De Jager, and C. De Vries, *Atomic Data and Nuclear Data Tables* **36** (1987), 495.

[9] von G. Moliere, *Z. Naturforsh* A2 (1947), 133-145; A3 (1948), 78.

[10] A.V. Butkevich et al. *Nucl. Instr. and Meth. in Phys. Res.* A 488 (2002), 282-294.

Chapter 7

Energy loss of Charged Particles

7.1 Mean Energy Loss

Energy loss processes are very similar for $e+/e-$, $\mu+/\mu-$ and charged hadrons, so a common description for them was a natural choice in Geant4 [1], [2]. Any energy loss process must calculate the continuous and discrete energy loss in a material. Below a given energy threshold the energy loss is continuous and above it the energy loss is simulated by the explicit production of secondary particles - gammas, electrons, and positrons.

7.1.1 Method

Let

$$\frac{d\sigma(Z,E,T)}{dT}$$

be the differential cross-section per atom (atomic number Z) for the ejection of a secondary particle with kinetic energy T by an incident particle of total energy E moving in a material of density ρ. The value of the *kinetic energy cut-off* or *production threshold* is denoted by T_{cut}. Below this threshold the soft secondaries ejected are simulated as continuous energy loss by the incident particle, and above it they are explicitly generated. The mean rate of energy loss is given by:

$$\frac{dE_{soft}(E,T_{cut})}{dx} = n_{at} \cdot \int_0^{T_{cut}} \frac{d\sigma(Z,E,T)}{dT} T\, dT \tag{7.1}$$

where n_{at} is the number of atoms per volume in the material. The total cross section per atom for the ejection of a secondary of energy $T > T_{cut}$ is

$$\sigma(Z,E,T_{cut}) = \int_{T_{cut}}^{T_{max}} \frac{d\sigma(Z,E,T)}{dT}\, dT \tag{7.2}$$

where T_{max} is the maximum energy transferable to the secondary particle. If there are several processes providing energy loss for a given particle, then the total continuous part of the energy loss is the sum:

$$\frac{dE^{tot}_{soft}(E,T_{cut})}{dx} = \sum_i \frac{dE_{soft,i}(E,T_{cut})}{dx}. \tag{7.3}$$

These values are pre-calculated during the initialization phase of GEANT4 and stored in the dE/dx table. Using this table the ranges of the particle in given materials are calculated and stored in the *Range* table. The *Range* table is then inverted to provide the $InverseRange$ table. At run time, values of the particle's continuous energy loss and range are obtained using these

tables. Concrete processes contributing to the energy loss are not involved in the calculation at that moment. In contrast, the production of secondaries with kinetic energies above the production threshold is sampled by each concrete energy loss process.

The default energy interval for these tables extends from $100eV$ to $10TeV$ and the default number of bins is 77. For muons and for heavy particles energy loss processes models are valid for higher energies and can be extended. For muons uppper limit may be set to $1000PeV$.

7.1.2 General Interfaces

There are a number of similar functions for discrete electromagnetic processes and for electromagnetic (EM) packages an additional base classes were designed to provide common computations [2]. Common calculations for discrete EM processes are performed in the class $G4VEnergyLossProcess$. Derived classes (7.1) are concrete processes providing initialisation. The physics models are implemented using the $G4VEmModel$ interface. Each process may have one or many models defined to be active over a given energy range and set of $G4Regions$. Models are implementing computation of energy loss, cross section and sampling of final state. The list of EM processes and models for gamma incident is shown in Table 7.1.

7.1.3 Step-size Limit

Continuous energy loss imposes a limit on the step-size because of the energy dependence of the cross sections. It is generally assumed in MC programs (for example, Geant3) that the cross sections are approximately constant along a step, i.e. the step size should be small enough, so that the change in cross section along the step is also small. In principle one must use very small steps in order to insure an accurate simulation, however the computing time increases as the step-size decreases.

For EM processes the exact solution is available (see 7.3) but is is not implemented yet for all physics processes including hadronics. A good compromise is to limit the step-size by not allowing the stopping range of the particle to decrease by more than $\sim$ 20 % during the step. This condition works well for particles with kinetic energies $>$ 1 MeV, but for lower energies it gives too short step-sizes, so must be relaxed. To solve this problem a lower limit on the step-size was introduced. A smooth *StepFunction*, with 2 parameters, controls the step size. At high energy the maximum step size is defined by Step/Range $\sim \alpha_R$ (parameter *dRoverRange*). By default $\alpha_R = 0.2$. As the particle travels the maximum step size decreases gradually

Table 7.1: List of process and model classes for charged particles.

EM process	EM model	Ref.
G4eIonisation	G4MollerBhabhaModel	8.1
	G4LivermoreIonisationModel	9.8
	G4PenelopeIonisationModel	10.1.7
	G4PAIModel	7.5
	G4PAIPhotModel	7.5
G4ePolarizedIonisation	G4PolarizedMollerBhabhaModel	17.1
G4MuIonisation	G4MuBetheBlochModel	13.1
	G4PAIModel	7.5
	G4PAIPhotModel	7.5
G4hIonisation	G4BetheBlochModel	12.1
	G4BraggModel	12.1
	G4ICRU73QOModel	12.2.1
	G4PAIModel	7.5
	G4PAIPhotModel	7.5
G4ionIonisation	G4BetheBlochModel	12.1
	G4BraggIonModel	12.1
	G4IonParametrisedLossModel	12.2.4
G4NuclearStopping	G4ICRU49NuclearStoppingModel	12.1.3
G4mplIonisation	G4mplIonisationWithDeltaModel	
G4eBremsstrahlung	G4SeltzerBergerModel	8.2.1
	G4eBremsstrahlungRelModel	8.2.2
	G4LivermoreBremsstrahlungModel	9.9
	G4PenelopeBremsstrahlungModel	10.1.6
G4ePolarizedBremsstrahlung	G4PolarizedBremsstrahlungModel	17.1
G4MuBremsstrahlung	G4MuBremsstrahlungModel	13.2
G4hBremsstrahlung	G4hBremsstrahlungModel	
G4MuPairProduction	G4MuPairProductionModel	13.3
G4hPairProduction	G4hPairProductionModel	

until the range becomes lower than ρ_R (parameter *finalRange*). Default *finalRange* $\rho_R = 1mm$. For the case of a particle range $R > \rho_R$ the *StepFunction* provides limit for the step size ΔS_{lim} by the following formula:

$$\Delta S_{lim} = \alpha_R R + \rho_R(1 - \alpha_R)\left(2 - \frac{\rho_R}{R}\right). \tag{7.4}$$

In the opposite case of a small range $\Delta S_{lim} = R$. The figure below shows the ratio step/range as a function of range if step limitation is determined only by the expression (7.4).

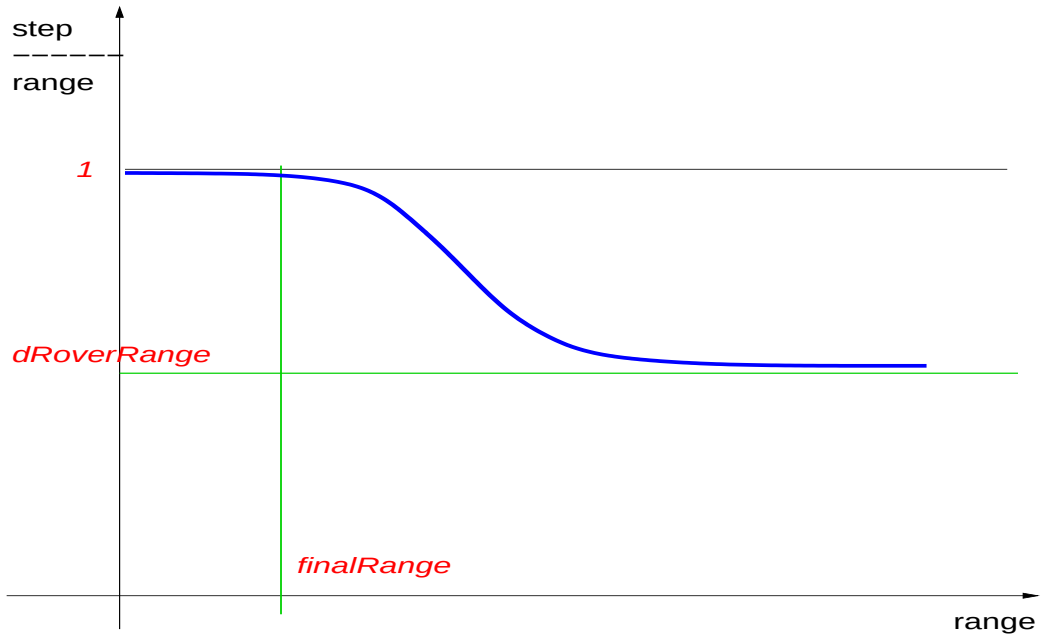

The parameters of *StepFunction* can be overwritten using an UI command:

/process/eLoss/StepFunction 0.2 1 mm
To provide more accurate simulation of particle ranges in physics constructors *G4EmStandardPhysics_option3* and *G4EmStandardPhysics_option4* more strict step limitation is chosen for different particle types.

7.1.4 Run Time Energy Loss Computation

The computation of the *mean energy loss* after a given step is done by using the dE/dx, *Range*, and *InverseRange* tables. The dE/dx table is used if the energy deposition (ΔT) is less than allowed limit $\Delta T < \xi T_0$, where ξ is

linearLossLimit parameter (by default $\xi = 0.01$), T_0 is the kinetic energy of the particle. In that case

$$\Delta T = \frac{dE}{dx}\Delta s, \tag{7.5}$$

where ΔT is the energy loss, Δs is the *true step length*. When a larger percentage of energy is lost, the mean loss can be written as

$$\Delta T = T_0 - f_T(r_0 - \Delta s) \tag{7.6}$$

where r_0 the range at the beginning of the step, the function $f_T(r)$ is the inverse of the *Range* table (i.e. it gives the kinetic energy of the particle for a range value of r). By default spline approximation is used to retrieve a value from dE/dx, *Range*, and $InverseRange$ tables. The spline flag can be changed using an UI command:

/process/em/spline false
After the mean energy loss has been calculated, the process computes the *actual* energy loss, i.e. the loss with fluctuations. The fluctuation models are described in Section 7.2.

If deexcitation module (see 14.1) is enabled then simulation of atomic deexcitation is performed using information on step length and ionisation cross section. Fluorescence gamma and Auger electrons are produced above the same threshold energy as δ-electrons and bremsstrahlung gammas. Following UI commands can be used to enable atomic relaxation:
/process/em/deexcitation myregion true true true
/process/em/fluo true
/process/em/auger true
/process/em/pixe true

7.1.5 Energy Loss by Heavy Charged Particles

To save memory in the case of positively charged hadrons and ions energy loss, dE/dx, *Range* and $InverseRange$ tables are constructed only for *proton, antiproton, muons, pions, kaons, and Generic Ion*. The energy loss for other particles is computed from these tables at the *scaled kinetic energy* T_{scaled} :

$$T_{scaled} = T\frac{M_{base}}{M_{particle}}, \tag{7.7}$$

where T is the kinetic energy of the particle, M_{base} and $M_{particle}$ are the masses of the base particle (*proton or kaon*) and particle. For positively changed hadrons with non-zero spin *proton* is used as a based particle, for negatively charged hadrons with non-zero spin - *antiproton*, for charged particles with zero spin - K^+ or K^- correspondingly. The virtual particle *Generic Ion* is used as a base particle for for all ions with $Z > 2$. It has mass, change and other quantum numbers of the *proton*. The energy loss can be defined via scaling relation:

$$\frac{dE}{dx}(T) = q_{eff}^2(F_1(T)\frac{dE}{dx}_{base}(T_{scaled}) + F_2(T, q_{eff})), \tag{7.8}$$

where q_{eff} is particle effective change in units of positron charge, F_1 and F_2 are correction function taking into account Birks effect, Block correction, low-energy corrections based on data from evaluated data bases [5]. For a hadron q_{eff} is equal to the hadron charge, for a slow ion effective charge is different from the charge of the ion's nucleus, because of electron exchange between transporting ion and the media. The effective charge approach is used to describe this effect [3]. The scaling relation (7.7) is valid for any combination of two heavy charged particles with accuracy corresponding to high order mass, charge and spin corrections [4].

7.1.6 Status of This Document

09.10.98 created by L. Urbán
01.12.03 revised by V. Ivanchenko
02.12.03 spelling and grammar check by D.H. Wright
09.12.05 minor update by V. Ivanchenko
14.06.07 added formula of StepFunction (M. Maire)
15.06.07 updated last sub-charter, list of processes and models by V. Ivanchenko
11.12.08 revised by V. Ivanchenko
09.12.10 revised by V. Ivanchenko

Bibliography

[1] S. Agostinelli et al., Geant4 – a simulation toolkit *Nucl. Instr. Meth. A506 (2003) 250.*

[2] J. Apostolakis et al., Geometry and physics of the Geant4 toolkit for high and medium energy applications. *Rad. Phys. Chem. 78 (2009) 859.*

[3] J.F. Ziegler and J.M. Manoyan, *Nucl. Instr. and Meth. B35 (1988) 215.*

[4] ICRU (A. Allisy et al), Stopping Powers and Ranges for Protons and Alpha Particles, *ICRU Report 49, 1993.*

[5] ICRU (R. Bimbot et al), Stopping of Ions Heavier than Helium, *Journal of the ICRU Vol5 No1 (2005) Report 73.*

7.2 Energy Loss Fluctuations

The total continuous energy loss of charged particles is a stochastic quantity with a distribution described in terms of a straggling function. The straggling is partially taken into account in the simulation of energy loss by the production of δ-electrons with energy $T > T_{cut}$ (Eq.7.2). However, continuous energy loss (Eq.7.1) also has fluctuations. Hence in the current GEANT4 implementation different models of fluctuations implementing the $G4VEmFluctuationModel$ interface:

- G4BohrFluctuations;
- G4IonFluctuations;
- G4PAIModel;
- G4PAIPhotModel;
- G4UniversalFluctuation.

The last model is the default one used in main Physics List and will be described below. Other models have limited applicability and will be described in chapters for ion ionisation and PAI models.

7.2.1 Fluctuations in Thick Absorbers

The total continuous energy loss of charged particles is a stochastic quantity with a distribution described in terms of a straggling function. The straggling is partially taken into account in the simulation of energy loss by the production of δ-electrons with energy $T > T_c$. However, continuous energy loss also has fluctuations. Hence in the current GEANT4 implementation two different models of fluctuations are applied depending on the value of the parameter κ which is the lower limit of the number of interactions of the particle in a step. The default value chosen is $\kappa = 10$. In the case of a high range cut (i.e. energy loss without delta ray production) for thick absorbers the following condition should be fulfilled:

$$\Delta E > \kappa \, T_{max} \tag{7.9}$$

where ΔE is the mean continuous energy loss in a track segment of length s, and T_{max} is the maximum kinetic energy that can be transferred to the atomic electron. If this condition holds the fluctuation of the total (unrestricted) energy loss follows a Gaussian distribution. It is worth noting that this

condition can be true only for heavy particles, because for electrons, $T_{max} = T/2$, and for positrons, $T_{max} = T$, where T is the kinetic energy of the particle. In order to simulate the fluctuation of the continuous (restricted) energy loss, the condition should be modified. After a study, the following conditions have been chosen:

$$\Delta E > \kappa \; T_c \tag{7.10}$$

$$T_{max} <= 2 \; T_c \tag{7.11}$$

where T_c is the cut kinetic energy of δ-electrons. For thick absorbers the straggling function approaches the Gaussian distribution with Bohr's variance [4]:

$$\Omega^2 = 2\pi r_e^2 m_e c^2 N_{el} \frac{Z_h^2}{\beta^2} T_c s \left(1 - \frac{\beta^2}{2}\right), \tag{7.12}$$

where r_e is the classical electron radius, N_{el} is the electron density of the medium, Z_h is the charge of the incident particle in units of positron charge, and β is the relativistic velocity.

7.2.2 Fluctuations in Thin Absorbers

If the conditions 7.10 and 7.11 are not satisfied the model of energy fluctuations in thin absorbers is applied. The formulas used to compute the energy loss fluctuation (straggling) are based on a very simple physics model of the atom. It is assumed that the atoms have only two energy levels with binding energies E_1 and E_2. The particle-atom interaction can be an excitation with energy loss E_1 or E_2, or ionisation with energy loss distributed according to a function $g(E) \sim 1/E^2$:

$$\int_{E_0}^{T_{up}} g(E) \; dE = 1 \Longrightarrow g(E) = \frac{E_0 T_{up}}{T_{up} - E_0} \frac{1}{E^2}. \tag{7.13}$$

The macroscopic cross section for excitation ($i = 1, 2$) is

$$\Sigma_i = C \frac{f_i}{E_i} \frac{\ln[2mc^2 \; (\beta\gamma)^2/E_i] - \beta^2}{\ln[2mc^2 \; (\beta\gamma)^2/I] - \beta^2} \; (1 - r) \tag{7.14}$$

and the ionisation cross section is

$$\Sigma_3 = C \frac{T_{up} - E_0}{E_0 T_{up} \ln(\frac{T_{up}}{E_0})} \; r \tag{7.15}$$

where E_0 denotes the ionisation energy of the atom, I is the mean ionisation energy, T_{up} is the production threshold for delta ray production (or the maximum energy transfer if this value smaller than the production threshold),

E_i and f_i are the energy levels and corresponding oscillator strengths of the atom, and C and r are model parameters.

The oscillator strengths f_i and energy levels E_i should satisfy the constraints

$$f_1 + f_2 = 1 \tag{7.16}$$

$$f_1 \cdot lnE_1 + f_2 \cdot lnE_2 = lnI. \tag{7.17}$$

The cross section formulas 7.14,7.15 and the sum rule equations 7.16,7.17 can be found e.g. in Ref. [1]. The model parameter C can be defined in the following way. The numbers of collisions (n_i, $i = 1, 2$ for excitation and 3 for ionisation) follow the Poisson distribution with a mean value $\langle n_i \rangle$. In a step of length Δx the mean number of collisions is given by

$$\langle n_i \rangle = \Delta x \ \Sigma_i \tag{7.18}$$

The mean energy loss in a step is the sum of the excitation and ionisation contributions and can be written as

$$\frac{dE}{dx} \cdot \Delta x = \left\{ \Sigma_1 E_1 + \Sigma_2 E_2 + \int_{E_0}^{T_{up}} E g(E) dE \right\} \Delta x. \tag{7.19}$$

From this, using Eq. 7.14 - 7.17, one can see that

$$C = dE/dx. \tag{7.20}$$

The other parameters in the fluctuation model have been chosen in the following way. $Z \cdot f_1$ and $Z \cdot f_2$ represent in the model the number of loosely/tightly bound electrons

$$f_2 = 0 \quad for \quad Z = 1 \tag{7.21}$$

$$f_2 = 2/Z \quad for \quad Z \geq 2 \tag{7.22}$$

$$E_2 = 10 \text{ eV } Z^2 \tag{7.23}$$

$$E_0 = 10 \text{ eV } . \tag{7.24}$$

Using these parameter values, E_2 corresponds approximately to the K-shell energy of the atoms (and $Zf_2 = 2$ is the number of K-shell electrons). The parameters f_1 and E_1 can be obtained from Eqs. 7.16 and 7.17. The parameter r is the only variable in the model which can be tuned. This parameter determines the relative contribution of ionisation and excitation to the energy loss. Based on comparisons of simulated energy loss distributions to experimental data, its value has been fixed as

$$r = 0.55 \tag{7.25}$$

7.2.3 Width Correction Algorithm

This simple parametrization and sampling in the model give good values for the most probable energy loss in thin layers. The width of the energy loss distribution (Full Width at Half Maximum, FWHM) in most of the cases is too small. In order to get good FWHM values a relatively simple width correction algorithm has been applied. This algorithm rescales the energy levels E_1, E_2 and the number of excitations n_1, n_2 in such a way that the mean energy loss remains the same. Using this width correction scheme the model gives not only good most probable energy loss, but good FWHM value too.

Width correction algorithm is in the model since version 9.2. The updated version in the model (in version 9.4) causes an important change in the behaviour of the model: the results become much more stable, i.e. the results do not change practically when the cuts and/or the stepsizes are changing. Another important change: the (unphysical) second peak or shoulder in the energy loss distribution which can be seen in some cases (energy loss in thin gas layers) in older versions of the model disappeared. Limit of validity of the model for thin targets: the model gives good (reliable) energy loss distribution if the mean energy loss in the target is $\geq (few\ times) * I_{exc}$, where I_{exc} is the mean excitation energy of the target material.

This simple model of energy loss fluctuations is rather fast and can be used for any thickness of material. This has been verified by performing many simulations and comparing the results with experimental data, such as those in Ref.[2]. As the limit of validity of Landau's theory is approached, the loss distribution approaches the Landau form smoothly.

7.2.4 Sampling of Energy Loss

If the mean energy loss and step are in the range of validity of the Gaussian approximation of the fluctuation (7.10 and 7.11), the Gaussian sampling is used to compute the actual energy loss (7.12). For smaller steps the energy loss is computed in the model under the assumption that the step length (or relative energy loss) is small and, in consequence, the cross section can be considered constant along the step. The loss due to the excitation is

$$\Delta E_{exc} = n_1 E_1 + n_2 E_2 \tag{7.26}$$

where n_1 and n_2 are sampled from a Poisson distribution. The energy loss due to ionisation can be generated from the distribution $g(E)$ by the inverse

transformation method :

$$u = F(E) = \int_{E_0}^{E} g(x)dx \tag{7.27}$$

$$E = F^{-1}(u) = \frac{E_0}{1 - u\frac{T_{up}-E_0}{T_{up}}} \tag{7.28}$$

where u is a uniformly distributed random number $\in [0,\ 1]$. The contribution coming from the ionisation will then be

$$\Delta E_{ion} = \sum_{j=1}^{n3} \frac{E_0}{1 - u_j\frac{T_{up}-E_0}{T_{up}}} \tag{7.29}$$

where n_3 is the number of ionisations sampled from the Poisson distribution. The total energy loss in a step will be $\Delta E = \Delta E_{exc} + \Delta E_{ion}$ and the energy loss fluctuation comes from fluctuations in the number of collisions n_i and from the sampling of the ionisation loss.

7.2.5 Status of This Document

30.01.02 created by L. Urbán
28.08.02 updated by V. Ivanchenko
17.08.04 moved to common to all charged particles (M. Maire)
04.12.04 spelling and grammar check by D.H. Wright
04.05.05 updated by L. Urbán
09.12.05 updated by V. Ivanchenko
29.03.07 updated by L. Urbán
11.12.08 updated by V. Ivanchenko
03.12.10 updated by L. Urbán
29.11.13 updated by V. Ivanchenko

Bibliography

[1] H. Bichsel *Rev.Mod.Phys. 60 (1988) 663.*

[2] K. Lassila-Perini, L. Urbán *Nucl.Inst.Meth. A362(1995) 416.*

[3] GEANT3 manual *Cern Program Library Long Writeup W5013 (1994)*

[4] ICRU (A. Allisy et al), Stopping Powers and Ranges for Protons and Alpha Particles, *ICRU Report 49 (1993).*

7.3 Correcting the Cross Section for Energy Variation

As described in Sections 7.1 and 3.2.2 the step size limitation is provided by energy loss processes in order to insure the precise calculation of the probability of particle interaction. It is generally assumed in Monte Carlo programs that the particle cross sections are approximately constant during a step, hence the reaction probability p at the end of the step can be expressed as

$$p = 1 - \exp\left(-ns\sigma(E_i)\right), \tag{7.30}$$

where n is the density of atoms in the medium, s is the step length, E_i is the energy of the incident particle at the beginning of the step, and $\sigma(E_i)$ is the reaction cross section at the beginning of the step.

However, it is possible to sample the reaction probability from the exact expression

$$p = 1 - \exp\left(-\int_{E_i}^{E_f} n\sigma(E)ds\right), \tag{7.31}$$

where E_f is the energy of the incident particle at the end of the step, by using the integral approach to particle transport. This approach is available for processes implemented via the $G4VEnergyLossProcess$ and $G4VEmProcess$ interfaces.

The Monte Carlo method of integration is used for sampling the reaction probability [1]. It is assumed that during the step the reaction cross section smaller, than some value $\sigma(E) < \sigma_m$. The mean free path for the given step is computed using σ_m. If the process is chosen as the process happens at the step, the sampling of the final state is performed only with the probability $p = \sigma(E_f)/\sigma_m$, alternatively no interaction happen and tracking of the particle is continued. To estimate the maximum value σ_m for the given tracking step at Geant4 initialisation the energy E_m of absoluted maximum σ_{max} of the cross section for given material is determined and stored. If at the tracking time particle energy $E < E_m$, then $\sigma_m = \sigma(E)$. For higher initial energies if $\xi E > E_m$ then $\sigma_m = min(\sigma(E), \sigma(\xi E))$. In the opposit case $\sigma_m = \sigma_{max}$. Here ξ is a parameter of the algorithm. Its optimal value is connected with the value of the *dRoverRange* parameter (see sub-chapter 7.1), by default $\xi = 1 - \alpha_R = 0.8$. Note, that described method is precise if the cross section has only one maximum, which is a typical case for electromagnetic processes.

The integral variant of step limitation is the default for the $G4eIonisation$, $G4eBremsstrahlung$ and some otehr process but is not automatically activated for others. To do so the boolean UI command can be used:

/process/eLoss/integral true

The integral variant of the energy loss sampling process is less dependent on values of the production cuts [2] and allows to have less step limitation, however it should be applied on a case-by-case basis because may require extra CPU.

7.3.1 Status of This Document

01.12.03 integral method subsection added by V. Ivanchenko
17.08.04 moved to common to all charged particles by M. Maire
25.11.06 revised by V. Ivanchenko
09.12.10 revised by V. Ivanchenko

Bibliography

[1] V.N.Ivanchenko et al., Proc. of Int. Conf. MC91: Detector and event simulation in high energy physics, Amsterdam 1991, pp. 79-85. (HEP INDEX 30 (1992) No. 3237).

[2] J. Apostolakis et al., Geometry and physics of the Geant4 toolkit for high and medium energy applications. *Rad. Phys. Chem. 78 (2009) 859.*

7.4 Conversion from Cut in Range to Energy Threshold

In Geant4 charged particles are tracked to the end of their range. The differential cross section of δ-electron productions and bremsstrahlung grow rapidly when secondary energy decrease. If all secondary particles will be tracked the CPU performance of any Monte Carlo code will be pure. The traditional solution is to use cuts. The specific of Geant4 [1] is that user provides value of cut in term of *cut in range*, which is unique for defined *G4Region* or for the complete geometry [2].

Range is used, rather than energy, as a more natural concept for designing a coherent policy for different particles and materials. Definition of the certain value of the *cut in range* means the requirement for precision of spatial radioactive dose deposition. This conception is more strict for a simulation code and provides less handles for user to modify final results. At the same time, it ensures that simulation validated in one geometry is valid also for the other geometries.

The value of cut is defined for electrons, positrons, gamma and protons. At the beginning of initialization of Geant4 physics the conversion is performed from unique *cut in range* to cuts (production thresholds) in kinetic energy for each *G4MaterialCutsCouple* [2]. At that moment no energy loss or range table is created, so computation should be performed using original formulas. For electrons and positrons ionization above $10keV$ a simplified Berger-Seltzer energy loss formula (8.2) is used, in which the density correction term is omitted. The contribution of the bremsstrahlung is added using empirical parameterized formula. For $T < 10keV$ the linear dependence of ionization losses on electron velocity is assumed, bremsstrahlung contribution is neglected. The stopping range is defined as

$$R(T) = \int_0^T \frac{1}{(dE/dx)}\, dE. \tag{7.32}$$

The integration has been done analytically for the low energy part and numerically above an energy limit 1 keV. For each *cut in range* the corresponding kinetic energy can be found out. If obtained production threshold in kinetic energy cannot be below the parameter *lowlimit* (default 1 keV) and above *highlimit* (default 10 GeV). If in specific application lower threshold is required, then the allowed energy cut needs to be extended:

G4ProductionCutsTable::GetProductionCutsTable()→SetEnergyRange(lowlimit,highlimit);
or via UI commands

/cuts/setMinCutEnergy 100 eV
/cuts/setMaxCutEnergy 100 TeV

In contrary to electrons, gammas has no range, so some approximation should be used for range to energy conversion. An approximate empirical formula is used to compute the *absorption cross section* of a photon in an element σ_{abs}. Here, the *absorption cross section* means the sum of the cross sections of the gamma conversion, Compton scattering and photoelectric effect. These processes are the "destructive" processes for photons: they destroy the photon or decrease its energy. The coherent or Rayleigh scattering changes the direction of the gamma only; its cross section is not included in the *absorption cross section*. The `AbsorptionLength` L_{abs} vector is calculated for every material as

$$L_{abs} = 5/\sigma_{abs}. \tag{7.33}$$

The factor 5 comes from the requirement that the probability of having no 'destructive' interaction should be small, hence

$$\exp(-L_{abs}\sigma_{abs}) = \exp(-5) = 6.7 \times 10^{-3}. \tag{7.34}$$

The photon cross section for a material has a minimum at a certain energy E_{min}. Correspondingly L_{abs} has a maximum at $E = E_{min}$, the value of the maximal L_{abs} is the biggest "meaningful" cut in absorption length. If the cut given by the user is bigger than this maximum, a warning is printed and the cut in kinetic energy is set to the *highlimit*.

The cut for proton is introduced with Geant4 v9.3. The main goal of this cut is to limit production of all recoil ions including protons in elastic scattering processes. A simple linear conversion formula is used to compute energy threshold from the value of cut in range, in particular, the cut in range 1 mm corresponds to the production threshold $100keV$.

The conversion from range to energy can be studied using *G4EmCalculator* class. This class allows access or recalculation of energy loss, ranges and other values. It can be instantiated and at any place of user code and can be used after initialisation of Physics Lists:

```
G4EmCalculator calc;
calc.ComputeEnergyCutFromRangeCut(range, particle, material);
```

here particle and material may be string names or corresponding const pointers to *G4ParticleDefinition* and *G4Material*.

7.4.1 Status of This Document

09.10.98 created by L. Urbán.
27.07.01 minor revision M.Maire
17.08.04 moved to common to all charged particles (mma)
04.12.04 minor re-wording by D.H. Wright
18.05.07 rewritten by V. Ivanchenko
11.12.08 minor revision by V. Ivanchenko, Geant4 v9.2
11.12.09 minor revision by V. Ivanchenko, Geant4 v9.3
09.12.10 minor revision by V. Ivanchenko, Geant4 v9.4

Bibliography

[1] Geant4 Collaboration (S. Agostinelli et al.), *Nucl. Instr. Meth. A506 (2003) 250.*

[2] J. Allison et al., *IEEE Trans. Nucl. Sci., 53 (2006) 270.*

7.5 Photoabsorption Ionization Model

7.5.1 Cross Section for Ionizing Collisions

The Photoabsorption Ionization (PAI) model describes the ionization energy loss of a relativistic charged particle in matter. For such a particle, the differential cross section $d\sigma_i/d\omega$ for ionizing collisions with energy transfer ω can be expressed most generally by the following equations [1]:

$$\begin{aligned}\frac{d\sigma_i}{d\omega} &= \frac{2\pi Ze^4}{mv^2}\left\{\frac{f(\omega)}{\omega\left|\varepsilon(\omega)\right|^2}\left[\ln\frac{2mv^2}{\omega\left|1-\beta^2\varepsilon\right|}-\right.\right.\\ &\left.\left.-\frac{\varepsilon_1-\beta^2\left|\varepsilon\right|^2}{\varepsilon_2}\arg(1-\beta^2\varepsilon^*)\right]+\frac{\tilde{F}(\omega)}{\omega^2}\right\}, \qquad (7.35)\end{aligned}$$

$$\tilde{F}(\omega)=\int_0^{\omega}\frac{f(\omega')}{\left|\varepsilon(\omega')\right|^2}d\omega',$$

$$f(\omega)=\frac{m\omega\varepsilon_2(\omega)}{2\pi^2ZN\hbar^2}.$$

Here m and e are the electron mass and charge, $\hbar$ is Planck's constant, $\beta = v/c$ is the ratio of the particle's velocity v to the speed of light c, Z is the effective atomic number, N is the number of atoms (or molecules) per unit volume, and $\varepsilon = \varepsilon_1 + i\varepsilon_2$ is the complex dielectric constant of the medium. In an isotropic non-magnetic medium the dielectric constant can be expressed in terms of a complex index of refraction, $n(\omega) = n_1 + in_2$, $\varepsilon(\omega) = n^2(\omega)$. In the energy range above the first ionization potential I_1 for all cases of practical interest, and in particular for all gases, $n_1 \sim 1$. Therefore the imaginary part of the dielectric constant can be expressed in terms of the photoabsorption cross section $\sigma_\gamma(\omega)$:

$$\varepsilon_2(\omega)=2n_1n_2\sim 2n_2=\frac{N\hbar c}{\omega}\sigma_\gamma(\omega).$$

The real part of the dielectric constant is calculated in turn from the dispersion relation

$$\varepsilon_1(\omega)-1=\frac{2N\hbar c}{\pi}V.p.\int_0^{\infty}\frac{\sigma_\gamma(\omega')}{\omega'^2-\omega^2}d\omega',$$

where the integral of the pole expression is considered in terms of the principal value. In practice it is convenient to calculate the contribution from the continuous part of the spectrum only. In this case the normalized photoabsorption cross section

$$\tilde{\sigma}_\gamma(\omega) = \frac{2\pi^2\hbar e^2 Z}{mc}\sigma_\gamma(\omega)\left[\int_{I_1}^{\omega_{max}}\sigma_\gamma(\omega')d\omega'\right]^{-1},\ \omega_{max}\sim 100\ keV$$

is used, which satisfies the quantum mechanical sum rule [2]:

$$\int_{I_1}^{\omega_{max}}\tilde{\sigma}_\gamma(\omega')d\omega' = \frac{2\pi^2\hbar e^2 Z}{mc}.$$

The differential cross section for ionizing collisions is expressed by the photoabsorption cross section in the continuous spectrum region:

$$\begin{aligned}\frac{d\sigma_i}{d\omega} &= \frac{\alpha}{\pi\beta^2}\left\{\frac{\tilde{\sigma}_\gamma(\omega)}{\omega\left|\varepsilon(\omega)\right|^2}\left[\ln\frac{2mv^2}{\omega\left|1-\beta^2\varepsilon\right|}-\right.\right.\\ &\left.\left.-\frac{\varepsilon_1-\beta^2\left|\varepsilon\right|^2}{\varepsilon_2}\arg(1-\beta^2\varepsilon^*)\right]+\frac{1}{\omega^2}\int_{I_1}^{\omega}\frac{\tilde{\sigma}_\gamma(\omega')}{\left|\varepsilon(\omega')\right|^2}d\omega'\right\},\quad (7.36)\end{aligned}$$

$$\varepsilon_2(\omega) = \frac{N\hbar c}{\omega}\tilde{\sigma}_\gamma(\omega),$$

$$\varepsilon_1(\omega) - 1 = \frac{2N\hbar c}{\pi}V.p.\int_{I_1}^{\omega_{max}}\frac{\tilde{\sigma}_\gamma(\omega')}{\omega'^2-\omega^2}d\omega'.$$

For practical calculations using Eq. 7.35 it is convenient to represent the photoabsorption cross section as a polynomial in ω^{-1} as was proposed in [3]:

$$\sigma_\gamma(\omega) = \sum_{k=1}^{4} a_k^{(i)}\omega^{-k},$$

where the coefficients, $a_k^{(i)}$ result from a separate least-squares fit to experimental data in each energy interval i. As a rule the interval borders are equal to the corresponding photoabsorption edges. The dielectric constant can now be calculated analytically with elementary functions for all ω, except near the photoabsorption edges where there are breaks in the photoabsorption cross section and the integral for the real part is not defined in the sense of the principal value.

The third term in Eq. (7.35), which can only be integrated numerically, results in a complex calculation of $d\sigma_i/d\omega$. However, this term is dominant

for energy transfers $\omega > 10\ keV$, where the function $|\varepsilon(\omega)|^2 \sim 1$. This is clear from physical reasons, because the third term represents the Rutherford cross section on atomic electrons which can be considered as quasifree for a given energy transfer [4]. In addition, for high energy transfers, $\varepsilon(\omega) = 1 - \omega_p^2/\omega^2 \sim 1$, where ω_p is the plasma energy of the material. Therefore the factor $|\varepsilon(\omega)|^{-2}$ can be removed from under the integral and the differential cross section of ionizing collisions can be expressed as:

$$\frac{d\sigma_i}{d\omega} = \frac{\alpha}{\pi\beta^2 |\varepsilon(\omega)|^2} \left\{ \frac{\tilde{\sigma}_\gamma(\omega)}{\omega} \left[\ln \frac{2mv^2}{\omega |1-\beta^2\varepsilon|} - \right.\right. \\ \left.\left. - \frac{\varepsilon_1 - \beta^2 |\varepsilon|^2}{\varepsilon_2} \arg(1-\beta^2\varepsilon^*) \right] + \frac{1}{\omega^2} \int_{I_1}^{\omega} \tilde{\sigma}_\gamma(\omega') d\omega' \right\}. \quad (7.37)$$

This is especially simple in gases when $|\varepsilon(\omega)|^{-2} \sim 1$ for all $\omega > I_1$ [4].

7.5.2 Energy Loss Simulation

For a given track length the number of ionizing collisions is simulated by a Poisson distribution whose mean is proportional to the total cross section of ionizing collisions:

$$\sigma_i = \int_{I_1}^{\omega_{max}} \frac{d\sigma(\omega')}{d\omega'} d\omega'.$$

The energy transfer in each collision is simulated according to a distribution proportional to

$$\sigma_i(> \omega) = \int_{\omega}^{\omega_{max}} \frac{d\sigma(\omega')}{d\omega'} d\omega'.$$

The sum of the energy transfers is equal to the energy loss. PAI ionisation is implemented according to the model approach (class G4PAIModel) allowing a user to select specific models in different regions. Here is an example physics list:

```
const G4RegionStore* theRegionStore = G4RegionStore::GetInstance();
G4Region* gas = theRegionStore->GetRegion("VertexDetector");
...
if (particleName == "e-")
{
  ...
  G4eIonisation* eion = new G4eIonisation();
```

```
    G4PAIModel*     pai = new G4PAIModel(particle,"PAIModel");

    // here 0 is the highest priority in region 'gas'
    eion->AddEmModel(0,pai,pai,gas);
    ...
  }
  ...
```

It shows how to select the G4PAIModel to be the preferred ionisation model for electrons in a *G4Region* named *VertexDetector*. The first argument in *AddEmModel* is 0 which means highest priority.

The class *G4PAIPhotonModel* generates both δ-electrons and photons as secondaries and can be used for more detailed descriptions of ionisation space distribution around the particle trajectory.

7.5.3 Photoabsorption Cross Section at Low Energies

The photoabsorption cross section, $\sigma_\gamma(\omega)$, where ω is the photon energy, is used in Geant4 for the description of the photo-electric effect, X-ray transportation and ionization effects in very thin absorbers. As mentioned in the discussion of photoabsorption ionization (see section 7.5), it is convenient to represent the cross section as a polynomial in ω^{-1} [5] :

$$\sigma_\gamma(\omega) = \sum_{k=1}^{4} a_k^{(i)} \omega^{-k}. \tag{7.38}$$

Using cross sections from the original Sandia data tables, calculations of primary ionization and energy loss distributions produced by relativistic charged particles in gaseous detectors show clear disagreement with experimental data, especially for gas mixtures which include xenon.

Therefore a special investigation was performed [6] by fitting the coefficients $a_k^{(i)}$ to modern data from synchrotron radiation experiments in the energy range of $10 - 50\ eV$. The fits were performed for elements typically used in detector gas mixtures: hydrogen, fluorine, carbon, nitrogen and oxygen. Parameters for these elements were extracted from data on molecular gases such as N_2, O_2, CO_2, CH_4, and CF_4 [7, 8]. Parameters for the noble gases were found using data given in the tables [9, 10].

7.5.4 Status of this document

01.12.05 expanded discussion by V. Grichine
08.05.02 re-written by D.H. Wright
16.11.98 created by V. Grichine
20.11.12 updated by V. Ivanchenko

Bibliography

[1] Asoskov V.S., Chechin V.A., Grichine V.M. at el, Lebedev Institute annual report, v. 140, p. 3 (1982)

[2] Fano U., and Cooper J.W. Rev.Mod.Phys., v. 40, p. 441 (1968)

[3] Biggs F., and Lighthill R., Preprint Sandia Laboratory, SAND 87-0070 (1990)

[4] Allison W.W.M., and Cobb J. Ann.Rev.Nucl.Part.Sci., v.30,p.253 (1980)

[5] Biggs F., and Lighthill R., Preprint Sandia Laboratory, SAND 87-0070 (1990)

[6] Grichine V.M., Kostin A.P., Kotelnikov S.K. et al., Bulletin of the Lebedev Institute no. 2-3, 34 (1994).

[7] Lee L.C. et al., J.Q.S.R.T., v. 13, p. 1023 (1973).

[8] Lee L.C. et al., Journ. of Chem. Phys., v. 67, p. 1237 (1977).

[9] G.V. Marr and J.B. West, Atom. Data Nucl. Data Tabl., v. 18, p. 497 (1976).

[10] J.B. West and J. Morton, Atom. Data Nucl. Data Tabl., v. 30, p. 253 (1980).

Chapter 8

Electron and Positron Incident

8.1 Ionization

8.1.1 Method

The *G4eIonisation* class provides the continuous and discrete energy losses of electrons and positrons due to ionization in a material according to the approach described in Section 7.1. The value of the maximum energy transferable to a free electron T_{max} is given by the following relation:

$$T_{max} = \begin{cases} E - mc^2 & for\ e^+ \\ (E - mc^2)/2 & for\ e^- \end{cases} \tag{8.1}$$

where mc^2 is the electron mass. Above a given threshold energy the energy loss is simulated by the explicit production of delta rays by Möller scattering (e^-e^-), or Bhabha scattering (e^+e^-). Below the threshold the soft electrons ejected are simulated as continuous energy loss by the incident $e^{\pm}$.

8.1.2 Continuous Energy Loss

The integration of 7.1 leads to the Berger-Seltzer formula [1]:

$$\left.\frac{dE}{dx}\right]_{T<T_{cut}} = 2\pi r_e^2 mc^2 n_{el} \frac{1}{\beta^2}\left[\ln\frac{2(\gamma+1)}{(I/mc^2)^2} + F^{\pm}(\tau,\tau_{up}) - \delta\right] \tag{8.2}$$

with

r_e	classical electron radius: $e^2/(4\pi\epsilon_0 mc^2)$
mc^2	mass energy of the electron
n_{el}	electron density in the material
I	mean excitation energy in the material
γ	E/mc^2
β^2	$1-(1/\gamma^2)$
τ	$\gamma - 1$
T_{cut}	minimum energy cut for δ -ray production
τ_c	T_{cut}/mc^2
τ_{max}	maximum energy transfer: τ for e^+, $\tau/2$ for e^-
τ_{up}	$\min(\tau_c, \tau_{max})$
δ	density effect function.

In an elemental material the electron density is

$$n_{el} = Z\, n_{at} = Z\, \frac{\mathcal{N}_{av}\rho}{A}.$$

$\mathcal{N}_{av}$ is Avogadro's number, ρ is the material density, and A is the mass of a mole. In a compound material

$$n_{el} = \sum_i Z_i \, n_{ati} = \sum_i Z_i \, \frac{\mathcal{N}_{av} w_i \rho}{A_i},$$

where w_i is the proportion by mass of the i^{th} element, with molar mass A_i .
The mean excitation energies I for all elements are taken from [2].
The functions $F^{\pm}$ are given by :

$$\begin{aligned} F^+(\tau, \tau_{up}) &= \ln(\tau\tau_{up}) \\ &\quad -\frac{\tau_{up}^2}{\tau}\left[\tau + 2\tau_{up} - \frac{3\tau_{up}^2 y}{2} - \left(\tau_{up} - \frac{\tau_{up}^3}{3}\right) y^2 - \left(\frac{\tau_{up}^2}{2} - \tau\frac{\tau_{up}^3}{3} + \frac{\tau_{up}^4}{4}\right) y^3\right] \end{aligned} \tag{8.3}$$

$$\begin{aligned} F^-(\tau, \tau_{up}) &= -1 - \beta^2 \\ &\quad + \ln\left[(\tau - \tau_{up})\tau_{up}\right] + \frac{\tau}{\tau - \tau_{up}} + \frac{1}{\gamma^2}\left[\frac{\tau_{up}^2}{2} + (2\tau + 1)\ln\left(1 - \frac{\tau_{up}}{\tau}\right)\right] \end{aligned} \tag{8.4}$$

where $y = 1/(\gamma + 1)$.

The density effect correction is calculated according to the formalism of Sternheimer [3]:
x is a kinetic variable of the particle : $x = \log_{10}(\gamma\beta) = \ln(\gamma^2\beta^2)/4.606$, and $\delta(x)$ is defined by

$$\begin{array}{lll} \text{for} \quad x < x_0 : & \delta(x) = 0 \\ \text{for} \quad x \in [x_0,\ x_1] : & \delta(x) = 4.606x - C + a(x_1 - x)^m \\ \text{for} \quad x > x_1 : & \delta(x) = 4.606x - C \end{array} \tag{8.5}$$

where the matter-dependent constants are calculated as follows:

$$\begin{aligned} h\nu_p &= \text{ plasma energy of the medium } = \sqrt{4\pi n_{el} r_e^3} mc^2/\alpha = \sqrt{4\pi n_{el} r_e}\hbar c \\ C &= 1 + 2\ln(I/h\nu_p) \\ x_a &= C/4.606 \\ a &= 4.606(x_a - x_0)/(x_1 - x_0)^m \\ m &= 3. \end{aligned} \tag{8.6}$$

For condensed media

$$\begin{array}{lll} I < 100\,\text{eV} & \left\{ \begin{array}{lll} \text{for } C \le 3.681 & x_0 = 0.2 & x_1 = 2 \\ \text{for } C > 3.681 & x_0 = 0.326C - 1.0 & x_1 = 2 \end{array} \right. \\ I \ge 100\,\text{eV} & \left\{ \begin{array}{lll} \text{for } C \le 5.215 & x_0 = 0.2 & x_1 = 3 \\ \text{for } C > 5.215 & x_0 = 0.326C - 1.5 & x_1 = 3 \end{array} \right. \end{array}$$

and for gaseous media

for	$C < 10.$	$x_0 = 1.6$	$x_1 = 4$
for	$C \in [10.0,\ 10.5[$	$x_0 = 1.7$	$x_1 = 4$
for	$C \in [10.5,\ 11.0[$	$x_0 = 1.8$	$x_1 = 4$
for	$C \in [11.0,\ 11.5[$	$x_0 = 1.9$	$x_1 = 4$
for	$C \in [11.5,\ 12.25[$	$x_0 = 2.$	$x_1 = 4$
for	$C \in [12.25,\ 13.804[$	$x_0 = 2.$	$x_1 = 5$
for	$C \geq 13.804$	$x_0 = 0.326C - 2.5$	$x_1 = 5.$

8.1.3 Total Cross Section per Atom and Mean Free Path

The total cross section per atom for Möller scattering (e^-e^-) and Bhabha scattering (e^+e^-) is obtained by integrating Eq. 7.2. In GEANT4 T_{cut} is always 1 keV or larger. For delta ray energies much larger than the excitation energy of the material ($T \gg I$), the total cross section becomes [1] for Möller scattering,

$$\begin{aligned}\sigma(Z,E,T_{cut}) &= \frac{2\pi r_e^2 Z}{\beta^2(\gamma-1)} \times \\ &\left[\frac{(\gamma-1)^2}{\gamma^2}\left(\frac{1}{2}-x\right)+\frac{1}{x}-\frac{1}{1-x}-\frac{2\gamma-1}{\gamma^2}\ln\frac{1-x}{x}\right],\end{aligned} \tag{8.7}$$

and for Bhabha scattering (e^+e^-),

$$\begin{aligned}\sigma(Z,E,T_{cut}) &= \frac{2\pi r_e^2 Z}{(\gamma-1)} \times \\ &\left[\frac{1}{\beta^2}\left(\frac{1}{x}-1\right)+B_1\ln x+B_2(1-x)-\frac{B_3}{2}(1-x^2)+\frac{B_4}{3}(1-x^3)\right].\end{aligned} \tag{8.8}$$

Here

$$\begin{array}{lllllll}\gamma &=& E/mc^2 & & B_1 &=& 2-y^2 \\ \beta^2 &=& 1-(1/\gamma^2) & & B_2 &=& (1-2y)(3+y^2) \\ x &=& T_{cut}/(E-mc^2) & & B_3 &=& (1-2y)^2+(1-2y)^3 \\ y &=& 1/(\gamma+1) & & B_4 &=& (1-2y)^3.\end{array}$$

The above formulas give the total cross section for scattering above the threshold energies

$$T^{\rm thr}_{\rm Moller} = 2T_{cut} \qquad \text{and} \qquad T^{\rm thr}_{\rm Bhabha} = T_{cut}. \tag{8.9}$$

In a given material the mean free path is then

$$\lambda = (n_{at}\cdot\sigma)^{-1} \quad or \quad \lambda = \left(\textstyle\sum_i n_{ati}\cdot\sigma_i\right)^{-1}. \tag{8.10}$$

8.1.4 Simulation of Delta-ray Production

Differential Cross Section

For $T \gg I$ the differential cross section per atom becomes [1] for Möller scattering,

$$\begin{aligned}\frac{d\sigma}{d\epsilon} &= \frac{2\pi r_e^2 Z}{\beta^2(\gamma-1)} \times \\ &\left[\frac{(\gamma-1)^2}{\gamma^2} + \frac{1}{\epsilon}\left(\frac{1}{\epsilon} - \frac{2\gamma-1}{\gamma^2}\right) + \frac{1}{1-\epsilon}\left(\frac{1}{1-\epsilon} - \frac{2\gamma-1}{\gamma^2}\right)\right]\end{aligned} \tag{8.11}$$

and for Bhabha scattering,

$$\frac{d\sigma}{d\epsilon} = \frac{2\pi r_e^2 Z}{(\gamma-1)}\left[\frac{1}{\beta^2\epsilon^2} - \frac{B_1}{\epsilon} + B_2 - B_3\epsilon + B_4\epsilon^2\right]. \tag{8.12}$$

Here $\epsilon = T/(E - mc^2)$. The kinematical limits of ϵ are

$$\epsilon_0 = \frac{T_{cut}}{E-mc^2} \le \epsilon \le \frac{1}{2} \quad \text{for } e^-e^- \qquad\qquad \epsilon_0 = \frac{T_{cut}}{E-mc^2} \le \epsilon \le 1 \quad \text{for } e^+e^-.$$

Sampling

The delta ray energy is sampled according to methods discussed in Chapter 2. Apart from normalization, the cross section can be factorized as

$$\frac{d\sigma}{d\epsilon} = f(\epsilon)g(\epsilon). \tag{8.13}$$

For e^-e^- scattering

$$f(\epsilon) = \frac{1}{\epsilon^2}\frac{\epsilon_0}{1-2\epsilon_0} \tag{8.14}$$

$$g(\epsilon) = \frac{4}{9\gamma^2 - 10\gamma + 5}\left[(\gamma-1)^2\epsilon^2 - (2\gamma^2+2\gamma-1)\frac{\epsilon}{1-\epsilon} + \frac{\gamma^2}{(1-\epsilon)^2}\right] \tag{8.15}$$

and for e^+e^- scattering

$$f(\epsilon) = \frac{1}{\epsilon^2}\frac{\epsilon_0}{1-\epsilon_0} \tag{8.16}$$

$$g(\epsilon) = \frac{B_0 - B_1\epsilon + B_2\epsilon^2 - B_3\epsilon^3 + B_4\epsilon^4}{B_0 - B_1\epsilon_0 + B_2\epsilon_0^2 - B_3\epsilon_0^3 + B_4\epsilon_0^4}. \tag{8.17}$$

Here $B_0 = \gamma^2/(\gamma^2-1)$ and all other quantities have been defined above.

To choose ϵ, and hence the delta ray energy,

1. ϵ is sampled from $f(\epsilon)$
2. the rejection function $g(\epsilon)$ is calculated using the sampled value of ϵ
3. ϵ is accepted with probability $g(\epsilon)$.

After the successful sampling of ϵ, the direction of the ejected electron is generated with respect to the direction of the incident particle. The azimuthal angle ϕ is generated isotropically and the polar angle θ is calculated from energy-momentum conservation. This information is used to calculate the energy and momentum of both the scattered incident particle and the ejected electron, and to transform them to the global coordinate system.

8.1.5 Status of this document

9.10.98 created by L. Urbán.
29.07.01 revised by M.Maire.
13.12.01 minor cosmetic by M.Maire.
24.05.02 re-written by D.H. Wright.
01.12.03 revised by V. Ivanchenko.

Bibliography

[1] H. Messel and D.F. Crawford, *Pergamon Press, Oxford (1970).*

[2] ICRU (A. Allisy et al), Stopping Powers for Electrons and Positrons, *ICRU Report No.37 (1984).*

[3] R.M. Sternheimer. *Phys.Rev. B3 (1971) 3681.*

8.2 Bremsstrahlung

The class *G4eBremsstrahlung* provides the energy loss of electrons and positrons due to the radiation of photons in the field of a nucleus according to the approach described in Section 7.1. Above a given threshold energy the energy loss is simulated by the explicit production of photons. Below the threshold the emission of soft photons is treated as a continuous energy loss.

Below electron/positron energies of 1 GeV, the cross section evaluation is based on a dedicated parameterization, above this limit an analytic cross section is used. In GEANT4 the Landau-Pomeranchuk-Migdal effect has also been implemented.

8.2.1 Seltzer-Berger bremsstrahlung model

In order to iprove accuracy of the model described above a new model *G4SeltzerBergerModel* have been design which implementing cross section based on interpolation of published tables [5, 15]. Single-differential cross section can be written as a sum of a contribution of bremsstrahlung produced in the field of the screened atomic nucleus $d\sigma_n/dk$, and the part $Z\,d\sigma_e/dk$ corresponding to bremsstrahlung produced in the field of the Z atomic electrons,

$$\frac{d\sigma}{dk} = \frac{d\sigma_n}{dk} + Z\frac{d\sigma_e}{dk}\,. \tag{8.18}$$

The differential cross section depends on the energy k of the emitted photon, the kinetic energy T_1 of the incident electron and the atomic number Z of the target atom.

Seltzer and Berger have published extensive tables for the differential cross section $d\sigma_n/dk$ and $d\sigma_e/dk$ [5, 15], covering electron energies from 1 keV up to 10 GeV, substantially extending previous publications [16]. The results are in good agreement with experimental data, and provided also the basis of bremsstrahlung implementations in many Monte Carlo programs (e.g. Penelope, EGS). The estimated uncertainties for $d\sigma/dk$ are:

- 3% to 5% in the high energy region ($T_1 \geq 50\,\mathrm{MeV}$),
- 5% to 10% in the intermediate energy region ($2 \geq T_1 \leq 50\,\mathrm{MeV}$),
- and 10% at low energies region compared with Pratt results. ($T_1 \leq 2\,\mathrm{MeV}$).

The restricted cross section (7.2) and the energy loss (7.3) are obtained by numerical integration performed at initialisation stage of Geant4. This

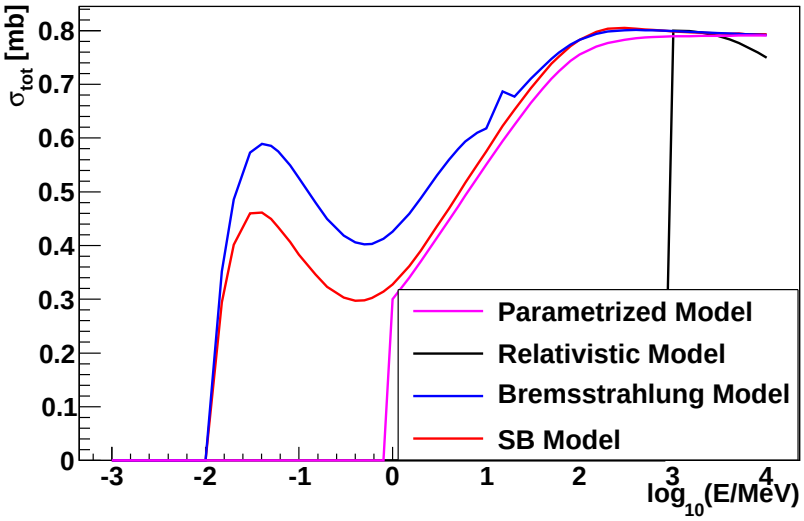

Figure 8.1: Total cross section comparison between models for $Z = 29$: Parametrized Bremsstrahlung Model, Relativistic Model, Bremsstrahlung Model (Geant4 9.4) and Seltzer-Berger Model. The discontinuities in the Parametized Model and the Relativistic Model at 1 Mev and 1 GeV, respectively, mark the validity range of these models.

method guarantees consistent description independent of the energy cutoff. The current version uses an interpolation in tables for 52 available electron energy points versus 31 photon energy points, and for atomic number Z ranging from 1 to 99. It is the default bremsstrahlung model in Geant4 since version 9.5. Figure 8.1 shows a comparison of the total bremsstrahlung cross sections with the previous implementation, and with the relativistic model. After the successful sampling of ϵ, the polar angles of the radiated photon are generated with respect to the parent electron's momentum. It is difficult to find simple formulae for this angle in the literature. For example the double

differential cross section reported by Tsai [12, 13] is

$$\begin{aligned}
\frac{d\sigma}{dkd\Omega} &= \frac{2\alpha^2 e^2}{\pi k m^4}\left\{\left[\frac{2\epsilon-2}{(1+u^2)^2}+\frac{12u^2(1-\epsilon)}{(1+u^2)^4}\right]Z(Z+1)\right. \\
&\quad \left.+\left[\frac{2-2\epsilon-\epsilon^2}{(1+u^2)^2}-\frac{4u^2(1-\epsilon)}{(1+u^2)^4}\right]\left[X-2Z^2 f_c((\alpha Z)^2)\right]\right\} \\
u &= \frac{E\theta}{m} \\
X &= \int_{t_{min}}^{m^2(1+u^2)^2}\left[G_Z^{el}(t)+G_Z^{in}(t)\right]\frac{t-t_{min}}{t^2}dt \\
G_Z^{el,in}(t) &\quad \text{atomic form factors} \\
t_{min} &= \left[\frac{km^2(1+u^2)}{2E(E-k)}\right]^2=\left[\frac{\epsilon m^2(1+u^2)}{2E(1-\epsilon)}\right]^2 .
\end{aligned}$$

The sampling of this distribution is complicated. It is also only an approximation to within a few percent, due at least to the presence of the atomic form factors. The angular dependence is contained in the variable $u = E\theta m^{-1}$. For a given value of u the dependence of the shape of the function on Z, E and $\epsilon = k/E$ is very weak. Thus, the distribution can be approximated by a function

$$f(u) = C\left(ue^{-au}+due^{-3au}\right) \tag{8.19}$$

where

$$C=\frac{9a^2}{9+d} \qquad a=0.625 \qquad d=27$$

where E is in GeV. While this approximation is good at high energies, it becomes less accurate around a few MeV. However in that region the ionization losses dominate over the radiative losses.

The sampling of the function $f(u)$ can be done with three random numbers r_i, uniformly distributed on the interval [0,1]:

1. choose between ue^{-au} and due^{-3au}:

$$b=\begin{cases} a & \text{if} \quad r_1 < 9/(9+d) \\ 3a & \text{if} \quad r_1 \geq 9/(9+d) \end{cases}$$

2. sample ue^{-bu}:

$$u=-\frac{\log(r_2 r_3)}{b}$$

$$P = \int_{u_{max}}^{\infty} f(u)\, du$$

E (MeV)	P(%)
0.511	3.4
0.6	2.2
0.8	1.2
1.0	0.7
2.0	< 0.1

Table 8.1: Angular sampling efficiency

3. check that:

$$u \leq u_{max} = \frac{E\pi}{m}$$

otherwise go back to 1.

The probability of failing the last test is reported in table 8.1.

The function $f(u)$ can also be used to describe the angular distribution of the photon in μ bremsstrahlung and to describe the angular distribution in photon pair production.

The azimuthal angle ϕ is generated isotropically. Along with θ, this information is used to calculate the momentum vectors of the radiated photon and parent recoiled electron, and to transform them to the global coordinate system. The momentum transfer to the atomic nucleus is neglected.

8.2.2 Bremsstrahlung of high-energy electrons

Above an electron energy of 1 GeV an analytic differential cross section representation is used [17], which was modified to account for the density effect and the Landau-Pomeranchuk-Migdal (LPM) effect [18, 19].

Relativistic Bremsstrahlung cross section

The basis of the implementation is the well known high energy limit of the Bremsstrahlung process [17],

$$\frac{d\sigma}{dk} = \frac{4\alpha r_e^2}{3k}\left[\{y^2 + 2[1 + (1-y)^2]\}[Z^2(F_{el} - f) + ZF_{inel}] + (1-y)\frac{Z^2 + Z}{3}\right] \quad (8.20)$$

The *elastic from factor* F_{el} and *inelastic form factor* F_{inel}, describe the scattering on the nucleus and on the shell electrons, respectively, and for $Z > 4$ are given by [14]

$$F_{el} = \log\left(\frac{184.15}{Z^{\frac{1}{3}}}\right) \qquad \text{and} \quad F_{inel} = \log\left(\frac{1194.}{Z^{\frac{2}{3}}}\right).$$

This corresponds to the complete screening approximation. The Coulomb correction is defined as [14]

$$f = \alpha^2 Z^2 \sum_{n=1}^{\infty} \frac{1}{n(n^2 + \alpha^2 Z^2)}$$

This approach provides an analytic differential cross section for an efficient evaluation in a Monte Carlo computer code. Note that in this approximation the differential cross section $d\sigma/dk$ is independent of the energy of the initial electron and is also valid for positrons.

The total integrated cross section $\int d\sigma/dk\, dk$ is divergent, but the energy loss integral $\int k d\sigma/dk\, dk$ is finite. This allows the usual separation into continuous enery loss, and discrete photon production according to Eqs. (7.3) and (7.2).

Landau Pomeranchuk Migdal (LPM) effect

At higher energies matter effects become more and more important. In GEANT4 the two leading matter effects, the LPM effect and the dielectric suppresion (or Ter-Mikaelian effect), are considered. The analytic cross section representation, eq. (8.20), provides the basis for the incorporation of these matter effects.

The LPM effect (see for example [3, 4, 20]) is the suppression of photon production due to the multiple scattering of the electron. If an electron undergoes multiple scattering while traversing the so called "formation zone", the bremsstrahlung amplitudes from before and after the scattering can interfere, reducing the probability of bremsstrahlung photon emission (a similar suppression occurs for pair production). The suppression becomes significant for photon energies below a certain value, given by

$$\frac{k}{E} < \frac{E}{E_{LPM}}, \tag{8.21}$$

where

k	photon energy
E	electron energy
E_{LPM}	characteristic energy for LPM effect (depend on the medium).

The value of the LPM characteristic energy can be written as

$$E_{LPM} = \frac{\alpha m^2 X_0}{4hc}, \tag{8.22}$$

where

α	fine structure constant
m	electron mass
X_0	radiation length in the material
h	Planck constant
c	velocity of light in vacuum.

At high energies (approximately above 1 GeV) the differential cross section including the Landau-Pomeranchuk-Migdal effect, can be expressed using an evaluation based on [8, 19, 18]

$$\frac{d\sigma}{dk} = \frac{4\alpha r_e^2}{3k}\Bigg[\xi(s)\{y^2 G(s) + 2[1+(1-y)^2]\phi(s)\} \times [Z^2(F_{el}-f) + ZF_{inel}] + (1-y)\frac{Z^2+Z}{3}\Bigg] \tag{8.23}$$

where LPM suppression functions are defined by [8]

$$G(s) = 24s^2\left(\frac{\pi}{2} - \int_0^\infty e^{-st}\frac{\sin(st)}{\sinh(\frac{t}{2})}dt\right) \tag{8.24}$$

and

$$\phi(s) = 12s^2\left(-\frac{\pi}{2} + \int_0^\infty e^{-st}\sin(st)\sinh\left(\frac{t}{2}\right)dt\right) \tag{8.25}$$

They can be piecewise approximated with simple analytic functions, see e.g. [19]. The suppression function $\xi(s)$ is recursively defined via

$$s = \sqrt{\frac{k\,E_{\mathrm{LPM}}}{8E(E-k)\xi(s)}}$$

but can be well approximated using an algorithm introduced by [19]. The material dependent characteristic energy E_{LPM} is defined in Eq. (8.22) according to [4]. Note that this definition differs from other definition (e.g. [18]) by a factor $\frac{1}{2}$.

An additional multiplicative factor governs the dielectric suppression effect (Ter-Mikaelian effect) [21].

$$S(k) = \frac{k^2}{k^2 + k_p^2}$$

The characteristic photon energy scale k_p is given by the plasma frequency of the media, defined as

$$k_p = \hbar\omega_p \frac{E_e}{m_e c^2} = \frac{\hbar E_e}{m_e c^2} \cdot \sqrt{\frac{n_e e^2}{\epsilon_0 m_e}} \,.$$

Both suppression effects, dielectric suppresion and LPM effect, reduce the effective formation length of the photon, so the suppressions *do not simply multiply.*

A consistent treatment of the overlap region, where both suppression mechanism, was suggested by [22]. The algorithm garanties that the LPM suppression is turned off as the density effect becomes important. This is achieved by defining a modified suppression variable $\hat{s}$ via

$$\hat{s} = s \cdot \left(1 + \frac{k_p^2}{k^2}\right)$$

and using $\hat{s}$ in the LPM suppression functions $G(s)$ and $\phi(s)$ instead of s in Eq. (8.23).

8.2.3 Status of this document

09.10.98 created by L. Urbán.
21.03.02 modif in angular distribution (M.Maire)
27.05.02 re-written by D.H. Wright
01.12.03 minor update by V. Ivanchenko
20.05.04 updated by L.Urban
09.12.05 minor update by V. Ivanchenko
15.03.07 modify definition of Elpm (M.Maire)
12.12.08 update LPM effect and relativistic Model
03.12.09 correct total cross section, formula 3 (M.Maire)
21.11.12 updated by V. Ivanchenko
29.11.13 updated by V. Ivanchenko

Bibliography

[1] S.T.Perkins, D.E.Cullen, S.M.Seltzer, UCRL-50400 Vol.31

[2] GEANT3 manual ,CERN Program Library Long Writeup W5013 (October 1994).

[3] V.M. Galitsky and I.I. Gurevich, Nuovo Cimento 32 (1964) 1820.

[4] P.L. Anthony et al., Phys. Rev. D **56** (1997) 1373, SLAC-PUB-7413/LBNL-40054 (February 1997).

[5] S.M.Seltzer and M.J.Berger, Nucl. Inst. Meth. **B12** (1985) 95.

[6] W.R. Nelson et al.:The EGS4 Code System. *SLAC-Report-265 , December 1985*

[7] H.Messel and D.F.Crawford. Pergamon Press,Oxford,1970.

[8] A.B. Migdal, Phys. Rev. **103** (1956) 1811.

[9] L. Kim et al., Phys. Rev. **A33** (1986) 3002.

[10] R.W. Williams, Fundamental Formulas of Physics, vol.2., Dover Pubs. (1960).

[11] J.C. Butcher and H. Messel., Nucl. Phys. **20** (1960) 15.

[12] Y-S. Tsai, Rev. Mod. Phys **46** (1974) 815.

[13] Y-S. Tsai, Rev. Mod. Phys **49** (1977) 421.

[14] C. Amsler et al., Phys. Lett. **B67** (2008) 1.

[15] S.M. Seltzer and M.J. Berger, Atomic Data and Nuclear Data **35** (1986) 345.

[16] R.H. Pratt et al, Atomic Data and Nuclear Data Tables **20** (1977) 175.

[17] M.L. Perl, in Procede Les Rencontres de physique de la Valle D'Aoste, SLAC-PUB-6514.

[18] S. Klein, Rev. Mod. Phys. **71** (1999) 1501-1538.

[19] T. Stanev et.al., Phys. Rev. D25 (1982) 1291.

[20] H.D. Hansen et al., Phys. Rev. D **69** (2004) 032001.

[21] M.L. Ter-Mikaelian, Dokl. Akad. Nauk SSSR 94 (1954) 1033.

[22] M.L. Ter-Mikaelian, *High-energy Electromagnetic Processes in Condensed Media*, Wiley, (1972).

8.3 Positron - Electron Annihilation

8.3.1 Introduction

The process `G4eplusAnnihilation` simulates the in-flight annihilation of a positron with an atomic electron. As is usually done in shower programs [1], it is assumed here that the atomic electron is initially free and at rest. Also, annihilation processes producing one, or three or more, photons are ignored because these processes are negligible compared to the annihilation into two photons [1, 2].

8.3.2 Cross Section

The annihilation in flight of a positron and electron is described by the cross section formula of Heitler [3, 1]:

$$\sigma(Z,E) = \frac{Z\pi r_e^2}{\gamma+1}\left[\frac{\gamma^2+4\gamma+1}{\gamma^2-1}\ln\left(\gamma+\sqrt{\gamma^2-1}\right)-\frac{\gamma+3}{\sqrt{\gamma^2-1}}\right] \quad (8.26)$$

where

E = total energy of the incident positron

γ = E/mc^2

r_e = classical electron radius

8.3.3 Sampling the final state

The final state of the $e+e-$ annihilation process

$$e^+\ e^-\ \rightarrow \gamma_a\ \gamma_b$$

is simulated by first determining the kinematic limits of the photon energy and then sampling the photon energy within those limits using the differential cross section. Conservation of energy-momentum is then used to determine the directions of the final state photons.

If the incident e^+ has a kinetic energy T, then the total energy is $E_e = T + mc^2$ and the momentum is $Pc = \sqrt{T(T+2mc^2)}$. The total available energy is $E_{tot} = E_e + mc^2 = E_a + E_b$ and momentum conservation requires $\vec{P} = \vec{P}_{\gamma_a} + \vec{P}_{\gamma_b}$. The fraction of the total energy transferred to one photon (say γ_a) is

$$\epsilon = \frac{E_a}{E_{tot}} \equiv \frac{E_a}{T+2mc^2}. \quad (8.27)$$

The energy transfered to γ_a is largest when γ_a is emitted in the direction of the incident e^+. In that case $E_{amax} = (E_{tot} + Pc)/2$. The energy transfered to γ_a is smallest when γ_a is emitted in the opposite direction of the incident e^+. Then $E_{amin} = (E_{tot} - Pc)/2$. Hence,

$$\epsilon_{max} = \frac{E_a\mathsf{max}}{E_{tot}} = \frac{1}{2}\left[1 + \sqrt{\frac{\gamma-1}{\gamma+1}}\right] \tag{8.28}$$

$$\epsilon_{min} = \frac{E_a\mathsf{min}}{E_{tot}} = \frac{1}{2}\left[1 - \sqrt{\frac{\gamma-1}{\gamma+1}}\right] \tag{8.29}$$

where $\gamma = (T + mc^2)/mc^2$. Therefore the range of ϵ is $[\epsilon_{min}\ ;\ \epsilon_{max}]$ $(\equiv [\epsilon_{min}\ ;\ 1 - \epsilon_{min}])$.

8.3.4 Sampling the Gamma Energy

A short overview of the sampling method is given in Chapter 2. The differential cross section of the two-photon positron-electron annihilation can be written as [3, 1]:

$$\frac{d\sigma(Z,\epsilon)}{d\epsilon} = \frac{Z\pi r_e^2}{\gamma-1}\ \frac{1}{\epsilon}\ \left[1 + \frac{2\gamma}{(\gamma+1)^2} - \epsilon - \frac{1}{(\gamma+1)^2}\frac{1}{\epsilon}\right] \tag{8.30}$$

where Z is the atomic number of the material, r_e the classical electron radius, and $\epsilon \in [\epsilon_{min}\ ;\ \epsilon_{max}]$. The differential cross section can be decomposed as

$$\frac{d\sigma(Z,\epsilon)}{d\epsilon} = \frac{Z\pi r_e^2}{\gamma-1}\alpha f(\epsilon) g(\epsilon) \tag{8.31}$$

where

$$\alpha = \ln(\epsilon_{max}/\epsilon_{min})$$

$$f(\epsilon) = \frac{1}{\alpha\epsilon} \tag{8.32}$$

$$g(\epsilon) = \left[1 + \frac{2\gamma}{(\gamma+1)^2} - \epsilon - \frac{1}{(\gamma+1)^2}\frac{1}{\epsilon}\right] \equiv 1 - \epsilon + \frac{2\gamma\epsilon - 1}{\epsilon(\gamma+1)^2} \tag{8.33}$$

Given two random numbers $r, r' \in [0, 1]$, the photon energies are chosen as follows:

1. sample ϵ from $f(\epsilon) : \epsilon = \epsilon_{min}\left(\frac{\epsilon_{max}}{\epsilon_{min}}\right)^r$
2. test the rejection function: if $g(\epsilon) \geq r'$ accept ϵ, otherwise return to step 1.

Then the photon energies are $E_a = \epsilon E_{tot}$ $E_b = (1 - \epsilon)E_{tot}$.

Computing the Final State Kinematics

If θ is the angle between the incident e^+ and γ_a, then from energy-momentum conservation,

$$\cos\theta = \frac{1}{Pc}\left[T + mc^2\frac{2\epsilon - 1}{\epsilon}\right] = \frac{\epsilon(\gamma+1)-1}{\epsilon\sqrt{\gamma^2-1}}. \tag{8.34}$$

The azimuthal angle, ϕ, is generated isotropically and the photon momentum vectors, $\vec{P_{\gamma_a}}$ and $\vec{P_{\gamma_b}}$, are computed from energy-momentum conservation and transformed into the lab coordinate system.

Annihilation at Rest

The method `AtRestDoIt` treats the special case when a positron comes to rest before annihilating. It generates two photons, each with energy $k = mc^2$ and an isotropic angular distribution.

8.3.5 Status of This Document

09.10.98 created by M. Maire
01.08.01 minor corrections by M. Maire
09.01.02 MeanFreePath by M. Maire
01.12.02 Re-written by D.H. Wright

Bibliography

[1] R. Ford and W. Nelson. *SLAC-265, UC-32* (1985)

[2] H. Messel and D. Crawford. *Electron-Photon shower distribution, Pergamon Press* (1970)

[3] W. Heitler. *The Quantum Theory of Radiation, Clarendon Press, Oxford* (1954)

8.4 Positron Annihilation into $\mu^+\mu^-$ Pair in Media

The class `G4AnnihiToMuPair` simulates the electromagnetic production of muon pairs by the annihilation of high-energy positrons with atomic electrons [1]. Details of the implementation are given below and can also be found in Ref.[2].

8.4.1 Total Cross Section

The annihilation of positrons and target electrons producing muon pairs in the final state ($e^+e^- \to \mu^+\mu^-$) may give an appreciable contribution to the total number of muons produced in high-energy electromagnetic cascades. The threshold positron energy in the laboratory system for this process with the target electron at rest is

$$E_{\rm th} = 2m_\mu^2/m_e - m_e \approx 43.69\,{\rm GeV}\,, \tag{8.35}$$

where m_μ and m_e are the muon and electron masses, respectively. The total cross section for the process on the electron is

$$\sigma = \frac{\pi\, r_\mu^2}{3}\,\xi\left(1+\frac{\xi}{2}\right)\sqrt{1-\xi}\,, \tag{8.36}$$

where $r_\mu = r_e\, m_e/m_\mu$ is the classical muon radius, $\xi = E_{\rm th}/E$, and E is the total positron energy in the laboratory frame. In Eq. 8.36, approximations are made that utilize the inequality $m_e^2 \ll m_\mu^2$.
The cross section as a function of the positron energy E is shown in Fig.8.2. It has a maximum at $E = 1.396\,E_{\rm th}$ and the value at the maximum is $\sigma_{\rm max} = 0.5426\,r_\mu^2 = 1.008\,\mu$b.

8.4.2 Sampling of Energies and Angles

It is convenient to simulate the muon kinematic parameters in the center-of-mass (c.m.) system, and then to convert into the laboratory frame.

The energies of all particles are the same in the c.m. frame and equal to

$$E_{\rm cm} = \sqrt{\frac{1}{2}\,m_e(E+m_e)}\,. \tag{8.37}$$

The muon momenta in the c.m. frame are $P_{\rm cm} = \sqrt{E_{\rm cm}^2 - m_\mu^2}$. In what follows, let the cosine of the angle between the c.m. momenta of the μ^+ and e^+ be denoted as $x = \cos\theta_{\rm cm}$.

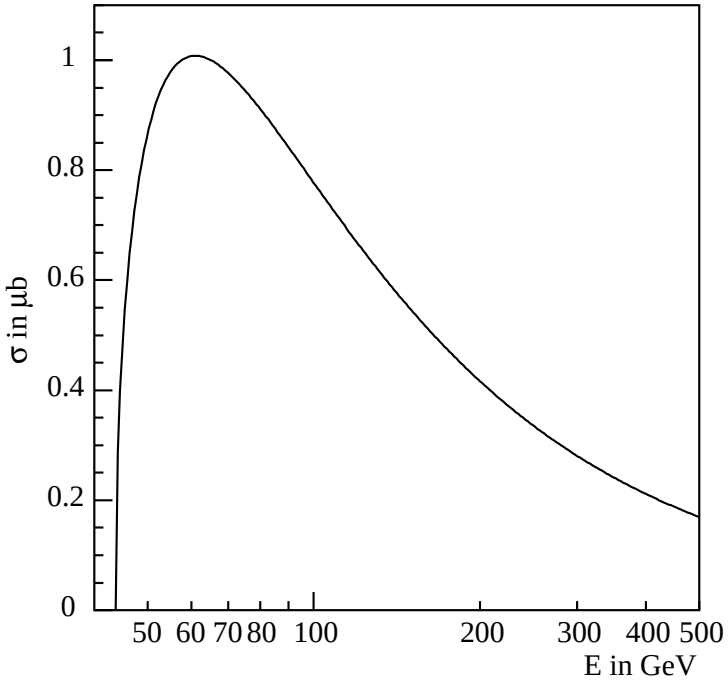

Figure 8.2: Total cross section for the process $e^+e^- \to \mu^+\mu^-$ as a function of the positron energy E in the laboratory system.

From the differential cross section it is easy to derive that, apart from normalization, the distribution in x is described by

$$f(x)\,dx = (1 + \xi + x^2\,(1 - \xi))\,dx\,, \quad -1 \le x \le 1\,. \tag{8.38}$$

The value of this function is contained in the interval $(1+\xi) \le f(x) \le 2$ and the generation of x is straightforward using the rejection technique. Fig. 8.3 shows both generated and analytic distributions.

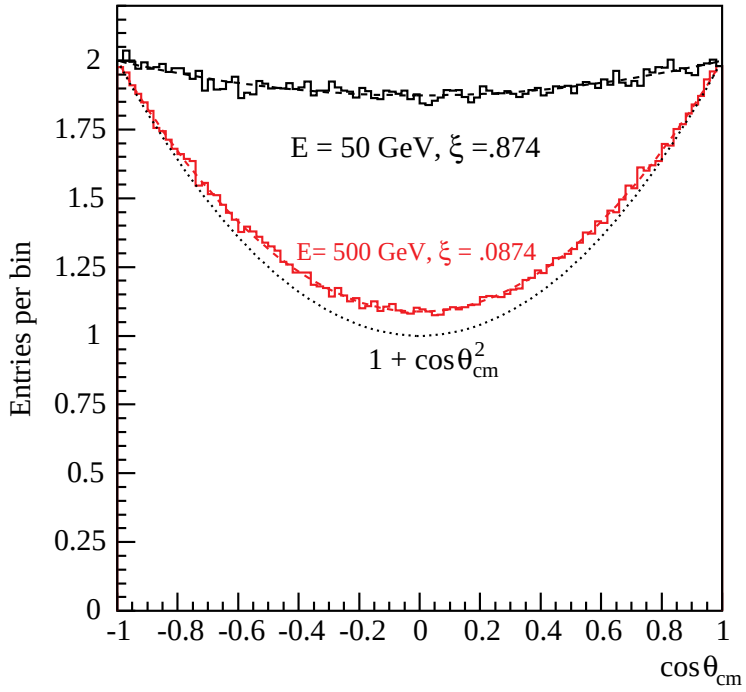

Figure 8.3: Generated histograms with 10^6 entries each and the expected $\cos\theta_{\rm cm}$ distributions (dashed lines) at $E = 50$ and 500 GeV positron energy in the lab frame. The asymptotic $1 + \cos\theta^2_{\rm cm}$ distribution valid for $E \to \infty$ is shown as dotted line.

The transverse momenta of the μ^+ and μ^- particles are the same, both in the c.m. and the lab frame, and their absolute values are equal to

$$P_\perp = P_{\rm cm}\,\sin\theta_{\rm cm} = P_{\rm cm}\,\sqrt{1 - x^2}\,. \tag{8.39}$$

The energies and longitudinal components of the muon momenta in the lab system may be obtained by means of a Lorentz transformation. The velocity and Lorentz factor of the center-of-mass in the lab frame may be written as

$$\beta = \sqrt{\frac{E - m_e}{E + m_e}}\,, \quad \gamma \equiv \frac{1}{\sqrt{1 - \beta^2}} = \sqrt{\frac{E + m_e}{2m_e}} = \frac{E_{\rm cm}}{m_e}\,. \tag{8.40}$$

The laboratory energies and longitudinal components of the momenta of the positive and negative muons may then be obtained:

$$E_+ = \gamma\,(E_{\rm cm} + x\,\beta\,P_{\rm cm})\,, \quad P_{+_\parallel} = \gamma\,(\beta E_{\rm cm} + x\,P_{\rm cm})\,, \tag{8.41}$$
$$E_- = \gamma\,(E_{\rm cm} - x\,\beta\,P_{\rm cm})\,, \quad P_{-_\parallel} = \gamma\,(\beta E_{\rm cm} - x\,P_{\rm cm})\,. \tag{8.42}$$

Finally, for the vectors of the muon momenta one obtains:

$$\mathbf{P}_+ = (+P_\perp \cos\varphi, +P_\perp \sin\varphi, P_{+_\parallel})\,, \tag{8.43}$$
$$\mathbf{P}_- = (-P_\perp \cos\varphi, -P_\perp \sin\varphi, P_{-_\parallel})\,, \tag{8.44}$$

where φ is a random azimuthal angle chosen between 0 and $2\,\pi$. The z-axis is directed along the momentum of the initial positron in the lab frame.

The maximum and minimum energies of the muons are given by

$$E_{\rm max} \approx \frac{1}{2}\,E\left(1 + \sqrt{1-\xi}\right)\,, \tag{8.45}$$

$$E_{\rm min} \approx \frac{1}{2}\,E\left(1 - \sqrt{1-\xi}\right) = \frac{E_{\rm th}}{2\left(1+\sqrt{1-\xi}\right)}\,. \tag{8.46}$$

The fly-out polar angles of the muons are approximately

$$\theta_+ \approx P_\perp/P_{+_\parallel}, \quad \theta_- \approx P_\perp/P_{-_\parallel}\,; \tag{8.47}$$

the maximal angle $\theta_{\rm max} \approx \dfrac{m_e}{m_\mu}\sqrt{1-\xi}$ is always small compared to 1.

Validity

The process described is assumed to be purely electromagnetic. It is based on virtual γ exchange, and the Z-boson exchange and $\gamma - Z$ interference processes are neglected. The Z-pole corresponds to a positron energy of $E = M_Z^2/2m_e = 8136\,\text{TeV}$. The validity of the current implementation is therefore restricted to initial positron energies of less than about 1000 TeV.

8.4.3 Status of this document

05.02.03 created by H.Burkhardt
14.04.03 minor re-wording by D.H. Wright

Bibliography

[1] A.G. Bogdanov et al., Geant4 simulation of production and interaction of muons, *IEEE Trans. Nucl. Sci. 53 (2006) 513.*

[2] H. Burkhardt, S. Kelner, and R. Kokoulin, "Production of muon pairs in annihilation of high-energy positrons with resting electrons," CERN-AB-2003-002 (ABP) and CLIC Note 554, January 2003.

8.5 Positron Annihilation into Hadrons in Media

8.5.1 Introduction

The process `G4eeToHadrons` simulates the in-flight annihilation of a positron with an atomic electron into hadrons [1]. It is assumed here that the atomic electron is initially free and at rest. Currently only two-pion production is available with a validity range up to 1 TeV.

8.5.2 Cross Section

The annihilation of positrons and target electrons producing pion pairs in the final state ($e^+e^- \to \pi^+\pi^-$) may give an appreciable contribution to electron-jet conversion at the LHC, and for the increasing total number of muons produced in the beam pipe of the linear collider [1]. The threshold positron energy in the laboratory system for this process with the target electron at rest is

$$E_{\rm th} = 2m_\pi^2/m_e - m_e \approx 70.35\,{\rm GeV}\,, \tag{8.48}$$

where m_π and m_e are the pion and electron masses, respectively. The total cross section is dominated by the reaction

$$e^+e^- \to \rho\gamma \to \pi^+\pi^-\gamma, \tag{8.49}$$

where γ is a radiative photon and $\rho(770)$ is a well known vector meson. This radiative correction is essential, because it significantly modifies the shape of the resonance. Details of the theory are described in [2], in which the main term and the leading α^2 corrections are taken into account.

8.5.3 Sampling the final state

The final state of the $e + e-$ annihilation process 8.49 is simulated by first determining the kinematic limits of the photon energy in the center of mass system and then sampling the photon energy within those limits using the differential cross section. Conservation of energy-momentum is then used to determine the four-momentum of the pion final state. Then the backward transformation to the laboratory system is performed.

8.5.4 Status of this document

09.12.05 created by V. Ivanchenko
10.12.10 revised by V. Ivanchenko

Bibliography

[1] A.G. Bogdanov et al., Geant4 simulation of production and interaction of muons, *IEEE Trans. Nucl. Sci. 53 (2006) 513.*

[2] M. Benayoun et al., *Mod. Phys. Lett. A14, 2605 (1999).*

Chapter 9

Low Energy Livermore

9.1 Introduction

Additional electromagnetic physics processes for photons, electrons, hadrons and ions have been implemented in Geant4 in order to extend the validity range of particle interactions to lower energies than those available in the standard Geant4 electromagnetic processes [1] Because atomic shell structure is more important in most cases at low energies than it is at higher energies, the low energy processes make direct use of shell cross section data. The standard processes, which are optimized for high energy physics applications, rely on parameterizations of these data.

The low energy processes include the photo-electric effect, Compton scattering, Rayleigh scattering, gamma conversion, bremsstrahlung and ionization. Fluorescence and Auger electron emission of excited atoms is also considered.

Some features common to all low energy processes currently implemented in Geant4 are summarized in this section. Subsequent sections provide more detailed information for each process.

9.1.1 Physics

The low energy processes of Geant4 represent electromagnetic interactions at lower energies than those covered by the equivalent Geant4 standard electromagnetic processes.

The current implementation of low energy processes is valid for energies down to $10eV$ and can be used up to approximately $100GeV$ for gamma processes. For electron processes upper limit is significantly below. It covers elements with atomic number between 1 and 99.

All processes involve two distinct phases:

- the calculation and use of total cross sections, and
- the generation of the final state.

Both phases are based on the theoretical models and on exploitation of evaluated data.

9.1.2 Data Sources

The data used for the determination of cross-sections and for sampling of the final state are extracted from a set of publicly distributed evaluated data libraries:

- EPDL97 (Evaluated Photons Data Library) [2];

- EEDL (Evaluated Electrons Data Library) [3];
- EADL (Evaluated Atomic Data Library) [4];
- binding energy values based on data of Scofield [5].

Evaluated data sets are produced through the process of critical comparison, selection, renormalization and averaging of the available experimental data, normally complemented by model calculations. These libraries provide the following data relevant for the simulation of Geant4 low energy processes:

- total cross-sections for photoelectric effect, Compton scattering, Rayleigh scattering, pair production and bremsstrahlung;
- subshell integrated cross sections for photo-electric effect and ionization;
- energy spectra of the secondaries for electron processes;
- scattering functions for the Compton effect;
- binding energies for electrons for all subshells;
- transition probabilities between subshells for fluorescence and the Auger effect.

The energy range covered by the data libraries extends from 100 GeV down to 1 eV for Rayleigh and Compton effects, down to the lowest binding energy for each element for photo-electric effect and ionization, and down to 10 eV for bremsstrahlung.

9.1.3 Distribution of the Data Sets

The author of EPDL97 [2], who is also responsible for the EEDL [3] and EADL [4] data libraries, Dr. Red Cullen, has kindly permitted the libraries and their related documentation to be distributed with the Geant4 toolkit. The data are reformatted for Geant4 input. They can be downloaded from the source code section of the Geant4 page: http://cern.ch/geant4/geant4.html.

The EADL, EEDL and EPDL97 data-sets are also available from several public distribution centres in a format different from the one used by Geant4 [6].

9.1.4 Calculation of Total Cross Sections

The energy dependence of the total cross section is derived for each process from the evaluated data libraries. For ionisation, bremsstrahlung and Compton scattering the total cross is obtained by interpolation according to the formula [7]:

$$\log(\sigma(E)) = \frac{log(\sigma_1)log(E_2/E) + log(\sigma_2)log(E/E_1)}{log(E_2/E_1)} \tag{9.1}$$

where E is actial energy, E_1 and E_2 are respectively the closest lower and higher energy points for which data (σ_1 and σ_2) are available. For other processes interpolation method is chosen depending on cross section shape.

9.1.5 Status of the document

30.09.1999 created by Alessandra Forti
07.02.2000 modified by Véronique Lefébure
08.03.2000 reviewed by Petteri Nieminen and Maria Grazia Pia
04.12.2001 reviewed by Vladimir Ivanchenko
26.01.2003 minor re-write by D.H. Wright
25.11.2011 reviewed by Vladimir Ivanchenko
21.11.2012 reviewed by Vladimir Ivanchenko

Bibliography

[1] "Geant4 Low Energy Electromagnetic Models for Electrons and Photons", J.Apostolakis et al., CERN-OPEN-99-034(1999), INFN/AE-99/18(1999)

[2] "EPDL97: the Evaluated Photon Data Library, '97 version", D.Cullen, J.H.Hubbell, L.Kissel, UCRL–50400, Vol.6, Rev.5

[3] "Tables and Graphs of Electron-Interaction Cross-Sections from 10 eV to 100 GeV Derived from the LLNL Evaluated Electron Data Library (EEDL), Z=1-100" S.T.Perkins, D.E.Cullen, S.M.Seltzer, UCRL-50400 Vol.31

[4] "Tables and Graphs of Atomic Subshell and Relaxation Data Derived from the LLNL Evaluated Atomic Data Library (EADL), Z=1-100" S.T.Perkins, D.E.Cullen, M.H.Chen, J.H.Hubbell, J.Rathkopf, J.Scofield, UCRL-50400 Vol.30

[5] J.H. Scofield, "Radiative Transitions", in "Atomic Inner-Shell Processes", B.Crasemann ed. (Academic Press, New York, 1975),pp.265-292.

[6] http://www.nea.fr/html/dbdata/nds_evaluated.htm

[7] "New Photon, Positron and Electron Interaction Data for Geant in Energy Range from 1 eV to 10 TeV", J. Stepanek, Draft to be submitted for publication

9.2 Compton Scattering

9.2.1 Total Cross Section

The total cross section for the Compton scattering process is determined from the data as described in section 9.1.4.

9.2.2 Sampling of the Final State

For low energy incident photons, the simulation of the Compton scattering process is performed according to the same procedure used for the "standard" Compton scattering simulation, with the addition that Hubbel's atomic form factor [1] or scattering function, SF, is taken into account. The angular and energy distribution of the incoherently scattered photon is then given by the product of the Klein-Nishina formula $\Phi(\epsilon)$ and the scattering function, $SF(q)$ [2]

$$P(\epsilon, q) = \Phi(\epsilon) \times SF(q). \tag{9.2}$$

ϵ is the ratio of the scattered photon energy E', and the incident photon energy E. The momentum transfer is given by $q = E \times \sin^2(\theta/2)$, where θ is the polar angle of the scattered photon with respect to the direction of the parent photon. $\Phi(\epsilon)$ is given by

$$\Phi(\epsilon) \cong [\frac{1}{\epsilon} + \epsilon][1 - \frac{\epsilon}{1+\epsilon^2} sin^2\theta]. \tag{9.3}$$

The effect of the scattering function becomes significant at low energies, especially in suppressing forward scattering [2].

The sampling method of the final state is based on composition and rejection Monte Carlo methods [3, 4, 5], with the SF function included in the rejection function

$$g(\epsilon) = \left[1 - \frac{\epsilon}{1+\epsilon^2} \sin^2\theta\right] \times SF(q), \tag{9.4}$$

with $0 < g(\epsilon) < Z$. Values of the scattering functions at each momentum transfer, q, are obtained by interpolating the evaluated data for the corresponding atomic number, Z.

The polar angle θ is deduced from the sampled ϵ value. In the azimuthal direction, the angular distributions of both the scattered photon and the recoil electron are considered to be isotropic [6].

Since the incoherent scattering occurs mainly on the outermost electronic subshells, the binding energies can be neglected, as stated in reference [6].

The momentum vector of the scattered photon, $\overrightarrow{P'_\gamma}$, is transformed into the `World` coordinate system. The kinetic energy and momentum of the recoil electron are then

$$\begin{aligned} T_{el} &= E - E' \\ \overrightarrow{P_{el}} &= \overrightarrow{P_\gamma} - \overrightarrow{P'_\gamma}. \end{aligned}$$

9.2.3 Status of the document

30.09.1999 created by Alessandra Forti
07.02.2000 modified by Véronique Lefébure
08.03.2000 reviewed by Petteri Nieminen and Maria Grazia Pia
26.01.2003 minor re-write by D.H. Wright

Bibliography

[1] "Summary of Existing Information on the Incoherent Scattering of Photons particularly on the Validity of the Use of the Incoherent Scattering Function", Radiat. Phys. Chem. Vol. 50, No 1, pp 113-124 (1997)

[2] "A simple model of photon transport", D.E. Cullen, Nucl. Instr. Meth. in Phys. Res. B 101(1995)499-510

[3] J.C. Butcher and H. Messel. *Nucl. Phys. 20* 15 (1960)

[4] H. Messel and D. Crawford. *Electron-Photon shower distribution, Pergamon Press* (1970)

[5] R. Ford and W. Nelson. *SLAC-265, UC-32* (1985)

[6] "New Photon, Positron and Electron Interaction Data for Geant in Energy Range from 1 eV to 10 TeV", J. Stepanek, Draft to be submitted for publication

9.3 Compton Scattering by Linearly Polarized Gamma Rays

9.3.1 The Cross Section

The quantum mechanical Klein - Nishina differential cross section for polarized photons is [Heitler 1954]:

$$\frac{d\sigma}{d\Omega} = \frac{1}{4} r_0^2 \frac{h\nu^2}{h\nu_o^2} \frac{h\nu_o^2}{h\nu^2} \left[\frac{h\nu_o}{h\nu} + \frac{h\nu}{h\nu_o} - 2 + 4cos^2\Theta \right]$$

where Θ is the angle between the two polarization vectors. In terms of the polar and azimuthal angles (θ, ϕ) this cross section can be written as

$$\frac{d\sigma}{d\Omega} = \frac{1}{2} r_0^2 \frac{h\nu^2}{h\nu_o^2} \frac{h\nu_o^2}{h\nu^2} \left[\frac{h\nu_o}{h\nu} + \frac{h\nu}{h\nu_o} - 2cos^2\phi sin^2\theta \right]$$

.

9.3.2 Angular Distribution

The integration of this cross section over the azimuthal angle produces the standard cross section. The angular and energy distribution are then obtained in the same way as for the standard process. Using these values for the polar angle and the energy, the azimuthal angle is sampled from the following distribution:

$$P(\phi) = 1 - \frac{a}{b} cos^2\phi$$

where $a = sin^2\theta$ and $b = \epsilon + 1/\epsilon$. ϵ is the ratio between the scattered photon energy and the incident photon energy.

9.3.3 Polarization Vector

The components of the vector polarization of the scattered photon are calculated from

$$\vec{\epsilon'_\perp} = \frac{1}{N} \left(\hat{j} cos\theta - \hat{k} sin\theta sin\phi \right) sin\beta$$

$$\vec{\epsilon'_\parallel} = \left[N\hat{i} - \frac{1}{N} \hat{j} sin^2\theta sin\phi cos\phi - \frac{1}{N} \hat{k} sin\theta cos\theta cos\phi \right] cos\beta$$

where

$$N = \sqrt{1 - sin^2\theta cos^2\phi}.$$

$cos\beta$ is calculated from $cos\Theta = Ncos\beta$, while $cos\Theta$ is sampled from the Klein - Nishina distribution.

The binding effects and the Compton profile are neglected. The kinetic energy and momentum of the recoil electron are then

$$T_{el} = E - E'$$
$$\vec{P}_{el} = \vec{P}_{\gamma} - \vec{P}'_{\gamma}.$$

The momentum vector of the scattered photon $\vec{P}_{\gamma}$ and its polarization vector are transformed into the `World` coordinate system. The polarization and the direction of the scattered gamma in the final state are calculated in the reference frame in which the incoming photon is along the z-axis and has its polarization vector along the x-axis. The transformation to the `World` coordinate system performs a linear combination of the initial direction, the initial poalrization and the cross product between them, using the projections of the calculated quantities along these axes.

9.3.4 Unpolarized Photons

A special treatment is devoted to unpolarized photons. In this case a random polarization in the plane perpendicular to the incident photon is selected.

9.3.5 Status of this document

18.06.2001 created by Gerardo Depaola and Francesco Longo
10.06.2002 revision by Francesco Longo
26.01.2003 minor re-wording and correction of equations by D.H. Wright

Bibliography

[1] W. Heitler *The Quantum Theory of Radiation, Oxford Clarendom Press* (1954)

9.4 Rayleigh Scattering

9.4.1 Total Cross Section

The total cross section for the Rayleigh scattering process is determined from the data as described in section 9.1.4.

9.4.2 Sampling of the Final State

The coherent scattered photon angle θ is sampled according to the distribution obtained from the product of the Rayleigh formula $(1+\cos^2\theta)\sin\theta$ and the square of Hubbel's form factor $FF^2(q)$ [1] [2]

$$\Phi(E,\theta) = [1+\cos^2\theta]\sin\theta \times FF^2(q), \tag{9.5}$$

where $q = 2E\sin(\theta/2)$ is the momentum transfer.

Form factors introduce a dependency on the initial energy E of the photon that is not taken into account in the Rayleigh formula. At low energies, form factors are isotropic and do not affect angular distribution, while at high energies they are forward peaked. For effective sampling of final state a method proposed by D.E. Cullen [2] has been implemented: form factor data were fitted and fitted parameters included in the *G4LivermoreRayleighModel*.

The sampling procedure is following:

1. atom is selected randomly according to cross section;
2. $cos\theta$ is sampled as proposed in [2];
3. azimuthal angle is sampled uniformly.

9.4.3 Status of this document

30.09.1999 created by Alessandra Forti
07.02.2000 modified by Véronique Lefébure
08.03.2000 reviewed by Petteri Nieminen and Maria Grazia Pia
10.06.2002 modified by Francesco Longo and Gerardo Depaola
26.01.2003 minor re-write and correction of equations by D.H. Wright
21.11.2012 modified by Vladimir Ivanchenko

Bibliography

[1] "Relativistic Atom Form Factors and Photon Coherent Scattering Cross Sections", J.H. Hubbell et al., J.Phys.Chem.Ref.Data, **8** (1979) 69.

[2] "A simple model of photon transport", D.E. Cullen, Nucl. Instr. Meth. in Phys. Res. **B101** (1995) 499-510.

9.5 Gamma Conversion

9.5.1 Total cross-section

The total cross-section of the Gamma Conversion process is determined from the data as described in section 9.1.4.

9.5.2 Sampling of the final state

For low energy incident photons, the simulation of the Gamma Conversion final state is performed according to [1].

The secondary $e^{\pm}$ energies are sampled using the Bethe-Heitler cross-sections with Coulomb correction.

The Bethe-Heitler differential cross-section with the Coulomb correction for a photon of energy E to produce a pair with one of the particles having energy ϵE (ϵ is the fraction of the photon energy carried by one particle of the pair) is given by [2]:

$$\begin{aligned}\frac{d\sigma(Z,E,\epsilon)}{d\epsilon} &= \frac{r_0^2\alpha Z(Z+\xi(Z))}{E^2}\left[(\epsilon^2+(1-\epsilon)^2)\left(\Phi_1(\delta)-\frac{F(Z)}{2}\right)+\right.\\ &\left.+\frac{2}{3}\epsilon(1-\epsilon)\left(\Phi_2(\delta)-\frac{F(Z)}{2}\right)\right]\end{aligned}$$

where $\Phi_i(\delta)$ are the screening functions depending on the screening variable δ [1].

The value of ϵ is sampled using composition and rejection Monte Carlo methods [1, 3, 4].

After the successful sampling of ϵ, the process generates the polar angles of the electron with respect to an axis defined along the direction of the parent photon. The electron and the positron are assumed to have a symmetric angular distribution. The energy-angle distribution is given by[5]:

$$\begin{aligned}\frac{d\sigma}{dpd\Omega} &= \frac{2\alpha^2e^2}{\pi km^4}\left[\left(\frac{2x(1-x)}{(1+l)}^2-\frac{12lx(1-x)}{(1+l)^4}\right)(Z^2+Z)+\right.\\ &\left.+\left(\frac{2x^2-2x+1}{(1+l)^2}+\frac{4lx(1-x)}{(1+l)^4}\right)(X-2Z^2f((\alpha Z)^2))\right]\end{aligned}$$

where k is the photon energy, p the momentum and E the energy of the electron of the $e^{\pm}$ pair $x = E/k$ and $l = E^2\theta^2/m^2$. The sampling of this cross-section is obtained according to [1].

The azimuthal angle ϕ is generated isotropically.

This information together with the momentum conservation is used to calculate the momentum vectors of both decay products and to transform them to the GEANT coordinate system. The choice of which particle in the pair is the electron/positron is made randomly.

9.5.3 Status of the document

18.06.2001 created by Francesco Longo

Bibliography

[1] Urban L., in Brun R. et al. (1993), *Geant. Detector Description and Simulation Tool*, CERN Program Library, section `Phys/211`

[2] R. Ford and W. Nelson., *SLAC-210, UC-32* (1978)

[3] J.C. Butcher and H. Messel. *Nucl. Phys. 20* 15 (1960)

[4] H. Messel and D. Crawford. *Electron-Photon shower distribution, Pergamon Press* (1970)

[5] Y. S. Tsai, *Rev. Mod. Phys. 46* 815 (1974), Y. S. Tsai, *Rev. Mod. Phys. 49* 421 (1977)

9.6 Triple Gamma Conversion

A new model class *G4BoldyshevTripletModel* was developed to simulate the pair production by linearly polarized gamma rays on electrons For the angular distribution of electron recoil we used the cross section by Vinokurov and Kuraev [1] using the Borsellino diagrams in the high energy For energy distribution for the pair, we used Boldyshev [2] formula that differs only in the normalization from Wheeler-Lamb. The cross sections include a cut off for momentum detections.

9.6.1 Method

The first step is sample the probability to have an electron recoil with momentum greater than a threshold define by the user (by default, this value is $p_0 = 1$ in units of mc). This probability is

$$\sigma(p \geq p_0) = \alpha r_0^2 \left(\frac{82}{27} - \frac{14}{9} ln X_0 + \frac{4}{15} X_0 - 0.0348 X_0^2 + 0.008 X_0^3 - ... \right) \tag{9.6}$$

$$X_0 = 2 \left(\sqrt{p_0^2 +} - 1 \right). \tag{9.7}$$

Since that total cross section is $\sigma = \alpha r_0^2 \left(\frac{28}{4} ln 2E_\gamma - \frac{218}{27} \right)$, if a random number is $\xi \geq \sigma(p \geq p_0)/\sigma$ we create the electron recoil, otherwise we deposited the energy in the local point.

9.6.2 Azimuthal Distribution for Electron Recoil

The expression for the differential cross section is composed of two terms which express the azimuthal dependence as follows:

$$d\sigma = d\sigma^{(t)} - P d\sigma^{(l)} cos(2\varphi) \tag{9.8}$$

Where, both $d\sigma_{(t)}$ and $d\sigma_{(l)}$, are independent of the azimuthal angle, φ, referred to an origin chosen in the direction of the polarization vector $\vec{P}$ of the incoming photons.

9.6.3 Monte Carlo Simulation of the Asymptotic Expression

In this section we present an algorithm for Monte Carlo simulation of the asymptotic expressions calculate by Vinokurov et.al. [1].

We must generate random values of θ and φ distributed with probability proportional to the following function $f(\theta, \varphi)$, for θ restricted inside of its allowed interval value [2] (0, or $\theta_{max}(p_0)$):

$$f(\theta, \varphi) = \frac{\sin\theta}{\cos^3\theta}\left(F_1(\theta) - \mathrm{P}\cos(2\varphi) F_P(\theta)\right) \tag{9.9}$$

$$F_1(\theta) = 1 - \frac{1 - 5\cos^2\theta}{\cos\theta}\ln(\cot(\theta/2)) \tag{9.10}$$

$$F_P(\theta) = 1 - \frac{\sin^2\theta}{\cos\theta}\ln(\cot(\theta/2)) \tag{9.11}$$

As we will see, for $\theta < \pi/2$, F_1 is several times greater than F_P, and since both are positive, it follows that f is positive for any possible value of P ($0 \leq P \leq 1$).

Since F_1 is the dominant term in expression , it is more convenient to begin developing the algorithm of this term, belonging to the unpolarized radiation.

9.6.4 Algorithm for Non Polarized Radiation

The algorithm was described in Ref.[3]. We must generate random values of θ between 0 and $\theta_{max} = arccos\left(\frac{E_1 - mc^2}{p_0} + mc^2\frac{E_1 + mc^2}{E_\gamma p_0}\right)$, $E_1 = \sqrt{p_0^2 + (mc^2)^2}$ distributed with probability proportional to the following function $f_1(\theta)$:

$$\begin{aligned} f_1(\theta) &= \frac{\sin(\theta)}{\cos^3(\theta)}\left(1 - \frac{1 - 5\cos^2(\theta)}{\cos(\theta)}\ln(\cot(\theta/2))\right) \\ &= \frac{\sin(\theta)}{\cos^3(\theta)} \times F_1(\theta) \end{aligned} \tag{9.12}$$

By substitution $\cos(\theta/2) = \sqrt{\frac{1+cos\theta}{2}}$ and $\sin(\theta/2) = \sqrt{\frac{1-cos\theta}{2}}$, We can write:

$$\ln(\cot(\theta/2)) = \frac{1}{2}\ln\left(\frac{1 + \cos\theta}{1 - \cos\theta}\right) \tag{9.13}$$

In order to simulate the f_1 function, it may be decomposed in two factors: the first, $sin(\theta)/cos^3(\theta)$, easy to integrate, and the other, $F_1(\theta)$, which may constitute a reject function, on despite of its $\theta = 0$ divergence. This is possible because they have very low probability. On other hand, θ values near to zero are not useful to measure polarization because for those angles it is very difficult to determine the azimuthal distribution (due to multiple scattering).

Then, it is possible to choose some value of θ_0, small enough that it is not important that the sample is fitted rigorously for $\theta < \theta_0$, and at the same time $F_1(\theta_0)$ is not too big.

Modifying F_1 so that it is constant for $\theta \leq \theta_0$, we may obtain an adequate reject function. Doing this, we introduce only a very few missed points, all of which lie totally outside of the interesting region.

Expanding F_1 for great values of θ, we see it is proportional to $cos^2\theta$:

$$F_1(\theta) \to \frac{14}{3}\cos^2\theta\left(1+\frac{33}{35}\cos^2\theta+\ldots\right), \quad \text{if } \theta \to \pi/2$$

Thus, it is evident that F_1 divided by $cos^2(\theta)$ will be a better reject function, because it tends softly to a some constant value $(14/3 = 4,6666...)$ for large θs, whereas its behavior is not affected in the region of small θs, where $cos(\theta) \to 1$.

It seems adequate to choose θ_0 near 5^0, and, after some manipulation looking for round numbers we obtain:

$$\frac{F_1(4.47^0)}{\cos^2(4.47^0)} \cong 14.00$$

Finally we define a reject function:

$$\begin{array}{rcll} r(\theta) & = & \frac{1}{14}\frac{F_1(\theta)}{\cos^2(\theta)} = \frac{1}{14\cos^2(\theta)} & \\ & & \left(1-\frac{1-5\cos^2(\theta)}{2\cos(\theta)}\ln\left(\frac{1+\cos\theta}{1-\cos\theta}\right)\right) & ; \quad \text{for } \theta \geq 4.47^0 \\ r(\theta) & = & 1 & ; \quad \text{for} \theta \leq 4.47^0 \end{array} \tag{9.14}$$

Now we have a probability distribution function (PDF) for θ, $p(\theta) = Cf_1(\theta)$, expressed as a product of another PDF, $\pi(\theta)$, by the reject function:

$$p(\theta) = Cf_1(\theta) \cong C'\pi(\theta)\, r(\theta) \tag{9.15}$$

where C is the normalization constant belonging to the function $p(\theta)$.

One must note that the equality between $C \sim f_1(\theta)$ and $C'\pi(\theta)r(\theta)$ is not exact for small values of θ, where we have truncated the infinity of $F_1(\theta)$; but this can not affect appreciably the distribution because $f_1 \to 0$ there. Now the PDF $\pi(\theta)$ is:

$$\pi(\theta) = C_\pi \frac{14sin(\theta)}{cos(\theta)} \tag{9.16}$$

From the normalization, the constant C_π results:

$$C_\pi = \frac{1}{14\int_0^{\theta_{max}} \frac{sin(\theta)}{cos(\theta)} d\theta} = \frac{-1}{14\ln\left(cos(\theta_{max})\right)} = \frac{1}{7}\ln\left(\frac{\omega}{4m}\right) \tag{9.17}$$

And the relation with C is given by:

$$C = \frac{1}{\int_0^{\theta_{max}} f_1(\theta) d\theta} \cong C' C_\pi \tag{9.18}$$

Then we obtain the cumulative probability by integrating the PDF $\pi(\theta)$:

$$P_\pi = \int_0^\theta \pi(\theta') d\theta' = \frac{-14\ln(\cos(\theta))}{7\ln\left(\frac{\omega}{4m}\right)} = \frac{2\ln(\cos(\theta))}{\ln\left(4m/\omega\right)} \tag{9.19}$$

Finally for the Monte Carlo method we sample a random number ξ_1 (between 0 and 1), which is defined as equal to P_π , and obtain the corresponding θ value:

$$\xi_1 = \frac{2\ln(\cos\theta)}{\ln\left(4\mathrm{m}/\omega\right)} = \frac{\ln(\cos\theta)}{\ln\left(\cos(\theta_{\mathrm{max}})\right)}$$

Then,

$$\theta = \arccos\left(\left(\frac{4m}{\omega}\right)^{\frac{\xi_1}{2}}\right) \tag{9.20}$$

Another random number ξ_2 is sampled for the reject process: the θ value is accepted if $\xi_2 \leq r(\theta)$, and reject in the contrary.

For $\theta \leq 4,47^0$ all values are accepted. It happens automatically without any modification in the algorithm previously defined (it is not necessary to define the truncated reject function for $\theta < \theta_0$).

9.6.5 Algorithm for Polarized Radiation

The algorithm was also described in Ref.[3]. As we have seen, the azimuthal dependence of the differential cross section is given by the expressions and :

$$f\left(\theta,\varphi\right) = \frac{\sin\theta}{\cos^3\theta}\left(F_1\left(\theta\right) - \mathrm{P}\cos\left(2\varphi\right)F_P\left(\theta\right)\right) \tag{9.21}$$

$$F_P\left(\theta\right) = 1 - \frac{\sin^2\theta}{\cos\theta}\ln\left(\cot\left(\theta/2\right)\right) \tag{9.22}$$

We see that F_P tends to 1 at $\theta = 0$, decreases monotonically to 0 as θ goes to $\pi/2$.

Furthermore, the expansion of F_P for θ near $\pi/2$ shows that it is proportional to $cos^2(\theta)$, in virtue of which $F_P/cos^2(\theta)$ tends to a non null value, 2/3. This value is exactly 7 times the value of $F_1/cos^2(\theta)$.

This suggests applying the combination method, rearranging the whole function as follows:

$$f(\theta,\varphi) = \tan(\theta)\frac{F_1(\theta)}{cos^2(\theta)}\left(1 - cos(2\varphi)P\frac{F_P(\theta)}{F_1(\theta)}\right) \tag{9.23}$$

and the normalized PDF $p(\theta,\varphi)$:

$$p(\theta,\varphi) = Cf(\theta,\varphi) \tag{9.24}$$

where is C the normalization constant

$$\frac{1}{C} = \int_0^{\theta_{\max}}\int_0^{2\pi} f(\theta,\varphi)\, d\varphi d\theta \tag{9.25}$$

Taking account that $\int_0^{2\pi}\cos(2\varphi)\, d\varphi = 0$, then:

$$\frac{1}{C} = 2\pi\int_0^{\theta_{\max}}\tan(\theta)\frac{F_1(\theta)}{\cos^2(\theta)}d\theta \tag{9.26}$$

On the other hand the integration over the azimuthal angle is straightforward and gives:

$$q(\theta) = \int_0^{2\pi} p(\theta,\varphi)d\varphi = 2\pi C\tan(\theta)\frac{F_1(\theta)}{cos^2(\theta)} \tag{9.27}$$

and $p(\varphi/\theta)$ is the conditional probability of φ given θ:

$$\begin{aligned} p(\varphi/\theta) &= \frac{p(\theta,\varphi)}{q(\theta)} = \frac{1}{2\pi C\tan(\theta)\frac{F_1(\theta)}{cos^2(\theta)}}C\frac{sin(\theta)}{cos^3(\theta)}F_1(\theta)\left(1 - cos(2\varphi)P\frac{F_P(\theta)}{F_1(\theta)}\right) \\ &= \frac{1}{2\pi}\left(1 - \cos(2\varphi)P\frac{F_P(\theta)}{F_1(\theta)}\right) \end{aligned} \tag{9.28}$$

Now the procedure consists of sampling θ according the PDF $q(\theta)$; then, for each value of θ we must sample φ according to the conditional PDF $p(\varphi/\theta)$.

Knowing that F_1 is several times greater than F_P, we can see that P $F_1/F_P << 1$, and thus $p(\varphi/\theta)$ maintains a nearly constant value slightly diminished in some regions of φ. Consequently the φ sample can be done directly by the rejecting method with high efficiency.

On the other hand, $q(\theta)$ is the same function $p(\theta)$ given by , that is the PDF for unpolarized radiation, $q(\theta) \cong C'\pi(\theta)r(\theta)$, so we can sample θ with

exactly the same procedure, specified as follows:
1.- We begin sampling a random number ξ_1 and obtain θ from :

$$\theta = \arccos\left(\left(\frac{4m}{\omega}\right)^{\frac{\xi_1}{2}}\right)$$

2.- Then we sample a second random number $\xi 2$ and accept the values of θ if $\xi_2 \leq r(\theta)$, where $r(\theta)$ is the same expression defined before:

$$\mathrm{r}\left(\theta\right) = \frac{1}{14\cos^2\theta}\left(1 - \frac{1 - 5\cos^2\theta}{2\cos\theta}\ln\left(\frac{1+\cos\theta}{1-\cos\theta}\right)\right)$$

For $\theta \geq 4,47^0$ and for $\theta \leq 4,47^0$ all values are accepted.
3.- Now we sample φ. According to the reject method, we sample a third random number ξ_3 (which is defined as $\varphi/2\pi$) and evaluate the reject function (which is essentially):

$$r_\theta(\xi_3) = \frac{1}{2\pi}\left(1 - \cos\left(4\pi\xi_3\right)P\frac{F_P\left(\theta\right)}{F_1\left(\theta\right)}\right) \tag{9.29}$$

$$= \frac{1}{2\pi}\left(1 - \cos(4\pi\xi_3)P\frac{\cos\theta - \sin^2\theta\ln\left(\cot\left(\frac{\theta}{2}\right)\right)}{cos\theta - (1-5cos^2\theta)\ln\left(\cot\left(\frac{\theta}{2}\right)\right)}\right) \tag{9.30}$$

4.- Finally, with a fourth random number ξ_4 , we accept the values of $\varphi = 2\pi\xi_4$ if $\xi_4 \leq r_\theta(\xi_3)$.

9.6.6 Sampling of Energy

For the electron recoil we calculate the energy from the maximum momentum that can take according with the θ angle

$$E_r = mc^2\frac{(S + (mc^2)^2)}{D2} \tag{9.31}$$

Where

$$\begin{aligned} S &= mc^2\left(2E_{gamma} + mc^2\right) \\ D2 &= 4Smc^2 + \left(S - (mc^2)^2\right)^2\sin^2(\theta) \end{aligned}$$

The remnant energy is distributed to the pair according to the Boldyshev formula [2](x is the fraction of the positron energy):

$$2\pi\frac{d^2\sigma}{dxd\phi} = 2\alpha r_0^2\left\{\left[1 - 2x\left(1-x\right)\right]J_1(p_0) + 2x\left(1-x\right)\left[1 - P\cos(\phi)\right]J_2(p_0)\right\} \tag{9.32}$$

$$J_1(p_0) = 2\left(t\frac{\cosh(t)}{\sinh(t)} - ln(2\sinh(t))\right)$$

$$J_2(p_0) = -\frac{2}{3}\ln(2\sinh(t)) + t\frac{\cosh(t)}{\sinh(t)} + \frac{\sinh(t) - t\cosh^3(t)}{3\sinh^3(t)}, \qquad \sinh(2t) = p_0$$

This distribution can by write like a PDF for x:

$$P(x) = N\left(1 - Jx(1-x)\right) \tag{9.33}$$

where N is a normalization constant and $J = (J_1 - J_2)/J_1$.
Solving for x (ξ is a random number):

$$x = \frac{c_1^{1/3}}{2J} + \frac{J-4}{2c_1^{1/3}} + \frac{1}{2} \tag{9.34}$$

$$\begin{aligned} c_1 &= (-6 + 12r_n + J + 2a)\,J^2 \\ a &= \left(\tfrac{16-3J-36r_n+36Jr_n^2+6r_nJ^2}{J}\right) \\ r_n &= \xi\left(1 - \tfrac{J}{6}\right) \end{aligned}$$

9.6.7 Status of This Document

10.12.10 created by G. Depaola
10.12.10 minor edition by V. Ivanchenko

Bibliography

[1] E.A. Vinokurov and E.A. Kuraev, *Zh. Eksp. Teor. Fiz. 63 (1972) 1142, in Russian; Sov. Phys. JETP 36, 602 (1973).*

[2] V.F. Boldyshev, E.A. Vinokurov, N.P. Merenkov, Yu.P. Peresunko, *Phys. Part. Nucl. 25 (1994) 292.*

[3] G.O. Depaola, M.L. Iparraguirre, *Nucl. Instr. Meth. A611 (2009) 84.*

9.7 Photoelectric effect

Two model classes are available *G4LivermorePhotoElectricModel* and *G4LivermorePolarizedPhotoelEctricModel*.

9.7.1 Cross sections

The total photoelectric and single shell cross-sections are tabulated from threshold to $600keV$. Above $600keV$ EPDL97 cross sections [1] are parameterized as following:

$$\sigma(E) = \frac{a_1}{E} + \frac{a_2}{E^2} + \frac{a_3}{E^3} + \frac{a_4}{E^4} + \frac{a_5}{E^5}. \tag{9.35}$$

The accuracy of such parameterisation is better than 1%.

9.7.2 Sampling of the final state

The incident photon is absorbed and an electron is emitted.

The electron kinetic energy is the difference between the incident photon energy and the binding energy of the electron before the interaction. The sub-shell, from which the electron is emitted, is randomly selected according to the relative cross-sections of all subshells, determined at the given energy. The interaction leaves the atom in an excited state. The deexcitation of the atom is simulated as described in section 14.1.

9.7.3 Angular distribution of the emmited photoelectron

For sampling of the direction of the emmited photoelectron by default the angular generator *G4SauterGavrilaAngularDistribution* is used. The algorithm is described in 5.2.

For polarized model alternative angular generator is applied *G4PhotoElectricAngularGeneratorPolarized*. This model models the double differential cross section (for angles θ and ϕ) and thus it is capable of account for polarization of the incident photon. The developed generator was based in the research of Sauter in 1931[2]. The Sauter's formula was recalculated by Gavrila in 1959 for the K-shell [3] and in 1961 for the L-shells [4]. These new double differential formulas have some limitations, αZ<<1 and have a range between 0.1< β <0.99 c.

The double differential photoeffect for K–shell can be written as [3]:

$$\frac{d\sigma}{d\omega}(\theta,\phi) = \frac{4}{m^2}\alpha^6 Z^5 \frac{\beta^3(1-\beta^2)^3}{[1-(1-\beta^2)^{1/2}]}\left(F\left(1-\frac{\pi\alpha Z}{\beta}\right)+\pi\alpha Z G\right) \quad (9.36)$$

where

$$\begin{aligned} F &= \frac{\sin^2\theta\cos^2\phi}{(1-\beta\cos\theta)^4} - \frac{1-(1-\beta^2)^{1/2}}{2(1-\beta^2)}\frac{\sin^2\theta\cos^2\phi}{(1-\beta\cos\theta)^3} \\ &+ \frac{\left[1-(1-\beta^2)^{1/2}\right]^2}{4(1-\beta^2)^{3/2}}\frac{\sin^2\theta}{(1-\beta\cos\theta)^3} \end{aligned}$$

$$\begin{aligned} G &= \frac{[1-(1-\beta^2)^{1/2}]^{1/2}}{2^{7/2}\beta^2(1-\beta\cos\theta)^{5/2}}\left[\frac{4\beta^2}{(1-\beta^2)^{1/2}}\frac{\sin^2\theta\cos^2\phi}{1-\beta\cos\theta}+\frac{4\beta}{1-\beta^2}\cos\theta\cos^2\phi-\right. \\ &- 4\,\frac{1-(1-\beta^2)^{1/2}}{1-\beta^2}(1-\cos^2\phi)-\beta^2\,\frac{1-(1-\beta^2)^{1/2}}{1-\beta^2}\frac{\sin^2\theta}{1-\beta\cos\theta}- \\ &+ \left.4\beta^2\frac{1-(1-\beta^2)^{1/2}}{(1-\beta^2)^{3/2}}-4\beta\frac{\left[1-(1-\beta^2)^{1/2}\right]^2}{(1-\beta^2)^{3/2}}\right] \\ &+ \frac{1-(1-\beta^2)^{1/2}}{4\beta^2(1-\beta\cos\theta)^2}\left[\frac{\beta}{1-\beta^2}-\frac{2}{1-\beta^2}\cos\theta\cos^2\phi+\frac{1-(1-\beta^2)^{1/2}}{(1-\beta^2)^{3/2}}\cos\theta\right. \\ &- \left.\beta\frac{1-(1-\beta^2)^{1/2}}{(1-\beta^2)^{3/2}}\right] \end{aligned}$$

where β is the electron velocity, α is the fine–structure constant, Z is the atomic number of the material and θ, ϕ are the emission angles with respect to the electron initial direction.

The double differential photoeffect distribution for L1–shell is the same as for K–shell despising a constant [4]:

$$B = \xi\frac{1}{8} \quad (9.37)$$

where ξ is equal to 1 when working with unscreened Coulomb wave functions as it is done in this development.

Since the polarized Gavrila cross–section is a 2–dimensional non–factorized distribution an acceptance–rejection technique was the adopted [5]. For the Gravrila distribution, two functions were defined $g_1(\phi)$ and $g_2(\theta)$:

$$g_1(\phi) = a \quad (9.38)$$

$$g_2(\theta) = \frac{\theta}{1+c\theta^2} \quad (9.39)$$

such that:

$$Ag_1(\phi)g_2(\theta) \geq \frac{d^2\sigma}{d\phi d\theta} \tag{9.40}$$

where A is a global constant. The method used to calculate the distribution is the same as the one used in Low Energy 2BN Bremsstrahlung Generator, being the difference $g_1(\phi) = a$.

9.7.4 Status of the document

30.09.1999 created by Alessandra Forti
07.02.2000 modified by Véronique Lefébure
08.03.2000 reviewed by Petteri Nieminen and Maria Grazia Pia
13.05.2002 modified by Vladimir Ivanchenko
01.05.2006 modified by Ana Farinha, Andreia Trindade, Luís Peralta and Pedro Rodrigues
21.11.2012 modified by Vladimir Ivanchenko

Bibliography

[1] "EPDL97: the Evaluated Photon Data Library, '97 version", D.Cullen, J.H.Hubbell, L.Kissel, UCRL–50400, Vol.6, Rev.5

[2] "K–Shell Photoelectric Cross Sections from 200 keV to 2 MeV", R H Pratt, R D Levee, R L Pexton and W Aron, Phys. Rev. 134 (1964) 4A

[3] "Relativistic K–Shell Photoeffect", M. Gavrila, Phys. Rev. 113 (1959) 2

[4] "Relativistic L–Shell Photoeffect", M. Gavrila, Phys. Rev. 124 (1961) 4

[5] "Monte Carlo Generation of 2BNBremsstrahlung Distribution", L. Peralta, P. Rodrigues, A. Trindade CERN EXT–2004–039 (July, 2003)

9.8 Electron ionisation

The class *G4LivermoreIonisationModel* calculates the continuous energy loss due to electron ionisation and simulates δ-ray production by electrons. The *delta*-electron production threshold for a given material, T_c, is used to separate the continuous and the discrete parts of the process. The energy loss of an electron with the incident energy, T, is expressed via the sum over all atomic shells, s, and the integral over the energy, t, of *delta*-electrons:

$$\frac{dE}{dx} = \sum_s \left(\sigma_s(T) \frac{\int_{0.1eV}^{T_c} t \frac{d\sigma}{dt} dt}{\int_{0.1eV}^{T_{max}} \frac{d\sigma}{dt} dt} \right), \tag{9.41}$$

where $T_{max} = 0.5T$ is the maximum energy transfered to a δ-electron, $\sigma_s(T)$ is the total cross-section for the shell, s, at a given incident kinetic energy, T, and $0.1eV$ is the low energy limit of the EEDL data. The δ-electron production cross-section is a complimentary function:

$$\sigma(T) = \sum_s \left(\sigma_s(T) \frac{\int_{T_c}^{T_{max}} \frac{d\sigma}{dt} dt}{\int_{0.1eV}^{T_{max}} \frac{d\sigma}{dt} dt} \right). \tag{9.42}$$

The partial sub-shell cross-sections, σ_s, are obtained from an interpolation of the evaluated cross-section data in the EEDL library [1], according to the formula (9.1) in Section 9.1.4.

The probability of emission of a δ-electron with kinetic energy, t, from a sub-shell, s, of binding energy, B_s, as the result of the interaction of an incoming electron with kinetic energy, T, is described by:

$$\frac{d\sigma}{dt} = \frac{P(x)}{x^2}, \quad \text{with} x = \frac{t + B_s}{T + B_s}, \tag{9.43}$$

where the parameter x is varied from $x_{min} = (0.1eV + B_s)/(T + B_s)$ to 0.5. The function, $P(x)$, is parametrised differently in 3 regions of x: from x_{min} to x_1 the linear interpolation with linear scale of 4 points is used; from x_1 to x_2 the linear interpolation with logarithmic scale of 16 points is used; from x_2 to 0.5 the following interpolation is applied:

$$P(x) = 1 - gx + (1 - g)x^2 + \frac{x^2}{1 - x}\left(\frac{1}{1 - x} - g\right) + A * (0.5 - x)/x, \tag{9.44}$$

where A is a fit coefficient, g is expressed via the gamma factor of the incoming electron:

$$g = (2\gamma - 1)/\gamma^2. \tag{9.45}$$

For the high energy case ($x >> 1$) the formula (9.44) is transformed to the Möller electron-electron scattering formula [2, 3].

The value of the coefficient, A, for each element is obtained as a result of the fit on the spectrum from the EEDL data for those energies which are available in the database. The values of x_1 and x_2 are chosen for each atomic shell according to the spectrum of δ-electrons in this shell. Note that x_1 corresponds to the maximum of the spectrum, if the maximum does not coincide with x_{min}. The dependence of all 24 parameters on the incident energy, T, is evaluated from a logarithmic interpolation (9.1).

The sampling of the final state proceeds in three steps. First a shell is randomly selected, then the energy of the *delta*-electron is sampled, finally the angle of emission of the scattered electron and of the δ-ray is determined by energy-momentum conservation taken into account electron motion on the atomic orbit.

The interaction leaves the atom in an excited state. The deexcitation of the atom is simulated as described in section 14.1. Sampling of the excitations is carried out for both the continuous and the discrete parts of the process.

9.8.1 Status of the document

30.09.1999 created by Alessandra Forti
07.02.2000 modified by Véronique Lefébure
08.03.2000 reviewed by Petteri Nieminen and Maria Grazia Pia
05.12.2001 modified by Vladimir Ivanchenko
13.05.2002 modified by Vladimir Ivanchenko

Bibliography

[1] "Tables and Graphs of Electron-Interaction Cross-Sections from 10 eV to 100 GeV Derived from the LLNL Evaluated Electron Data Library (EEDL), Z=1-100" S.T.Perkins, D.E.Cullen, S.M.Seltzer, UCRL-50400 Vol.31

[2] GEANT3 manual ,CERN Program Library Long Writeup W5013 (October 1994).

[3] H.Messel and D.F.Crawford. Pergamon Press,Oxford,1970.

9.9 Bremsstrahlung

The class G4LivermoreBremsstrahlungModel calculates the continuous energy loss due to low energy gamma emission and simulates the gamma production by electrons. The gamma production threshold for a given material ω_c is used to separate the continuous and the discrete parts of the process. The energy loss of an electron with the incident energy T are expressed via the integrand over energy of the gammas:

$$\frac{dE}{dx} = \sigma(T)\frac{\int_{0.1eV}^{\omega_c} t\frac{d\sigma}{d\omega}d\omega}{\int_{0.1eV}^{T}\frac{d\sigma}{d\omega}d\omega}, \tag{9.46}$$

where $\sigma(T)$ is the total cross-section at a given incident kinetic energy, T, $0.1eV$ is the low energy limit of the EEDL data. The production cross-section is a complimentary function:

$$\sigma = \sigma(T)\frac{\int_{\omega_c}^{T}\frac{d\sigma}{d\omega}d\omega}{\int_{0.1eV}^{T}\frac{d\sigma}{d\omega}d\omega}. \tag{9.47}$$

The total cross-section, σ_s, is obtained from an interpolation of the evaluated cross-section data in the EEDL library [1], according to the formula (9.1) in Section 9.1.4.

The EEDL data [1] of total cross-sections are parametrised [2] according to (9.1). The probability of the emission of a photon with energy, ω, considering an electron of incident kinetic energy, T, is generated according to the formula:

$$\frac{d\sigma}{d\omega} = \frac{F(x)}{x}, \quad \text{with} x = \frac{\omega}{T}. \tag{9.48}$$

The function, $F(x)$, describing energy spectra of the outcoming photons is taken from the EEDL library. For each element 15 points in x from 0.01 to 1 are used for the linear interpolation of this function. The function F is normalised by the condition $F(0.01) = 1$. The energy distributions of the emitted photons available in the EEDL library are for only a few incident electron energies (about 10 energy points between 10 eV and 100 GeV). For other energies a logarithmic interpolation formula (9.1) is used to obtain values for the function, $F(x)$. For high energies, the spectral function is very close to:

$$F(x) = 1 - x + 0.75x^2. \tag{9.49}$$

9.9.1 Bremsstrahlung angular distributions

The angular distribution of the emitted photons with respect to the incident electron can be sampled according to three alternative generators described below. The direction of the outcoming electron is determined from the energy-momentum balance. This generators are currently implemented in G4ModifiedTsai, G4Generator2BS and G4Generator2BN classes.

G4ModifiedTsai

The angular distribution of the emitted photons is obtained from a simplified [3] formula based on the Tsai cross-section [4], which is expected to become isotropic in the low energy limit.

G4Generator2BS

In G4Generator2BS generator, the angular distribution of the emitted photons is obtained from the 2BS Koch and Motz bremsstrahlung double differential cross-section [5]:

$$\begin{aligned} d\sigma_{k,\theta} &= \frac{4Z^2 r_0^2}{137}\frac{dk}{k} y dy \left\{ \frac{16y^2 E}{(y^2+1)^4 E_0} - \right. \\ &\left. \frac{(E_0+E)^2}{(y^2+1)^2 E_0^2} + \left[\frac{E_0^2+E^2}{(y^2+1)^2 E_0^2} - \frac{4y^2 E}{(y^2+1)^4 E_0} \right] lnM(y) \right\} \end{aligned}$$

where k the photon energy, θ the emission angle, E_0 and E are the initial and final electron energy in units of $m_e c^2$, r_0 is the classical electron radius and Z the atomic number of the material. y and $M(y)$ are defined as:

$$\begin{aligned} y &= E_0 \theta \\ \frac{1}{M(y)} &= \left(\frac{k}{2E_0 E} \right)^2 + \left(\frac{Z^{1/3}}{111(y^2+1)} \right)^2 \end{aligned}$$

The adopted sampling algorithm is based on the sampling scheme developed by A. F. Bielajew et al. [6], and latter implemented in EGS4. In this sampling algorithm only the angular part of 2BS is used, with the emitted photon energy, k, determined by GEANT4 $\left(\frac{d\sigma}{dk}\right)$ differential cross-section.

G4Generator2BN

The angular distribution of the emitted photons is obtained from the 2BN Koch and Motz bremsstrahlung double differential cross-section [5] that can be written as:

$$
\begin{aligned}
d\sigma_{k,\theta} &= \frac{Z^2 r_0^2}{8\pi 137}\frac{dk}{k}\frac{p}{p_0}d\Omega_k\left\{\frac{8\sin^2\theta(2E_0^2-1)}{p_0^2\Delta_0^4}-\right. \\
&\frac{2(5E_0^2+2EE_0+3)}{p_0^2\Delta_0^2}-\frac{2(p_0^2-k^2)}{Q^2\Delta_0}+\frac{4E}{p_2^2\Delta_0}+\frac{L}{pp_0} \\
&\left[\frac{4E_0\sin^2\theta(3k-p_0^2E)}{p_0^2\Delta^4}+\frac{4E_0^2(E_0^2+E^2)}{p_0^2\Delta_0^2}+\right. \\
&\left.\frac{2-2(E_0^2-3EE_0+E^2)}{p_0^2\Delta_0^2}+\frac{2k(E_0^2+EE_0-1)}{p_0^2\Delta_0}\right] \\
&\left.-\left(\frac{4\epsilon}{p\Delta 0}\right)+\left(\frac{\epsilon^Q}{pQ}\right)\left[\frac{4}{\Delta_0^2}-\frac{6k}{\Delta_0}-\frac{2k(p_0^2-k^2)}{Q^2\Delta_0}\right]\right\}
\end{aligned}
$$

in which:

$$
\begin{aligned}
L &= \ln\left[\frac{EE_0-1+pp_0}{EE_0-1-pp_0}\right] \\
\Delta_0 &= E_0-p_0\cos\theta \\
Q^2 &= p_0^2+k^2-2p_0k\cos\theta \\
\epsilon &= \ln\left[\frac{E+p}{E-p}\right] \qquad \epsilon^Q=\ln\left[\frac{Q+p}{Q-p}\right]
\end{aligned}
$$

where k is the photon energy, θ the emission angle and (E_0, p_0) and (E, p) are the total (energy, momentum) of the electron before and after the radiative emission, all in units of $m_e c^2$.
Since the 2BN cross–section is a 2-dimensional non-factorized distribution an acceptance-rejection technique was the adopted. For the 2BN distribution, two functions $g_1(k)$ and $g_2(\theta)$ were defined:

$$
g_1(k)=k^{-b} \qquad\qquad g_2(\theta)=\frac{\theta}{1+c\theta^2} \tag{9.50}
$$

such that:

$$
Ag_1(k)g_2(\theta)\geq\frac{d\sigma}{dkd\theta} \tag{9.51}
$$

where A is a global constant to be completed. Both functions have an analytical integral G and an analytical inverse G^{-1}. The b parameter of $g_1(k)$ was empirically tuned and set to 1.2. For positive θ values, $g_2(\theta)$ has a maximum at $\frac{1}{\sqrt{(c)}}$. c parameter controls the function global shape and it was used to tune $g_2(\theta)$ according to the electron kinetic energy.

To generate photon energy k according to g_1 and θ according to g_2 the inverse-transform method was used. The integration of these functions gives

$$G_1 = C_1 \int_{k_{min}}^{k_{max}} k'^{-b} dk' = C_1 \frac{k^{1-b} - k_{min}^{1-b}}{1-b} \tag{9.52}$$

$$G_2 = C_2 \int_0^{\theta} \frac{\theta'}{1 + c\theta'^2} d\theta' = C_2 \frac{\log(1 + c\theta^2)}{2c} \tag{9.53}$$

where C_1 and C_2 are two global constants chosen to normalize the integral in the overall range to the unit. The photon momentum k will range from a minimum cut value k_{min} (required to avoid infrared divergence) to a maximum value equal to the electron kinetic energy E_k, while the polar angle ranges from 0 to π, resulting for C_1 and C_2:

$$C_1 = \frac{1-b}{E_k^{1-b}} \qquad C_2 = \frac{2c}{\log(1 + c\pi^2)} \tag{9.54}$$

k and θ are then sampled according to:

$$k = \left[\frac{1-b}{C_1} \xi_1 + k_{min}^{1-b} \right] \qquad \theta = \sqrt{\frac{\exp\left(\frac{2c\xi_2}{C_1}\right)}{2c}} \tag{9.55}$$

where ξ_1 and ξ_2 are uniformly sampled in the interval (0,1). The event is accepted if:

$$u A g_1(k) g_2(\theta) \leq \frac{d\sigma}{dk d\theta} \tag{9.56}$$

where u is a random number with uniform distribution in (0,1). The A and c parameters were computed in a logarithmic grid, ranging from 1 keV to 1.5 MeV with 100 points per decade. Since the $g_2(\theta)$ function has a maximum at $\theta = \frac{1}{\sqrt{c}}$, the c parameter was computed using the relation $c = \frac{1}{\theta_{max}}$. At the point (k_{min}, θ_{max}) where k_{min} is the k cut value, the double differential cross-section has its maximum value, since it is monotonically decreasing in k and thus the global normalization parameter A is estimated from the relation:

$$A g_1(k_{min}) g_2(\theta_{max}) = \left(\frac{d^2\sigma}{dk d\theta} \right)_{max} \tag{9.57}$$

where $g_1(k_{min}) g_2(\theta_{max}) = \frac{k_{min}^{-b}}{2\sqrt{c}}$. Since A and c can only be retrieved for a fixed number of electron kinetic energies there exists the possibility that $A g_1(k_{min}) g_2(\theta_{max}) \leq \left(\frac{d^2\sigma}{dk d\theta}\right)_{max}$ for a given E_k. This is a small violation that

can be corrected introducing an additional multiplicative factor to the A parameter, which was empirically determined to be 1.04 for the entire energy range.

Comparisons between Tsai, 2BS and 2BN generators

The currently available generators can be used according to the user required precision and timing requirements. Regarding the energy range, validation results indicate that for lower energies ($\leq$ 100 keV) there is a significant deviation on the most probable emission angle between Tsai/2BS generators and the 2BN generator - Figure 9.1. The 2BN generator maintains however a good agreement with Kissel data [7], derived from the work of Tseng and co-workers [8], and it should be used for energies between 1 keV and 100 keV [9]. As the electron kinetic energy increases, the different distributions tend to overlap and all generators present a good agreement with Kissel data.

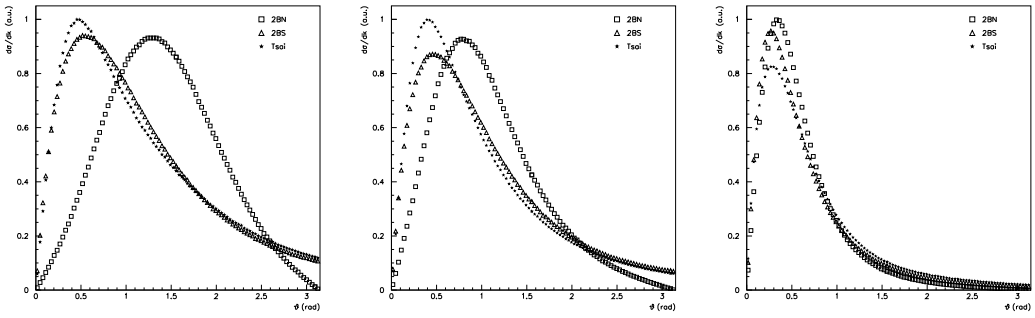

Figure 9.1: Comparison of polar angle distribution of bremsstrahlung photons ($k/T = 0.5$) for 10 keV (*left*) and 100 keV (*middle*) and 500 keV (*right*) electrons in silver, obtained with Tsai, 2BS and 2BN generator

In figure 9.2 the sampling efficiency for the different generators are presented. The sampling generation efficiency was defined as the ratio between the number of generated events and the total number of trials. As energies increases the sampling efficiency of the 2BN algorithm decreases from 0.65 at 1 keV electron kinetic energy down to almost 0.35 at 1 MeV. For energies up to 10 keV the 2BN sampling efficiency is superior or equivalent to the one of the 2BS generator. These results are an indication that precision simulation of low energy bremsstrahlung can be obtained with little performance degradation. For energies above 500 keV, Tsai generator can be used, retain-

ing a good physics accuracy and a sampling efficiency superior to the 2BS generator.

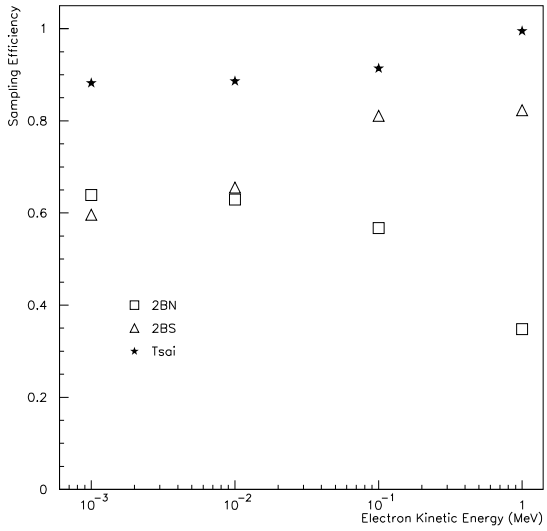

Figure 9.2: Sampling efficiency for Tsai generator, 2BS and 2BN Koch and Motz generators.

9.9.2 Status of the document

30.09.1999 created by Alessandra Forti
07.02.2000 modified by Véronique Lefébure
08.03.2000 reviewed by Petteri Nieminen and Maria Grazia Pia
05.12.2001 modified by Vladimir Ivanchenko
13.05.2002 modified by Vladimir Ivanchenko
24.11.2003 modified by Andreia Trindade, Pedro Rodrigues and Luis Peralta

Bibliography

[1] "Geant4 Low Energy Electromagnetic Models for Electrons and Photons", J.Apostolakis et al., CERN-OPEN-99-034(1999), INFN/AE-99/18(1999)

[2] "Tables and Graphs of Electron-Interaction Cross-Sections from 10 eV to 100 GeV Derived from the LLNL Evaluated Electron Data Library (EEDL), Z=1-100" S.T.Perkins, D.E.Cullen, S.M.Seltzer, UCRL-50400 Vol.31

[3] "GEANT, Detector Description and Simulation Tool", CERN Application Software Group, CERN Program Library Long Writeup W5013

[4] "Pair production and bremsstrahlung of charged leptons", Y. Tsai, Rev. Mod. Phys., Vol.46, 815(1974), Vol.49, 421(1977)

[5] "Bremsstrahlung Cross-Section Formulas and Related Data", H. W. Koch and J. W. Motz, Rev. Mod. Phys., Vol.31, 920(1959)

[6] "Improved bremsstrahlung photon angular sampling in the EGS4 code system", A. F. Bielajew, R. Mohan and C.-S. Chui, Report NRCC/PIRS-0203 (1989)

[7] "Bremsstrahlung from electron collisions with neutral atoms", L. Kissel, C. A. Quarls and R. H. Pratt, At. Data Nucl. Data Tables, Vol. 28, 382(1983)

[8] "Electron bremsstrahlung angular distributions in the 1-500 keV energy range", H. K. Tseng, R. H. Pratt and C. M. Lee , Phys. Rev. A, Vol. 19, 187(1979)

[9] "GEANT4 Applications and Developments for Medical Physics Experiments", P. Rodrigues et al. IEEE 2003 NSS/MIC Conference Record

Chapter 10

Low Energy Penelope

10.1 Penelope physics

10.1.1 Introduction

A new set of physics processes for photons, electrons and positrons is implemented in Geant4: it includes Compton scattering, photoelectric effect, Rayleigh scattering, gamma conversion, bremsstrahlung, ionization (to be released) and positron annihilation (to be released). These processes are the Geant4 implementation of the physics models developed for the PENELOPE code (PENetration and Energy LOss of Positrons and Electrons), version 2001, that are described in detail in Ref. [1]. The Penelope models have been specifically developed for Monte Carlo simulation and great care was given to the low energy description (i.e. atomic effects, etc.). Hence, these implementations provide reliable results for energies down to a few hundred eV and can be used up to ∼1 GeV [1, 2]. For this reason, they may be used in Geant4 as an alternative to the Low Energy processes. For the same physics processes, the user now has more alternative descriptions from which to choose, including the cross section calculation and the final state sampling.

10.1.2 Compton scattering

Total cross section

The total cross section of the Compton scattering process is determined from an analytical parameterization. For γ energy E greater than 5 MeV, the usual Klein-Nishina formula is used for $\sigma(E)$. For $E < 5$ MeV a more accurate parameterization is used, which takes into account atomic binding effects and Doppler broadening [3]:

$$\begin{aligned}\sigma(E) &= 2\pi \int_{-1}^{1} \frac{r_e^2}{2} \frac{E_C^2}{E^2} \left(\frac{E_C}{E} + \frac{E}{E_C} - \sin^2\theta\right) \cdot \\ &\quad \sum_{shells} f_i \Theta(E - U_i) n_i(p_z^{max}) \; d(\cos\theta) \end{aligned} \tag{10.1}$$

where:
r_e = classical radius of the electron;
m_e = mass of the electron;
θ = scattering angle;
E_C = Compton energy

$$= \frac{E}{1 + \frac{E}{m_e c^2}(1 - \cos\theta)}$$

f_i = number of electrons in the i-th atomic shell;
U_i = ionisation energy of the i-th atomic shell;
Θ = Heaviside step function;
p_z^{max} = highest possible value of p_z (projection of the initial momentum of the electron in the direction of the scattering angle)

$$= \frac{E(E-U_i)(1-\cos\theta) - m_e c^2 U_i}{c\sqrt{2E(E-U_i)(1-\cos\theta)+U_i^2}}.$$

Finally,

$$n_i(x) = \begin{array}{ll} \frac{1}{2}e^{[\frac{1}{2}-(\frac{1}{2}-\sqrt{2}J_{i0}x)^2]} & \text{if} \quad x<0 \\ 1-\frac{1}{2}e^{[\frac{1}{2}-(\frac{1}{2}+\sqrt{2}J_{i0}x)^2]} & \text{if} \quad x>0 \end{array} \tag{10.2}$$

where J_{i0} is the value of the p_z-distribution profile $J_i(p_z)$ for the i-th atomic shell calculated in $p_z = 0$. The values of J_{i0} for the different shells of the different elements are tabulated from the Hartree-Fock atomic orbitals of Ref. [4].
The integration of Eq.(10.1) is performed numerically using the 20-point Gaussian method. For this reason, the initialization of the Penelope Compton process is somewhat slower than the Low Energy process.

Sampling of the final state

The polar deflection $\cos\theta$ is sampled from the probability density function

$$P(\cos\theta) = \frac{r_e^2}{2}\frac{E_C^2}{E^2}\Big(\frac{E_C}{E}+\frac{E}{E_C}-\sin^2\theta\Big)\sum_{shells} f_i\Theta(E-U_i)n_i(p_z^{max}) \tag{10.3}$$

(see Ref. [1] for details on the sampling algorithm). Once the direction of the emerging photon has been set, the active electron shell i is selected with relative probability equal to $Z_i\Theta(E-U_i)n_i[p_z^{max}(E,\theta)]$. A random value of p_z is generated from the analytical Compton profile [4]. The energy of the emerging photon is

$$E' = \frac{E\tau}{1-\tau t}\Big[(1-\tau t\cos\theta)+\frac{p_z}{|p_z|}\sqrt{(1-\tau t\cos\theta)^2-(1-t\tau^2)(1-t)}\Big], \tag{10.4}$$

where

$$t = \Big(\frac{p_z}{m_e c}\Big)^2 \quad \text{and} \quad \tau = \frac{E_C}{E}. \tag{10.5}$$

The azimuthal scattering angle ϕ of the photon is sampled uniformly in the interval (0,2π). It is assumed that the Compton electron is emitted with

energy $E_e = E - E' - U_i$, with polar angle θ_e and azimuthal angle $\phi_e = \phi + \pi$, relative to the direction of the incident photon. In this case $\cos\theta_e$ is given by

$$\cos\theta_e \;=\; \frac{E - E'\cos\theta}{\sqrt{E^2 + E'^2 - 2EE'\cos\theta}}. \tag{10.6}$$

Since the active electron shell is known, characteristic x-rays and electrons emitted in the de-excitation of the ionized atom can also be followed. The de-excitation is simulated as described in section 14.1. For further details see [1].

10.1.3 Rayleigh scattering

Total cross section

The total cross section of the Rayleigh scattering process is determined from an analytical parameterization. The atomic cross section for coherent scattering is given approximately by [5]

$$\sigma(E) \;=\; \pi r_e^2 \int_{-1}^{1} \frac{1+\cos^2\theta}{2} [F(q,Z)]^2 \; d\cos\theta, \tag{10.7}$$

where $F(q,Z)$ is the atomic form factor, Z is the atomic number and q is the magnitude of the momentum transfer, i.e.

$$q \;=\; 2\,\frac{E}{c}\,\sin\Big(\frac{\theta}{2}\Big). \tag{10.8}$$

In the numerical calculation the following analytical approximations are used for the form factor:

$$F(q,Z) = f(x,Z) = \begin{array}{ll} Z\,\frac{1+a_1x^2+a_2x^3+a_3x^4}{(1+a_4x^2+a_5x^4)^2} & \text{or} \\ \max[f(x,Z), F_K(x,Z)] & \text{if } Z > 10 \text{ and } f(x,Z) < 2 \end{array} \tag{10.9}$$

where

$$F_K(x,Z) \;=\; \frac{\sin(2b\arctan Q)}{bQ(1+Q^2)^b}, \tag{10.10}$$

with

$$x = 20.6074\frac{q}{m_e c}, \quad Q = \frac{q}{2m_e c a}, \quad b = \sqrt{1-a^2}, \quad a = \alpha\Big(Z - \frac{5}{16}\Big), \tag{10.11}$$

where α is the fine-structure constant. The function $F_K(x,Z)$ is the contribution to the atomic form factor due to the two K-shell electrons (see [6]).

The parameters of expression $f(x, Z)$ have been determined in Ref. [6] for Z=1 to 92 by numerically fitting the atomic form factors tabulated in Ref. [7]. The integration of Eq.(10.7) is performed numerically using the 20-point Gaussian method. For this reason the initialization of the Penelope Rayleigh process is somewhat slower than the Low Energy process.

Sampling of the final state

The angular deflection $\cos\theta$ of the scattered photon is sampled from the probability distribution function

$$P(\cos\theta) \;=\; \frac{1+\cos^2\theta}{2}[F(q,Z)]^2. \tag{10.12}$$

For details on the sampling algorithm (which is quite heavy from the computational point of view) see Ref. [1]. The azimuthal scattering angle ϕ of the photon is sampled uniformly in the interval (0,2π).

10.1.4 Gamma conversion

Total cross section

The total cross section of the γ conversion process is determined from the data [8], as described in section 9.1.4.

Sampling of the final state

The energies E_- and E_+ of the secondary electron and positron are sampled using the Bethe-Heitler cross section with the Coulomb correction, using the semiempirical model of Ref. [6]. If

$$\epsilon \;=\; \frac{E_- + m_e c^2}{E} \tag{10.13}$$

is the fraction of the γ energy E which is taken away from the electron,

$$\kappa \;=\; \frac{E}{m_e c^2} \quad \text{and} \quad a = \alpha Z, \tag{10.14}$$

the differential cross section, which includes a low-energy correction and a high-energy radiative correction, is

$$\frac{d\sigma}{d\epsilon} \;=\; r_e^2 a(Z+\eta) C_r \frac{2}{3}\Big[2\Big(\frac{1}{2}-\epsilon\Big)^2\phi_1(\epsilon)+\phi_2(\epsilon)\Big], \tag{10.15}$$

where:

$$\begin{aligned}\phi_1(\epsilon) &= \frac{7}{3} - 2\ln(1+b^2) - 6b\arctan(b^{-1}) \\ &\quad -b^2[4 - 4b\arctan(b^{-1}) - 3\ln(1+b^{-2})] \\ &\quad +4\ln(Rm_ec/\hbar) - 4f_C(Z) + F_0(\kappa, Z) \end{aligned} \tag{10.16}$$

and

$$\begin{aligned}\phi_2(\epsilon) &= \frac{11}{6} - 2\ln(1+b^2) - 3b\arctan(b^{-1}) \\ &\quad +\frac{1}{2}b^2[4 - 4b\arctan(b^{-1}) - 3\ln(1+b^{-2})] \\ &\quad +4\ln(Rm_ec/\hbar) - 4f_C(Z) + F_0(\kappa, Z), \end{aligned} \tag{10.17}$$

with

$$b = \frac{Rm_ec}{\hbar}\frac{1}{2\kappa}\frac{1}{\epsilon(1-\epsilon)}. \tag{10.18}$$

In this case R is the screening radius for the atom Z (tabulated in [10] for Z=1 to 92) and η is the contribution of pair production in the electron field (rather than in the nuclear field). The parameter η is approximated as

$$\eta = \eta_\infty(1 - e^{-v}), \tag{10.19}$$

where

$$\begin{aligned} v &= (0.2840 - 0.1909a)\ln(4/\kappa) + (0.1095 + 0.2206a)\ln^2(4/\kappa) \\ &\quad +(0.02888 - 0.04269a)\ln^3(4/\kappa) \\ &\quad +(0.002527 + 0.002623)\ln^4(4/\kappa) \end{aligned} \tag{10.20}$$

and η_∞ is the contribution for the atom Z in the high-energy limit and is tabulated for Z=1 to 92 in Ref. [10]. In the Eq.(10.15), the function $f_C(Z)$ is the high-energy Coulomb correction of Ref. [9], given by

$$\begin{aligned} f_C(Z) &= a^2[(1+a^2)^{-1} + 0.202059 - 0.03693a^2 + 0.00835a^4 \\ &\quad -0.00201a^6 + 0.00049a^8 - 0.00012a^{10} + 0.00003a^{12}]; \end{aligned} \tag{10.21}$$

$C_r = 1.0093$ is the high-energy limit of Mork and Olsen's radiative correction (see Ref. [10]); $F_0(\kappa, Z)$ is a Coulomb-like correction function, which has been analytically approximated as [1]

$$\begin{aligned} F_0(\kappa, Z) &= (-0.1774 - 12.10a + 11.18a^2)(2/\kappa)^{1/2} \\ &\quad +(8.523 + 73.26a - 44.41a^2)(2/\kappa) \\ &\quad -(13.52 + 121.1a - 96.41a^2)(2/\kappa)^{3/2} \\ &\quad +(8.946 + 62.05a - 63.41a^2)(2/\kappa)^2. \end{aligned} \tag{10.22}$$

The kinetic energy E_+ of the secondary positron is obtained as

$$E_+ \;=\; E - E_- - 2m_e c^2. \tag{10.23}$$

The polar angles θ_- and θ_+ of the directions of movement of the electron and the positron, relative to the direction of the incident photon, are sampled from the leading term of the expression obtained from high-energy theory (see Ref. [11])

$$p(\cos\theta_\pm) \;=\; a(1-\beta_\pm\cos\theta_\pm)^{-2}, \tag{10.24}$$

where a is the a normalization constant and $\beta_\pm$ is the particle velocity in units of the speed of light. As the directions of the produced particles and of the incident photon are not necessarily coplanar, the azimuthal angles ϕ_- and ϕ_+ of the electron and of the positron are sampled independently and uniformly in the interval $(0,2\pi)$.

10.1.5 Photoelectric effect

Total cross section

The total photoelectric cross section at a given photon energy E is calculated from the data [12], as described in section 9.1.4.

Sampling of the final state

The incident photon is absorbed and one electron is emitted. The direction of the electron is sampled according to the Sauter distribution [13]. Introducing the variable $\nu = 1-\cos\theta_e$, the angular distribution can be expressed as

$$p(\nu) \;=\; (2-\nu)\Big[\frac{1}{A+\nu}+\frac{1}{2}\beta\gamma(\gamma-1)(\gamma-2)\Big]\frac{\nu}{(A+\nu)^3}, \tag{10.25}$$

where

$$\gamma = 1+\frac{E_e}{m_e c^2}, \quad A=\frac{1}{\beta}-1, \tag{10.26}$$

E_e is the electron energy, m_e its rest mass and β its velocity in units of the speed of light c. Though the Sauter distribution, strictly speaking, is adequate only for ionisation of the K-shell by high-energy photons, in many practical simulations it does not introduce appreciable errors in the description of any photoionisation event, irrespective of the atomic shell or of the photon energy.
The subshell from which the electron is emitted is randomly selected according to the relative cross sections of subshells, determined at the energy E

by interpolation of the data of Ref. [11]. The electron kinetic energy is the difference between the incident photon energy and the binding energy of the electron before the interaction in the sampled shell. The interaction leaves the atom in an excited state; the subsequent de-excitation is simulated as described in section 14.1.

10.1.6 Bremsstrahlung

Introduction

The class `G4PenelopeBremsstrahlung` calculates the continuous energy loss due to soft γ emission and simulates the photon production by electrons and positrons. As usual, the gamma production threshold T_c for a given material is used to separate the continuous and the discrete parts of the process.

Electrons

The total cross sections are calculated from the data [15], as described in sections 9.1.4 and 9.9.
The energy distribution $\frac{d\sigma}{dW}(E)$, i.e. the probability of the emission of a photon with energy W given an incident electron of kinetic energy E, is generated according to the formula

$$\frac{d\sigma}{dW}(E) \;=\; \frac{F(\kappa)}{\kappa}, \quad \kappa \;=\; \frac{W}{E}. \tag{10.27}$$

The functions $F(\kappa)$ describing the energy spectra of the outgoing photons are taken from Ref. [14]. For each element Z from 1 to 92, 32 points in κ, ranging from 10^{-12} to 1, are used for the linear interpolation of this function. $F(\kappa)$ is normalized using the condition $F(10^{-12}) = 1$. The energy distribution of the emitted photons is available in the library [14] for 57 energies of the incident electron between 1 keV and 100 GeV. For other primary energies, logarithmic interpolation is used to obtain the values of the function $F(\kappa)$.
The direction of the emitted bremsstrahlung photon is determined by the polar angle θ and the azimuthal angle ϕ. For isotropic media, with randomly oriented atoms, the bremsstrahlung differential cross section is independent of ϕ and can be expressed as

$$\frac{d^2\sigma}{dW\, d\cos\theta} \;=\; \frac{d\sigma}{dW} p(Z, E, \kappa; \cos\theta). \tag{10.28}$$

Numerical values of the "shape function" $p(Z, E, \kappa; \cos\theta)$, calculated by partial-wave methods, have been published in Ref. [16] for the following

benchmark cases: Z= 2, 8, 13, 47, 79 and 92; E= 1, 5, 10, 50, 100 and 500 keV; κ= 0, 0.6, 0.8 and 0.95. It was found in Ref. [1] that the benchmark partial-wave shape function of Ref. [16] can be closely approximated by the analytical form (obtained in the Lorentz-dipole approximation)

$$p(\cos\theta) = A\frac{3}{8}\Big[1+\Big(\frac{\cos\theta-\beta'}{1-\beta'\cos\theta}\Big)^2\Big]\frac{1-\beta'^2}{(1-\beta'\cos\theta)^2}$$
$$+(1-A)\frac{3}{4}\Big[1-\Big(\frac{\cos\theta-\beta'}{1-\beta'\cos\theta}m\Big)^2\Big]\frac{1-\beta'^2}{(1-\beta'\cos\theta)^2}, \qquad (10.29)$$

with $\beta' = \beta(1+B)$, if one considers A and B as adjustable parameters. The parameters A and B have been determined, by least squares fitting, for the 144 combinations of atomic numbers, electron energies and reduced photon energies corresponding to the benchmark shape functions tabulated in [16]. The quantities $\ln(AZ\beta)$ and $B\beta$ vary smoothly with Z, β and κ and can be obtained by cubic spline interpolation of their values for the benchmark cases. This permits the fast evaluation of the shape function $p(Z, E, \kappa; \cos\theta)$ for any combination of Z, β and κ.
The stopping power $\frac{dE}{dx}$ due to soft bremsstrahlung is calculated by interpolating in E and κ the numerical data of scaled cross sections of Ref. [17]. The energy and the direction of the outgoing electron are determined by using energy-momentum balance.

Positrons

The radiative differential cross section $\frac{d\sigma^+}{dW}(E)$ for positrons reduces to that for electrons in the high-energy limit, but is smaller for intermediate and low energies. Owing to the lack of more accurate calculations, the differential cross section for positrons is obtained by multiplying the electron differential cross section $\frac{d\sigma^-}{dW}(E)$ by a $\kappa-$indendent factor, i.e.

$$\frac{d\sigma^+}{dW} \;=\; F_p(Z,E)\frac{d\sigma^-}{dW}. \qquad (10.30)$$

The factor $F_p(Z, E)$ is set equal to the ratio of the radiative stopping powers for positrons and electrons, which has been calculated in Ref. [18]. For the actual calculation, the following analytical approximation is used:

$$F_p(Z,E) \;=\; 1-\exp(-1.2359\cdot10^{-1}t+6.1274\cdot10^{-2}t^2-3.1516\cdot10^{-2}t^3$$
$$+7.7446\cdot10^{-3}t^4-1.0595\cdot10^{-3}t^5+7.0568\cdot10^{-5}t^6$$
$$-1.8080\cdot10^{-6}t^7), \qquad (10.31)$$

where

$$t \;=\; \ln\Big(1+\frac{10^6}{Z^2}\frac{E}{m_e c^2}\Big). \tag{10.32}$$

Because the factor $F_p(Z,E)$ is independent on κ, the energy distribution of the secondary γ's has the same shape as electron bremsstrahlung. Similarly, owing to the lack of numerical data for positrons, it is assumed that the shape of the angular distribution $p(Z,E,\kappa;\cos\theta)$ of the bremsstrahlung photons for positrons is the same as for the electrons.
The energy and direction of the outgoing positron are determined from energy-momentum balance.

10.1.7 Ionisation

The `G4PenelopeIonisation` class calculates the continuous energy loss due to electron and positron ionisation and simulates the δ-ray production by electrons and positrons. The electron production threshold T_c for a given material is used to separate the continuous and the discrete parts of the process.
The simulation of inelastic collisions of electrons and positrons is performed on the basis of a Generalized Oscillation Strength (GOS) model (see Ref. [1] for a complete description). It is assumed that GOS splits into contributions from the different atomic electron shells.

Electrons

The total cross section $\sigma^-(E)$ for the inelastic collision of electrons of energy E is calculated analytically. It can be split into contributions from distant longitudinal, distant transverse and close interactions,

$$\sigma^-(E) \;=\; \sigma_{dis,l}+\sigma_{dis,t}+\sigma^-_{clo}. \tag{10.33}$$

The contributions from distant longitudinal and transverse interactions are

$$\sigma_{dis,l} \;=\; \frac{2\pi e^4}{m_e v^2}\sum_{shells} f_k \frac{1}{W_k}\ln\Big(\frac{W_k}{Q_k^{min}}\,\frac{Q_k^{min}+2m_e c^2}{W_k+2m_e c^2}\Big)\Theta(E-W_k) \tag{10.34}$$

and

$$\sigma_{dis,t} \;=\; \frac{2\pi e^4}{m_e v^2}\sum_{shells} f_k \frac{1}{W_k}\Big[\ln\Big(\frac{1}{1-\beta^2}\Big)-\beta^2-\delta_F\Big]\Theta(E-W_k) \tag{10.35}$$

respectively, where:
m_e = mass of the electron;

v = velocity of the electron;
β = velocity of the electron in units of c;
f_k = number of electrons in the k-th atomic shell;
Θ = Heaviside step function;
W_k = resonance energy of the k-th atomic shell oscillator;
Q_k^{min} = minimum kinematically allowed recoil energy for energy transfer W_k

$$= \sqrt{\left[\sqrt{E(E+2m_ec^2)} - \sqrt{(E-W_k)(E-W_k+2m_ec^2)}\right]^2 + m_e^2c^4} - m_ec^2;$$

δ_F = Fermi density effect correction, computed as described in Ref. [19].

The value of W_k is calculated from the ionisation energy U_k of the k-th shell as $W_k = 1.65\ U_k$. This relation is derived from the hydrogenic model, which is valid for the innermost shells. In this model, the shell ionisation cross sections are only roughly approximated; nevertheless the ionisation of inner shells is a low-probability process and the approximation has a weak effect on the global transport properties[1].
The integrated cross section for close collisions is the Møller cross section

$$\sigma_{clo}^- = \frac{2\pi e^4}{m_e v^2} \sum_{shells} f_k \int_{W_k}^{\frac{E}{2}} \frac{1}{W^2} F^-(E,W) dW, \tag{10.36}$$

where

$$F^-(E,W) = 1 + \left(\frac{W}{E-W}\right)^2 - \frac{W}{E-W} + \left(\frac{E}{E+m_ec^2}\right)^2 \left(\frac{W}{E-W} + \frac{W^2}{E^2}\right). \tag{10.37}$$

The integral of Eq.(10.36) can be evaluated analytically. In the final state there are two indistinguishable free electrons and the fastest one is considered as the "primary"; accordingly, the maximum allowed energy transfer in close collisions is $\frac{E}{2}$.
The GOS model also allows evaluation of the spectrum $\frac{d\sigma^-}{dW}$ of the energy W lost by the primary electron as the sum of distant longitudinal, distant transverse and close interaction contributions,

$$\frac{d\sigma^-}{dW} = \frac{d\sigma_{clo}^-}{dW} + \frac{d\sigma_{dis,l}}{dW} + \frac{d\sigma_{dis,t}}{dW}. \tag{10.38}$$

[1] In cases where inner-shell ionisation is directly observed, a more accurate description of the process should be used.

In particular,

$$\frac{d\sigma_{dis,l}}{dW} = \frac{2\pi e^4}{m_e v^2}\sum_{shells} f_k \frac{1}{W_k}\ln\Big(\frac{W_k}{Q_-}\,\frac{Q_- + 2m_e c^2}{W_k + 2m_e c^2}\Big)\delta(W - W_k)\Theta(E - W_k), \tag{10.39}$$

where

$$Q_- = \sqrt{\Big[\sqrt{E(E+2m_e c^2)} - \sqrt{(E-W)(E-W+2m_e c^2)}\Big]^2 + m_e^2 c^4} - m_e c^2, \tag{10.40}$$

$$\frac{d\sigma_{dis,t}}{dW} = \frac{2\pi e^4}{m_e v^2}\sum_{shells} f_k \frac{1}{W_k}\Big[\ln\Big(\frac{1}{1-\beta^2}\Big) - \beta^2 - \delta_F\Big] \Theta(E - W_k)\delta(W - W_k) \tag{10.41}$$

and

$$\frac{d\sigma^-_{clo}}{dW} = \frac{2\pi e^4}{m_e v^2}\sum_{shells} f_k \frac{1}{W^2} F^-(E,W)\Theta(W - W_k). \tag{10.42}$$

Eqs. (10.34), (10.35) and (10.36) derive respectively from the integration in dW of Eqs. (10.39), (10.41) and (10.42) in the interval [0,W_{max}], where $W_{max} = E$ for distant interactions and $W_{max} = \frac{E}{2}$ for close. The analytical GOS model provides an accurate *average* description of inelastic collisions. However, the continuous energy loss spectrum associated with single distant excitations of a given atomic shell is approximated as a single resonance (a δ distribution). As a consequence, the simulated energy loss spectra show unphysical narrow peaks at energy losses that are multiples of the resonance energies. These spurious peaks are automatically smoothed out after multiple inelastic collisions.
The explicit expression of $\frac{d\sigma^-}{dW}$, Eq. (10.38), allows the analytic calculation of the partial cross sections for soft and hard ionisation events, i.e.

$$\sigma^-_{soft} = \int_0^{T_c} \frac{d\sigma^-}{dW} dW \quad \text{and} \quad \sigma^-_{hard} = \int_{T_c}^{W_{max}} \frac{d\sigma^-}{dW} dW. \tag{10.43}$$

The first stage of the simulation is the selection of the active oscillator k and the oscillator branch (distant or close).
In distant interactions with the k-th oscillator, the energy loss W of the primary electron corresponds to the excitation energy W_k, i.e. W=W_k. If the interaction is transverse, the angular deflection of the projectile is neglected, i.e. $\cos\theta$=1. For longitudinal collisions, the distribution of the recoil energy

Q is given by

$$P_k(Q) = \begin{cases} \frac{1}{Q[1+Q/(2m_ec^2)]} & \text{if } Q_- < Q < W_{max} \\ 0 & \text{otherwise} \end{cases} \tag{10.44}$$

Once the energy loss W and the recoil energy Q have been sampled, the polar scattering angle is determined as

$$\cos\theta = \frac{E(E+2m_ec^2)+(E-W)(E-W+2m_ec^2)-Q(Q+2m_ec^2)}{2\sqrt{E(E+2m_ec^2)(E-W)(E-W+2m_ec^2)}}. \tag{10.45}$$

The azimuthal scattering angle ϕ is sampled uniformly in the interval (0,2π). For close interactions, the distributions for the reduced energy loss $\kappa \equiv W/E$ for electrons are

$$P_k^-(\kappa) = \Big[\frac{1}{\kappa^2}+\frac{1}{(1-\kappa)^2}-\frac{1}{\kappa(1-\kappa)}+\Big(\frac{E}{E+m_ec^2}\Big)^2\Big(1+\frac{1}{\kappa(1-\kappa)}\Big)\Big] \Theta(\kappa-\kappa_c)\Theta(\frac{1}{2}-\kappa) \tag{10.46}$$

with $\kappa_c = \max(W_k, T_c)/E$. The maximum allowed value of κ is 1/2, consistent with the indistinguishability of the electrons in the final state. After the sampling of the energy loss $W = \kappa E$, the polar scattering angle θ is obtained as

$$\cos^2\theta = \frac{E-W}{E}\,\frac{E+2m_ec^2}{E-W+2m_ec^2}. \tag{10.47}$$

The azimuthal scattering angle ϕ is sampled uniformly in the interval (0,2π). According to the GOS model, each oscillator W_k corresponds to an atomic shell with f_k electrons and ionisation energy U_k. In the case of ionisation of an inner shell i (K or L), a secondary electron (δ-ray) is emitted with energy $E_s = W - U_i$ and the residual ion is left with a vacancy in the shell (which is then filled with the emission of fluorescence x-rays and/or Auger electrons). In the case of ionisation of outer shells, the simulated δ-ray is emitted with kinetic energy $E_s = W$ and the target atom is assumed to remain in its ground state. The polar angle of emission of the secondary electron is calculated as

$$\cos^2\theta_s = \frac{W^2/\beta^2}{Q(Q+2m_ec^2)}\Big[1+\frac{Q(Q+2m_ec^2)-W^2}{2W(E+m_ec^2)}\Big]^2 \tag{10.48}$$

(for close collisions $Q = W$), while the azimuthal angle is $\phi_s = \phi + \pi$. In this model, the Doppler effects on the angular distribution of the δ rays are

neglected.
The stopping power due to soft interactions of electrons, which is used for the computation of the continuous part of the process, is analytically calculated as

$$S_{in}^{-} \;=\; N\int_0^{T_c} W\frac{d\sigma^-}{dW}dW \tag{10.49}$$

from the expression (10.38), where N is the number of scattering centers (atoms or molecules) per unit volume.

Positrons

The total cross section $\sigma^+(E)$ for the inelastic collision of positrons of energy E is calculated analytically. As in the case of electrons, it can be split into contributions from distant longitudinal, distant transverse and close interactions,

$$\sigma^+(E) \;=\; \sigma_{dis,l} + \sigma_{dis,t} + \sigma^+_{clo}. \tag{10.50}$$

The contributions from distant longitudinal and transverse interactions are the same as for electrons, Eq. (10.34) and (10.35), while the integrated cross section for close collisions is the Bhabha cross section

$$\sigma^+_{clo} \;=\; \frac{2\pi e^4}{m_e v^2}\sum_{shells} f_k \int_{W_k}^{E}\frac{1}{W^2}F^+(E,W)dW, \tag{10.51}$$

where

$$F^+(E,W) \;= 1 - b_1\frac{W}{E} + b_2\frac{W^2}{E^2} - b_3\frac{W^3}{E^3} + b_4\frac{W^4}{E^4}; \tag{10.52}$$

the Bhabha factors are

$$b_1 = \Big(\frac{\gamma-1}{\gamma}\Big)^2\,\frac{2(\gamma+1)^2-1}{\gamma^2-1} \qquad b_2 = \Big(\frac{\gamma-1}{\gamma}\Big)^2\,\frac{3(\gamma+1)^2+1}{(\gamma+1)^2},$$
$$b_3 = \Big(\frac{\gamma-1}{\gamma}\Big)^2\,\frac{2(\gamma-1)\gamma}{(\gamma+1)^2}, \qquad b_4 = \Big(\frac{\gamma-1}{\gamma}\Big)^2\,\frac{(\gamma-1)^2}{(\gamma+1)^2}, \tag{10.53}$$
$$\tag{10.54}$$

and γ is the Lorentz factor of the positron. The integral of Eq. (10.51) can be evaluated analytically. The particles in the final state are not undistinguishable so the maximum energy transfer W_{max} in close collisions is E.
As for electrons, the GOS model allows the evaluation of the spectrum $\frac{d\sigma^+}{dW}$ of

the energy W lost by the primary positron as the sum of distant longitudinal, distant transverse and close interaction contributions,

$$\frac{d\sigma^+}{dW} = \frac{d\sigma^+_{clo}}{dW} + \frac{d\sigma_{dis,l}}{dW} + \frac{d\sigma_{dis,t}}{dW}, \tag{10.55}$$

where the distant terms $\frac{d\sigma_{dis,l}}{dW}$ and $\frac{d\sigma_{dis,t}}{dW}$ are those from Eqs. (10.39) and (10.41), while the close contribution is

$$\frac{d\sigma^+_{clo}}{dW} = \frac{2\pi e^4}{m_e v^2} \sum_{shells} f_k \frac{1}{W^2} F^+(E,W)\Theta(W - W_k). \tag{10.56}$$

Also in this case, the explicit expression of $\frac{d\sigma^+}{dW}$, Eq. (10.55), allows an analytic calculation of the partial cross sections for soft and hard ionisation events, i.e.

$$\sigma^+_{soft} = \int_0^{T_c} \frac{d\sigma^+}{dW} dW \quad \text{and} \quad \sigma^+_{hard} = \int_{T_c}^{E} \frac{d\sigma^+}{dW} dW. \tag{10.57}$$

The sampling of the final state in the case of distant interactions (transverse or longitudinal) is performed in the same way as for primary electrons, see section 10.1.7. For close positron interactions with the k-th oscillator, the distribution for the reduced energy loss $\kappa \equiv W/E$ is

$$P^+_k(\kappa) = \Big[\frac{1}{\kappa^2} - \frac{b_1}{\kappa} + b_2 - b_3\kappa + b_4\kappa^2\Big]\Theta(\kappa - \kappa_c)\Theta(1 - \kappa) \tag{10.58}$$

with $\kappa_c = \max(W_k, T_c)/E$. In this case, the maximum allowed reduced energy loss κ is 1. After sampling the energy loss $W = \kappa E$, the polar angle θ and the azimuthal angle ϕ are obtained using the equations introduced for electrons in section 10.1.7. Similarly, the generation of δ rays is performed in the same way as for electrons.
Finally, the stopping power due to soft interactions of positrons, which is used for the computation of the continuous part of the process, is analytically calculated as

$$S^+_{in} = N \int_0^{T_c} W \frac{d\sigma^+}{dW} dW \tag{10.59}$$

from the expression (10.55), where N is the number of scattering centers per unit volume.

10.1.8 Positron Annihilation

Total Cross Section

The total cross section (per target electron) for the annihilation of a positron of energy E into two photons is evaluated from the analytical formula [20, 21]

$$\sigma(E) = \frac{\pi r_e^2}{(\gamma+1)(\gamma^2-1)} \times \left\{(\gamma^2+4\gamma+1)\ln\left[\gamma+\sqrt{\gamma^2-1}\right]-(3+\gamma)\sqrt{\gamma^2-1}\right\}. \quad (10.60)$$

where
r_e = classical radius of the electron, and
γ = Lorentz factor of the positron.

Sampling of the Final State

The target electrons are assumed to be free and at rest: binding effects, that enable one-photon annihilation [20], are neglected. When the annihilation occurs in flight, the two photons may have different energies, say E_- and E_+ (the photon with lower energy is denoted by the superscript "$-$"), whose sum is $E + 2m_ec^2$. Each annihilation event is completely characterized by the quantity

$$\zeta = \frac{E_-}{E+2m_ec^2}, \quad (10.61)$$

which is in the interval $\zeta_{min} \le \zeta \le \frac{1}{2}$, with

$$\zeta_{min} = \frac{1}{\gamma+1+\sqrt{\gamma^2-1}}. \quad (10.62)$$

The parameter ζ is sampled from the differential distribution

$$P(\zeta) = \frac{\pi r_e^2}{(\gamma+1)(\gamma^2-1)}[S(\zeta)+S(1-\zeta)], \quad (10.63)$$

where γ is the Lorentz factor and

$$S(\zeta) = -(\gamma+1)^2+(\gamma^2+4\gamma+1)\frac{1}{\zeta}-\frac{1}{\zeta^2}. \quad (10.64)$$

From conservation of energy and momentum, it follows that the two photons are emitted in directions with polar angles

$$\cos\theta_- = \frac{1}{\sqrt{\gamma^2-1}}\left(\gamma+1-\frac{1}{\zeta}\right) \quad (10.65)$$

and

$$\cos\theta_+ \;=\; \frac{1}{\sqrt{\gamma^2-1}}\Big(\gamma+1-\frac{1}{1-\zeta}\Big) \tag{10.66}$$

that are completely determined by ζ; in particuar, when $\zeta=\zeta_{min}$, $\cos\theta_-=-1$. The azimuthal angles are ϕ_- and $\phi_+=\phi_-+\pi$; owing to the axial symmetry of the process, the angle ϕ_- is uniformly distributed in $(0,2\pi)$.

10.1.9 Status of the document

09.06.2003 created by L. Pandola
20.06.2003 spelling and grammar check by D.H. Wright
07.11.2003 Ionisation and Annihilation section added by L. Pandola
01.06.2005 Added text in the PhotoElectric effect section, L. Pandola

Bibliography

[1] *Penelope - A Code System for Monte Carlo Simulation of Electron and Photon Transport*, Workshop Proceedings Issy-les-Moulineaux, France, 5−7 November 2001, AEN-NEA;

[2] J.Sempau *et al.*, *Experimental benchmarks of the Monte Carlo code PENELOPE*, submitted to NIM B (2002);

[3] D.Brusa *et al.*, *Fast sampling algorithm for the simulation of photon Compton scattering*, NIM A379,167 (1996);

[4] F.Biggs *et al.*, *Hartree-Fock Compton profiles for the elements*, At.Data Nucl.Data Tables 16,201 (1975);

[5] M.Born, *Atomic physics*, Ed. Blackie and Sons (1969);

[6] J.Baró *et al.*, *Analytical cross sections for Monte Carlo simulation of photon transport*, Radiat.Phys.Chem. 44,531 (1994);

[7] J.H.Hubbel *et al.*, *Atomic form factors, incoherent scattering functions and photon scattering cross sections*, J. Phys.Chem.Ref.Data 4,471 (1975). Erratum: *ibid.* 6,615 (1977);

[8] M.J.Berger and J.H.Hubbel, *XCOM: photom cross sections on a personal computer*, Report NBSIR 87-3597 (National Bureau of Standards) (1987);

[9] H.Davies *et al.*, *Theory of bremsstrahlung and pair production. II.Integral cross section for pair production*, Phys.Rev. 93,788 (1954);

[10] J.H.Hubbel *et al.*, *Pair, triplet and total atomic cross sections (and mass attenuation coefficients) for 1 MeV − 100 GeV photons in element Z=1 to 100*, J.Phys.Chem.Ref.Data 9,1023 (1980);

[11] J.W.Motz *et al.*, *Pair production by photons*, Rev.Mod.Phys 41,581 (1969);

[12] D.E.Cullen *et al.*, *Tables and graphs of photon-interaction cross sections from 10 eV to 100 GeV derived from the LLNL evaluated photon data library (EPDL)*, Report UCRL-50400 (Lawrence Livermore National Laboratory) (1989);

[13] , F. Sauter, Ann. Phys. 11 (1931) 454

[14] S.M.Seltzer and M.J.Berger, *Bremsstrahlung energy spectra from electrons with kinetic energy 1 keV - 100 GeV incident on screened nuclei and orbital electrons of neutral atoms with Z=1-100*, At.Data Nucl.Data Tables 35,345 (1986);

[15] D.E.Cullen *et al.*, *Tables and graphs of electron-interaction cross sections from 10 eV to 100 GeV derived from the LLNL evaluated photon data library (EEDL)*, Report UCRL-50400 (Lawrence Livermore National Laboratory) (1989);

[16] L.Kissel *et al.*, *Shape functions for atomic-field bremsstrahlung from electron of kinetic energy 1−500 keV on selected neutral atoms* $1 \leq Z \leq 92$, At.Data Nucl.Data.Tab. 28,381 (1983);

[17] M.J.Berger and S.M.Seltzer, *Stopping power of electrons and positrons*, Report NBSIR 82-2550 (National Bureau of Standards) (1982);

[18] L.Kim *et al.*, *Ratio of positron to electron bremsstrahlung energy loss: an approximate scaling law*, Phys.Rev.A 33,3002 (1986);

[19] U.Fano, *Penetration of protons, alpha particles and mesons*, Ann.Rev.Nucl.Sci. 13,1 (1963);

[20] W.Heitler, *The quantum theory of radiation*, Oxford University Press, London (1954);

[21] W.R.Nelson *et al.*, *The EGS4 code system*, Report SLAC-265 (1985).

Chapter 11

Monash University low energy photon processes

11.1 Monash Low Energy Photon Processes

11.1.1 Introduction

The Monash Compton Scattering Model is an alternative Compton scattering model to those of Livermore and Penelope that were constructed using Ribberfors' theoretical framework [1, 2, 3]. The limitation of the Livermore and Penelope models is that only the components of the pre-collision momentum of the target electron contained within the photon plane, two-dimensional plane defined by the incident and scattered photon, is incorporated into their scattering frameworks [4]. Both models are forced to constrain the ejected direction of the Compton electron into the photon plane as a result. The Monash Compton scattering model avoids this limitation through the use of a two-body fully relativistic three-dimensional scattering framework to ensure the conservation of energy and momentum in the Relativistic Impulse Approximation (RIA) [5].

11.1.2 Physics and Simulation

Total Cross Section

The Monash Compton scattering model has been built using the Livermore Compton scattering model as a template. As a result the total cross section for the Compton scattering process mimics the process outlined in Section 9.

Sampling of the Final State

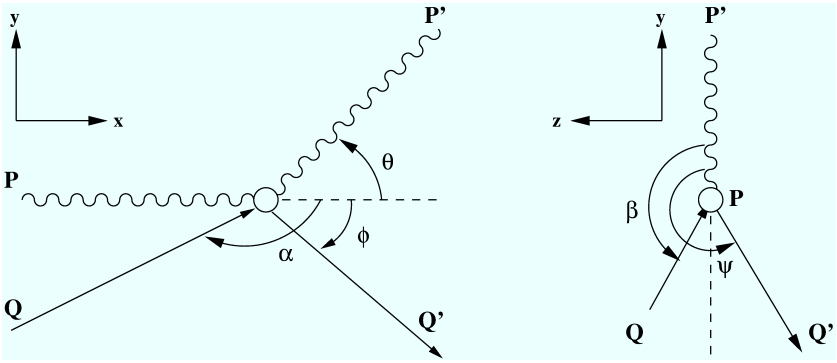

Figure 11.1: Scattering diagram of atomic bound electron Compton scattering. $\mathbf{P}$ is the incident photon momentum, $\mathbf{Q}$ the electron pre-collision momentum, $\mathbf{P}'$ the scattered photon momentum and $\mathbf{Q}'$ the recoil electron momentum.

The scattering diagram seen in Figure 11.1 outlines the basic principles of Compton scattering with an electron of non-zero pre-collision momentum in the RIA.

The process of sampling the target atom, atomic shell and target electron pre-collision momentum mimic that outlined in Section 9. After the sampling of these parameters the following four equations are utilised to model the scattered photon energy E', recoil electron energy T_{el} and recoil electron polar and azimuthal angles (ϕ and ψ) with respect to the incident photon direction:

$$E' = \frac{\gamma mc\left(c - u\cos\alpha\right)}{1 - \cos\theta + \frac{\gamma mc(c - u\cos\theta\cos\alpha - u\sin\theta\sin\alpha\cos\beta)}{E}}, \tag{11.1}$$

$$T_{el} = E - E' - E_B, \tag{11.2}$$

$$\cos\phi = \frac{-Y \pm \sqrt{Y^2 - 4WZ}}{2W}, \tag{11.3}$$

$$\cos\psi = \frac{C - B\cos\phi}{A\sin\phi}, \tag{11.4}$$

where:

$$A = E'u'\sin\theta, \tag{11.5}$$

$$B = E'u'\cos\theta - Eu', \tag{11.6}$$

$$C = c\left(E' - E\right) - \frac{EE'}{\gamma' mc}\left(1 - \cos\theta\right), \tag{11.7}$$

$$D = \frac{\gamma mE'}{c}\left(c - u\cos\theta\cos\alpha - u\sin\theta\cos\beta\sin\alpha\right) + m^2c^2\left(\gamma\gamma' - 1\right) - \gamma' mE', \tag{11.8}$$

$$F = (\gamma\gamma' m^2 uu'\cos\beta\sin\alpha - \frac{\gamma' mE'u'}{c}\sin\theta), \tag{11.9}$$

$$G = \gamma\gamma' m^2 uu'\sin\beta\sin\alpha, \tag{11.10}$$

$$H = (\gamma\gamma' m^2 uu'\cos\alpha - \frac{\gamma' mE'}{c}u'\cos\theta), \tag{11.11}$$

$$W = (FB - HA)^2 + G^2A^2 + G^2B^2, \tag{11.12}$$

$$Y = 2\left((AD - FC)(FB - HA) - G^2BC\right), \tag{11.13}$$

$$Z = (AD - FC)^2 + G^2\left(C^2 - A^2\right), \tag{11.14}$$

and c is the speed of light, m is the rest mass of an electron, u is the speed of the target electron, u' is the speed of the recoil electron, $\gamma = (1 - (u^2/c^2))^{-1/2}$ and $\gamma' = (1 - (u'^2/c^2))^{-1/2}$. Further information regarding the Monash Compton scattering model can be found in [6].

11.1.3 Status of the document

16.11.2012 created by Jeremy Brown

Bibliography

[1] Ribberfors R., Phys. Rev. B. 12 2067-2074, 1975.

[2] Brusa D. et al., Nucl. Instrum. Methods Phys. Res. A 379 167-175, 1996.

[3] Kippen, R. M., New Astro. Reviews 48, 221-225, 2004.

[4] Salvat F. et al., PENELOPE, A Code System for Monte Carlo Simulation of Electron and Photon Transport, Proceedings of a Workshop/Training Course, OECD/NEA 5-7 November 2001.

[5] Du Mond J. W. M., Phys. Rev. 33 643-658, 1929.

[6] Brown J. M. C. et al., Nucl. Instrum. Methods Phys. Res. A, under review, 2012.

Chapter 12

Charged Hadron Incident

12.1 Hadron and Ion Ionization

12.1.1 Method

The class *G4hIonisation* provides the continuous energy loss due to ionization and simulates the 'discrete' part of the ionization, that is, delta rays produced by charged hadrons. The class *G4ionIonisation* is intended for the simulation of energy loss by positive ions with change greater than unit. Inside these classes the following models are used:

- *G4BetherBlochModel* (valid for protons with $T > 2\ MeV$)
- *G4BraggModel* (valid for protons with $T < 2\ MeV$)
- *G4BraggIonModel* (valid for protons with $T < 2\ MeV$)
- *G4ICRU73QOModel* (valid for anti-protons with $T < 2\ MeV$)

The scaling relation (7.7) is a basic conception for the description of ionization of heavy charged particles. It is used both in energy loss calculation and in determination of the validity range of models. Namely the $T_p = 2MeV$ limit for protons is scaled for a particle with mass M_i by the ratio of the particle mass to the proton mass $T_i = T_p M_p / M_i$.

For all ionization models the value of the maximum energy transferable to a free electron T_{max} is given by the following relation [1]:

$$T_{max} = \frac{2m_e c^2(\gamma^2 - 1)}{1 + 2\gamma(m_e/M) + (m_e/M)^2}, \tag{12.1}$$

where m_e is the electron mass and M is the mass of the incident particle. The method of calculation of the continuous energy loss and the total cross-section are explained below.

12.1.2 Continuous Energy Loss

The integration of 7.1 leads to the Bethe-Bloch restricted energy loss ($T < T_{cut}$ formula [1], which is modified taken into account various corrections [2]:

$$\frac{dE}{dx} = 2\pi r_e^2 mc^2 n_{el} \frac{z^2}{\beta^2} \left[\ln\left(\frac{2mc^2\beta^2\gamma^2 T_{up}}{I^2} \right) - \beta^2 \left(1 + \frac{T_{up}}{T_{max}} \right) - \delta - \frac{2C_e}{Z} + F \right] \tag{12.2}$$

where

r_e	classical electron radius: $e^2/(4\pi\epsilon_0 mc^2)$
mc^2	mass-energy of the electron
n_{el}	electrons density in the material
I	mean excitation energy in the material
Z	atomic number of the material
z	charge of the hadron in units of the electron change
γ	E/mc^2
β^2	$1-(1/\gamma^2)$
T_{up}	$\min(T_{cut}, T_{max})$
δ	density effect function
C_e	shell correction function
F	high order corrections

In a single element the electron density is

$$n_{el} = Z\, n_{at} = Z\, \frac{\mathcal{N}_{av}\rho}{A}$$

($\mathcal{N}_{av}$: Avogadro number, ρ: density of the material, A: mass of a mole). In a compound material

$$n_{el} = \sum_i Z_i\, n_{ati} = \sum_i Z_i\, \frac{\mathcal{N}_{av} w_i \rho}{A_i}.$$

w_i is the proportion by mass of the i^{th} element, with molar mass A_i.

The mean excitation energy I for all elements is tabulated according to the ICRU recommended values [3].

Shell Correction

$2C_e/Z$ is the so-called *shell correction term* which accounts for the fact of interaction of atomic electrons with atomic nucleus. This term more visible at low energies and for heavy atoms. The classical expression for the term [4] is used

$$C = \sum C_\nu(\theta_\nu, \eta_\nu),\ \ \nu = K, L, M, ...,\ \theta = \frac{J_\nu}{\epsilon_\nu},\ \ \eta_\nu = \frac{\beta^2}{\alpha^2 Z_\nu^2}, \qquad (12.3)$$

where α is the fine structure constant, β is the hadron velocity, J_ν is the ionisation energy of the shell ν, ϵ_ν is Bohr ionisation energy of the shell ν, Z_ν is the effective charge of the shell ν. First terms C_K and C_L can

be analytically computed in using an assumption non-relativistic hydrogenic wave functions [5, 6]. The results [7] of tabulation of these computations in the interval of parameters $\eta_\nu = 0.005 \div 10$ and $\theta_\nu = 0.25 \div 0.95$ are used directly. For higher values of η_ν the parameterization [7] is applied:

$$C_\nu = \frac{K_1}{\eta} + \frac{K_2}{\eta^2} + \frac{K_3}{\eta^3}, \tag{12.4}$$

where coefficients K_i provide smooth shape of the function. The effective nuclear charge for the L-shell can be reproduced as $Z_L = Z - d$, d is a parameter shown in Table 12.24. For outer shells the calculations are not available, so

Z	3	4	5	6	7	8	9	>9
d	1.72	2.09	2.48	2.82	3.16	3.53	3.84	4.15

Table 12.1: Effective nuclear charge for the L-shell [4].

L-shell parameterization is used and the following scaling relation [4, 8] is applied:

$$C_\nu = V_\nu C_L(\theta_L, H_\nu \eta_L), \;\; V_\nu = \frac{n_\nu}{n_L}, \;\; H_\nu = \frac{J_\nu}{J_L}, \tag{12.5}$$

where V_ν is a vertical scaling factor proportional to number of electrons at the shell n_ν. The contribution of the shell correction term is about 10% for protons at $T = 2MeV$.

Density Correction

δ is a correction term which takes into account the reduction in energy loss due to the so-called *density effect*. This becomes important at high energies because media have a tendency to become polarized as the incident particle velocity increases. As a consequence, the atoms in a medium can no longer be considered as isolated. To correct for this effect the formulation of Sternheimer [9] is used:
x is a kinetic variable of the particle : $x = \log_{10}(\gamma\beta) = \ln(\gamma^2\beta^2)/4.606$, and $\delta(x)$ is defined by

$$\begin{array}{lll} \text{for} \quad x < x_0 : & \delta(x) = 0 & \\ \text{for} \quad x \in [x_0,\ x_1] : & \delta(x) = 4.606x - C + a(x_1 - x)^m & \\ \text{for} \quad x > x_1 : & \delta(x) = 4.606x - C & \end{array} \tag{12.6}$$

where the matter-dependent constants are calculated as follows:

$$\begin{array}{lcl} h\nu_p & = & \text{plasma energy of the medium } = \sqrt{4\pi n_{el} r_e^3} mc^2/\alpha = \sqrt{4\pi n_{el} r_e}\hbar c \\ C & = & 1 + 2\ln(I/h\nu_p) \\ x_a & = & C/4.606 \\ a & = & 4.606(x_a - x_0)/(x_1 - x_0)^m \\ m & = & 3. \end{array} \tag{12.7}$$

For condensed media

$$\begin{array}{lll} I < 100\,\text{eV} & \left\{ \begin{array}{lll} \text{for } C \le 3.681 & x_0 = 0.2 & x_1 = 2 \\ \text{for } C > 3.681 & x_0 = 0.326C - 1.0 & x_1 = 2 \end{array} \right. \\ I \ge 100\,\text{eV} & \left\{ \begin{array}{lll} \text{for } C \le 5.215 & x_0 = 0.2 & x_1 = 3 \\ \text{for } C > 5.215 & x_0 = 0.326C - 1.5 & x_1 = 3 \end{array} \right. \end{array}$$

and for gaseous media

$$\begin{array}{llll} \text{for} & C < 10. & x_0 = 1.6 & x_1 = 4 \\ \text{for} & C \in [10.0,\ 10.5[& x_0 = 1.7 & x_1 = 4 \\ \text{for} & C \in [10.5,\ 11.0[& x_0 = 1.8 & x_1 = 4 \\ \text{for} & C \in [11.0,\ 11.5[& x_0 = 1.9 & x_1 = 4 \\ \text{for} & C \in [11.5,\ 12.25[& x_0 = 2. & x_1 = 4 \\ \text{for} & C \in [12.25,\ 13.804[& x_0 = 2. & x_1 = 5 \\ \text{for} & C \ge 13.804 & x_0 = 0.326C - 2.5 & x_1 = 5. \end{array}$$

High Order Corrections

High order corrections term to Bethe-Bloch formula (12.2) can be expressed as

$$F = G - S + 2(zL_1 + z^2 L_2), \tag{12.8}$$

where G is the Mott correction term, S is the finite size correction term, L_1 is the Barkas correction, L_2 is the Bloch correction. The Mott term [2] describes the close-collision corrections tend to become more important at large velocities and higher charge of projectile. The Fermi result is used:

$$G = \pi\alpha z\beta. \tag{12.9}$$

The Barkas correction term describes distant collisions. The parameterization of Ref. is expressed in the form:

$$L_1 = \frac{1.29F_A(b/x^{1/2})}{Z^{1/2}x^{3/2}}, \quad x = \frac{\beta^2}{Z\alpha^2}, \tag{12.10}$$

Z	1 (H_2 gas)	1	2	3 - 10	11 - 17	18	19 - 25	26 - 50	> 50
d	0.6	1.8	0.6	1.8	1.4	1.8	1.4	1.35	1.3

Table 12.2: Scaled minimum impact parameter b [4].

where F_A is tabulated function [10], b is scaled minimum impact parameter shown in Table 12.2. This and other corrections depending on atomic properties are assumed to be additive for mixtures and compounds. For the Bloch correction term the classical expression [4] is following:

$$z^2 L_2 = -y^2 \sum_{n=1}^{\infty} \frac{1}{n(n^2+y^2)}, \quad y = \frac{z\alpha}{\beta}. \tag{12.11}$$

The finite size correction term takes into account the space distribution of charge of the projectile particle. For muon it is zero, for hadrons this term become visible at energies above few hundred GeV and the following parameterization [2] is used:

$$S = ln(1+q), \quad q = \frac{2m_e T_{max}}{\varepsilon^2}, \tag{12.12}$$

where T_{max} is given in relation (12.1), ε is proportional to the inverse effective radius of the projectile (Table 12.3). All these terms break scaling

mesons, spin = 0 ($\pi^{\pm}$, $K^{\pm}$)	0.736 GeV
baryons, spin = 1/2	0.843 GeV
ions	0.843 $A^{1/3}$ GeV

Table 12.3: The values of the ε parameter for different particle types.

relation (7.7) if the projectile particle charge differs from ± 1. To take this circumstance into account in *G4ionIonisation* process at initialisation time the term F is ignored for the computation of the dE/dx table. At run time this term is taken into account by adding to the mean energy loss a value

$$\Delta T' = 2\pi r_e^2 mc^2 n_{el} \frac{z^2}{\beta^2} F \Delta s, \tag{12.13}$$

where Δs is the *true step length* and F is the high order correction term (12.8).

Parameterizations at Low Energies

For scaled energies below $T_{lim} = 2\ MeV$ shell correction becomes very large and precision of the Bethe-Bloch formula degrades, so parameterisation of

evaluated data for stopping powers at low energies is required. These parameterisations for all atoms is available from ICRU'49 report [4]. The proton parametrisation is used in *G4BraggModel*, which is included by default in the process *G4hIonisation*. The alpha particle parameterisation is used in the *G4BraggIonModel*, which is included by default in the process *G4ionIonisation*. To provide a smooth transition between low-energy and high-energy models the modified energy loss expression is used for high energy

$$S(T) = S_H(T) + (S_L(T_{lim}) - S_H(T_{lim}))\frac{T_{lim}}{T}, \;\; T > T_{lim}, \tag{12.14}$$

where S is smoothed stopping power, S_H is stopping power from formula (12.2) and S_L is the low-energy parameterisation.

The precision of Bethe-Bloch formula for $T > 10MeV$ is within 2%, below the precision degrades and at $1keV$ only 20% may be garanteed. In the energy interval $1 - 10MeV$ the quality of description of the stopping power varied from atom to atom. To provide more stable and precise parameterisation the data from the NIST databases are included inside the standard package. These data are provided for 74 materials of the NIST material database [11]. The data from the PSTAR database are included into *G4BraggModel*. The data from the ASTAR database are included into *G4BraggIonModel*. So, if Geant4 material is defined as a NIST material, than NIST data are used for low-energy parameterisation of stopping power. If material is not from the NIST database, then the ICRU'49 parameterisation is used.

12.1.3 Nuclear Stopping

Nuclear stopping due to elastic ion-ion scattering since Geant4 v9.3 can be simulated with the continuous process *G4NuclearStopping*. By default this correction is active and the ICRU'49 parameterisation [4] is used, which is implemented in the model class *G4ICRU49NuclearStoppingModel*.

12.1.4 Total Cross Section per Atom

For $T \gg I$ the differential cross section can be written as

$$\frac{d\sigma}{dT} = 2\pi r_e^2 mc^2 Z \frac{z_p^2}{\beta^2}\frac{1}{T^2}\left[1 - \beta^2\frac{T}{T_{max}} + \frac{T^2}{2E^2}\right] \tag{12.15}$$

[1]. In GEANT4 $T_{cut} \geq 1$ keV. Integrating from T_{cut} to T_{max} gives the total cross section per atom :

$$\begin{aligned} \sigma(Z, E, T_{cut}) &= \frac{2\pi r_e^2 Z z_p^2}{\beta^2} mc^2 \times \\ &\left[\left(\frac{1}{T_{cut}} - \frac{1}{T_{max}}\right) - \frac{\beta^2}{T_{max}} \ln \frac{T_{max}}{T_{cut}} + \frac{T_{max} - T_{cut}}{2E^2}\right] \end{aligned} \tag{12.16}$$

The last term is for spin 1/2 only. In a given material the mean free path is:

$$\lambda = (n_{at} \cdot \sigma)^{-1} \quad or \quad \lambda = \left(\textstyle\sum_i n_{ati} \cdot \sigma_i\right)^{-1} \tag{12.17}$$

The mean free path is tabulated during initialization as a function of the material and of the energy for all kinds of charged particles.

12.1.5 Simulating Delta-ray Production

A short overview of the sampling method is given in Chapter 2. Apart from the normalization, the cross section 12.15 can be factorized :

$$\frac{d\sigma}{dT} = f(T)g(T) \quad with \quad T \in [T_{cut},\ T_{max}] \tag{12.18}$$

where

$$f(T) = \left(\frac{1}{T_{cut}} - \frac{1}{T_{max}}\right) \frac{1}{T^2} \tag{12.19}$$

$$g(T) = 1 - \beta^2 \frac{T}{T_{max}} + \frac{T^2}{2E^2}. \tag{12.20}$$

The last term in $g(T)$ is for spin 1/2 only. The energy T is chosen by

1. sampling T from $f(T)$
2. calculating the rejection function $g(T)$ and accepting the sampled T with a probability of $g(T)$.

After the successful sampling of the energy, the direction of the scattered electron is generated with respect to the direction of the incident particle. The azimuthal angle ϕ is generated isotropically. The polar angle θ is calculated from energy-momentum conservation. This information is used to calculate the energy and momentum of both scattered particles and to transform them into the *global* coordinate system.

12.1.6 Ion Effective Charge

As ions penetrate matter they exchange electrons with the medium. In the implementation of *G4ionIonisation* the effective charge approach is used [12]. A state of equilibrium between the ion and the medium is assumed, so that the ion's effective charge can be calculated as a function of its kinetic energy in a given material. Before and after each step the dynamic charge of the ion is recalculated and saved in *G4DynamicParticle*, where it can be used not only for energy loss calculations but also for the sampling of transportation in an electromagnetic field.

The ion effective charge is expressed via the ion charge z_i and the fractional effective charge of ion γ_i:

$$z_{eff} = \gamma_i z_i. \tag{12.21}$$

For helium ions fractional effective charge is parameterized for all elements

$$\begin{aligned} (\gamma_{He})^2 &= \left(1 - \exp\left[-\sum_{j=0}^{5} C_j Q^j\right]\right)\left(1 + \frac{7 + 0.05Z}{1000}\exp(-(7.6 - Q)^2)\right)^2, \\ Q &= \max(0, \ln T), \end{aligned} \tag{12.22}$$

where the coefficients C_j are the same for all elements, and the helium ion kinetic energy T is in keV/amu.

The following expression is used for heavy ions [13]:

$$\gamma_i = \left(q + \frac{1-q}{2}\left(\frac{v_0}{v_F}\right)^2 \ln\left(1 + \Lambda^2\right)\right)\left(1 + \frac{(0.18 + 0.0015Z)\exp(-(7.6 - Q)^2)}{Z_i^2}\right), \tag{12.23}$$

where q is the fractional average charge of the ion, v_0 is the Bohr velocity, v_F is the Fermi velocity of the electrons in the target medium, and Λ is the term taking into account the screening effect:

$$\Lambda = 10\frac{v_F}{v_0}\frac{(1-q)^{2/3}}{Z_i^{1/3}(6+q)}. \tag{12.24}$$

The Fermi velocity of the medium is of the same order as the Bohr velocity, and its exact value depends on the detailed electronic structure of the medium. The expression for the fractional average charge of the ion is the following:

$$q = [1 - \exp(0.803y^{0.3} - 1.3167y^{0.6} - 0.38157y - 0.008983y^2)], \tag{12.25}$$

where y is a parameter that depends on the ion velocity v_i

$$y = \frac{v_i}{v_0 Z^{2/3}} \left(1 + \frac{v_F^2}{5 v_i^2}\right). \tag{12.26}$$

The parametrisation of the effective charge of the ion applied if the kinetic energy is below limit value

$$T < 10 z_i \frac{M_i}{M_p}\, MeV, \tag{12.27}$$

where M_i is the ion mass and M_p is the proton mass.

12.1.7 Status of this document

09.10.98 created by L. Urbán.
14.12.01 revised by M.Maire
29.11.02 re-worded by D.H. Wright
01.12.03 revised by V. Ivanchenko
21.06.07 revised by V. Ivanchenko
25.11.11 revised by V. Ivanchenko

Bibliography

[1] W.-M. Yao et al., Jour. of Phys. G33 (2006) 1.

[2] S.P. Ahlen, Rev. Mod. Phys. 52 (1980) 121.

[3] ICRU (A. Allisy et al), Stopping Powers for Electrons and Positrons, ICRU Report 37, 1984.

[4] ICRU (A. Allisy et al), Stopping Powers and Ranges for Protons and Alpha Particles, ICRU Report 49, 1993.

[5] M.C. Walske, Phys. Rev. 88 (1952) 1283.

[6] M.C. Walske, Phys. Rev. 181 (1956) 940.

[7] G.S. Khandelwal, Nucl. Phys. A116 (1968) 97.

[8] H. Bichsel, Phys. Rev. A46 (1992) 5761.

[9] R.M. Sternheimer. Phys.Rev. B3 (1971) 3681.

[10] J.C. Ashley, R.H. Ritchie and W. Brandt, Phys. Rev. A8 (1973) 2402.

[11] http://physics.nist.gov/PhysRevData/contents-radi.html

[12] J.F. Ziegler, J.P. Biersack, U. Littmark, The Stopping and Ranges of Ions in Solids. Vol.1, Pergamon Press, 1985.

[13] W. Brandt and M. Kitagawa, Phys. Rev. B25 (1982) 5631.

12.2 Low energy extentions

12.2.1 Energy losses of slow negative particles

At low energies, e.g. below a few MeV for protons/antiprotons, the Bethe-Bloch formula is no longer accurate in describing the energy loss of charged hadrons and higher Z terms should be taken in account. Odd terms in Z lead to a significant difference between energy loss of positively and negatively charged particles. The energy loss of negative hadrons is scaled from that of antiprotons. The antiproton energy loss is calculated according to the quantum harmonic oscillator model is used, as described in [1] and references therein. The lower limit of applicability of the model is chosen for all materials at 10 keV. Below this value stopping power is set to constant equal to the dE/dx at 10 keV.

12.2.2 Energy losses of hadrons in compounds

To obtain energy losses in a mixture or compound, the absorber can be thought of as made up of thin layers of pure elements with weights proportional to the electron density of the element in the absorber (Bragg's rule):

$$\frac{dE}{dx} = \sum_i \left(\frac{dE}{dx}\right)_i, \tag{12.28}$$

where the sum is taken over all elements of the absorber, i is the number of the element, $(\frac{dE}{dx})_i$ is energy loss in the pure i-th element.

Bragg's rule is very accurate for relativistic particles when the interaction of electrons with a nucleus is negligible. But at low energies the accuracy of Bragg's rule is limited because the energy loss to the electrons in any material depends on the detailed orbital and excitation structure of the material. In the description of Geant4 materials there is a special attribute: the chemical formula. It is used in the following way:

- if the data on the stopping power for a compound as a function of the proton kinetic energy is available (Table 12.4), then the direct parametrisation of the data for this material is performed;
- if the data on the stopping power for a compound is available for only one incident energy (Table 12.5), then the computation is performed based on Bragg's rule and the chemical factor for the compound is taken into account;

Table 12.4: The list of chemical formulae of compounds for which parametrisation of stopping power as a function of kinetic energy is in Ref.[3].

Number	Chemical formula
1.	AlO
2.	C_2O
3.	CH_4
4.	(C_2H_4)_N-Polyethylene
5.	(C_2H_4)_N-Polypropylene
6.	(C_8H_8)_N
7.	C_3H_8
8.	SiO_2
9.	H_2O
10.	H_2O-Gas
11.	Graphite

- if there are no data for the compound, the computation is performed based on Bragg's rule.

In the review [2] the parametrisation stopping power data are presented as

$$S_e(T_p) = S_{Bragg}(T_p)\left[1 + \frac{f(T_p)}{f(125\ keV)}\left(\frac{S_{exp}(125\ keV)}{S_{Bragg}(125\ keV)} - 1\right)\right], \quad (12.29)$$

where $S_{exp}(125\ keV)$ is the experimental value of the energy loss for the compound for 125 keV protons or the reduced experimental value for He ions, $S_{Bragg}(T_p)$ is a value of energy loss calculated according to Bragg's rule, and $f(T_p)$ is a universal function, which describes the disappearance of deviations from Bragg's rule for higher kinetic energies according to:

$$f(T_p) = \frac{1}{1 + \exp\left[1.48(\frac{\beta(T_p)}{\beta(25\ keV)} - 7.0)\right]}, \quad (12.30)$$

where $\beta(T_p)$ is the relative velocity of the proton with kinetic energy T_p.

12.2.3 Fluctuations of energy losses of hadrons

The total continuous energy loss of charged particles is a stochastic quantity with a distribution described in terms of a straggling function. The straggling is partially taken into account by the simulation of energy loss by the

Table 12.5: The list of chemical formulae of compounds for which the *chemical factor* is calculated from the data of Ref.[2].

Number	Chemical formula	Number	Chemical formula
1.	H_2O	28.	C_2H_6
2.	C_2H_4O	29.	C_2F_6
3.	C_3H_6O	30.	C_2H_6O
4.	C_2H_2	31.	C_3H_6O
5.	C_H_3OH	32.	C_4H_10O
6.	C_2H_5OH	33.	C_2H_4
7.	C_3H_7OH	34.	C_2H_4O
8.	C_3H_4	35.	C_2H_4S
9.	NH_3	36.	SH_2
10.	C_14H_10	37.	CH_4
11.	C_6H_6	38.	CCLF_3
12.	C_4H_10	39.	CCl_2F_2
13.	C_4H_6	40.	CHCl_2F
14.	C_4H_8O	41.	(CH_3)_2S
15.	CCl_4	42.	N_2O
16.	CF_4	43.	C_5H_10O
17.	C_6H_8	44.	C_8H_6
18.	C_6H_12	45.	(CH_2)_N
19.	C_6H_10O	46.	(C_3H_6)_N
20.	C_6H_10	47.	(C_8H_8)_N
21.	C_8H_16	48.	C_3H_8
22.	C_5H_10	49.	C_3H_6-Propylene
23.	C_5H_8	50.	C_3H_6O
24.	C_3H_6-Cyclopropane	51.	C_3H_6S
25.	C_2H_4F_2	52.	C_4H_4S
26.	C_2H_2F_2	53.	C_7H_8
27.	C_4H_8O_2		

production of δ-electrons with energy $T > T_c$. However, continuous energy loss also has fluctuations. Hence in the current GEANT4 implementation two different models of fluctuations are applied depending on the value of the parameter κ which is the lower limit of the number of interactions of the particle in the step. The default value chosen is $\kappa = 10$. To select a model for thick absorbers the following boundary conditions are used:

$$\Delta E > T_c\kappa) \ \ or \ \ T_c < I\kappa, \tag{12.31}$$

where ΔE is the mean continuous energy loss in a track segment of length s, T_c is the cut kinetic energy of δ-electrons, and I is the average ionisation potential of the atom.

For long path lengths the straggling function approaches the Gaussian distribution with Bohr's variance [3]:

$$\Omega^2 = KN_{el}\frac{Z_h^2}{\beta^2}T_c s f\left(1 - \frac{\beta^2}{2}\right), \tag{12.32}$$

where f is a screening factor, which is equal to unity for fast particles, whereas for slow positively charged ions with $\beta^2 < 3Z(v_0/c)^2$ $f = a + b/Z_{eff}^2$, where parameters a and b are parametrised for all atoms [4, 5].

For short path lengths, when the condition 12.31 is not satisfied, the model described in the charter 7.2 is applied.

12.2.4 ICRU 73-based energy loss model

The ICRU 73 [1] report contains stopping power tables for ions with atomic numbers 3–18 and 26, covering a range of different elemental and compound target materials. The stopping powers derive from calculations with the PASS code [6], which implements the binary stopping theory described in [6, 7]. Tables in ICRU 73 extend over an energy range up to 1 GeV/nucleon. All stopping powers were incorporated into Geant4 and are available through a parameterisation model (`G4IonParametrisedLossModel`). For a few materials revised stopping powers were included (water, water vapor, nylon type 6 and 6/6 from P. Sigmund et al [8] and copper from P. Sigmund [9]), which replace the corresponding tables of the original ICRU 73 report.

To account for secondary electron production above T_c, the continuous energy loss per unit path length is calculated according to

$$\left.\frac{dE}{dx}\right|_{T<T_C} = \left(\frac{dE}{dx}\right)_{ICRU73} - \left(\frac{dE}{dx}\right)_{\delta} \tag{12.33}$$

where $(dE/dx)_{ICRU73}$ refers to stopping powers obtained by interpolating ICRU 73 tables and $(dE/dx)_\delta$ is the mean energy transferred to δ-electrons per path length given by

$$\left(\frac{dE}{dx}\right)_\delta = \sum_i n_{at,i} \int_{T_c}^{T_{max}} \frac{d\sigma_i(T)}{dT} T dT \tag{12.34}$$

where the index i runs over all elements composing the material, $n_{at,i}$ is the number of atoms of the element i per volume, T_{max} is the maximum energy transferable to an electron according to formula and $d\sigma_i/dT$ specifies the differential cross section per atom for producing an δ-electron following equation

For compound targets not considered in the ICRU 73 report, the first term on the rightern side in equation (12.33) is computed by applying Bragg's additivity rule [3] if tables for all elemental components are available in ICRU 73.

12.2.5 Status of this document

21.11.2000 Created by V.Ivanchenko
30.05.2001 Modified by V.Ivanchenko
23.11.2001 Modified by M.G. Pia to add PIXE section.
19.01.2002 Minor corrections (mma)
13.05.2002 Minor corrections (V.Ivanchenko)
28.08.2002 Minor corrections (V.Ivanchenko)
11.12.2009 Modified by A. Lechner to add ICRU 73 section
20.11.2011 Updated by V.Ivanchenko

Bibliography

[1] Stopping of Ions Heavier Than Helium, ICRU Report 73, Oxford University Press (2005).

[2] J.F. Ziegler and J.M. Manoyan, Nucl. Instr. and Meth. B35 (1988) 215.

[3] ICRU (A. Allisy et al), Stopping Powers and Ranges for Protons and Alpha Particles, ICRU Report 49, 1993.

[4] Q. Yang, D.J. O'Connor, Z. Wang, Nucl. Instr. and Meth. B61 (1991) 149.

[5] W.K. Chu, in: Ion Beam Handbook for Material Analysis, edt. J.W. Mayer and E. Rimini, Academic Press, NY, 1977.

[6] P. Sigmund and A. Schinner, Nucl. Instr. Meth. in Phys. Res. B 195 (2002) 64.

[7] P. Sigmund and A. Schinner, Eur. Phys. J. D 12 (2000) 425.

[8] P. Sigmund, A. Schinner and H. Paul, Errata and Addenda for ICRU Report 73, Stopping of Ions Heavier than Helium (2009).

[9] Personal communication with P. Sigmund (2009).

Chapter 13

Muon Incident

13.1 Muon Ionization

The class *G4MuIonisation* provides the continuous energy loss due to ionization and simulates the 'discrete' part of the ionization, that is, delta rays produced by muons. Inside this class the following models are used:

- *G4BraggModel* (valid for protons with $T < 0.2\ MeV$)
- *G4BetherBlochModel* (valid for protons with $0.2\ MeV < T < 1\ GeV$)
- *G4MuBetherBlochModel* (valid for protons with $T > 1\ GeV$)

The limit energy $0.2\ MeV$ is equivalent to the proton limit energy $2MeV$ because of scaling relation (7.7), which allows simulation for muons with energy below $1\ GeV$ in the same way as for point-like hadrons with spin 1/2 described in the section 7.1.

For higher energies the *G4MuBetherBlochModel* is applied, in which leading radiative corrections are taken into account [1]. Simple analytical formula for the cross section, derived with the logarithmic are used. Calculation results appreciably differ from usual elastic $\mu - e$ scattering in the region of high energy transfers $m_e << T < T_{max}$ and give non-negligible correction to the total average energy loss of high-energy muons. The total cross section is written as following:

$$\sigma(E,\epsilon) = \sigma_{BB}(E,\epsilon)\left[1 + \frac{\alpha}{2\pi} ln\left(1 + \frac{2\epsilon}{m_e}\right) ln\left(\frac{4m_e E(E-\epsilon)}{m_\mu^2(2\epsilon + m_e)}\right)\right], \quad (13.1)$$

here $\sigma(E,\epsilon)$ is the differential cross sections, $\sigma(E,\epsilon)_{BB}$ is the Bethe-Bloch cross section (12.15), m_e is the electron mass, m_μ is the muon mass, E is the muon energy, ϵ is the energy transfer, $\epsilon = \omega + T$, where T is the electron kinetic energy and ω is the energy of radiative gamma.

For computation of the truncated mean energy loss (7.1) the partial integration of the expression (13.1) is performed

$$S(E,\epsilon_{up}) = S_{BB}(E,\epsilon_{up}) + S_{RC}(E,\epsilon_{up}), \;\; \epsilon_{up} = min(\epsilon_{max},\epsilon_{cut}), \quad (13.2)$$

where term S_{BB} is the Bethe-Bloch truncated energy loss (12.2) for the interval of energy transfer $(0 - \epsilon_{up})$ and term S_{RC} is a correction due to radiative effects. The function become smooth after log-substitution and is computed by numerical integration

$$S_{RC}(E,\epsilon_{up}) = \int_{\ln\epsilon_1}^{\ln\epsilon_{up}} \epsilon^2(\sigma(E,\epsilon) - \sigma_{BB}(E,\epsilon))d(\ln\epsilon), \quad (13.3)$$

where lower limit ϵ_1 does not effect result of integration in first order and in the class *G4MuBetheBlochModel* the default value $\epsilon_1 = 100keV$ is used.

For computation of the discrete cross section (7.2) another substitution is used in order to perform numerical integration of a smooth function

$$\sigma(E) = \int_{1/\epsilon_{max}}^{1/\epsilon_{up}} \epsilon^2 \sigma(E, \epsilon) d(1/\epsilon). \tag{13.4}$$

The sampling of energy transfer is performed between $1/\epsilon_{up}$ and $1/\epsilon_{max}$ using rejection constant for the function $\epsilon^2\sigma(E, \epsilon)$. After the successful sampling of the energy transfer, the direction of the scattered electron is generated with respect to the direction of the incident particle. The energy of radiative gamma is neglected. The azimuthal electron angle ϕ is generated isotropically. The polar angle θ is calculated from energy-momentum conservation. This information is used to calculate the energy and momentum of both scattered particles and to transform them into the *global* coordinate system.

13.1.1 Status of this document

09.10.98 created by L. Urbán.
14.12.01 revised by M.Maire
30.11.02 re-worded by D.H. Wright
01.12.03 revised by V. Ivanchenko
22.06.07 rewritten by V. Ivanchenko

Bibliography

[1] S.R. Kelner, R.P. Kokoulin, A.A. Petrukhin, Phys. Atomic Nuclei 60 (1997) 576.

13.2 Bremsstrahlung

Bremsstrahlung dominates other muon interaction processes in the region of catastrophic collisions ($v \geq 0.1$), that is at "moderate" muon energies above the kinematic limit for knock–on electron production. At high energies ($E \geq 1$ TeV) this process contributes about 40% of the average muon energy loss.

13.2.1 Differential Cross Section

The differential cross section for muon bremsstrahlung (in units of $\mathrm{cm}^2/(\mathrm{g\ GeV})$) can be written as

$$\begin{aligned} \frac{d\sigma(E,\epsilon,Z,A)}{d\epsilon} &= \frac{16}{3}\alpha N_A(\frac{m}{\mu}r_e)^2\frac{1}{\epsilon A}Z(Z\Phi_n+\Phi_e)(1-v+\frac{3}{4}v^2) \\ &= 0 \quad \text{if} \quad \epsilon \geq \epsilon_{\max} = E-\mu, \end{aligned} \tag{13.5}$$

where μ and m are the muon and electron masses, Z and A are the atomic number and atomic weight of the material, and N_A is Avogadro's number. If E and T are the initial total and kinetic energy of the muon, and ϵ is the emitted photon energy, then $\epsilon = E - E'$ and the relative energy transfer $v = \epsilon/E$.

Φ_n represents the contribution of the nucleus and can be expressed as

$$\begin{aligned} \Phi_n &= \ln\frac{BZ^{-1/3}(\mu+\delta(D'_n\sqrt{e}-2))}{D'_n(m+\delta\sqrt{e}BZ^{-1/3})}; \\ &= 0 \quad \text{if} \quad \text{negative.} \end{aligned}$$

Φ_e represents the contribution of the electrons and can be expressed as

$$\begin{aligned} \Phi_e &= \ln\frac{B'Z^{-2/3}\mu}{\left(1+\dfrac{\delta\mu}{m^2\sqrt{e}}\right)(m+\delta\sqrt{e}B'Z^{-2/3})}; \\ &= 0 \quad \text{if} \quad \epsilon \geq \epsilon'_{\max} = E/(1+\mu^2/2mE); \\ &= 0 \quad \text{if} \quad \text{negative.} \end{aligned}$$

In Φ_n and Φ_e, for all nuclei except hydrogen,

$$\begin{aligned} \delta &= \mu^2\epsilon/2EE' = \mu^2 v/2(E-\epsilon); \\ D'_n &= D_n^{(1-1/Z)}, \quad D_n = 1.54A^{0.27}; \\ B &= 183, \quad B' = 1429, \quad \sqrt{e} = 1.648(721271). \end{aligned}$$

For hydrogen (Z=1) $B = 202.4$, $B' = 446$, $D'_n = D_n$.

These formulae are taken mostly from Refs. [1] and [2]. They include improved nuclear size corrections in comparison with Ref. [3] in the region $v \sim 1$ and low Z. Bremsstrahlung on atomic electrons (taking into account target recoil and atomic binding) is introduced instead of a rough substitution $Z(Z+1)$. A correction for processes with nucleus excitation is also included [4].

Applicability and Restrictions of the Method

The above formulae assume that:
1. $E \gg \mu$, hence the ultrarelativistic approximation is used;
2. $E \leq 10^{20}$ eV; above this energy, LPM suppression can be expected;
3. $v \geq 10^{-6}$; below 10^{-6} Ter-Mikaelyan suppression takes place. However, in the latter region the cross section of muon bremsstrahlung is several orders of magnitude less than that of other processes.
The Coulomb correction (for high Z) is not included. However, existing calculations [5] show that for muon bremsstrahlung this correction is small.

13.2.2 Continuous Energy Loss

The restricted energy loss for muon bremsstrahlung $(dE/dx)_{\rm rest}$ with relative transfers $v = \epsilon/(T+\mu) \leq v_{\rm cut}$ can be calculated as follows :

$$\left(\frac{dE}{dx}\right)_{\rm rest} = \int_0^{\epsilon_{\rm cut}} \epsilon\,\sigma(E,\epsilon)\,d\epsilon = (T+\mu)\int_0^{v_{\rm cut}} \epsilon\,\sigma(E,\epsilon)\,dv\,.$$

If the user cut $v_{\rm cut} \geq v_{\rm max} = T/(T+\mu)$, the total average energy loss is calculated. Integration is done using Gaussian quadratures, and binning provides an accuracy better than about 0.03% for $T = 1$ GeV, $Z = 1$. This rapidly improves with increasing T and Z.

13.2.3 Total Cross Section

The integration of the differential cross section over $d\epsilon$ gives the total cross section for muon bremsstrahlung:

$$\sigma_{\rm tot}(E,\epsilon_{\rm cut}) = \int_{\epsilon_{\rm cut}}^{\epsilon_{\rm max}} \sigma(E,\epsilon)d\epsilon = \int_{\ln v_{\rm cut}}^{\ln v_{\rm max}} \epsilon\sigma(E,\epsilon)d(\ln v), \qquad (13.6)$$

where $v_{\rm max} = T/(T+\mu)$. If $v_{\rm cut} \geq v_{\rm max}$, $\sigma_{\rm tot} = 0$.

13.2.4 Sampling

The photon energy ϵ_p is found by numerically solving the equation :

$$P = \int_{\epsilon_p}^{\epsilon_{\max}} \sigma(E, \epsilon, Z, A)\, d\epsilon \Big/ \int_{\epsilon_{\rm cut}}^{\epsilon_{\max}} \sigma(E, \epsilon, Z, A)\, d\epsilon \,.$$

Here P is the random uniform probability, $\epsilon_{\max} = T$, and $\epsilon_{\rm cut} = (T + \mu) \cdot v_{\rm cut}$. $v_{min.cut} = 10^{-5}$ is the minimal relative energy transfer adopted in the algorithm.

For fast sampling, the solution of the above equation is tabulated at initialization time for selected Z, T and P. During simulation, this table is interpolated in order to find the value of ϵ_p corresponding to the probability P.

The tabulation routine uses accurate functions for the differential cross section. The table contains values of

$$x_p = \ln(v_p/v_{\max})/\ln(v_{\max}/v_{\rm cut}), \tag{13.7}$$

where $v_p = \epsilon_p/(T + \mu)$ and $v_{\max} = T/(T + \mu)$. Tabulation is performed in the range $1 \le Z \le 128$, $1 \le T \le 1000$ PeV, $10^{-5} \le P \le 1$ with constant logarithmic steps. Atomic weight (which is a required parameter in the cross section) is estimated here with an iterative solution of the approximate relation:

$$A = Z\,(2 + 0.015\,A^{2/3}).$$

For $Z = 1$, $A = 1$ is used.

To find x_p (and thus ϵ_p) corresponding to a given probability P, the sampling method performs a linear interpolation in $\ln Z$ and $\ln T$, and a cubic, 4 point Lagrangian interpolation in $\ln P$. For $P \le P_{\rm min}$, a linear interpolation in (P, x) coordinates is used, with $x = 0$ at $P = 0$. Then the energy ϵ_p is obtained from the inverse transformation of 13.7 :

$$\epsilon_p = (T + \mu) v_{\max} (v_{\max}/v_{\rm cut})^{x_p}$$

The algorithm with the parameters described above has been tested for various Z and T. It reproduces the differential cross section to within 0.2 – 0.7 % for $T \ge 10$ GeV. The average total energy loss is accurate to within 0.5%. While accuracy improves with increasing T, satisfactory results are also obtained for $1 \le T \le 10$ GeV.

It is important to note that this sampling scheme allows the generation of ϵ_p for different user cuts on v which are above $v_{\rm min.cut}$. To perform such a simulation, it is sufficient to define a new probability variable

$$P' = P\,\sigma_{\rm tot}\,(v_{\rm user.cut})/\sigma_{\rm tot}(v_{\rm min.cut})$$

and use it in the sampling method. Time consuming re-calculation of the 3-dimensional table is therefore not required because only the tabulation of $\sigma_{\rm tot}(v_{\rm user.cut})$ is needed.

The small-angle, ultrarelativistic approximation is used for the simulation (with about 20% accuracy at $\theta \leq \theta^* \approx 1$) of the angular distribution of the final state muon and photon. Since the target recoil is small, the muon and photon are directed symmetrically (with equal transverse momenta and coplanar with the initial muon):

$$p_{\perp\mu} = p_{\perp\gamma}, \quad \text{where} \quad p_{\perp\mu} = E'\theta_\mu, \quad p_{\perp\gamma} = \epsilon\theta_\gamma. \tag{13.8}$$

θ_μ and θ_γ are muon and photon emission angles. The distribution in the variable $r = E\theta_\gamma/\mu$ is given by

$$f(r)dr \sim rdr/(1+r^2)^2. \tag{13.9}$$

Random angles are sampled as follows:

$$\theta_\gamma = \frac{\mu}{E} r \quad \theta_\mu = \frac{\epsilon}{E'}\theta_\gamma, \tag{13.10}$$

where

$$r = \sqrt{\frac{a}{1-a}}, \quad a = \xi \frac{r_{\rm max}^2}{1+r_{\rm max}^2}, \quad r_{\rm max} = \min(1, E'/\epsilon) \cdot E\,\theta^*/\mu\,,$$

and ξ is a random number uniformly distributed between 0 and 1.

13.2.5 Status of this document

09.10.98 created by R.Kokoulin and A.Rybin
17.05.00 updated by S.Kelner, R.Kokoulin and A.Rybin
30.11.02 re-written by D.H. Wright

Bibliography

[1] S.R.Kelner, R.P.Kokoulin, A.A.Petrukhin. Preprint MEPhI 024-95, Moscow, 1995; CERN SCAN-9510048.

[2] S.R.Kelner, R.P.Kokoulin, A.A.Petrukhin. Phys. Atomic Nuclei, **60** (1997) 576.

[3] A.A.Petrukhin, V.V.Shestakov. Canad.J.Phys., **46** (1968) S377.

[4] Yu.M.Andreyev, L.B.Bezrukov, E.V.Bugaev. Phys. Atomic Nuclei, **57** (1994) 2066.

[5] Yu.M.Andreev, E.V.Bugaev, Phys. Rev. D, **55** (1997) 1233.

13.3 Positron - Electron Pair Production by Muons

Direct electron pair production is one of the most important muon interaction processes. At TeV muon energies, the pair production cross section exceeds those of other muon interaction processes over a range of energy transfers between 100 MeV and $0.1E_\mu$. The average energy loss for pair production increases linearly with muon energy, and in the TeV region this process contributes more than half the total energy loss rate.

To adequately describe the number of pairs produced, the average energy loss and the stochastic energy loss distribution, the differential cross section behavior over an energy transfer range of 5 MeV $\leq \epsilon \leq 0.1 \cdot E_\mu$ must be accurately reproduced. This is is because the main contribution to the total cross section is given by transferred energies 5 MeV $\leq \epsilon \leq 0.01 \cdot E_\mu$, and because the contribution to the average muon energy loss is determined mostly in the region $0.001 \cdot E_\mu \leq \epsilon \leq 0.1 \cdot E_\mu$.

For a theoretical description of the cross section, the formulae of Ref. [1] are used, along with a correction for finite nuclear size [2]. To take into account electron pair production in the field of atomic electrons, the inelastic atomic form factor contribution of Ref. [3] is also applied.

13.3.1 Differential Cross Section

Definitions and Applicability

In the following discussion, these definitions are used:

- m and μ are the electron and muon masses, respectively
- $E \equiv E_\mu$ is the total muon energy, $E = T + \mu$
- Z and A are the atomic number and weight of the material
- ϵ is the total pair energy or, approximately, the muon energy loss ($E - E'$)
- $v = \epsilon/E$
- $e = 2.718\ldots$
- $A^\star = 183$.

The formula for the differential cross section applies when:

- $E_\mu \gg \mu$ ($E \geq 2$ – 5 GeV) and $E_\mu \leq 10^{15}$ – 10^{17} eV. If muon energies exceed this limit, the LPM (Landau Pomeranchuk Migdal) effect may become important, depending on the material
- the muon energy transfer ϵ lies between $\epsilon_{\min} = 4\,m$ and $\epsilon_{\max} = E_\mu - \frac{3\sqrt{e}}{4}\,\mu\,Z^{1/3}$, although the formal lower limit is $\epsilon \gg 2\,m$, and the formal upper limit requires $E'_\mu \gg \mu$.
- $Z \leq 40$ – 50. For higher Z, the Coulomb correction is important but has not been sufficiently studied theoretically.

Formulae

The differential cross section for electron pair production by muons $\sigma(Z, A, E, \epsilon)$ can be written as :

$$\sigma(Z, A, E, \epsilon) = \frac{4}{3\pi}\,\frac{Z(Z+\zeta)}{A}\,N_A\,(\alpha r_0)^2\,\frac{1-v}{\epsilon}\int_0^{\rho_{\max}} G(Z, E, v, \rho)\,d\rho, \tag{13.11}$$

where

$$G(Z, E, v, \rho) = \Phi_e + (m/\mu)^2\Phi_\mu,$$

$$\Phi_{e,\mu} = B_{e,\mu}L'_{e,\mu}$$

and

$$\Phi_{e,\mu} = 0 \quad \text{whenever} \quad \Phi_{e,\mu} < 0.$$

B_e and B_μ do not depend on Z, A, and are given by

$$B_e = [(2+\rho^2)(1+\beta) + \xi(3+\rho^2)]\ln\left(1+\frac{1}{\xi}\right) + \frac{1-\rho^2-\beta}{1+\xi} - (3+\rho^2);$$

$$B_e \approx \frac{1}{2\xi}\,[(3-\rho^2) + 2\beta(1+\rho^2)] \quad \text{for} \quad \xi \geq 10^3;$$

$$B_\mu = \left[(1+\rho^2)\left(1+\frac{3\beta}{2}\right) - \frac{1}{\xi}(1+2\beta)(1-\rho^2)\right]\ln(1+\xi) + \frac{\xi(1-\rho^2-\beta)}{1+\xi} + (1+2\beta)(1-\rho^2);$$

$$B_\mu \approx \frac{\xi}{2}\,[(5-\rho^2) + \beta(3+\rho^2)] \quad \text{for} \quad \xi \leq 10^{-3};$$

Also,

$$\xi = \frac{\mu^2 v^2}{4m^2}\,\frac{(1-\rho^2)}{(1-v)}; \quad \beta = \frac{v^2}{2(1-v)};$$

$$L'_e = \ln \frac{A^* Z^{-1/3}\sqrt{(1+\xi)(1+Y_e)}}{1+\dfrac{2m\sqrt{e}A^* Z^{-1/3}(1+\xi)(1+Y_e)}{Ev(1-\rho^2)}}$$

$$-\frac{1}{2}\ln\left[1+\left(\frac{3mZ^{1/3}}{2\mu}\right)^2(1+\xi)(1+Y_e)\right];$$

$$L'_\mu = \ln \frac{(\mu/m)A^* Z^{-1/3}\sqrt{(1+1/\xi)(1+Y_\mu)}}{1+\dfrac{2m\sqrt{e}A^* Z^{-1/3}(1+\xi)(1+Y_\mu)}{Ev(1-\rho^2)}}$$

$$-\ln\left[\frac{3}{2}\,Z^{1/3}\sqrt{(1+1/\xi)(1+Y_\mu)}\right].$$

For faster computing, the expressions for $L'_{e,\mu}$ are further algebraically transformed. The functions $L'_{e,\mu}$ include the nuclear size correction [2] in comparison with parameterization [1] :

$$Y_e = \frac{5-\rho^2+4\,\beta\,(1+\rho^2)}{2(1+3\beta)\ln(3+1/\xi)-\rho^2-2\beta(2-\rho^2)};$$

$$Y_\mu = \frac{4+\rho^2+3\,\beta\,(1+\rho^2)}{(1+\rho^2)(\frac{3}{2}+2\beta)\ln(3+\xi)+1-\frac{3}{2}\,\rho^2};$$

$$\rho_{\max} = [1-6\mu^2/E^2(1-v)]\sqrt{1-4m/Ev}.$$

Comment on the Calculation of the Integral $\int d\rho$ in Eq. 13.11

The integral $\int\limits_0^{\rho_{\max}} G(Z,E,v,\rho)\;d\rho$ is computed with the substitutions:

$$\begin{aligned} t &= \ln(1-\rho), \\ 1-\rho &= \exp(t), \\ 1+\rho &= 2-\exp(t), \\ 1-\rho^2 &= e^t\,(2-e^t). \end{aligned}$$

After that,

$$\int_0^{\rho_{\max}} G(Z,E,v,\rho)\;d\rho = \int_{t_{\min}}^{0} G(Z,E,v,\rho)\,e^t\,dt, \qquad (13.12)$$

where

$$t_{\min} = \ln \frac{\dfrac{4m}{\epsilon} + \dfrac{12\mu^2}{EE'}\left(1 - \dfrac{4m}{\epsilon}\right)}{1 + \left(1 - \dfrac{6\mu^2}{EE'}\right)\sqrt{1 - \dfrac{4m}{\epsilon}}}.$$

To compute the integral of Eq. 13.12 with an accuracy better than 0.5%, Gaussian quadrature with $N = 8$ points is sufficient.

The function $\zeta(E, Z)$ in Eq. 13.11 serves to take into account the process on atomic electrons (inelastic atomic form factor contribution). To treat the energy loss balance correctly, the following approximation, which is an algebraic transformation of the expression in Ref. [3], is used:

$$\zeta(E, Z) = \frac{0.073 \ln \dfrac{E/\mu}{1 + \gamma_1 Z^{2/3} E/\mu} - 0.26}{0.058 \ln \dfrac{E/\mu}{1 + \gamma_2 Z^{1/3} E/\mu} - 0.14};$$

$$\zeta(E, Z) = 0 \quad \text{if the numerator is negative.}$$

For E $\leq 35\,\mu$, $\zeta(E, Z) = 0$. Also $\gamma_1 = 1.95 \cdot 10^{-5}$ and $\gamma_2 = 5.30 \cdot 10^{-5}$.

The above formulae make use of the Thomas-Fermi model which is not good enough for light elements. For hydrogen ($Z = 1$) the following parameters must be changed:
$A^* = 183 \;\Rightarrow\; 202.4$;
$\gamma_1 = 1.95 \cdot 10^{-5} \;\Rightarrow\; 4.4 \cdot 10^{-5}$;
$\gamma_2 = 5.30 \cdot 10^{-5} \;\Rightarrow\; 4.8 \cdot 10^{-5}$.

13.3.2 Total Cross Section and Restricted Energy Loss

If the user's cut for the energy transfer ϵ_{cut} is greater than $\epsilon_{\min}$, the process is represented by continuous restricted energy loss for interactions with $\epsilon \leq \epsilon_{\text{cut}}$, and discrete collisions with $\epsilon > \epsilon_{\text{cut}}$. Respective values of the total cross section and restricted energy loss rate are defined as:

$$\sigma_{\text{tot}} = \int_{\epsilon_{\text{cut}}}^{\epsilon_{\max}} \sigma(E, \epsilon)\, d\epsilon; \quad (dE/dx)_{\text{restr}} = \int_{\epsilon_{\min}}^{\epsilon_{\text{cut}}} \epsilon\, \sigma(E, \epsilon)\, d\epsilon.$$

For faster computing, $\ln \epsilon$ substitution and Gaussian quadratures are used.

13.3.3 Sampling of Positron - Electron Pair Production

The e^+e^- pair energy ϵ_P, is found numerically by solving the equation

$$P = \int_{\epsilon_P}^{\epsilon_{\max}} \sigma(Z, A, T, \epsilon) d\epsilon \quad / \int_{cut}^{\epsilon_{\max}} \sigma(Z, A, T, \epsilon) d\epsilon \tag{13.13}$$

or

$$1 - P = \int_{cut}^{\epsilon_P} \sigma(Z, A, T, \epsilon) d\epsilon \quad / \int_{cut}^{\epsilon_{\max}} \sigma(Z, A, T, \epsilon) d\epsilon \tag{13.14}$$

To reach high sampling speed, solutions of Eqs. 13.13, 13.14 are tabulated at initialization time. Two 3-dimensional tables (referred to here as A and B) of $\epsilon_P(P, T, Z)$ are created, and then interpolation is used to sample ϵ_P. The number and spacing of entries in the table are chosen as follows:

- a constant increment in $\ln T$ is chosen such that there are four points per decade in the range $T_{\min} - T_{\max}$. The default range of muon kinetic energies in Geant4 is $T = 1\,\text{GeV} - 1000\,\text{PeV}$.
- a constant increment in $\ln Z$ is chosen. The shape of the sampling distribution does depend on Z, but very weakly, so that eight points in the range $1 \leq Z \leq 128$ are sufficient. There is practically no dependence on the atomic weight A.
- for probabilities $P \leq 0.5$, Eq. 13.13 is used and Table A is computed with a constant increment in $\ln P$ in the range $10^{-7} \leq P \leq 0.5$. The number of points in $\ln P$ for Table A is about 100.
- for $P \geq 0.5$, Eq. 13.14 is used and Table B is computed with a constant increment in $\ln(1 - P)$ in the range $10^{-5} \leq (1 - P) \leq 0.5$. In this case 50 points are sufficient.

The values of $\ln(\epsilon_P - cut)$ are stored in both Table A and Table B.

To create the "probability tables" for each (T, Z) pair, the following procedure is used:

- a temporary table of ~ 2000 values of $\epsilon \cdot \sigma(Z, A, T, \epsilon)$ is constructed with a constant increment (~ 0.02) in $\ln \epsilon$ in the range $(cut, \epsilon_{\max})$. ϵ is taken in the middle of the corresponding bin in $\ln \epsilon$.
- the accumulated cross sections

$$\sigma_1 = \int_{\ln \epsilon}^{\ln \epsilon_{\max}} \epsilon \, \sigma(Z, A, T, \epsilon) \, d(\ln \epsilon)$$

and

$$\sigma_2 = \int_{\ln(cut)}^{\ln\epsilon} \epsilon\,\sigma(Z,A,T,\epsilon)\,d(\ln\epsilon)$$

are calculated by summing the temporary table over the values above $\ln\epsilon$ (for σ_1) and below $\ln\epsilon$ (for σ_2) and then normalizing to obtain the accumulated probability functions.

- finally, values of $\ln(\epsilon_P - cut)$ for corresponding values of $\ln P$ and $\ln(1-P)$ are calculated by linear interpolation of the above accumulated probabilities to form Tables A and B. The monotonic behavior of the accumulated cross sections is very useful in speeding up the interpolation procedure.

The random transferred energy corresponding to a probability P, is then found by linear interpolation in $\ln Z$ and $\ln T$, and a cubic interpolation in $\ln P$ for Table A or in $\ln(1-P)$ for Table B. For $P \leq 10^{-7}$ and $(1-P) \leq 10^{-5}$, linear extrapolation using the entries at the edges of the tables may be safely used. Electron pair energy is related to the auxiliary variable $x = \ln(\epsilon_P - cut)$ found by the trivial interpolation $\epsilon_P = e^x + cut$.

Similar to muon bremsstrahlung (section 13.2), this sampling algorithm does not re-initialize the tables for user cuts greater than cut_{min}. Instead, the probability variable is redefined as

$$P' = P\sigma_{\rm tot}(cut_{user})/\sigma_{\rm tot}(cut_{min}),$$

and P' is used for sampling.

In the simulation of the final state, the muon deflection angle (which is of the order of m/E) is neglected. The procedure for sampling the energy partition between e^+ and e^- and their emission angles is similar to that used for the $\gamma \to e^+\,e^-$ conversion.

13.3.4 Status of this document

12.10.98 created by R.Kokoulin and A.Rybin
18.05.00 edited by S.Kelner, R.Kokoulin, and A.Rybin
27.01.03 re-written by D.H. Wright

Bibliography

[1] R.P.Kokoulin and A.A.Petrukhin, Proc. 11th Intern. Conf. on Cosmic Rays, Budapest, 1969 [Acta Phys. Acad. Sci. Hung.,**29, Suppl.4**, p.277, 1970].

[2] R.P.Kokoulin and A.A.Petrukhin, Proc. 12th Int. Conf. on Cosmic Rays, Hobart, 1971, **vol.6**, p.2436.

[3] S.R.Kelner, Phys. Atomic Nuclei, **61** (1998) 448.

13.4 Muon Photonuclear Interaction

The inelastic interaction of muons with nuclei is important at high muon energies ($E \geq 10$ GeV), and at relatively high energy transfers ν ($\nu/E \geq 10^{-2}$). It is especially important for light materials and for the study of detector response to high energy muons, muon propagation and muon-induced hadronic background. The average energy loss for this process increases almost lineary with energy, and at TeV muon energies constitutes about 10% of the energy loss rate.

The main contribution to the cross section $\sigma(E,\nu)$ and energy loss comes from the low Q^2–region ($Q^2 \ll 1$ GeV^2). In this domain, many simplifications can be made in the theoretical consideration of the process in order to obtain convenient and simple formulae for the cross section. Most widely used are the expressions given by Borog and Petrukhin [1], and Bezrukov and Bugaev [2]. Results from these authors agree within 10% for the differential cross section and within about 5% for the average energy loss, provided the same photonuclear cross section, $\sigma_{\gamma N}$, is used in the calculations.

13.4.1 Differential Cross Section

The Borog and Petrukhin formula for the cross section is based on:

- Hand's formalism [3] for inelastic muon scattering,
- a semi-phenomenological inelastic form factor, which is a Vector Dominance Model with parameters estimated from experimental data, and
- nuclear shadowing effects with a reasonable theoretical parameterization [4].

For $E \geq 10$ GeV, the Borog and Petrukhin cross section (cm^2/g GeV), differential in transferred energy, is

$$\sigma(E,\nu) = \Psi(\nu)\Phi(E,v), \tag{13.15}$$

$$\Psi(\nu) = \frac{\alpha}{\pi}\frac{A_{\text{eff}}N_{AV}}{A}\sigma_{\gamma N}(\nu)\frac{1}{\nu}, \tag{13.16}$$

$$\Phi(E,v) = v - 1 + \left[1 - v + \frac{v^2}{2}\left(1 + \frac{2\mu^2}{\Lambda^2}\right)\right]\ln\frac{\dfrac{E^2(1-v)}{\mu^2}\left(1 + \dfrac{\mu^2 v^2}{\Lambda^2(1-v)}\right)}{1 + \dfrac{Ev}{\Lambda}\left(1 + \dfrac{\Lambda}{2M} + \dfrac{Ev}{\Lambda}\right)}, \tag{13.17}$$

where ν is the energy lost by the muon, $v = \nu/\mathrm{E}$, and μ and M are the muon and nucleon (proton) masses, respectively. Λ is a Vector Dominance Model parameter in the inelastic form factor which is estimated to be $\Lambda^2 = 0.4\ \mathrm{GeV}^2$.

For A_{eff}, which includes the effect of nuclear shadowing, the parameterization [4]

$$A_{\mathrm{eff}} = 0.22A + 0.78A^{0.89} \tag{13.18}$$

is chosen.

A reasonable choice for the photonuclear cross section, $\sigma_{\gamma N}$, is the parameterization obtained by Caldwell et al. [5] based on the experimental data on photoproduction by real photons:

$$\sigma_{\gamma N} = (49.2 + 11.1 \ln K + 151.8/\sqrt{K}) \cdot 10^{-30}\mathrm{cm}^2 \quad K \text{ in GeV}. \tag{13.19}$$

The upper limit of the transferred energy is taken to be $\nu_{\max} = E - M/2$. The choice of the lower limit $\nu_{\min}$ is less certain since the formula 13.15, 13.16, 13.17 is not valid in this domain. Fortunately, $\nu_{\min}$ influences the total cross section only logarithmically and has no practical effect on the average energy loss for high energy muons. Hence, a reasonable choice for $\nu_{\min}$ is 0.2 GeV.

In Eq. 13.16, A_{eff} and $\sigma_{\gamma N}$ appear as factors. A more rigorous theoretical approach may lead to some dependence of the shadowing effect on ν and E; therefore in the differential cross section and in the sampling procedure, this possibility is forseen and the atomic weight A of the element is kept as an explicit parameter.

The total cross section is obtained by integration of Eq. 13.15 between $\nu_{\min}$ and $\nu_{\max}$; to facilitate the computation, a $\ln(\nu)$–substitution is used.

13.4.2 Sampling

Sampling the Transferred Energy

The muon photonuclear interaction is always treated as a discrete process with its mean free path determined by the total cross section. The total cross section is obtained by the numerical integration of Eq. 13.15 within the limits $\nu_{\min}$ and $\nu_{\max}$. The process is considered for muon energies $1\mathrm{GeV} \leq \mathrm{T} \leq 1000\mathrm{PeV}$, though it should be noted that above 100 TeV the extrapolation (Eq. 13.19) of $\sigma_{\gamma N}$ may be too crude.

The random transferred energy, ν_p, is found from the numerical solution of the equation :

$$P = \int_{\nu_p}^{\nu_{\max}} \sigma(E,\nu)d\nu \Big/ \int_{\nu_{\min}}^{\nu_{\max}} \sigma(E,\nu)d\nu \ . \tag{13.20}$$

Here P is the random uniform probability, with $\nu_{\max} = E - M/2$ and $\nu_{\min} = 0.2$ GeV.

For fast sampling, the solution of Eq. 13.20 is tabulated at initialization time. During simulation, the sampling method returns a value of ν_p corresponding to the probability P, by interpolating the table. The tabulation routine uses Eq. 13.15 for the differential cross section. The table contains values of

$$x_p = \ln(\nu_p/\nu_{\max})/\ln(\nu_{\max}/\nu_{\min}), \tag{13.21}$$

calculated at each point on a three-dimensional grid with constant spacings in $\ln(T)$, $\ln(A)$ and $\ln(P)$. The sampling uses linear interpolations in $\ln(T)$ and $\ln(A)$, and a cubic interpolation in $\ln(P)$. Then the transferred energy is calculated from the inverse transformation of Eq. 13.21, $\nu_p = \nu_{\max}(\nu_{\max}/\nu_{\min})^{x_p}$. Tabulated parameters reproduce the theoretical dependence to better than 2% for $T > 1$ GeV and better than 1% for $T > 10$ GeV.

Sampling the Muon Scattering Angle

According to Refs. [1, 6], in the region where the four-momentum transfer is not very large ($Q^2 \leq 3\text{GeV}^2$), the t – dependence of the cross section may be described as:

$$\frac{d\sigma}{dt} \sim \frac{(1 - t/t_{\max})}{t(1 + t/\nu^2)(1 + t/m_0^2)}[(1 - y)(1 - t_{\min}/t) + y^2/2], \tag{13.22}$$

where t is the square of the four-momentum transfer, $Q^2 = 2(EE' - PP'\cos\theta - \mu^2)$. Also, $t_{\min} = (\mu y)^2/(1 - y)$, $y = \nu/E$ and $t_{\max} = 2M\nu$. $\nu = E - E'$ is the energy lost by the muon and E is the total initial muon energy. M is the nucleon (proton) mass and $m_0^2 \equiv \Lambda^2 \simeq 0.4$ GeV^2 is a phenomenological parameter determing the behavior of the inelastic form factor. Factors which depend weakly, or not at all, on t are omitted.

To simulate random t and hence the random muon deflection angle, it is convenient to represent Eq. 13.22 in the form :

$$\sigma(t) \sim f(t)g(t), \tag{13.23}$$

where

$$f(t) = \frac{1}{t(1+t/t_1)}, \tag{13.24}$$

$$g(t) = \frac{1-t/t_{\max}}{1+t/t_2} \cdot \frac{(1-y)(1-t_{\min}/t)+y^2/2}{(1-y)+y^2/2},$$

and

$$t_1 = \min(\nu^2, m_0^2) \quad t_2 = \max(\nu^2, m_0^2). \tag{13.25}$$

t_P is found analytically from Eq. 13.24 :

$$t_P = \frac{t_{\max} t_1}{(t_{\max}+t_1)\left[\frac{t_{\max}(t_{\min}+t_1)}{t_{\min}(t_{\max}+t_1)}\right]^P - t_{\max}},$$

where P is a random uniform number between 0 and 1, which is accepted with probability $g(t)$. The conditions of Eq. 13.25 make use of the symmetry between ν^2 and m_0^2 in Eq. 13.22 and allow increased selection efficiency, which is typically ≥ 0.7. The polar muon deflection angle θ can easily be found from [1]

$$\sin^2(\theta/2) = \frac{t_P - t_{\min}}{4\,(EE' - \mu^2) - 2\,t_{\min}}.$$

The hadronic vertex is generated by the hadronic processes taking into account the four-momentum transfer.

13.4.3 Status of this document

12.10.98 created by R.Kokoulin, A.Rybin.
18.05.00 edited by S.Kelner, R.Kokoulin, and A.Rybin.
07.12.02 re-worded by D.H. Wright
30.08.04 correction of eq. 8.24 (to 1/sqrt) from H. Araujo

Bibliography

[1] V.V.Borog and A.A.Petrukhin, Proc. 14th Int.Conf. on Cosmic Rays, Munich,1975, **vol.6**, p.1949.

[2] L.B.Bezrukov and E.V.Bugaev, Sov. J. Nucl. Phys., **33**, 1981, p.635.

[1] This convenient formula has been shown to the authors by D.A. Timashkov.

[3] L.N.Hand. Phys. Rev., **129**, 1834 (1963).

[4] S.J.Brodsky, F.E.Close and J.F.Gunion, Phys. Rev. **D6**, 177 (1972).

[5] D.O. Caldwell et al., Phys. Rev. Lett., **42**, 553 (1979).

[6] V.V.Borog, V.G.Kirillov-Ugryumov, A.A.Petrukhin, Sov. J. Nucl. Phys., **25**, 1977, p.46.

Chapter 14

Atomic Relaxation

14.1 Atomic relaxation

Atomic relaxation processes can be induced by any ionisation process that leaves the interested atom in an excited state (i.e. with a vacancy in its electronic structure). Processes inducing atomic relaxation in Geant4 are photoelectric effect, Compton and ionization (both Standard and Lowenergy).

Geant4 uses the Livermore Evaluation Atomic Data Library EADL [1], that contains data to describe the relaxation of atoms back to neutrality after they are ionised.

It is assumed that the binding energy of all subshells (from now on shells are the same for neutral ground state atoms as for ionised atoms [1]).

Data in EADL includes the radiative and non-radiative transition probabilities for each sub-shell of each element, for Z=1 to 100. The atom has been ionised by a process that has caused an electron to be ejected from an atom, leaving a vacancy or "hole" in a given subshell. The EADL data are then used to calculate the complete radiative and non-radiative spectrum of X-rays and electrons emitted as the atom relaxes back to neutrality.

Non-radiative de-excitation can occur via the Auger effect (the initial and secondary vacancies are in different shells) or Coster-Kronig effect (transitions within the same shell).

14.1.1 Fluorescence

The simulation procedure for the fluorescence process is the following:

1. If the vacancy shell is not included in the data, energy equal to the binding energy of the shell is deposited locally

2. If the vacancy subshell is included in the data, an outer subshell is randomly selected taking into account the relative transition probabilities for all possible outer subshells.

3. In the case where the energy corresponding to the selected transition is larger than a user defined cut value (equal to zero by default), a photon particle is created and emitted in a random direction in 4π, with an energy equal to the transition energy, provided by EADL.

4. the procedure is repeated from step 1, for the new vacancy subshell.

The final local energy deposit is the difference between the binding energy of the initial vacancy subshell and the sum of all transition energies which

were taken by fluorescence photons. The atom is assumed to be initially ionised with an electric charge of $+1e$.

Sub-shell data are provided in the EADL data bank [1] for Z=1 through 100. However, transition probabilities are only explicitly included for Z=6 through 100, from the subshells of the K, L, M, N shells and some O subshells. For subshells O,P,Q: transition probabilities are negligible (of the order of 0.1%) and smaller than the precision with which they are known. Therefore, for the time being, for Z=1 through 5, only a local energy deposit corresponding to the binding energy B of an electron in the ionised subshell is simulated. For subshells of the O, P, and Q shells, a photon is emitted with that energy B.

14.1.2 Auger process

The Auger effect is complimentary to fluorescence, hence the simulation process is the same as for the fluorescence, with the exception that two random shells are selected, one for the transition electron that fills the original vacancy, and the other for selecting the shell generating the Auger electron.

Subshell data are provided in the EADL data bank [1] for $Z = 6$ through 100. Since in EADL no data for elements with $Z < 5$ are provided, Auger effects are only considered for $5 < Z < 100$ and always due to the EADL data tables, only for those transitions which have a probabiliy to occur $> 0.1\%$ of the total non-radiative transition probability. EADL probability data used are, however, normalized to one for Fluorescence + Auger.

14.1.3 PIXE

PIXE (Particle Induced X-Ray Emission) can be simulated for ionisation continuous processes perfomed by ions. Ionised shells are selected randomly according the ionisation cross section of each shell once known the (continuous) energy loss along the step 7.1.

Different shell ionisation cross sections models are available in different energy ranges:

- ECPSSR[2],[3] internal Geant4 calculation for K and L shells.
- ECPSSR calculations from Factor Form according to Reis[4] for K and L shells from 0.1 to 100 MeV and for M shells from 0.1 to 10 MeV.
- empirical "reference" K-shell values from Paul for protons[5] and for for alphas[6]. Energies ranges are 0.1 - 10 MeV/amu circa, depending on the atomic number that varies between 4 and 32.

- empirical Li-shell values from Orlic[7]. Energy Range 0.1-10 MeV for Z between 41 and 92.

Otside Z and energy of limited shell ionisation cross sections, the ECPSSR internal calculation method is applied.

Please refer to ref.[8] and original papers to have detailed information of every model.

14.1.4 Status of the document

08.02.2000 created by Véronique Lefébure
08.03.2000 reviewed by Petteri Nieminen and Maria Grazia Pia
05.06.2002 added Auger Effect description by Alfonso Mantero
27.11.2002 slight review and added PIXE section by Alfonso Mantero
12.11.2012 energy ranges and shell updates by Alfonso Mantero

Bibliography

[1] "Tables and Graphs of Atomic Subshell and Relaxation Data Derived from the LLNL Evaluated Atomic Data Library (EADL), Z=1-100" S.T.Perkins, D.E.Cullen, M.H.Chen, J.H.Hubbell, J.Rathkopf, J.Scofield, UCRL-50400 Vol.30

[2] W.Brandt and G.Lapicki, Phys.Rev.A23(1981)

[3] W. Brandt and G. Lapicki, Phys.Rev.A20 N2 (1979)

[4] A. Taborda et al., X-Ray Spec. 40 (2011) 127-134

[5] H. Paul, J.Sacher, Atom.Dat. and Nucl. Dat. Tabl. Volume 42, Issue 1, May 1989, Pages 105-156

[6] H. Paul, O. Bolik, Atom. Dat. and Nucl. Dat. Tabl. Volume 54, Issue 1, May 1993, Pages 75-131

[7] I. Orlic et al., International Journal of PIXE.Vol.4(1994) 217-230

[8] A. Mantero et al., X-Ray Spec. 40 (2011) 135-140

Chapter 15

Geant4-DNA

15.1 Geant4-DNA processes and models

The Geant4-DNA processes and models (theoretical, semi-empirical) are adapted for track structure simulations in liquid water down to the eV scale. They are described on a dedicated web site: http://geant4-dna.org, which includes a full list of publications.

Any report or published results obtained using the Geant4-DNA software shall cite the following publication : Comparison of Geant4 very low energy cross section models with experimental data in water, S. Incerti et al., Med. Phys. 37 (2010) 4692-4708

15.1.1 Status of the document

12.11.2012 created by Sebastien Incerti

Chapter 16

Microelectronics

16.1 The MicroElec[1] extension for microelectronics applications

The Geant4-MicroElec extension [1], developed by CEA, aims at modeling the effect of ionizing radiation in highly integrated microelectronic components. It describes the transport and generation of very low energy electrons by incident electrons, protons and heavy ions in silicon.

All Geant4-MicroElec physics processes and models simulate step-by-step interactions of particles in silicon down to the eV scale; they are pure discrete processes. Table 16.1 summarizes the list of physical interactions per particle type that can be modeled using the Geant4-MicroElec extension, along with the corresponding process classes, model classes, low energy limit applicability of models, high energy applicability of models and energy threshold below which the incident particle is killed (stopped and the kinetic energy is locally deposited). All models are interpolated. For now, they are valid for silicon only (use the **G4_Si** Geant4-NIST material).

Particle	**Interaction**	**Process, Model, Range**	**Kill**
Electron	Elastic scattering	`G4MicroElastic` `G4MicroElecElasticModel`	16.7 eV (*)
		$5\text{ eV} < E < 100\text{ MeV}$	
Electron	Ionisation	`G4MicroElecInelastic` `G4MicroElecInelasticModel`	—
		$16.7\text{ eV} < E < 100\text{ MeV}$	
Protons, ions	Ionisation	`G4MicroElecInelastic` `G4MicroElecInelasticModel`	—
		$50\text{ keV}/u < E < 23\text{ MeV/u}$	

(*) because of the low energy limit applicability of the inelastic model.

Table 16.1: List of G4MicroElec physical interactions

All details regarding the physics and formula used for these processes and models and available in [2] for incident electrons and in [3] for incident protons and heavy ions.

[1]Previously called MuElec.

16.1.1 Status of the document

12.11.2012 created by Melanie Raine

Bibliography

[1] Geant4-MicroElec online available at: https://twiki.cern.ch/twiki/bin/-view/Geant4LoweMuElec

[2] A. Valentin, M. Raine, J.-E. Sauvestre, M. Gaillardin and P. Paillet, "Geant4 physics processes for microdosimetry simulation: very low energy electromagnetic models for electrons in silicon", Nuclear Instruments and Methods in Physics Research B, vol. 288, pp. 66 - 73, 2012.

[3] A. Valentin, M. Raine, M. Gaillardin and P. Paillet, "Geant4 physics processes for microdosimetry simulation: very low energy electromagnetic models for protons and heavy ions in silicon", Nuclear Instruments and Methods in Physics Research B, vol. 287, pp. 124 - 129, 2012.

Chapter 17

Polarized Electron/Positron/Gamma Incident

17.1 Introduction

With the EM polarization extension it is possible to track polarized particles (leptons and photons). Special emphasis will be put in the proper treatment of polarized matter and its interaction with longitudinal polarized electrons/positrons or circularly polarized photons, which is for instance essential for the simulation of positron polarimetry. The implementation is base on Stokes vectors [1]. Further details can be found in [2].

In its current state, the following polarization dependent processes are considered

- Bhabha/Møller scattering,
- Positron Annihilation,
- Compton scattering,
- Pair creation,
- Bremsstrahlung.

Several simulation packages for the realistic description of the development of electromagnetic showers in matter have been developed. A prominent example of such codes is EGS (Electron Gamma Shower)[3]. For this simulation framework extensions with the treatment of polarized particles exist [4, 5, 6]; the most complete has been developed by K. Flöttmann [4]. It is based on the matrix formalism [1], which enables a very general treatment of polarization. However, the Flöttmann extension concentrates on evaluation of polarization transfer, i.e. the effects of polarization induced asymmetries are neglected, and interactions with polarized media are not considered.

Another important simulation tool for detector studies is GEANT3 [7]. Here also some effort has been made to include polarization [8, 9], but these extensions are not publicly available.

In general the implementation of polarization in this EM polarization library follows very closely the approach by K. Flöttmann [4]. The basic principle is to associate a *Stokes vector* to each particle and track the mean polarization from one interaction to another. The basics for this approach is the matrix formalism as introduced in [1].

17.1.1 Stokes vector

The *Stokes vector* [10, 1] is a rather simple object (in comparison to e.g. the spin density matrix), three real numbers are sufficient for the characterization

of the polarization state of any single electron, positron or photon. Using *Stokes vectors* **all** possible polarization states can be described, i.e. circular and linear polarized photons can be handled with the same formalism as longitudinal and transverse polarized electron/positrons.

The *Stokes vector* can be used also for beams, in the sense that it defines a mean polarization.

In the EM polarization library the Stokes vector is defined as follows:

	Photons	Electrons
ξ_1	linear polarization	polarization in x direction
ξ_2	linear polarization but $\pi/4$ to right	polarization in y direction
ξ_3	circular polarization	polarization in z direction

This definition is assumed in the *particle reference frame*, i.e. with the momentum of the particle pointing to the z direction, cf. also next section about coordinate transformations. Correspondingly a 100% longitudinally polarized electron or positron is characterized by

$$\boldsymbol{\xi} = \begin{pmatrix} 0 \\ 0 \\ \pm 1 \end{pmatrix}, \tag{17.1}$$

where ± 1 corresponds to spin parallel (anti parallel) to particle's momentum. Note that this definition is similar, but not identical to the definition used in McMaster [1].

Many scattering cross sections of polarized processes using Stokes vectors for the characterization of initial and final states are available in [1]. In general a differential cross section has the form

$$\frac{d\sigma(\boldsymbol{\zeta}^{(1)}, \boldsymbol{\zeta}^{(2)}, \boldsymbol{\xi}^{(1)}, \boldsymbol{\xi}^{(2)})}{d\Omega}\,, \tag{17.2}$$

i.e. it is a function of the polarization states of the initial particles $\boldsymbol{\zeta}^{(1)}$ and $\boldsymbol{\zeta}^{(2)}$, as well as of the polarization states of the final state particles $\boldsymbol{\xi}^{(1)}$ and $\boldsymbol{\xi}^{(2)}$ (in addition to the kinematic variables E, θ, and ϕ).

Consequently, in a simulation we have to account for

- Asymmetries:

  Polarization of beam ($\boldsymbol{\zeta}^{(1)}$) and target ($\boldsymbol{\zeta}^{(2)}$) can induce azimuthal and polar asymmetries, and may also influence on the total cross section (`Geant4: GetMeanFreePath()`).

- Polarization transfer / depolarization effects

  The dependence on the final state polarizations defines a possible transfer from initial polarization to final state particles.

17.1.2 Transfer matrix

Using the formalism of McMaster, differential cross section and polarization transfer from the initial state ($\boldsymbol{\zeta}^{(1)}$) to one final state particle ($\boldsymbol{\xi}^{(1)}$) are combined in an interaction matrix T:

$$\begin{pmatrix} O \\ \boldsymbol{\xi}^{(1)} \end{pmatrix} = T \begin{pmatrix} I \\ \boldsymbol{\zeta}^{(1)} \end{pmatrix} , \tag{17.3}$$

where I and O are the incoming and outgoing currents, respectively. In general the 4×4 matrix T depends on the target polarization $\boldsymbol{\zeta}^{(2)}$ (and of course on the kinematic variables E, θ, ϕ). Similarly one can define a matrix defining the polarization transfer to second final state particle like

$$\begin{pmatrix} O \\ \boldsymbol{\xi}^{(2)} \end{pmatrix} = T' \begin{pmatrix} I \\ \boldsymbol{\zeta}^{(1)} \end{pmatrix} . \tag{17.4}$$

In this framework the transfer matrix T is of the form

$$T = \begin{pmatrix} S & A_1 & A_2 & A_3 \\ P_1 & M_{11} & M_{21} & M_{31} \\ P_2 & M_{12} & M_{22} & M_{32} \\ P_3 & M_{13} & M_{23} & M_{33} \end{pmatrix} . \tag{17.5}$$

The matrix elements T_{ij} can be identified as (unpolarized) differential cross section (S), polarized differential cross section (A_j), polarization transfer (M_{ij}), and (de)polarization (P_i). In the Flöttmann extension the elements A_j and P_i have been neglected, thus concentrating on polarization transfer only. Using the full matrix takes now all polarization effects into account.

The transformation matrix, i.e. the dependence of the mean polarization of final state particles, can be derived from the asymmetry of the differential cross section w.r.t. this particular polarization. Where the asymmetry is defined as usual by

$$A = \frac{\sigma(+1) - \sigma(-1)}{\sigma(+1) + \sigma(-1)} . \tag{17.6}$$

The mean final state polarizations can be determined coefficient by coefficient.

In general, the differential cross section is a linear function of the polarizations, i.e.

$$\begin{aligned}\frac{d\sigma(\boldsymbol{\zeta}^{(1)},\boldsymbol{\zeta}^{(2)},\boldsymbol{\xi}^{(1)},\boldsymbol{\xi}^{(2)})}{d\Omega} &= \Phi_{(\zeta^{(1)},\zeta^{(2)})} + \boldsymbol{A}_{(\zeta^{(1)},\zeta^{(2)})}\cdot\boldsymbol{\xi}^{(1)} + \boldsymbol{B}_{(\zeta^{(1)},\zeta^{(2)})}\cdot\boldsymbol{\xi}^{(2)} \\ &\quad + \boldsymbol{\xi}^{(1)^T} M_{(\zeta^{(1)},\zeta^{(2)})}\,\boldsymbol{\xi}^{(2)} \qquad (17.7)\end{aligned}$$

In this form, the mean polarization of the final state can be read off easily, and one obtains

$$\langle\boldsymbol{\xi}^{(1)}\rangle = \frac{1}{\Phi_{(\zeta^{(1)},\zeta^{(2)})}}\boldsymbol{A}_{(\zeta^{(1)},\zeta^{(2)})} \text{ and} \qquad (17.8)$$

$$\langle\boldsymbol{\xi}^{(2)}\rangle = \frac{1}{\Phi_{(\zeta^{(1)},\zeta^{(2)})}}\boldsymbol{B}_{(\zeta^{(1)},\zeta^{(2)})}\,. \qquad (17.9)$$

Note, that the *mean* polarization states do not depend on the correlation matrix $M_{(\zeta^{(1)},\zeta^{(2)})}$. In order to account for correlation one has to generate *single* particle Stokes vector explicitly, i.e. on an event by event basis. However, this implementation generates *mean* polarization states, and neglects correlation effects.

17.1.3 Coordinate transformations

Three different coordinate systems are used in the evaluation of polarization states:

- **World frame**

  The geometry of the target, and the momenta of all particles in Geant4 are noted in the world frame X, Y, Z (the *global reference frame*, GRF). It is the basis of the calculation of any other coordinate system.

- **Particle frame**

  Each particle is carrying its own coordinate system. In this system the direction of motion coincides with the z-direction. Geant4 provides a transformation from any particle frame to the World frame by the method `G4ThreeMomemtum::rotateUz()`. Thus, the y-axis of the *particle reference frame* (PRF) lies in the X-Y-plane of the world frame.

  The Stokes vector of any moving particle is defined w.r.t. the corresponding particle frame. Particles at rest (e.g. electrons of a media) use the world frame as particle frame.

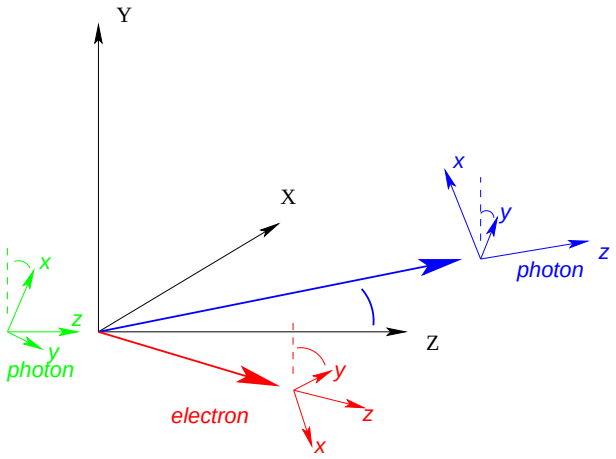

Figure 17.1: The *interaction frame* and the *particle frames* for the example of Compton scattering. The momenta of all participating particle lie in the x-z-plane, the scattering plane. The incoming photon gives the z direction. The outgoing photon is defined as *particle 1* and gives the x-direction, perpendicular to the z-axis. The y-axis is then perpendicular to the scattering plane and completes the definition of a right handed coordinate system called *interaction frame*. The *particle frame* is defined by the Geant4 routine `G4ThreeMomemtum::rotateUz()`.

- **Interaction frame**

  For the evaluation of the polarization transfer another coordinate system is used, defined by the scattering plane, cf. fig. 17.1. There the z-axis is defined by the direction of motion of the incoming particle. The scattering plane is spanned by the z-axis and the x-axis, in a way, that the direction of *particle 1* has a positive x component. The definition of *particle 1* depends on the process, for instance in Compton scattering, the outgoing photon is referred as *particle 1*[1].

All frames are right handed.

17.1.4 Polarized beam and material

Polarization of beam particles is well established. It can be used for simulating low-energy Compton scattering of linear polarized photons. The interpretation as Stokes vector allows now the usage in a more general framework. The polarization state of a (initial) beam particle can be fixed using standard

[1]Note, for an incoming particle travelling on the Z-axis (of GRF), the y-axis of the PRF of both outgoing particles is parallel to the y-axis of the *interaction frame*.

the ParticleGunMessenger class. For example, the class `G4ParticleGun` provides the method `SetParticlePolarization()`, which is usually accessable via

```
/gun/polarization <Sx> <Sy> <Sz>
```

in a macro file.

In addition for the simulation of polarized media, a possibility to assign Stokes vectors to physical volumes is provided by a new class, the so-called *G4PolarizationManager*. The procedure to assign a polarization vector to a media, is done during the *detector construction*. There the *logical volumes* with certain polarization are made known to *polarization manager*. One example `DetectorConstruction` might look like follows:

```
G4double Targetthickness = .010*mm;
G4double Targetradius    = 2.5*mm;

G4Tubs *solidTarget =
  new G4Tubs("solidTarget",
             0.0,
             Targetradius,
             Targetthickness/2,
             0.0*deg,
             360.0*deg );

G4LogicalVolume * logicalTarget =
  new G4LogicalVolume(solidTarget,
                      iron,
                      "logicalTarget",
                      0,0,0);

G4VPhysicalVolume *  physicalTarget =
  new G4PVPlacement(0,G4ThreeVector(0.*mm, 0.*mm, 0.*mm),
                    logicalTarget,
                    "physicalTarget",
                    worldLogical,
                    false,
                    0);

G4PolarizationManager * polMgr = G4PolarizationManager::GetInstance();
polMgr->SetVolumePolarization(logicalTarget,G4ThreeVector(0.,0.,0.08));
```

Once a logical volume is known to the `G4PolarizationManager`, its polarization vector can be accessed from a macro file by its name, e.g. the polarization of the logical volume called "logicalTarget" can be changed via

```
/polarization/volume/set logicalTarget 0. 0. -0.08
```

Note, the polarization of a material is stated in the world frame.

17.1.5 Status of this document

20.11.06 created by A.Schälicke

Bibliography

[1] W. H. McMaster, Rev. Mod. Phys. **33** (1961) 8; and references therein.

[2] K. Laihem, PhD thesis, Measurement of the positron polarization at an helical undulator based positron source for the International Linear Collider ILC, Humboldt University Berlin, Germany, (2008).

[3] W. R. Nelson, H. Hirayama, D. W. O. Rogers, SLAC-R-0265.

[4] K. Flöttmann, PhD thesis, DESY Hamburg (1993); DESY-93-161.

[5] Y. Namito, S. Ban, H. Hirayama, Nucl. Instrum. Meth. A **332** (1993) 277.

[6] J. C. Liu, T. Kotseroglou, W. R. Nelson, D. C. Schultz, SLAC-PUB-8477.

[7] R. Brun, M. Caillat, M. Maire, G. N. Patrick, L. Urban, CERN-DD/85/1.

[8] G. Alexander *et al.*, SLAC-TN-04-018, SLAC-PROPOSAL-E-166.

[9] J. Hoogduin, PhD thesis, Rijksuniversiteit Groningen (1997).

[10] G. Stokes, Trans. Cambridge Phil. Soc. **9** (1852) 399.

17.2 Ionization

17.2.1 Method

The class *G4ePolarizedIonization* provides continuous and discrete energy losses of polarized electrons and positrons in a material. It evaluates polarization transfer and – if the material is polarized – asymmetries in the explicit delta rays production. The implementation baseline follows the approach derived for the class *G4eIonization* described in sections 7.1 and 8.1. For continuous energy losses the effects of a polarized beam or target are negligible provided the separation cut $T_{\rm cut}$ is small, and are therefore not considered separately. On the other hand, in the explicit production of delta rays by Møller or Bhabha scattering, the effects of polarization on total cross section and mean free path, on distribution of final state particles and the average polarization of final state particles are taken into account.

17.2.2 Total cross section and mean free path

Kinematics of Bhabha and Møller scattering is fixed by initial energy

$$\gamma = \frac{E_{k_1}}{mc^2} \tag{17.10}$$

and variable

$$\epsilon = \frac{E_{p_2} - mc^2}{E_{k_1} - mc^2}, \tag{17.11}$$

which is the part of kinetic energy of initial particle carried out by scatter. Lower kinematic limit for ϵ is 0, but in order to avoid divergencies in both total and differential cross sections one sets

$$\epsilon_{min} = x = \frac{T_{min}}{E_{k_1} - mc^2}, \tag{17.12}$$

where T_{min} has meaning of minimal kinetic energy of secondary electron. And, $\epsilon_{\rm max} = 1(1/2)$ for Bhabha(Møller) scatterings.

Total Møller cross section

The total cross section of the polarized Møller scattering can be expressed as follows

$$\sigma^M_{pol} = \frac{2\pi\gamma^2 r_e^2}{(\gamma-1)^2(\gamma+1)} \left[\sigma^M_0 + \zeta^{(1)}_3\zeta^{(2)}_3\sigma^M_L + \left(\zeta^{(1)}_1\zeta^{(2)}_1 + \zeta^{(1)}_2\zeta^{(2)}_2\right)\sigma^M_T\right], \tag{17.13}$$

where the r_e is classical electron radius, and

$$\begin{aligned}
\sigma_0^M &= -\frac{1}{1-x} + \frac{1}{x} - \frac{(\gamma-1)^2}{\gamma^2}\left(\frac{1}{2} - x\right) + \frac{2-4\,\gamma}{2\,\gamma^2}\,\ln\left(\frac{1-x}{x}\right) \\
\sigma_L^M &= \frac{(-3+2\,\gamma+\gamma^2)\,(1-2\,x)}{2\,\gamma^2} + \frac{2\,\gamma\,(-1+2\,\gamma)}{2\,\gamma^2}\,\ln\left(\frac{1-x}{x}\right) \\
\sigma_T^M &= \frac{2\,(\gamma-1)\,(2\,x-1)}{2\,\gamma^2} + \frac{(1-3\,\gamma)}{2\,\gamma^2}\,\ln\left(\frac{1-x}{x}\right)
\end{aligned} \tag{17.14}$$

Total Bhabha cross section

The total cross section of the polarized Bhabha scattering can be expressed as follows

$$\sigma_{pol}^B = \frac{2\pi r_e^2}{\gamma-1}\left[\sigma_0^B + \zeta_3^{(1)}\zeta_3^{(2)}\sigma_L^B + \left(\zeta_1^{(1)}\zeta_1^{(2)} + \zeta_2^{(1)}\zeta_2^{(2)}\right)\sigma_T^B\right], \tag{17.15}$$

where

$$\begin{aligned}
\sigma_0^B &= \frac{1-x}{2\,(\gamma-1)\,x} + \frac{2\,(-1+3\,x-6\,x^2+4\,x^3)}{3\,(1+\gamma)^3} \\
&+ \frac{-1-5\,x+12\,x^2-10\,x^3+4\,x^4}{2\,(1+\gamma)\,x} + \frac{-3-x+8\,x^2-4\,x^3-\ln(x)}{(1+\gamma)^2} \\
&+ \frac{3+4\,x-9\,x^2+3\,x^3-x^4+6\,x\,\ln(x)}{3\,x} \\
\sigma_L^B &= \frac{2\,(1-3\,x+6\,x^2-4\,x^3)}{3\,(1+\gamma)^3} + \frac{-14+15\,x-3\,x^2+2\,x^3-9\,\ln(x)}{3\,(1+\gamma)} \\
&+ \frac{5+3\,x-12\,x^2+4\,x^3+3\,\ln(x)}{3\,(1+\gamma)^2} + \frac{7-9\,x+3\,x^2-x^3+6\,\ln(x)}{3} \\
\sigma_T^B &= \frac{2\,(-1+3\,x-6\,x^2+4\,x^3)}{3\,(1+\gamma)^3} + \frac{-7-3\,x+18\,x^2-8\,x^3-3\,\ln(x)}{3\,(1+\gamma)^2} \\
&+ \frac{5+3\,x-12\,x^2+4\,x^3+9\,\ln(x)}{6\,(1+\gamma)}
\end{aligned} \tag{17.16}$$

Mean free path

With the help of the total polarized Møller cross section one can define a longitudinal asymmetry A_L^M and the transverse asymmetry A_T^M, by

$$A_L^M = \frac{\sigma_L^M}{\sigma_0^M} \qquad \text{and} \qquad A_T^M = \frac{\sigma_T^M}{\sigma_0^M}\,.$$

Similarly, using the polarized Bhabha cross section one can introduce a longitudinal asymmetry A_L^B and the transverse asymmetry A_T^B via

$$A_L^B = \frac{\sigma_L^B}{\sigma_0^B} \qquad \text{and} \qquad A_T^B = \frac{\sigma_T^B}{\sigma_0^B} \ .$$

These asymmetries are depicted in figures 17.2 and 17.3 respectively.

If both beam and target are polarized the mean free path as defined in section 8.1 has to be modified. In the class *G4ePolarizedIonization* the polarized mean free path $\lambda^{\rm pol}$ is derived from the unpolarized mean free path $\lambda^{\rm unpol}$ via

$$\lambda^{\rm pol} = \frac{\lambda^{\rm unpol}}{1 + \zeta_3^{(1)}\zeta_3^{(2)}\, A_L + \left(\zeta_1^{(1)}\zeta_1^{(2)} + \zeta_2^{(1)}\zeta_2^{(2)}\right) A_T} \tag{17.17}$$

17.2.3 Sampling the final state

Differential cross section

The polarized differential cross section is rather complicated, the full result can be found in [1, 2, 3]. In *G4PolarizedMollerCrossSection* the complete result is available taking all mass effects into account, only binding effects are neglected. Here we state only the ultra-relativistic approximation (URA), to show the general dependencies.

$$\begin{aligned}
&\frac{d\sigma_{URA}^M}{d\epsilon d\varphi} = \frac{{r_\epsilon}^2}{\gamma+1} \times \\
&\left[\frac{\left(1-\epsilon+\epsilon^2\right)^2}{4\left(\epsilon-1\right)^2\epsilon^2} + \zeta_3^{(1)}\zeta_3^{(2)}\frac{2-\epsilon+\epsilon^2}{-4\,\epsilon(1-\epsilon)} + \left(\zeta_2^{(1)}\zeta_2^{(2)} - \zeta_1^{(1)}\zeta_1^{(2)}\right)\frac{1}{4}\right. \\
&\left. + \left(\xi_3^{(1)}\zeta_3^{(1)} - \xi_3^{(2)}\zeta_3^{(2)}\right)\frac{1-\epsilon+2\,\epsilon^2}{4\,(1-\epsilon)\,\epsilon^2} + \left(\xi_3^{(2)}\zeta_3^{(1)} - \xi_3^{(1)}\zeta_3^{(2)}\right)\frac{2-3\,\epsilon+2\,\epsilon^2}{4\left(1-\epsilon\right)^2\epsilon}\right]
\end{aligned} \tag{17.18}$$

The corresponding cross section for Bhabha cross section is implemented in *G4PolarizedBhabhaCrossSection*. In the ultra-relativistic approximation it

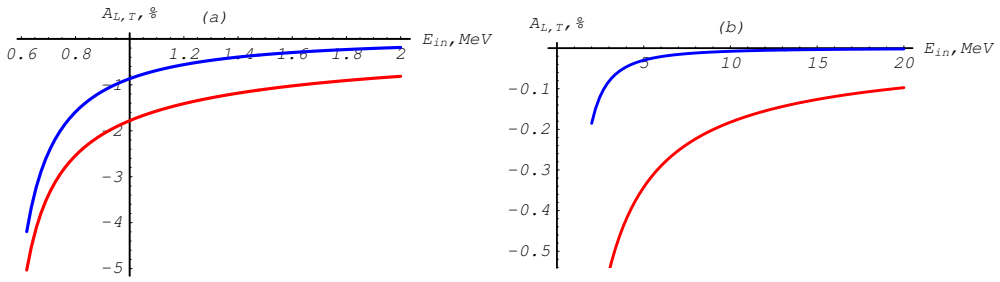

Figure 17.2: Møller total cross section asymmetries depending on the total energy of the incoming electron, with a cut-off $T_{\rm cut} = 1$keV. Transverse asymmetry is plotted in blue, longitudinal asymmetry in red. Left part, between 0.5 MeV and 2 MeV, right part up to 10 MeV.

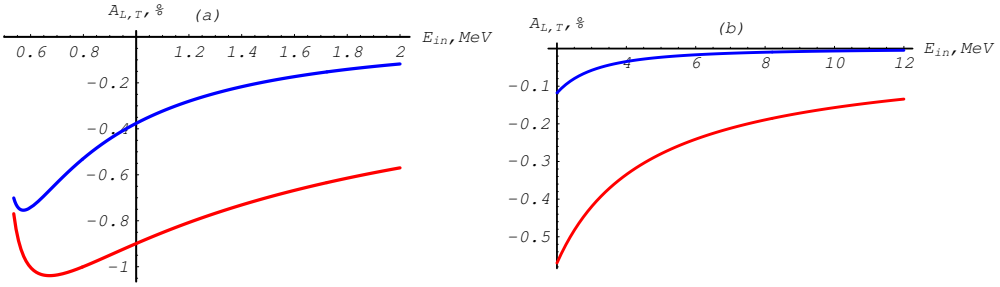

Figure 17.3: Bhabha total cross section asymmetries depending on the total energy of the incoming positron, with a cut-off $T_{\rm cut} = 1$keV. Transverse asymmetry is plotted in blue, longitudinal asymmetry in red. Left part, between 0.5 MeV and 2 MeV, right part up to 10 MeV.

reads

$$\frac{d\sigma^B_{URA}}{d\epsilon d\varphi} = \frac{{r_\epsilon}^2}{\gamma-1}\times$$
$$\left[\frac{\left(1-\epsilon+\epsilon^2\right)^2}{4\,\epsilon^2}+\zeta_3^{(1)}\zeta_3^{(2)}\frac{(\epsilon-1)\,\left(2-\epsilon+\epsilon^2\right)}{4\,\epsilon}+\left(\zeta_2^{(1)}\zeta_2^{(2)}-\zeta_1^{(1)}\zeta_1^{(2)}\right)\frac{(1-\epsilon)^2}{4}\right.$$
$$\left.+\left(\xi_3^{(1)}\zeta_3^{(1)}-\xi_3^{(2)}\zeta_3^{(2)}\right)\frac{1-2\,\epsilon+3\,\epsilon^2-2\,\epsilon^3}{4\,\epsilon^2}+\left(\xi_3^{(2)}\zeta_3^{(1)}-\xi_3^{(1)}\zeta_3^{(2)}\right)\frac{2-3\,\epsilon+2\,\epsilon^2}{4\epsilon}\right] \tag{17.19}$$

where r_e = classical electron radius
γ = $E_{k_1}/m_e c^2$
ϵ = $(E_{p_1} - m_e c^2)/(E_{k_1} - m_e c^2)$
E_{k_1} = energy of the incident electron/positron
E_{p_1} = energy of the scattered electron/positron
$m_e c^2$ = electron mass
$\boldsymbol{\zeta}^{(1)}$ = Stokes vector of the incoming electron/positron
$\boldsymbol{\zeta}^{(2)}$ = Stokes vector of the target electron
$\boldsymbol{\xi}^{(1)}$ = Stokes vector of the outgoing electron/positron
$\boldsymbol{\xi}^{(2)}$ = Stokes vector of the outgoing (2nd) electron .

Sampling

The delta ray is sampled according to methods discussed in Chapter 2. After exploitation of the symmetry in the Møller cross section under exchanging ϵ versus $(1-\epsilon)$, the differential cross section can be approximated by a simple function $f^M(\epsilon)$:

$$f^M(\epsilon) = \frac{1}{\epsilon^2}\frac{\epsilon_0}{1-2\epsilon_0} \tag{17.20}$$

with the kinematic limits given by

$$\epsilon_0 = \frac{T_{\text{cut}}}{E_{k_1} - m_e c^2} \leq \epsilon \leq \frac{1}{2} \tag{17.21}$$

A similar function $f^B(\epsilon)$ can be found for Bhabha scattering:

$$f^B(\epsilon) = \frac{1}{\epsilon^2}\frac{\epsilon_0}{1-\epsilon_0} \tag{17.22}$$

with the kinematic limits given by

$$\epsilon_0 = \frac{T_{\text{cut}}}{E_{k_1} - m_e c^2} \leq \epsilon \leq 1 \tag{17.23}$$

The kinematic of the delta ray production is constructed by the following steps:

1. ϵ is sampled from $f(\epsilon)$
2. calculate the differential cross section, depending on the initial polarizations $\boldsymbol{\zeta}^{(1)}$ and $\boldsymbol{\zeta}^{(2)}$.
3. ϵ is accepted with the probability defined by ratio of the differential cross section over the approximation function.

4. The φ is diced uniformly.

5. φ is determined from the differential cross section, depending on the initial polarizations $\boldsymbol{\zeta}^{(1)}$ and $\boldsymbol{\zeta}^{(2)}$

Note, for initial states without transverse polarization components, the φ distribution is always uniform. In figure 17.4 the asymmetries indicate the influence of polarization. In general the effect is largest around $\epsilon = \frac{1}{2}$.

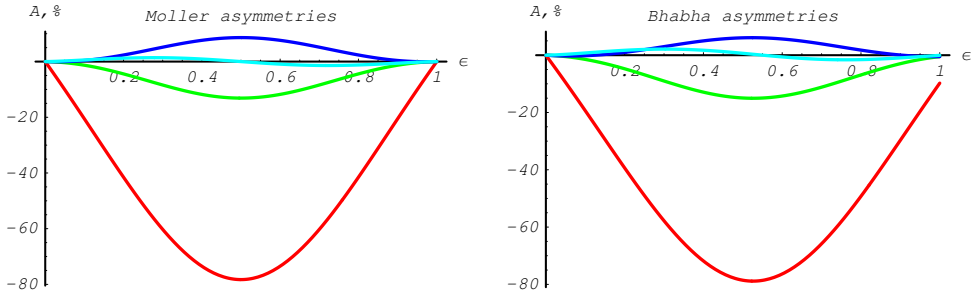

Figure 17.4: Differential cross section asymmetries in% for Møller (left) and Bhabha (right) scattering (red - $A_{ZZ}(\epsilon)$, green - $A_{XX}(\epsilon)$, blue - $A_{YY}(\epsilon)$, lightblue - $A_{ZX}(\epsilon)$)

After both ϕ and ϵ are known, the kinematic can be constructed fully. Using momentum conservation the momenta of the scattered incident particle and the ejected electron are constructed in global coordinate system.

Polarization transfer

After the kinematics is fixed the polarization properties of the outgoing particles are determined. Using the dependence of the differential cross section on the final state polarization a mean polarization is calculated according to method described in section 17.1.

The resulting polarization transfer functions $\xi_3^{(1,2)}(\epsilon)$ are depicted in figures 17.5 and 17.6.

17.2.4 Status of this document

20.11.06 created by P.Starovoitov
21.02.07 minor update by A.Schälicke

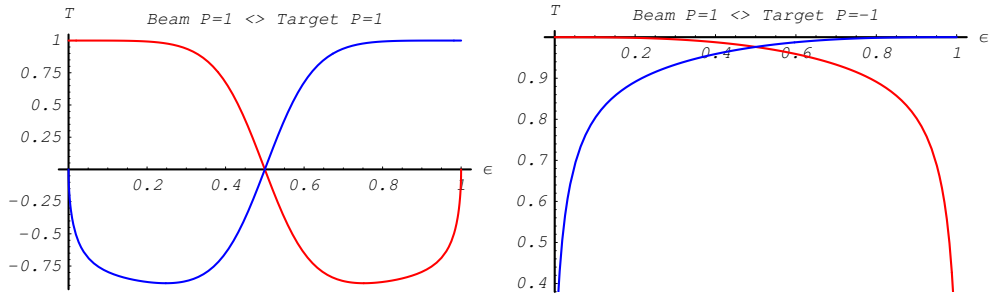

Figure 17.5: Polarization transfer functions in Møller scattering. Longitudinal polarization $\xi_3^{(2)}$ of electron with energy E_{p_2} in blue; longitudinal polarization $\xi_3^{(1)}$ of second electron in red. Kinetic energy of incoming electron $T_{k_1} = 10\text{MeV}$

.

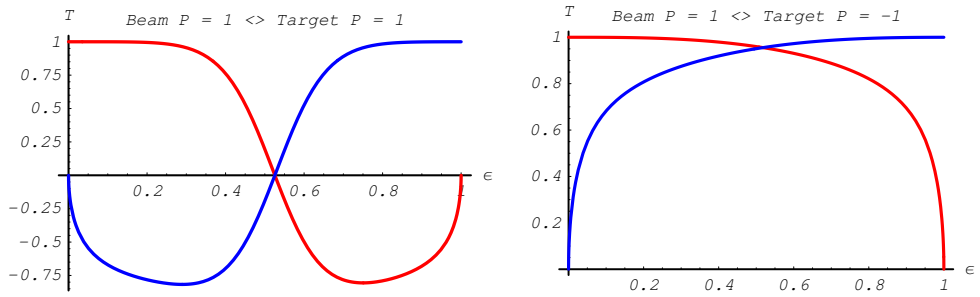

Figure 17.6: Polarization Transfer in Bhabha scattering. Longitudinal polarization $\xi_3^{(2)}$ of electron with energy E_{p_2} in blue; longitudinal polarization $\xi_3^{(1)}$ of scattered positron. Kinetic energy of incoming positron $T_{k_1} = 10\text{MeV}$

.

Bibliography

[1] P. Starovoitov *et.al.*, in preparation.

[2] G. W. Ford, C. J. Mullin, Phys. Rev. **108** (1957) 477.

[3] P. Stehle, Phys. Rev. **110** (1958) 1458.

17.3 Positron - Electron Annihilation

17.3.1 Method

The class *G4eplusPolarizedAnnihilation* simulates annihilation of polarized positrons with electrons in a material. The implementation baseline follows the approach derived for the class *G4eplusAnnihilation* described in section 8.3. It evaluates polarization transfer and – if the material is polarized – asymmetries in the produced photons. Thus, it takes the effects of polarization on total cross section and mean free path, on distribution of final state photons into account. And calculates the average polarization of these generated photons. The material electrons are assumed to be free and at rest.

17.3.2 Total cross section and mean free path

Kinematics of annihilation process is fixed by initial energy

$$\gamma = \frac{E_{k_1}}{mc^2} \tag{17.24}$$

and variable

$$\epsilon = \frac{E_{p_1}}{E_{k_1} + mc^2}, \tag{17.25}$$

which is the part of total energy available in initial state carried out by first photon. This variable has the following kinematical limits

$$\frac{1}{2}\left(1 - \sqrt{\frac{\gamma-1}{\gamma+1}}\right) \;<\; \epsilon \;<\; \frac{1}{2}\left(1 + \sqrt{\frac{\gamma-1}{\gamma+1}}\right) \;. \tag{17.26}$$

Total Cross Section

The total cross section of the annihilation of a polarized e^+e^- pair into two photons could be expressed as follows

$$\sigma^A_{pol} = \frac{\pi r_e^2}{\gamma+1}\left[\sigma^A_0 + \zeta^{(1)}_3\zeta^{(2)}_3\sigma^A_L + \left(\zeta^{(1)}_1\zeta^{(2)}_1 + \zeta^{(1)}_2\zeta^{(2)}_2\right)\sigma^A_T\right], \tag{17.27}$$

where

$$\sigma^A_0 = \frac{-\left(3+\gamma\right)\,\sqrt{-1+\gamma^2} + \left(1+\gamma\,\left(4+\gamma\right)\right)\,\ln(\gamma+\sqrt{-1+\gamma^2})}{4\,\left(\gamma^2-1\right)} \tag{17.28}$$

$$\sigma_L^A = \frac{-\sqrt{-1+\gamma^2}\,(5+\gamma\,(4+3\,\gamma))+(3+\gamma\,(7+\gamma+\gamma^2))\,\ln(\gamma+\sqrt{\gamma^2-1})}{4\,(\gamma-1)^2\,(1+\gamma)} \tag{17.29}$$

$$\sigma_T^A = \frac{(5+\gamma)\,\sqrt{-1+\gamma^2}-(1+5\,\gamma)\,\ln(\gamma+\sqrt{-1+\gamma^2})}{4\,(-1+\gamma)^2\,(1+\gamma)} \tag{17.30}$$

Mean free path

With the help of the total polarized annihilation cross section one can define a longitudinal asymmetry A_L^A and the transverse asymmetry A_T^A, by

$$A_L^A = \frac{\sigma_L^A}{\sigma_0^A} \qquad \text{and} \qquad A_T^A = \frac{\sigma_T^A}{\sigma_0^A}\,.$$

These asymmetries are depicted in figure 17.7.

If both incident positron and target electron are polarized the mean free path as defined in section 8.3 has to be modified. The polarized mean free path λ^{pol} is derived from the unpolarized mean free path λ^{unpol} via

$$\lambda^{\text{pol}} = \frac{\lambda^{\text{unpol}}}{1+\zeta_3^{(1)}\zeta_3^{(2)}\,A_L+\left(\zeta_1^{(1)}\zeta_1^{(2)}+\zeta_2^{(1)}\zeta_2^{(2)}\right)\,A_T} \tag{17.31}$$

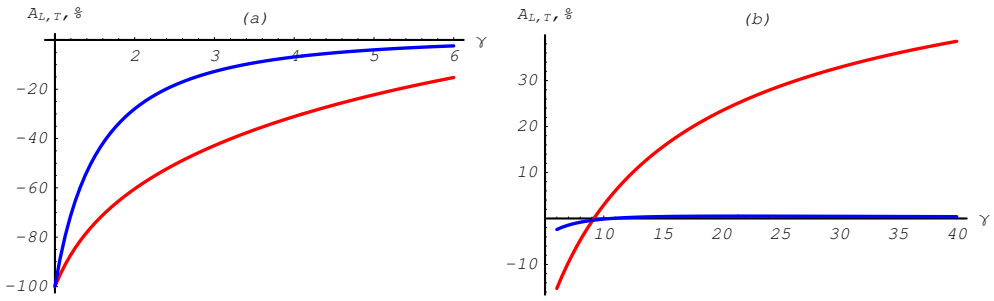

Figure 17.7: Annihilation total cross section asymmetries depending on the total energy of the incoming positron E_{k_1}. The transverse asymmetry is shown in blue, the longitudinal asymmetry in red.

17.3.3 Sampling the final state

Differential Cross Section

The fully polarized differential cross section is implemented in the class *G4PolarizedAnnihilationCrossSection*, which takes all mass effects into account, but binding effects are neglected [1, 2]. In the ultra-relativistic approximation (URA) and concentrating on longitudinal polarization states only the cross section is rather simple:

$$\begin{aligned}\frac{d\sigma^A_{URA}}{d\epsilon d\varphi} &= \frac{{r_e}^2}{\gamma-1}\times\left(\frac{1-2\,\epsilon+2\,\epsilon^2}{8\,\epsilon-8\,\epsilon^2}\left(1+\zeta_3^{(1)}\zeta_3^{(2)}\right)\right.\\ &\left.+\frac{(1-2\,\epsilon)\,\left(\zeta_3^{(1)}+\zeta_3^{(2)}\right)\,\left(\xi_3^{(1)}-\xi_3^{(2)}\right)}{8\,(\epsilon-1)\,\epsilon}\right)\end{aligned} \tag{17.32}$$

where
r_e = classical electron radius
γ = E_{k_1}/m_ec^2
E_{k_1} = energy of the incident positron
m_ec^2 = electron mass
$\boldsymbol{\zeta}^{(1)}$ = Stokes vector of the incoming positron
$\boldsymbol{\zeta}^{(2)}$ = Stokes vector of the target electron
$\boldsymbol{\xi}^{(1)}$ = Stokes vector of the 1st photon
$\boldsymbol{\xi}^{(2)}$ = Stokes vector of the 2nd photon .

Sampling

The photon energy is sampled according to methods discussed in Chapter 2. After exploitation of the symmetry in the Annihilation cross section under exchanging ϵ versus $(1-\epsilon)$, the differential cross section can be approximated by a simple function $f(\epsilon)$:

$$f(\epsilon)=\frac{1}{\epsilon}\ln^{-1}\left(\frac{\epsilon_{\max}}{\epsilon_{\min}}\right) \tag{17.33}$$

with the kinematic limits given by

$$\begin{aligned}\epsilon_{\min} &= \frac{1}{2}\left(1-\sqrt{\frac{\gamma-1}{\gamma+1}}\right)\ ,\\ \epsilon_{\max} &= \frac{1}{2}\left(1+\sqrt{\frac{\gamma-1}{\gamma+1}}\right)\ .\end{aligned} \tag{17.34}$$

The kinematic of the two photon final state is constructed by the following steps:

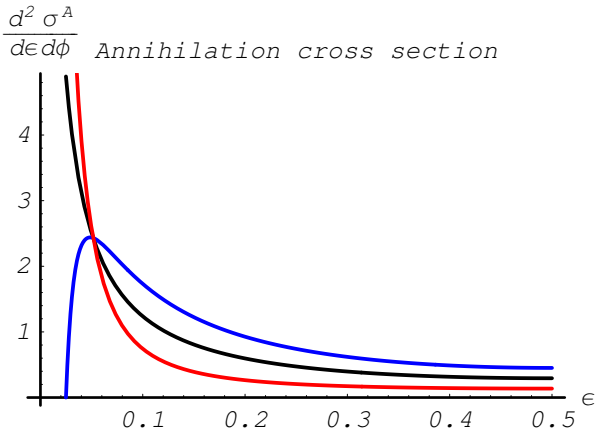

Figure 17.8: Annihilation differential cross section in arbitrary units. Black line corresponds to unpolarized cross section; red line – to the antiparallel spins of initial particles, and blue line – to the parallel spins. Kinetic energy of the incoming positron $T_{k_1} = 10\text{MeV}$.

1. ϵ is sampled from $f(\epsilon)$
2. calculate the differential cross section, depending on the initial polarizations $\boldsymbol{\zeta}^{(1)}$ and $\boldsymbol{\zeta}^{(2)}$.
3. ϵ is accepted with the probability defined by the ratio of the differential cross section over the approximation function $f(\epsilon)$.
4. The φ is diced uniformly.
5. φ is determined from the differential cross section, depending on the initial polarizations $\boldsymbol{\zeta}^{(1)}$ and $\boldsymbol{\zeta}^{(2)}$.

A short overview over the sampling method is given in Chapter 2. In figure 17.9 the asymmetries indicate the influence of polarization for an 10MeV incoming positron. The actual behavior is very sensitive to the energy of the incoming positron.

Polarization transfer

After the kinematics is fixed the polarization of the outgoing photon is determined. Using the dependence of the differential cross section on the final state polarizations a mean polarization is calculated for each photon according to method described in section 17.1.

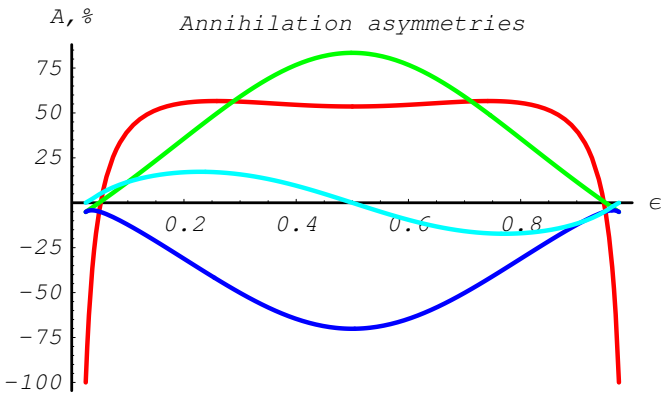

Figure 17.9: Annihilation differential cross section asymmetries in%. Red line corrsponds to $A_{ZZ}(\epsilon)$, green line – $A_{XX}(\epsilon)$, blue line – $A_{YY}(\epsilon)$, lightblue line – $A_{ZX}(\epsilon)$). Kinetic energy of the incoming positron $T_{k_1} = 10\text{MeV}$.

The resulting polarization transfer functions $\xi^{(1,2)}(\epsilon)$ are depicted in figure 17.10.

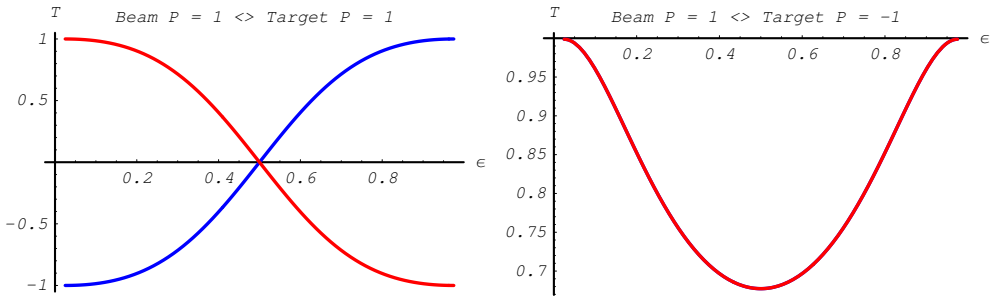

Figure 17.10: Polarization Transfer in annihilation process. Blue line corresponds to the circular polarization $\xi_3^{(1)}$ of the photon with energy $m(\gamma+1)\epsilon$; red line – circular polarization $\xi_3^{(2)}$ of the photon photon with energy $m(\gamma+1)(1-\epsilon)$.

17.3.4 Annihilation at Rest

The method `AtRestDoIt` treats the special case where a positron comes to rest before annihilating. It generates two photons, each with energy $E_{p_{1/2}} = mc^2$ and an isotropic angular distribution. Starting with the differential cross section for annihilation with positron and electron spins opposed and parallel,

respectively,[2]

$$d\sigma_1 = \sim \frac{(1-\beta^2)+\beta^2(1-\beta^2)(1-\cos^2\theta)^2}{(1-\beta^2\cos^2\theta)^2} d\cos\theta \qquad (17.35)$$

$$d\sigma_2 = \sim \frac{\beta^2(1-\cos^4\theta)}{(1-\beta^2\cos^2\theta)^2} d\cos\theta \qquad (17.36)$$

In the limit $\beta \to 0$ the cross section $d\sigma_1$ becomes one, and the cross section $d\sigma_2$ vanishes. For the opposed spin state, the total angular momentum is zero and we have a uniform photon distribution. For the parallel case the total angular momentum is 1. Here the two photon final state is forbidden by angular momentum conservation, and it can be assumed that higher order processes (e.g. three photon final state) play a dominant role. However, in reality 100% polarized electron targets do not exist, consequently there are always electrons with opposite spin, where the positron can annihilate with. Final state polarization does not play a role for the decay products of a spin zero state, and can be safely neglected. (Is set to zero)

17.3.5 Status of this document

20.11.06 created by P.Starovoitov
21.02.07 minor update by A.Schälicke

Bibliography

[1] P. Starovoitov *et.al.*, in preparation.

[2] L. A. Page, Phys. Rev. **106** (1957) 394-398.

17.4 Polarized Compton scattering

17.4.1 Method

The class *G4PolarizedCompton* simulates Compton scattering of polarized photons with (possibly polarized) electrons in a material. The implementation follows the approach described for the class *G4ComptonScattering* introduced in section 5.3. Here the explicit production of a Compton scattered photon and the ejected electron is considered taking the effects of polarization on total cross section and mean free path as well as on the distribution of final state particles into account. Further the average polarizations of the scattered photon and electron are calculated. The material electrons are assumed to be free and at rest.

17.4.2 Total cross section and mean free path

Kinematics of the Compton process is fixed by the initial energy

$$X = \frac{E_{k_1}}{mc^2} \tag{17.37}$$

and the variable

$$\epsilon = \frac{E_{p_1}}{E_{k_1}}, \tag{17.38}$$

which is the part of total energy avaible in initial state carried out by scattered photon, and the scattering angle

$$\cos\theta = 1 - \frac{1}{X}\left(\frac{1}{\epsilon} - 1\right) \tag{17.39}$$

The variable ϵ has the following limits:

$$\frac{1}{1+2X} \;<\; \epsilon \;<\; 1 \tag{17.40}$$

Total Cross Section

The total cross section of Compton scattering reads

$$\sigma^C_{pol} = \frac{\pi\, {r_e}^2}{X^2\,(1+2\,X)^2}\left[\sigma^C_0 + \zeta_3^{(1)}\zeta_3^{(2)}\sigma^C_L\right] \tag{17.41}$$

where

$$\sigma^C_0 = \frac{2\,X\;(2+X\;(1+X)\;(8+X)) - (1+2\,X)^2\;(2+(2-X)\;X)\;\ln(1+2\,X)}{X} \tag{17.42}$$

and

$$\sigma_L^C = 2\,X\,(1 + X\,(4 + 5\,X)) - (1 + X)\,(1 + 2\,X)^2\,\ln(1 + 2\,X) \qquad (17.43)$$

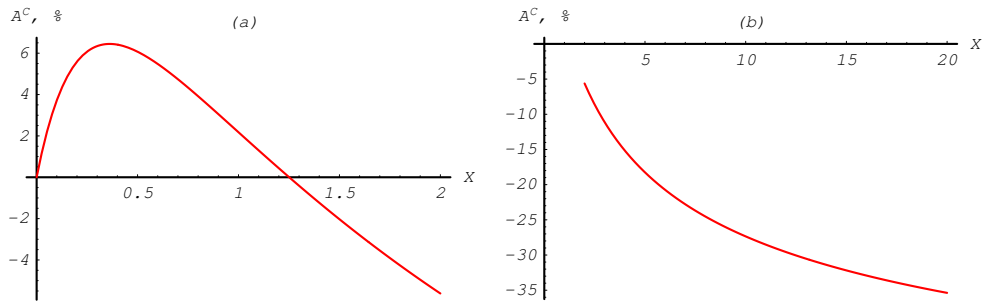

Figure 17.11: Compton total cross section asymmetry depending on the energy of incoming photon. Left part, between 0 and $\sim$ 1 MeV, right part – up to 10MeV.

Mean free path

When simulating the Compton scattering of a photon with an atomic electron, an empirical cross section formula is used, which reproduces the cross section data down to 10 keV (see section 5.3). If both, beam and target, are polarized this mean free path has to be corrected.

In the class *G4ComptonScattering* the polarized mean free path $\lambda^{\rm pol}$ is defined on the basis of the the unpolarized mean free path $\lambda^{\rm unpol}$ via

$$\lambda^{\rm pol} = \frac{\lambda^{\rm unpol}}{1 + \zeta_3^{(1)}\zeta_3^{(2)}\,A_L^C} \qquad (17.44)$$

where

$$A_L^C = \frac{\sigma_L^A}{\sigma_0^A} \qquad (17.45)$$

is the expected asymmetry from the the total polarized Compton cross section given above. This asymmetry is depicted in figure 17.11.

17.4.3 Sampling the final state

Differential Compton Cross Section

In the ultra-relativistic approximation the dependence of the differential cross section on the longitudinal/circular degree of polarization is very simple. It

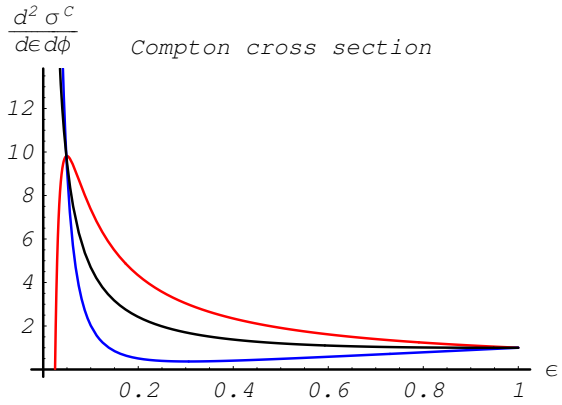

Figure 17.12: Compton scattering differential cross section in arbitrary units. Black line corresponds to the unpolarized cross section; red line – to the antiparallel spins of initial particles, and blue line – to the parallel spins. Energy of the incoming photon $E_{k_1} = 10\text{MeV}$.

reads

$$\frac{d\sigma^C_{URA}}{ded\varphi} = \frac{{r_e}^2}{X}\left(\frac{\epsilon^2+1}{2\,\epsilon} + \frac{\epsilon^2-1}{2\,\epsilon}\left(\zeta_3^{(1)}\zeta_3^{(2)} + \zeta_3^{(2)}\,\xi_3^{(1)} - \zeta_3^{(1)}\,\xi_3^{(2)}\right)\right.$$
$$\left. + \frac{\epsilon^2+1}{2\,\epsilon}\left(\zeta_3^{(1)}\,\xi_3^{(1)} - \zeta_3^{(2)}\,\xi_3^{(2)}\right)\right) \qquad (17.46)$$

where r_e = classical electron radius
X = $E_{k_1}/m_e c^2$
E_{k_1} = energy of the incident photon
$m_e c^2$ = electron mass

The fully polarized differential cross section is available in the class *G4PolarizedComptonCross*
It takes all mass effects into account, but binding effects are neglected [1, 2]. The cross section dependence on ϵ for right handed circularly polarized photons and longitudinally polarized electrons is plotted in figure 17.12

Sampling

The photon energy is sampled according to methods discussed in Chapter 2. The differential cross section can be approximated by a simple function $\Phi(\epsilon)$:

$$\Phi(\epsilon) = \frac{1}{\epsilon} + \epsilon \qquad (17.47)$$

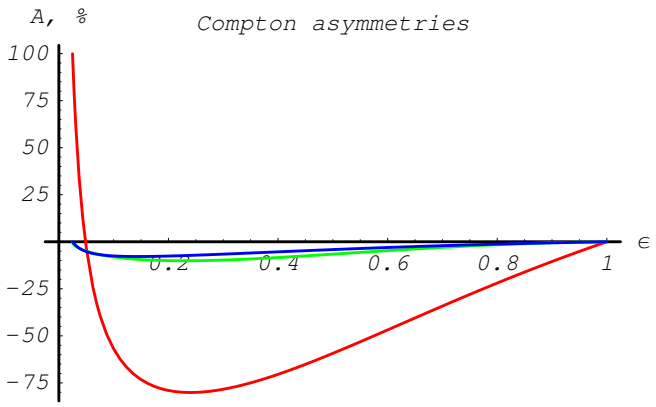

Figure 17.13: Compton scattering differential cross section asymmetries in%. Red line corresponds to the asymmetry due to circular photon and longitudinal electron initial state polarization, green line – due to circular photon and transverse electron initial state polarization, blue line – due to linear photon and transverse electron initial state polarization.

with the kinematic limits given by

$$\epsilon_{\min} = \frac{1}{1+2X} \tag{17.48}$$

$$\epsilon_{\max} = 1 \tag{17.49}$$

The kinematic of the scattered photon is constructed by the following steps:

1. ϵ is sampled from $\Phi(\epsilon)$
2. calculate the differential cross section, depending on the initial polarizations $\boldsymbol{\zeta}^{(1)}$ and $\boldsymbol{\zeta}^{(2)}$, which the correct normalization.
3. ϵ is accepted with the probability defined by ratio of the differential cross section over the approximation function.
4. The φ is diced uniformly.
5. φ is determined from the differential cross section, depending on the initial polarizations $\boldsymbol{\zeta}^{(1)}$ and $\boldsymbol{\zeta}^{(2)}$.

In figure 17.13 the asymmetries indicate the influence of polarization for an 10MeV incoming positron. The actual behavior is very sensitive to energy of the incoming positron.

Polarization transfer

After the kinematics is fixed the polarization of the outgoing photon is determined. Using the dependence of the differential cross section on the final state polarizations a mean polarization is calculated for each photon according to the method described in section 17.1.

The resulting polarization transfer functions $\xi^{(1,2)}(\epsilon)$ are depicted in figure 17.14.

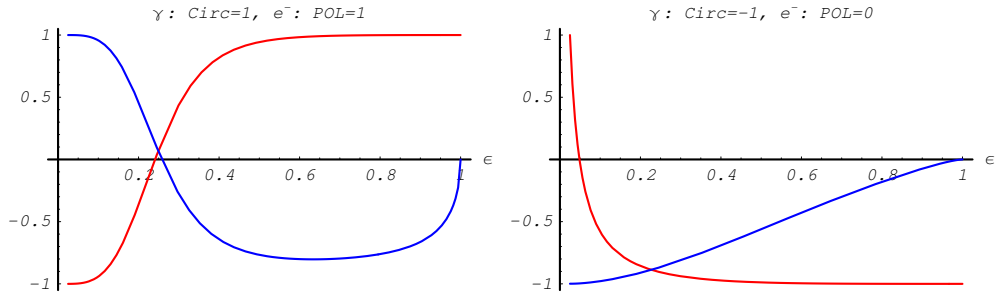

Figure 17.14: Polarization Transfer in Compton scattering. Blue line corresponds to the longitudinal polarization $\xi_3^{(2)}$ of the electron, red line – circular polarization $\xi_3^{(1)}$ of the photon.

17.4.4 Status of this document

20.11.06 created by P.Starovoitov
21.02.07 corrected cross section and some minor update by A.Schälicke

Bibliography

[1] P. Starovoitov *et.al.*, in preparation.

[2] F.W. Lipps, H.A. Tolhoek, Physica **20** (1954) 85; F.W. Lipps, H.A. Tolhoek, Physica **20** (1954) 395.

17.5 Polarized Bremsstrahlung for electron and positron

17.5.1 Method

The polarized version of Bremsstrahlung is based on the unpolarized cross section. Energy loss, mean free path, and distribution of explicitly generated final state particles are treated by the unpolarized version *G4eBremsstrahlung*. For details consult section 8.2.

The remaining task is to attribute polarization vectors to the generated final state particles, which is discussed in the following.

17.5.2 Polarization in gamma conversion and bremsstrahlung

Gamma conversion and bremsstrahlung are cross-symmetric processes (i.e. the Feynman diagram for electron bremsstrahlung can be obtained from the gamma conversion diagram by flipping the incoming photon and outgoing positron lines) and their cross sections closely related. For both processes, the interaction occurs in the field of the nucleus and the total and differential cross section are polarization independent. Therefore, only the polarization transfer from the polarized incoming particle to the outgoing particles is taken into account.

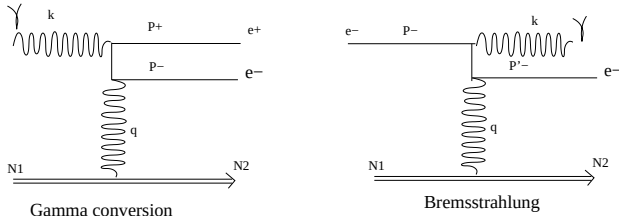

Figure 17.15: Feynman diagrams of Gamma conversion and bremsstrahlung processes.

For both processes, the scattering can be formulated by:

$$\mathcal{K}_1(k_1, \boldsymbol{\zeta}^{(1)}) + \mathcal{N}_1(k_{\mathcal{N}_1}, \boldsymbol{\zeta}^{(\mathcal{N}_1)}) \longrightarrow \mathcal{P}_1(p_1, \boldsymbol{\xi}^{(1)}) + \mathcal{P}_2(p_2, \boldsymbol{\xi}^{(2)}) + \mathcal{N}_2(p_{\mathcal{N}_2}, \boldsymbol{\xi}^{(\mathcal{N}_2)}) \tag{17.50}$$

Where $\mathcal{N}_1(k_{\mathcal{N}_1}, \boldsymbol{\zeta}^{(\mathcal{N}_1)})$ and $\mathcal{N}_2(p_{\mathcal{N}_2}, \boldsymbol{\xi}^{(\mathcal{N}_2)})$ are the initial and final state of the field of the nucleus respectively assumed to be unchanged, at rest and unpolarized. This leads to $k_{\mathcal{N}_1} = k_{\mathcal{N}_2} = 0$ and $\boldsymbol{\zeta}^{(\mathcal{N}_1)} = \boldsymbol{\xi}^{(\mathcal{N}_2)} = 0$

In the case of gamma conversion process:
$\mathcal{K}_1(k_1, \boldsymbol{\zeta}^{(1)})$ is the incoming photon initial state with momentum k_1 and polarization state $\boldsymbol{\zeta}^{(1)}$.
$\mathcal{P}_1(p_1, \boldsymbol{\xi}^{(1)})$ and $\mathcal{P}_2(p_2, \boldsymbol{\xi}^{(2)})$ are the two photons final states with momenta p_1 and p_2 and polarization states $\boldsymbol{\xi}^{(1)}$ and $\boldsymbol{\xi}^{(2)}$.

In the case of bremsstrahlung process:
$\mathcal{K}_1(k_1, \boldsymbol{\zeta}^{(1)})$ is the incoming lepton $e^-(e^+)$ initial state with momentum k_1 and polarization state $\boldsymbol{\zeta}^{(1)}$.
$\mathcal{P}_1(p_1, \boldsymbol{\xi}^{(1)})$ is the lepton $e^-(e^+)$ final state with momentum p_1 and polarization state $\boldsymbol{\xi}^{(1)}$.
$\mathcal{P}_2(p_2, \boldsymbol{\xi}^{(2)})$ is the bremsstrahlung photon in final state with momentum p_2 and polarization state $\boldsymbol{\xi}^{(2)}$.

17.5.3 Polarization transfer from the lepton $e^-(e^+)$ to a photon

The polarization transfer from an electron (positron) to a photon in a bremsstrahlung process was first calculated by Olsen and Maximon [1] taking into account both Coulomb and screening effects. In the Stokes vector formalism, the $e^-(e^+)$ polarization state can be transformed to a photon polarization finale state by means of interaction matrix T_γ^b. It defined via

$$\begin{pmatrix} O \\ \boldsymbol{\xi}^{(2)} \end{pmatrix} = T_\gamma^b \begin{pmatrix} 1 \\ \boldsymbol{\zeta}^{(1)} \end{pmatrix} , \tag{17.51}$$

and

$$T_\gamma^b \approx \begin{pmatrix} 1 & 0 & 0 & 0 \\ D & 0 & 0 & 0 \\ 0 & 0 & 0 & 0 \\ 0 & T & 0 & L \end{pmatrix} , \tag{17.52}$$

where

$$I = (\epsilon_1^2 + \epsilon_2^2)(3 + 2\Gamma) - 2\epsilon_1\epsilon_2(1 + 4u^2\hat{\xi}^2\Gamma) \tag{17.53}$$

$$D = \left\{8\epsilon_1\epsilon_2 u^2\hat{\xi}^2\Gamma\right\}/I \tag{17.54}$$

$$T = \left\{-4k\epsilon_2\hat{\xi}(1 - 2\hat{\xi})u\Gamma\right\}/I \tag{17.55}$$

$$L = k\{(\epsilon_1 + \epsilon_2)(3 + 2\Gamma) - 2\epsilon_2(1 + 4u^2\hat{\xi}^2\Gamma)\}/I \tag{17.56}$$

and

ϵ_1 Total energy of the incoming lepton $e^+(e^-)$ in units mc^2
ϵ_2 Total energy of the outgoing lepton $e^+(e^-)$ in units mc^2
k $= (\epsilon_1 - \epsilon_2)$, the energy of the bremsstrahlung photon in units of mc^2
$\boldsymbol{p}$ Electron (positron) initial momentum in units mc
$\boldsymbol{k}$ Bremsstrahlung photon momentum in units mc
$\boldsymbol{u}$ Component of $\boldsymbol{p}$ perpendicular to $\boldsymbol{k}$ in units mc and $u = |\boldsymbol{u}|$
$\hat{\xi}$ $= 1/(1+u^2)$

Coulomb and screening effects are contained in Γ, defined as follows

$$\Gamma = \ln\left(\frac{1}{\delta}\right) - 2 - f(Z) + \mathcal{F}\left(\frac{\hat{\xi}}{\delta}\right) \quad \text{for } \Delta \leq 120 \tag{17.57}$$

$$\Gamma = \ln\left(\frac{111}{\hat{\xi} Z^{\frac{1}{3}}}\right) - 2 - f(z) \quad \text{for } \Delta \geq 120 \tag{17.58}$$

with

$$\Delta = \frac{12 Z^{\frac{1}{3}} \epsilon_1 \epsilon_2 \hat{\xi}}{121 k} \quad \text{with } Z \text{ the atomic number and } \delta = \frac{k}{2\epsilon_1 \epsilon 2} \tag{17.59}$$

$f(Z)$ is the coulomb correction term derived by Davies, Bethe and Maximon [6]. $\mathcal{F}(\hat{\xi}/\delta)$ contains the screening effects and is zero for $\Delta \leq 0.5$ (No screening effects). For $0.5 \leq \Delta \leq 120$ (intermediate screening) it is a slowly decreasing function. The $\mathcal{F}(\hat{\xi}/\delta)$ values versus Δ are given in table 17.1 and used with a linear interpolation in between.

The polarization vector of the incoming $e^-(e^+)$ must be rotated into the frame defined by the scattering plane (x-z-plane) and the direction of the outgoing photon (z-axis). The resulting polarization vector of the bremsstrahlung photon is also given in this frame. Using Eq. (17.51) and the transfer matrix given by Eq. (17.52) the bremsstrahlung photon polarization state in the Stokes formalism [2, 3] is given by

$$\xi^{(2)} = \begin{pmatrix} \xi_1^{(2)} \\ \xi_2^{(2)} \\ \xi_3^{(2)} \end{pmatrix} \approx \begin{pmatrix} D \\ 0 \\ \zeta_1^{(1)} L + \zeta_2^{(1)} T \end{pmatrix} \tag{17.60}$$

17.5.4 Remaining polarization of the lepton after emitting a bremsstrahlung photon

The $e^-(e^+)$ polarization final state after emitting a bremsstrahlung photon can be calculated using the interaction matrix T_l^b which describes the lepton

Table 17.1: $\mathcal{F}(\hat{\xi}/\delta)$ for intermediate values of the screening factor [7].

Δ	$-\mathcal{F}\left(\hat{\xi}/\delta\right)$	Δ	$-\mathcal{F}\left(\hat{\xi}/\delta\right)$
0.5	0.0145	40.0	2.00
1.0	0.0490	45.0	2.114
2.0	0.1400	50.0	2.216
4.0	0.3312	60.0	2.393
8.0	0.6758	70.0	2.545
15.0	1.126	80.0	2.676
20.0	1.367	90.0	2.793
25.0	1.564	100.0	2.897
30.0	1.731	120.0	3.078
35.0	1.875		

depolarization. The polarization vector for the outgoing $e^-(e^+)$ is not given by Olsen and Maximon. However, their results can be used to calculate the following transfer matrix [4, 5].

$$\begin{pmatrix} O \\ \boldsymbol{\xi}^{(1)} \end{pmatrix} = T_l^b \begin{pmatrix} 1 \\ \boldsymbol{\zeta}^{(1)} \end{pmatrix} \tag{17.61}$$

$$T_l^b \approx \begin{pmatrix} 1 & 0 & 0 & 0 \\ D & M & 0 & E \\ 0 & 0 & M & 0 \\ 0 & F & 0 & M+P \end{pmatrix} \tag{17.62}$$

where

$$I = (\epsilon_1^2 + \epsilon_2^2)(3 + 2\Gamma) - 2\epsilon_1\epsilon_2(1 + 4u^2\hat{\xi}^2\Gamma) \tag{17.63}$$

$$F = \epsilon_2 \left\{ 4k\hat{\xi}u(1 - 2\hat{\xi})\Gamma \right\} / I \tag{17.64}$$

$$E = \epsilon_1 \left\{ 4k\hat{\xi}u(2\hat{\xi} - 1)\Gamma \right\} / I \tag{17.65}$$

$$M = \left\{ 4k\epsilon_1\epsilon_2(1 + \Gamma - 2u^2\hat{\xi}^2\Gamma) \right\} / I \tag{17.66}$$

$$P = \left\{ k^2(1 + 8\Gamma(\hat{\xi} - 0.5)^2 \right\} / I \tag{17.67}$$

and

ϵ_1	Total energy of the incoming e^+/e^- in units mc^2
ϵ_2	Total energy of the outgoing e^+/e^- in units mc^2
k	$= (\epsilon_1 - \epsilon_2)$, energy of the photon in units of mc^2
$\boldsymbol{p}$	Electron (positron) initial momentum in units mc
$\boldsymbol{k}$	Photon momentum in units mc
$\boldsymbol{u}$	Component of $\boldsymbol{p}$ perpendicular to $\boldsymbol{k}$ in units mc and $u = \|\boldsymbol{u}\|$

Using Eq. (17.61) and the transfer matrix given by Eq. (17.62) the $e^-(e^+)$ polarization state after emitting a bremsstrahlung photon is given in the Stokes formalism by

$$\xi^{(1)} = \begin{pmatrix} \xi_1^{(1)} \\ \xi_2^{(1)} \\ \xi_3^{(1)} \end{pmatrix} \approx \begin{pmatrix} \zeta_1^{(1)} M + \zeta_3^{(1)} E \\ \zeta_2^{(1)} M \\ \zeta_3^{(1)} (M + P) + \zeta_1^{(1)} F \end{pmatrix} . \tag{17.68}$$

17.5.5 Status of this document

20.11.06 created by K.Laihem
21.02.07 minor update by A.Schälicke
27.11.08 correction in Eq. (17.56) by A.Schälicke

Bibliography

[1] H. Olsen and L.C. Maximon. Photon and electron polarization in high-energy bremsstrahlung and pair production with screening. Physical Review, 114:887-904, 1959.

[2] W.H. McMaster. Polarization and the Stokes parameters. American Journal of Physics, 22(6):351-362, 1954.

[3] W.H. McMaster. Matrix representation of polarization. Reviews of Modern Physics, 33(1):8-29, 1961.

[4] K. Flöttmann. Investigations toward the development of polarized and unpolarized high intensity positron sources for linear colliders. PhD thesis, Universitat Hamburg, 1993.

[5] Hoogduin, Johannes Marinus, Electron, positron and photon polarimetry. PhD thesis, Rijksuniversiteit Groningen 1997.

[6] H. Davies, H.A. Bethe and L.C. Maximon, Theory of Bremsstrahlung and Pair Production. II. Integral Cross Section for Pair Production, Physical Review, 93(4):788-795, 1954.

[7] H.W. Koch and J.W. Motz, Bremsstrahlung cross-section formulas and related data. Review Mod. Phys., 31(4):920-955, 1959.

[8] K. Laihem, PhD thesis, Measurement of the positron polarization at an helical undulator based positron source for the International Linear Collider ILC, Humboldt University Berlin, Germany, (2008).

17.6 Polarized Gamma conversion into an electron–positron pair

17.6.1 Method

The polarized version of gamma conversion is based on the EM standard process *G4GammaConversion*. Mean free path and the distribution of explicitly generated final state particles are treated by this version. For details consult section 5.4.

The remaining task is to attribute polarization vectors to the generated final state leptons, which is discussed in the following.

17.6.2 Polarization transfer from the photon to the two leptons

Gamma conversion process is essentially the inverse process of Bremsstrahlung and the interaction matrix is obtained by inverting the rows and columns of the bremsstrahlung matrix and changing the sign of ϵ_2, cf. section 17.5. It follows from the work by Olsen and Maximon [1] that the polarization state $\xi^{(1)}$ of an electron or positron after pair production is obtained by

$$\begin{pmatrix} O \\ \boldsymbol{\xi}^{(1)} \end{pmatrix} = T_l^p \begin{pmatrix} 1 \\ \boldsymbol{\zeta}^{(1)} \end{pmatrix} \tag{17.69}$$

and

$$T_l^p \approx \begin{pmatrix} 1 & D & 0 & 0 \\ 0 & 0 & 0 & T \\ 0 & 0 & 0 & 0 \\ 0 & 0 & 0 & L \end{pmatrix} , \tag{17.70}$$

where

$$\begin{aligned} I &= (\epsilon_1^2 + \epsilon_2^2)(3 + 2\Gamma) + 2\epsilon_1\epsilon_2(1 + 4u^2\hat{\xi}^2\Gamma) && (17.71) \\ D &= \left\{-8\epsilon_1\epsilon_2 u^2\hat{\xi}^2\Gamma\right\}/I && (17.72) \\ T &= \left\{-4k\epsilon_2\hat{\xi}(1 - 2\hat{\xi})u\Gamma\right\}/I && (17.73) \\ L &= k\{(\epsilon_1 - \epsilon_2)(3 + 2\Gamma) + 2\epsilon_2(1 + 4u^2\hat{\xi}^2\Gamma)\}/I && (17.74) \end{aligned}$$

and

ϵ_1	total energy of the first lepton $e^+(e^-)$ in units mc^2
ϵ_2	total energy of the second lepton $e^-(e^+)$ in units mc^2
$k = (\epsilon_1 + \epsilon_2)$	energy of the incoming photon in units of mc^2
$\boldsymbol{p}$	electron=positron initial momentum in units mc
$\boldsymbol{k}$	photon momentum in units mc
$\boldsymbol{u}$	electron/positron initial momentum in units mc
u	$= \lvert\boldsymbol{u}\rvert$

Coulomb and screening effects are contained in Γ, defined in section 17.5.

Using Eq. (17.69) and the transfer matrix given by Eq. (17.70) the polarization state of the produced $e^-(e^+)$ is given in the Stokes formalism by:

$$\xi^{(1)} = \begin{pmatrix} \xi_1^{(1)} \\ \xi_2^{(1)} \\ \xi_3^{(1)} \end{pmatrix} \approx \begin{pmatrix} \zeta_3^{(1)} T \\ 0 \\ \zeta_3^{(1)} L \end{pmatrix} \tag{17.75}$$

17.6.3 Status of this document

20.11.06 created by K.Laihem
21.02.07 minor update by A.Schälicke
27.11.08 correction in Eq. (17.74) by A.Schälicke

Bibliography

[1] H. Olsen and L.C. Maximon. Photon and electron polarization in high-energy bremsstrahlung and pair production with screening. Physical Review, 114:887-904, 1959.

[2] K. Laihem, PhD thesis, Measurement of the positron polarization at an helical undulator based positron source for the International Linear Collider ILC, Humboldt University Berlin, Germany, (2008).

17.7 Polarized Photoelectric Effect

17.7.1 Method

This section describes the basic formulas of polarization transfer in the photoelectric effect class (*G4PolarizedPhotoElectricEffect*). The photoelectric effect is the emission of electrons from matter upon the absorption of electromagnetic radiation, such as ultraviolet radiation or x-rays. The energy of the photon is completely absorbed by the electron and, if sufficient, the electron can escape from the material with a finite kinetic energy. A single photon can only eject a single electron, as the energy of one photon is only absorbed by one electron. The electrons that are emitted are often called photoelectrons. If the photon energy is higher than the binding energy the remaining energy is transferred to the electron as a kinetic energy

$$E_{kin}^{e^-} = k - B_{shell} \tag{17.76}$$

In Geant4 the photoelectric effect process is taken into account if:

$$k > B_{shell} \tag{17.77}$$

Where k is the incoming photon energy and B_{shell} the electron binding energy provided by the class *G4AtomicShells*.

The polarized version of the photoelectric effect is based on the EM standard process *G4PhotoElectricEffect*. Mean free path and the distribution of explicitly generated final state particles are treated by this version. For details consult section 5.2.

The remaining task is to attribute polarization vectors to the generated final state electron, which is discussed in the following.

17.7.2 Polarization transfer

The polarization state of an incoming polarized photon is described by the Stokes vector $\vec{\zeta}^{(1)}$. The polarization transfer to the photoelectron can be described in the Stokes formalism using the same approach as for the Bremsstrahlung and gamma conversion processes, cf. 17.5 and 17.6. The relation between the photoelectron's Stokes parameters and the incoming photon's Stokes parameters is described by the interaction matrix T_l^p derived from H. Olsen [1] and reviewed by H.W McMaster [2]:

$$\begin{pmatrix} I' \\ \vec{\xi}^{(1)} \end{pmatrix} = T_l^p \begin{pmatrix} I_0 \\ \vec{\zeta}^{(1)} \end{pmatrix} \tag{17.78}$$

In general, for the photoelectric effect as a two-body scattering, the cross section should be correlated with the spin states of the incoming photon and the target electron. In our implementation the target electron is not polarized and only the polarization transfer from the photon to the photoelectron is taken into account. In this case the cross section of the process remains polarization independent. To compute the matrix elements we take advantage of the available kinematic variables provided by the generic *G4PhotoelectricEffect* class. To compute the photoelectron spin state (Stokes parameters), four main parameters are needed:

- The incoming photon Stokes vector $\vec{\zeta}^{(1)}$
- The incoming photon's energy k.
- the photoelectron's kinetic energy $E^{e^-}_{kin}$ or the Lorentz factors β and γ.
- The photoelectron's polar angle θ or $\cos\theta$.

The interaction matrix derived by H. Olsen [1] is given by:

$$T_l^P = \begin{pmatrix} 1+D & -D & 0 & 0 \\ 0 & 0 & 0 & B \\ 0 & 0 & 0 & 0 \\ 0 & 0 & 0 & A \end{pmatrix} \tag{17.79}$$

Where

$$D = \frac{1}{k}\left[\frac{2}{k\epsilon(1-\beta\cos\theta)} - 1\right] \tag{17.80}$$

$$A = \frac{\epsilon}{\epsilon+1}\left[\frac{2}{k\epsilon} + \beta\cos\theta + \frac{2}{k\epsilon^2(1-\beta\cos\theta)}\right] \tag{17.81}$$

$$B = \frac{\epsilon}{\epsilon+1}\beta\sin\theta\left[\frac{2}{k\epsilon(1-\beta\cos\theta)} - 1\right] \tag{17.82}$$

Using Eq. (17.78) and the transfer matrix given by Eq. (17.79) the polarization state of the produced e^- is given in the Stokes formalism by:

$$\vec{\xi}^{(1)} = \begin{pmatrix} \xi_1^{(1)} \\ \xi_2^{(1)} \\ \xi_3^{(1)} \end{pmatrix} = \begin{pmatrix} \zeta_3^{(1)} B \\ 0 \\ \zeta_3^{(1)} A \end{pmatrix} \tag{17.83}$$

From equation (17.83) one can see that a longitudinally (transversally) polarized photoelectron can only be produced if the incoming photon is circularly polarized.

17.7.3 Status of this document

20.11.07 created by K.Laihem
03.12.07 minor update by A.Schälicke

Bibliography

[1] H. Olsen, Kgl. N. Videnskab. Selskabs Forh. 31, Nos 11, 11a (1958).

[2] W.H. McMaster. Matrix representation of polarization. Reviews of Modern Physics, 33(1):8-29, 1961.

[3] K. Laihem, PhD thesis, Measurement of the positron polarization at an helical undulator based positron source for the International Linear Collider ILC, Humboldt University Berlin, Germany, (2008).

Chapter 18

X-Ray Production

18.1 Transition radiation

18.1.1 The Relationship of Transition Radiation to X-ray Cherenkov Radiation

X-ray transition radiation (XTR) occurs when a relativistic charged particle passes from one medium to another of a different dielectric permittivity. In order to describe this process it is useful to begin with an explanation of X-ray Cherenkov radiation, which is closely related.

The mean number of X-ray Cherenkov radiation (XCR) photons of frequency ω emitted into an angle θ per unit distance along a particle trajectory is [1]

$$\frac{d^3\bar{N}_{xcr}}{\hbar d\omega\, dx\, d\theta^2} = \frac{\alpha}{\pi\hbar c}\frac{\omega}{c}\theta^2 \mathrm{Im}\left\{Z\right\}. \tag{18.1}$$

Here the quantity Z is introduced as the *complex formation zone* of XCR in the medium:

$$Z = \frac{L}{1 - i\dfrac{L}{l}}, \quad L = \frac{c}{\omega}\left[\gamma^{-2} + \frac{\omega_p^2}{\omega^2} + \theta^2\right]^{-1}, \quad \gamma^{-2} = 1 - \beta^2. \tag{18.2}$$

with l and ω_p the photon absorption length and the plasma frequency, respectively, in the medium. For the case of a transparent medium, $l \to \infty$ and the complex formation zone reduces to the *coherence length* L of XCR. The coherence length roughly corresponds to that part of the trajectory in which an XCR photon can be created.

Introducing a complex quantity Z with its imaginary part proportional to the absorption cross-section ($\sim l^{-1}$) is required in order to account for absorption in the medium. Usually, $\omega_p^2/\omega^2 \gg c/\omega l$. Then it can be seen from Eqs. 18.1 and 18.2 that the number of emitted XCR photons is considerably suppressed and disappears in the limit of a transparent medium. This is caused by the destructive interference between the photons emitted from different parts of the particle trajectory.

The destructive interference of X-ray Cherenkov radiation is removed if the particle crosses a boundary between two media with different dielectric permittivities, ϵ, where

$$\epsilon = 1 - \frac{\omega_p^2}{\omega^2} + i\frac{c}{\omega l}. \tag{18.3}$$

Here the standard high-frequency approximation for the dielectric permittivity has been used. This is valid for energy transfers larger than the K-shell excitation potential.

If layers of media are alternated with spacings of order L, the X-ray radiation yield from a trajectory of unit length can be increased by roughly l/L times. The radiation produced in this case is called X-ray transition radiation (XTR).

18.1.2 Calculating the X-ray Transition Radiation Yield

Using the methods developed in Ref. [2] one can derive the relation describing the mean number of XTR photons generated per unit photon frequency and θ^2 *inside* the radiator for a general XTR radiator consisting of n different absorbing media with fluctuating thicknesses:

$$\frac{d^2\bar{N}_{in}}{\hbar d\omega\, d\theta^2} = \frac{\alpha}{\pi\hbar c^2}\omega\theta^2 \mathrm{Re}\left\{\sum_{i=1}^{n-1}(Z_i - Z_{i+1})^2 + \right. \tag{18.4}$$

$$\left. + \quad 2\sum_{k=1}^{n-1}\sum_{i=1}^{k-1}(Z_i - Z_{i+1})\left[\prod_{j=i+1}^{k} F_j\right](Z_k - Z_{k+1})\right\},\ F_j = \exp\left[-\frac{t_j}{2Z_j}\right].$$

In the case of gamma distributed gap thicknesses (foam or fiber radiators) the values F_j, $(j = 1, 2)$ can be estimated as:

$$F_j = \int_0^\infty dt_j \left(\frac{\nu_j}{\bar{t}_j}\right)^{\nu_j} \frac{t_j^{\nu_j - 1}}{\Gamma(\nu_j)} \exp\left[-\frac{\nu_j t_j}{\bar{t}_j} - i\frac{t_j}{2Z_j}\right] = \left[1 + i\frac{\bar{t}_j}{2Z_j\nu_j}\right]^{-\nu_j}, \tag{18.5}$$

where Z_j is the complex formation zone of XTR (similar to relation 18.2 for XCR) in the j-th medium [2, 6]. Γ is the Euler gamma function, $\bar{t}_j$ is the mean thickness of the j-th medium in the radiator and $\nu_j > 0$ is the parameter roughly describing the relative fluctuations of t_j. In fact, the relative fluctuation is $\delta t_j/\bar{t}_j \sim 1/\sqrt{\nu_j}$.

In the particular case of n foils of the first medium (Z_1, F_1) interspersed with gas gaps of the second medium (Z_2, F_2), one obtains:

$$\frac{d^2\bar{N}_{in}}{\hbar d\omega\, d\theta^2} = \frac{2\alpha}{\pi\hbar c^2}\omega\theta^2 \mathrm{Re}\left\{\langle R^{(n)}\rangle\right\}, \quad F = F_1F_2, \tag{18.6}$$

$$\langle R^{(n)}\rangle = (Z_1 - Z_2)^2\left\{n\frac{(1-F_1)(1-F_2)}{1-F} + \frac{(1-F_1)^2F_2[1-F^n]}{(1-F)^2}\right\}. \tag{18.7}$$

Here $\langle R^{(n)}\rangle$ is the stack factor reflecting the radiator geometry. The integration of (18.6) with respect to θ^2 can be simplified for the case of a regular radiator ($\nu_{1,2} \to \infty$), transparent in terms of XTR generation media, and

$n \gg 1$ [3]. The frequency spectrum of emitted XTR photons is given by:

$$\frac{d\bar{N}_{in}}{\hbar d\omega} = \int_0^{\sim 10\gamma^{-2}} d\theta^2 \frac{d^2\bar{N}_{in}}{\hbar d\omega\, d\theta^2} = \frac{4\alpha n}{\pi\hbar\omega}(C_1 + C_2)^2 \cdot \sum_{k=k_{min}}^{k_{max}} \frac{(k - C_{min})}{(k - C_1)^2(k + C_2)^2} \sin^2\left[\frac{\pi t_1}{t_1 + t_2}(k + C_2)\right], \tag{18.8}$$

$$C_{1,2} = \frac{t_{1,2}(\omega_1^2 - \omega_2^2)}{4\pi c\omega}, \quad C_{min} = \frac{1}{4\pi c}\left[\frac{\omega(t_1 + t_2)}{\gamma^2} + \frac{t_1\omega_1^2 + t_2\omega_2^2}{\omega}\right].$$

The sum in (18.8) is defined by terms with $k \geq k_{min}$ corresponding to the region of $\theta \geq 0$. Therefore k_{min} should be the nearest to C_{min} integer $k_{min} \geq C_{min}$. The value of k_{max} is defined by the maximum emission angle $\theta_{max}^2 \sim 10\gamma^{-2}$. It can be evaluated as the integer part of

$$C_{max} = C_{min} + \frac{\omega(t_1 + t_2)}{4\pi c}\frac{10}{\gamma^2}, \quad k_{max} - k_{min} \sim 10^2 \div 10^3 \gg 1.$$

Numerically, however, only a few tens of terms contribute substantially to the sum, that is, one can choose $k_{max} \sim k_{min} + 20$. Equation (18.8) corresponds to the spectrum of the total number of photons emitted inside a regular transparent radiator. Therefore the mean interaction length, λ_{XTR}, of the XTR process in this kind of radiator can be introduced as:

$$\lambda_{XTR} = n(t_1 + t_2)\left[\int_{\hbar\omega_{min}}^{\hbar\omega_{max}} \hbar d\omega \frac{d\bar{N}_{in}}{\hbar d\omega}\right]^{-1},$$

where $\hbar\omega_{min} \sim 1$ keV, and $\hbar\omega_{max} \sim 100$ keV for the majority of high energy physics experiments. Its value is constant along the particle trajectory in the approximation of a transparent regular radiator. The spectrum of the total number of XTR photons *after* regular transparent radiator is defined by (18.8) with:

$$n \to n_{eff} = \sum_{k=0}^{n-1} \exp[-k(\sigma_1 t_1 + \sigma_2 t_2)] = \frac{1 - \exp[-n(\sigma_1 t_1 + \sigma_2 t_2)]}{1 - \exp[-(\sigma_1 t_1 + \sigma_2 t_2)]},$$

where σ_1 and σ_2 are the photo-absorption cross-sections corresponding to the photon frequency ω in the first and the second medium, respectively. With this correction taken into account the XTR absorption in the radiator (18.8) corresponds to the results of [4]. In the more general case of the flux of XTR

photons *after* a radiator, the XTR absorption can be taken into account with a calculation based on the stack factor derived in [5]:

$$\begin{aligned}\langle R^{(n)}_{flux}\rangle &= (L_1 - L_2)^2 \left\{ \frac{1-Q^n}{1-Q} \frac{(1+Q_1)(1+F) - 2F_1 - 2Q_1F_2}{2(1-F)} \right. \\ &+ \left. \frac{(1-F_1)(Q_1-F_1)F_2(Q^n - F^n)}{(1-F)(Q-F)} \right\}, \end{aligned} \tag{18.9}$$

$$Q = Q_1 \cdot Q_2, \quad Q_j = \exp\left[-t_j/l_j\right] = \exp\left[-\sigma_j t_j\right], \quad j = 1, 2.$$

Both XTR energy loss (18.7) and flux (18.9) models can be implemented as a discrete electromagnetic process (see below).

18.1.3 Simulating X-ray Transition Radiation Production

A typical XTR radiator consits of many (~ 100) boundaries between different materials. To improve the tracking performance in such a volume one can introduce an artificial material [6], which is the geometrical mixture of foil and gas contents. Here is an example:

```
// In DetectorConstruction of an application
// Preparation of mixed radiator material
foilGasRatio  = fRadThickness/(fRadThickness+fGasGap);
foilDensity  = 1.39*g/cm3;     // Mylar
gasDensity   = 1.2928*mg/cm3 ; // Air
totDensity   = foilDensity*foilGasRatio +
               gasDensity*(1.0-foilGasRatio);
fractionFoil =  foilDensity*foilGasRatio/totDensity;
fractionGas  =  gasDensity*(1.0-foilGasRatio)/totDensity;
G4Material* radiatorMat = new G4Material("radiatorMat",
                                         totDensity,
                                         ncomponents = 2 );
radiatorMat->AddMaterial( Mylar, fractionFoil );
radiatorMat->AddMaterial( Air,   fractionGas  );
G4cout << *(G4Material::GetMaterialTable()) << G4endl;
// materials of the TR radiator
fRadiatorMat = radiatorMat;   // artificial for geometry
fFoilMat     = Mylar;
fGasMat      = Air;
```

This artificial material will be assigned to the logical volume in which XTR will be generated:

```
solidRadiator = new G4Box("Radiator",
                          1.1*AbsorberRadius ,
                          1.1*AbsorberRadius,
                          0.5*radThick       );
logicRadiator = new G4LogicalVolume( solidRadiator,
                                      fRadiatorMat,  // !!!
                                     "Radiator");
physiRadiator = new G4PVPlacement(0,
                                  G4ThreeVector(0,0,zRad),
                                  "Radiator", logicRadiator,
                                  physiWorld, false, 0      );
```

XTR photons generated by a relativistic charged particle intersecting a radiator with $2n$ interfaces between different media can be simulated by using the following algorithm. First the total number of XTR photons is estimated using a Poisson distribution about the mean number of photons given by the following expression:

$$\bar{N}^{(n)} = \int_{\omega_1}^{\omega_2} d\omega \int_0^{\theta^2_{max}} d\theta^2 \frac{d^2\bar{N}^{(n)}}{d\omega\, d\theta^2} = \frac{2\alpha}{\pi c^2} \int_{\omega_1}^{\omega_2} \omega d\omega \int_0^{\theta^2_{max}} \theta^2 d\theta^2 \mathrm{Re}\left\{\langle R^{(n)}\rangle\right\}.$$

Here $\theta^2_{max} \sim 10\gamma^{-2}$, $\hbar\omega_1 \sim 1$ keV, $\hbar\omega_2 \sim 100$ keV, and $\langle R^{(n)}\rangle$ correspond to the geometry of the experiment. For events in which the number of XTR photons is not equal to zero, the energy and angle of each XTR quantum is sampled from the integral distributions obtained by the numerical integration of expression (18.6). For example, the integral energy spectrum of emitted XTR photons, $\bar{N}^{(n)}_{>\omega}$, is defined from the following integral distribution:

$$\bar{N}^{(n)}_{>\omega} = \frac{2\alpha}{\pi c^2} \int_{\omega}^{\omega_2} \omega d\omega \int_0^{\theta^2_{max}} \theta^2 d\theta^2 \mathrm{Re}\left\{\langle R^{(n)}\rangle\right\}.$$

In GEANT4 XTR generation *inside* or *after* radiators is described as a discrete electromagnetic process. It is convenient for the description of tracks in magnetic fields and can be used for the cases when the radiating charge experiences a scattering inside the radiator. The base class `G4VXTRenergyLoss` is responsible for the creation of tables with integral energy and angular distributions of XTR photons. It also contains the `PostDoIt` function providing XTR photon generation and motion (if fExitFlux=true) through a XTR radiator to its boundary. Particular models like `G4RegularXTRadiator` implement the pure virtual function `GetStackFactor`, which calculates the response of the XTR radiator reflecting its geometry. Included below are some comments for the declaration of XTR in a user application.

In the physics list one should pass to the XTR process additional details of the XTR radiator involved:

```
// In PhysicsList of an application
else if (particleName == "e-")  // Construct processes for electron with XTR
{
   pmanager->AddProcess(new G4MultipleScattering, -1, 1,1 );
   pmanager->AddProcess(new G4eBremsstrahlung(),  -1,-1,1 );
   pmanager->AddProcess(new Em10StepCut(),        -1,-1,1 );
// in regular radiators:
   pmanager->AddDiscreteProcess(
   new G4RegularXTRadiator        // XTR dEdx in general regular radiator
// new G4XTRRegularRadModel        - XTR flux after general regular radiator
// new G4TransparentRegXTRadiator  - XTR dEdx in transparent
//                                   regular radiator
// new G4XTRTransparentRegRadModel - XTR flux after transparent
//                                   regular radiator
                          (pDet->GetLogicalRadiator(), // XTR radiator

                           pDet->GetFoilMaterial(), // real foil
                           pDet->GetGasMaterial(),  // real gas
                           pDet->GetFoilThick(),    // real geometry
                           pDet->GetGasThick(),
                           pDet->GetFoilNumber(),
                           "RegularXTRadiator"));
// or for foam/fiber radiators:
   pmanager->AddDiscreteProcess(
   new G4GammaXTRadiator    - XTR dEdx in general foam/fiber radiator
// new G4XTRGammaRadModel   - XTR flux after general foam/fiber radiator
                           ( pDet->GetLogicalRadiator(),
                             1000.,
                             100.,
                             pDet->GetFoilMaterial(),
                             pDet->GetGasMaterial(),
                             pDet->GetFoilThick(),
                             pDet->GetGasThick(),
                             pDet->GetFoilNumber(),
                             "GammaXTRadiator"));
}
```

Here for the foam/fiber radiators the values 1000 and 100 are the ν parameters (which can be varied) of the Gamma distribution for the foil and gas gaps,

respectively. Classes G4TransparentRegXTRadiator and G4XTRTransparentRegRadModel correspond (18.8) to n and n_{eff}, respectively.

18.1.4 Status of this document

18.11.05 modified by V.Grichine
29.11.02 re-written by D.H. Wright
29.05.02 created by V.Grichine

Bibliography

[1] V.M. Grichine, *Nucl. Instr. and Meth.*, **A482** (2002) 629.

[2] V.M. Grichine, *Physics Letters*, **B525** (2002) 225-239

[3] G.M. Garibyan, *Sov. Phys. JETP* **32** (1971) 23.

[4] C.W. Fabian and W. Struczinski *Physics Letters*, **B57** (1975) 483.

[5] G.M. Garibian, L.A. Gevorgian, and C. Yang, *Sov. Phys.- JETP, 39 (1975) 265.*

[6] J. Apostolakis, S. Giani, V. Grichine et al., *Comput. Phys. Commun.* **132** (2000) 241.

18.2 Scintillation

Every scintillating material has a characteristic light yield, Y $(photons/MeV)$, and an intrinsic resolution which generally broadens the statistical distribution, $\sigma_i/\sigma_s > 1$, due to impurities which are typical for doped crystals like NaI(Tl) and CsI(Tl). The average yield can have a non-linear dependence on the local energy deposition. Scintillators also have a time distribution spectrum with one or more exponential decay time constants, τ_i, with each decay component having its intrinsic photon emission spectrum. These are empirical parameters typical for each material.

The generation of scintillation light can be simulated by sampling the number of photons from a Poisson distribution. This distribution is based on the energy lost during a step in a material and on the scintillation properties of that material. The frequency of each photon is sampled from the empirical spectra. The photons are generated evenly along the track segment and are emitted uniformly into 4π with a random linear polarization.

18.2.1 Status of this document

07.12.98 created by P.Gumplinger

18.3 Čerenkov Effect

The radiation of Čerenkov light occurs when a charged particle moves through a dispersive medium faster than the speed of light in that medium. A dispersive medium is one whose index of refraction is an increasing function of photon energy. Two things happen when such a particle slows down:

1. a cone of Čerenkov photons is emitted, with the cone angle (measured with respect to the particle momentum) decreasing as the particle loses energy;

2. the momentum of the photons produced increases, while the number of photons produced decreases.

When the particle velocity drops below the local speed of light, photons are no longer emitted. At that point, the Čerenkov cone collapses to zero.

In order to simulate Čerenkov radiation the number of photons per track length must be calculated. The formulae used for this calculation can be found below and in [1, 2]. Let n be the refractive index of the dielectric material acting as a radiator. Here $n = c/c'$ where c' is the group velocity of light in the material, hence $1 \leq n$. In a dispersive material n is an increasing function of the photon energy ϵ ($dn/d\epsilon \geq 0$). A particle traveling with speed $\beta = v/c$ will emit photons at an angle θ with respect to its direction, where θ is given by

$$\cos\theta = \frac{1}{\beta n}.$$

From this follows the limitation for the momentum of the emitted photons:

$$n(\epsilon_{min}) = \frac{1}{\beta}.$$

Photons emitted with an energy beyond a certain value are immediately re-absorbed by the material; this is the window of transparency of the radiator. As a consequence, all photons are contained in a cone of opening angle $\cos\theta_{max} = 1/(\beta n(\epsilon_{max}))$.

The average number of photons produced is given by the relations :

$$\begin{aligned} dN &= \frac{\alpha z^2}{\hbar c}\sin^2\theta d\epsilon dx = \frac{\alpha z^2}{\hbar c}(1 - \frac{1}{n^2\beta^2})d\epsilon dx \\ &\approx 370 z^2 \frac{photons}{eV\ cm}(1 - \frac{1}{n^2\beta^2})d\epsilon dx \end{aligned}$$

and the number of photons generated per track length is

$$\frac{dN}{dx} \approx 370z^2 \int_{\epsilon_{min}}^{\epsilon_{max}} d\epsilon \left(1 - \frac{1}{n^2\beta^2}\right) = 370z^2 \left[\epsilon_{max} - \epsilon_{min} - \frac{1}{\beta^2} \int_{\epsilon_{min}}^{\epsilon_{max}} \frac{d\epsilon}{n^2(\epsilon)}\right]$$

.

The number of photons produced is calculated from a Poisson distribution with a mean of $\langle n \rangle$ = StepLength dN/dx. The energy distribution of the photon is then sampled from the density function

$$f(\epsilon) = \left[1 - \frac{1}{n^2(\epsilon)\beta^2}\right]$$

.

18.3.1 Status of this document

07.12.98 created by P.Gumplinger
11.12.01 SI units (mma)
08.05.02 re-written by D.H. Wright

Bibliography

[1] J.D.Jackson, Classical Electrodynamics, John Wiley and Sons (1998)

[2] D.E. Groom et al. Particle Data Group . Rev. of Particle Properties. Eur. Phys. J. C15,1 (2000) http://pdg.lbl.gov/

18.4 Synchrotron Radiation

18.4.1 Photon spectrum

Synchrotron radiation photons are emitted by relativistic charged particles traveling in magnetic fields. The properties of synchrotron radiation are well understood and described in textbooks [1, 2, 3].

In the simplest case, we have an electron of momentum p moving perpendicular to a homogeneous magnetic field B. The magnetic field will keep the particle on a circular path, with radius

$$\rho = \frac{p}{e\,B} = \frac{m\gamma\beta c}{e\,B}\,. \quad \text{Numerically we have} \quad \rho[\mathrm{m}] = p[\mathrm{GeV/c}]\,\frac{3.336\,\mathrm{m}}{B[\mathrm{T}]}\,. \tag{18.10}$$

In general, there will be an arbitrary angle θ between the local magnetic field $\mathbf{B}$ and momentum vector $\mathbf{p}$ of the particle. The motion has a circular component in the plane perpendicular to the magnetic field, and in addition a constant momentum component parallel to the magnetic field. For a constant homogeneous field, the resulting trajectory is a helix.

The critical energy of the synchrotron radiation can be calculated using the radius ρ of Eq.18.10 and angle θ or the magnetic field perpendicular to the particle direction $B_\perp = B\sin\theta$ according to

$$E_c = \frac{3}{2}\,\hbar c\,\frac{\gamma^3\sin\theta}{\rho} = \frac{3\,\hbar}{2\,m}\,\gamma^2\,eB_\perp\,. \tag{18.11}$$

Half of the synchrotron radiation power is radiated by photons above the critical energy.

With x we denote the photon energy E_γ, expressed in units of the critical energy E_c

$$x = \frac{E_\gamma}{E_c}\,. \tag{18.12}$$

The photon spectrum (number of photons emitted per path length s and relative energy x) can be written as

$$\frac{d^2\,N}{ds\,dx} = \frac{\sqrt{3}\,\alpha}{2\pi}\,\frac{eB_\perp}{mc}\int_x^\infty K_{5/3}(\xi)\,d\xi \tag{18.13}$$

where $\alpha = e^2/\,4\pi\epsilon_0\hbar c$ is the dimensionless electromagnetic coupling (or fine structure) constant and $K_{5/3}$ is the modified Bessel function of the third kind.

The number of photons emitted per unit length and the mean free path λ between two photon emissions is obtained by integration over all photon

energies. Using

$$\int_0^\infty dx \int_x^\infty K_{5/3}(\xi)\, d\xi = \frac{5\pi}{3} \tag{18.14}$$

we find that

$$\frac{dN}{ds} = \frac{5\,\alpha}{2\sqrt{3}}\,\frac{eB_\perp}{m\beta c} = \frac{1}{\lambda}\,. \tag{18.15}$$

Here we are only interested in ultra-relativistic ($\beta \approx 1$) particles, for which λ only depends on the field B and not on the particle energy. We define a constant λ_B such that

$$\lambda = \frac{\lambda_B}{B_\perp} \qquad \text{where} \quad \lambda_B = \frac{2\sqrt{3}}{5}\,\frac{m\,c}{\alpha\,e} = 0.16183\,\mathrm{Tm}\,. \tag{18.16}$$

As an example, consider a 10 GeV electron, travelling perpendicular to a 1 T field. It moves along a circular path of radius $\rho = 33.356\,\mathrm{m}$. For the Lorentz factor we have $\gamma = 19569.5$ and $\beta = 1 - 1.4\times10^{-9}$. The critical energy is $E_c = 66.5\,\mathrm{keV}$ and the mean free path between two photon emissions is $\lambda = 0.16183\,\mathrm{m}$.

18.4.2 Validity

The spectrum given in Eq. 18.13 can generally be expected to provide a very accurate description for the synchrotron radiation spectrum generated by GeV electrons in magnetic fields.

Here we discuss some known limitations and possible extensions.

For particles traveling on a circular path, the spectrum observed in one location will in fact not be a continuous spectrum, but a discrete spectrum, consisting only of harmonics or modes n of the revolution frequency. In practice, the mode numbers will generally be too high to make this a visible effect. The critical mode number corresponding to the critical energy is $n_c = 3/2\,\gamma^3$. 10 GeV electrons for example have $n_c \approx 10^{13}$.

Synchrotron radiation can be neglected for slower particles and only becomes relevant for ultra-relativistic particles with $\gamma > 10^3$. Using $\beta = 1$ introduces an uncertainty of about $1/2\gamma^2$ or less than 5×10^{-7}.

It is rather straightforward to extend the formulas presented here to particles other than electrons, with arbitrary charge q and mass m, see [4]. The number of photons and the power scales with the square of the charge.

The standard synchrotron spectrum of Eq. 18.13 is only valid as long as the photon energy remains small compared to the particle energy [5, 6]. This is a very safe assumption for GeV electrons and standard magnets with fields of order of Tesla.

An extension of synchrotron radiation to fields exceeding several hundred Tesla, such as those present in the beam-beam interaction in linear-colliders, is also known as beamstrahlung. For an introduction see [7].

The standard photon spectrum applies to homogeneous fields and remains a good approximation for magnetic fields which remain approximately constant over a the length ρ/γ, also known as the formation length for synchrotron radiation. Short magnets and edge fields will result instead in more energetic photons than predicted by the standard spectrum.

We also note that short bunches of many particles will start to radiate coherently like a single particle of the equivalent charge at wavelengths which are longer than the bunch dimensions.

Low energy, long-wavelength synchrotron radiation may destructively interfere with conducting surfaces [8].

The soft part of the synchrotron radiation spectrum emitted by charged particles travelling through a medium will be modified for frequencies close to and lower than the plasma frequency [9].

18.4.3 Direct inversion and generation of the photon energy spectrum

The task is to find an algorithm that effectively transforms the flat distribution given by standard pseudo-random generators into the desired distribution proportional to the expressions given in Eqs. 18.13, 18.17. The transformation is obtained from the inverse F^{-1} of the cumulative distribution function $F(x) = \int_0^x f(t)dt$.

Leaving aside constant factors, the probability density function relevant for the photon energy spectrum is

$$\mathrm{SynRad}(x) = \int_x^\infty K_{5/3}(t)dt \ . \tag{18.17}$$

Numerical methods to evaluate $K_{5/3}$ are discussed in [10]. An efficient algorithm to evaluate the integral SynRad using Chebyshev polynomials is described in [11]. This has been used in an earlier version of the Monte Carlo generator for synchrotron radiation using approximate transformations and the rejection method [12].

The cumulative distribution function is the integral of the probability density function. Here we have

$$\mathrm{SynRadInt}(z) = \int_z^\infty \mathrm{SynRad}(x)\, dx \ , \tag{18.18}$$

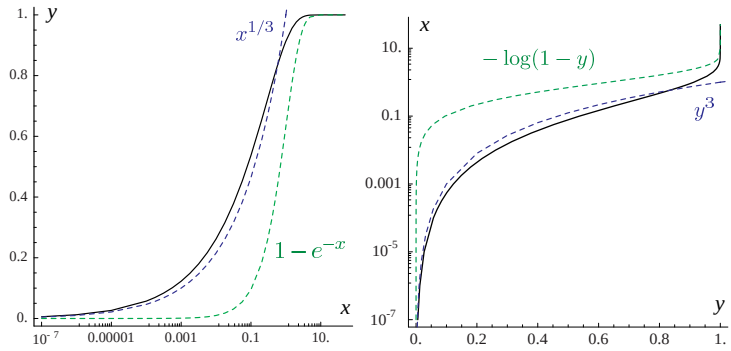

Figure 18.1: SynFracInt (left) and its inverse InvSynFracInt (right), on a $\log x$ scale. The functions $x^{1/3}$, y^3 and $1-e^{-x}$, $-\log(1-y)$ are shown as dashed lines.

with normalization

$$\text{SynRadInt}(0) = \int_0^\infty \text{SynRad}(x)\,dx \;= \frac{5\pi}{3}\,, \tag{18.19}$$

such that $\frac{3}{5\pi}\text{SynRadInt}(x)$ gives the fraction of photons above x.

It is possible to directly obtain the desired distribution with a fast and accurate algorithm using an analytical description based on simple transformations and Chebyshev polynomials. This approach is used here.

We now describe in some detail how the analytical description was obtained. For more details see [13].

It turned out to be convenient to start from the normalized complement rather then Eq. 18.18 directly, that is

$$\text{SynFracInt}(x) = \frac{3}{5\pi}\int_0^x \int_x^\infty K_{5/3}(t)dt\,dx = 1 - \frac{3}{5\pi}\,\text{SynRadInt}(x)\,, \tag{18.20}$$

which gives the fraction of photons below x.

Figure 18.1 shows on the left hand side $y = \text{SynFracInt(x)}$ and on the right hand side the inverse $x = \text{InvSynFracInt}(y)$ together with simple approximate functions. We can see, that SynFracInt can be approximated by $x^{1/3}$ for small arguments, and by $1-e^{-x}$ for large x. Consequently, we have for the inverse, $\text{InvSynFracInt}(y)$, which can be approximated for small y by y^3 and for large y by $-\log(1-y)$.

Good convergence for $\text{InvSynFracInt}(y)$ was obtained using Chebyshev polynomials combined with the approximate expressions for small and large arguments. For intermediate values, a Chebyshev polynomial can be used directly. Table 18.1 summarizes the expressions used in the different intervals.

Table 18.1: InvSynFracInt.

y	$x = \mathrm{InvSynFracInt}(y)$
$y < 0.7$	$y^3\,\mathrm{P_{Ch}}(y)$
$0.7 \leq y \leq 0.9999$	$\mathrm{P_{Ch}}(y)$
$y > 0.9999$	$-\log(1-y)\mathrm{P_{Ch}}(-\log(1-y))$

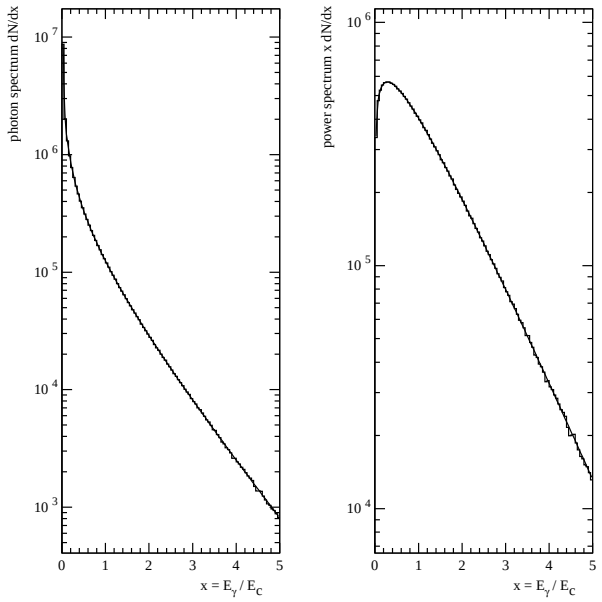

Figure 18.2: Comparison of the exact (smooth curve) and generated (histogram) spectra for 2×10^7 events. The photon spectrum is shown on the left and the power spectrum on the right side.

The procedure for Monte Carlo simulation is to generate y at random uniformly distributed between 0 at 1, as provided by standard random generators, and then to calculate the energy x in units of the critical energy according to $x = \mathrm{InvSynFracInt}(y)$.

The numerical accuracy of the energy spectrum presented here is about 14 decimal places, close to the machine precision. Fig. 18.2 shows a comparison of generated and expected spectra. A Geant4 display of an electron moving in a magnetic field radiating synchrotron photons is presented in Fig. 18.3

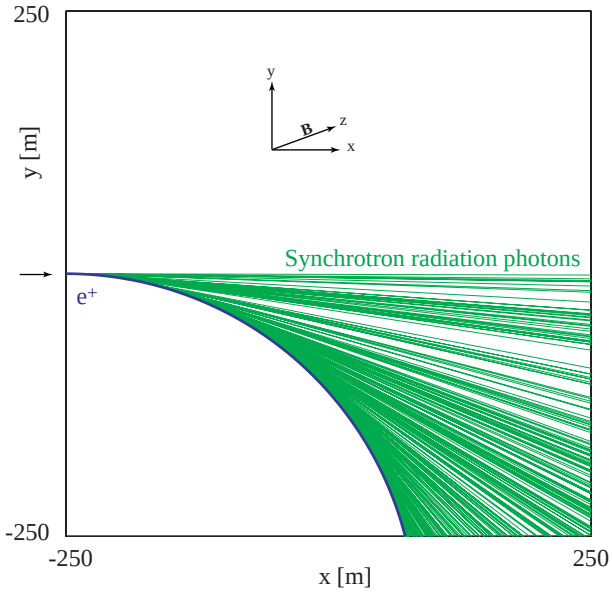

Figure 18.3: Geant4 display. 10 GeV e^+ moving initially in x-direction, bends downwards on a circular path by a 0.1 T magnetic field in z-direction.

18.4.4 Properties of the Power Spectra

The normalised probability function describing the photon energy spectrum is

$$n_\gamma(x) = \frac{3}{5\pi} \int_x^\infty K_{5/3}(t) dt \; . \tag{18.21}$$

$n_\gamma(x)$ gives the fraction of photons in the interval x to $x + dx$, where x is the photon energy in units of the critical energy. The first moment or mean value is

$$\mu = \int_0^\infty x \, n_\gamma(x) \, dx = \frac{8}{15\sqrt{3}} \; . \tag{18.22}$$

implying that the mean photon energy is $\frac{8}{15\sqrt{3}} = 0.30792$ of the critical energy.

The second moment about the mean, or variance, is

$$\sigma^2 = \int_0^\infty (x - \mu)^2 \, n_\gamma(x) \, dx = \frac{211}{675} \; , \tag{18.23}$$

and the r.m.s. value of the photon energy spectrum is $\sigma = \sqrt{\frac{211}{675}} = 0.5591$.

The normalised power spectrum is

$$P_\gamma(x) = \frac{9\sqrt{3}}{8\pi}\, x \int_x^\infty K_{5/3}(t)dt \ . \tag{18.24}$$

$P_\gamma(x)$ gives the fraction of the power which is radiated in the interval x to $x + dx$.

Half of the power is radiated below the critical energy

$$\int_0^1 P_\gamma(x)\, dx = 0.5000 \tag{18.25}$$

The mean value of the power spectrum is

$$\mu = \int_0^\infty x\, P_\gamma(x)\, dx = \frac{55}{24\,\sqrt{3}} = 1.32309 \ . \tag{18.26}$$

The variance is

$$\sigma^2 = \int_0^\infty (x-\mu)^2\, P_\gamma(x)\, dx = \frac{2351}{1728} \ , \tag{18.27}$$

and the r.m.s. width is $\sigma = \sqrt{\frac{2351}{1728}} = 1.16642$.

18.4.5 Status of This Document

08.06.06 created by H. Burkhardt
10.12.10 minor edition by V. Ivanchenko

Bibliography

[1] A.A.Sokolov and I.M.Ternov, *Radiation from Relativistic Electrons*, Amer. Inst of Physics, 1986.

[2] J. Jackson, *Classical Electrodynamics*. John Wiley & Sons, third ed., 1998.

[3] A. Hofmann, *The Physics of Synchrotron Radiation*. Cambridge University Press, 2004.

[4] H. Burkhardt, "Reminder of the Edge Effect in Synchrotron Radiation", LHC Project Note 172, CERN Geneva 1998.

[5] F. Herlach, R. McBroom, T. Erber, J. .Murray, and R. Gearhart, "Experiments with Megagauss targets at SLAC", IEEE Trans Nucl Sci, NS 18, 3 (1971) 809-814.

[6] T. Erber, G. B. Baumgartner, D. White, and H. G. Latal, "Megagauss Bremsstrahlung and Radiation Reaction", in *Batavia 1983, proceedings, High Energy Accelerators*, 372-374.

[7] P. Chen, "An Introduction to Beamstrahlung and Disruption", in *Frontiers of Particle Beams*, M. Month and S. Turner, eds., Lecture Notes in Physics 296, pp. 481–494. Springer-Verlag, 1986.

[8] J. B. Murphy, S. Krinsky, and R. L. Gluckstern, "Longitudinal wakefield for an electron moving on a circular orbit", *Part. Acc.* 57 (1997) 9.

[9] V. M. Grichine, "Radiation of accelerated charge in absorbing medium", CERN-OPEN-2002-056.

[10] Y. Luke, "The special functions and their approximations", New York, NY: Academic Press, 1975.- 585 p.

[11] H.H.Umstätter. CERN/PS/SM/81-13, CERN Geneva 1981.

[12] H. Burkhardt, "Monte Carlo Generator for Synchrotron Radiation", LEP Note 632, CERN, December, 1990.

[13] H. Burkhardt, "Monte Carlo Generation of the Energy Spectrum of Synchrotron Radiation", to be published as CERN-AB and EuroTeV report.

Chapter 19

Optical Photons

19.1 Interactions of optical photons

Optical photons are produced when a charged particle traverses:

1. a dielectric material with velocity above the Čerenkov threshold;
2. a scintillating material.

19.1.1 Physics processes for optical photons

A photon is called optical when its wavelength is much greater than the typical atomic spacing, for instance when $\lambda \geq 10nm$ which corresponds to an energy $E \leq 100eV$. Production of an optical photon in a HEP detector is primarily due to:

1. Čerenkov effect;
2. Scintillation.

Optical photons undergo three kinds of interactions:

1. Elastic (Rayleigh) scattering;
2. Absorption;
3. Medium boundary interactions.

Rayleigh scattering

For optical photons Rayleigh scattering is usually unimportant. For $\lambda = .2\mu m$ we have $\sigma_{Rayleigh} \approx .2b$ for N_2 or O_2 which gives a mean free path of $\approx 1.7km$ in air and $\approx 1m$ in quartz. Two important exceptions are aerogel, which is used as a Čerenkov radiator for some special applications and large water Čerenkov detectors for neutrino detection.

The differential cross section in Rayleigh scattering, $d\sigma/d\Omega$, is proportional to $1 + \cos^2\theta$, where θ is the polar angle of the new polarization with respect to the old polarization.

Absorption

Absorption is important for optical photons because it determines the lower λ limit in the window of transparency of the radiator. Absorption competes with photo-ionization in producing the signal in the detector, so it must be treated properly in the tracking of optical photons.

Medium boundary effects

When a photon arrives at the boundary of a dielectric medium, its behaviour depends on the nature of the two materials which join at that boundary:

- Case dielectric → dielectric.
  The photon can be transmitted (refracted ray) or reflected (reflected ray). In case where the photon can only be reflected, total internal reflection takes place.

- Case dielectric → metal.
  The photon can be absorbed by the metal or reflected back into the dielectric. If the photon is absorbed it can be detected according to the photoelectron efficiency of the metal.

- Case dielectric → black material.
  A black material is a tracking medium for which the user has not defined any optical property. In this case the photon is immediately absorbed undetected.

19.1.2 Photon polarization

The photon polarization is defined as a two component vector normal to the direction of the photon:

$$\begin{pmatrix} a_1 e^{i\Phi_1} \\ a_2 e^{i\Phi_2} \end{pmatrix} = e^{\Phi_o} \begin{pmatrix} a_1 e^{i\Phi_c} \\ a_2 e^{-i\Phi_c} \end{pmatrix}$$

where $\Phi_c = (\Phi_1 - \Phi_2)/2$ is called circularity and $\Phi_o = (\Phi_1 + \Phi_2)/2$ is called overall phase. Circularity gives the left- or right-polarization characteristic of the photon. RICH materials usually do not distinguish between the two polarizations and photons produced by the Čerenkov effect and scintillation are linearly polarized, that is $\Phi_c = 0$.

The overall phase is important in determining interference effects between coherent waves. These are important only in layers of thickness comparable with the wavelength, such as interference filters on mirrors. The effects of such coatings can be accounted for by the empirical reflectivity factor for the surface, and do not require a microscopic simulation. GEANT4 does not keep track of the overall phase.

Vector polarization is described by the polarization angle $\tan \Psi = a_2/a_1$. Reflection/transmission probabilities are sensitive to the state of linear polarization, so this has to be taken into account. One parameter is sufficient to

describe vector polarization, but to avoid too many trigonometrical transformations, a unit vector perpendicular to the direction of the photon is used in GEANT4. The polarization vector is a data member of `G4DynamicParticle`.

19.1.3 Tracking of the photons

Optical photons are subject to in flight absorption, Rayleigh scattering and boundary action. As explained above, the status of the photon is defined by two vectors, the photon momentum ($\vec{p} = \hbar\vec{k}$) and photon polarization ($\vec{e}$). By convention the direction of the polarization vector is that of the electric field. Let also $\vec{u}$ be the normal to the material boundary at the point of intersection, pointing out of the material which the photon is leaving and toward the one which the photon is entering. The behaviour of a photon at the surface boundary is determined by three quantities:

1. refraction or reflection angle, this represents the kinematics of the effect;
2. amplitude of the reflected and refracted waves, this is the dynamics of the effect;
3. probability of the photon to be refracted or reflected, this is the quantum mechanical effect which we have to take into account if we want to describe the photon as a particle and not as a wave.

As said above, we distinguish three kinds of boundary action, dielectric $\rightarrow$ black material, dielectric $\rightarrow$ metal, dielectric $\rightarrow$ dielectric. The first case is trivial, in the sense that the photon is immediately absorbed and it goes undetected.

To determine the behaviour of the photon at the boundary, we will at first treat it as an homogeneous monochromatic plane wave:

$$\vec{E} = \vec{E}_0 e^{i\vec{k}\cdot\vec{x} - i\omega t}$$

$$\vec{B} = \sqrt{\mu\epsilon}\frac{\vec{k}\times\vec{E}}{k}$$

Case dielectric $\rightarrow$ dielectric

In the classical description the incoming wave splits into a reflected wave (quantities with a double prime) and a refracted wave (quantities with a single prime). Our problem is solved if we find the following quantities:

$$\vec{E}' = \vec{E}'_0 e^{i\vec{k}'\cdot\vec{x} - i\omega t}$$

$$\vec{E}'' = \vec{E}_0'' e^{i\vec{k}''\cdot\vec{x} - i\omega t}$$

For the wave numbers the following relations hold:

$$|\vec{k}| = |\vec{k}''| = k = \frac{\omega}{c}\sqrt{\mu\epsilon}$$
$$|\vec{k}'| = k' = \frac{\omega}{c}\sqrt{\mu'\epsilon'}$$

Where the speed of the wave in the medium is $v = c/\sqrt{\mu\epsilon}$ and the quantity $n = c/v = \sqrt{\mu\epsilon}$ is called refractive index of the medium. The condition that the three waves, refracted, reflected and incident have the same phase at the surface of the medium, gives us the well known Fresnel law:

$$(\vec{k}\cdot\vec{x})_{surf} = (\vec{k}'\cdot\vec{x})_{surf} = (\vec{k}''\cdot\vec{x})_{surf}$$

$$k\sin i = k'\sin r = k''\sin r'$$

where i, r, r' are, respectively, the angle of the incident, refracted and reflected ray with the normal to the surface. From this formula the well known condition emerges:

$$i = r'$$
$$\frac{\sin i}{\sin r} = \sqrt{\frac{\mu'\epsilon'}{\mu\epsilon}} = \frac{n'}{n}$$

The dynamic properties of the wave at the boundary are derived from Maxwell's equations which impose the continuity of the normal components of $\vec{D}$ and $\vec{B}$ and of the tangential components of $\vec{E}$ and $\vec{H}$ at the surface boundary. The resulting ratios between the amplitudes of the the generated waves with respect to the incoming one are expressed in the two following cases:

1. a plane wave with the electric field (polarization vector) perpendicular to the plane defined by the photon direction and the normal to the boundary:

$$\frac{E_0'}{E_0} = \frac{2n\cos i}{n\cos i = \frac{\mu}{\mu'}n'\cos r} = \frac{2n\cos i}{n\cos i + n'\cos r}$$
$$\frac{E_0''}{E_0} = \frac{n\cos i - \frac{\mu}{\mu'}n'\cos r}{n\cos i + \frac{\mu}{\mu'}n'\cos r} = \frac{n\cos i - n'\cos r}{n\cos i + n'\cos r}$$

   where we suppose, as it is legitimate for visible or near-visible light, that $\mu/\mu' \approx 1$;

2. a plane wave with the electric field parallel to the above surface:

$$\frac{E_0'}{E_0} = \frac{2n\cos i}{\frac{\mu}{\mu'}n'\cos i + n\cos r} = \frac{2n\cos i}{n'\cos i + n\cos r}$$
$$\frac{E_0''}{E_0} = \frac{\frac{\mu}{\mu'}n'\cos i - n\cos r}{\frac{\mu}{\mu'}n'\cos i + n\cos r} = \frac{n'\cos i - n\cos r}{n'\cos i + n\cos r}$$

with the same approximation as above.

We note that in case of photon perpendicular to the surface, the following relations hold:

$$\frac{E_0'}{E_0} = \frac{2n}{n'+n} \qquad \frac{E_0''}{E_0} = \frac{n'-n}{n'+n}$$

where the sign convention for the parallel field has been adopted. This means that if $n' > n$ there is a phase inversion for the reflected wave.

Any incoming wave can be separated into one piece polarized parallel to the plane and one polarized perpendicular, and the two components treated accordingly.

To maintain the particle description of the photon, the probability to have a refracted or reflected photon must be calculated. The constraint is that the number of photons be conserved, and this can be imposed via the conservation of the energy flux at the boundary, as the number of photons is proportional to the energy. The energy current is given by the expression:

$$\vec{S} = \frac{1}{2}\frac{c}{4\pi}\sqrt{\mu\epsilon}\vec{E}\times\vec{H} = \frac{c}{8\pi}\sqrt{\frac{\epsilon}{\mu}}E_0^2\hat{k}$$

and the energy balance on a unit area of the boundary requires that:

$$\vec{S}\cdot\vec{u} = \vec{S}'\cdot\vec{u} - \vec{S}''\cdot\vec{u}$$
$$S\cos i = S'cosr + S''cosi$$
$$\frac{c}{8\pi}\frac{1}{\mu}nE_0^2\cos i = \frac{c}{8\pi}\frac{1}{\mu'}n'E_0'^2\cos r + \frac{c}{8\pi}\frac{1}{\mu}nE_0''^2\cos i$$

If we set again $\mu/\mu' \approx 1$, then the transmission probability for the photon will be:

$$T = (\frac{E_0'}{E_0})^2\frac{n'\cos r}{n\cos i}$$

and the corresponding probability to be reflected will be $R = 1 - T$.

In case of reflection, the relation between the incoming photon $(\vec{k}, \vec{e})$, the refracted one $(\vec{k}', \vec{e}')$ and the reflected one $(\vec{k}'', \vec{e}'')$ is given by the following relations:

$$\vec{q} = \vec{k} \times \vec{u}$$

$$\vec{e}_\perp = (\frac{\vec{e} \cdot \vec{q}}{|\vec{q}|}) \frac{\vec{q}}{|\vec{q}|}$$

$$\vec{e}_\parallel = \vec{e} - \vec{e}_\perp$$

$$e'_\parallel = e_\parallel \frac{2n \cos i}{n' \cos i + n \cos r}$$

$$e'_{\perp|} = e_\perp \frac{2n \cos i}{n \cos i + n' \cos r}$$

$$e''_\parallel = \frac{n'}{n} e'_\parallel - e_\parallel$$

$$e''_\perp = e'_\perp - e_\perp$$

After transmission or reflection of the photon, the polarization vector is re-normalized to 1. In the case where $\sin r = n \sin i / n' > 1$ then there cannot be a refracted wave, and in this case we have a total internal reflection according to the following formulas:

$$\vec{k}'' = \vec{k} - 2(\vec{k} \cdot \vec{u})\vec{u}$$

$$\vec{e}'' = -\vec{e} + 2(\vec{e} \cdot \vec{u})\vec{u}$$

Case dielectric → metal

In this case the photon cannot be transmitted. So the probability for the photon to be absorbed by the metal is estimated according to the table provided by the user. If the photon is not absorbed, it is reflected.

19.1.4 Mie Scattering in Henyey-Greensterin Approximation

(Author: X. Qian, 2010-07-04)

Mie Scattering (or Mie solution) is an analytical solution of Maxwell's equations for the scattering of optical photon by spherical particles. The general introduction of Mie scattering can be found in Ref. [2]. The analytical express of Mie Scattering are very complicated since they are a series

sum of Bessel functions [3]. Therefore, the exact expression of Mie scattering is not suitable to be included in the Monte Carlo simulation.

One common approximation made is called "Henyey-Greensterin" [5]. It has been used by Vlasios Vasileiou in GEANT4 simulation of Milagro experiment [6]. In the HG approximation,

$$\frac{d\sigma}{d\Omega} \sim \frac{1-g^2}{(1+g^2-2g\cos(\theta))^{3/2}} \tag{19.1}$$

where

$$d\Omega = d\cos(\theta)d\phi \tag{19.2}$$

and $g =< \cos(\theta) >$ can be viewed as a free constant labeling the angular distribution.

Therefore, the normalized density function of HG approximation can be expressed as:

$$P(\cos(\theta_0)) = \frac{\int_{-1}^{\cos(\theta_0)} \frac{d\sigma}{d\Omega} d\cos(\theta)}{\int_{-1}^{1} \frac{d\sigma}{d\Omega} d\cos(\theta)} = \frac{1-g^2}{2g}\left(\frac{1}{(1+g^2-2g\cos(\theta_0))} - \frac{1}{1+g}\right) \tag{19.3}$$

Therefore,

$$\cos(\theta) = \frac{1}{2g}\cdot(1+g^2-(\frac{1-g^2}{1-g+2g\cdot p})^2) = 2p\frac{(1+g)^2(1-g+gp)}{(1-g+2gp)^2} - 1 \tag{19.4}$$

where p is a uniform random number between 0 and 1.

Similarly, the backward angle where $\theta_b = \pi - \theta_f$ can also be simulated by replacing θ_f to θ_b. Therefore the final differential cross section can be viewed as:

$$\frac{d\sigma}{d\Omega} = r\frac{d\sigma}{d\Omega}(\theta_f, g_f) + (1-r)\frac{d\sigma}{d\Omega}(\theta_b, g_b) \tag{19.5}$$

This is the exact approach used in Ref. [4]. Here r is the ratio factor between the forward angle and backward angle.

In implementing the above MC method into GEANT4, the treatment of polarization and momentum are similar to that of Rayleigh scattering. We require the final polarization direction to be perpendicular to the momentum direction. We also require the final momentum, initial polarization and final polarization to be in the same plane.

Bibliography

[1] J.D. Jackson, *Classical Electrodynamics*, J. Wiley & Sons Inc., New York, 1975.

[2] http://en.wikipedia.org/wiki/Mie_theory

[3] http://farside.ph.utexas.edu/teaching/jk1/lectures/node103.html

[4] Vlasios Vasileiou *private communication.*

[5] G. Zhao and X. Sun Prog. in Elec. Res. Sym. Proc. Xi'an, China, 1449, (March 22nd 2010).

[6] http://umdgrb.umd.edu/cosmic/milagro.html

Chapter 20

Phonon-Lattice Interactions

20.1 Introduction

Phonons are quantized vibrations in solid-state lattices or amorphous solids, of interest to the low-temperature physics community. Phonons are typically produced when a heat source excites lattice vibrations, or when energy from radiation is deposited through elastic interactions with nuclei of lattice atoms. Below 1 K, thermal phonons are highly suppressed; this leaves only *acoustic* and *optical* phonons to propagate.

There is significant interest from the condensed-matter community and direct dark-matter searches to integrate phonon production and propagation with the excellent nuclear and electromagnetic simulations available in Geant4. An effort in this area began in 2011 by the SuperCDMS Collaboration[1] and is continuing; initial developments in phonon propagation have been incorporated into the Geant4 toolkit for Release 10.0.

As quasiparticles, phonons at low temparatures may be treated in the Geant4 particle-tracking framework, carrying well defined momenta, and propagating in specific directions until they interact[1]. The present implementation handles ballistic transport, scattering with mode-mixing, and anharmonic downcoversion[2][3][4] of acoustic phonons. Optical phonon transport and interactions between propagating phonons and thermal background phonons are not treated.

Production of phonons from charged particle energy loss or by photon-lattice interactions are in development, but are not yet included in the Geant4 toolkit.

20.2 Phonon Propagation

The propagation of phonons is governed by the three-dimensional wave equation[5]:

$$\rho\omega^2 e_i = C_{ijlm} k_j k_m e_l \tag{20.1}$$

where ρ is the crystal mass density and C_{ijml} is the elasticity tensor; the phonon is described by its wave vector $\vec{k}$, frequency ω and polarization $\vec{e}$.

For a given wave vector $\vec{k}$, Eq. 20.1 has three eigenvalues ω and three polarization eigenvectors $\vec{e}$. The three polarization states are labelled *Fast Transverse (FT)*, *Slow Transverse (ST)* and *Longitudinal (L)*. The direction and speed of propagation of the phonon are given by the *group velocity* $\vec{v_g} = d\omega/dk$, which may be computed from Eq. 20.1:

$$\vec{v_g} = \frac{d\omega(\vec{k})}{d\vec{k}} = \nabla_k \omega(\vec{k}) \ . \tag{20.2}$$

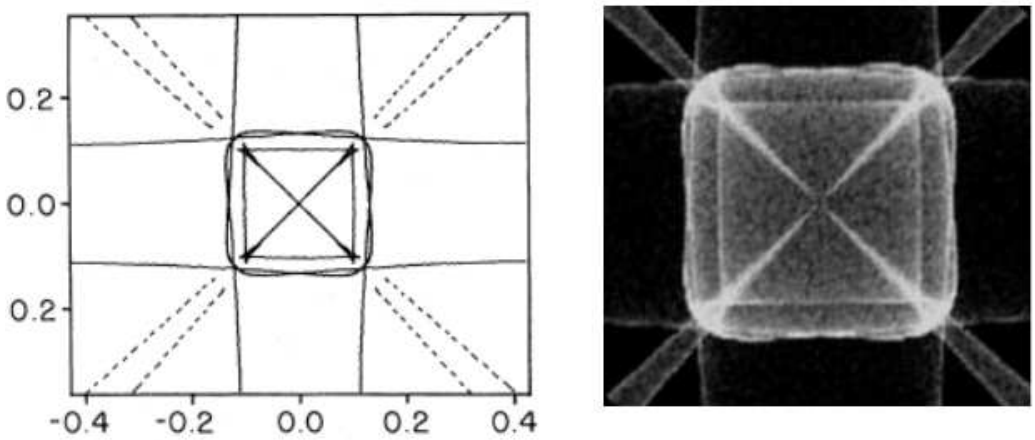

Figure 20.1: **Left:** outline of phonon caustics in germanium as predicted by Nothrop and Wolfe [6]. **Right:** Phonon caustics as simulated using the Geant4 phonon transport code.

Since the lattice tensor C_{ijml} is anisotropic in general, the phonon group velocity $\vec{v_g}$ is not parallel to the momentum vector $\hbar\vec{k}$. This anisotropic transport leads to a focussing effect, where phonons are driven to directions which correspond to the highest density of eigenvectors $\vec{k}$. Experimentally, this is seen[6] as caustics in the energy distribution resulting from a point-like phonon source isotropic in $\vec{k}$-space, as shown in Figure 20.1.

20.3 Lattice Parameters

20.4 Scattering and Mode Mixing

In a pure crystal, *isotope scattering* occurs when a phonon interacts with an isotopic substitution site in the lattice. We treat it as an elastic scattering process, where the phonon momentum direction (wave vector) and polarization are both randomized. The scattering rate for a phonon of frequency ν ($\omega/2\pi$) is given by[3]

$$\Gamma_{scatter} = B\nu^4 \tag{20.3}$$

where $\Gamma_{scatter}$ is the number of scattering events per unit time, and B is a constant of proportionality derived from the elasticity tensor (see Eq. 11 and Table 1 in [4]). For germanium, $B = 3.67 \times 10^{-41}$ s^3. [4]

At each scattering event, the phonon polarziation may change between

any of the three states L, ST, FT. The branching ratios for the polarizations are determined by the relative density of allowed states in the lattice. This process is often referred to as *mode mixing*.

20.5 Anharmonic Downconversion

An energetic phonon may interact in the crystal to produce two phonons of reduced energy. This *anharmonic downconversion* conserves energy ($\vec{k} = \vec{k}' + \vec{k}''$), but not momentum, since momentum is exchanged with the bulk lattice. In principle, all three polarization states may decay through downconversion. In practice, however, the rate for L-phonons completely dominates the energy evolution of the system, with downconversion events from other polarization states being negligigible[3].

The total downconversion rate Γ_{anh} for an L-phonon of frequency ν is given by[3]

$$\Gamma_{anh} = A\nu^5 \tag{20.4}$$

where (as in Eq. 20.3) A is a constant of proportionality derived from the elasticity tensor (see Eq. 11 and Table 1 in [4]). For germanium, $A = 6.43 \times 10^{-55}$ s^4. [4]

Downconversion may produce either two transversely polarized phonons, or one transverse and one longitudinal. The relative rates are determined by dynamical constants derived from the elasticity tensor C_{ijkl}.

As can be seen from Eqs. 20.3 and 20.4, phonon interactions depend strongly on energy $\hbar\nu$. High energy phonons ($\nu \sim$ THz) start out in a diffusive regime with high isotope scattering and downconversion rates and mean free paths of order microns. After several such interactions, mean free paths increase to several centimeters or more. This transition from a diffuse to a ballistic transport mode is commonly referred to as "quasi-diffuse" and it controls the time evolution of phonon heat pulses.

Simulation of heat pulse propagation using our Geant4 transport code has been described previously[1] and shows good agreement with experiment.

20.6 References

Bibliography

[1] D. Brandt et al., *Journal of Low Temperature Physics* **167**, 485–490, (2012)

[2] S. Tamura, *J. Lo. T. Phys.* **93**, 433, (1993)

[3] S. Tamura, *Phys. Rev. B.* **48**, 13502, (1993)

[4] S. Tamura, *Phys. Rev. B.* **31**, (1985)

[5] J.P. Wolfe, *Imaging Phonons, Chapter 2*,42, Cambridge University Press, United Kingdom (1998)

[6] G.A. Nothrop and J.P. Wolfe, *Phys. Rev. Lett.* **19**, 1424, (1979)

Chapter 21

Precision multi-scale modeling

21.1 Overview

The physics simulation tools grouped in this domain reflect ongoing research in key issues of particle transport:

- multi-scale simulation and its implications on condensed and discrete transport schemes [1], [2], [3], [4], [5],
- epistemic uncertainties in physics models and parameters [6],
- innovative software design techniques [7], [9], [8], [10], [11] in support of physics modeling,
- the assessment of the accuracy of data libraries used by Monte Carlo simulation codes [12], [13], [14], [15], [16], [17],
- precision models of particle interactions with matter, quantitatively assessed through comparison with experimental measurements of the model constituents [1], [16], [17].

The main features of the simulation tools developed in this research context, which are so far released in Geant4, are summarized below. They concern impact ionisation by protons and α particles, and the following particle induced X-ray emission (PIXE), which are encompassed in the Geant4 "electromagnetic/pii" package.

21.2 Impact ionisation by hadrons and PIXE

Despite the simplicity of its nature as a physical effect, PIXE represents a conceptual challenge for general-purpose Monte Carlo codes, since it involves an intrinsically discrete effect (the atomic relaxation) intertwined with a process (ionisation) affected by infrared divergence, therefore usually treated in Monte Carlo codes by means of con The largely incomplete knowledge of ionisation cross sections by hadron impact, limited to the innermost atomic shells both as theoretical calculations and experimental measurements, further complicates the achievement of a conceptually consistent description of this process.

Early developments of proton and α particle impact ionisation cross sections in Geant4 are reviewed in a detailed paper devoted to PIXE simulation with Geant4 [1]. This article also presents new, extensive developments for PIXE simulation, their validation with respect to experimental data and the first Geant4-based simulation involving PIXE in a concrete experimental use

case: the optimization of the graded shielding of the X-ray detectors of the eROSITA [18] mission. The new developments described in [1] are released in Geant4 in the *pii* package (in *source/processes/electromagnetic/pii*).

The developments for PIXE simulation described in [1] provide a variety of proton and α particle cross sections for the ionisation of K, L and M shells:

- theoretical calculations based on the ECPSSR [19] model and its variants (with Hartree-Slater corrections [20], with the united atom approximation [21] and specialized for high energies [22]),
- theoretical calculations based on plane wave Born approximation (PWBA),
- empirical models based on fits to experimental data collected by Paul and Sacher [23] (for protons, K shell), Paul and Bolik [24] (for α, K shell), Kahoul et al. [25]) (for protons, K, shell), Miyagawa et al. [26], Orlic et al. [27] and Sow et al. [28] for L shell.

The cross section models available in Geant4 are listed in Table 21.1.

The calculation of cross sections in the course of the simulation is based on the interpolation of tabulated values, which are collected in a data library. The tabulations corresponding to theoretical calculations span the energy range between 10 keV and 10 GeV; empirical models are tabulated consistently with the energy range of validity documented by their authors, that corresponds to the range of the data used in the empirical fits and varies along with the atomic number and sub-shell.

ECPSSR tabulations have been produced using the ISICS software [29, 30], 2006 version; an extended version, kindly provided by ISICS author S. Cipolla [31], has been exploited to produce tabulations associated with recent high energy modelling developments [22].

An example of the characteristics of different cross section models is illustrated in Fig. 21.1. Fig. 21.2 shows various cross section models for the ionisation of carbon K shell by proton, compared to experimental data reported in [23].

The implemented cross section models have been subject to rigorous statistical analysis to evaluate their compatibility with experimental measurements reported in [23], [32], [33] and to compare the relative accuracy of the various modelling options.

The validation process involved two stages: first goodness-of-fit analysis based on the χ^2 test to evaluate the hypothesis of compatibility with experimental data, then categorical analysis exploiting contingency tables to determine whether the various modelling options differ significantly in accuracy. Contingency tables were analyzed with the χ^2 test and with Fishers exact test.

Table 21.1: Ionisation cross section models available for PIXE simulation with Geant4

Protons, K shell	
Model	Z range
ECPSSR	6-92
ECPSSR High Energy	6-92
ECPSSR Hartree-Slater	6-92
ECPSSR United Atom	6-92
ECPSSR reference [23]	6-92
PWBA	6-92
Paul and Sacher	6-92
Kahoul et al.	6-92
Protons, L shell	
Model	Z range
ECPSSR	6-92
ECPSSR United Atom	6-92
PWBA	6-92
Miyagawa et al.	40-92
Orlic et al.	43-92
Sow et al.	43-92
Protons, M shell	
Model	Z range
ECPSSR	6-92
PWBA	6-92
α, K shell	
Model	Z range
ECPSSR	6-92
ECPSSR Hartree-Slater	6-92
ECPSSR reference [24]	6-92
PWBA	6-92
Paul and Bolik	6-92
α, L and M shell	
Model	Z range
ECPSSR	6-92
PWBA	6-92

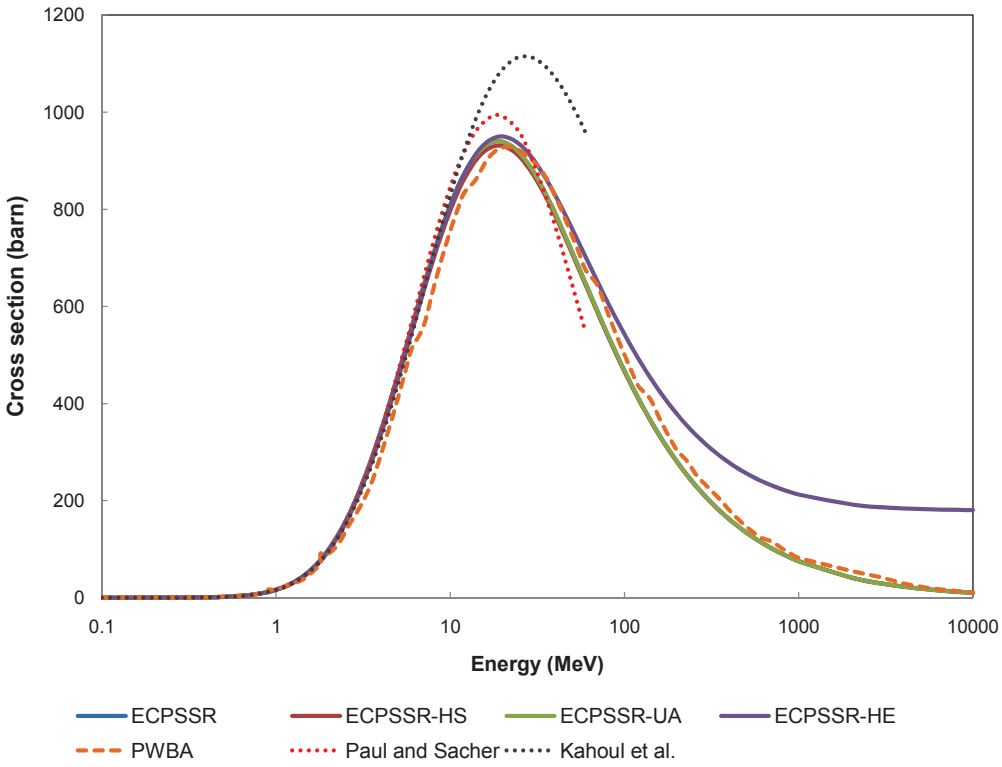

Figure 21.1: Cross section for the ionisation of copper K shell by proton impact according to the various implemented modeling options: ECPSSR model, ECPSSR model with "united atom" (UA) approximation, Hartree-Slater (HS) corrections and specialized for high energies (HE); plane wave Born approximation (PWBA); empirical models by Paul and Sacher and Kahoul et al. The curves reproducing some of the model implementations can be hardly distinguished in the plot due to their similarity.

The complete set of validation results is documented in [1]. Only the main ones are summarized here; Geant4 users interested in detailed results, like the accuracy of different cross section models for specific target elements, should should refer to [1] for detailed information.

Regarding the K shell, the statistical analysis identified the ECPSSR model with Hartree-Slater correction as the most accurate in the energy range up to approximately 10 MeV; at higher energies the ECPSSR model in its plain formulation or the empirical Paul and Sacher one (within its range of applicability) exhibit the best performance. The scarceness of high energy data prevents a definitive appraisal of the ECPSSR specialization for high energies.

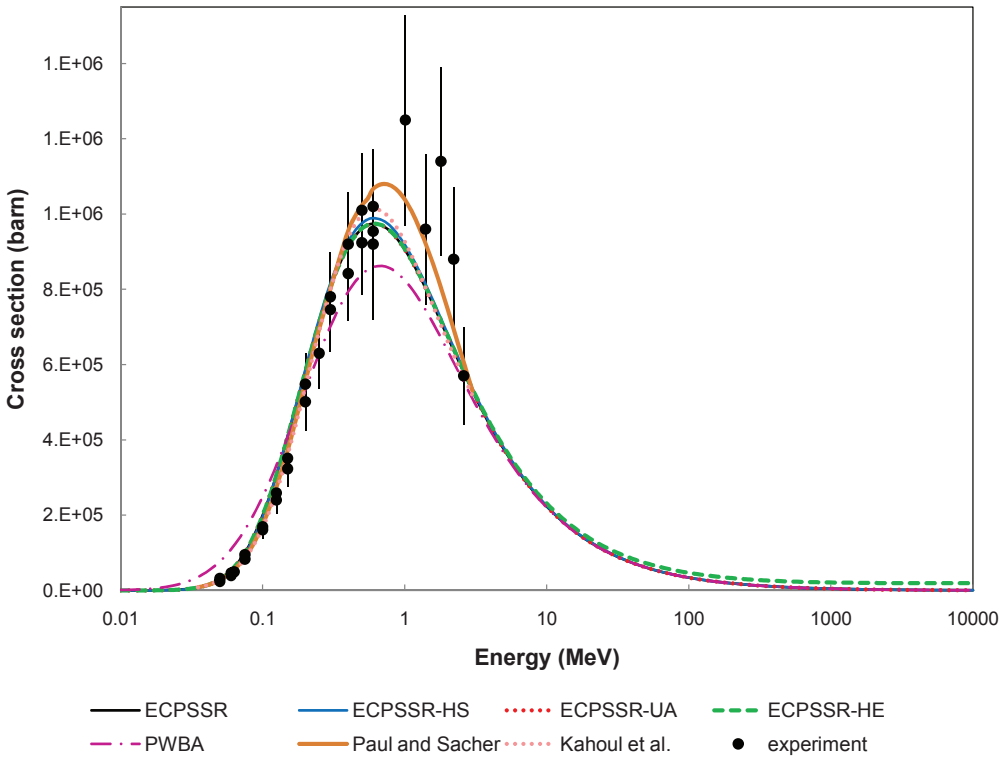

Figure 21.2: Cross section for the ionisation of carbon K shell by proton impact according to the various implemented modeling options, and comparison with experimental data [23]: ECPSSR model, ECPSSR model with "united atom" (UA) approximation, Hartree-Slater (HS) corrections and specialized for high energies (HE); plane wave Born approximation (PWBA); empirical models by Paul and Sacher and Kahoul et al. The curves reproducing some of the model implementations can be hardly distinguished in the plot due to their similarity.

Regarding the L shell, the ECPSSR model with "united atom" approximation exhibits the best accuracy among the various implemented models; its compatibility with experimental measurements at 95% confidence level ranges from approximately 90% of the test cases for the L_3 sub-shell to approximately 65% for the L_1 sub-shell. According to the results of the categorical analysis, the ECPSSR model in its original formulation can be considered an equivalently accurate alternative. The Orlic et al. model exhibits the worst accuracy with respect to experimental data; its accuracy is significantly different from the one of the ECPSSR model in the united atom variant.

In the current Geant4 release the implementation of the hadron impact ionisation process (*G4ImpactIonisation*) is largely based on the original *G4hLowEnergyIonisation* process [34],[35], [36]. Thanks to the adopted component-based software design, the simulation of PIXE currently exploits the existing Geant4 atomic relaxation [37] component to produce secondary X-rays resulting from impact ionisation.

Bibliography

[1] M. G. Pia, G. Weidenspointner, M. Augelli, L. Quintieri, P. Saracco, M. Sudhakar, and A. Zoglauer, "PIXE simulation with Geant4", *IEEE Trans. Nucl. Sci.*, vol. 56, no. 6, pp. 3614-3649, 2009.

[2] M. G. Pia et al., "R&D for co-working condensed and discrete transport methods in Geant4 kernel", in *Proc. Int. Conf. on Mathematics, Computational Methods & Reactor Physics (M&C 2009)*, New York, 2009.

[3] M. Augelli et al., "Geant4-related R&D for new particle transport methods", in *Proc. IEEE Nucl. Sci. Symp.*, 2009.

[4] M. Augelli et al., "Environmental Adaptability and Mutants: Exploring New Concepts in Particle Transport for Multi-Scale Simulation", in *Proc. IEEE Nucl. Sci. Symp.*, 2010.

[5] M. Augelli et al., "Environmental adaptability and mutants: exploring new concepts in particle transport for multi-scale simulation", in *Proc. Int. Conf. on Supercomp. in Nucl. Appl. and Monte Carlo (SNA + MC2010)*, 2010.

[6] M. G. Pia, M. Begalli, A. Lechner, L. Quintieri, and P. Saracco, "Physics-related epistemic uncertainties of proton depth dose simulation", *IEEE Trans. Nucl. Sci.*, vol. 57, no. 5, pp. , 2010.

[7] M. G. Pia et al., "Design and performance evaluations of generic programming techniques in a R&D prototype of Geant4 physics", *J. Phys.: Conf. Ser.*, vol. 219, pp. 042019, 2009.

[8] M. Augelli et al., "Research in Geant4 electromagnetic physics design, and its effects on computational performance and quality assurance", in *Proc. IEEE Nucl. Sci. Symp.*, 2009.

[9] M. G. Pia et al., "New techniques in Monte Carlo simulation: experience with a prototype of generic programming application to Geant4 physics

processes", in *Proc. Int. Conf. on Supercomp. in Nucl. Appl. and Monte Carlo (SNA + MC2010)*, 2010.

[10] M. Han, C. H. Kim, L. Moneta, M. G. Pia, and H. Seo, "Physics data management tools: computational evolutions and benchmarks", in *Proc. Int. Conf. on Supercomp. in Nucl. Appl. and Monte Carlo (SNA + MC2010)*, 2010.

[11] M. Han, C. H. Kim, L. Moneta, M. G. Pia, and H. Seo, "Physics Data Management Tools for Monte Carlo Transport: Computational Evolutions and Benchmarks", in *Proc. IEEE Nucl. Sci. Symp.*, 2010.

[12] M. G. Pia, P. Saracco, M. Sudhakar, "Validation of radiative transition probability calculations", *IEEE Trans. Nucl. Sci.*, vol. 56, no. 6, pp. 3650-3661, 2009.

[13] H. Seo, M. G. Pia, M. Begalli, L. Quintieri, P. Saracco and C. H. Kim, "Atomic Parameters for Monte Carlo Transport Simulation: Survey, Validation and Induced Systematic Effects", in *Proc. IEEE Nucl. Sci. Symp.*, 2010.

[14] M. Augelli et al., "New Physics Data Libraries for Monte Carlo Transport", in *Proc. IEEE Nucl. Sci. Symp.*, 2010.

[15] M. Augelli et al., "Data libraries as a collaborative tool across Monte Carlo codes", in *Proc. Int. Conf. on Supercomp. in Nucl. Appl. and Monte Carlo (SNA + MC2010)*, 2010.

[16] H. Seo, M. G. Pia, P. Saracco and C. H. Kim, "Design, development and validation of electron ionisation models for nano-scale simulation", in *Proc. Int. Conf. on Supercomp. in Nucl. Appl. and Monte Carlo (SNA + MC2010)*, 2010.

[17] H. Seo, M. G. Pia, P. Saracco and C. H. Kim, "Ionisation Models for Nano-Scale Simulation", in *Proc. IEEE Nucl. Sci. Symp.*, 2010.

[18] P. Predehl et al., "eROSITA", in *Proc. of the SPIE*, vol. 6686, pp. 668617-668617-9, 2007.

[19] W. Brandt and G. Lapicki, "Energy-loss effect in inner-shell Coulomb ionization by heavy charged particles", *Phys. Rev.A*, vol. 23, pp. 1717-1729, 1981.

[20] G. Lapicki, "The status of theoretical K-shell ionization cross sections by protons", *X-Ray Spectrom.*, vol. 34, pp. 269-278, 2005.

[21] S. J. Cipolla, "The united atom approximation option in the ISICS program to calculate K-, L-, and M-shell cross sections from PWBA and ECPSSR theory", *Nucl. Instrum. Meth. B*, vol. 261, pp. 142-144, 2007.

[22] G. Lapicki, "Scaling of analytical cross sections for K-shell ionization by nonrelativistic protons to cross sections by protons at relativistic velocities", *J. Phys. B*, vol. 41, pp. 115201 (13pp), 2008.

[23] H. Paul and J. Sacher, "Fitted empirical reference cross sections for K-shell ionization by protons", *At. Data Nucl. Data Tab.*, vol. 42, pp. 105-156, 1989.

[24] H. Paul and O. Bolik, "Fitted Empirical Reference Cross Sections for K-Shell Ionization by Alpha Particles", *At. Data Nucl. Data Tab.*, vol. 54, pp. 75-131, 1993.

[25] A. Kahoul, M. Nekkab, and B. Deghfel, "Empirical K-shell ionization cross-sections of elements from ^{4}Be to ^{9}2U by proton impact", *Nucl. Instrum. Meth. B*, vol. 266, pp. 4969-4975, 2008.

[26] Y. Miyagawa, S. Nakamura and S. Miyagawa, "Analytical Formulas for Ionization Cross Sections and Coster-Kronig Corrected Fluorescence Yields of the Ll, L2, and L3 Subshells", *Nucl. Instrum. Meth. B*, vol. 30, pp. 115-122, 1988.

[27] I. Orlic, C. H. Sow, and S. M. Tang, "Semiempirical Formulas for Calculation of L Subshell Ionization Cross Sections", *Int. J. PIXE*, vol. 4, no. 4, pp. 217-230, 1994.

[28] C. H. Sow, I. Orlic, K. K. Lob and S. M. Tang, "New parameters for the calculation of L subshell ionization cross sections", *Nucl. Instrum. Meth. B*, vol. 75, pp. 58-62, 1993.

[29] Z. Liu and S. J. Cipolla, "ISICS: A program for calculating K-, L-, and M-shell cross sections from ECPSSR theory using a personal computer", *Comp. Phys. Comm.*, vol. 97, pp. 315-330, 1996.

[30] S. J. Cipolla, "An improved version of ISICS: a program for calculating K-, L-, and M-shell cross sections from PWBA and ECPSSR theory using a personal computer", *Comp. Phys. Comm.*, vol. 176, pp. 157-159, 2007.

[31] S. Cipolla, ISICS, 2008 version. Private communication: S Cipolla, Creighton Univ., Omaha NE 68178.

[32] I. Orlic, J. Sow, and S. M. Tang, "Experimental L-shell X-ray production and ionization cross sections for proton impact", *At. Data Nucl. Data Tab.*, vol. 56, pp. 159-210, 1994.

[33] R. S. Sokhi and D. Crumpton, "Experimental L-Shell X-Ray Production and Ionization Cross Sections for Proton Impact", *At. Data Nucl. Data Tab.*, vol. 30, pp. 49-124, 1984.

[34] S. Chauvie et al., "Geant4 Low Energy Electromagnetic Physics", in *Proc. Computing in High Energy and Nuclear Physics*, Beijing, China, pp. 337-340, 2001.

[35] S. Chauvie et al., "Geant4 Low Energy Electromagnetic Physics", in *Conf. Rec. IEEE Nucl. Sci. Symp.*, N33-165, 2004.

[36] S. Chauvie, P. Nieminen, M. G. Pia, "Geant4 model for the stopping power of low energy negatively charged hadrons", *IEEE Trans. Nucl. Sci.*, vol. 54, no. 3, pp. 578-584, 2007.

[37] S. Guatelli et al., "Geant4 Atomic Relaxation", *IEEE Trans. Nucl. Sci.*, vol. 54, no. 3, pp. 585-593, 2007.

21.3 Status of the document

30.11.10 created by Maria Grazia Pia

Chapter 22

Shower Parameterizations

22.1 Gflash Shower Parameterizations

The computing time needed for the simulation of high energy electromagnetic showers can become very large, since it increases approximately linearly with the energy absorbed in the detector. Using parameterizations instead of individual particle tracking for electromagnetic (sub)showers can speed up the simulations considerably without sacrificing much precision. The Gflash package allows the parameterization of electron and positron showers in homogeneous (for the time being) calorimeters and is based on the parameterization described in Ref. [1] .

22.1.1 Parameterization Ansatz

The spatial energy distribution of electromagnetic showers is given by three probability density functions (pdf),

$$dE(\vec{r}) \;=\; E\, f(t)dt\, f(r)dr\, f(\phi)d\phi, \tag{22.1}$$

describing the longitudinal, radial, and azimuthal energy distributions. Here t denotes the longitudinal shower depth in units of radiation length, r measures the radial distance from the shower axis in Molière units, and ϕ is the azimuthal angle. The start of the shower is defined by the space point where the electron or positron enters the calorimeter, which is different from the original Gflash. A gamma distribution is used for the parameterization of the longitudinal shower profile, $f(t)$. The radial distribution $f(r)$, is described by a two-component ansatz. In ϕ, it is assumed that the energy is distributed uniformly: $f(\phi) = 1/2\pi$.

22.1.2 Longitudinal Shower Profiles

The average longitudinal shower profiles can be described by a gamma distribution [2]:

$$\left\langle \frac{1}{E}\frac{dE(t)}{dt} \right\rangle \;=\; f(t) \;=\; \frac{(\beta t)^{\alpha-1}\beta \exp(-\beta t)}{\Gamma(\alpha)}. \tag{22.2}$$

The center of gravity, $\langle t \rangle$, and the depth of the maximum, T, are calculated from the shape parameter α and the scaling parameter β according to:

$$\langle t \rangle \;=\; \frac{\alpha}{\beta} \tag{22.3}$$

$$T \;=\; \frac{\alpha - 1}{\beta}. \tag{22.4}$$

In the parameterization all lengths are measured in units of radiation length (X_0), and energies in units of the critical energy ($E_c = 2.66\left(X_0\frac{Z}{A}\right)^{1.1}$). This allows material independence, since the longitudinal shower moments are equal in different materials, according to Ref. [3]. The following equations are used for the energy dependence of T_{hom} and (α_{hom}), with $y = E/E_c$ and $t = x/X_0$, x being the longitudinal shower depth:

$$T_{hom} = \ln y + t_1 \tag{22.5}$$
$$\alpha_{hom} = a_1 + (a_2 + a_3/Z)\ln y. \tag{22.6}$$

The y-dependence of the fluctuations can be described by:

$$\sigma = (s_1 + s_2 \ln y)^{-1}. \tag{22.7}$$

The correlation between $\ln T_{hom}$ and $\ln \alpha_{hom}$ is given by:

$$\rho(\ln T_{hom}, \ln \alpha_{hom}) \equiv \rho = r_1 + r_2 \ln y. \tag{22.8}$$

From these formulae, correlated and varying parameters α_i and β_i are generated according to

$$\begin{pmatrix} \ln T_i \\ \ln \alpha_i \end{pmatrix} = \begin{pmatrix} \langle \ln T \rangle \\ \langle \ln \alpha \rangle \end{pmatrix} + C \begin{pmatrix} z_1 \\ z_2 \end{pmatrix} \tag{22.9}$$

with

$$C = \begin{pmatrix} \sigma(\ln T) & 0 \\ 0 & \sigma(\ln \alpha) \end{pmatrix} \begin{pmatrix} \sqrt{\frac{1+\rho}{2}} & \sqrt{\frac{1-\rho}{2}} \\ \sqrt{\frac{1+\rho}{2}} & -\sqrt{\frac{1-\rho}{2}} \end{pmatrix}$$

$\sigma(\ln \alpha)$ and $\sigma(\ln T)$ are the fluctuations of T_{hom} and (α_{hom}. The values of the coefficients can be found in Ref. [1].

22.1.3 Radial Shower Profiles

For the description of average radial energy profiles,

$$f(r) = \frac{1}{dE(t)}\frac{dE(t,r)}{dr}, \tag{22.10}$$

a variety of different functions can be found in the literature. In Gflash the following two-component ansatz, an extension of that in Ref.[4], was used:

$$\begin{aligned} f(r) &= p f_C(r) + (1-p) f_T(r) \\ &= p\frac{2rR_C^2}{(r^2+R_C^2)^2} + (1-p)\frac{2rR_T^2}{(r^2+R_T^2)^2} \end{aligned} \tag{22.11}$$

with

$$0 \leq p \leq 1.$$

Here R_C (R_T) is the median of the core (tail) component and p is a probability giving the relative weight of the core component. The variable $\tau = t/T$, which measures the shower depth in units of the depth of the shower maximum, is used in order to generalize the radial profiles. This makes the parameterization more convenient and separates the energy and material dependence of various parameters. The median of the core distribution, R_C, increases linearly with τ. The weight of the core, p, is maximal around the shower maximum, and the width of the tail, R_T, is minimal at $\tau \approx 1$.

The following formulae are used to parameterize the radial energy density distribution for a given energy and material:

$$R_{C,hom}(\tau) = z_1 + z_2\tau \tag{22.12}$$

$$R_{T,hom}(\tau) = k_1\{\exp(k_3(\tau - k_2)) + \exp(k_4(\tau - k_2))\} \tag{22.13}$$

$$p_{hom}(\tau) = p_1 \exp\left\{\frac{p_2 - \tau}{p_3} - \exp\left(\frac{p_2 - \tau}{p_3}\right)\right\} \tag{22.14}$$

The parameters $z_1 \cdots p_3$ are either constant or simple functions of $\ln E$ or Z.

Radial shape fluctuations are also taken into account. A detailed explanation of this procedure, as well as a list of all the parameters used in Gflash, can be found in Ref. [1].

22.1.4 Gflash Performance

The parameters used in this Gflash implementation were extracted from full simulation studies with Geant 3. They also give good results inside the Geant4 fast shower framework when compared with the full electromagnetic shower simulation. However, if more precision or higher particle energies are required, retuning may be necessary. For the longitudinal profiles the difference between full simulation and Gflash parameterization is at the level of a few percent. Because the radial profiles are slightly broader in Geant3 than in Geant4, the differences may reach $> 10\%$. The gain in speed, on the other hand, is impressive. The simulation of a 1 TeV electron in a $PbWO_4$ cube is 160 times faster with Gflash. Gflash can also be used to parameterize electromagnetic showers in sampling calorimeters. So far, however, only homogeneous materials are supported.

22.1.5 Status of this document

02.12.04 created by J.Weng
03.12.04 grammar check and minor re-wording by D.H. Wright

Bibliography

[1] G. Grindhammer, S. Peters, *The Parameterized Simulation of Electromagnetic Showers in Homogeneous and Sampling Calorimeters, hep-ex/0001020* (1993).

[2] E. Longo and I. Sestili,*Nucl. Instrum. Meth. 128, 283* (1975).

[3] Rossi *rentice Hall, New York* (1952).

[4] G. Grindhammer, M. Rudowicz, and S. Peters, *Nucl. Instrum. Meth. A290, 469* (1990).

Part IV

Hadronic Interactions

Chapter 23

Total Reaction Cross Section in Nucleus-nucleus Reactions

The transportation of heavy ions in matter is a subject of much interest in several fields of science. An important input for simulations of this process is the total reaction cross section, which is defined as the total (σ_T) minus the elastic (σ_{el}) cross section for nucleus-nucleus reactions:

$$\sigma_R = \sigma_T - \sigma_{el}.$$

The total reaction cross section has been studied both theoretically and experimentally and several empirical parameterizations of it have been developed. In Geant4 the total reaction cross sections are calculated using four such parameterizations: the Sihver[1], Kox[2], Shen[3] and Tripathi[4] formulae. Each of these is discussed in order below.

23.1 Sihver Formula

Of the four parameterizations, the Sihver formula has the simplest form:

$$\sigma_R = \pi r_0^2 [A_p^{1/3} + A_t^{1/3} - b_0 [A_p^{-1/3} + A_t^{-1/3}]]^2 \tag{23.1}$$

where A_p and A_t are the mass numbers of the projectile and target nuclei, and

$$b_0 = 1.581 - 0.876(A_p^{-1/3} + A_t^{-1/3}),$$

$$r_0 = 1.36 fm.$$

It consists of a nuclear geometrical term $(A_p^{1/3} + A_t^{1/3})$ and an overlap or transparency parameter (b_0) for nucleons in the nucleus. The cross section is independent of energy and can be used for incident energies greater than 100 MeV/nucleon.

23.2 Kox and Shen Formulae

Both the Kox and Shen formulae are based on the strong absorption model. They express the total reaction cross section in terms of the interaction radius R, the nucleus-nucleus interaction barrier B, and the center-of-mass energy of the colliding system E_{CM}:

$$\sigma_R = \pi R^2 [1 - \frac{B}{E_{CM}}]. \tag{23.2}$$

Kox formula: Here B is the Coulomb barrier (B_c) of the projectile-target system and is given by

$$B_c = \frac{Z_t Z_p e^2}{r_C (A_t^{1/3} + A_p^{1/3})},$$

where $r_C = 1.3$ fm, e is the electron charge and Z_t, Z_p are the atomic numbers of the target and projectile nuclei. R is the interaction radius R_{int} which in the Kox formula is divided into volume and surface terms:

$$R_{int} = R_{vol} + R_{surf}.$$

R_{vol} and R_{surf} correspond to the energy-independent and energy-dependent components of the reactions, respectively. Collisions which have relatively small impact parameters are independent of both energy and mass number. These core collisions are parameterized by R_{vol}. Therefore R_{vol} can depend only on the volume of the projectile and target nuclei:

$$R_{vol} = r_0 (A_t^{1/3} + A_p^{1/3}).$$

The second term of the interaction radius is a nuclear surface contribution and is parameterized by

$$R_{surf} = r_0 [a \frac{A_t^{1/3} A_p^{1/3}}{A_t^{1/3} + A_p^{1/3}} - c] + D.$$

The first term in brackets is the mass asymmetry which is related to the volume overlap of the projectile and target. The second term c is

an energy-dependent parameter which takes into account increasing surface transparency as the projectile energy increases. D is the neutron-excess which becomes important in collisions of heavy or neutron-rich targets. It is given by

$$D = \frac{5(A_t - Z_t)Z_p}{A_p A_r}.$$

The surface component (R_{surf}) of the interaction radius is actually not part of the simple framework of the strong absorption model, but a better reproduction of experimental results is possible when it is used.

The parameters r_0, a and c are obtained using a χ^2 minimizing procedure with the experimental data. In this procedure the parameters r_0 and a were fixed while c was allowed to vary only with the beam energy per nucleon. The best χ^2 fit is provided by $r_0 = 1.1$ fm and $a = 1.85$ with the corresponding values of c listed in Table III and shown in Fig. 12 of Ref. [2] as a function of beam energy per nucleon. This reference presents the values of c only in chart and figure form, which is not suitable for Monte Carlo calculations. Therefore a simple analytical function is used to calculate c in Geant4. The function is:

$$c = -\frac{10}{x^5} + 2.0 \text{ for x} \geq 1.5$$

$$c = (-\frac{10}{1.5^5} + 2.0) \times (\frac{x}{1.5})^3 \text{ for x} < 1.5,$$

$$x = log(KE),$$

where KE is the projectile kinetic energy in units of MeV/nucleon in the laboratory system.

Shen formula: as mentioned earlier, this formula is also based on the strong absorption model, therefore it has a structure similar to the Kox formula:

$$\sigma_R = 10\pi R^2[1 - \frac{B}{E_{CM}}]. \tag{23.3}$$

However, different parameterized forms for R and B are applied. The interaction radius R is given by

$$R = r_0[A_t^{1/3} + A_p^{1/3} + 1.85\frac{A_t^{1/3}A_p^{1/3}}{A_t^{1/3} + A_p^{1/3}} - C'(KE)]$$
$$+\alpha\frac{5(A_t - Z_t)Z_p}{A_p A_r} + \beta E_{CM}^{-1/3}\frac{A_t^{1/3}A_p^{1/3}}{A_t^{1/3} + A_p^{1/3}}$$

where α, β and r_0 are

$$\alpha = 1fm$$

$$\beta = 0.176MeV^{1/3} \cdot fm$$

$$r_0 = 1.1fm$$

In Ref. [3] as well, no functional form for $C'(KE)$ is given. Hence the same simple analytical function is used by Geant4 to derive c values.

The second term B is called the nuclear-nuclear interaction barrier in the Shen formula and is given by

$$B = \frac{1.44 Z_t Z_p}{r} - b\frac{R_t R_p}{R_t + R_p}(MeV)$$

where r, b, R_t and R_p are given by

$$r = R_t + R_p + 3.2fm$$

$$b = 1MeV \cdot fm^{-1}$$

$$R_i = 1.12A_i^{1/3} - 0.94A_i^{-1/3} \ (i = t, p)$$

The difference between the Kox and Shen formulae appears at energies below 30 MeV/nucleon. In this region the Shen formula shows better agreement with the experimental data in most cases.

23.3 Tripathi formula

Because the Tripathi formula is also based on the strong absorption model its form is similar to the Kox and Shen formulae:

$$\sigma_R = \pi r_0^2 (A_p^{1/3} + A_t^{1/3} + \delta_E)^2 [1 - \frac{B}{E_{CM}}], \tag{23.4}$$

where $r_0 = 1.1$ fm. In the Tripathi formula B and R are given by

$$B = \frac{1.44 Z_t Z_p}{R}$$

$$R = r_p + r_t + \frac{1.2(A_p^{1/3} + A_t^{1/3})}{E_{CM}^{1/3}}$$

where r_i is the equivalent sphere radius and is related to the $r_{rms,i}$ radius by

$$r_i = 1.29 r_{rms,i} \ (i = p, t).$$

δ_E represents the energy-dependent term of the reaction cross section which is due mainly to transparency and Pauli blocking effects. It is given by

$$\delta_E = 1.85S + (0.16S/E_{CM}^{1/3}) - C_{KE} + [0.91(A_t - 2Z_t)Z_p/(A_pA_t)],$$

where S is the mass asymmetry term given by

$$S = \frac{A_p^{1/3} A_t^{1/3}}{A_p^{1/3} + A_t^{1/3}}.$$

This is related to the volume overlap of the colliding system. The last term accounts for the isotope dependence of the reaction cross section and corresponds to the D term in the Kox formula and the second term of R in the Shen formula.

The term C_{KE} corresponds to c in Kox and $C'(KE)$ in Shen and is given by

$$C_E = D_{Pauli}[1 - \exp(-KE/40)] - 0.292 \exp(-KE/792) \times \cos(0.229 KE^{0.453}).$$

Here D_{Pauli} is related to the density dependence of the colliding system, scaled with respect to the density of the ^{12}C+^{12}C colliding system:

$$D_{Pauli} = 1.75 \frac{\rho_{A_p} + \rho_{A_t}}{\rho_{A_C} + \rho_{A_C}}.$$

The nuclear density is calculated in the hard sphere model. D_{Pauli} simulates the modifications of the reaction cross sections caused by Pauli blocking and is being introduced to the Tripathi formula for the first time. The modification of the reaction cross section due to Pauli blocking plays an important role at energies above 100 MeV/nucleon. Different forms of D_{Pauli} are used in the Tripathi formula for alpha-nucleus and lithium-nucleus collisions. For alpha-nucleus collisions,

$$D_{Pauli} = 2.77 - (8.0 \times 10^{-3} A_t) + (1.8 \times 10^{-5} A_t^2) \\ -0.8/\{1 + \exp[(250 - KE)/75]\}$$

For lithium-nucleus collisions,

$$D_{Pauli} = D_{Pauli}/3.$$

Note that the Tripathi formula is not fully implemented in Geant4 and can only be used for projectile energies less than 1 GeV/nucleon.

23.4 Representative Cross Sections

Representative cross section results from the Sihver, Kox, Shen and Tripathi formulae in Geant4 are displayed in Table I and compared to the experimental measurements of Ref. [2].

23.5 Tripathi Formula for "light" Systems

For nuclear-nuclear interactions in which the projectile and/or target are light, Tripathi *et al* [6] propose an alternative algorithm for determining the interaction cross section (implemented in the new class G4TripathiLightCrossSection). For such systems, Eq.23.4 becomes:

$$\sigma_R = \pi r_0^2 [A_p^{1/3} + A_t^{1/3} + \delta_E]^2 (1 - R_C \frac{B}{E_{CM}}) X_m \tag{23.5}$$

R_C is a Coulomb multiplier, which is added since for light systems Eq. 23.4 overestimates the interaction distance, causing B (in Eq. 23.4) to be underestimated. Values for R_C are given in Table 23.2.

$$X_m = 1 - X_1 \exp\left(-\frac{E}{X_1 S_L}\right) \tag{23.6}$$

where:

$$X_1 = 2.83 - \left(3.1 \times 10^{-2}\right) A_T + \left(1.7 \times 10^{-4}\right) A_T^2 \tag{23.7}$$

except for neutron interactions with ^{4}He, for which X_1 is better approximated to 5.2, and the function S_L is given by:

$$S_L = 1.2 + 1.6 \left[1 - \exp\left(-\frac{E}{15}\right)\right] \tag{23.8}$$

For light nuclear-nuclear collisions, a slightly more general expression for C_E is used:

$$C_E = D\left[1 - \exp\left(-\frac{E}{T_1}\right)\right] - 0.292\exp\left(-\frac{E}{792}\right)\cdot\cos\left(0.229E^{0.453}\right) \quad (23.9)$$

D and T_1 are dependent on the interaction, and are defined in table 23.3.

23.6 Status of this document

25.11.03 created by Tatsumi Koi
28.11.03 grammar check and re-wording by D.H. Wright
18.06.04 light system section added by Peter Truscott

Bibliography

[1] L. Sihver et al., Phys. Rev. C47, 1225 (1993).

[2] Kox et al. Phys. Rev. C35, 1678 (1987).

[3] Shen et al. Nucl. Phys. A491, 130 (1989).

[4] Tripathi et al, NASA Technical Paper 3621 (1997).

[5] Jaros et al, Phys. Rev. C 18 2273 (1978).

[6] R K Tripathi, F A Cucinotta, and J W Wilson, "Universal parameterization of absorption cross-sections - Light systems," NASA Technical Paper TP-1999-209726, 1999.

Table 23.1: Representative total reaction cross sections

Proj.	Target	Elab [MeV/n]	Exp. Results [mb]	Sihver	Kox	Shen	Tripathi
^{12}C	^{12}C	30	1316±40	—	1295.04	1316.07	1269.24
		83	965±30	—	957.183	969.107	989.96
		200	864±45	868.571	885.502	893.854	864.56
		300	858±60	868.571	871.088	878.293	857.414
		870[1]	939±50	868.571	852.649	857.683	939.41
		2100[1]	888±49	868.571	846.337	850.186	936.205
	^{27}Al	30	1748±85	—	1801.4	1777.75	1701.03
		83	1397±40	—	1407.64	1386.82	1405.61
		200	1270±70	1224.95	1323.46	1301.54	1264.26
		300	1220±85	1224.95	1306.54	1283.95	1257.62
	^{89}Y	30	2724±300	—	2898.61	2725.23	2567.68
		83	2124±140	—	2478.61	2344.26	2346.54
		200	1885±120	2156.47	2391.26	2263.77	2206.01
		300	1885±150	2156.47	2374.17	2247.55	2207.01
^{16}O	^{27}Al	30	1724±80	—	1965.85	1935.2	1872.23
	^{89}Y	30	2707±330	—	3148.27	2957.06	2802.48
^{20}Ne	^{27}Al	30	2113±100	—	2097.86	2059.4	2016.32
		100	1446±120	1473.87	1684.01	1658.31	1667.17
		300	1328±120	1473.87	1611.88	1586.17	1559.16
	^{108}Ag	300	2407±200[2]	2730.69	3095.18	2939.86	2893.12

1. Data measured by Jaros et al. [5]
2. Natural silver was used in this measurement.

Table 23.2: Coulomb multiplier for light systems [6].

System	R_C
p + d	13.5
p + ^{3}He	21
p + ^{4}He	27
p + Li	2.2
d + d	13.5
d + ^{4}He	13.5
d + C	6.0
^{4}He + Ta	0.6
^{4}He + Au	0.6

Table 23.3: Parameters D and T1 for light systems [6].

System	T1 [MeV]	D	G [MeV] (^{4}He + X only)
p + X	23	$1.85 + \frac{0.16}{1+\exp\left(\frac{500-E}{200}\right)}$	(Not applicable)
n + X	18	$1.85 + \frac{0.16}{1+\exp\left(\frac{500-E}{200}\right)}$	(Not applicable)
d + X	23	$1.65 + \frac{0.1}{1+\exp\left(\frac{500-E}{200}\right)}$	(Not applicable)
^{3}He + X	40	1.55	(Not applicable)
^{4}He + ^{4}He	40	$D = 2.77 - 8.0 \times 10^{-3} A_T$ $+1.8 \times 10^{-5} A_T^2$ $-\frac{0.8}{1+\exp\left(\frac{250-E}{G}\right)}$	300
^{4}He + Be	25	(as for ^{4}He + ^{4}He)	300
^{4}He + N	40	(as for ^{4}He + ^{4}He)	500
^{4}He + Al	25	(as for ^{4}He + ^{4}He)	300
^{4}He + Fe	40	(as for ^{4}He + ^{4}He)	300
^{4}He + X (general)	40	(as for ^{4}He + ^{4}He)	75

Chapter 24

Coherent elastic scattering

24.1 Nucleon-Nucleon elastic Scattering

The classes G4LEpp and G4LEnp provide data-driven models for proton-proton (or neutron-neutron) and neutron-proton elastic scattering over the range 10-1200 MeV. Final states (primary and recoil particle) are derived by sampling from tables of the cumulative distribution function of the centre-of-mass scattering angle, tabulated for a discrete set of lab kinetic energies from 10 MeV to 1200 MeV. The CDF's are tabulated at 1 degree intervals and sampling is done using bi-linear interpolation in energy and CDF values. The data are derived from differential cross sections obtained from the SAID database, R. Arndt, 1998.

In class G4LEpp there are two data sets: one including Coulomb effects (for p-p scattering) and one with no Coulomb effects (for n-n scattering or p-p scattering with Coulomb effects suppressed). The method G4LEpp::SetCoulombEffects can be used to select the desired data set:

- SetCoulombEffects(0): No Coulomb effects (the default)
- SetCoulombEffects(1): Include Coulomb effects

The recoil particle will be generated as a new secondary particle. In class G4LEnp, the possiblity of a charge-exchange reaction is included, in which case the incident track will be stopped and both the primary and recoil particles will be generated as secondaries.

Chapter 25

Hadron-nucleus Elastic Scattering at Medium and High Energy

25.1 Method of Calculation

The Glauber model [1] is used as an alternative method of calculating differential cross sections for elastic and quasi-elastic hadron-nucleus scattering at high and intermediate energies.

For high energies this includes corrections for inelastic screening and for quasi-elastic scattering the exitation of a discrete level or a state in the continuum is considered.

The usual expression for the Glauber model amplitude for multiple scattering was used

$$F(q) = \frac{ik}{2\pi} \int d^2b e^{\vec{q}\cdot\vec{b}} M(\vec{b}). \tag{25.1}$$

Here $M(\vec{b})$ is the hadron-nucleus amplitude in the impact parameter representation

$$M(\vec{b}) = 1 - [1 - e^{-A\int d^3r \Gamma(\vec{b}-\vec{s})\rho(\vec{r})}]^A, \tag{25.2}$$

k is the incident particle momentum, $\vec{q} = \vec{k}' - \vec{k}$ is the momentum transfer, and $\vec{k}'$ is the scattered particle momentum. Note that $|\vec{q}|^2 = -t$ - invariant momentum transfer squared in the center of mass system. $\Gamma(\vec{b})$ is the hadron-nucleon amplitude of elastic scattering in the impact-parameter representation

$$\Gamma(\vec{b}) = \frac{1}{2\pi i k^{hN}} \int d\vec{q} e^{-\vec{q}\cdot\vec{b}} f(\vec{q}). \tag{25.3}$$

The exponential parameterization of the hadron-nucleon amplitude is usually used:

$$f(\vec{q}) = \frac{i k^{hN} \sigma^{hN}}{2\pi} e^{-0.5 q^2 B}. \tag{25.4}$$

Here $\sigma^{hN} = \sigma_{tot}^{hN}(1 - i\alpha)$, σ_{tot}^{hN} is the total cross section of a hadron-nucleon scattering, B is the slope of the diffraction cone and α is the ratio of the real to imaginary parts of the amplitude at $q = 0$. The value k^{hN} is the hadron momentum in the hadron-nucleon coordinate system.

The important difference of these calculations from the usual ones is that the two-gaussian form of the nuclear density was used

$$\rho(r) = C(e^{-(r/R_1)^2} - p e^{-(r/R_2)^2}), \tag{25.5}$$

where R_1, R_2 and p are the fitting parameters and C is a normalization constant.

This density representation allows the expressions for amplitude and differential cross section to be put into analytical form. It was earlier used for light [2, 3] and medium [4] nuclei. Described below is an extension of this method to heavy nuclei. The form 25.5 is not physical for a heavy nucleus, but nevertheless works rather well (see figures below). The reason is that the nucleus absorbs the hadrons very strongly, especially at small impact parameters where the absorption is full. As a result only the peripherial part of the nucleus participates in elastic scattering. Eq. 25.5 therefore describes only the edge of a heavy nucleus.

Substituting Eqs. 25.5 and 25.4 into Eqs. 25.1, 25.2 and 25.3 yields the following formula

$$F(q) = \frac{ik\pi}{2} \sum_{k=1}^{A} (-1)^k \binom{A}{k} \left[\frac{\sigma^{hN}}{2\pi(R_1^3 - pR_2^3)}\right]^k \sum_{m=0}^{k} (-1)^m \binom{k}{m} \left[\frac{R_1^3}{R_1^2 + 2B}\right]^{k-m}$$

$$\times \left[\frac{pR_2^3}{R_2^2 + 2B}\right]^m \left(\frac{m}{R_2^2 + 2B} + \frac{k-m}{R_1^2 + 2B}\right)^{-1}$$

$$\times \exp\left[-\frac{-q^2}{4}\left(\frac{m}{R_2^2 + 2B} + \frac{k-m}{R_1^2 + 2B}\right)^{-1}\right]. \tag{25.6}$$

An analogous procedure can be used to get the inelastic screening corrections to the hadron-nucleus amplitude $\Delta M(\vec{b})$ [5]. In this case an intermediate inelastic diffractive state is created which rescatters on the nucleons of the nucleus and then returns into the initial hadron. Hence it is nessesary to integrate the production cross section over the mass distribution of the exited system $\frac{d\sigma^{diff}}{dtdM_x^2}$. The expressions for the corresponding amplitude are quite long and so are not presented here. The corrections for the total cross-sections can be found in [5].

The full amplitude is the sum $M(\vec{b}) + \Delta M(\vec{b})$.

The differential cross section is connected with the amplitude in the following way

$$\frac{d\sigma}{d\Omega_{CM}} = |F(q)|^2 , \qquad \frac{d\sigma}{|dt|} = \frac{d\sigma}{dq_{CM}^2} = \frac{\pi}{k_{CM}^2} |F(q)|^2 . \tag{25.7}$$

The main energy dependence of the hadron-nucleus elastic scattering cross section comes from the energy dependence of the parameters of hadron-nucleon scattering ($\sigma_{tot}^{hN}\alpha$, B and $\frac{d\sigma^{diff}}{dtdM_x^2}$). At interesting energies these parameters were fixed at their well-known values. The fitting of the nuclear density parameters was performed over a wide range of atomic numbers ($A = 4-208$) using experimental data on proton-nuclei elastic scattering at a kinetic energy of $T_p = 1GeV$.

The fitting was perfomed both for individual nuclei and for the entire set of nuclei at once.

It is necessary to note that for every nucleus an optimal set of density parameters exists and it differs slightly from the one derived for the full set of nuclei.

A comparision of the phenomenological cross sections [6] with experiment is presented in Figs. 25.1 - 25.9

In this comparison, the individual nuclei parameters were used. The experimental data were obtained in Gatchina (Russia) and in Saclay (France) [6]. The horizontal axis is the scattering angle in the center of mass system Θ_{CM} and the vertical axis is $\frac{d\sigma}{d\Omega_{CM}}$ in $\frac{mb}{Ster}$.

Comparisions were also made for p^4He elastic scatering at $T_{=}1GeV$[7], $45GeV$ and $301GeV$ [3]. The resulting cross sections $\frac{d\sigma}{d|t|}$ are shown in the Figs. 25.10 - 25.12.

In order to generate events the distribution function $\mathcal{F}$ of a corresponding process must be known. The differential cross section is proportional to the density distribution. Therefore to get the distribution function it is sufficient to integrate the differential cross section and normalize it:

$$\mathcal{F}(q^2) = \frac{\int\limits_0^{q^2} d(q^2)\frac{d\sigma}{d(q^2)}}{\int\limits_0^{q^2_{max}} d(q^2)\frac{d\sigma}{d(q^2)}}. \qquad (25.8)$$

Expressions 25.6 and 25.7 allow analytic integration in Eq. 25.8 but the result is too long to be given here.

For light and medium nuclei the analytic expression is more convenient for calculations than the numerical integration of Eq. 25.8, but for heavy nuclei the latter is preferred due to the large number of terms in the analytic expression.

25.2 Status of this document

18.06.04 created by Nikolai Starkov
19.06.04 re-written for spelling and grammar by D.H. Wright

Bibliography

[1] R.J. Glauber, in "High Energy Physics and Nuclear Structure", edited by S. Devons (Plenum Press, NY 1970).

[2] R. H. Bassel, W. Wilkin, Phys. Rev., 174, p. 1179, 1968;
T. T. Chou, Phys. Rev., 168, 1594, 1968;
M. A. Nasser, M. M. Gazzaly, J. V. Geaga et al., Nucl. Phys., A312, pp. 209-216, 1978.

[3] Bujak, P. Devensky, A. Kuznetsov et al., Phys. Rev., D23, N 9, pp. 1895-1910, 1981.

[4] V. L. Korotkikh, N. I. Starkov, Sov. Journ. of Nucl. Phys., v. 37, N 4, pp. 610-613, 1983;
N. T. Ermekov, V. L. Korotkikh, N. I. Starkov, Sov. Journ. of Nucl. Phys., 33, N 6, pp. 775-777, 1981.

[5] R.A. Nam, S. I. Nikol'skii, N. I. Starkov et al., Sov. Journ. of Nucl. Phys., v. 26, N 5, pp. 550-555, 1977.

[6] G.D. Alkhazov et al., Phys. Rep., 1978, C42, N 2, pp. 89-144;

[7] J. V. Geaga, M. M. Gazzaly, G. J. Jgo et al., Phys. Rev. Lett. 38, N 22, pp. 1265-1268;
S. J. Wallace. Y. Alexander, Phys. Rev. Lett. 38, N 22, pp. 1269-1272.

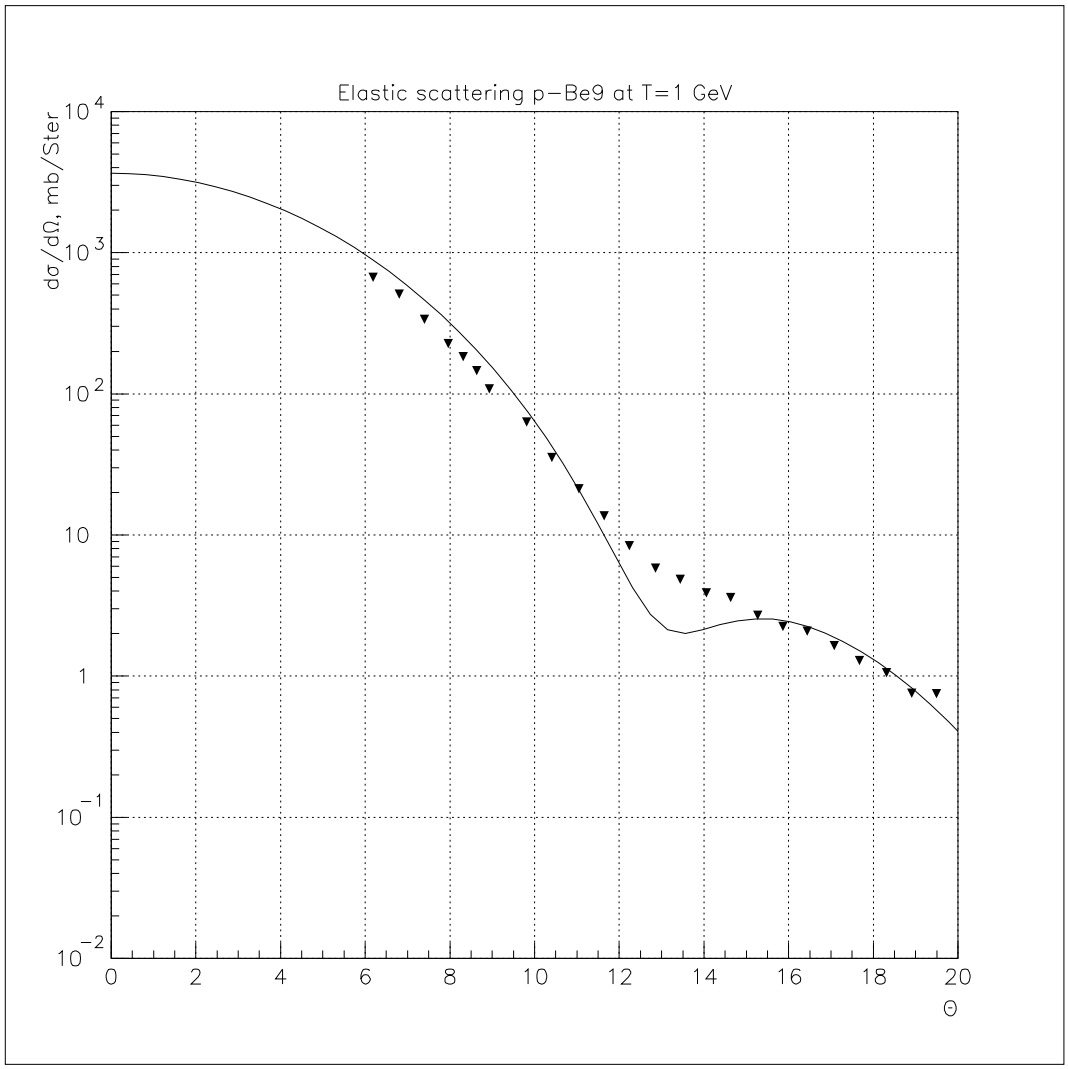

Figure 25.1: Elastic proton scattering on ^{9}Be at 1 GeV

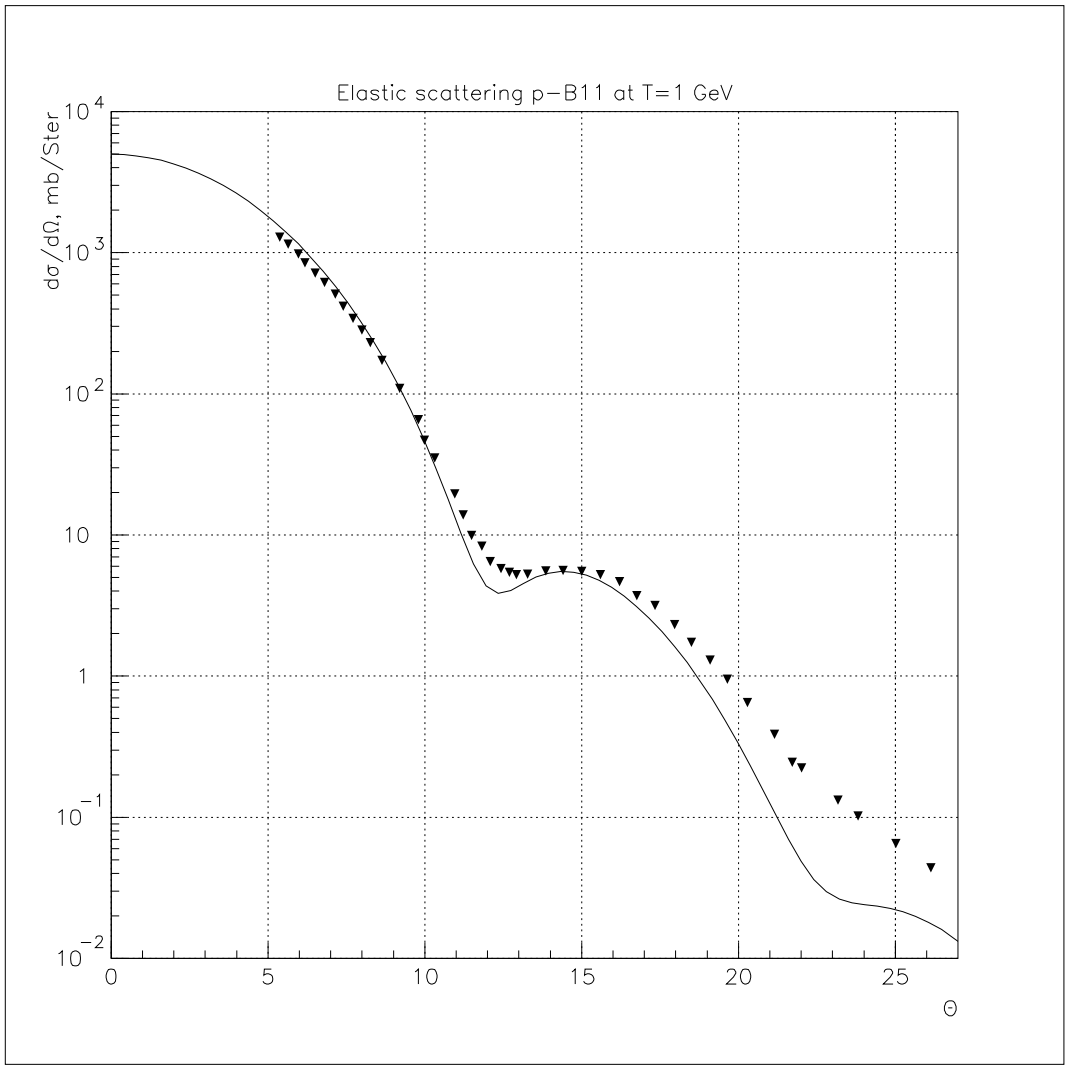

Figure 25.2: Elastic proton scattering on ^{11}B at 1 GeV

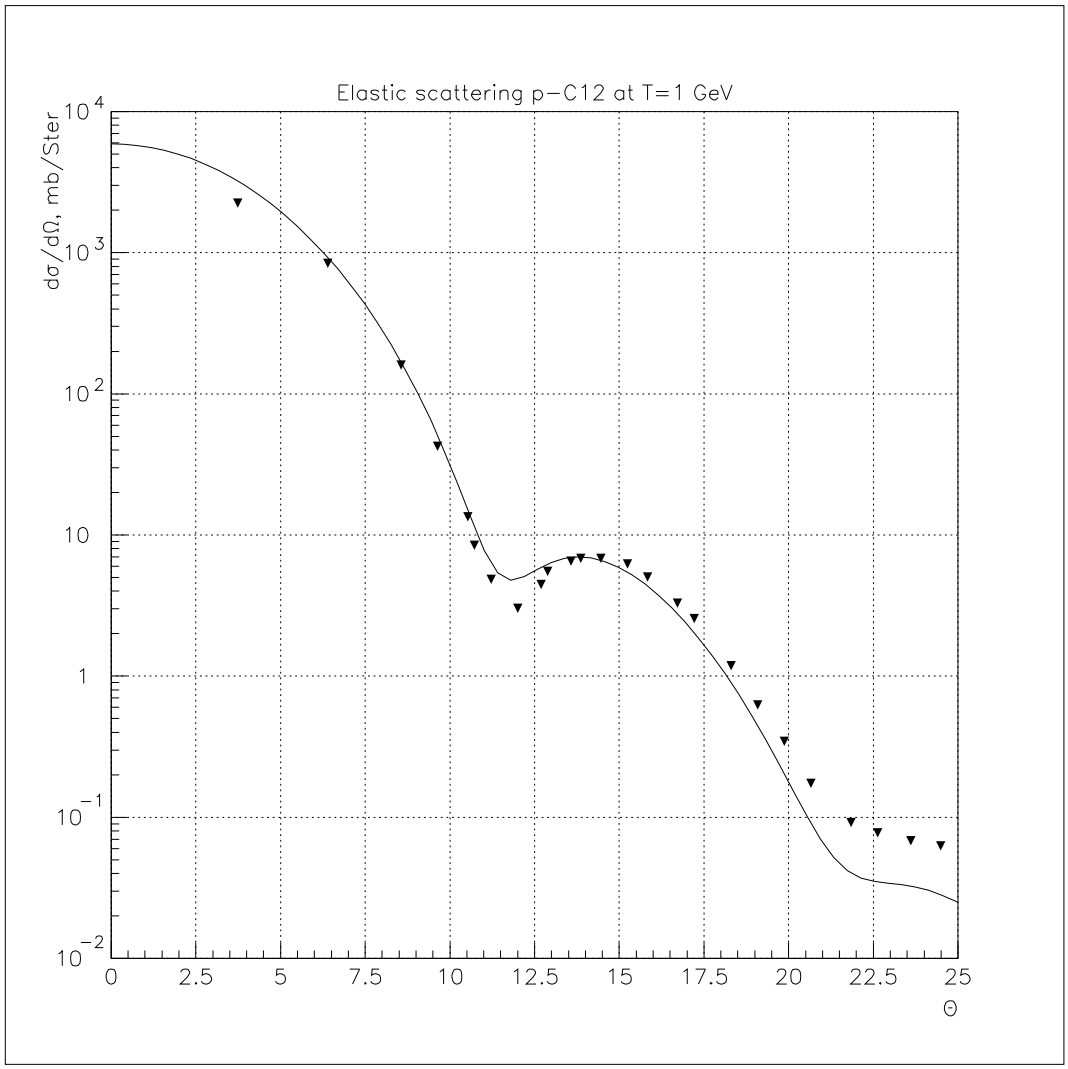

Figure 25.3: Elastic proton scattering on ^{12}C at 1 GeV

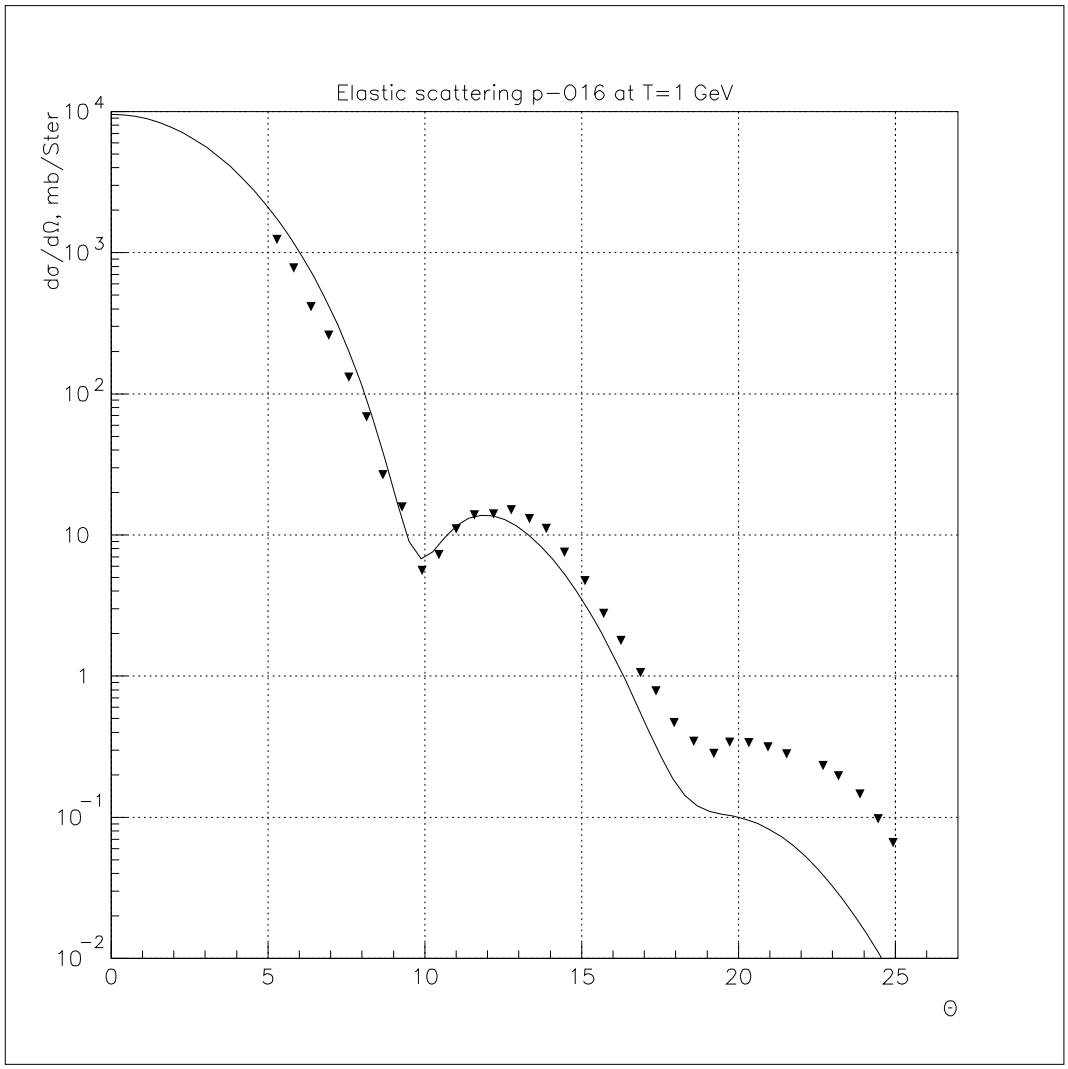

Figure 25.4: Elastic proton scattering on ^{16}O at 1 GeV

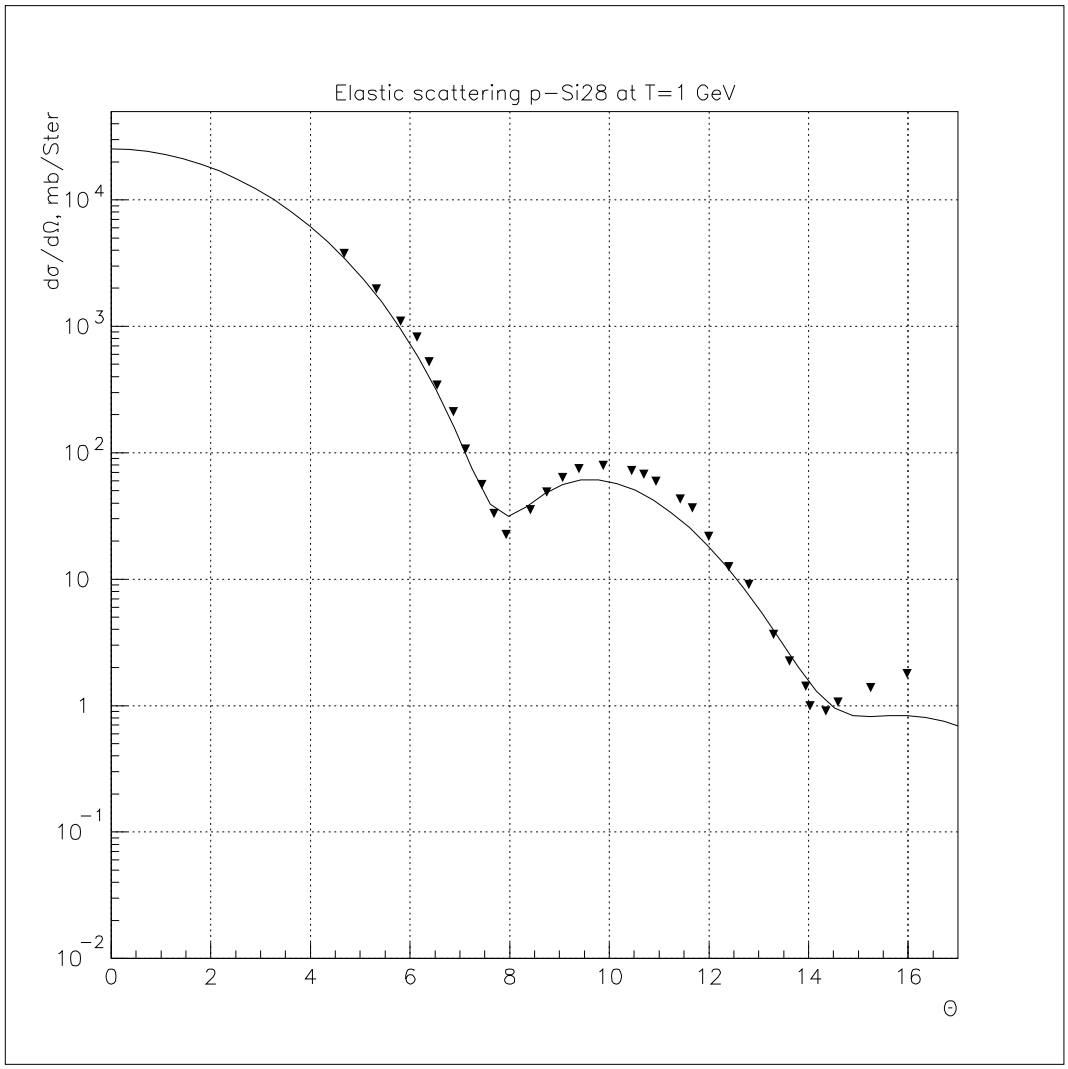

Figure 25.5: Elastic proton scattering on ^{28}Si at 1 GeV

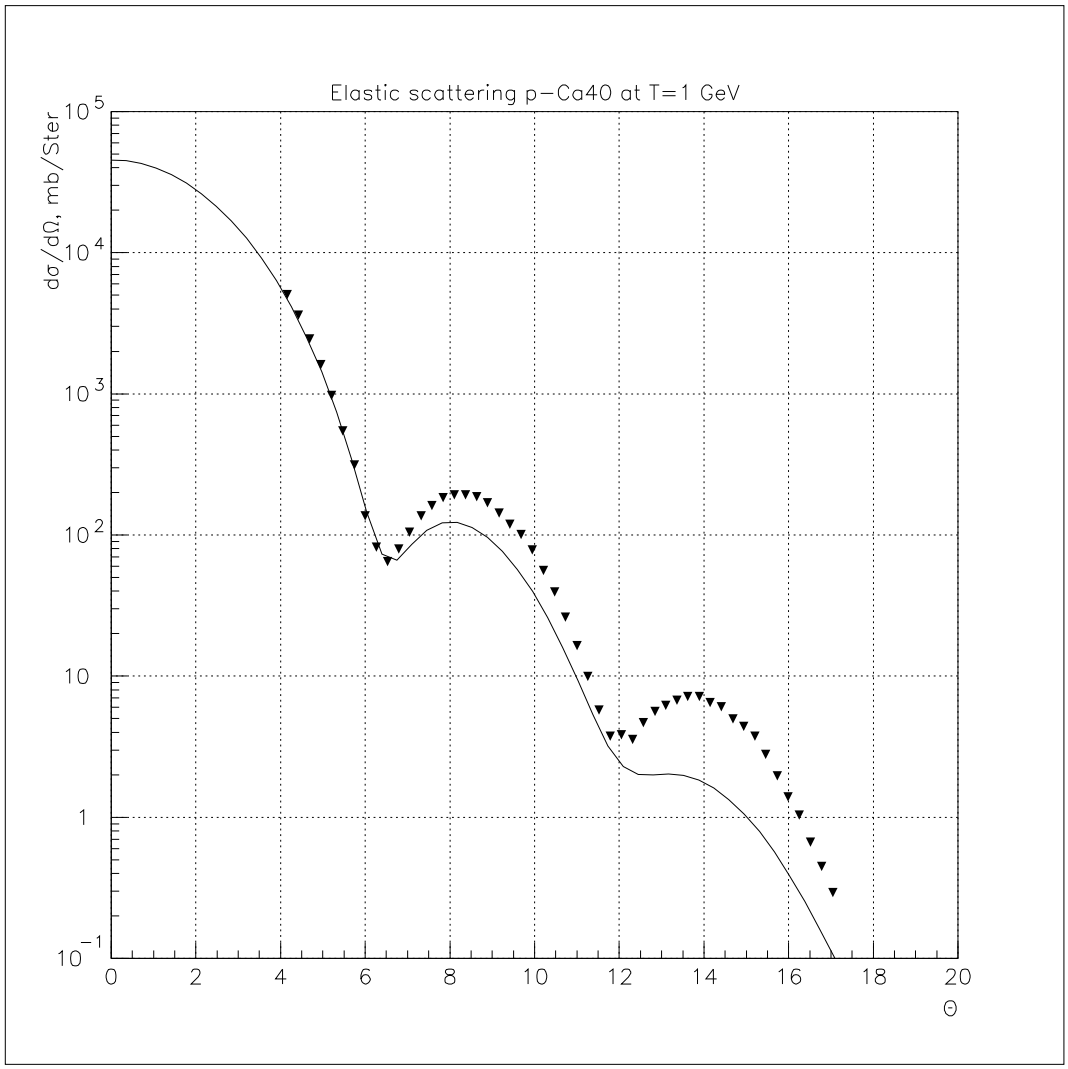

Figure 25.6: Elastic proton scattering on ^{40}Ca at 1 GeV

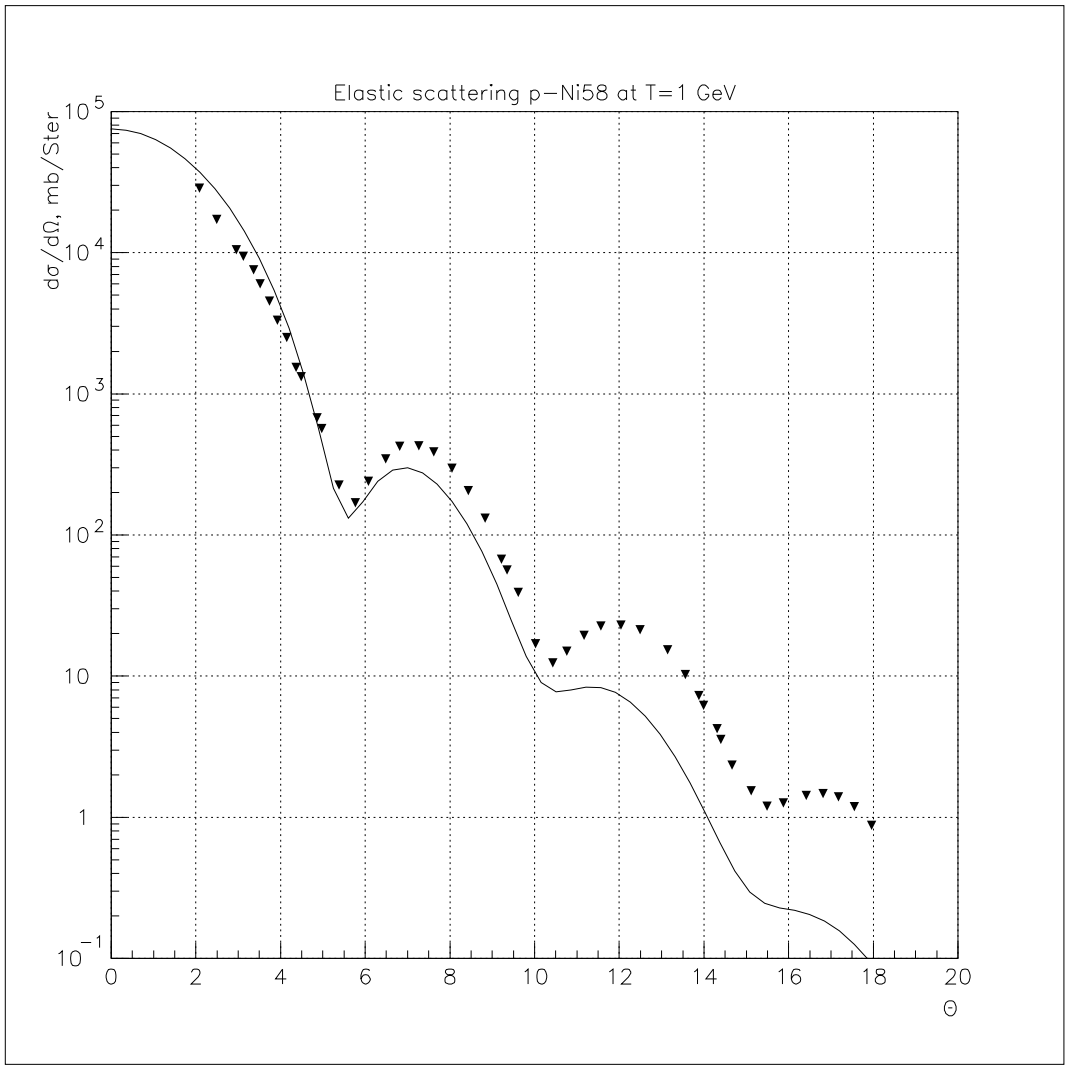

Figure 25.7: Elastic proton scattering on ^{58}Ni at 1 GeV

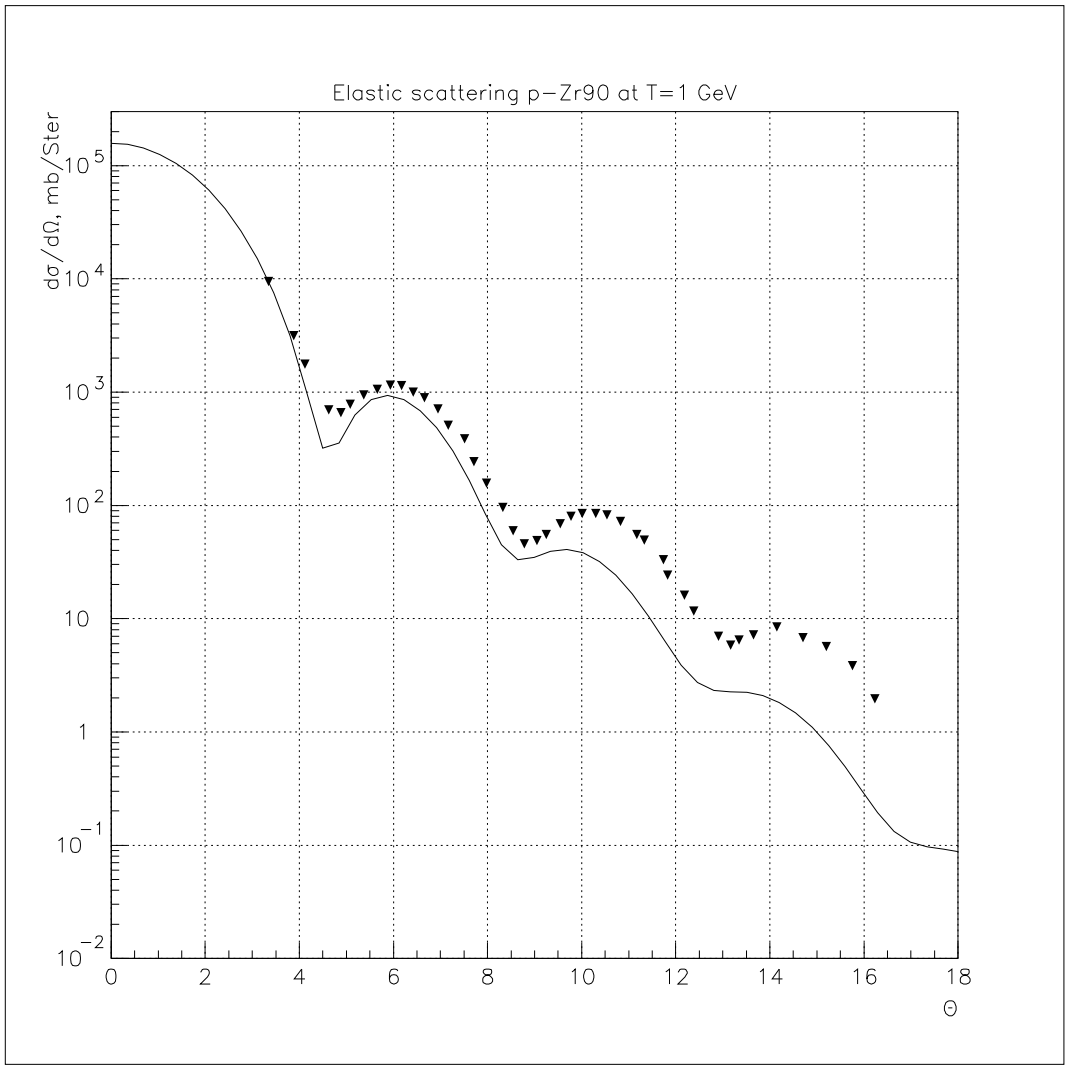

Figure 25.8: Elastic proton scattering on ^{90}Zr at 1 GeV

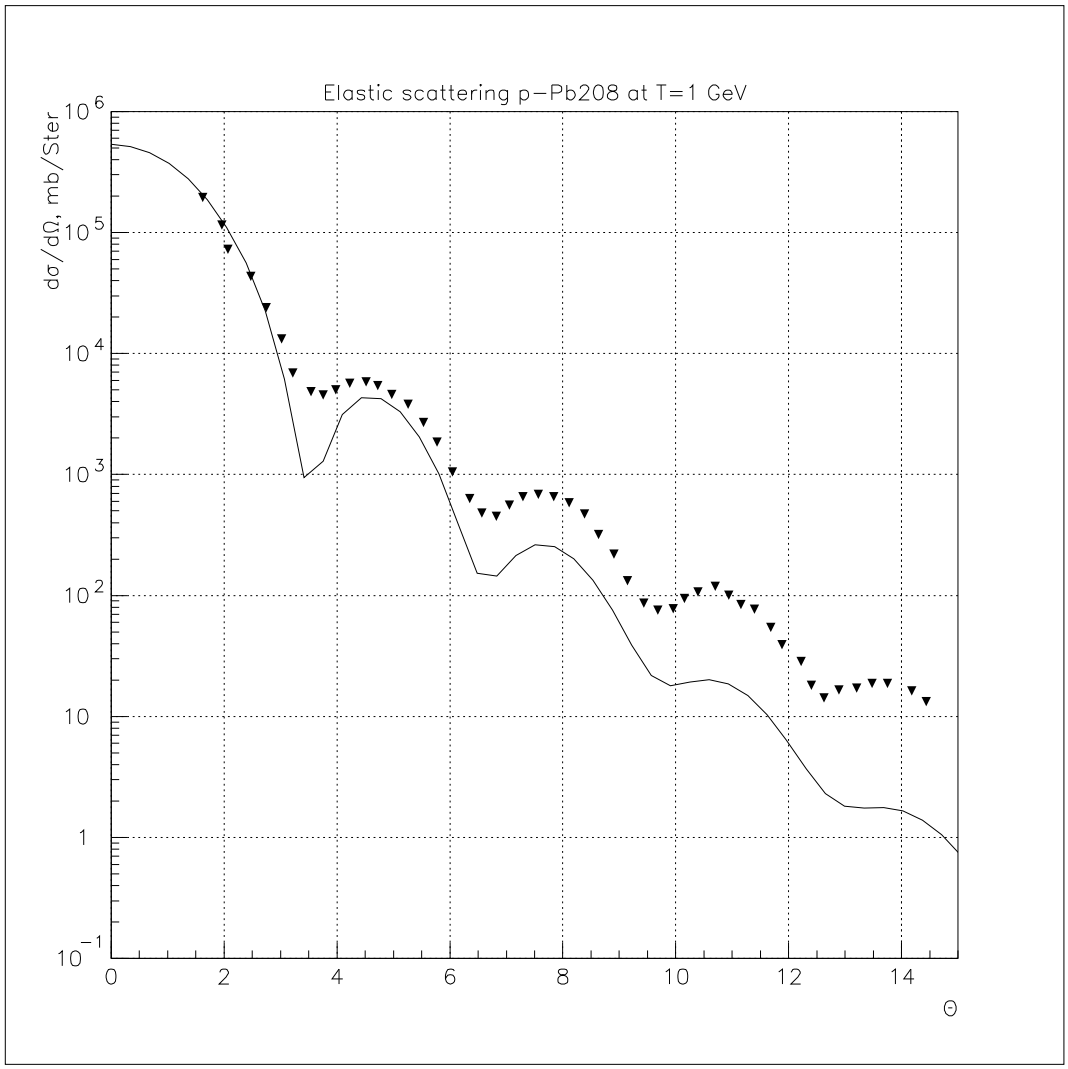

Figure 25.9: Elastic proton scattering on ^{208}Pb at 1 GeV

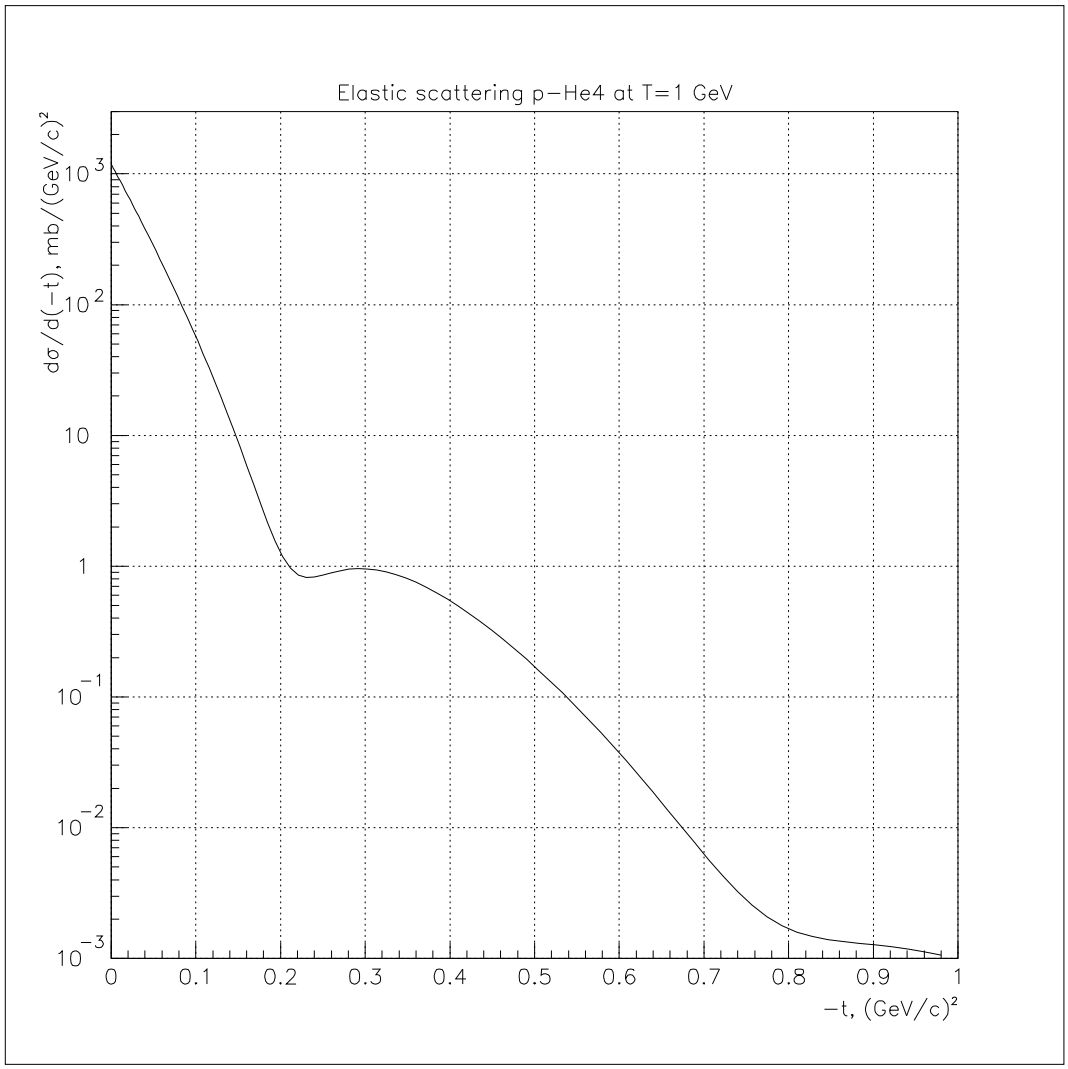

Figure 25.10: Elastic proton scattering on ^{4}He at 1 GeV

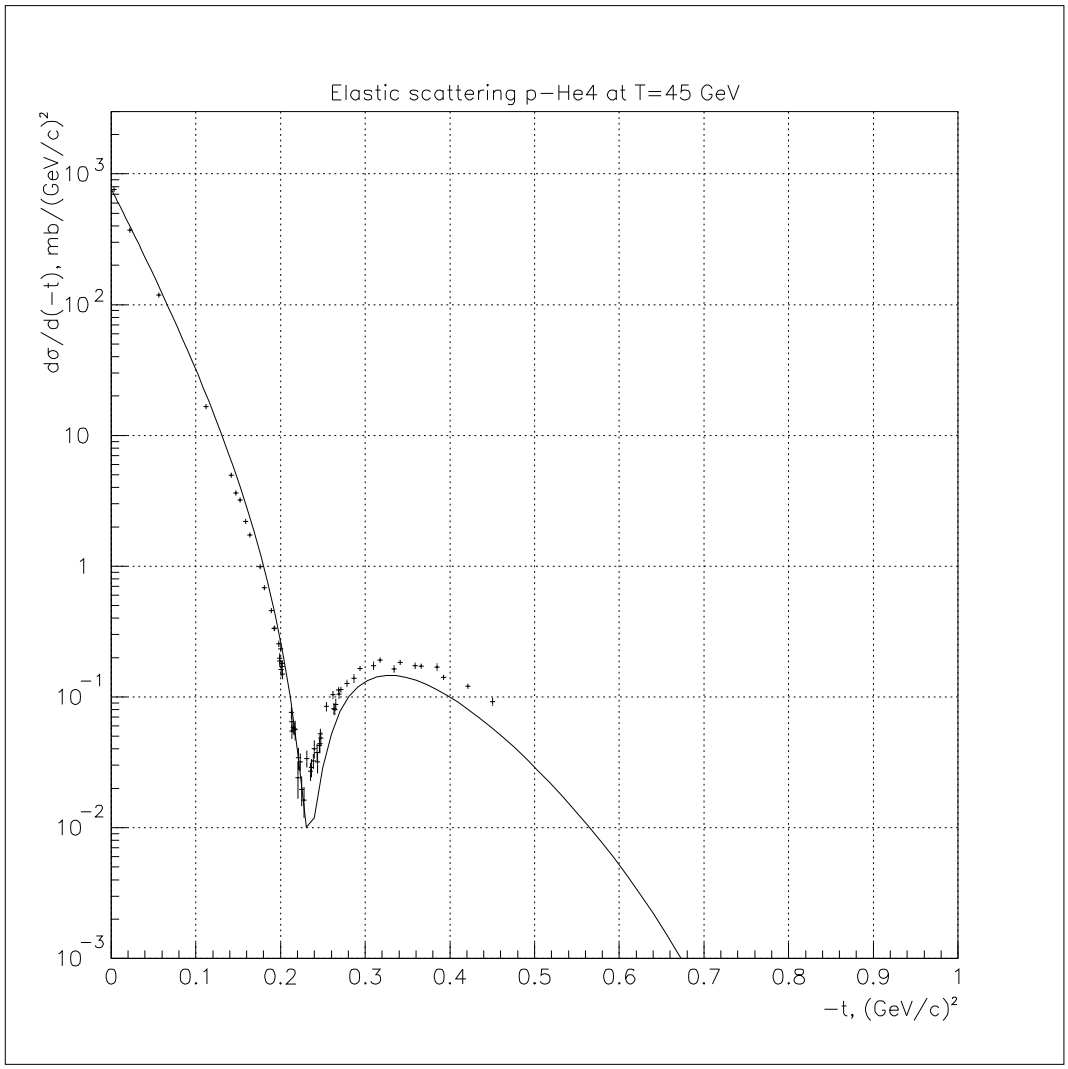

Figure 25.11: Elastic proton scattering on ^{4}He at 45 GeV

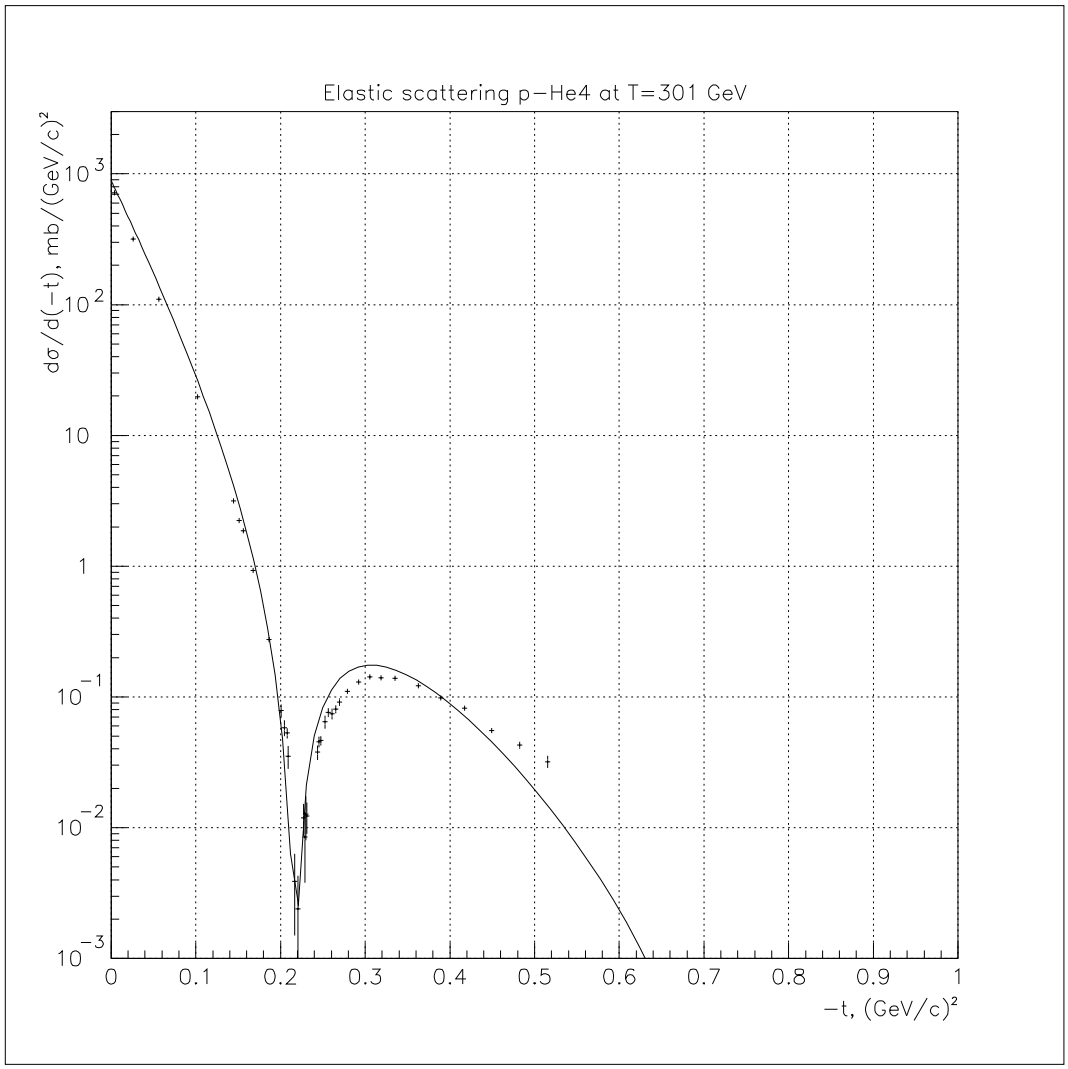

Figure 25.12: Elastic proton scattering on ^{4}He at 301 GeV

Chapter 26

Interactions of Stopping Particles

26.1 Complementary parameterised and theoretical treatment

Absorption of negative pions and kaons at rest from a nucleus is described in literature [1], [2], [3], [4] as consisting of two main components:

- a primary absorption process, involving the interaction of the incident stopped hadron with one or more nucleons of the target nucleus;
- the deexcitation of the remnant nucleus, left in an excitated state as a result of the occurrence of the primary absorption process.

This interpretation is supported by several experiments [5], [6], [7], [8], [9], [10], [11], that have measured various features characterizing these processes. In many cases the experimental measurements are capable to distinguish the final products originating from the primary absorption process and those resulting from the nuclear deexcitation component.

A set of stopped particle absorption processes is implemented in GEANT4, based on this two-component model (PiMinusAbsorptionAtRest and KaonMinusAbsorptionAtRest classes, for π^- and K^- respectively. Both implementations adopt the same approach: the primary absorption component of the process is parameterised, based on available experimental data; the nuclear deexcitation component is handled through the theoretical models described elsewhere in this Manual.

26.1.1 Pion absorption at rest

The absorption of stopped negative pions in nuclei is interpreted [1], [2], [3], [4] as starting with the absorption of the pion by two or more correlated nucleons; the total energy of the pion is transferred to the absorbing nucleons, which then may leave the nucleus directly, or undergo final-state interactions with the residual nucleus. The remaining nucleus de-excites by evaporation of low energetic particles.

G4PiMinusAbsorptionAtRest generates the primary absorption component of the process through the parameterisation of existing experimental data; the primary absorption component is handled by class G4PiMinusStopAbsorption. In the current implementation only absorption on a nucleon pair is considered, while contributions from absorption on nucleon clusters are neglected; this approximation is supported by experimental results [1], [13] showing that it is the dominating contribution.

Several features of stopped pion absorption are known from experimental measurements on various materials [5], [6], [7], [8], [9], [10], [11], [12]:

- the average number of nucleons emitted, as resulting from the primary absorption process;
- the ratio of nn vs np as nucleon pairs involved in the absorption process;
- the energy spectrum of the resulting nucleons emitted and their opening angle distribution.

The corresponding final state products and related distributions are generated according to a parameterisation of the available experimental measurements listed above. The dependence on the material is handled by a strategy pattern: the features pertaining to material for which experimental data are available are treated in G4PiMinusStopX classes (where X represents an element), inheriting from G4StopMaterial base class. In case of absorption on an element for which experimental data are not available, the experimental distributions for the elements closest in Z are used.

The excitation energy of the residual nucleus is calculated by difference between the initial energy and the energy of the final state products of the primary absorption process.

Another strategy handles the nucleus deexcitation; the current default implementation consists in handling the deexcitatoin component of the process through the evaporation model described elsewhere in this Manual.

Bibliography

[1] E. Gadioli and E. Gadioli Erba *Phys. Rev. C 36* 741 (1987)

[2] H.C. Chiang and J. Hufner *Nucl. Phys. A352* 442 (1981)

[3] D. Ashery and J. P. Schiffer *Ann. Rev. Nucl. Part. Sci. 36* 207 (1986)

[4] H. J. Weyer *Phys. Rep. 195* 295 (1990)

[5] R. Hartmann et al., *Nucl. Phys. A300* 345 (1978)

[6] R. Madley et al., *Phys. Rev. C 25* 3050 (1982)

[7] F. W. Schleputz et al., *Phys. Rev. C 19* 135 (1979)

[8] C.J. Orth et al., *Phys. Rev. C 21* 2524 (1980)

[9] H.S. Pruys et al., *Nucl. Phys. A316* 365 (1979)

[10] P. Heusi et al., *Nucl. Phys. A407* 429 (1983)

[11] H.P. Isaak et al., *Nucl. Phys. A392* 368 (1983)

[12] H.P. Isaak et al., *Helvetica Physica Acta 55* 477 (1982)

[13] H. Machner *Nucl. Phys. A395* 457 (1983)

Chapter 27

Parametrization Driven Models

27.1 Introduction

Two sets of parameterized models are provided for the simulation of high energy hadron-nucleus interactions. The so-called "low energy model" is intended for hadronic projectiles with incident energies between 1 GeV and 25 GeV, while the "high energy model" is valid for projectiles between 25 GeV and 10 TeV. Both are based on the well-known GHEISHA package of GEANT3. The physics underlying these models comes from an old-fashioned multi-chain model in which the incident particle collides with a nucleon inside the nucleus. The final state of this interaction consists of a recoil nucleon, the scattered incident particle, and possibly many hadronic secondaries. Hadron production is approximated by the formation zone concept, in which the interacting quark-partons require some time and therefore some range to hadronize into real particles. All of these particles are able to re-interact within the nucleus, thus developing an intra-nuclear cascade.

In these models only the first hadron-nucleon collision is simulated in detail. The remaining interactions within the nucleus are simulated by generating additional hadrons and treating them as secondaries from the initial collision. The numbers, types and distributions of the extra hadrons are determined by functions which were fitted to experimental data or which reproduce general trends in hadron-nucleus collisions. Numerous tunable parameters are used throughout these models to obtain reasonable physical behavior. This restricts the use of these models as generators for hadron-nucleus interactions because it is not always clear how the parameters relate to physical quantities. On the other hand a precise simulation of minimum bias events is possible, with significant predictive power for calorimetry.

27.2 Low Energy Model

In the low energy parameterized model the mean number of hadrons produced in a hadron-nucleus collision is given by

$$N_m = C(s)A^{1/3}N_{ic} \tag{27.1}$$

where A is the atomic mass, $C(s)$ is a function only of the center of mass energy s, and N_{ic} is approximately the number of hadrons generated in the initial collision. Assuming that the collision occurs at the center of the nucleus, each of these hadrons must traverse a distance roughly equal to the nuclear radius. They may therefore potentially interact with a number of nucleons proportional to $A^{1/3}$. If the energy-dependent cross section for interaction in the nuclear medium is included in C then Eq. 27.1 can be interpreted as the number of target nucleons excited by the initial collision. Some of these nucleons are added to the intra-nuclear cascade. The rest, especially at higher momenta where nucleon production is suppressed, are replaced by pions and kaons.

Once the mean number of hadrons, N_m is calculated, the total number of hadrons in the intra-nuclear cascade is sampled from a Poisson distribution about the mean. Sampling from additional distribution functions provides

- the combined multiplicity $w(\vec{a}, n_i)$ for all particles i, $i = \pi^+, \pi^0, \pi^-, p, n, ...$, including the correlations between them,
- the additive quantum numbers E (energy), Q (charge), S (strangeness) and B (baryon number) in the entire phase space region, and
- the reaction products from nuclear fission and evaporation.

A universal function $f(\vec{b}, x/p_T, m_T)$ is used for the distribution of the additive quantum numbers, where x is the Feynman variable, p_T is the transverse momentum and m_T is the transverse mass. $\vec{a}$ and $\vec{b}$ are parameter vectors, which depend on the particle type of the incoming beam and the atomic number A of the target. Any dependence on the beam energy is completely restricted to the multiplicity distribution and the available phase space.

The low energy model can be applied to the π^+, π^-, K^+, K^-, K^0 and $\overline{K^0}$ mesons. It can also be applied to the baryons p, n, Λ, Σ^+, Σ^-, Ξ^0, Ξ^-, Ω^-, and their anti-particles, as well as the light nuclei, d, t and α. The model can in principal be applied down to zero projectile energy, but the assumptions used to develop it begin to break down in the sub-GeV region.

27.3 High Energy Model

The high energy model is valid for incident particle energies from 10-20 GeV up to 10-20 TeV. Individual implementations of the model exist for π^+, π^-, K^+, K^-, K_S^0 and K_L^0 mesons, and for p, n, Λ, Σ^+, Σ^-, Ξ^0, Ξ^-, and Ω^- baryons and their anti-particles.

27.3.1 Initial Interaction

In a given implementation, the generation of the final state begins with the selection of a nucleon from the target nucleus. The pion multiplicities resulting from the initial interaction of the incident particle and the target nucleon are then calculated. The total pion multiplicity is taken to be a function of the log of the available energy in the center of mass of the incident particle and target nucleon, and the π^+, π^- and π^0 multiplicities are given by the KNO distribution.

From this initial set of particles, two are chosen at random to be replaced with either a kaon-anti-kaon pair, a nucleon-anti-nucleon pair, or a kaon and a hyperon. The relative probabilities of these options are chosen according to a logarithmically interpolated table of strange-pair and nucleon-anti-nucleon pair cross sections. The particle types of the pair are chosen according to averaged, parameterized cross sections typical at energies of a few GeV. If the increased mass of the new pair causes the total available energy to be exceeded, particles are removed from the initial set as necessary.

27.3.2 Intra-nuclear Cascade

The cascade of these particles through the nucleus, and the additional particles generated by the cascade are simulated by several models. These include high energy cascading, high energy cluster production, medium energy cascading and medium energy cluster production. For each event, high energy cascading is attempted first. If the available energy is sufficient, this method will likely succeed in producing the final state and the interaction will have been completely simulated. If it fails due to lack of energy or other reasons, the remaining models are called in succession until the final state is produced. If none of these methods succeeds, quasi-elastic scattering is attempted and finally, as a last resort, elastic scattering is performed. These models are responsible for assigning final state momenta to all generated particles, and for checking that, on average, energy and momentum are conserved.

27.3.3 High Energy Cascading

As particles from the initial collision cascade through the nucleus more particles will be generated. The number and type of these particles are parameterized in terms of the CM energy of the initial particle-nucleon collision. The number of particles produced from the cascade is given roughly by

$$N_m = C(s)[A^{1/3} - 1]N_{ic} \tag{27.2}$$

where A is the atomic mass, $C(s)$ is a function only of s, the square of the center of mass energy, and N_{ic} is approximately the number of hadrons generated in the initial collision. This can be understood qualitatively by assuming that the collision occurs, on average, at the center of the nucleus. Then each of the N_{ic} hadrons must traverse a distance roughly equal to the nuclear radius. They may therefore potentially interact with a number of nucleons proportional to $A^{1/3}$. If the energy-dependent cross section for interaction in the nuclear medium is included in $C(s)$ then Eq. 27.2 can be interpreted as the number of target nucleons excited by the initial collision and its secondaries.

Some of these nucleons are added to the intra-nuclear cascade. The rest, especially at higher momenta where nucleon production is suppressed, are replaced by pions, kaons and hyperons. The mean of the total number of hadrons generated in the cascade is partitioned into the mean number of nucleons, N_n, pions, N_π and strange particles, N_s. Each of these is used as the mean of a Poisson distribution which produces the randomized number of each type of particle.

The momenta of these particles are generated by first dividing the final state phase space into forward and backward hemispheres, where forward is in the direction of the original projectile. Each particle is assigned to one hemisphere or the other according to the particle type and origin:

- the original projectile, or its substitute if charge or strangeness exchange occurs, is assigned to the forward hemisphere and the target nucleon is assigned to the backward hemisphere;
- the remainder of the particles from the initial collision are assigned at random to either hemisphere;
- pions and strange particles generated in the intra-nuclear cascade are assigned 80% to the backward hemisphere and 20% to the forward hemisphere;
- nucleons generated in the intra-nuclear cascade are all assigned to the backward hemisphere.

It is assumed that energy is separately conserved for each hemisphere. If too many particles have been added to a given hemisphere, randomly chosen particles are deleted until the energy budget is met. The final state momenta are then generated according to two different algorithms, a cluster model for the backward nucleons from the intra-nuclear cascade, and a fragmentation model for all other particles. Several corrections are then applied to the final state particles, including momentum re-scaling, effects due to Fermi motion, and binding energy subtraction. Finally the de-excitation of the residual nucleus is treated by adding lower energy protons, neutrons and light ions to the final state particle list.

Fragmentation Model. This model simulates the fragmentation of the highly excited hadrons formed in the initial projectile-nucleon collision. Particle momenta are generated by first sampling the average transverse momentum p_T from an exponential distribution:

$$exp[-a{p_T}^b] \tag{27.3}$$

where

$$1.70 \leq a \leq 4.00;\ 1.18 \leq b \leq 1.67. \tag{27.4}$$

The values of a and b depend on particle type and result from a parameterization of experimental data. The value selected for p_T is then used to set the scale for the determination of x, the fraction of the projectile's momentum carried by the fragment. The sampling of x assumes that the invariant cross section for the production of fragments can be given by

$$E\frac{d^3\sigma}{dp^3} = \frac{K}{(M^2x^2 + {p_T}^2)^{3/2}} \tag{27.5}$$

where E and p are the energy and momentum, respectively, of the produced fragment, and K is a proportionality constant. M is the average transverse mass which is parameterized from data and varies from 0.75 GeV to 0.10 GeV, depending on particle type. Taking m to be the mass of the fragment and noting that

$$p_z \simeq xE_{proj} \tag{27.6}$$

in the forward hemisphere and

$$p_z \simeq xE_{targ} \tag{27.7}$$

in the backward hemisphere, Eq. 27.5 can be re-written to give the sampling function for x:

$$\frac{d^3\sigma}{dp^3} = \frac{K}{(M^2x^2 + {p_T}^2)^{3/2}} \frac{1}{\sqrt{m^2 + {p_T}^2 + x^2E_i^2}}, \tag{27.8}$$

where $i = proj$ or $targ$.

x-sampling is performed for each fragment in the final-state candidate list. Once a fragment's momentum is assigned, its total energy is checked to see if it exceeds the energy budget in its hemisphere. If so, the momentum of the particle is reduced by 10%, as is p_T and the integral of the x-sampling function, and the momentum selection process is repeated. If the offending particle starts out in the forward hemisphere, it is moved to the backward hemisphere, provided the budget for the backward hemisphere is not exceeded. If, after six iterations, the particle still does not fit, it is removed from the candidate list and the kinetic energies of the particles selected up to this point are reduced by 5%. The entire procedure is repeated up to three times for each fragment.

The incident and target particles, or their substitutes in the case of charge- or strangeness-exchange, are guaranteed to be part of the final state. They are the last particles to be selected and the remaining energy in their respective hemispheres is used to set the p_z components of their momenta. The p_T components selected by x-sampling are retained.

Cluster Model. This model groups the nucleons produced in the intra-nuclear cascade together with the target nucleon or hyperon, and treats them as a cluster moving forward in the center of mass frame. The cluster disintegrates in such a way that each of its nucleons is given a kinetic energy

$$40 < T_{nuc} < 600\text{MeV} \tag{27.9}$$

if the kinetic energy of the original projectile, T_{inc}, is 5 GeV or more. If T_{inc} is less than 5 GeV,

$$40(T_{inc}/5\text{GeV})^2 < \mathrm{T_{nuc}} < 600(\mathrm{T_{inc}}/5\text{GeV})^2. \tag{27.10}$$

In each range the energy is sampled from a distribution which is skewed strongly toward the high energy limit. In addition, the angular distribution of the nucleons is skewed forward in order to simulate the forward motion of the cluster.

Momentum Re-scaling. Up to this point, all final state momenta have been generated in the center of mass of the incident projectile and the target nucleon. However, the interaction involves more than one nucleon as evidenced by the intra-nuclear cascade. A more correct center of mass should then be defined by the incident projectile and all of the baryons generated by the cascade, and the final state momenta already calculated must be re-scaled to reflect the new center of mass.

This is accomplished by correcting the momentum of each particle in the final state candidate list by the factor T_1/T_2. T_2 is the total kinetic energy in the lab frame of all the final state candidates generated assuming a projectile-nucleon center of mass. T_1 is the total kinetic energy in the lab frame of the same final state candidates, but whose momenta have been calculated by the phase space decay of an imaginary particle. This particle has the total CM energy of the original projectile and a cluster consisting of all the baryons generated from the intra-nuclear cascade.

Corrections. Part of the Fermi motion of the target nucleons is taken into account by smearing the transverse momentum components of the final state particles. The Fermi momentum is first sampled from an average distribution and a random direction for its transverse component is chosen. This component, which is proportional to the number of baryons produced in the cascade, is then included in the final state momenta.

Each final state particle must escape the nucleus, and in the process reduce its kinetic energy by the nuclear binding energy. The binding energy is parameterized as a function of A:

$$E_B = 25\mathrm{MeV}\left(\frac{\mathrm{A}-1}{120}\right)\mathrm{e}^{-(\mathrm{A}-1)/120)}. \tag{27.11}$$

Another correction reduces the kinetic energy of final state π^0s when the incident particle is a π^+ or π^-. This reduction increases as the log of the incident pion energy, and is done to reproduce experimental data. In order to conserve energy on average, the energy removed from the π^0s is re-distributed among the final state π^+s, π^-s and π^0s.

Nuclear De-excitation. After the generation of initial interaction and cascade particles, the target nucleus is left in an excited state. De-excitation is accomplished by evaporating protons, neutrons, deuterons, tritons and alphas from the nucleus according to a parameterized model. The total kinetic energy given to these particles is a function of the incident particle kinetic energy:

$$T_{evap} = 7.716\mathrm{GeV}\left(\frac{\mathrm{A}-1}{120}\right)\mathrm{F(T)e}^{-\mathrm{F(T)}-(\mathrm{A}-1)/120}, \tag{27.12}$$

where

$$F(T) = \max[0.35 + 0.1304\mathrm{ln(T)}, 0.15], \tag{27.13}$$

and

$$T = 0.1\text{GeV} \quad \text{for} \quad \text{T}_{\text{inc}} < 0.1\text{GeV} \tag{27.14}$$

$$T = T_{inc} \quad \text{for} \quad 0.1\text{GeV} \leq \text{T}_{\text{inc}} \leq 4\text{GeV} \tag{27.15}$$

$$T = 4\text{GeV} \quad \text{for} \quad \text{T}_{\text{inc}} > 4\text{GeV}. \tag{27.16}$$

The mean energy allocated for proton and neutron emission is $\overline{T_{pn}}$ and that for deuteron, triton and alpha emission is $\overline{T_{dta}}$. These are determined by partitioning T_{evap} :

$$\overline{T_{pn}} = T_{evap}R \quad , \quad \overline{T_{dta}} = T_{evap}(1-R) \quad \text{with}$$

$$R = \max[1 - (\text{T}/4\text{GeV})^2, 0.5]. \tag{27.17}$$

The simulated values of T_{pn} and T_{dta} are sampled from normal distributions about $\overline{T_{pn}}$ and $\overline{T_{dta}}$ and their sum is constrained not to exceed the incident particle's kinetic energy, T_{inc}.

The number of proton and neutrons emitted, N_{pn}, is sampled from a Poisson distribution about a mean which depends on R and the number of baryons produced in the intranuclear cascade. The average kinetic energy per emitted particle is then $T_{av} = T_{pn}/N_{pn}$. T_{av} is used to parameterize an exponential which qualitatively describes the nuclear level density as a function of energy. The simulated kinetic energy of each evaporated proton or neutron is sampled from this exponential. Next, the nuclear binding energy is subtracted and the final momentum is calculated assuming an isotropic angular distribution. The number of protons and neutrons emitted is $(Z/A)N_{pn}$ and $(N/A)N_{pn}$, respectively.

A similar procedure is followed for the deuterons, tritons and alphas. The number of each species emitted is $0.6N_{dta}$, $0.3N_{dta}$ and $0.1N_{dta}$, respectively.

Tuning of the High Energy Cascade The final stage of the high energy cascade method involves adjusting the momenta of the produced particles so that they agree better with data. Currently, five such adjustments are performed, the first three of which apply only to charged particles incident upon light and medium nuclei at incident energies above $\simeq$ 65 GeV.

- If the final state particle is a nucleon or light ion with a momentum of less than 1.5 GeV/c, its momentum will be set to zero some fraction of the time. This fraction increases with the logarithm of the kinetic energy of the incident particle and decreases with $log_{10}(A)$.

- If the final state particle with the largest momentum happens to be a π^0, its momentum is exchanged with either the π^+ or π^- having the largest momentum, depending on whether the incident particle charge is positive or negative.

- If the number of baryons produced in the cascade is a significant fraction (> 0.3) of A, about 25% of the nucleons and light ions already produced will be removed from the final particle list, provided their momenta are each less than 1.2 GeV/c.

- The final state of the interaction is of course heavily influenced by the quantum numbers of the incident particle, particularly in the forward direction. This influence is enforced by compiling, for each forward-going final state particle, the sum

$$S_{forward} = \Delta_M + \Delta_Q + \Delta_S + \Delta_B, \tag{27.18}$$

  where each Δ corresponds to the absolute value of the difference of the quantum number between the incident particle and the final state particle. M, Q, S, and B refer to mass, charge, strangeness and baryon number, respectively. For final state particles whose character is significantly different from the incident particle (S is large), the momentum component parallel to the incident particle momentum is reduced. The transverse component is unchanged. As a result, large-S particles are driven away from the axis of the hadronic shower. For backward-going particles, a similar procedure is followed based on the calculation of $S_{backward}$.

- Conservation of energy is imposed on the particles in the final state list in one of two ways, depending on whether or not a leading particle has been chosen from the list. If all the particles differ significantly from the incident particle in momentum, mass and other quantum numbers, no leading particle is chosen and the kinetic energy of each particle is scaled by the same correction factor. If a leading particle is chosen, its kinetic energy is altered to balance the total energy, while all the remaining particles are unaltered.

27.3.4 High Energy Cluster Production

As in the high energy cascade model, the high energy cluster model randomly assigns particles from the initial collision to either a forward- or backward-going cluster. Instead of performing the fragmentation process, however,

the two clusters are treated kinematically as the two-body final state of the hadron-nucleon collision. Each cluster is assigned a kinetic energy T which is sampled from a distribution

$$exp[-aT^{1/b}] \tag{27.19}$$

where both a and b decrease with the number of particles in a cluster. If the combined total energy of the two clusters is larger than the center of mass energy, the energy of each cluster is reduced accordingly. The center of mass momentum of each cluster can then be found by sampling the 4-momentum transfer squared, t, from the distribution

$$exp[t(4.0 + 1.6ln(p_{inc}))] \tag{27.20}$$

where $t < 0$ and p_{inc} is the incident particle momentum. Then,

$$cos\theta = 1 + \frac{t - (E_c - E_i)^2 + (p_c - p_i)^2}{2p_c p_i}, \tag{27.21}$$

where the subscripts c and i refer to the cluster and incident particle, respectively. Once the momentum of each cluster is calculated, the cluster is decomposed into its constituents. The momenta of the constituents are determined using a phase space decay algorithm.

The particles produced in the intra-nuclear cascade are grouped into a third cluster. They are treated almost exactly as in the high energy cascade model, where Eq. 27.2 is used to estimate the number of particles produced. The main difference is that the cluster model does not generate strange particles from the cascade. Nucleon suppression is also slightly stronger, leading to relatively higher pion production at large incident momenta. Kinetic energy and direction are assigned to the cluster as described in the cluster model paragraph in the previous section.

The remaining steps to produce the final state particle list are the same as those in high energy cascading:

- re-scaling of the momenta to reflect a center of mass which involves the cascade baryons,
- corrections due to Fermi motion and binding energy,
- reduction of final state π^0 energies,
- nuclear de-excitation and
- high energy tuning.

27.3.5 Medium Energy Cascading

The medium energy cascade algorithm is very similar to the high energy cascade algorithm, but it may be invoked for lower incident energies (down to 1 GeV). The primary difference between the two codes is the parameterization of the fragmentation process. The medium energy cascade samples larger transverse momenta for pions and smaller transverse momenta for kaons and baryons.

A second difference is in the treatment of the cluster consisting of particles generated in the cascade. Instead of parameterizing the kinetic energies and angles of the outgoing particles, the phase space decay approach is used.

Another difference is that the high energy tuning of the final state distribution is not performed.

27.3.6 Medium Energy Cluster Production

The medium energy cluster algorithm is nearly identical to the high energy cluster algorithm, but it may be invoked for incident energies down to 10 MeV. There are three significant differences at medium energy: less nucleon suppression, fewer particles generated in the intra-nuclear cascade, and no high energy tuning of the final state particle distributions.

27.3.7 Elastic and Quasi-elastic Scattering

When no additional particles are produced in the initial interaction, either elastic or quasi-elastic scattering is performed. If there is insufficient energy to induce an intra-nuclear cascade, but enough to excite the target nucleus, quasi-elastic scattering is performed. The final state is calculated using two-body scattering of the incident particle and the target nucleon, with the scattering angle in the center of mass sampled from an exponential:

$$exp[-2bp_{in}p_{cm}(1 - cos\theta)]. \tag{27.22}$$

Here p_{in} is the incident particle momentum, p_{cm} is the momentum in the center of mass, and b is a logarithmic function of the incident momentum in the lab frame as parameterized from data. As in the cascade and cluster production models, the residual nucleus is then de-excited by evaporating nucleons and light ions.

If the incident energy is too small to excite the nucleus, elastic scattering is performed. The angular distribution of the scattered particle is sampled from the sum of two exponentials whose parameters depend on A.

27.4 Status of this document

7.10.02 re-written by D.H. Wright
1.11.04 new section on high energy model by D.H. Wright

Chapter 28

Parton string model.

28.1 Reaction initial state simulation.

28.1.1 Allowed projectiles and bombarding energy range for interaction with nucleon and nuclear targets

The GEANT4 parton string models are capable to predict final states (produced hadrons which belong to the scalar and vector meson nonets and the baryon (antibaryon) octet and decuplet) of reactions on nucleon and nuclear targets with nucleon, pion and kaon projectiles. The allowed bombarding energy $\sqrt{s} > 5$ GeV is recommended. Two approaches, based on diffractive excitation or soft scattering with diffractive admixture according to cross-section, are considered. Hadron-nucleus collisions in the both approaches (diffractive and parton exchange) are considered as a set of the independent hadron-nucleon collisions. However, the string excitation procedures in these approaches are rather different.

28.1.2 MC initialization procedure for nucleus.

The initialization of each nucleus, consisting from A nucleons and Z protons with coordinates $\mathbf{r}_i$ and momenta $\mathbf{p}_i$, where $i = 1, 2, ..., A$ is performed. We use the standard initialization Monte Carlo procedure, which is realized in the most of the high energy nuclear interaction models:

- Nucleon radii r_i are selected randomly in the rest of nucleus according to proton or neutron density $\rho(r_i)$. For heavy nuclei with $A > 16$ [1] nucleon density is

$$\rho(r_i) = \frac{\rho_0}{1 + \exp\left[(r_i - R)/a\right]} \tag{28.1}$$

where

$$\rho_0 \approx \frac{3}{4\pi R^3}(1+\frac{a^2\pi^2}{R^2})^{-1}. \tag{28.2}$$

Here $R = r_0 A^{1/3}$ fm and $r_0 = 1.16(1-1.16A^{-2/3})$ fm and $a \approx 0.545$ fm. For light nuclei with $A < 17$ nucleon density is given by a harmonic oscillator shell model [2], e. g.

$$\rho(r_i) = (\pi R^2)^{-3/2} \exp{(-r_i^2/R^2)}, \tag{28.3}$$

where $R^2 = 2/3 < r^2 >= 0.8133A^{2/3}$ fm^2. To take into account nucleon repulsive core it is assumed that internucleon distance $d > 0.8$ fm;

- The initial momenta of the nucleons are randomly choosen between 0 and p_F^{max}, where the maximal momenta of nucleons (in the local Thomas-Fermi approximation [3]) depends from the proton or neutron density ρ according to

$$p_F^{max} = \hbar c(3\pi^2\rho)^{1/3} \tag{28.4}$$

with $\hbar c = 0.197327$ GeV fm;

- To obtain coordinate and momentum components, it is assumed that nucleons are distributed isotropicaly in configuration and momentum spaces;

- Then perform shifts of nucleon coordinates $\mathbf{r'_j} = \mathbf{r_j} - 1/A\sum_i \mathbf{r_i}$ and momenta $\mathbf{p'_j} = \mathbf{p_j} - 1/A\sum_i \mathbf{p_i}$ of nucleon momenta. The nucleus must be centered in configuration space around $\mathbf{0}$, *i. e.* $\sum_i \mathbf{r}_i = \mathbf{0}$ and the nucleus must be at rest, i. e. $\sum_i \mathbf{p_i} = \mathbf{0}$;

- We compute energy per nucleon $e = E/A = m_N + B(A,Z)/A$, where m_N is nucleon mass and the nucleus binding energy $B(A,Z)$ is given by the Bethe-Weizsäcker formula[4]:

$$B(A,Z) = \\ = -0.01587A + 0.01834A^{2/3} + 0.09286(Z-\tfrac{A}{2})^2 + 0.00071Z^2/A^{1/3}, \tag{28.5}$$

and find the effective mass of each nucleon $m_i^{eff} = \sqrt{(E/A)^2 - p_i^{2\prime}}$.

28.1.3 Random choice of the impact parameter.

The impact parameter $0 \leq b \leq R_t$ is randomly selected according to the probability:

$$P(\mathbf{b})d\mathbf{b} = bd\mathbf{b}, \tag{28.6}$$

where R_t is the target radius, respectively. In the case of nuclear projectile or target the nuclear radius is determined from condition:

$$\frac{\rho(R)}{\rho(0)} = 0.01. \tag{28.7}$$

28.2 Sample of collision participants in nuclear collisions.

28.2.1 MC procedure to define collision participants.

The inelastic hadron–nucleus interactions at ultra–relativistic energies are considered as independent hadron–nucleon collisions. It was shown long time ago [5] for the hadron–nucleus collision that such a picture can be obtained starting from the Regge–Gribov approach [6], when one assumes that the hadron-nucleus elastic scattering amplitude is a result of reggeon exchanges between the initial hadron and nucleons from target–nucleus. This result leads to simple and efficient MC procedure [7] to define the interaction cross sections and the number of the nucleons participating in the inelastic hadron–nucleus collision:

- We should randomly distribute B nucleons from the target-nucleus on the impact parameter plane according to the weight function $T([\vec{b}_j^B])$. This function represents probability density to find sets of the nucleon impact parameters $[\vec{b}_j^B]$, where $j = 1, 2, ..., B$.
- For each pair of projectile hadron i and target nucleon j with choosen impact parameters $\vec{b}_i$ and $\vec{b}_j^B$ we should check whether they interact inelastically or not using the probability $p_{ij}(\vec{b}_i - \vec{b}_j^B, s)$, where $s_{ij} = (p_i + p_j)^2$ is the squared total c.m. energy of the given pair with the 4–momenta p_i and p_j, respectively.

In the Regge–Gribov approach[6] the probability for an inelastic collision of pair of i and j as a function at the squared impact parameter difference $b_{ij}^2 = (\vec{b}_i - \vec{b}_j^B)^2$ and s is given by

$$p_{ij}(\vec{b}_i - \vec{b}_j^B, s) = c^{-1}[1 - \exp\{-2u(b_{ij}^2, s)\}] = \sum_{n=1}^{\infty} p_{ij}^{(n)}(\vec{b}_i - \vec{b}_j^B, s), \tag{28.8}$$

where

$$p_{ij}^{(n)}(\vec{b}_i - \vec{b}_j^B, s) = c^{-1} \exp\{-2u(b_{ij}^2, s)\} \frac{[2u(b_{ij}^2, s)]^n}{n!}. \quad (28.9)$$

is the probability to find the n cut Pomerons or the probability for $2n$ strings produced in an inelastic hadron-nucleon collision. These probabilities are defined in terms of the (eikonal) amplitude of hadron–nucleon elastic scattering with Pomeron exchange:

$$u(b_{ij}^2, s) = \frac{z(s)}{2} \exp(-b_{ij}^2/4\lambda(s)). \quad (28.10)$$

The quantities $z(s)$ and $\lambda(s)$ are expressed through the parameters of the Pomeron trajectory, $\alpha_P^{'} = 0.25\ GeV^{-2}$ and $\alpha_P(0) = 1.0808$, and the parameters of the Pomeron-hadron vertex R_P and γ_P:

$$z(s) = \frac{2c\gamma_P}{\lambda(s)}(s/s_0)^{\alpha_P(0)-1} \quad (28.11)$$

$$\lambda(s) = R_P^2 + \alpha_P^{'} \ln(s/s_0), \quad (28.12)$$

respectively, where s_0 is a dimensional parameter.

In Eqs. (28.8,28.9) the so–called shower enhancement coefficient c is introduced to determine the contribution of diffractive dissociation[6]. Thus, the probability for diffractive dissociation of a pair of nucleons can be computed as

$$p_{ij}^d(\vec{b}_i - \vec{b}_j^B, s) = \frac{c-1}{c}[p_{ij}^{tot}(\vec{b}_i - \vec{b}_j^B, s) - p_{ij}(\vec{b}_i - \vec{b}_j^B, s)], \quad (28.13)$$

where

$$p_{ij}^{tot}(\vec{b}_i - \vec{b}_j^B, s) = (2/c)[1 - \exp\{-u(b_{ij}^2, s)\}]. \quad (28.14)$$

The Pomeron parameters are found from a global fit of the total, elastic, differential elastic and diffractive cross sections of the hadron–nucleon interaction at different energies.

For the nucleon-nucleon, pion-nucleon and kaon-nucleon collisions the Pomeron vertex parameters and shower enhancement coefficients are found: $R_P^{2N} = 3.56\ GeV^{-2}$, $\gamma_P^N = 3.96\ GeV^{-2}$, $s_0^N = 3.0\ GeV^2$, $c^N = 1.4$ and $R_P^{2\pi} = 2.36\ GeV^{-2}$, $\gamma_P^\pi = 2.17\ GeV^{-2}$, and $R_P^{2K} = 1.96\ GeV^{-2}$, $\gamma_P^K = 1.92\ GeV^{-2}$, $s_0^K = 2.3\ GeV^2$, $c^\pi = 1.8$.

28.2.2 Separation of hadron diffraction excitation.

For each pair of target hadron i and projectile nucleon j with choosen impact parameters $\vec{b}_i$ and $\vec{b}_j^B$ we should check whether they interact inelastically or not using the probability

$$p_{ij}^{in}(\vec{b}_i - \vec{b}_j^B, s) = p_{ij}(\vec{b}_i - \vec{b}_j^B, s) + p_{ij}^d(\vec{b}_i^A - \vec{b}_j^B, s). \quad (28.15)$$

If interaction will be realized, then we have to consider it to be diffractive or nondiffractive with probabilities

$$\frac{p_{ij}^{d}(\vec{b}_i - \vec{b}_j^B, s)}{p_{ij}^{in}(\vec{b}_i^A - \vec{b}_j^B, s)} \tag{28.16}$$

and

$$\frac{p_{ij}(\vec{b}_i - \vec{b}_j^B, s)}{p_{ij}^{in}(\vec{b}_i^A - \vec{b}_j^B, s)}. \tag{28.17}$$

28.3 Longitudinal string excitation

28.3.1 Hadron–nucleon inelastic collision

Let us consider collision of two hadrons with their c. m. momenta $P_1 = \{E_1^+, m_1^2/E_1^+, \mathbf{0}\}$ and $P_2 = \{E_2^-, m_2^2/E_2^-, \mathbf{0}\}$, where the light-cone variables $E_{1,2}^{\pm} = E_{1,2} \pm P_{z1,2}$ are defined through hadron energies $E_{1,2} = \sqrt{m_{1,2}^2 + P_{z1,2}^2}$, hadron longitudinal momenta $P_{z1,2}$ and hadron masses $m_{1,2}$, respectively. Two hadrons collide by two partons with momenta $p_1 = \{x^+E_1^+, 0, \mathbf{0}\}$ and $p_2 = \{0, x^-E_2^-, \mathbf{0}\}$, respectively.

28.3.2 The diffractive string excitation

In the diffractive string excitation (the Fritiof approach [9]) only momentum can be transferred:

$$\begin{aligned} P_1' &= P_1 + q \\ P_2' &= P_2 - q, \end{aligned} \tag{28.18}$$

where

$$q = \{-q_t^2/(x^-E_2^-), q_t^2/(x^+E_1^+), \mathbf{q_t}\} \tag{28.19}$$

is parton momentum transferred and $\mathbf{q_t}$ is its transverse component. We use the Fritiof approach to simulate the diffractive excitation of particles.

28.3.3 The string excitation by parton exchange

For this case the parton exchange (rearrangement) and the momentum exchange are allowed [10],[11],[7]:

$$\begin{aligned} P_1' &= P_1 - p_1 + p_2 + q \\ P_2' &= P_2 + p_1 - p_2 - q, \end{aligned} \tag{28.20}$$

where $q = \{0, 0, \mathbf{q_t}\}$ is parton momentum transferred, i. e. only its transverse components $\mathbf{q_t} = 0$ is taken into account.

28.3.4 Transverse momentum sampling

The transverse component of the parton momentum transferred is generated according to probability

$$P(\mathbf{q_t})d\mathbf{q_t} = \sqrt{\frac{a}{\pi}}\exp\left(-aq_t^2\right)d\mathbf{q_t}, \tag{28.21}$$

where parameter $a = 0.6$ GeV^{-2}.

28.3.5 Sampling x-plus and x-minus

Light cone parton quantities x^+ and x^- are generated independently and according to distribution:

$$u(x) \sim x^\alpha(1-x)^\beta, \tag{28.22}$$

where $x = x^+$ or $x = x^-$. Parameters $\alpha = -1$ and $\beta = 0$ are chosen for the FRITIOF approach [9]. In the case of the QGSM approach [7] $\alpha = -0.5$ and $\beta = 1.5$ or $\beta = 2.5$. Masses of the excited strings should satisfy the kinematical constraints:

$$P_1'^+P_1'^- \geq m_{h1}^2 + q_t^2 \tag{28.23}$$

and

$$P_2'^+P_2'^- \geq m_{h2}^2 + q_t^2, \tag{28.24}$$

where hadronic masses m_{h1} and m_{h2} (model parameters) are defined by string quark contents. Thus, the random selection of the values x^+ and x^- is limited by above constraints.

28.3.6 The diffractive string excitation

In the diffractive string excitation (the FRITIOF approach [9]) for each inelastic hadron–nucleon collision we have to select randomly the transverse momentum transferred $\mathbf{q_t}$ (in accordance with the probability given by Eq. (28.21)) and select randomly the values of $x^\pm$ (in accordance with distribution defined by Eq. (28.22)). Then we have to calculate the parton momentum transferred q using Eq. (28.19) and update scattered hadron and nucleon or scatterred nucleon and nucleon momenta using Eq. (28.20). For each collision we have to check the constraints (28.23) and (28.24), which can be written more explicitly:

$$[E_1^+ - \frac{q_t^2}{x^-E_2^-}][\frac{m_1^2}{E_1^+} + \frac{q_t^2}{x^+E_1^+}] \geq m_{h1}^2 + q_t^2 \tag{28.25}$$

and

$$[E_2^- + \frac{q_t^2}{x^- E_2^-}][\frac{m_2^2}{E_2^-} - \frac{q_t^2}{x^+ E_1^+}] \geq m_{h1}^2 + q_t^2. \tag{28.26}$$

28.3.7 The string excitation by parton rearrangement

In this approach [7] strings (as result of parton rearrangement) should be spanned not only between valence quarks of colliding hadrons, but also between valence and sea quarks and between sea quarks. The each participant hadron or nucleon should be splitted into set of partons: valence quark and antiquark for meson or valence quark (antiquark) and diquark (antidiquark) for baryon (antibaryon) and additionaly the $(n-1)$ sea quark-antiquark pairs (their flavours are selected according to probability ratios $u:d:s=1:1:0.35$), if hadron or nucleon is participating in the n inelastic collisions. Thus for each participant hadron or nucleon we have to generate a set of light cone variables x_{2n}, where $x_{2n} = x_{2n}^+$ or $x_{2n} = x_{2n}^-$ according to distribution:

$$f^h(x_1, x_2, ..., x_{2n}) = f_0 \prod_{i=1}^{2n} u_{q_i}^h(x_i) \delta(1 - \sum_{i=1}^{2n} x_i), \tag{28.27}$$

where f_0 is the normalization constant. Here, the quark structure functions $u_{q_i}^h(x_i)$ for valence quark (antiquark) q_v, sea quark and antiquark q_s and valence diquark (antidiquark) qq are:

$$u_{q_v}^h(x_v) = x_v^{\alpha_v},\ u_{q_s}^h(x_s) = x_s^{\alpha_s},\ u_{qq}^h(x_{qq}) = x_{qq}^{\beta_{qq}}, \tag{28.28}$$

where $\alpha_v = -0.5$ and $\alpha_s = -0.5$ [10] for the non-strange quarks (antiquarks) and $\alpha_v = 0$ and $\alpha_s = 0$ for strange quarks (antiquarks), $\beta_{uu} = 1.5$ and $\beta_{ud} = 2.5$ for proton (antiproton) and $\beta_{dd} = 1.5$ and $\beta_{ud} = 2.5$ for neutron (antineutron). Usualy x_i are selected between $x_i^{min} \leq x_i \leq 1$, where model parameter x^{min} is a function of initial energy, to prevent from production of strings with low masses (less than hadron masses), when whole selection procedure should be repeated. Then the transverse momenta of partons $\mathbf{q_{it}}$ are generated according to the Gaussian probability Eq. (28.21) with $a = 1/4\Lambda(s)$ and under the constraint: $\sum_{i=1}^{2n} \mathbf{q_{it}} = 0$. The partons are considered as the off-shell partons, i. e. $m_i^2 \neq 0$.

28.4 Longitudinal string decay.

28.4.1 Hadron production by string fragmentation.

A string is stretched between flying away constituents: quark and antiquark or quark and diquark or diquark and antidiquark or antiquark and antidiquark. From knowledge of the constituents longitudinal $p_{3i} = p_{zi}$ and transversal $p_{1i} = p_{xi}$, $p_{2i} = p_{yi}$ momenta as well as their energies $p_{0i} = E_i$, where $i = 1, 2$, we can calculate string mass squared:

$$M_S^2 = p^\mu p_\mu = p_0^2 - p_1^2 - p_2^2 - p_3^2, \tag{28.29}$$

where $p_\mu = p_{\mu 1} + p_{\mu 2}$ is the string four momentum and $\mu = 0, 1, 2, 3$.

The fragmentation of a string follows an iterative scheme:

$$string \Rightarrow hadron + new\ string, \tag{28.30}$$

i. e. a quark-antiquark (or diquark-antidiquark) pair is created and placed between leading quark-antiquark (or diquark-quark or diquark-antidiquark or antiquark-antidiquark) pair.

The values of the strangeness suppression and diquark suppression factors are

$$u : d : s : qq = 1 : 1 : 0.35 : 0.1. \tag{28.31}$$

A hadron is formed randomly on one of the end-points of the string. The quark content of the hadrons determines its species and charge. In the chosen fragmentation scheme we can produce not only the groundstates of baryons and mesons, but also their lowest excited states. If for baryons the quark-content does not determine whether the state belongs to the lowest octet or to the lowest decuplet, then octet or decuplet are choosen with equal probabilities. In the case of mesons the multiplet must also be determined before a type of hadron can be assigned. The probability of choosing a certain multiplet depends on the spin of the multiplet.

The zero transverse momentum of created quark-antiquark (or diquark-antidiquark) pair is defined by the sum of an equal and opposite directed transverse momenta of quark and antiquark.

The transverse momentum of created quark is randomly sampled according to probability (28.21) with the parameter $a = 0.25$ GeV^{-2}. Then a hadron transverse momentum $\mathbf{p_t}$ is determined by the sum of the transverse momenta of its constituents.

The fragmentation function $f^h(z, p_t)$ represents the probability distribution for hadrons with the transverse momenta $\mathbf{p_t}$ to aquire the light cone momentum fraction $z = z^\pm = (E^h \pm p_z^h/(E^q \pm p_z^q)$, where E^h and E^q

are the hadron and fragmented quark energies, respectively and p_z^h and p_z^q are hadron and fragmented quark longitudinal momenta, respectively, and $z_{min}^{\pm} \leq z^{\pm} \leq z_{max}^{\pm}$, from the fragmenting string. The values of $z_{min,max}^{\pm}$ are determined by hadron m_h and constituent transverse masses and the available string mass. One of the most common fragmentation function is used in the LUND model [12]:

$$f^h(z, p_t) \sim \frac{1}{z}(1-z)^a \exp\,[-\frac{b(m_h^2 + p_t^2)}{z}]. \tag{28.32}$$

One can use this fragmentation function for the decay of the excited string.

One can use also the fragmentation functions are derived in [13]:

$$f_q^h(z, p_t) = [1 + \alpha_q^h(< p_t >)](1-z)^{\alpha_q^h(<p_t>)}. \tag{28.33}$$

The advantage of these functions as compared to the LUND fragmentation function is that they have correct three–reggeon behaviour at $z \to 1$ [13].

28.4.2 The hadron formation time and coordinate.

To calculate produced hadron formation times and longitudinal coordinates we consider the $(1+1)$-string with mass M_S and string tension κ, which decays into hadrons at string rest frame. The i-th produced hadron has energy E_i and its longitudinal momentum p_{zi}, respectively. Introducing light cone variables $p_i^{\pm} = E_i \pm p_{iz}$ and numbering string breaking points consecutively from right to left we obtain $p_0^+ = M_S$, $p_i^+ = \kappa(z_{i-1}^+ - z_i^+)$ and $p_i^- = \kappa x_i^-$.

We can identify the hadron formation point coordinate and time as the point in space-time, where the quark lines of the quark-antiquark pair forming the hadron meet for the first time (the so-called 'yo-yo' formation point [12]):

$$t_i = \frac{1}{2\kappa}[M_S - 2\sum_{j=1}^{i-1} p_{zj} + E_i - p_{zi}] \tag{28.34}$$

and coordinate

$$z_i = \frac{1}{2\kappa}[M_S - 2\sum_{j=1}^{i-1} E_j + p_{zi} - E_i]. \tag{28.35}$$

28.5 Status of this document

05.12.05 corrected units on hbarc in section 1 - D.H. Wright
00.00.00 created by ??

Bibliography

[1] Grypeos M. E., Lalazissis G. A., Massen S. E., Panos C. P., J. Phys. **G17** 1093 (1991).

[2] Elton L. R. B., Nuclear Sizes, Oxford University Press, Oxford, 1961.

[3] DeShalit A., Feshbach H., Theoretical Nuclear Physics, Vol. 1: Nuclear Structure, Wyley, 1974.

[4] Bohr A., Mottelson B. R., Nuclear Structure, W. A. Benjamin, New York, Vol. 1, 1969.

[5] Capella A. and Krzywicki A., Phys. Rev. **D18** (1978) 4120.

[6] Baker M. and Ter–Martirosyan K. A., Phys. Rep. **28C** (1976) 1.

[7] Amelin N. S., Gudima K. K., Toneev V. D., Sov. J. Nucl. Phys. **51** (1990) 327; Amelin N. S., JINR Report **P2-86-56** (1986).

[8] Abramovskii V. A., Gribov V. N., Kancheli O. V., Sov. J. Nucl. Phys. **18** (1974) 308.

[9] Andersson B., Gustafson G., Nielsson-Almquist, Nucl. Phys. **281** 289 (1987).

[10] Kaidalov A. B., Ter-Martirosyan K. A., Phys. Lett. **B117** 247 (1982).

[11] Capella A., Sukhatme U., Tan C. I., Tran Thanh Van. J., Phys. Rep. **236** 225 (1994).

[12] Andersson B., Gustafson G., Ingelman G., Sjöstrand T., Phys. Rep. **97** 31 (1983).

[13] Kaidalov A. B., Sov. J. Nucl. Phys. **45** 1452 (1987).

Chapter 29

Fritiof (FTF) Model

The Fritiof model, or FTF for short, is used in Geant4 for simulation of the following interactions: hadron-nucleus at Plab > 3–4 GeV/c, nucleus-nucleus at Plab > 2–3 GeV/c/nucleon, antibaryon-nucleus at all energies, and antinucleus-nucleus. Because the model does not include multi-jet production in hadron-nucleon interactions, the upper limit of its validity range is estimated to be 1000 GeV/c per hadron or nucleon.

The model assumes that one or two unstable objects (quark-gluon strings) are produced in elementary interactions. If only one object is created, the process is called diffraction dissociation. It is assumed also that the objects can interact with other nucleons in hadron-nucleus and nucleus-nucleus collisions, and can produce other objects. The number of produced objects in these non-diffractive interactions is proportional to the number of participating nucleons. Thus, multiplicities in the hadron-nucleus and nucleus-nucleus interactions are larger than those in elementary ones.

The modeling of hadron-nucleon interactions in the FTF model includes simulations of elastic scattering, binary reactions like $NN \to N\Delta$, $\pi N \to \pi\Delta$, single diffractive and non-diffractive events, and annihilation in antibaryon-nucleon interactions. It is assumed that the unstable objects created in hadron-nucleus and nucleus-nucleus collisions can have analogous reactions.

Parameterizations of the CHIPS Geant4 model are used for calculations of elastic and inelastic hadron-nucleon cross sections. Data-driven parameterizations of the binary reaction cross sections and the diffraction dissociation cross sections in the elementary interactions are implemented in the FTF model. It is assumed in the model that the unstable object cross sections are equal to the cross sections of stable objects having the same quark content.

The LUND string fragmentation model is used for the simulation of unstable object decays. The formation time of hadrons is considered also. Pa-

rameters of the fragmentation model were tuned to experimental data. A restriction of the available phase space is taken into account in low mass string fragmentation.

A simplified Glauber model is used for sampling the multiplicity of intra-nuclear collisions. Gribov inelastic screening is not considered. For medium and heavy nuclei a Saxon-Woods parameterization of the one-particle nuclear density is used, while for light nuclei a harmonic oscillator shape is used. Center-of-mass correlations and short range nucleon-nucleon correlations are taken into account.

The reggeon theory inspired model (RTIM) of nuclear destruction is applied for a description of secondary particle intra-nuclear cascading. A new algorithm to simulate "Fermi motion" in nuclear reactions is used.

Excitation energies of residual nuclei are estimated in the wounded nucleon approximation. This allows for a direct coupling of the FTF model to the Precompound model of Geant4 and hence with the GEM nuclear fragmentation model. The determination of the particle formation time allows one to couple the FTF model with the Binary cascade model of Geant4.

29.1 Main assumptions of the FTF model

The Fritiof model[1, 2] assumes that all hadron-hadron interactions are binary reactions, $h_1 + h_2 \rightarrow h_1' + h_2'$, where h_1' and h_2' are excited states of the hadrons with discrete or continuous mass spectra (see Fig. 29.1). If one of the final hadrons is in its ground state ($h_1 + h_2 \rightarrow h_1 + h_2'$) the reaction is called "single diffraction dissociation", and if neither hadron is in its ground state it is called a "non-diffractive" interaction.

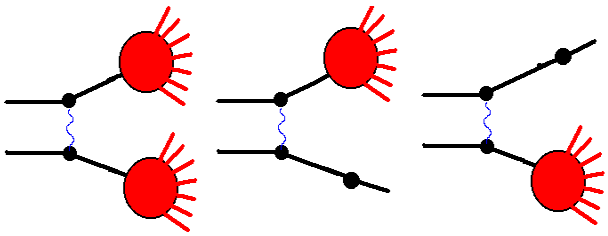

Figure 29.1: Non-diffractive and diffractive interactions considered in the Fritiof model.

The excited hadrons are considered as QCD-strings, and the corresponding LUND-string fragmentation model is applied in order to simulate their decays.

The key ingredient of the Fritiof model is the sampling of the string masses. In general, the set of final state of interactions can be represented by Fig. 29.2, where samples of possible string masses are shown. There is a point corresponding to elastic scattering, a group of points which represents final states of binary hadron-hadron interactions, lines corresponding to the diffractive interactions, and various intermediate regions. The region populated with the red points is responsible for the non-diffractive interactions. In the model, the mass sampling threshold is set equal to the ground state hadron masses, but in principle the threshold can be lower than these masses. The string masses are sampled in the triangular region restricted by the diagonal line corresponding to the kinematical limit $M_1 + M_2 = E_{cms}$ where M_1 and M_2 are the masses of the h'_1 and h'_2 hadrons, and also of the threshold lines. If a point is below the string mass threshold, it is shifted to the nearest diffraction line.

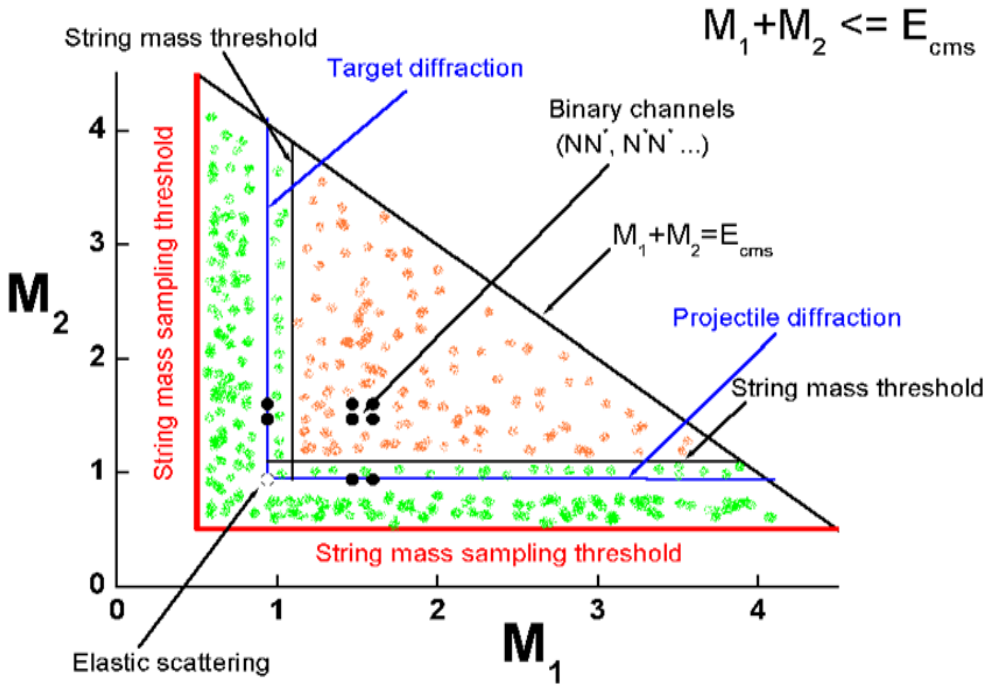

Figure 29.2: Diagram of the final states of hadron-hadron interactions.

Unlike the original Fritiof model, the final state diagram of the current model is complicated, which leads to a mass sampling algorithm that is not simple. This will be considered below. The original model had no points corresponding to elastic scattering or to the binary final states. As it was known at the time, the mass of an object produced by diffraction dissociation,

M_x, for example from the reaction $p+p \to p+X$, is distributed as $dM_x/M_x \propto dM_x^2/M_x^2$, so it was natural to assume that the object mass distributions in all inelastic interactions obeyed the same law. This can be re-written using the light-cone momentum variables, P^+ or P^-,

$$P^+ = E + p_z, \quad P^- = E - p_z,$$

where E is an energy of a particle, and p_z is its longitudinal momentum along the collision axis. At large energy and positive p_z, $P^- \simeq (M^2 + P_T^2)/2p_z$. At negative p_z, $P^+ \simeq (M^2 + P_T^2)/2|p_z|$. Usually, the transferred transverse momentum, P_T, is small and can be neglected. Thus, it was assumed that P^- and P^+ of a projectile, or target associated hadron, respectively, are distributed as

$$dP^-/P^-, \quad dP^+/P^+.$$

A gaussian distribution was used to sample P_T.

In the case of hadron-nucleus or nucleus-nucleus interactions it was assumed that the created objects can interact further with other nuclear nucleons and create new objects. Assuming equal masses of the objects, the multiplicity of particles produced in these interactions will be proportional to the number of participating nuclear nucleons, or to the multiplicity of intra-nuclear collisions. Due to this, the multiplicity of particles produced in hadron-nucleus or nucleus-nucleus interactions is larger than that in hadron-hadron ones. The probabilities of multiple intra-nuclear collisions were sampled with the help of a simplified Glauber model. Cascading of secondary particles was not considered.

Because the Fermi motion of nuclear nucleons was simulated in a simple manner, the original Fritiof model could not work at $P_{lab} < 10$–20 GeV/c.

It was assumed in the model that the created objects are quark-gluon strings with constituent quarks at their ends originating from the primary colliding hadrons. Thus, the LUND-string fragmentation model was applied for a simulation of the object decays. It was assumed also that the strings with sufficiently large masses have "kinks" – additional radiated gluons. This was very important for a correct reproduction of particle multiplicities in the interactions.

All of the above assumptions were reconsidered in the implementation of the Geant4 Fritiof model, and new features were added. These will be presented below.

29.2 General properties of hadron-nucleon interactions

Before going into details of the FTF model implementation it would be better to consider briefly the general properties of hadron-nucleon interactions in order to understand what needs to be simulated. These properties include total and elastic cross sections, and cross sections of various other reactions. There is so much data on inclusive spectra that not all of it can be addressed in this work. It is hoped that the remaining data will be the subject of a future paper. Inclusive data present kinematical properties of produced particles. Their description requires additional methods and parameters, which will be considered later.

29.2.1 $\pi^- p$-interactions

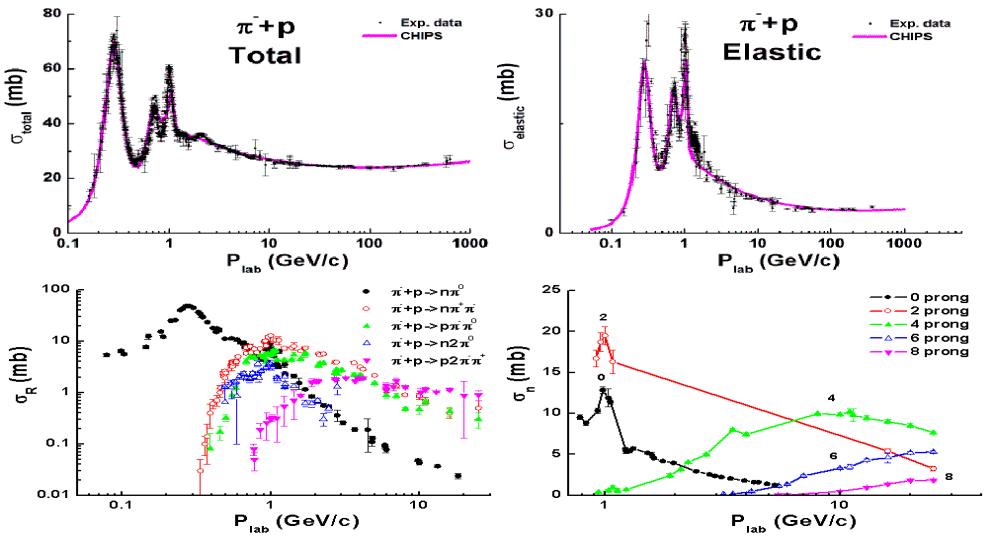

Figure 29.3: General properties of $\pi^- p$-interactions. Points are experimental data: data on total and elastic cross sections from PDG data-base [3], other data from [4].

Total, elastic and reaction cross sections of $\pi^- p$-interactions are presented in Fig. 29.3. As seen, there are peaks in the total cross section connected with Δ-isobar production ($\Delta(1232)$, $\Delta(1600)$, $\Delta(1700)$ and so on) in the s-channel, $\pi^- + p \to \Delta^0$. The main channel of a Δ^0-isobar decay is $\Delta^0 \to \pi^- + p$. These resonances are reflected in the elastic cross section. The other important de-

cay channel is $\Delta^0 \to \pi^0 + n$, which is the main inelastic reaction channel at $P_{lab} < 700$ MeV/c. At higher energy two-meson production channels start to dominate, and at $P_{lab} > 3$ GeV/c there is practically no structure in the cross sections. Cross sections of final states with defined charged particle multiplicity, so-called prong cross sections according to the old terminology, are presented in the last figure. As seen, real multi-particle production processes ($n \geq 4$) dominate at $P_{lab} > 5$–7 GeV/c.

In the constituent quark model of hadrons, the creation of s-channel Δ-isobars is explained by quark–anti-quark annihilation (see Fig. 29.4a). The production of two mesons may result from quark exchange (see Fig. 29.4b, 29.4c). A quark–di-quark (q–qq) system created in the process can be in a resonance state (29.4b), or in a state with a continuous mass spectrum (29.4c). In the latter case, multi-meson production is possible. Amplitudes of these two channels are connected by crossing symmetry to annihilation in the t-channel, and with non-vacuum exchanges in the elastic scattering according to the reggeon phenomenology. According to that phenomenology, pomeron exchange must dominate in elastic scattering at high energies. In a simple approach, this corresponds to two-gluon exchange between colliding hadrons. It reflects also one or many non-perturbative gluon exchanges in the inelastic reaction. Due to these exchanges, a state with subdivided colors is created (see Fig. 29.4d). The state can decay into two colorless objects. The quark content of the objects coincides with the quark content of the primary hadrons, according to the FTF model, or it is a mixture of the primary hadron's quarks, according to the Quark-Gluon-String model (QGSM).

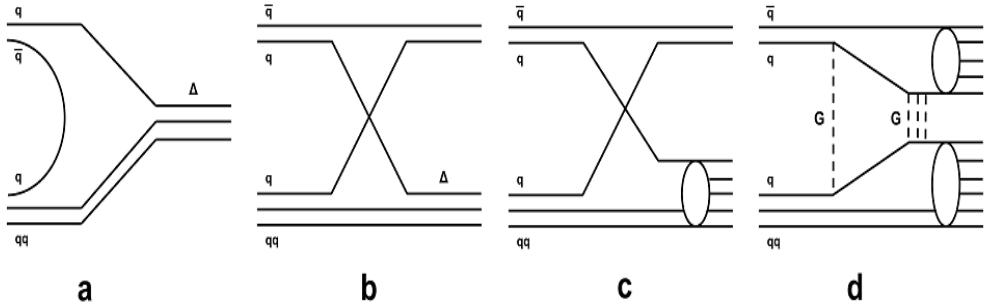

Figure 29.4: Quark flow diagrams of πN-interactions.

The original Fritiof model contains only the pomeron exchange process shown in Fig. 29.4d. It would be useful to extend the model by adding the exchange processes shown in Figs. 29.4b and 29.4c, and the annihilation process of Fig. 29.4a . This could probably be done by introducing a restricted

set of mesonic and baryonic resonances and a corresponding set of parameters. This procedure was employed in the binary cascade model of Geant4 (BIC) [5] and in the Ultra-Relativistic-Quantum-Molecular-Dynamic model (UrQMD) [6]. However, it is complicated to use this solution for a simulation of hadron-nucleus and nucleus-nucleus interactions. The problem is that one has to consider resonance propagation in the nuclear medium and take into account their possible decays which enormously increases computing time. Thus, in the current version of the FTF model only quark exchange processes have been added to account for meson and baryon interactions with nucleons, without considering resonance propagation and decay. This is a reasonable hypothesis at sufficiently high energies.

29.2.2 π^+p-interactions

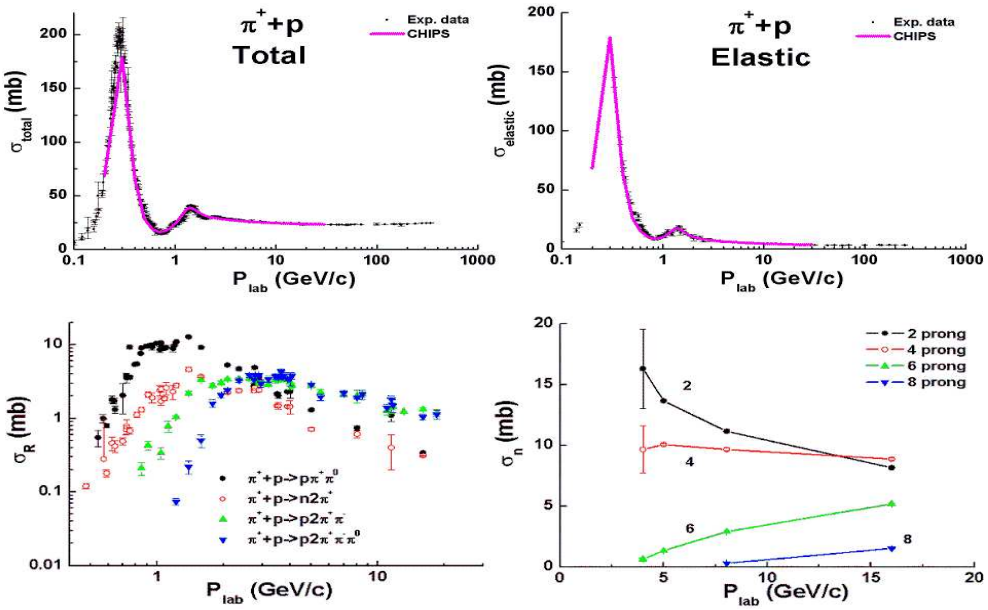

Figure 29.5: General properties of π^+p-interactions. Points are experimental data: data on total and elastic cross sections from PDG data-base [3], other data from [4].

Total, elastic and reaction cross sections of π^+p-interactions are presented in Fig. 29.5. As seen, there are fewer peaks in the total cross section than in π^-p-collisions. The creation of Δ^{++}-isobars in the s-channel ($\pi^+ + p \to \Delta^{++}$) is mainly seen in the elastic cross section because the main channel of Δ^{++}-isobar decay is $\Delta^{++} \to \pi^+ + p$. This process is due to quark–anti-quark

annihilation. At $P_{lab} > 400$ MeV/c two-meson production channels appear. They can be connected with quark exchange and with the formation of Δ^{++} and Δ^{+} isobars at the proton site. The corresponding cross sections of the reactions – $\pi^+ + p \to \pi^0 + \Delta^{++} \to \pi^0 + \pi^+ + p$, $\pi^+ + p \to \pi^+ + \Delta^+ \to \pi^+ + \pi^0 + p$, $\pi^+ + p \to \pi^+ + \Delta^+ \to \pi^+ + \pi^+ + n$ have structures at $P_{lab} \simeq 1.5$ and 2.8 GeV/c. At higher energies there is no structure. The cross sections of other reactions are rather smooth.

29.2.3 *pp*-interactions

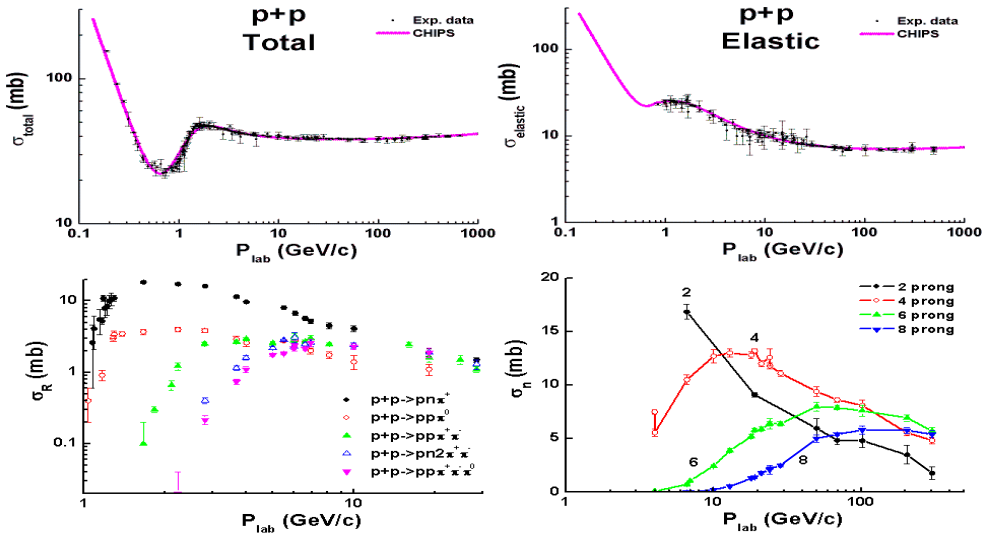

Figure 29.6: General properties of *pp*-interactions. Points are experimental data: data on total and elastic cross sections from PDG data-base [3], other data from [7]

Total, elastic and reaction cross sections of *pp*-interactions are presented in Fig. 29.6. The total cross section is seen to decrease with energy below the meson production threshold ($P_{lab} \leq 800$ MeV/c). Above the threshold the cross section starts to increase and becomes nearly constant. The main reaction channel below 6–8 GeV/c is $p + p \to p + n + \pi^+$. Because there cannot be quark–anti-quark annihilation in the interaction, the reaction must be connected to quark exchange. Intermediate states can be $p + p \to p + \Delta^+$ and $p + p \to n + \Delta^{++}$. In the first case, quarks of the same flavor in the projectile and the target are exchanged. In the second case quarks with different flavors take part in the exchange. Because the cross section of the

$p+p \to p+n+\pi^+$ reaction is larger than the that of $p+p \to p+p+\pi^0$, one has to assume that the exchange of quarks with the same flavors is suppressed.

All the reactions shown can also be caused by diffraction dissociation. Although there can be a yield of the $p+p \to \Delta^0+\Delta^{++}$ reaction in the cross section of the channel $p+p \to (p+\pi^-)+(p+\pi^+)$ at $P_{lab} \sim$ 2–3 GeV/c. Because there are no defined structures in the cross sections, one can assume that diffraction plays an essential role in the interactions.

Summing up the consideration of the interactions, one can conclude that the probability of quark exchanges can depend on quark flavors, and that pp-collisions could be a source of information about diffraction.

29.2.4 K^+p- and K^-p-interactions

For completeness, the properties of K^+p- and K^-p-interactions are presented. Total and elastic cross sections are shown in Fig. 29.7. As the s-anti-quark in the K^+-mesons cannot annihilate in the K^+p-interactions, the structure of the corresponding cross sections is rather simple, and is very like the structure of pp cross sections. The u-anti-quark in the K^--mesons can annihilate, and the structure of the cross sections is more complicated. Due to these features, inelastic reactions are very different even though all of them can be connected with various quark flow diagrams like that shown in Fig. 29.4

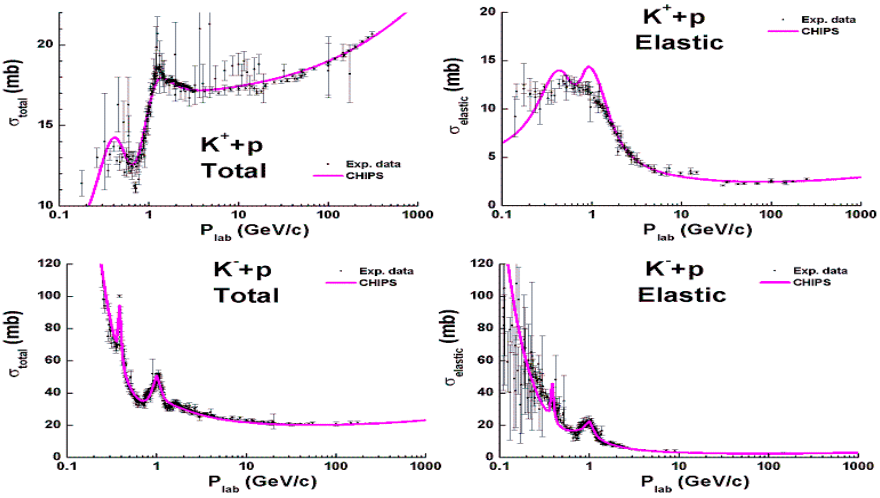

Figure 29.7: Total and elastic cross sections of Kp-interactions. Points are experimental data from PDG data-base [3].

The reactions $K^- + p \to \Sigma^- + \pi^+$ and $K^- + p \to \Sigma^0 + \pi^0$ can be explained by the annihilation of the u-anti-quark of the K^- and the formation of s-

channel resonances. The other reactions – $K^- + p \to \Sigma^+ + \pi^-$ and $K^- + p \to \Lambda + \pi^0$, are connected with quark exchange. As seen, the energy dependence of the cross sections of the two types of processes are different. The $K^- + p \to n + K^0$ reaction must be caused by annihilation, but the dependence of its cross section on energy is closer to that of the quark exchange processes. The cross section of the reaction has a resonance structure only at $P_{lab} < 2$ GeV/c. Above that energy there is no structure. Because the cross section of the reaction is sufficiently small at high energies, one can omit its correct description.

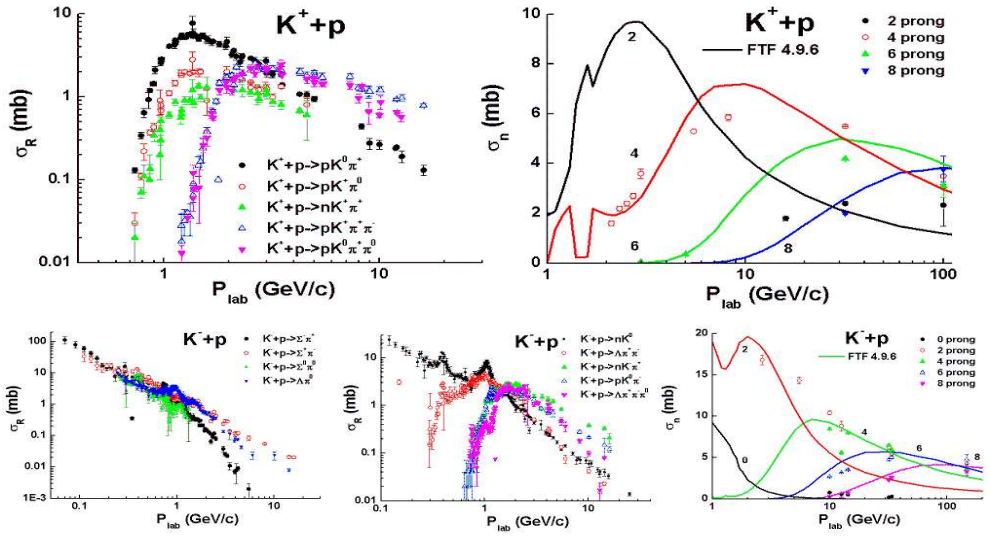

Figure 29.8: Reaction cross sections of Kp-interactions. Points are experimental data [8].

$K^- + p \to n + K^- + \pi^+$ and $K^- + p \to p + K^0 + \pi^-$ reactions are mainly caused by the diffraction dissociation of a projectile or a target hadron. The energy dependence of their cross sections are different from those of annihilation and quark exchange.

The same regularities can be seen in K^+p reactions. The energy dependence of the cross sections of the $K^+ + p \to p + K^0 + \pi^+$, $K^+ + p \to p + K^+ + \pi^0$ and $K^+ + p \to n + K^+ + \pi^+$ reactions are quite different from those of $K^- + p$.

In summary, there are three types of energy dependence in the reaction cross sections. The rapidly decreasing one is due to annihilation. The cross sections of the quark exchange processes decrease more slowly. Finally, the diffraction cross sections grow with energy and reach near-constant values.

29.2.5 Proton–anti-proton interactions

Proton–anti-proton interactions provide the beautiful possibility of studying annihilation processes in detail. The general properties of the interactions are presented in Fig. 29.9. Almost no structure is seen in the cross sections and their energy dependence is very different from the previously described reactions.

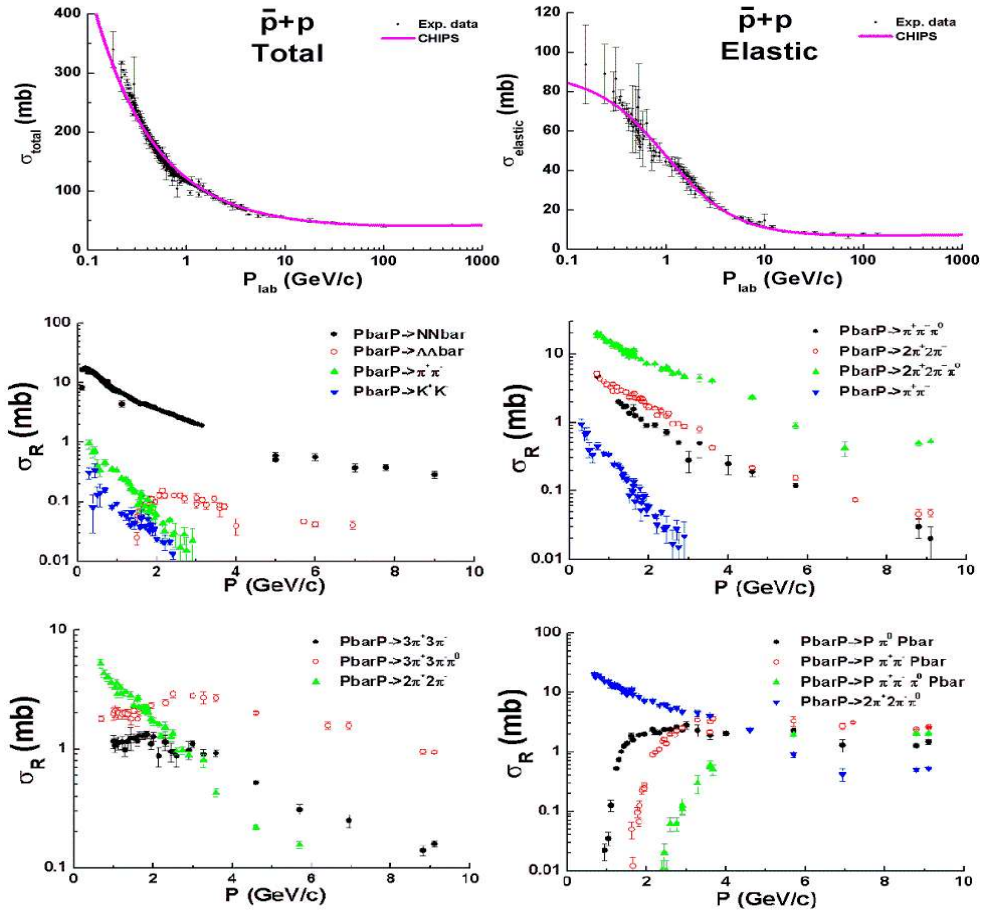

Figure 29.9: General properties of $\bar{p}p$-interactions. Points are experimental data: data on total and elastic cross sections from PDG data-base [3], other data from [7].

Cross sections of the reactions – $\bar{p}+p \to \pi^+ + \pi^-$ and $\bar{p}+p \to K^+ + K^-$, decrease faster than other cross sections as a functions of energy. $\bar{p}+p \to \pi^+ + \pi^- + \pi^0$ and $\bar{p}+p \to 2\pi^+ + 2\pi^-$ cross sections decrease less rapidly, nearly in the same manner as cross sections of the reactions – $\bar{p}+p \to n+\bar{n}$ and

$\bar{p}+p \to \Lambda+\bar{\Lambda}$. The cross sections of the reaction – $\bar{p}+p \to 2\pi^+ + 2\pi^- + \pi^0$, is a slowly decreasing function. The cross section of the process – $\bar{p}+p \to 3\pi^+ + 3\pi^- + \pi^0$ varies only a little over the studied energy range. Cross sections of other reactions ($\bar{p}+p \to p+\pi^0+\bar{p}$, $\bar{p}+p \to p+\pi^+ + \pi^- + \bar{p}$ and so on) show behaviour typical of diffraction cross sections.

The main channel of $\bar{p}p$ interactions at $P_{lab} < 4$ GeV/c is $\bar{p}+p \to 2\pi^+ + 2\pi^- + \pi^0$. At higher energies, there is a mixture of various channels. Such variety in the processes is indicative of complicated quark interactions. Possible quark flow diagrams are shown in Fig. 29.10.

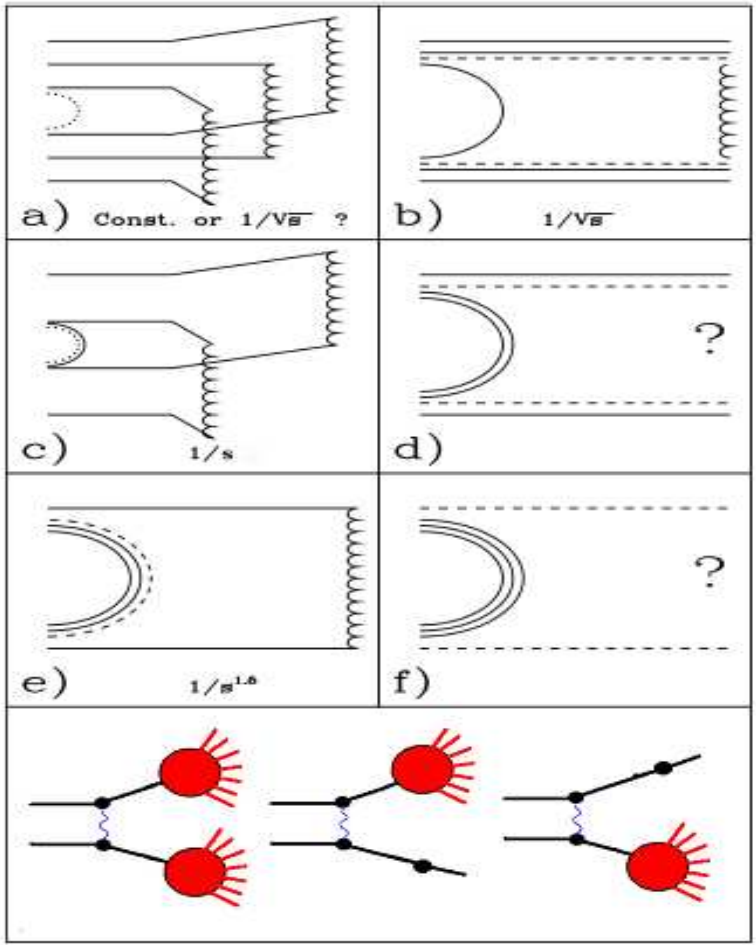

Figure 29.10: Quark flow diagrams of $\bar{p}p$-interactions.

As usual, quarks and anti-quarks are shown by solid lines. Dashed lines present so-called string junctions. It is assumed that the gluon field in baryons has a non-trivial topology. This heterogeneity is called a "string

junction". Quark-gluon strings produced in the reaction are shown by wavy lines.

The diagram of 29.10a represents a process with a string junction annihilation and the creation of three strings. Diagram 29.10b describes quark-antiquark annihilation and string creation between the di-quark and anti-di-quark. Quark-anti-quark and string junction annihilation is shown in Fig. 29.10c. Finally, one string is created in the process of 29.10e. Hadrons appear at the fragmentation of the strings in the same way that they appear in e^+e^--annihilation. One can assume that excited strings with complicated gluonic field configurations are created in processes 29.10d and 29.10f. If the collision energy is sufficiently small glueballs can be formed in the process 29.10f. Mesons with constituent gluons or with hidden baryon number can be created in process 29.10d. Of course the standard FTF processes shown in the bottom of the figure are also allowed.

In the simplest approach it is assumed that the energy dependence of the cross sections of these processes vary inversely with a power of s as depicted in Fig. 29.10 . Here s is CMS energy squared. This is dictated by the reggeon phenomenology. Calculating the cross sections of binary reactions is a rather complicated procedure (see [9]) because there can be interactions in the initial and final states. These interactions reflect also on cross sections of other reactions [10].

29.3 Hadron-nucleon process cross section

29.3.1 Total, elastic and inelastic hadron-nucleon cross sections

Parameterizations of the cross sections implemented in the CHIPS model of Geant4 (Authors: M.V. Kossov and P.V. Degtyarenko) are used in the FTF model. The general form of the parameterization is

$$\sigma = \sigma_{LE} + \sigma_{As},$$

where σ_{LE} is a low energy parameterization depending on the types of colliding particles, and σ_{As} is the asymptotic part of cross sections. The COMPLETE Collaboration proposed a hypothesis [11] that σ_{As} of total cross sections at very high energies does not depend on the types of colliding particles:

$$\sigma_{As}^{tot} = Z_{h_1h_2} + B\ \left(log(s/s_0)\right)^2,$$

$$B = 0.3152, \quad s_0 = 34.0 \qquad [(GeV/c)^2] \quad (COMPLETE,\ 2002) \quad (29.1)$$
$$B = 0.308\ , \quad s_0 = 28.9 \qquad [(GeV/c)^2] \quad (PDG,\ 2006) \quad (29.2)$$
$$B = 0.304\ , \quad s_0 = 33.1 \qquad [(GeV/c)^2] \quad (M.Ishida,\ K.Igi,\ 2009) \quad (29.3)$$

while the pre-asymptotic part does depend on colliding particles (h_1, h_2).

The CHIPS model σ_{As} for total and elastic cross sections has the same form:

$$\sigma_{As} = \left\{A\ \left[ln(P_{lab}) - B\right]^2 + C + D/P_{lab}^{0.5} + E/P_{lab} + F/P_{lab}^2\right\} /$$
$$\left(1 + G/P_{lab}^{0.5} + H/P_{lab}^3 + I/P_{lab}^4\right) \quad [mb],$$
$$P_{lab}\ \ in\ [GeV/c]$$

where A, B, C and so on are parameters given in Tabl. 29.1, 29.2.

Table 29.1: CHIPS model parameters for total cross sections

$h_1\ h_2$	A	B	C	D	E	F	G	H	I
$\pi^- p$	0.3	3.5	22.3	12.0	0	0	0	0	0.4
$\pi^+ p$	0.3	3.5	22.3	5.0	0	0	0	0	1.0
pp	0.3	3.5	38.2	0	0	0	0	0	0.54
np	0.3	3.5	38.2	0	0	52.7	0	0	2.72
$K^+ p$	0.3	3.5	19.5	0	0	0	0.46	0	1.6
$K^- p$	0.3	3.5	19.5	0	0	0	-0.21	0	0.52
$\bar{p}p$	0.3	3.5	38.2	0	0	0	0	0	0

Table 29.2: CHIPS model parameters for elastic cross sections

$h_1\ h_2$	A	B	C	D	E	F	G	H	I
$\pi^- p$	0.0557	3.5	2.4	6.0	0	0	0	0	3.0
$\pi^+ p$	0.0557	3.5	2.4	7.0	0	0	0	0	0.7
pp	0.0557	3.5	6.72	0	30.0	0	0	0.49	0.
np	0.0557	3.5	6.72	0	32.6	0	0	0	1.0
$K^+ p$	0.0557	3.5	2.23	0	0	0	-0.7	0	0.1
$K^- p$	0.0557	3.5	2.23	0	0	0	-0.7	0	0.075

The low energy parts of the cross sections are very different for various projectiles, and they are not presented here. These can be found in the corresponding classes of Geant4.

It is obvious that $\sigma^{in} = \sigma^{tot} - \sigma^{el}$.

A comparison of the parameterizations with experimental data was presented in the previous figures.

29.3.2 Cross sections of quark exchange processes

Cross sections of quark exchange processes are parameterized as:

$$\sigma_{q.e.} = \sigma_{in}\ A\ e^{-B\ y_{lab}},$$

where y_{lab} is a projectile rapidity in a target rest frame. A and B are parameters given in Tabl. 29.3

Table 29.3: Parameters of quark exchange cross sections

$h_1\ h_2$	A	B
pp/pn	1.85	0.7
$\pi p/\pi n$	240	2
Kp/Kn	40	2.25

The parameters were determined from a description of reaction channel cross sections.

29.3.3 Cross sections of anti-proton processes

The annihilation cross section is given as:

$$\sigma_{ann} = \sigma_a\ +\ B\ X_b\ +\ C\ X_c\ +\ D\ X_d,$$

where X_i are yields of the diagrams of Fig. 29.10. All cross sections are given in $[mb]$.

$$\sigma_a = 25\ \sqrt{s}/\lambda^{1/2}(s, m_p^2, m_N^2),$$

$$\lambda(s, m_p^2, m_N^2) = s^2 + m_p^4 + m_N^4 - 2sm_p^2 - 2sm_N^2 - 2m_p^2 m_N^2,$$

$$X_b = 3.13\ +\ 140\ (s_{th} - s)^{2.5}, \quad s\ <\ s_{th}, \quad s_{th} = (m_p + m_N + 2m_\pi + \delta)^2$$

$$X_b = 6.8/\sqrt{s}, \qquad s\ >\ s_{th},$$

$$X_c = 2\ \frac{\sqrt{s}}{\lambda^{1/2}(s, m_p^2, m_N^2)} \frac{(m_p + m_N)^2}{s},$$

$$X_d = 23.3/s.$$

The coefficients B, C and D are pure combinatorial coefficients calculated on the assumption that the same conditions apply to all quarks and anti-quarks. For example, in $\bar{p}p$ interactions there are five possibilities to annihilate a quark and an anti-quark, and six possibilities to annihilate two quarks and two anti-quarks. Thus, $B = C = 5$ and $D = 6$.

Table 29.4: Coefficients B, C and D

	$\bar{p}p$	$\bar{p}n$	$\bar{n}p$	$\bar{n}n$	$\bar{\Lambda}p$	$\bar{\Lambda}n$	$\bar{\Sigma}^-p$	$\bar{\Sigma}^-n$	$\bar{\Sigma}^0p$	$\bar{\Sigma}^0n$	$\bar{\Sigma}^+p$	$\bar{\Sigma}^+n$
B	5	4	4	5	3	3	2	4	3	3	4	2
C	5	4	4	5	3	3	2	4	3	3	4	2
D	6	4	4	6	3	3	2	2	2	2	2	0

	$\bar{\Xi}^-p$	$\bar{\Xi}^-n$	$\bar{\Xi}^0p$	$\bar{\Xi}^0n$	$\bar{\Omega}^-p$	$\bar{\Omega}^-n$
B	1	2	2	1	0	0
C	1	2	2	1	0	0
D	0	0	0	0	0	0

Note that final state particles in the process of Fig. 29.10b can coincide with initial state particles. Thus the true elastic cross section is not given by the experimental cross section.

At $P_{lab} < 40$ MeV/c anti-proton-nucleon cross sections are:

$$\sigma^{tot} = 1512.9, \;\; \sigma^{el} = 473.2, \;\; \sigma_a = 625.1, \;\; \sigma_b = 9.78, \;\; \sigma_c = 49.99, \;\; \sigma_d = 6.61.$$

All cross sections are given in $[mb]$. $\sigma_b = 0$ for $\bar{p}p$-interactions because the process $\bar{p}p \to \bar{n}n$ is impossible at the energies ($P_{lab} < 40$ MeV/c).

29.3.4 Cross sections of diffractive and non-diffractive processes

As mentioned above, three processes are considered in the FTF model at high energies: projectile diffraction (pd), target diffraction (td) and non-diffractive interactions (nd). They are parameterized as:

$$\sigma^{pd}_{pp} = \sigma^{td}_{pp} = 6 \; + \; \sigma^{in}\frac{1.5}{s}, \quad (mb),$$

$$\sigma^{pd}_{\bar{p}p} = \sigma^{td}_{\bar{p}p} = 6 \; + \; \sigma^{in}\frac{1.5}{s}, \quad (mb),$$

$$\sigma^{pd}_{\pi p} = 6.2 \; - \; e^{-\frac{(\sqrt{s}-7)^2}{16}}, \quad \sigma^{td}_{\pi p} = 2 \; + \; 22/s, \quad (mb),$$

$$\sigma^{pd}_{Kp} = 4.7, \quad \sigma^{td}_{Kp} = 1.5, \quad (mb),$$

For the determination of the cross sections, inclusive spectra of particles in hadronic interactions were used. In Fig. 29.11 an inclusive spectrum of protons in the reaction $p + p \to p + X$ is shown in comparison with model predictions.

As seen, all the models have difficulties in describing the data. In the FTF model this was overcome by tuning the single diffraction dissociation

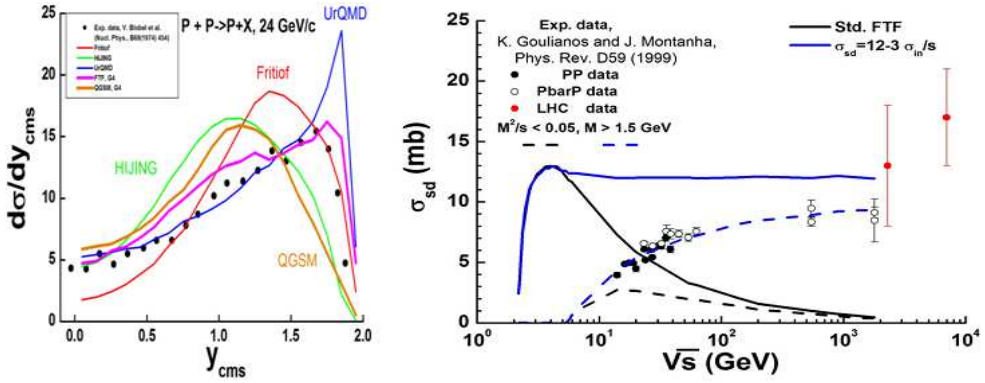

Figure 29.11: Left: inclusive spectrum of proton in pp-interactions at $P_{lab} = 24$ GeV/c. Points are experimental data [14], lines are model calculations. Right: single diffraction dissociation cross section in pp-interactions. Points are data gathered by K. Goulianos and J. Montanha [15]. Lines are FTF model calculations.

cross section. Tuning was made possible by the fact that the height of the proton peak at large rapidities depends on this cross section (see left Fig. 29.11).

The $2\sigma_{pp}^{pd}$ predicted by the expression (blue solid curve) is shown at the right of Fig. 29.11 in a comparison with experimental data gathered by K. Goulianos and J. Montanha [15]. The values are larger than experimental data. Though taking into account the restriction that the mass of a produced system, X, cannot be very small or very large ($M^2/s < 0.05$ and $M > 1.5$ GeV) brings the predictions closer to the data. So, the accounting of the restriction is very important for a correct reproduction of the data.

A more complicated situation arises with πp- and Kp-interactions. The set of experimental data on diffraction cross sections is very restricted. Thus, a refined tuning was used. The FTF processes discussed above give yields in various regions of particle spectra. The target diffraction dissociation, $\pi + p \to \pi + X$, gives its main yield at large values of $x_F = 2p_z/\sqrt{s}$ for π-mesons. The projectile diffraction dissociation yield ($\pi + p \to X + p$) has a maximum at $x_F \sim -1$. Thus, using various experimental data and varying the cross sections of the processes, the points presented in the lower left corner of Fig. 29.12 were obtained. They were parameterized by the expressions ???. A correct reproduction of particle spectra in the central region, $x_F \sim 0$, was very important for these. As a result, we have a good description of π-meson spectra in the interactions at various energies.

In Kp-interactions the projectile diffraction cross sections were deter-

mined by tuning on proton spectra from the reactions $K + p \to p + X$ (see Fig. 29.13). There are no data on leading K-meson spectra in the reactions $K + p \to K + X$. Thus, π^--meson spectra in the central region were tuned. At a given value of a projectile diffraction cross section, the central spectrum depends on a target diffraction. This was used to determine the target diffraction cross sections. The estimated cross sections are shown in the lower left corner of Fig. 29.13. As a result, a satisfactory description of meson spectra was obtained.

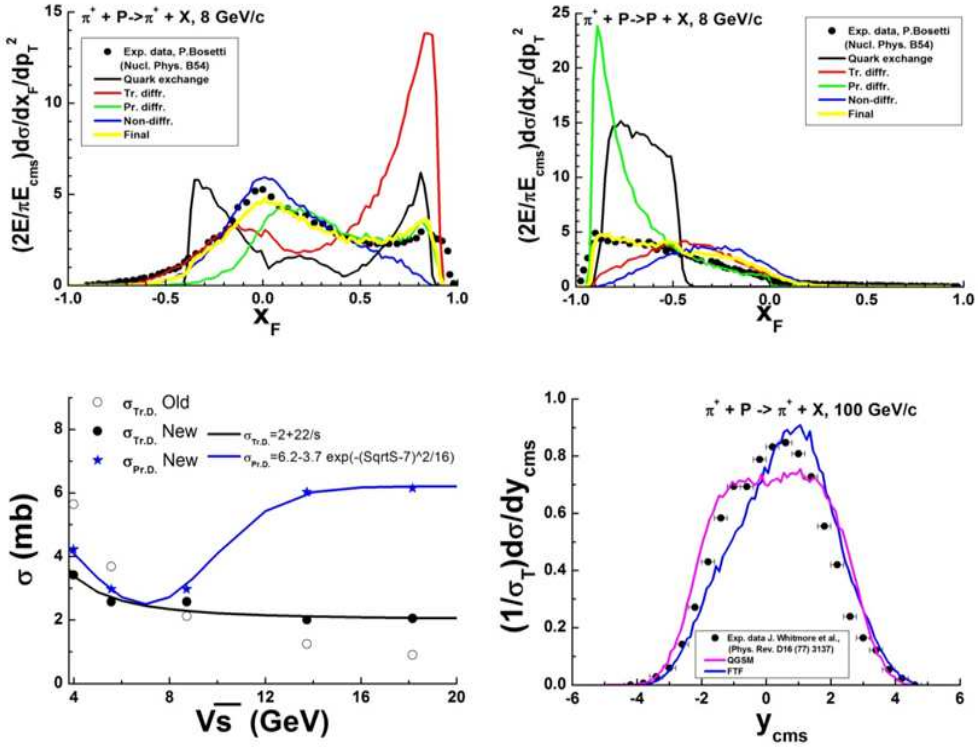

Figure 29.12: Upper figures: inclusive spectra of protons and π^+-mesons in π^+p-interactions. Points are experimental data [16]. Lines are yields of the FTF processes calculated on the assumption that the probability of a process is 100 %. Bottom left figure: diffraction dissociation cross sections obtained by tuning (points), and their description (lines) by the expressions ... Bottom right figure: Rapidity spectrum of π^+-mesons in π^+p-interactions at p_{lab} =100 GeV/c. Points are experimental data [17].

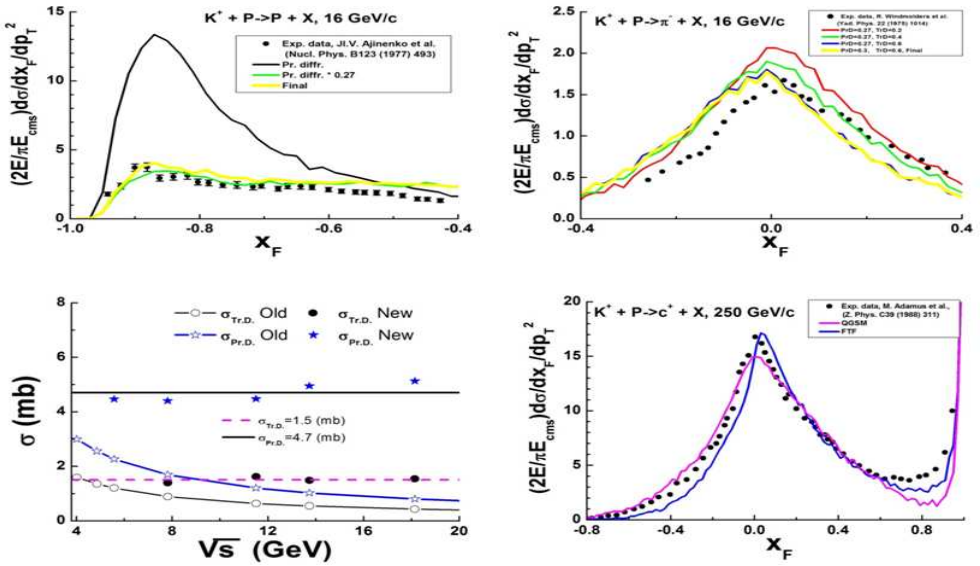

Figure 29.13: Upper figures: inclusive spectra of protons and π^--mesons in Kp-interactions. Points are experimental data [18]. Lines are FTF calculations. Bottom left figure: diffraction dissociation cross sections obtained by tuning (points), and their description (lines) by the expressions ... Bottom right figure: x_F spectrum of positive charged particles in Kp-interactions at p_{lab} =250 GeV/c. Points are experimental data [17], lines are model calculations.

29.4 Simulation of hadron-nucleon interactions

29.4.1 Simulation of meson-nucleon and nucleon-nucleon interactions

Colliding hadrons may either be on or off the mass shell when they are bound in nuclei. When they are off-shell the total mass of the hadrons is checked. If the sum of the masses is above the CMS energy of the collision, the simulated event is rejected. If below, the event is accepted. It is assumed that due to the interaction the hadrons go on-shell, and the CMS energy of the collision is not changed.

The simulation of an inelastic hadron-nucleon interaction starts with a choice: should a quark exchange or a diffractive excitation be simulated? The probability of a quark exchange is given by $W_{qe} = \sigma_{qe}/\sigma^{in}$. The probability

of a diffractive excitation is then $1 - W_{qe}$. σ_{qe} depends on the energies and flavors of the colliding hadron (see Eq.???).

If a quark exchange is sampled, the quark contents of the projectile and target are determined. After that the possibility of a quark exchange is checked. A meson consists of a quark and an anti-quark. Thus there is no alternative but to choose a quark. Let it be q_M. A baryon has three quarks, q_1, q_2 and q_3. The quark from the meson can be exchanged, in principle, with any of the baryon quarks, but the above description of the experimental data indicates that an exchange of quarks with the same flavor must be suppressed. So, only the exchange of quarks with different flavors is allowed. After the exchange ($q_M \leftrightarrow q_i$), the new contents of the meson and the baryon are determined. The new meson may be either pseudo-scalar or pseudo-vector with a 50% probability. The new baryon may be in its ground state, or in an excited state. The probability of an excited baryon state is 0.56 for πN-interactions, and 0.6 for KN-interactions. Only $\Delta(1232)$'s are considered as excited states. If all quarks of a baryon have the same flavor, the $\Delta(1232)$ is always created ($\Delta(1232)^{++}$ or $\Delta(1232)^{--}$).

The same procedure is followed for a projectile baryon, but in this case any quark of the projectile or target may participate in an exchange if they have different flavors. Only the ground state of the new baryon is considered.

Final state hadrons may undergo additional elastic scattering with probability $W_{el} = 2.256\ e^{-0.6\ y_{lab}}$, or a diffractive excitation with probability $1 - W_{el}$, where y_{lab} is the rapidity of the projectile in the target rest frame.

The above procedure is sufficient for a description of hadron-nucleon reaction cross sections at $p_{lab} < 3 - 5$ GeV/c. At higher energies the diffractive excitation must be simulated.

As mentioned above, there can be a projectile diffraction, or a target diffraction, or both of them. Probabilities of the corresponding processes at high energies are: σ^{pd}/σ^{in}, σ^{td}/σ^{in}, and $(\sigma^{in} - \sigma^{pd} - \sigma^{td})/\sigma^{in}$. The processes are sampled randomly.

Having a sampled a projectile diffraction or a target diffraction, the corresponding light-cone momentum (P^- or P^+) is choosing according to the distribution: dP^-/P^- or dP^+/P^+. Boundaries for a sampling have to be determined before.

Let us consider kinematics of a projectile diffraction, $P + T \to P' + T$, for a definition of these boundaries. It is obvious that a mass of the diffractive produced system, $m_{P'}$, must satisfy the conditions:

$$m_D \leq m_{P'} \leq \sqrt{s} - m_T,$$

where m_D is a minimal mass of the system, s is a CMS energy squared, m_T is a mass of the target. If there is not a transverse momentum transfer, and

$m_{P'}$ reaches the lower boundary then

$$P^-_{min} = \sqrt{m_D^2 + p_z^2} - p_z, \quad p_z = \lambda^{1/2}(s, m_D^2, m_T^2)/2\sqrt{s}.$$

When $m_{P'}$ reaches the upper boundary, the longitudinal momenta of the particles are zeros. Thus,

$$P^-_{max} = \sqrt{s} - m_T.$$

Having a sampled P^-, $m_{P'}$ and P^+ can be found with a help of the energy-momentum conservation law written is the CMS system:

$$\left\{ \begin{array}{l} E_{P'} + E_T = \sqrt{s} \\ P_{z,P'} + P_{z,T} = 0 \end{array} \right| \left. \begin{array}{l} P^-_{P'} + P^-_T = \sqrt{s} \\ P^+_{P'} + P^+_T = \sqrt{s} \end{array} \right| \left. \begin{array}{l} P^-_T = \sqrt{s} - P^-_{P'} \\ P^+_T = m_T^2/P^-_T \\ m^2_{P'} = P^-_{P'} \cdot (\sqrt{s} - P^+_T) \end{array} \right. \quad (29.4)$$

An accounting of a transferred transverse momentum sampled according to the distribution:

$$dW = \frac{1}{\pi < P_\perp^2 >} \, e^{-P_\perp^2/<P_\perp^2>} d^2P_\perp, \quad < P_\perp^2 >= 0.3 \ (GeV/c)^2,$$

leads to a replacement of masses by transverse masses, $m_\perp = \sqrt{m^2 + P_\perp^2}$.

Let us determine also light-cone momenta transferred to the projectile are:

$$Q^+ = P^+_{T,0} - P^+_T, \quad Q^- = P^-_{T,0} - P^-_T,$$

where $P^+_{T,0}$ and $P^-_{T,0}$ are light-cone momenta of the target in the initial state.

In the case of non-diffractive interaction ($P+T \to P'+T'$), $P^-_{P'}$ is sampled first of all as it was described above at $m_T = m_{T,nd}$, where $m_{T,nd}$ is a minimal mass of target originated particle produced in the non-diffractive interaction. After that, $P^+_{T'}$ is independently sampled at $m_P = m_{P,nd}$. The minimal light-cone momenta, $P^-_{P'}$ and $P^+_{T'}$, are calculated at $m_P = m_{P,nd}$ and $m_T = m_{T,nd}$. At the last step it is checked that $m_{P'} \geq m_{P,nd}$ and $m_{T'} \geq m_{T,nd}$. In the current version of the FTF model the same value is used for minimal masses in the diffractive and non-diffractive interactions.

Table 29.5: Minimal masses of diffractive produced strings

	p/n	π	K
m_D (MeV)	1160	500	600

29.4.2 Simulation of anti-baryon-nucleon interactions

At the beginning of an annihilation simulation, the cross sections of the processes (see Fig. 29.10) are calculated (see ???). After that a sampling of a process takes place.

In the cases of the processes 29.10b and 29.10e quarks for the annihilation are chosen randomly. In each of the processes only one string is created. Its mass is equal to a CMS energy of the interaction. After that the string is fragmented. It is required at the fragmentation, that in the process 29.10b there must not be a baryon and an anti-baryon in a final state.

At sufficiently high energies the standard FTF processes can be simulated as it was described above.

In the process 29.10c only 2 strings will be created. If their masses are given, kinematical properties of the strings can be determined with a help of the energy-momentum conservation law. The masses must be connected with quark's and anti-quark's momenta.

We believe that in the process all quarks and anti-quarks are in equal conditions. Thus, transverse momenta of them are sampled independently according to the gaussian distribution with $< P_\perp^2 >= 0.04\ (GeV/c)^2$. To put a sum of the momenta to zero, a transverse momentum of each particle is re-defined: $\vec{P}_{\perp i} \to \vec{P}_{\perp i} - \frac{1}{4}\sum_{j=1}^{4} \vec{P}_{\perp j}$.

To find longitudinal momenta of quarks let us use light-cone momenta: total light-cone momenta of projectile originated anti-quarks and target originated quarks,

$$P^+ = P^+_{\bar{q}_1} + P^+_{\bar{q}_2}, \quad P^- = P^-_{q_1} + P^-_{q_2}.$$

Let us introduce also light-cone momentum fractions:

$$x^+_{\bar{q}_1} = P^+_{\bar{q}_1}/P^+, \quad x^+_{\bar{q}_2} = 1 - x^+_{\bar{q}_1}$$

$$x^-_{q_1} = P^-_{q_1}/P^-, \quad x^-_{q_2} = 1 - x^-_{q_1}.$$

Using these variables, the energy-momentum conservation law in CMS system is written as:

$$P^+/2 + \frac{\alpha}{2\ P^+} \ + \ P^-/2 + \frac{\beta}{2\ P^-} = \sqrt{s}, \tag{29.5}$$

$$P^+/2 - \frac{\alpha}{2\ P^+} \ - \ P^-/2 + \frac{\beta}{2\ P^-} = 0, \tag{29.6}$$

$$\alpha = \frac{m^2_{\perp \bar{q}_1}}{x^+_{\bar{q}_1}} + \frac{m^2_{\perp \bar{q}_2}}{1 - x^+_{\bar{q}_1}},$$

$$\beta = \frac{m^2_{\perp q_1}}{x^-_{q_1}} + \frac{m^2_{\perp q_2}}{1 - x^-_{q_1}}.$$

A solution of the equations at $\sqrt{\alpha}+\sqrt{\beta} \leq \sqrt{s}$ is:

$$P^+ = \frac{s+\alpha-\beta+\lambda^{1/2}(s,\alpha,\beta)}{2\sqrt{s}}, \tag{29.7}$$

$$P^- = \frac{s-\alpha+\beta+\lambda^{1/2}(s,\alpha,\beta)}{2\sqrt{s}}. \tag{29.8}$$

If $\sqrt{\alpha}+\sqrt{\beta} > \sqrt{s}$, the transverse momenta and x's are re-sampled until the inequality will be broken.

Because quarks are in the equal conditions, a distribution on x can have a form $x^a\ (1-x)^a$. A recommended value of a can be zero or -0.5. We chose $a=-0.5$. We assumed also that quark masses are zeros. Probably, other values of the parameters can be used, but we have not found experimental data sensitive to the parameters.

At a simulation of the process 29.10a we follow the same line of the consideration, and introduce light-cone momentum fractions – $x^+_{\bar{q}1},\ x^+_{\bar{q}2},\ x^+_{\bar{q}3}$ and $x^-_{q_1},\ x^-_{q_2},\ x^-_{q_3}$. A distribution on x's is chosen in the form:

$$dW \propto x^a_{q_1}\ x^a_{q_2}\ x^a_{q_3}\delta(1-x_{q_1}-x_{q_2}-x_{q_3})dx_{q_1}\ dx_{q_2}\ dx_{q_3}, \quad a=-0.5.$$

It is obvious that in the case

$$\alpha = \sum_{i=1}^{3}\frac{m^2_{\perp\bar{q}_i}}{x^+_{\bar{q}_i}}, \quad \beta = \sum_{i=1}^{3}\frac{m^2_{\perp q_i}}{x^-_{q_i}}.$$

29.5 Flowchart of the FTF model

A simulation of hadron-nucleus or nucleus-nucleus interaction events starts with an initialization of the model variables: calculations of cross sections, setting up slopes, masses and so on. The next step is a determination of intra-nuclear collision multiplicity with a help of Glauber model. If energy of collisions is sufficiently high, a simulation of secondary particle cascading within the reggeon theory inspired model (RTIM [19]) is carried out. After that all involved nuclear nucleons are put on the mass-shell. If the energy is not high enough these steps are missed. A reason for this will be explained latter.

The main job is doing in the loop over intra-nuclear collisions. To the moment a time order of the collisions has determined. For each collision it is sampled what has to be simulated – elastic scattering, inelastic interaction or annihilation for projectile anti-baryons. For each branch an adjustment of a participating nuclear nucleon is performed at the low energy, and the

corresponding process is simulated. In the case of a sampling of the inelastic interaction at high energy there is an alternative – to reject the interaction or to process it.

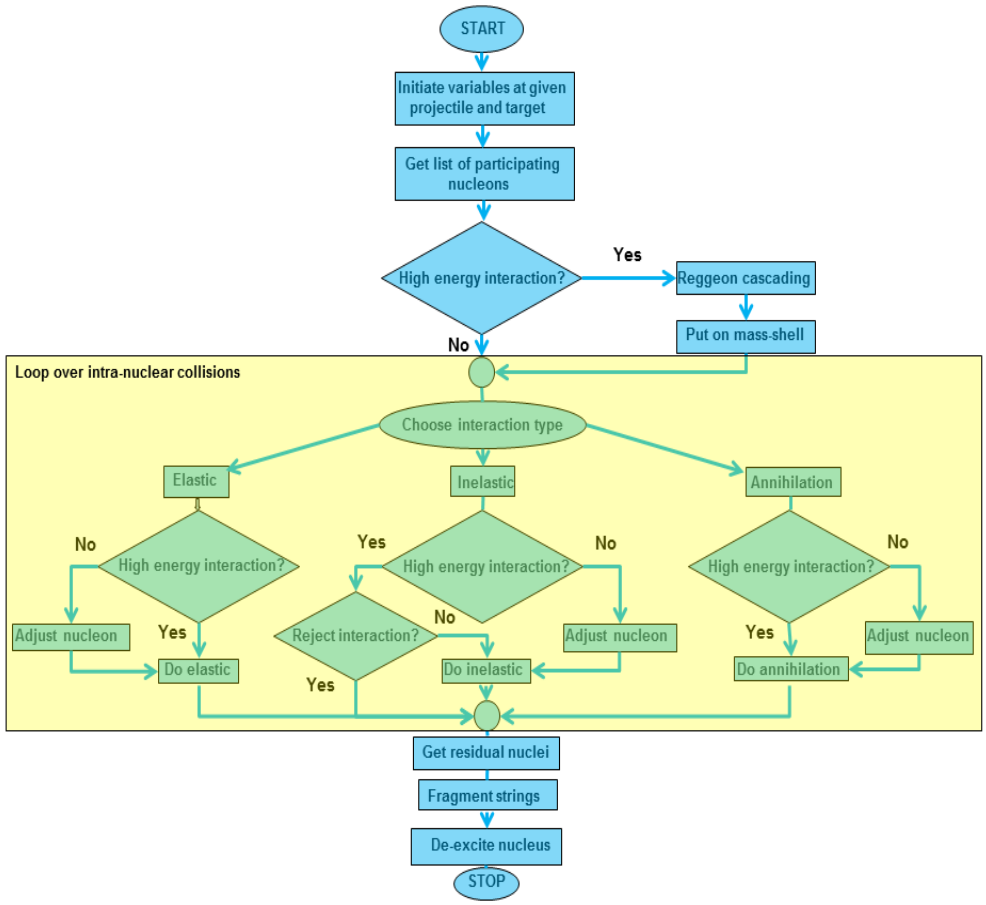

Figure 29.14: Flowchart of the FTF model

At the end of the loop properties of nuclear residuals (mass number, charge, excitation energy and 4-momentum) are transferred to a calling program. The program initiates the fragmentation of created strings and decays of excited residuals.

Simulations of elastic scattering, inelastic interactions and annihilation were considered above. Other steps of the FTF model will be presented below.

29.6 Simulation of nuclear interactions

29.6.1 Sampling of intra-nuclear collisions

Classical cascade-type sampling

As known, the intra-nuclear cascade models like that implemented in Geant4 – the Bertini model and the Binary cascade model, work well at projectile energies below 5 – 10 GeV. The first step in the model is a sampling of the impact parameter, b. The next step is a sampling of a point where a projectile will interact with nuclear matter (see Fig. 29.15a).

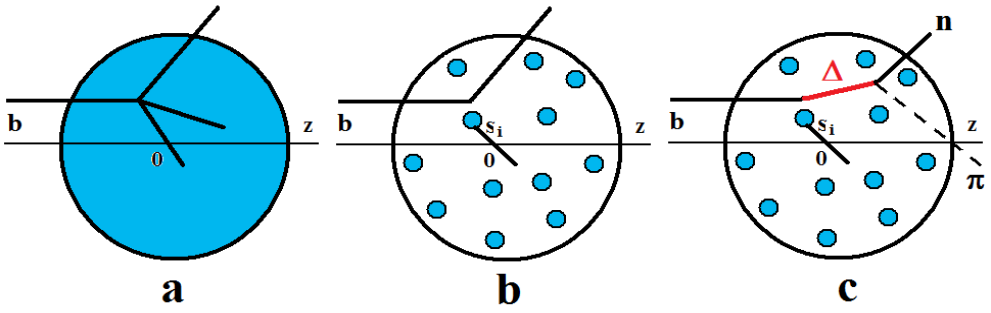

Figure 29.15: Cascade-type sampling.

The following consideration is used here: a probability that the projectile reaches a point z going from minus infinity to the point z is

$$P = e^{-\sigma^{tot} \int_{-\infty}^{z} \rho_A(\vec{b},z')\ dz'},$$

where σ^{tot} is the total cross section of the projectile-nucleon interaction, ρ_A is is a density of a nucleus considered as a continuous medium.

A probability that the projectile will have an interactions in the range z – $z + dz$ is equal $\sigma^{tot}\rho_A(\vec{b}, z)\ dz$. Thus, the total probability is:

$$P(\vec{b}, z) = \sigma^{tot}\rho_A(\vec{b}, z)\ e^{-\sigma^{tot} \int_{-\infty}^{z} \rho_A(\vec{b},z')\ dz'}\ dz,$$

$$P(\vec{b}) = \int_{-\infty}^{+\infty} P(\vec{b}, z)\ dz = 1 - e^{-\sigma^{tot} \int_{-\infty}^{\infty} \rho_A(\vec{b},z')\ dz'}.$$

Having sampled the interaction point, a choice between an elastic scattering and an inelastic interaction is implemented. In the case of the inelastic interaction, a multi-particle production process is simulated. After this, for each produced particles new interactions points are sampled, and so on. In the

case of the elastic scattering, the scattering is simulated, and new interactions points for a recoil nucleon and the projectile are sampled.

The prescription is changed a little bit at a replacing of the continuous medium by a collection of A nucleons located in the points $\{\vec{s}_i, z_i\}$, $i = 1$–A where $\{\vec{s}_i\}$ are coordinates of the nucleons in the impact parameter plane. The projectile can interact with a nearest nuclear nucleon, $\vec{s}_i$ of which satisfies a condition: $|\vec{b} - \vec{s}_i| \leq \sqrt{\sigma^{tot}/\pi}$ (see Fig. 29.15b).

In first versions of the cascade model, nucleons and pions were considered only. When it was recognized that most of inelastic reactions at intermediate energies are going through resonance productions, various baryonic and mesonic resonances were included, and the algorithm changed (see Fig. 29.15c). At energy growth more and more heavy resonances were produced. Thus an understanding of interactions was changed because properties of resonance-nucleon collisions were not known. Here an interpretation of Glauber approximation was very useful.

Short review of Glauber approximation

The Glauber approach [20] was proposed before a creation of the intra-nuclear cascade model in the framework of the potential theory. Its main assumption is that at sufficiently high energies many partial waves give yields in a particle elastic scattering amplitude, $f(\vec{q})$. Thus, a summation on angular momenta can be replaced by an integral:

$$f(\vec{q}) = \frac{iP}{2\pi)} \int e^{i\vec{q}\vec{b}} \left[1 - e^{i\chi(\vec{b})}\right] \, d^2b, \quad \frac{d\sigma}{d\Omega} = |f(\vec{q})|^2,$$

$$\gamma(\vec{b}) = \frac{1}{2\pi i P} \int e^{-i\vec{q}\vec{b}} \, f(\vec{q}) \, d^2q,$$

where P is a projectile momentum, q is transferred transverse momentum, $\vec{b}$ is the impact parameter, χ is a phase shift, and γ is the scattering amplitude in the impact parameter representation.

Due to the additivity of potentials, it was natural to assume that a summared phase shift for a projectile scattered on A centers located in the points $\{\vec{s}_i, z_i\}$, $i = 1$–A is a sum of corresponding shifts on each center:

$$\chi_{hA} = \sum_{i=1}^{A} \chi(\vec{b} - \vec{s}_i),$$

$$\gamma_{hA}(\vec{b}) = 1 - \prod_{i=1}^{A} \left[1 - \gamma(\vec{b} - \vec{s}_i)\right]. \tag{29.9}$$

Because positions of nucleons in nuclei are not fixed, the Eq. 29.9 has to be averaged, and a hadron-nucleus scattering amplitude takes a form:

$$F_{0\to f}^{hA} = \frac{iP}{2\pi}\int d^2b\, e^{-i\vec{q}\vec{b}}\,\left\{1-\prod_{i=1}^{A}\left[1-\gamma(\vec{b}-\vec{s}_i)\right]\right\}\,\Psi_0(\{r_A\})\Psi_f^*(\{r_A\})\prod_{i=1}^{A}d^3r_i, \tag{29.10}$$

where Ψ_0 and Ψ_f are wave functions of the nucleus in initial and final states, respectively.

In the case of elastic scattering, $\Psi_0 = \Psi_f$, we have:

$$F_{el}^{hA} = \frac{iP}{2\pi}\int d^2b\, e^{-i\vec{q}\vec{b}}\,\left\{1-\prod_{i=1}^{A}\left[1-\int\gamma(\vec{b}-\vec{s}_i)\rho_A(\vec{s}_i,z')d^2s_idz'\right]\right\}\simeq \tag{29.11}$$

$$\simeq \frac{iP}{2\pi}\int d^2b\, e^{-i\vec{q}\vec{b}}\,\left\{1-\left[1-\frac{1}{A}\int\gamma(\vec{b}-\vec{s})T_A(\vec{s})d^2s\right]^A\right\}$$

$$\simeq \frac{iP}{2\pi}\int d^2b\, e^{-i\vec{q}\vec{b}}\,\left\{1-e^{-\int\gamma(\vec{b}-\vec{s})T_A(\vec{s})d^2s}\right\}$$

$$\simeq \frac{iP}{2\pi}\int d^2b\, e^{-i\vec{q}\vec{b}}\,\left\{1-e^{-\sigma_{hN}^{tot}(1-i\alpha)T_A(\vec{b})/2}\right\}$$

A lot of assumptions and abbreviations was used at the derivations. First of all it was assumed that $|\Psi_0|^2 \simeq \prod_{i=1}^{A}\rho(\vec{s}_i,z_i)$ where ρ is one particle nuclear density. Because the nucleon coordinates must obey the obvious condition – $\sum_{i=1}^{A}\vec{r}_i = 0$, it would be better to use $|\Psi_0|^2 \simeq \delta(\sum_{i=1}^{A}\vec{r}_i)\prod_{i=1}^{A}\rho(\vec{s}_i,z_i)$. An accounting of this δ-function is called an accounting of center-of-mass correlation.

The second assumption is that A is sufficiently large, thus $(1-\frac{x}{A})^A_{A\to\infty} = e^{-x}$ (optical limit).

A thickness function of the nucleus was introduced:

$$T(\vec{b}) = A\int_{-\infty}^{+\infty}\rho(\vec{b},z)\;dz.$$

It was assumed also that a range of γ-function is much less than a range of the nuclear density: $\int\gamma(\vec{b}-\vec{s})T_A(\vec{s})d^2s \simeq \sigma_{hN}^{tot}(1-i\alpha)T_A(\vec{b})/2$, where σ_{hN}^{tot} is hadron-nucleon total cross section, and $\alpha = Re\; f(0)/Im\; f(0)$ is a ratio of real and imaginary parts of hadron-nucleon elastic scattering amplitude at zero momentum transfer.

There were many applications of the Glauber approach for calculations of elastic scattering cross sections, cross sections of nuclear excitations, coherent

particle production and so on. We consider only its application to inelastic reactions.

If energy resolution of a scattered projectile is not high, many nuclear excited states can give yields in scattering amplitude: $F^{hA} = \sum_f F^{hA}_{0\to f}$. Finding corresponding cross section, it is usually assumed that a set of final state wave functions satisfy the complitness relation: $\sum_f \Psi_f(\{\vec{r}_i\})\Psi^*_f(\{\vec{r}'_j\}) = \prod_{i=1}^{A} \delta(\vec{r}_i - \vec{r}'_i)$.

The cross section of the reactions called cross section of elastic and quasi-elastic scatterings is given as:

$$\sigma^{hA}_{el.+qel.} = \int d^2b \, \left\{1 - 2Re \, e^{-\sigma^{tot}_{hN}(1-i\alpha)T_A(\vec{b})/2} + e^{-\sigma^{in}_{hN}T_A(\vec{b})}\right\}. \qquad (29.12)$$

Subtracting from it the cross section of the elastic scattering, we have:

$$\sigma^{hA}_{qel.} = \int d^2b \, \left\{e^{-\sigma^{in}_{hN}T_A(\vec{b})} - e^{-\sigma^{tot}_{hN}T_A(\vec{b})}\right\} = \int d^2b \, e^{-\sigma^{tot}_{hN}T_A(\vec{b})} \left\{e^{\sigma^{el}_{hN}T_A(\vec{b})} - 1\right\} = \qquad (29.13)$$

$$= \int d^2b \, e^{-\sigma^{tot}_{hN}T_A(\vec{b})} \sum_{n=1}^{\infty} \frac{[\sigma^{el}_{hN}T_A(\vec{b})]^n}{n!}.$$

The last expression shows that the quasi-elastic cross section is a sum of cross sections with various multiplicities of elastic scatterings. It coincides with a prescription of the cascade model if only elastic scatterings of a projectile are considered.

Cross section of multi-particle production processes in the Glauber approach has a form:

$$\sigma^{hA}_{mpp} = \sigma^{hA}_{tot} - \sigma^{hA}_{el.+qel.} = \int d^2b \, \left\{1 - e^{-\sigma^{in}_{hN}T_A(\vec{b})}\right\} = \qquad (29.14)$$

$$= \int d^2b \, e^{-\sigma^{in}_{hN}T_A(\vec{b})} \sum_{n=1}^{\infty} \frac{[\sigma^{in}_{hN}T_A(\vec{b})]^n}{n!}.$$

It coincides with an analogous cascade expression if a projectile particle can be distinguished from produced particles. Of course, it cannot be so in the case of projectile pions.

In the FTF model of Geant4 it is assumed that projectile and target originated strings are distinguished. Thus, the cascade-type algorithm of the sampling of the multiplicities and types of interactions in nuclei is used.

A generalization of the Glauber approach for the case of nucleus-nucleus interactions was proposed by V. Franco [21]. In the theory, a cross section

of multi-particle production processes is given by the expression:

$$\sigma^{AB}_{mpp} = \int d^2b \left\{ 1 - \prod_{i=1}^{A} \prod_{j=1}^{B} \left[1 - g(\vec{b} + \tau_j - \vec{s}_i) \right] \right\} \cdot \tag{29.15}$$

$$\cdot |\Psi_0^A(\{r_A\})|^2 |\Psi_0^B(\{t_B\})|^2 \left[\prod_{i=1}^{A} d^3 r_i \right] \left[\prod_{j=1}^{B} d^3 t_i \right],$$

where $g(\vec{b}) = \gamma(\vec{b}) + \gamma^*(\vec{b}) - |\gamma(\vec{b})|^2$, A and B are mass numbers of colliding nuclei, $\{\vec{\tau}_j\}$ is a set of impact coordinates of projectile nucleons ($\vec{t} = (\vec{\tau}, z)$).

Considering $g(\vec{b})$ as a probability that two nucleons separated by the impact parameter $\vec{b}$ will have an inelastic interaction, a simple interpretation of the Eq. 29.15 can be given. The expression in the curly brackets of Eq. 29.15 is a probability that there will be at least one or more inelastic nucleon-nucleon interactions. $|\Psi_0^A(\{r_A\})|^2 \ |\Psi_0^B(\{t_B\})|^2 \ \left[\prod_{i=1}^{A} d^3 r_i\right] \ \left[\prod_{j=1}^{B} d^3 t_i\right]$ is a probability to find nucleons with coordinates $\{r_A\}$ and $\{t_B\}$. The interpretation allows a simple implementation in a program code which was done in many papers [22] sometimes with the simplifying assumptions that $g(\vec{b}) = \theta(|\vec{b}| - \sqrt{\sigma^{in}_{NN}/\pi})$. It is so-called Glauber Monte Carlo approach.

Because there is no expression in the Glauber theory that combines elastic and inelastic nucleon-nucleon collisions in nucleus-nucleus interactions, the cascade-type sampling is used in the FTF model in the case of these interactions.

Correction of interaction number

The Glauber cross section of multi-particle production processes in a hadron-nucleus interactions (Eq. 29.14) was obtained in the reggeon phenomenology [23] applying the asymptotical Abramovski-Gribov-Kancheli cutting rules [24] to the elastic scattering amplitude (Eq. 29.11). Thus, the summation in Eq. 29.14 is going from one to infinity. But a large number of intra-nuclear collisions cannot be reached in interactions with extra-heavy nuclei (like neutron star), or at low energy. To restrict the number of collisions it is needed to introduce finite energy corrections to the cutting rules. Because there is no defined prescription for accounting of these corrections, let us undertake a phenomenological consideration, and start with the cascade model.

As it was said above, a simple cascade model considers only pions and nucleons. Due to this it cannot work when resonance production is a dominating process in hadronic interactions. But if energy is sufficiently low the resonances can decay before a next possible collision, and the model can be

valid. Let p is a momentum of a produced resonance (Δ). The average life time of the resonance in its rest frame is $1/\Gamma$. In the laboratory frame the time is $E_\Delta/\Gamma\ m_\Delta$. During the time, the resonance will fly a distance $\bar{l} = v\ E_\Delta/\Gamma\ m_\Delta = p/\Gamma\ m_\Delta$. If the distance is less than an average distance between nucleons in nuclei ($\bar{d} \sim 2$ fm), the model can be applied. From the condition, we have:

$$p \leq \bar{d}\ \Gamma m_\Delta \sim 1.5 \quad (GeV/c).$$

Direct Δ-resonance production takes place in πN interactions at low energies. Thus the model cannot work quite well at momentum of pions above 2 GeV/c. In nucleon-nucleon interactions, due to momentum transfer to a target nucleon, the boundary can be higher.

Returned back to the FTF model, let us assume that projectile originated strings have average life time $1/\Gamma$, and an average mass m^*. The strings can interact at the average with $\bar{l}/\bar{d} = p/\Gamma\ m^*/\bar{d} = p/p_0$ nucleons. Here p_0 is a new parameters. According to our estimations it is about 3–5 GeV/c. Thus, we can assume that at given energy there can be a maximum number of intra-nuclear collisions in the FTF model – $\nu_{max} = p/p_0$.

Let us introduce this number in the Glauber expression for the cross section of multi-particle production processes.

$$\sigma^{hA}_{mpp} = \int d^2b\ \left\{1 - \left(1 - \frac{1}{A}\sigma^{in}_{hN}T_A(\vec{b})\right)^A\right\} = \tag{29.16}$$

$$= \int d^2b\ \left\{1 - \left[\left(1 - \frac{1}{A}\sigma^{in}_{hN}T_A(\vec{b})\right)^{A/\nu_{max}}\right]^{\nu_{max}}\right\} =$$

$$= \int d^2b\ \sum_{\nu=1}^{\nu_{max}} \frac{\nu_{max}!}{\nu!(\nu_{max}-\nu)!}\left[1 - \left(1 - \frac{1}{A}\sigma^{in}_{hN}T_A(\vec{b})\right)^{A/\nu_{max}}\right]^{\nu} \cdot$$

$$\cdot \left[\left(1 - \frac{1}{A}\sigma^{in}_{hN}T_A(\vec{b})\right)^{A/\nu_{max}}\right]^{\nu_{max}-\nu}.$$

As seen, the number of the intra-nuclear collisions is restricted according to the formula by ν_{max}.

The formula looks rather complicated, but a Monte Carlo algorithm for the rejection of the interaction number is quite simple.

An algorithm implementing of the idea look like that: at the beginning, a projectile has a power, P_w, to interact inelastically with ν_{max} nucleons ($P_w = \nu_{max}$), thus a probability of an interaction with the first nucleon,

P_w/ν_{max}, is equal to 1. The power decreases after the interaction on 1. Thus, a probability of an inelastic interaction with the second nucleon is equal to P_w/ν_{max}, where $P_w = \nu_{max} - 1$. If the second interaction is happened, the power is decreased one more. In other case, it is left on the same level. This is applied for each possible interaction.

The same algorithm is applied in the case of nucleus-nucleus interactions, but each of projectile or target nucleon is ascribed by the power.

29.6.2 Reggeon cascading

As known, the Glauber approximation used in the Fritiof model and in the other string models does not provide enough amount of intra-nuclear collisions for a correct description of a nuclear destruction. Additional cascading in nuclei is needed! An usage of a standard cascade for secondary particle interactions leads too large multiplicity of produced particles. Usually, it is assumed that an inclusion of a secondary particle's formation time can help to solve this problem. Hadrons are not point-like particles. They have defined space sizes. Thus, a production of a hadron cannon be considered as a process taking place in a point, but rather in a space region. To implement the idea in Monte Carlo generators, it is assumed that particles are appeared not in a nominal space-time point of production, but after some time interval called the formation time, and at some distance called the formation length. Because these time and length depend on a reference frame, it is assumed that for them standard relativistic formulae can be applied: $t_F = \tau_0 E/m, \quad l_F = \tau_0 p/m$, where E, p and m are energy, momentum and mass of the particle in a final state. τ_0 is a parameter. Now the problem is – How can one determine the "nominal" point of the production? We do not know a regular solution of the problem. Additional to this, reggeon theory experts criticized for long time the concept of the formation time and the "standard" model of particle cascading in nuclei – the approaches do not consider a space-time structure of strong interactions. It was assumed also that the cascading could be correctly treated in the reggeon theory at a consideration of so-called enhanced diagrams.

According to the phenomenology, an elastic hadron-hadron scattering amplitude is a sum of contributions connected with various exchanges in the t-channel. Each contribution has the following form in the impact parameter representation:

$$A^R_{NN}(\vec{b},\xi) = \eta_R g_R^2 e^{\Delta_R \xi} \frac{e^{-\frac{b^2}{4(R^2+\alpha'_R\xi)}}}{(R^2_{NN}+\alpha'_R\xi)}. \tag{29.17}$$

Here $|\vec{b}|$ is the impact parameter, $\xi = ln(s)$, s is the squared CMS energy,

η_R is the signature factor: $\eta_R = 1 + i\ cot(\pi(1+\Delta_R)/2)$ for a pole with positive signature, and $\eta_R = -1 + i\ cot(\pi(1+\Delta_R)/2)$ for a pole with negative signature. $1+\Delta_R$ is an intercept of the reggeon trajectory, α'_R is its slope, and the vertex of reggeon-nucleon interaction is parameterized as $g(t) = g_R\ exp(R^2_{NN}t/2)$, t is transferred 4-momentum.

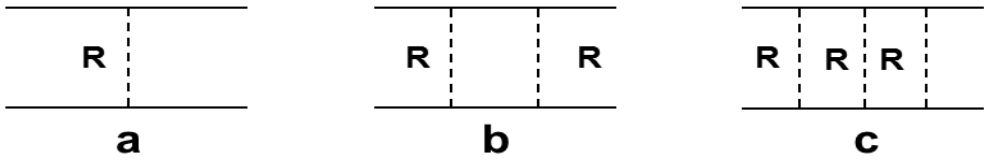

Figure 29.16: Nonenhanced diagrams of NN-scattering.

Taking into account contributions of other diagrams of Fig. 29.16, one can find NN-scattering amplitude:

$$\gamma_{NN}(\vec{b},\xi) = 1 - e^{-A^R_{NN}(\vec{b},\xi)}.$$

A calculation of amplitudes and cross sections for cascade interactions requires a consideration of so-called enhanced diagrams like that shown in Fig. 29.17.

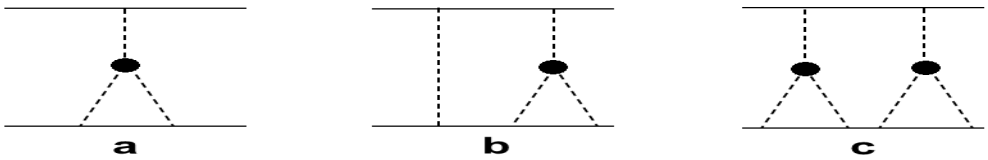

Figure 29.17: Simplest enhanced diagrams of NN-scattering.

A contribution of the diagram Fig. 29.17a to the elastic scattering amplitude is given by the expression:

$$GE_a(\vec{b},\xi) = -G\int\limits_{\epsilon}^{\xi-\epsilon} d\xi' \int d^2b' A^{R_1}_{N\pi}(\vec{b}-\vec{b'},\xi-\xi')A^{R_2}_{\pi N}(\vec{b'},\xi')A^{R_3}_{\pi N}(\vec{b'},\xi'), \quad (29.18)$$

where $A_{\pi N}$ is an amplitude of meson-nucleon scattering due to one-reggeon exchange, G is a three reggeon's coupling constant, ϵ is cutoff parameter ($\epsilon \sim 1$). Here we use the model of multi-reggeon vertices proposed in Refs. [25], where it was assumed that reggeon are coupled to one another via a created virtual meson (pion) pair.

The simplest enhanced diagrams were accounted for at a consideration of hadron-nucleus scattering in Ref. [26, 27]. An effective computational procedure was proposed in papers [28, 29], but it was not applied to an analysis of experimental data. The structure of the enhanced diagrams and their analytical properties were studied in [30].

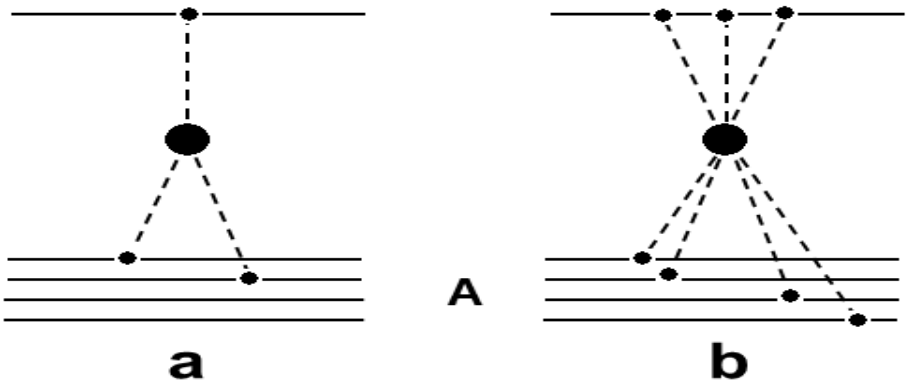

Figure 29.18: Possible enhanced diagrams of hA-interactions.

In the reggeon approach the interaction of secondary particles with a nucleus is described by cuttings of enhanced diagrams. Here the Abramovski-Gribov-Kancheli (AGK) cutting rules [24] are frequently applied. The corrections to them were discussed in [30] in an application to the problem of particle cascading into the nucleus. It was shown there that inelastic rescatterings occur for any secondary particles, both slow and fast ones, and the yield of enhanced diagrams leads to the enrichment of the spectrum by slow particles in the target fragmentation region.

As in [25] we shall assume that the reggeon interaction vertices are small. Therefore of the full set of enhanced diagrams the only important ones will be those containing vertices where one of the reggeons split into several, which then interact with different nucleons of the nucleus (figure 29.18a). In studying interactions with nuclei, however, it is convenient, in the spirit of the Glauber approach, to deal not with individual reggeons, but with sets of them interacting with a given nucleons of the nucleus (figure 29.18b). Unfortunately, the reggeon method of calculating the sum of the yields of enhanced diagrams in the case of hA- and AA-interactions is not developed for practical tasks. Hence we propose a simple model of estimating reggeon cascading in hA- and AA-interactions.

Let us consider an yield of the first diagram of Fig. 29.18a:

$$Y = G \int d\xi' d^2b' F_{N\pi}(\vec{b} - \vec{b'}, \xi - \xi') \times F_{\pi N}(\vec{b'} - \vec{s}_1, \xi') F_{\pi N}(\vec{b'} - \vec{s}_2, \xi'), \quad (29.19)$$

where $\vec{b}$ is the impact parameter of a projectile hadron, $\vec{s}_1$ and $\vec{s}_2$ are impact coordinates of two nuclear nucleons, $\vec{b'}$ is the position of the reggeon interaction vertex in the impact parameter plane, ξ' is its rapidity.

Using Gaussian parameterization for $F_{N\pi}$ ($F_{\pi N} = exp(-|\vec{b}|^2/R^2_{\pi N})$ and neglecting its dependence on energy, we have

$$Y \simeq G(\xi_0 - 2\epsilon)\frac{R^2_{\pi N}}{3} exp(-(\vec{b} - (\vec{s}_1 + \vec{s}_2)/2)^2/3R^2_{\pi N}) \times exp(-(\vec{s}_1 - \vec{s}_2)^2/2R^2_{\pi N}), \tag{29.20}$$

where $R_{\pi N}$ is the pion-nucleon interaction radius. According to the equation, the contribution reaches a maximum if the nucleon coordinates, $\vec{s}_1$ and $\vec{s}_2$, coincide, and decreases very fast with increasing the distance between the nucleons.

Cutting the diagram, one can obtain that a probability, ϕ, to involve 2 neighboring nucleons is

$$\phi(\mid \vec{s}_1 - \vec{s}_2 \mid) \sim exp(-\frac{\mid \vec{s}_1 - \vec{s}_2 \mid^2}{R^2_{\pi N}}) \tag{29.21}$$

Schematically, the hadron-nucleus interaction process in the impact parameter plane can be represented as in Fig. 29.19, where the position of the projectile hadron is marked by an open circle, the positions of nuclear nucleons by closed circles, reggeon exchanges by dashed lines and the small points are the coordinates of the reggeon interaction vertices.

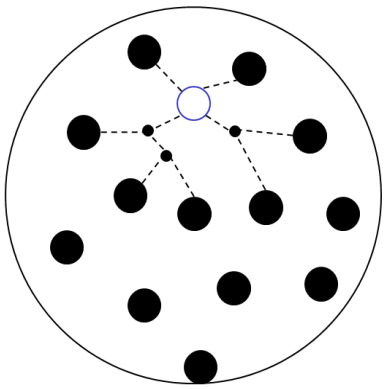

Figure 29.19: Reggeon "cascade" in hA-scattering.

Let us consider the problem using quark-gluon approach. There were some successful attempts to describe the hadron-nucleon elastic scattering at low and intermediate energies (below 1 – 2 GeV) within the approach

(see Refs. [31]). Especially, in Refs. [31] the amplitudes of $\pi\pi$-, KK- and NN-scatterings were found, and an agreement of the theoretical calculations with experimental data was reached at the assumption that in the elastic hadron scattering one-gluon exchange with following quark interchange between hadrons takes place (see Fig. 29.20a). At high energies, two-gluon exchange approximation (Fig. 29.20b) works quite well (see Ref. [32]). What kind of exchanges can dominate in hadron-nucleus and nucleus-nucleus interactions?

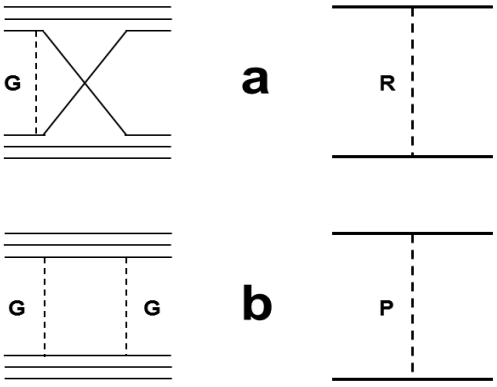

Figure 29.20: Diagrams of quark-gluon exchanges and corresponding reggeon diagrams for hadron-hadron interactions.

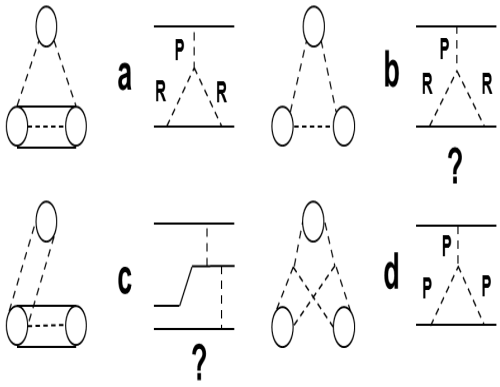

Figure 29.21: Diagrams of quark-gluon exchanges and corresponding reggeon diagrams for hadron-nucleus interactions.

The simplest possible diagrams of processes with three nucleons are given in Fig. 29.21. A calculation of their amplitudes according to Refs. [31] is a serious mathematical problem. It can be simplified if one takes into account an analogy between quark-gluon diagrams and reggeon diagrams: the quark diagram of Fig. 29.20a corresponds to a one-nonvacuum reggeon exchange; the diagram of Fig. 29.20b describes the pomeron exchange in the t-channe; the diagram of Fig. 29.21a is in a correspondence with the enhanced reggeon diagram of the pomeron splitting into two non-vacuum reggeons. The three pomeron diafram (Fig. 29.21d) represent the more complicated process. It is rather complicated to find a correspondence between reggeon diagrams and the diagrams of Fig. 29.21b. Fig. 29.21c.

It seems obvious that the processes like one in Fig. 29.21d cannot dominate in the elastic hadron-nucleus scattering because they are accompanied by a production of high mass diffraction beam of particles in the intermediate state. Thus, their yields are damped by a nuclear form-factor. According to the same reason, the yields of processes like ones in Figs. 29.21a, 29.21b can be small too. If it is not so, one can expect a large corrections to Glauber

cross sections. The practice shows that the corrections to hadron-nucleus cross sections must be lower than 5 – 7 %.

The yield of the diagram 29.21c can give a correction to the Glauber one-scattering amplitude. The analogous corrections can be to the other terms of Glauber series. They can re-normalize nuclear vertex constants. According to Refs. [31] the yield can have a form:

$$Y_c \propto \exp\left[-(\vec{b}-\vec{s}_1)/R_p^2\right] \exp\left[-(\vec{s}_1-\vec{s}_2)/R_c^2\right],$$

where R_p is a radius of high energy nucleon-nucleon interactions, R_c is another low energy radius. Let us note that Y_c does not depend as other reggeon diagram yields on longitudinal coordinates of nucleons and on multiplicity of produced particles. It is the main difference between "reggeon cascading" and usual cascading.

As well known, the intra-nuclear cascade model assumes that in a hadron-nucleus collision, secondary particles are produced in a first inelastic interaction of a projectile with a nuclear nucleon. The produced particles can interact with other target nucleons. A distribution for a distance l between the first interaction and a second one has a form:

$$W(l)dl \propto \frac{n}{< l >} exp(-\frac{n}{< l >}\ l),$$

where $< l >= 1/\sigma\rho_A$, σ is a hadron-nucleon cross section, n is a multiplicity of the produced particles, and $\rho_A \sim 0.15\ (fm)^{-3}$ is a nuclear density. At the same time, the amplitudes or a cross sections of processes like Fig. 29.21 have no dependence on l or n. Thus, one can expect that the "cascade" in the quark-gluon approach will be more restricted than in the cascade model. The difference between the approaches can lead to different predictions for hadron interactions with heavy nuclei due to a large multiplicity of the produced particles.

Because it is complicated to calculate yields of various diagrams, and take into account all possibilities, let us formulate a simple phenomenological model keeping the main features of the above given approaches.

The model formulation

1. As it was said above, the "reggeon" cascade is developed in the impact parameter plane, and has features typical for branching processes. Thus, for its description it is needed to determine a probability to involve a nuclear nucleons into the "cascade". It is obvious, that the probability depends on a difference of impact coordinates of new and

previous involved nucleons. Looking at the yield of diagram 29.21c, a functional form of the probability is chosen as:

$$P(|\vec{s_i} - \vec{s_j}|) = C_{nd}\ exp[-(\vec{s_i} - \vec{s_j})^2/R_c^2], \qquad (29.22)$$

where $\vec{s_i}$ and $\vec{s_j}$ are projections of the radii of i^{th} and j^{th} nucleons on the impact parameter plane.

2. The "cascade" is initiated by primary involved nucleons. These nucleons are determined with a help of the Glauber approach.

3. All involved nucleons are ejected from nuclei.

The "cascade" looks like that: a projectile particle interacts with some intra-nuclear nucleons. These nucleons are called "wounded" or participating nucleons. The nucleons initiate the "cascade". A wounded nucleon can involve a spectator nucleon into the "cascade" with the probability (29.22). The latter one can involve an other nucleon. The second nucleon can involve a third one and so on. This algorithm is implemented in the FTF model.

We have tuned C_{nd} using the HARP-CDP data on proton production in the $p + Cu$ interactions [33]. According to our estimations,

$$C_{nd} = e^{4\ (y-2.1)}/[1 + e^{4\ (y-2.1)}], \quad R_c^2 = 1.5\ \ (fm)^2.$$

where y is a projectile rapidity. The value, 2.1, standing in the exponents corresponds to $P_{lab} \sim 4$ GeV/c.

29.6.3 "Fermi motion" of nuclear nucleons

In a "standard" approach, a nucleus is considered as a potential well where nucleons are freely moving. A particle falling on the nucleus changes its momentum on a border of the well. Here a question appears, to whom the recoil momentum must be ascribed? If the particle is absorbed by the nucleus, probably, one has to imagine in a final state the potential well with its nucleons moving with a momentum of the particle!? If some nucleons are ejected from the nucleus, it is unknown in the case, what conditions have to satisfy the nucleon momenta, and how will the "residual" well be moving to satisfy the energy-momentum conservation law? In the case of 3-dimensional potential well it is unknown, how will be changed momentum components of the particle on the well surface? Only a component transverse to the surface will be changed, or a component which is parallel to the surface? A list of questions can be extended at a consideration of nucleus-nucleus interactions.

Two approaches are used at practice. According to the first one, the nucleus is considered as a continuous media, and nucleons are appeared only in points of the projectile interactions with the media. It seems natural in the approach to sum momenta of all ejected particles. Subtracting it from the initial momentum, one can find a momentum of residual nucleus. It is unclear, what has to be done in nucleus-nucleus interactions?

In the second approach, space coordinates and momenta of the nucleons are sampled according to some assumptions. In order to satisfy the energy-momentum conservation law, the projectile momentum does not changed, and each nucleon is ascribed by a new mass:

$$m = \sqrt{(m_0 - \epsilon_b)^2 - p^2},$$

where m_0 is a nucleon mass in the free state, ϵ_b is a nuclear binding energy per nucleon, and p is a momentum of the nucleon.

In the approach, the nucleus is a collection of off-mass-shell particles. Apparently, in the case of nucleus-nucleus interactions one has to consider two such collections.

The energy-momentum conservation law is satisfied in the approach, if it is satisfied in each collision of out-of-mass-shell nucleons. Though, there is a problem with excitation energy of a nuclear residual. In most of the cases, it is too small.

All the questions are absent in the approach proposed in the paper [34]. Let us consider it starting from simple example of a hadron interaction with a bound system of two nucleons, $(1, 2)$. It is assumed in the approach that the process has two stages. At the first one, the system is dissociated:

$$h + (1, 2) \to h + 1 + 2.$$

At the second stage a "hard" collision of the projectile with the first or second nucleon takes place. Neglecting transverse momenta let us write the energy-momentum conservation law in the form:

$$\begin{cases} p_h = p'_h + p_1 + p_2 \\ E_h + E_{(1,2)} = E'_h + E_1 + E_2 \end{cases}$$

As seen there are three variables and two equations. Thus, only one variable can be chosen as an independent one. It can be p'_h – hadron momentum in the final state, or p_1 or p_2 – nucleon momentum in the state. We choose as the variable the light cone momentum fraction:

$$x_1 = (E_1 - p_1)/(E_1 + E_2 - p_1 - p_2).$$

It is invariant under the Lorentz transform along the collision axis.

Using the variable and the energy-momentum conservation law, one can find:

$$W^- = E_1 + E_2 - p_1 - p_2 = [s - m_h^2 + \beta^2 - \lambda^{1/2}(s, m_h^2, \beta^2)]/2\ W_0^+,$$

where

$$W_0^+ = E_h + E_{(1,2)} + p_h, \quad W_0^- = E_h + E_{(1,2)} - p_h, \quad s = W_0^+ W_0^-,$$

$$\beta^2 = \frac{m_1^2}{x_1} + \frac{m_2^2}{1 - x_1}.$$

Other kinematical variables are:

$$p_1 = \frac{m_1^2}{2x_1 W^-} - \frac{x_1 W^-}{2}, \quad E_1 = \frac{m_1^2}{2x_1 W^-} - + \frac{x_1 W^-}{2},$$

$$p_2 = \frac{m_2^2}{2(1-x_1) W^-} - \frac{(1-x_1) W^-}{2}, \quad E_2 = \frac{m_2^2}{2(1-x_1) W^-} - + \frac{(1-x_1) W^-}{2},$$

$$p'_h = p_h - p_1 - p_2, \quad E'_h = E_h + E_{(1,2)} - E_1 - E_2.$$

So, for a simulation of the interactions, one has to determine only one function: $f(x_1)$ – a distribution for x_1. Distributions for p_1 and p_2 have interesting properties: at $p_h \to \infty$ they become stable. At $p_h \to 0, \quad E_h + E_{(1,2)} > m_h + m_1 + m_2$ they become narrow and narrow. Thus, a typical limiting fragmentation of bounded system takes place.

It is not complicated to introduce transverse momenta – $p'_{\perp h}$, $p_{\perp 1}$ and $p_{\perp 2}$, $p'_{\perp h} + p_{\perp 1} + p_{\perp 2} = 0$. It is sufficient to replace m_i by the transverse masses: $m_i \to m_{\perp i} = \sqrt{m_i^2 + p_{\perp i}^2}$.

In the case of interactions of two composed systems, A and B, consist of A and B constituents, respectively, let us describe i^{th} constituent of A by the variables:

$$x_i^+ = (E_{Ai} + p_{iz})/W_A^+ \quad and \quad \vec{p}_{i\perp},$$

and j^{th} constituent of B by the variables:

$$y_j^- = (E_{Bj} - q_{jz})/W_B^- \quad and \quad \vec{q}_{i\perp}.$$

Here $E_{Ai}(E_{Bi})$ and $\vec{p}_i(\vec{q}_i)$ are energy and momentum of i^{th} constituent of the system A (B).

$$W_A^+ = \sum_{i=1}^{A} (E_{Ai} + p_{iz}), \quad W_B^- = \sum_{i=1}^{B} (E_{Bi} - q_{iz}).$$

Using the variables, the energy-momentum conservation law takes the form:

$$\frac{W_A^+}{2}+\frac{1}{2W_A^+}\sum_{i=1}^{A}\frac{m_{i\perp}^2}{x_i^+}+\frac{W_B^-}{2}+\frac{1}{2W_B^-}\sum_{i=1}^{B}\frac{\mu_{i\perp}^2}{y_i^-}=E_A^0+E_B^0,$$

$$\frac{W_A^+}{2}-\frac{1}{2W_A^+}\sum_{i=1}^{A}\frac{m_{i\perp}^2}{x_i^+}-\frac{W_B^-}{2}+\frac{1}{2W_B^-}\sum_{i=1}^{B}\frac{\mu_{i\perp}^2}{y_i^-}=P_A^0+P_B^0, \qquad (29.23)$$

$$\sum_{i=1}^{A}\vec{p}_{i\perp}+\sum_{i=1}^{B}\vec{q}_{i\perp}=0,$$

where $m_{i\perp}^2=m_i^2+\vec{p}_{i\perp}^2$, $\mu_{i\perp}^2=\mu_i^2+\vec{q}_{i\perp}^2$, $m_i(\mu_i)$ is a mass of i^{th} constituent of ().

The system of the equations (29.23) allows one to find W_A^+, W_B^- and all kinematical properties of the particles at given $\{x_i^+,\vec{p}_{i\perp}\}$, $\{y_i^-,\vec{q}_{i\perp}\}$.

$$W_A^+=(W_0^-W_0^++\alpha-\beta+\sqrt{\Delta})/2W_0^-; \qquad (29.24)$$

$$W_B^-=(W_0^-W_0^+-\alpha+\beta+\sqrt{\Delta})/2W_0^+; \qquad (29.25)$$

$$W_0^+=(E_A^0+E_B^0)+(P_{Az}^0+P_{Bz}^0;$$

$$W_0^-=(E_A^0+E_B^0)-(P_{Az}^0+P_{Bz}^0;$$

$$\alpha=\sum_{i=1}^{A}\frac{m_{i\perp}^2}{x_i^+},\quad \beta=\sum_{i=1}^{B}\frac{\mu_{i\perp}^2}{y_i^-};$$

$$\Delta=(W_0^-W_0^+)^2+\alpha^2+\beta^2-2W_0^-W_0^+\alpha-2W_0^-W_0^+\beta-2\alpha\beta;$$

$$p_{iz}=(W_A^+x_i^+-\frac{m_{i\perp}^2}{x_i^+W_A^+})/2;\quad q_{iz}=-(W_B^-y_i^--\frac{\mu_{i\perp}^2}{y_i^-W_B^-})/2.$$

Consequently, the problem of binding energy and Fermi motion accounting at a simulation of composed system interactions comes to a definition of distributions for $x_i^+,y_i^-,\vec{p}_{i\perp},\vec{q}_{i\perp}$.

Transverse momentum of an ejected nucleon ($\vec{p}_\perp$) was sampled according to the distribution:

$$dW\propto exp(-\vec{p}_\perp^2/<p_\perp^2>)d^2p_\perp, \qquad (29.26)$$

$$<p_\perp^2>=0.035+0.04\frac{e^{4\ (y_{lab}-2.5)}}{1+e^{4\ (y_{lab}-2.5)}}\quad (GeV/c)^2. \qquad (29.27)$$

where y_{lab} is a projectile nucleus rapidity in the rest frame of a target nucleus. A sum of the transverse momenta with minus sign is ascribed to a residual of the target nucleus.

x^+ or y^- was sampled according to the distribution:

$$dW \propto exp[-(x^+ - 1/A)^2/(d/A)^2]dx^+, \quad d = 0.3. \tag{29.28}$$

x^+ of the nuclear residual is determined as $1 - \sum x_i^+$.

29.6.4 Excitation energy of nuclear residuals

According to the materials presented above, excitation energy of a nuclear residual has to be determined before a simulation of particle production. It seems natural to assume that the energy is connected with a multiplicity of ejected nuclear nucleons, as participating ones, as well as ones involved in the reggeon cascading. Without the involved nucleons, the energy will be proportional to a multiplicity of participating nucleons calculated in the Glauber approach. Such approach was used in the paper [35] where proton-nucleus interactions at intermediate energies were analyzed. There the multiplicity of the nucleons was calculated in the Glauber approach. It was assumed also that each recoil participating nucleon gives an yield in the excitation energy distributed according to the law:

$$dW(E) = \frac{1}{\langle E \rangle} e^{-E/\langle E \rangle} dE. \tag{29.29}$$

Sum of the yields determines the residual excitation energy. The authors of the paper [35] considered absorptions and ejections of the nucleons, and decreasing projectile energy during interactions. They obtained a good agreement of their calculations with experimental data on neutron production as a function of the residual excitation energy.

Extending the approach [35], we assume, as a first step, that each participating or involved nucleon adds 100 MeV to the nuclear residual excitation energy. The excited residual is fragmenting using the Generalized Evaporation Model (GEM) [36].

29.7 Validation of the FTF model

Bibliography

[1] B.Andersson et al. Nucl. Phys. **B281** 289 (1987).

[2] B.Nilsson-Almquist, E.Stenlund, Comp. Phys. Comm. **43** 387 (1987).

[3] http://pdg.lbl.gov/2012/hadronic-xsections/hadron.html

[4] E. Bracci et al. CERN–HERA 72-1 (1972).

[5] G. Folger, V.N. Ivanchenko, J.P. Wellisch, Eur. Phys. J. **A21** 407 (2004).

[6] S.A. Bass et al. Prog. Part. Nucl. Phys. **41** 225 (1998); M. Bleicher et al. J. Phys. **G25** 1859 (1999).

[7] E. Bracci et al. CERN–HERA 73-1 (1973); V. Flaminio et al.CERN–HERA 84-01 (1984).

[8] V. Flaminio et al. CERN–HERA 79-02 (1979).

[9] A.B. Kaidalov and P.E. Volkovitsky, Zeit. fur Phys. **C63** 517 (1994).

[10] V.V. Uzhinsky and A.S. Galoyan, arXiv: hep-ph/0212369 (2002).

[11] J.R. Cudell et al. (COMPLETE collab.) Phys. Rev. **D65** 074024 (2002).

[12] W.-M. Yao et al. (PDG), J. Phys. **G33** 337 (2006).

[13] M. Ishida and K. Igi, Phys. Rev. **D79** 096003 (2009).

[14] Bonn-Hamburg-Munich Collab. (V. Blobel et al.) Nucl. Phys. **B69** 454 (1974).

[15] K.A. Goulianos and J. Montanha, Phys. Rev. **D59** 114017 (1999).

[16] P. Bosettii et al., Nucl. Phys. **B54** 141 (1973).

[17] J. Whitmore, Phys. Rep. **10** 273 (1974).

[18] NA22 Collab. (M. Adamus et al.) Zeit. fur Phys. **C32** 475 (1986);
BBCMS Collab. (I.V. Azhinenko et al.) Nucl. Phys. **B123** 493 (1977).

[19] Kh. Abdel-Waged and V.V. Uzhinsky, Phys. Atom. Nucl. **60** 828 (1997) (Yad. Fiz. **60** 925 (1997)).
Kh. Abdel-Waged and V.V. Uzhinsky, J. Phys. **G24** 1723 (1997).

[20] R.J. Glauber, In: "Lectures in Theoretical Physics", Ed. W.E.Brittin et al., v. **1**, Interscience Publishers, N.Y., 1959.; R.J. Glauber, Proc. of the 2nd Int. Conf. on High Energy Physics and Nuclear structure, (Rehovoth, 1967) Ed. G.A.Alexander, North-Holland, Amsterdam, 1967.

[21] V. Franco, Phys. Rev. **175** 1376 (1968).

[22] S.Yu. Shmakov, V.V. Uzhinski and A.M. Zadorojny, Comp. Phys. Commun. **54** 125 (1989);
B. Alver, M. Baker, C. Loizides, and P. Steinberg, arxiv:0805.4411 [nucl-exp] (2005). M.L. Miller, K. Reygers, S.J. Sanders and P. Steinberg, Ann. Rev. Nucl. Part. Sci., **57** 205 (2007);
W. Broniowski, M. Rybczynski, and P. Bozek, Comp. Phys. Commun., **180** 69 (2009).

[23] Yu.M. Shabelski, Sov. J. Part. Nucl., **12** 430 (1981).

[24] V.A. Abramovsky, V.N. Gribov and O.V. Kancheli, Sov. J. Nucl. Phys. **18** 308 (1974) (Yad. Fiz. **18** 595 (1973)).

[25] A.B. Kaidalov, L.A. ponomarev and K.A. Ter-Martirosian, Sov. J. Nucl. Phys. **44** 468 (1986) (Yad. Fiz. **44** 722 (1986)).

[26] R. Jengo and D.Treliani, Nucl. Phys. **117B** 433 (1976).

[27] R.E. Camboa Saravi, Phys. Rev. **21** 2021 (1980).

[28] A. Schwimmer, Nucl. Phys. **94B** 445 (1975).

[29] L. Caneschi, A. Schwimmer and R.Jenco, Nucl. Phys. **108B** 82 (1976).

[30] K.G. Boreskov, A.B. Kaidalov, S.M. Kiselev and N.Ya. Smorodinskaya, Sov. J. Nucl. Phys. **53** 356 (1991) (Yad. Fiz. **53** 569 (1991)).

[31] T. Barnes and E.S.Swanson, Phys. Rev. **D46** 131 (1992);
T.Barnes, E.S.Swanson and J.Weinstein, Phys. Rev. **D46** 4868 (1992);
T.Barnes, S.Capstick, M.D.Kovarik and E.S. Swanson, Phys. Rev. **C48** 539 (1993);
T.Barnes and E.S.Swanson, Phys. Rev. **C49** 1166 (1992).

[32] F. Low, Phys. Rev. **D12** 163 (1975);
S. Nussinov, Phys. Rev. **D14** 246 (1976);
J. Gunion and D.Shoper, Phys. Rev. **D15** 2617 (1977);
E.M. Levin and M.G. Ryskin, Yad. Fiz. **34** 619 (1981).

[33] HARP-CDP Collab. (A. Bolshakova et al.) Eur. Phys. J. **C64** 181 (2009).

[34] EMU-01 Collab. (M.I. Adamovich et al.) Zeit. fur Phys. **A358** 337 (1997).

[35] A.Y. Abul-Magd, W.A.Friedman and J.Hufner, Phys. Rev. **C34** 113 (1986).

[36] S. Furihata, NIM **B171** 251 (2000).

Chapter 30

Chiral Invariant Phase Space Decay

30.1 Introduction

The CHIPS computer code is a quark-level event generator for the fragmentation of hadronic systems into hadrons. In contrast to other parton models [1] CHIPS is nonperturbative and three-dimensional. It is based on the Chiral Invariant Phase Space (ChIPS) model [2, 3, 4] which employs a 3D quark-level SU(3) approach. Thus Chiral Invariant Phase Space refers to the phase space of massless partons and hence only light (u, d, s) quarks can be considered. The c, b, and t quarks are not implemented in the model directly, while they can be created in the model as a result of the gluon-gluon or photo-gluon fusion. The main parameter of the CHIPS model is the critical temperature $T_c \approx 200\ MeV$. The probability of finding a quark with energy E drops with the energy approximately as $e^{-E/T}$, which is why the heavy flavors of quarks are suppressed in the Chiral Invariant Phase Space. The s quarks, which have masses less then the critical temperature, have an effective suppression factor in the model.

The critical temperature T_c defines the number of 3D partons in the hadronic system with total energy W. If masses of all partons are zero then the number of partons can be found from the equation $W^2 = 4T_c^2(n-1)n$. The mean squared total energy can be calculated for any "parton" mass (partons are usually massless). The corresponding formula can be found in [5]. In this treatment the masses of light hadrons are fitted better than by the chiral bag model of hadrons [6] with the same number of parameters. In both models any hadron consists of a few quark-partons, but in the CHIPS model the critical temperature defines the mass of the hadron, consisting of

N quark-partons, while in the bag model the hadronic mass is defined by the balance between the quark-parton internal pressure (which according to the uncertainty principle increases when the radius of the "bag" decreases) and the external pressure (B) of the nonperturbative vacuum, which has negative energy density.

In CHIPS the interactions between hadrons are defined by the Isgur quark-exchange diagrams, and the decay of excited hadronic systems in vacuum is treated as the fusion of quark-antiquark or quark-diquark partons. An important feature of the model is the homogeneous distribution of asymptotically free quark-partons over the invariant phase space, as applied to the fragmentation of various types of excited hadronic systems. In this sense the CHIPS model may be considered as a generalization of the well-known hadronic phase space distribution [7] approach, but it generates not only angular and momentum distributions for a given set of hadrons, but also the multiplicity distributions for different kinds of hadrons, which is defined by the multistep energy dissipation (decay) process.

The CHIPS event generator may be applied to nucleon excitations, hadronic systems produced in e^+e^- and $p\bar{p}$ annihilation, and high energy nuclear excitations, among others. Despite its quark nature, the nonperturbative CHIPS model can also be used successfully at very low energies. It is valid for photon and hadron projectiles and for hadron and nuclear targets. Exclusive event generation models multiple hadron production, conserving energy, momentum, and other quantum numbers. This generally results in a good description of particle multiplicities, inclusive spectra, and kinematic correlations in multihadron fragmentation processes. Thus, it is possible to use the CHIPS event generator in exclusive modeling of hadron cascades in materials.

In the CHIPS model, the result of a hadronic or nuclear interaction is the creation of a quasmon which is essentially an intermediate state of excited hadronic matter. When the interaction occurs in vacuum the quasmon can dissipate energy by radiating particles according to the quark fusion mechanism [2] described in section 30.4. When the interaction occurs in nuclear matter, the energy dissipation of a quasmon can be the result of quark exchange with surrounding nucleons or clusters of nucleons [3] (section 30.5), in addition to the vacuum quark fusion mechanism.

In this sense the CHIPS model can be a successful competitor of the cascade models, because it does not break the projectile, instead it captures it, creating a quasmon, and then decays the quasmon in nuclear matter. The perturbative mechanisms in deep inelastic scattering are in some sense similar to the cascade calculations, while the parton splitting functions are used instead of interactions. The nonperturbative CHIPS approach is making a "short cut" for the perturbative calculations too. Similar to the time-like

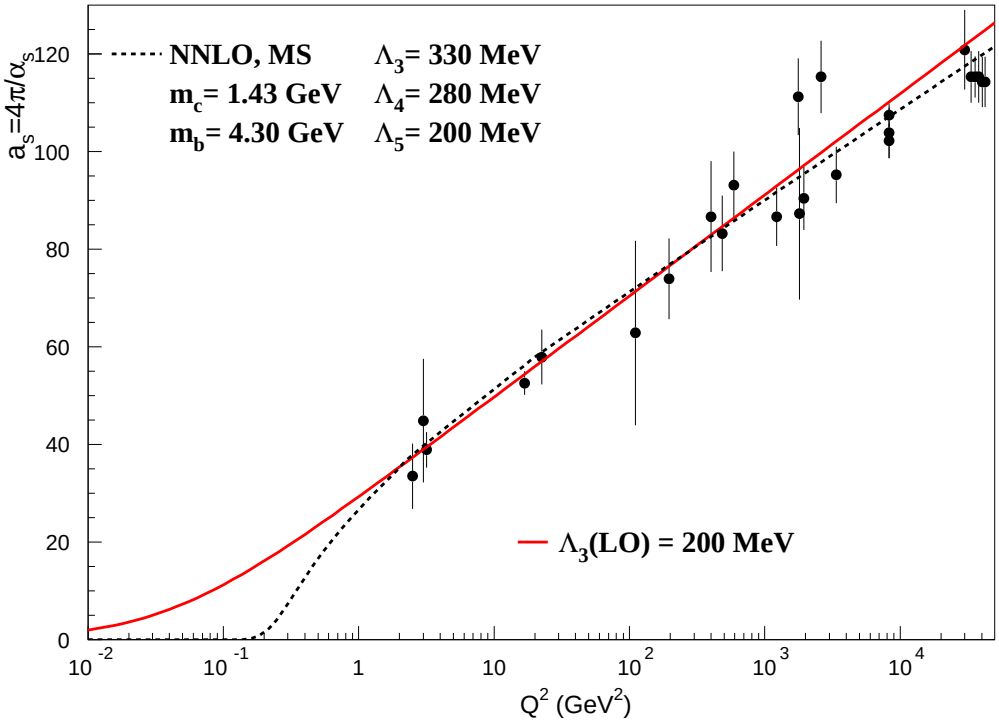

Figure 30.1: The CHIPS fit of the α_s measurements.

$s = W^2$ evolution of the number of partons in the nonperturbative chiral phase space (mentioned above) the space-like Q^2 evolution of the number of partons is given by $N(Q^2) = n_V + \frac{1}{2\alpha_s(Q^2)}$, where n_V is the number of valence quark-partons. The running $\alpha_s(Q^2)$ value is calculated in CHIPS as $\alpha_s(Q^2) = \frac{4\pi}{\beta_0 ln(1+Q^2/T_c^2)}$, where $\beta_0^{n_f=3)=9}$. In other words, the critical temperature T_c plays the role of Λ_QCD and still cuts out heavy flavors of quark-partons and high orders of the QCD calculation (NLO, NNLO, N^{3}LO, etc.), substituting for them the effective LO "short cut". This simple approximation of α_s fits all the present measurements of this value (Fig. 30.1). It is very important that α_s is defined in CHIPS for any Q^2, and that the number of partons at $Q^2 = 0$ converges to the number of valence quarks.

The effective α_s is defined for all Q^2, but at $Q^2 = 0$ it is infinite. In other words at $Q^2 = 0$ the number of the virtual interacting partons goes to infinity. This means that on the boundary between perturbative and non-perturbative vacuums a virtual "thermostate" of gluons with an effective temperature T_c exists. This "virtual thermostate" defines the phase space

distribution of partons, and the "thermalization" can happen very quickly. On the other hand, the CHIPS nonperturbative approach can be used below $Q^2 = 1\ GeV^2$. This was done for the neutrino-nuclear interactions (section 30.8).

30.2 Fundamental Concepts

The CHIPS model is an attempt to use a set of simple rules which govern microscopic quark-level behavior to model macroscopic hadronic systems with a large number of degrees of freedom. The invariant phase space distribution as a paradigm of thermalized chaos is applied to quarks, and simple kinematic mechanisms are used to model the hadronization of quarks into hadrons. Along with relativistic kinematics and the conservation of quantum numbers, the following concepts are used:

- **Quasmon:** in the CHIPS model, a quasmon is any excited hadronic system; it can be viewed as a continuous spectrum of a generalized hadron. At the constituent level, a quasmon may be thought of as a bubble of quark-parton plasma in which the quarks are massless and the quark-partons in the quasmon are homogeneously distributed over the invariant phase space. It may also be considered as a bubble of the three-dimensional Feynman-Wilson [8] parton gas. The traditional hadron is a particle defined by quantum numbers and a fixed mass or a mass with a width. The quark content of the hadron is a secondary concept constrained by the quantum numbers. The quasmon, however, is defined by its quark content and its mass, and the concept of a well defined particle with quantum numbers (a discrete spectrum) is of secondary importance. A given quasmon hadronic state with fixed mass and quark content can be considered as a superposition of traditional hadrons, with the quark content of the superimposed hadrons being the same as the quark content of the quasmon.

- **Quark fusion:** the quark fusion hypothesis determines the rules of final state hadron production, with energy spectra reflecting the momentum distribution of the quarks in the system. Fusion occurs when a quark-parton in a quasmon joins with another quark-parton from the same quasmon and forms a new white hadron, which can be radiated. If a neighboring nucleon (or the nuclear cluster) is present, quark-partons may also be exchanged between the quasmon and the neighboring nucleon (cluster). The kinematic condition applied to these mechanisms is that the resulting hadrons are produced on their mass shells. The

model assumes that the u, d and s quarks are effectively massless, which allows the integrals of the hadronization process to be done easily and the modeling decay algorithm to be accelerated. The quark mass is taken into account indirectly in the masses of outgoing hadrons. The type of the outgoing hadron is selected using combinatoric and kinematic factors consistent with conservation laws. In the present version of CHIPS all mesons with three-digit PDG Monte Carlo codes [9] up to spin 4, and all baryons with four-digit PDG codes up to spin $\frac{7}{2}$ are implemented.

- **Critical temperature** the only non-kinematic concept of the model is the hypothesis of the critical temperature of the quasmon. This has a 40-year history, starting with Ref. [10] and is based on the experimental observation of regularities in the inclusive spectra of hadrons produced in different reactions at high energies. Qualitatively, the hypothesis of a critical temperature assumes that the quark-gluon hadronic system (quasmon) cannot be heated above a certain temperature. Adding more energy to the hadronic system increases only the number of constituent quark-partons while the temperature remains constant. The critical temperature is the principal parameter of the model and is used to calculate the number of quark-partons in a quasmon. In an infinite thermalized system, for example, the mean energy of partons is $2T$ per particle, the same as for the dark body radiation.

30.3 Code Development

Because the CHIPS event generator was originally developed only for final state hadronic fragmentation, the initial interaction of projectiles with targets requires further development. Hence, the first applications of CHIPS described interactions at rest, for which the interaction cross section is not important [2], [3], and low energy photonuclear reactions [4], for which the interaction cross section can be calculated easily [11]. With modification of the first interaction algorithm the CHIPS event generator can be used for all kinds of hadronic interaction. The Geant4 String Model interface to the CHIPS generator [12], [13] also makes it possible to use the CHIPS code for nuclear fragmentation at extremely high energies.

In the first published versions of the CHIPS event generator the class `G4Quasmon` was the head of the model and all initial interactions were hidden in its constructor. More complicated applications of the model such as anti-proton nuclear capture at rest and the Geant4 String Model interface to

CHIPS led to the multi-quasmon version of the model. This required a change in the structure of the CHIPS event generator classes. In the case of at-rest anti-proton annihilation in a nucleus, for example, the first interaction occurs on the nuclear periphery. After this initial interaction, a fraction (defined by a special parameter of the model) of the secondary mesons independently penetrate the nucleus. Each of these mesons can create a separate quasmon in the interior of the nucleus. In this case the class `G4Quasmon` can no longer be the head of the model. A new head class, `G4QEnvironment`, was developed which can adopt a vector of projectile hadrons (`G4QHadronVector`) and create a vector of quasmons, `G4QuasmonVector`. All newly created quasmons then begin the energy dissipation process in parallel in the same nucleus. The `G4QEnvironment` instance can be used both for vacuum and for nuclear matter. If `G4QEnvironment` is created in vacuum, it is practically identical to the `G4Quasmon` class, because in this case only one instance of `G4Quasmon` is allowed. This leaves the model unchanged for hadronic interactions.

The convention adopted for the CHIPS model requires all its class names to use the prefix `G4Q` in order to distinguish them from other Geant4 classes, most of which use the `G4` prefix. The intent is that the `G4Q` prefix will not be used by other Geant4 projects.

30.4 Nucleon-Antinucleon Annihilation at Rest

In order to generate hadron spectra from the annihilation of a proton with an anti-proton at rest, the number of partons in the system must be found. For a finite system of N partons with a total center-of-mass energy M, the invariant phase space integral, Φ_N, is proportional to M^{2N-4}. According to the dimensional counting rule, $2N$ comes from $\prod_{i=1}^{N} \frac{d^3p_i}{E_i}$, and 4 comes from the energy and momentum conservation function, $\delta^4(\underline{\mathrm{P}} - \sum \underline{\mathrm{p}}_i)$. At a temperature T the statistical density of states is proportional to $e^{-\frac{M}{T}}$ so that the probability to find a system of N quark-partons in a state with mass M is $dW \propto M^{2N-4} e^{-\frac{M}{T}} dM$. For this kind of probability distribution the mean value of M^2 is

$$< M^2 >= 4N(N-1) \cdot T^2. \tag{30.1}$$

When N goes to infinity one obtains for massless particles the well-known $< M > \equiv \sqrt{< M^2 >} = 2NT$ result.

After a nucleon absorbs an incident quark-parton, such as a real or virtual photon, for example, the newly formed quasmon has a total of N quark-partons, where N is determined by Eq. 30.1. Choosing one of these quark-partons with energy k in the center of mass system (CMS) of N partons, the

spectrum of the remaining $N-1$ quark-partons is given by

$$\frac{dW}{kdk} \propto (M_{N-1})^{2N-6}, \tag{30.2}$$

where M_{N-1} is the effective mass of the $N-1$ quark-partons. This result was obtained by applying the above phase-space relation ($\Phi_N \propto M^{2N-4}$) to the residual $N-1$ quarks. The effective mass is a function of the total mass M,

$$M_{N-1}^2 = M^2 - 2kM, \tag{30.3}$$

so that the resulting equation for the quark-parton spectrum is:

$$\frac{dW}{kdk} \propto (1 - \frac{2k}{M})^{N-3}. \tag{30.4}$$

30.4.1 Meson Production

In this section, only the quark fusion mechanism of hadronization is considered. The quark exchange mechanism can take place only in nuclear matter where a quasmon has neighboring nucleons. In order to decompose a quasmon into an outgoing hadron and a residual quasmon, one needs to calculate the probability of two quark-partons combining to produce the effective mass of the outgoing hadron. This requires that the spectrum of the second quark-parton be calculated. This is done by following the same argument used to determine Eq. 30.4. One quark-parton is chosen from the residual $N-1$. It has an energy q in the CMS of the $N-1$ quark-partons. The spectrum is obtained by substituting $N-1$ for N and M_{N-1} for M in Eq. 30.4 and then using Eq. 30.3 to get

$$\frac{dW}{qdq} \propto \left(1 - \frac{2q}{M\sqrt{1-\frac{2k}{M}}}\right)^{N-4}. \tag{30.5}$$

Next, one of the residual quark-partons must be selected from this spectrum such that its fusion with the primary quark-parton makes a hadron of mass μ. This selection is performed by the mass shell condition for the outgoing hadron,

$$\mu^2 = 2\frac{k}{\sqrt{1-\frac{2k}{M}}} \cdot q \cdot (1 - \cos\theta). \tag{30.6}$$

Here θ is the angle between the momenta, $\mathbf{k}$ and $\mathbf{q}$ of the two quark-partons in the CMS of $N-1$ quarks. Now the kinematic quark fusion probability

can be calculated for any primary quark-parton with energy k:

$$P(k,M,\mu) = \int \left(1 - \frac{2q}{M\sqrt{1-\frac{2k}{M}}}\right)^{N-4} \times \delta\left(\mu^2 - \frac{2kq(1-\cos\theta)}{\sqrt{1-\frac{2k}{M}}}\right) qdqd\cos\theta. \tag{30.7}$$

Using the δ-function[1] to perform the integration over q one gets:

$$P(k,M,\mu) = \int \left(1 - \frac{\mu^2}{Mk(1-\cos\theta)}\right)^{N-4} \times \left(\frac{\mu^2\sqrt{1-\frac{2k}{M}}}{2k(1-\cos\theta)}\right)^2 d\left(\frac{1-\cos\theta}{\mu^2}\right), \tag{30.8}$$

or

$$P(k,M,\mu) = \frac{M-2k}{4k}\int \left(1 - \frac{\mu^2}{Mk(1-\cos\theta)}\right)^{N-4} \times d\left(1 - \frac{\mu^2}{Mk(1-\cos\theta)}\right). \tag{30.9}$$

After the substitution $z = 1 - \frac{2q}{M_{N-1}} = 1 - \frac{\mu^2}{Mk(1-\cos\theta)}$, this becomes

$$P(k,M,\mu) = \frac{M-2k}{4k}\int z^{N-4}dz, \tag{30.10}$$

where the limits of integration are 0 when $\cos\theta = 1 - \frac{\mu^2}{M\cdot k}$, and

$$z_{\max} = 1 - \frac{\mu^2}{2Mk}, \tag{30.11}$$

when $\cos\theta = -1$. The resulting range of θ is therefore $-1 < \cos\theta < 1 - \frac{\mu^2}{M\cdot k}$. Integrating from 0 to z yields

$$\frac{M-2k}{4k\cdot(N-3)}\cdot z^{N-3}, \tag{30.12}$$

[1] If $g(x_0)$=0, $\int f(x)\delta\left[g(x)\right]dx = \int \frac{f(x)\delta[g(x)]}{g'(x)}dg(x) = \frac{f(x_0)}{g'(x_0)}$

and integrating from 0 to z_{max} yields the total kinematic probability for hadronization of a quark-parton with energy k into a hadron with mass μ:

$$\frac{M-2k}{4k\cdot(N-3)}\cdot z_{\max}^{N-3}. \tag{30.13}$$

The ratio of expressions 30.12 and 30.13 can be treated as a random number, R, uniformly distributed on the interval [0,1]. Solving for z then gives

$$z = \sqrt[N-3]{R}\cdot z_{\max}. \tag{30.14}$$

In addition to the kinematic selection of the two quark-partons in the fusion process, the quark content of the quasmon and the spin of the candidate final hadron are used to determine the probability that a given type of hadron is produced. Because only the relative hadron formation probabilities are necessary, overall normalization factors can be dropped. Hence the relative probability can be written as

$$P_h(k,M,\mu) = (2s_h+1)\cdot z_{\max}^{N-3}\cdot C_Q^h. \tag{30.15}$$

Here, only the factor $z_{\max}^{N-3}$ is used since the other factors in equation 30.13 are constant for all candidates for the outgoing hadron. The factor $2s_h+1$ counts the spin states of a candidate hadron of spin s_h, and C_Q^h is the number of ways the candidate hadron can be formed from combinations of the quarks within the quasmon. In making these combinations, the standard quark wave functions for pions and kaons were used. For η and η' mesons the quark wave functions $\eta = \frac{\bar{u}u+\bar{d}d}{2} - \frac{\bar{s}s}{\sqrt{2}}$ and $\eta' = \frac{\bar{u}u+\bar{d}d}{2} + \frac{\bar{s}s}{\sqrt{2}}$ were used. No mixing was assumed for the ω and ϕ meson states, hence $\omega = \frac{\bar{u}u+\bar{d}d}{\sqrt{2}}$ and $\varphi = \bar{s}s$.

A final model restriction is applied to the hadronization process: after a hadron is emitted, the quark content of the residual quasmon must have a quark content corresponding to either one or two real hadrons. When the quantum numbers of a quasmon, determined by its quark content, cannot be represented by the quantum numbers of a real hadron, the quasmon is considered to be a virtual hadronic molecule such as $\pi^+\pi^+$ or $K^+\pi^+$, in which case it is defined in the CHIPS model to be a Chipolino pseudo-particle.

To fuse quark-partons and create the decay of a quasmon into a hadron and residual quasmon, one needs to generate randomly the residual quasmon mass m, which in fact is the mass of the residual $N-2$ quarks. Using an equation similar to 30.3) one finds that

$$m^2 = z\cdot(M^2-2kM). \tag{30.16}$$

Using Eqs. 30.14 and 30.11, the mass of the residual quasmon can be expressed in terms of the random number R:

$$m^2 = (M - 2k) \cdot (M - \frac{\mu^2}{2k}) \cdot \sqrt[N-3]{R}. \tag{30.17}$$

At this point, the decay of the original quasmon into a final state hadron and a residual quasmon of mass m has been simulated. The process may now be repeated on the residual quasmon.

This iterative hadronization process continues as long as the residual quasmon mass remains greater than $m_{\min}$, whose value depends on the type of quasmon. For hadron-type residual quasmons

$$m_{\min} = m_{\min}^{QC} + m_{\pi^0}, \tag{30.18}$$

where $m_{\min}^{QC}$ is the minimum hadron mass for the residual quark content (QC). For Chipolino-type residual quasmons consisting of hadrons h_1 and h_2,

$$m_{\min} = m_{h_1} + m_{h_2}. \tag{30.19}$$

These conditions insure that the quasmon always has enough energy to decay into at least two final state hadrons, conserving four-momentum and charge.

If the remaining CMS energy of the residual quasmon falls below $m_{\min}$, then the hadronization process terminates with a final two-particle decay. If the parent quasmon is a Chipolino consisting of hadrons h_1 and h_2, then a binary decay of the parent quasmon into m_{h_1} and m_{h_2} takes place. If the parent quasmon is not a Chipolino then a decay into $m_{\min}^{QC}$ and m_h takes place. The decay into $m_{\min}^{QC}$ and m_π^0 is always possible in this case because of condition 30.18.

If the residual quasmon is not Chipolino-type, and $m > m_{\min}$, the hadronization loop can still be finished by the resonance production mechanism, which is modeled following the concept of parton-hadron duality [14]. If the residual quasmon has a mass in the vicinity of a resonance with the same quark content (ρ or K^* for example), there is a probability for the residual quasmon to convert to this resonance.[2] In the present version of the CHIPS event generator the probability of convert to the resonance is given by

$$P_{\text{res}} = \frac{m_{\min}^2}{m^2}. \tag{30.20}$$

Hence the resonance with the mass-squared value m_r^2 closest to m^2 is selected, and the binary decay of the quasmon into m_h and m_r takes place.

[2]When comparing quark contents, the quark content of the quasmon is reduced by canceling quark-antiquark pairs of the same flavor.

With more detailed experimental data, it will be possible to take into account angular momentum conservation, as well as C-, P- and G-parity conservation. In the present version of the generator, η and η' are suppressed by a factor of 0.3. This factor was tuned using data from experiments on antiproton annihilation at rest in liquid hydrogen and can be different for other hadronic reactions. It is possible to vary it when describing other reactions.

Another parameter, s/u, controls the suppression of heavy quark production [15]. For proton-antiproton annihilation at rest the strange quark-antiquark sea was found to be suppressed by the factor $s/u = 0.1$. In the JETSET [15] event generator, the default value for this parameter is $s/u = 0.3$. The lower value may be due to quarks and anti-quarks of colliding hadrons initially forming a non-strange sea, with the strange sea suppressed by the OZI rule [16]. This question is still under discussion [17] and demands further experimental measurements. The s/u parameter may differ for other reactions. In particular, for e^+e^- reactions it can be closer to 0.3.

Finally, the temperature parameter has been fixed at $T = 180$ MeV. In earlier versions of the model it was found that this value successfully reproduced spectra of outgoing hadrons in different types of medium-energy reactions.

The above parameters were used to fit not only the spectrum of pions Fig. 30.2,a and the multiplicity distribution for pions Fig. 30.2,b but also branching ratios of various measured [18, 19] exclusive channels as shown in Figs. 30.3, 30.4, 30.5. In Fig. 30.5 one can see many decay channels with higher meson resonances. The relative contribution of events with meson resonances produced in the final state is 30 - 40 percent, roughly in agreement with experiment. The agreement between the model and experiment for particular decay modes is within a factor of 2-3 except for the branching ratios to higher resonances. In these cases it is not completely clear how the resonance is defined in a concrete experiment. In particular, for the $a_2\omega$ channel the mass sum of final hadrons is 2100 MeV with a full width of about 110 MeV while the total initial energy of the $p\bar{p}$ annihilation reaction is only 1876.5 MeV. This decay channel can be formally simulated by an event generator using the tail of the Breit-Wigner distribution for the a_2 resonance, but it is difficult to imagine how the a_2 resonance can be experimentally identified 2Γ away from its mean mass value.

30.4.2 Baryon Production

To model fragmentation into baryons the POPCORN idea [20] was used, which assumes the existence of diquark-partons. The assumption of massless

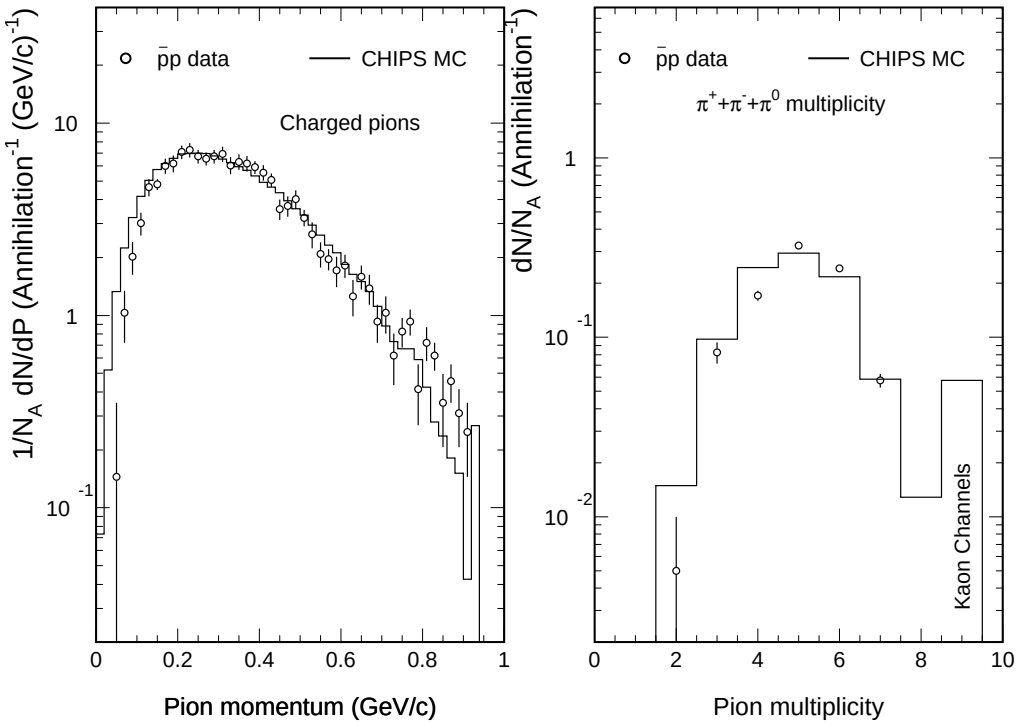

Figure 30.2: (a) (left): momentum distribution of charged pions produced in proton-antiproton annihilation at rest. The experimental data are from [18], and the histogram was produced by the CHIPS Monte Carlo. The experimental spectrum is normalized to the measured average charged pion multiplicity, 3.0. (b) (right): pion multiplicity distribution. Data points were taken from compilations of experimental data [19], and the histogram was produced by the CHIPS Monte Carlo. The number of events with kaons in the final state is shown in pion multiplicity bin 9, where no real 9-pion events are generated or observed experimentally. In the model, the percentage of annihilation events with kaons is close to the experimental value of 6% [19].

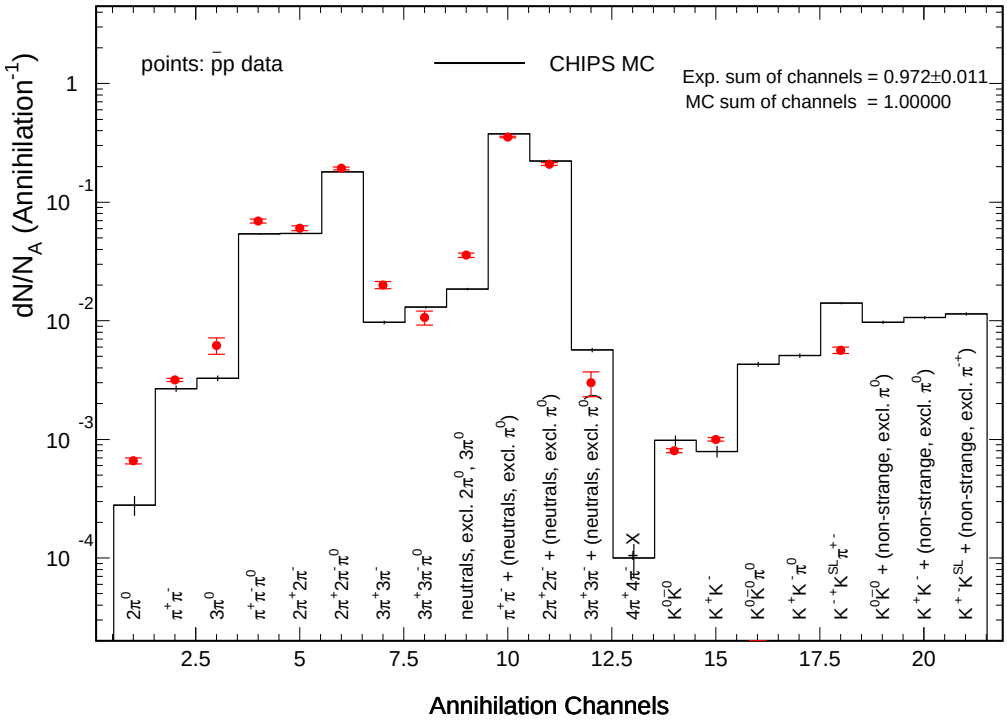

Figure 30.3: Branching probabilities for different channels in proton-antiproton annihilation at rest. The experimental data are from [19], and the histogram was produced by the CHIPS Monte Carlo.

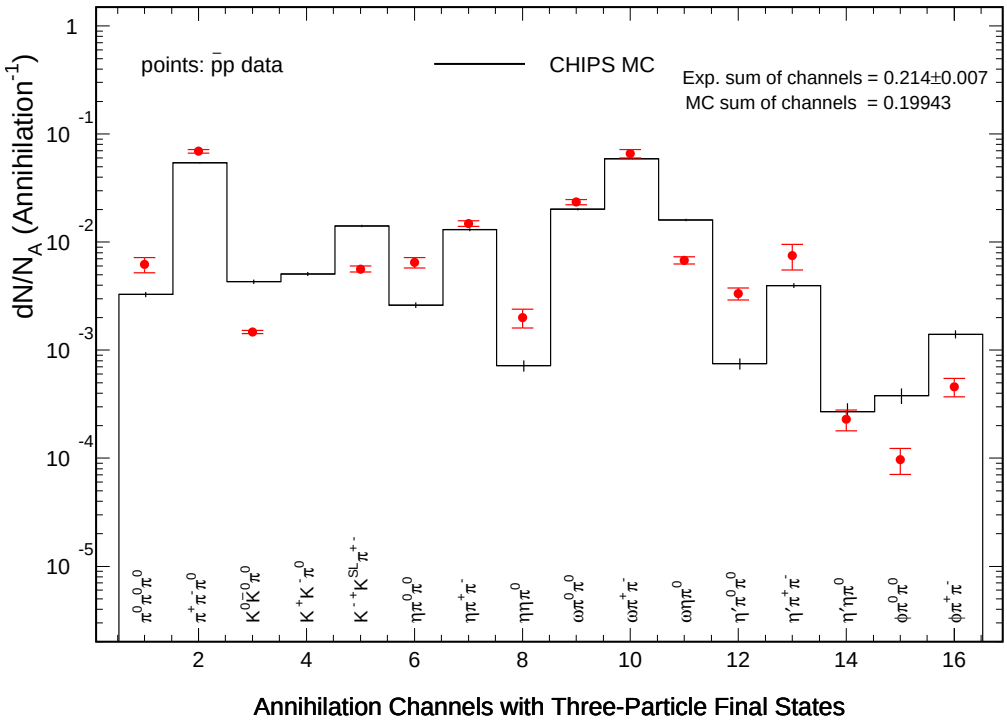

Figure 30.4: Branching probabilities for different channels with three-particle final states in proton-antiproton annihilation at rest. The points are experimental data [19] and the histogram is from the CHIPS Monte Carlo.

diquarks is somewhat inconsistent at low energies, as is the assumption of massless s-quarks, but it is simple and it helps to generate baryons in the same way as mesons.

Baryons are heavy, and the baryon production in $p\bar{p}$ annihilation reactions at medium energies is very sensitive to the value of the temperature. If the temperature is low, the baryon yield is small, and the mean multiplicity of pions increases very noticeably with center-of-mass energy as seen in Fig. 30.6. For higher temperature values the baryon yield reduces the pion multiplicity at higher energies. The existing experimental data [21], shown in Fig. 30.6, can be considered as a kind of "thermometer" for the model. This thermometer confirms that the critical temperature is about 200 MeV.

It can be used as a tool for the Monte Carlo simulation of a wide variety of hadronic reactions. The CHIPS event generator can be used not only for "phase-space background" calculations in place of the standard GENBOD

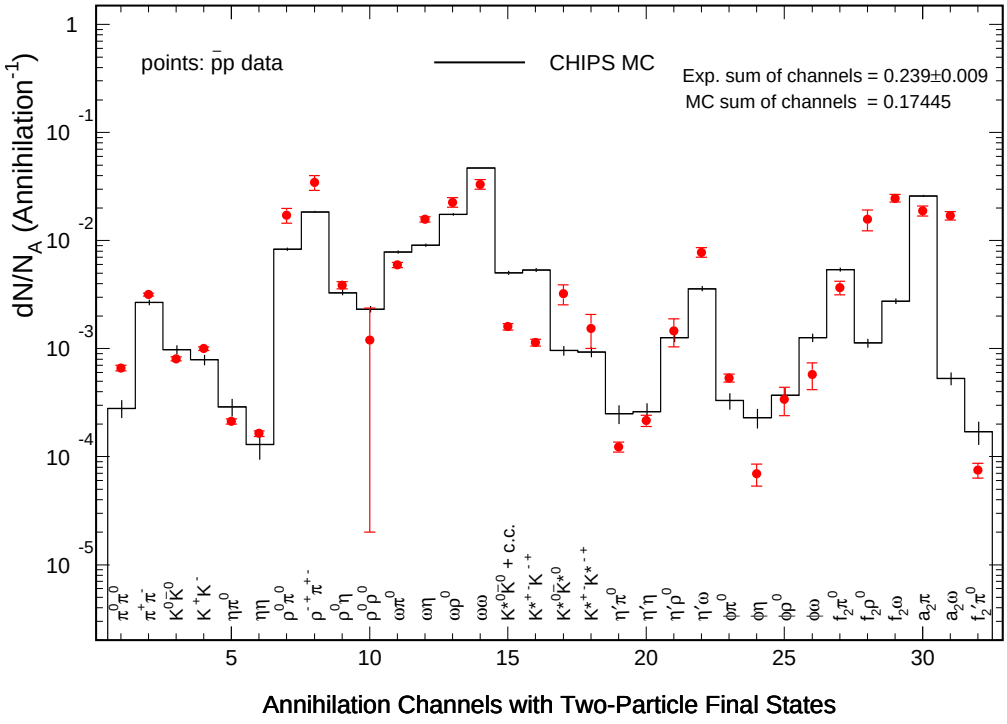

Figure 30.5: Branching probabilities for different channels with two-particle final states in proton-antiproton annihilation at rest. The points are experimental data [19] and the histogram is from the CHIPS Monte Carlo.

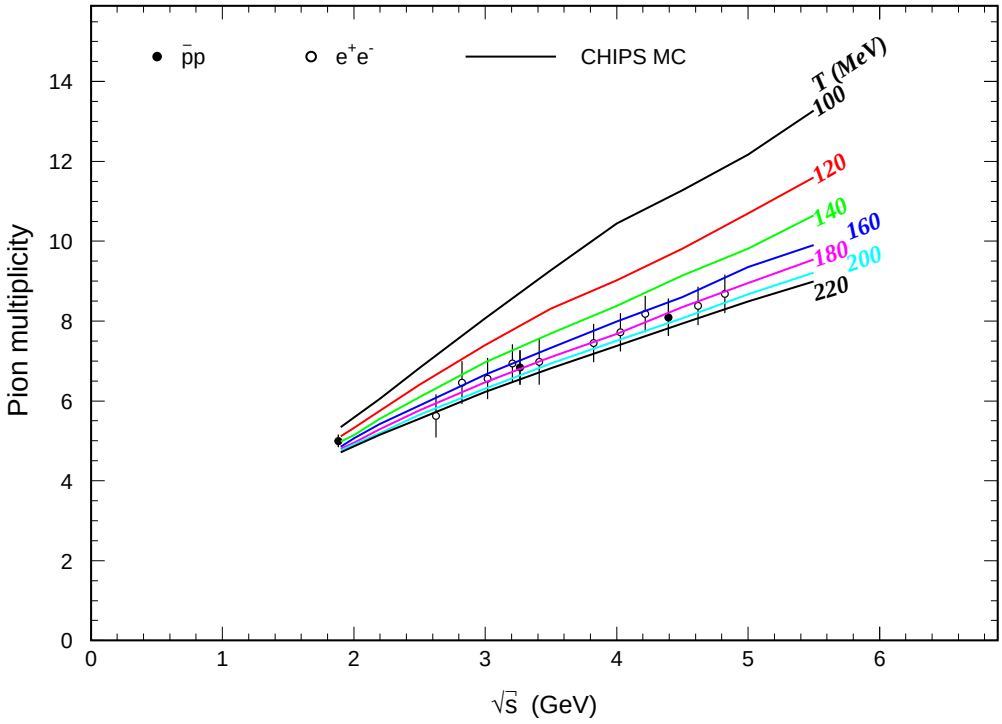

Figure 30.6: Average meson multiplicities in proton-antiproton and in electron-positron annihilation, as a function of the center-of-mass energy of the interacting hadronic system. The points are experimental data [21] and the lines are CHIPS Monte Carlo calculations at several values of the critical temperature parameter T.

routine [7], but even for taking into account the reflection of resonances in connected final hadron combinations. Thus it can be useful for physics analysis too, even though its main range of application is the simulation of the evolution of hadronic and electromagnetic showers in matter at medium energies.

30.5 Nuclear Pion Capture at Rest and Photonuclear Reactions Below the Delta(3,3) Resonance

When compared with the first "in vacuum" version of the model, described in Section 30.4, modeling hadronic fragmentation in nuclear matter is more complicated because of the much greater number of possible secondary fragments. However, the hadronization process itself is simpler in a way. In vacuum, the quark-fusion mechanism requires a quark-parton partner from the external (as in JETSET [15]) or internal (the quasmon itself, Section 30.4) quark-antiquark sea. In nuclear matter, there is a second possibility: quark exchange with a neighboring hadronic system, which could be a nucleon or multinucleon cluster.

In nuclear matter the spectra of secondary hadrons and nuclear fragments reflect the quark-parton energy spectrum within a quasmon. In the case of inclusive spectra that are decreasing steeply with energy, and correspondingly steeply decreasing spectra of the quark-partons in a quasmon, only those secondary hadrons which get the maximum energy from the primary quark-parton of energy k contribute to the inclusive spectra. This extreme situation requires the exchanged quark-parton with energy q, coming toward the quasmon from the cluster, to move in a direction opposite to that of the primary quark-parton. As a result the hadronization quark exchange process becomes one-dimensional along the direction of k. If a neighboring nucleon or nucleon cluster with bound mass $\tilde{\mu}$ absorbs the primary quark-parton and radiates the exchanged quark-parton in the opposite direction, then the energy of the outgoing fragment is $E = \tilde{\mu} + k - q$, and the momentum is $p = k + q$. Both the energy and the momentum of the outgoing nuclear fragment are known, as is the mass $\tilde{\mu}$ of the nuclear fragment in nuclear matter, so the momentum of the primary quark-parton can be reconstructed using the approximate relation

$$k = \frac{p + E - B \cdot m_N}{2}. \tag{30.21}$$

Here B is the baryon number of the outgoing fragment ($\tilde{\mu} \approx B \cdot m_N$) and m_N is the nucleon mass. In Ref. [22] it was shown that the invariant inclusive spectra of pions, protons, deuterons, and tritons in proton-nucleus reactions at 400 GeV [23] not only have the same exponential slope but almost coincide when they are plotted as a function of $k = \frac{p+E_{\rm kin}}{2}$. Using data at 10 GeV [24], it was shown that the parameter k, defined by Eq. 30.21, is also appropriate for the description of secondary anti-protons produced in high energy nuclear reactions. This means that the extreme assumption of one-dimensional hadronization is a good approximation.

The same approximation is also valid for the quark fusion mechanism. In the one-dimensional case, assuming that q is the momentum of the second quark fusing with the primary quark-parton of energy k, the total energy of the outgoing hadron is $E = q + k$ and the momentum is $p = k - q$. In the one-dimensional case the secondary quark-parton must move in the opposite direction with respect to the primary quark-parton, otherwise the mass of the outgoing hadron would be zero. So, for mesons $k = \frac{p+E}{2}$, in accordance with Eq. 30.21. In the case of anti-proton radiation, the baryon number of the quasmon is increased by one, and the primary antiquark-parton will spend its energy to build up the mass of the antiproton by picking up an anti-diquark. Thus, the energy conservation law for antiproton radiation looks like $E + m_N = q + k$ and $k = \frac{p+E+m_N}{2}$, which is again in accordance with Eq. 30.21.

The one-dimensional quark exchange mechanism was proposed in 1984 [22]. Even in its approximate form it was useful in the analysis of inclusive spectra of hadrons and nuclear fragments in hadron-nuclear reactions at high energies. Later the same approach was used in the analysis of nuclear fragmentation in electro-nuclear reactions [25]. Also in 1984 the quark-exchange mechanism developed in the framework of the non-relativistic quark model was found to be important for the explanation of the short distance features of NN interactions [26]. Later it was successfully applied to K^-p interactions [27]. The idea of the quark exchange mechanism between nucleons was useful even for the explanation of the EMC effect [28]. For the non-relativistic quark model, the quark exchange technique was developed as an alternative to the Feynman diagram technique at short distances [29].

The CHIPS event generator models quark exchange processes, taking into account kinematic and combinatorial factors for asymptotically free quark-partons. In the naive picture of the quark-exchange mechanism, one quark-parton tunnels from the asymptotically free region of one hadron to the asymptotically free region of another hadron. To conserve color, another quark-parton from the neighboring hadron must replace the first quark-parton in the quasmon. This makes the tunneling mutual, and the resulting

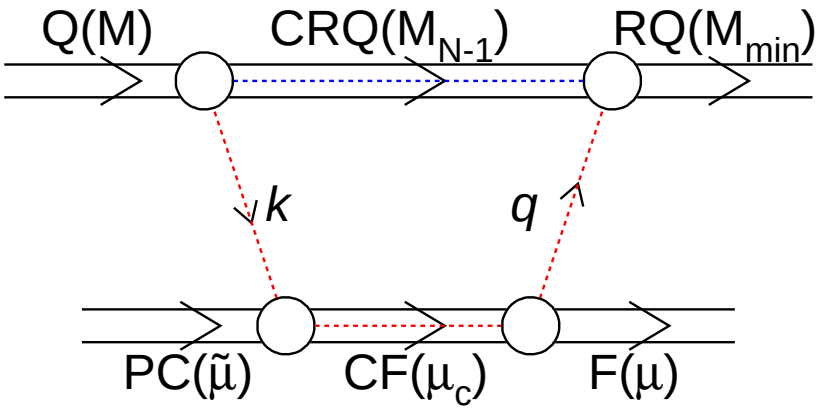

Figure 30.7: Diagram of the quark exchange mechanism.

process is quark exchange.

The experimental data available for multihadron production at high energies show regularities in the secondary particle spectra that can be related to the simple kinematic, combinatorial, and phase space rules of such quark exchange and fusion mechanisms. The CHIPS model combines these mechanisms consistently.

Fig. 30.7 shows a quark exchange diagram which helps to keep track of the kinematics of the process. It was shown in Section 30.4 that a quasmon, Q is kinematically determined by a few asymptotically free quark-partons homogeneously distributed over the invariant phase space. The quasmon mass M is related to the number of quark-partons N through

$$< M^2 >= 4N(N-1) \cdot T^2, \tag{30.22}$$

where T is the temperature of the system.

The spectrum of quark partons can be calculated as

$$\frac{dW}{k^* dk^*} \propto \left(1 - \frac{2k^*}{M}\right)^{N-3}, \tag{30.23}$$

where k^* is the energy of the primary quark-parton in the center-of-mass system of the quasmon. After the primary quark-parton is randomized and the neighboring cluster, or parent cluster, PC, with bound mass $\tilde{\mu}$ is selected, the quark exchange process begins. To follow the process kinematically one should imagine a colored, compound system consisting of a stationary, bound parent cluster and the primary quark. The primary quark has energy k in the lab system,

$$k = k^* \cdot \frac{E_N + p_N \cdot \cos(\theta_k)}{M_N}, \tag{30.24}$$

where M_N, E_N and p_N are the mass, energy, and momentum of the quasmon in the lab frame. The mass of the compound system, CF, is $\mu_c = \sqrt{(\tilde{\mu} + k)^2}$, where $\tilde{\mu}$ and k are the corresponding four-vectors. This colored compound system decays into a free outgoing nuclear fragment, F, with mass μ and a recoiling quark with energy q. q is measured in the CMS of $\tilde{\mu}$, which coincides with the lab frame in the present version of the model because no cluster motion is considered. At this point one should recall that a colored residual quasmon, CRQ, with mass M_{N-1} remains after the radiation of k. CRQ is finally fused with the recoil quark q to form the residual quasmon RQ. The minimum mass of RQ should be greater than $M_{\min}$, which is determined by the minimum mass of a hadron (or Chipolino double-hadron as defined in Section 30.4) with the same quark content.

All quark-antiquark pairs with the same flavor should be canceled in the minimum mass calculations. This imposes a restriction, which in the center-of-mass system of μ_c, can be written as

$$2q \cdot (E - p \cdot \cos\theta_{qCQ}) + M_{N-1}^2 > M_{\min}^2, \tag{30.25}$$

where E is the energy and p is the momentum of the colored residual quasmon with mass M_{N-1} in the CMS of μ_c. The restriction for $\cos\theta_{qCQ}$ then becomes

$$\cos\theta_{qCQ} < \frac{2qE - M_{\min}^2 + M_{N-1}^2}{2qp}, \tag{30.26}$$

which implies

$$q > \frac{M_{N-1}^2 - M_{\min}^2}{2 \cdot (E + p)}. \tag{30.27}$$

A second restriction comes from the nuclear Coulomb barrier for charged particles. The Coulomb barrier can be calculated in the simple form:

$$E_{CB} = \frac{Z_F \cdot Z_R}{A_F^{\frac{1}{3}} + A_R^{\frac{1}{3}}} \text{ (MeV)}, \tag{30.28}$$

where Z_F and A_F are the charge and atomic weight of the fragment, and Z_R and A_R are the charge and atomic weight of the residual nucleus. The obvious restriction is

$$q < k + \tilde{\mu} - \mu - E_{CB}. \tag{30.29}$$

In addition to 30.27 and 30.29, the quark exchange mechanism imposes restrictions which are calculated below. The spectrum of recoiling quarks is similar to the k^* spectrum in the quasmon (30.23):

$$\frac{dW}{q\ dq\ d\cos\theta} \propto \left(1 - \frac{2q}{\tilde{\mu}}\right)^{n-3}, \tag{30.30}$$

where n is the number of quark-partons in the nucleon cluster. It is assumed that $n = 3A_C$, where A_C is the atomic weight of the parent cluster. The tunneling of quarks from one nucleon to another provides a common phase space for all quark-partons in the cluster.

An additional equation follows from the mass shell condition for the outgoing fragment,

$$\mu^2 = \tilde{\mu}^2 + 2\tilde{\mu}\cdot k - 2\tilde{\mu}\cdot q - 2k\cdot q\cdot(1-\cos\theta_{kq}), \tag{30.31}$$

where θ_{kq} is the angle between quark-parton momenta in the lab frame. From this equation q can be calculated as

$$q = \frac{\tilde{\mu}\cdot(k-\Delta)}{\tilde{\mu} + k\cdot(1-\cos\theta_{kq})}, \tag{30.32}$$

where Δ is the covariant binding energy of the cluster $\Delta = \frac{\mu^2-\tilde{\mu}^2}{2\tilde{\mu}}$. The quark exchange probability integral can be then written in the form:

$$\begin{aligned} &P(k,\tilde{\mu},\mu) = \\ &\int \delta\left[\mu^2 - \tilde{\mu}^2 - 2\tilde{\mu}\cdot k + 2\tilde{\mu}\cdot q + 2k\cdot q\cdot(1-\cos\theta_{kq})\right] \\ &\qquad \times \left(1-\frac{2q}{\tilde{\mu}}\right)^{n-3} q dq\cdot d\cos\theta_{kq}. \end{aligned} \tag{30.33}$$

Using the δ-function to perform the integration over q one obtains

$$\begin{aligned} P(k,\tilde{\mu},\mu) &= \int \left(1-\frac{2(k-\Delta)}{\tilde{\mu}+k(1-\cos\theta_{kq})}\right)^{n-3} \\ &\quad \times \frac{\tilde{\mu}(k-\Delta)}{2[\tilde{\mu}+k(1-\cos\theta_{kq})]^2} d\cos\theta_{kq} \end{aligned} \tag{30.34}$$

or

$$\begin{aligned} P(k,\tilde{\mu},\mu) &= \int \left(1-\frac{2(k-\Delta)}{\tilde{\mu}+k(1-\cos\theta_{kq})}\right)^{n-3} \\ &\quad \times \left(\frac{\tilde{\mu}(k-\Delta)}{\tilde{\mu}+k(1-\cos\theta_{kq})}\right)^2 \\ &\quad \times d\left(\frac{\tilde{\mu}+k(1-\cos\theta_{kq})}{\tilde{\mu}(k-\Delta)}\right). \end{aligned} \tag{30.35}$$

The result of the integration is

$$\begin{aligned} &P(k,\tilde{\mu},\mu) = \frac{\tilde{\mu}}{4k(n-2)} \\ &\times \left[\left(1-\frac{2(k-\Delta)}{\tilde{\mu}+2k}\right)^{n-2}_{\text{high}} - \left(1-\frac{2(k-\Delta)}{\tilde{\mu}}\right)^{n-2}_{\text{low}}\right]. \end{aligned} \tag{30.36}$$

For randomization it is convenient to make z a random parameter

$$z = 1 - \frac{2(k-\Delta)}{\tilde{\mu} + k(1-\cos\theta_{kq})} = 1 - \frac{2q}{\tilde{\mu}}. \tag{30.37}$$

From (30.36) one can find the high and the low limits of the randomization. The first limit is for k: $k > \Delta$. It is similar to the restriction for quasmon fragmentation in vacuum: $k^* > \frac{\mu^2}{2M}$. The second limit is $k = \frac{\mu^2}{2\tilde{\mu}}$, when the low limit of randomization becomes equal to zero. If $k < \frac{\mu^2}{2\tilde{\mu}}$, then $-1 < \cos\theta_{kq} < 1$ and $z_{\rm low} = 1 - \frac{2(k-\Delta)}{\tilde{\mu}}$. If $k > \frac{\mu^2}{2\tilde{\mu}}$, then the range of $\cos\theta_{kq}$ is $-1 < \cos\theta_{kq} < \frac{\mu^2}{k\tilde{\mu}} - 1$ and $z_{\rm low} = 0$. This value of $z_{\rm low}$ should be corrected using the Coulomb barrier restriction (30.29), and the value of $z_{\rm high}$ should be corrected using the minimum residual quasmon restriction (30.27). In the case of a quasmon with momentum much less than k it is possible to impose tighter restrictions than (30.27) because the direction of motion of the CRQ is opposite to k. So $\cos\theta_{qCQ} = -\cos\theta_{kq}$, and from (30.32) one can find that

$$\cos\theta_{qCQ} = 1 - \frac{\tilde{\mu}\cdot(k-\Delta-q)}{k\cdot q}. \tag{30.38}$$

So in this case the equation (30.27) can be replaced by the more stringent one:

$$q > \frac{M_{N-1}^2 - M_{\rm min}^2 + 2\frac{p\cdot\tilde{\mu}}{k}(k-\Delta)}{2\cdot(E+p+\frac{p\cdot\tilde{\mu}}{k})}. \tag{30.39}$$

The integrated kinematical quark exchange probability (in the range from $z_{\rm low}$ to $z_{\rm high}$) is

$$\frac{\tilde{\mu}}{4k(n-2)}\cdot z^{n-2}, \tag{30.40}$$

and the total kinematic probability of hadronization of the quark-parton with energy k into a nuclear fragment with mass μ is

$$\frac{\tilde{\mu}}{4k(n-2)}\cdot\left(z_{\rm high}^{n-2} - z_{\rm low}^{n-2}\right). \tag{30.41}$$

This can be compared with the vacuum probability of the quark fusion mechanism from Section 30.4:

$$\frac{M-2k}{4k(N-3)} z_{\rm max}^{N-3}. \tag{30.42}$$

The similarity is very important, as the absolute probabilities define the competition between vacuum and nuclear channels.

Equations (30.40) and (30.41) can be used for randomization of z:

$$z = z_{\rm low} + \sqrt[n-2]{R} \cdot (z_{\rm high} - z_{\rm low}), \tag{30.43}$$

where R is a random number, uniformly distributed in the interval (0,1).

Eq. (30.41) can be used to control the competition between different nuclear fragments and hadrons in the hadronization process, but in contrast to the case of "in vacuum" hadronization it is not enough to take into account only the quark combinatorics of the quasmon and the outgoing hadron. In the case of hadronization in nuclear matter, different parent bound clusters should be taken into account as well. For example, tritium can be radiated as a result of quark exchange with a bound tritium cluster or as a result of quark exchange with a bound ^{3}He cluster.

To calculate the yield of fragments it is necessary to calculate the probability to find a cluster with certain proton and neutron content in a nucleus. One could consider any particular probability as an independent parameter, but in such a case the process of tuning the model would be difficult. We proposed the following scenario of clusterization. A gas of quasi-free nucleons is close to the phase transition to a liquid bound by strong quark exchange forces. Precursors of the liquid phase are nuclear clusters, which may be considered as "drops" of the liquid phase within the nucleus. Any cluster can meet another nucleon and absorb it (making it bigger), or it can release one of the nucleons (making it smaller). The first parameter ε_1 is the percentage of quasi-free nucleons not involved in the clusterization process. The rest of the nucleons $(1 - \varepsilon_1)$ clusterize. We assume that since on the periphery of the nucleus the density is lower, one can consider only dibaryon clusters, and neglect triple-baryon clusters. Still we denote the number of nucleons clusterized in dibaryons on the periphery by the parameter ε_2. In the dense part of the nucleus, strong quark exchange forces make clusters out of quasi-free nucleons with high probability. To characterize the distribution of clusters the clusterization probability parameter ω was used.

If the number of nucleons involved in clusterization is $a = (1-\varepsilon_1-\varepsilon_2)\cdot A$, then the probability to find a cluster consisting of ν nucleons is defined by the distribution

$$P_\nu \propto C_\nu^a \cdot \omega^{\nu-1}, \tag{30.44}$$

where C_ν^a is the corresponding binomial coefficient. The coefficient of proportionality can be found from the equation

$$a = b \cdot \sum_{\nu=1}^{a} \nu \cdot C_\nu^a \cdot \omega^{\nu-1} = b \cdot a \cdot (1+\omega)^{a-1}. \tag{30.45}$$

Thus, the number of clusters consisting of ν nucleons is

$$P_\nu = \frac{C_\nu^a \cdot \omega^{\nu-1}}{(1+\omega)^{a-1}}. \tag{30.46}$$

For clusters with an even number of nucleons we used only isotopically symmetric configurations ($\nu = 2n$, n protons and n neutrons) and for odd clusters ($\nu = 2n+1$) we used only two configurations: n neutrons with $n+1$ protons and $n+1$ neutrons with n protons. This restriction, which we call "isotopic focusing", can be considered an empirical rule of the CHIPS model which helps to describe data. It is applied in the case of nuclear clusterization (isotopically symmetric clusters) and in the case of hadronization in nuclear matter. In the hadronization process the quasmon is shifted from the isotopic symmetric state (e.g., by capturing a negative pion) and transfers excess charge to the outgoing nuclear cluster. This tendency is symmetric with respect to the quasmon and the parent cluster.

The temperature parameter used to calculate the number of quark-partons in a quasmon (see equation 30.22) was chosen to be $T = 180$ MeV, which is the same as in Section 30.4.

CHIPS is mostly a model of fragmentation, conserving energy, momentum, and charge. But to compare it with experimental data one needs to model also the first interaction of the projectile with the nucleus. For proton-antiproton annihilation this was easy, as we assumed that in the interaction at rest, a proton and antiproton always create a quasmon. In the case of pion capture the pion can be captured by different clusters. We assumed that the probability of capture is proportional to the number of nucleons in a cluster. After the capture the quasmon is formed, and the CHIPS generator produces fragments consecutively and recursively, choosing at each step the quark-parton four-momentum k, the type of parent and outgoing fragment, and the four-momentum of the exchange quark-parton q, to produce a final state hadron and the new quasmon with less energy.

In the CHIPS model we consider this process as a chaotic process with large number of degrees of freedom and do not take into account any final state interactions of outgoing hadrons. Nevertheless, when the excitation energy dissipates, and in some step the quasmon mass drops below the mass shell, the quark-parton mechanism of hadronization fails. To model the event exclusively, it becomes necessary to continue fragmentation at the hadron level. Such a fragmentation process is known as nuclear evaporation. It is modeled using the non-relativistic phase space approach. In the non-relativistic case the phase space of nucleons can be integrated as well as in the ultra-relativistic case of quark-partons.

The general formula for the non-relativistic phase space can be found starting with the phase space for two particles $\tilde{\Phi}_2$. It is proportional to the center-of-mass momentum:

$$\tilde{\Phi}_2(W_2) \propto \sqrt{W_2}, \tag{30.47}$$

where W_2 is a total kinetic energy of the two non-relativistic particles. If the phase space integral is known for $n-1$ hadrons then it is possible to calculate the phase space integral for n hadrons:

$$\begin{aligned} \tilde{\Phi}_n(W_n) &= \int \tilde{\Phi}_{n-1}(W_{n-1}) \cdot \delta(W_n - W_{n-1} - E_{\rm kin}) \\ &\quad \times \sqrt{E_{\rm kin}} dE_{\rm kin} dW_{n-1}. \end{aligned} \tag{30.48}$$

Using (30.47) and (30.48) one can find that

$$\tilde{\Phi}_n(W_n) \propto W_n^{\frac{3}{2}n-\frac{5}{2}} \tag{30.49}$$

and the spectrum of hadrons, defined by the phase space of residual $n-1$ nucleons, can be written as

$$\frac{dN}{\sqrt{E_{\rm kin}} dE_{\rm kin}} \propto \left(1 - \frac{E_{\rm kin}}{W_n}\right)^{\frac{3}{2}n-4}. \tag{30.50}$$

This spectrum can be randomized. The only problem is from which level one should measure the thermal kinetic energy when most nucleons in nuclei are filling nuclear levels with zero temperature. To model the evaporation process we used this unknown level as a parameter U of the evaporation process. Comparison with experimental data gives $U = 1.7$ MeV. Thus, the total kinetic energy of A nucleons is

$$W_A = U \cdot A + E_{\rm ex}, \tag{30.51}$$

where $E_{\rm ex}$ is the excitation energy of the nucleus.

To be radiated, the nucleon should overcome the threshold

$$U_{\rm thresh} = U + U_{\rm bind} + E_{CB}, \tag{30.52}$$

where $U_{\rm bind}$ is the separation energy of the nucleon, and E_{CB} is the Coulomb barrier energy which is non-zero only for positive particles and can be calculated using formula (30.28).

From several experimental investigations of nuclear pion capture at rest, four published results have been selected here, which constitute, in our opinion, a representative data set covering a wide range of target nuclei, types

of produced hadrons and nuclear fragments, and their energy range. In the first publication [47] the spectra of charged fragments (protons, deuterons, tritons, ^{3}He, ^{4}He) in pion capture were measured on 17 nuclei within one experimental setup. To verify the spectra we compared them for a carbon target with detailed measurements of the spectra of charged fragments given in Ref. [48]. In addition, we took ^{6}Li spectra for a carbon target from the same paper.

The neutron spectra were added from Ref. [49] and Ref. [50]. We present data and Monte Carlo distributions as the invariant phase space function $f = \frac{d\sigma}{pdE}$ depending on the variable $k = \frac{p+E_{\rm kin}}{2}$ as defined in equation (30.21).

Spectra on ^{9}Be, ^{12}C, ^{28}Si (^{27}Al for secondary neutrons), ^{59}Co (^{64}Cu for secondary neutrons), and ^{181}Ta are shown in Figs. 30.8 through 30.12. The data are well-described, including the total energy spent in the reaction to yield the particular type of fragments.

The evaporation process for nucleons is also well-described. It is exponential in k, and looks especially impressive for Si/Al and Co/Cu data, where the Coulomb barrier is low, and one can see proton evaporation as a continuation of the evaporation spectra from secondary neutrons. This way the exponential behavior of the evaporation process can be followed over 3 orders of magnitude. Clearly seen is the transition region at $k \approx 90$ MeV (kinetic energy $15 - 20$ MeV) between the quark-level hadronization process and the hadron-level evaporation process. For light target nuclei the evaporation process becomes much less prominent.

The ^{6}Li spectrum on a carbon target exhibits an interesting regularity when plotted as a function of k: it practically coincides with the spectrum of ^{4}He fragments, and shows exponential behavior in a wide range of k, corresponding to a few orders of magnitude in the invariant cross section. To keep the figure readable, the ^{6}Li spectrum generated by CHIPS was not plotted. It coincides with the ^{4}He spectrum at $k > 200$ MeV, and underestimates lithium emission at lower energies, similarly to the ^{3}He and tritium data.

Between the region where hadron-level processes dominate and the kinematic limit, all hadronic spectrum slopes become similar when plotted as a function of k. In addition to this general behavior there is the effect of strong proton-neutron splitting. For protons and neutrons it reaches almost an order of magnitude. To model such splitting in the CHIPS generator, the mechanism of "isotopic focusing" was used, which locally transfers the negative charge from the pion to the first radiated nuclear fragment.

Thus, the model qualitatively describes all typical features of the pion capture process. The question is what can be extracted from the experimental

Table 30.1: Clusterization parameters

	^{9}Be	^{12}C	^{28}Si	^{59}Co	^{181}Ta
ε_1	0.45	0.40	0.35	0.33	0.33
ε_2	0.15	0.15	0.05	0.03	0.02
ω	5.00	5.00	5.00	5.00	5.00

data with this tool. The clusterization parameters are listed in Table 30.1. No formal fitting procedure has been performed. A balanced qualitative agreement with all data was used to tune the parameters. The difference between the $\frac{\varepsilon_2}{\varepsilon_1}$ ratio and the parameter ω (which is the same for all nuclei) is an indication that there is a phase transition between the gas phase and the liquid phase of the nucleus. The large value of the parameter ω, determining the average size of a nuclear cluster, is critical in describing the model spectra at large k, where the fragment spectra approach the kinematic limits.

Using the same parameters of clusterization, the γ absorption data [51] on Al and Ca nuclei were compared in Fig. 30.13) to the CHIPS results. One can see that the spectra of secondary protons and deuterons are qualitatively described by the CHIPS model.

The CHIPS model covers a wide spectrum of hadronic reactions with a large number of degrees of freedom. In the case of nuclear reactions the CHIPS generator helps to understand phenomena such as the order-of-magnitude splitting of neutron and proton spectra, the high yield of energetic nuclear fragments, and the emission of nucleons which kinematically can be produced only if seven or more nucleons are involved in the reaction.

The CHIPS generator allows the extraction of collective parameters of a nucleus such as clusterization. The qualitative conclusion based on the fit to the experimental data is that most of the nucleons are clusterized, at least in heavy nuclei. The nuclear clusters can be considered as drops of a liquid nuclear phase. The quark exchange makes the phase space of quark-partons of each cluster common, stretching the kinematic limits for particle production.

The hypothetical quark exchange process is important not only for nuclear clusterization, but also for the nuclear hadronization process. The quark exchange between the excited cluster (quasmon) and a neighboring nuclear cluster, even at low excitation level, operates with quark-partons at energies comparable with the nucleon mass. As a result it easily reaches the kinematic limits of the reaction, revealing the multi-nucleon nature of the process.

Up to now the most under-developed part of the model has been the initial interaction between projectile and target. That is why we started with

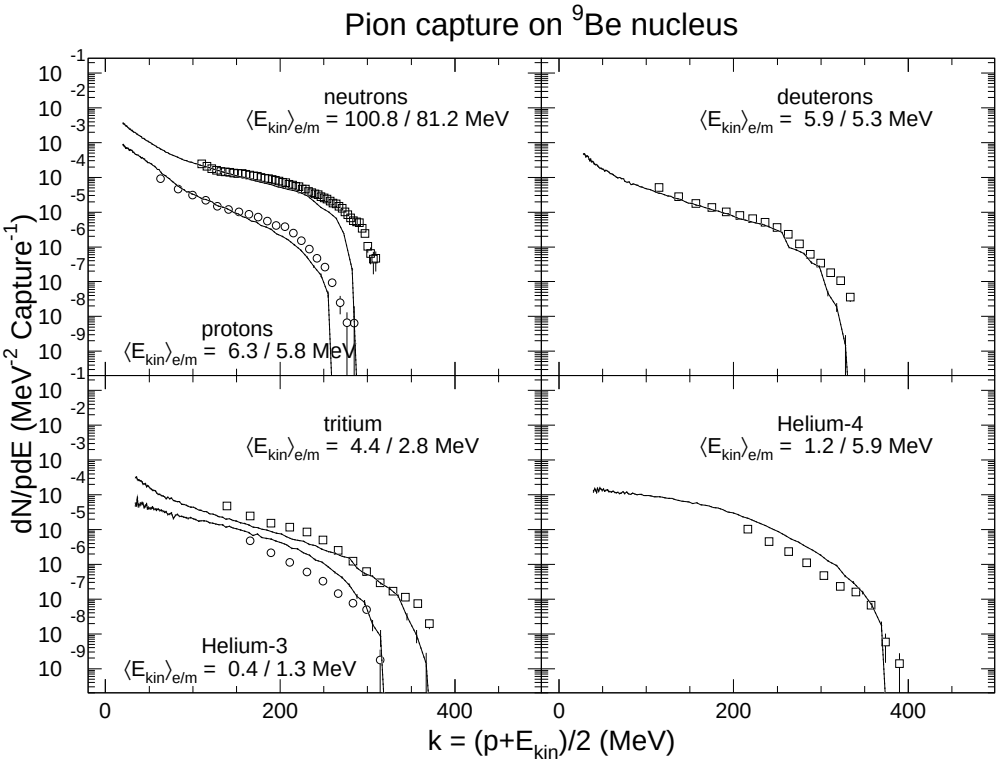

Figure 30.8: Comparison of the CHIPS model results with experimental data on proton, neutron, and nuclear fragment production in the capture of negative pions on ^{9}Be. Proton [47] and neutron [49] experimental spectra are shown in the upper left panel by open circles and open squares, respectively. The model calculations are shown by the two corresponding solid lines. The same arrangement is used to present ^{3}He [47] and tritium [47] spectra in the lower left panel. Deuterium [47] and ^{4}He [47] spectra are shown in the right panels of the figure by open squares and lines (CHIPS model). The average kinetic energy carried away by each nuclear fragment is shown in the panels by the two numbers: first is the average calculated using the experimental data shown; second is the model result.

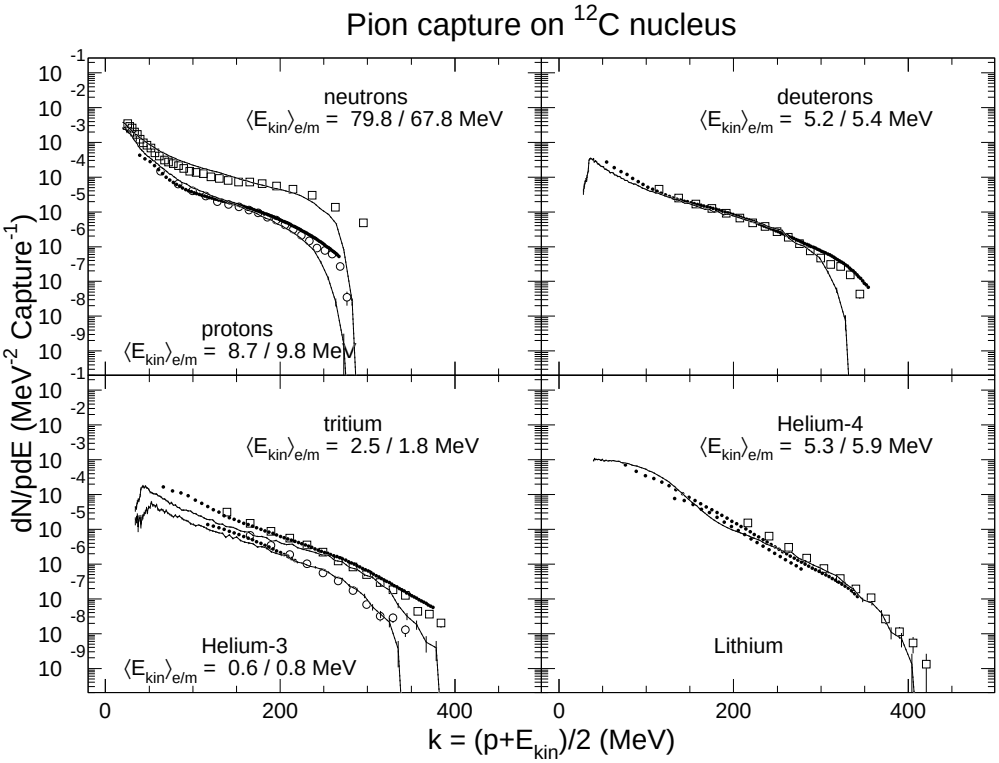

Figure 30.9: Same as in Figure 30.8, for pion capture on ^{12}C. The experimental neutron spectrum is taken from [50]. In addition, the detailed data on charged particle production, including the ^{6}Li spectrum, taken from Ref. [48], are superimposed on the plots as a series of dots.

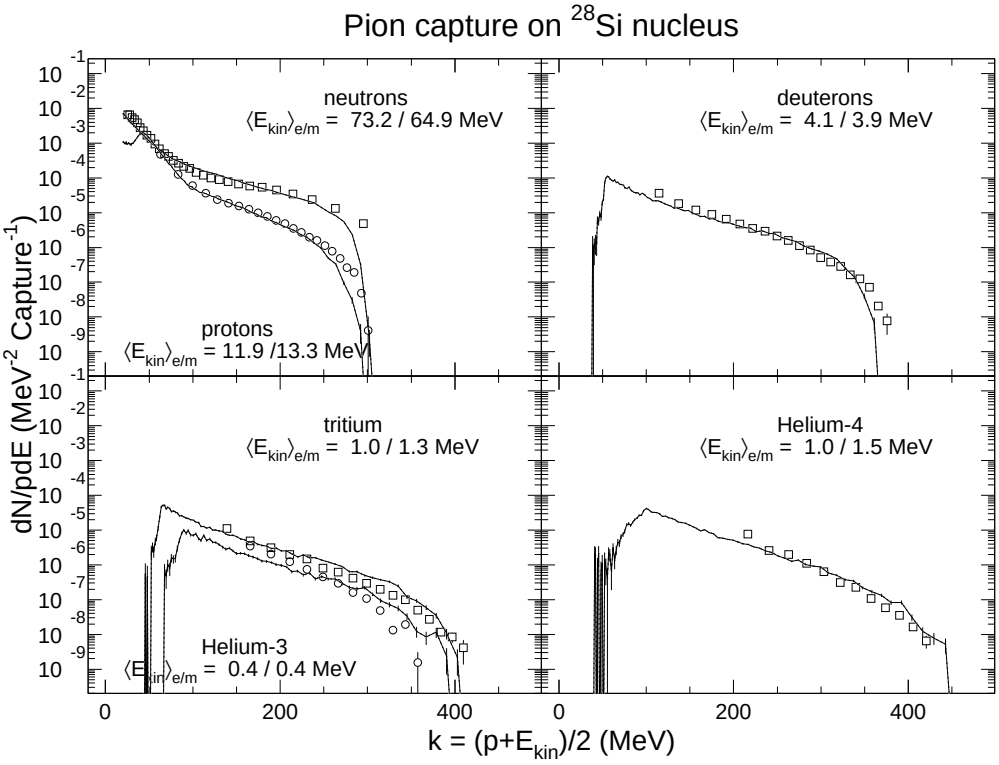

Figure 30.10: Same as in Figure 30.8, for pion capture on ^{28}Si nucleus. The experimental neutron spectrum is taken from [50], for the reaction on ^{27}Al.

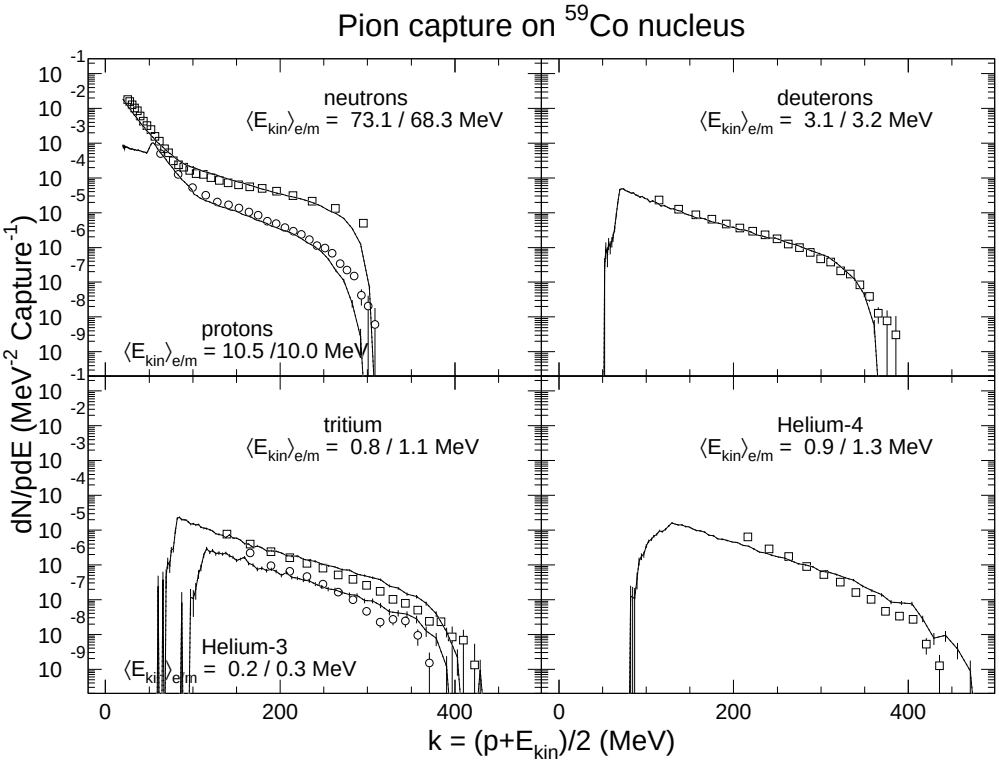

Figure 30.11: Same as in Figure 30.8, for pion capture on ^{59}Co. The experimental neutron spectrum is taken from [50], for the reaction on ^{64}Cu.

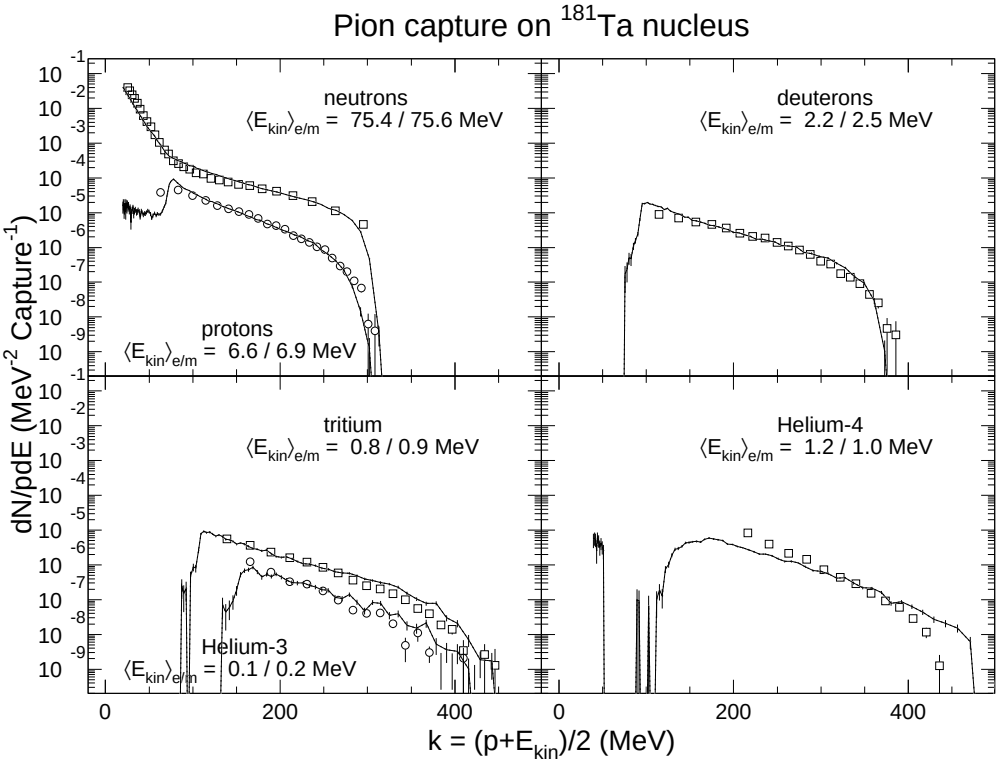

Figure 30.12: Same as in Figure 30.8, for pion capture on ^{181}Ta. The experimental neutron spectrum is taken from [50].

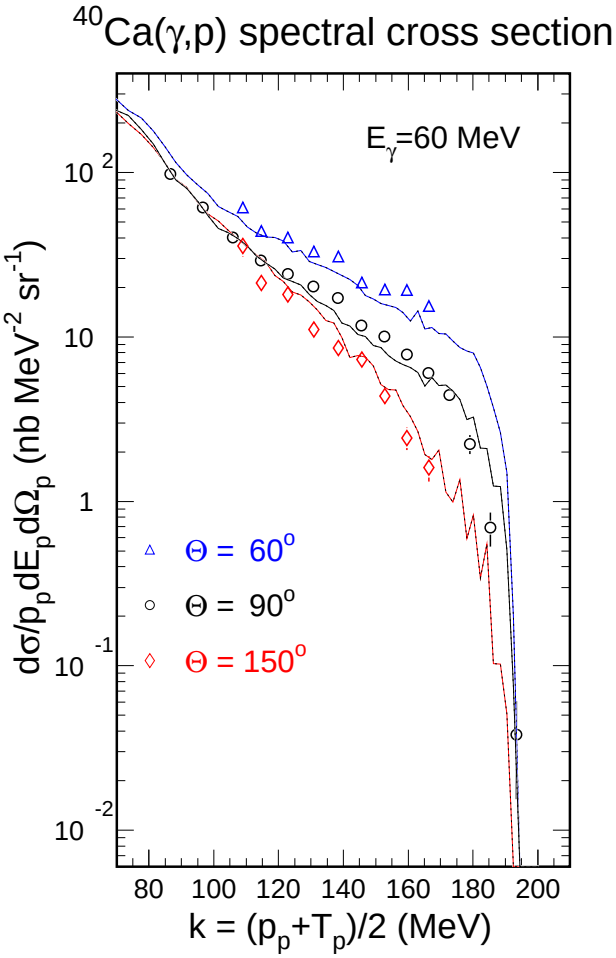

Figure 30.13: Comparison of CHIPS model with experimental data [51] on proton and deuteron production at 90° in photonuclear reactions on ^{27}Al and ^{40}Ca at 59 – 65 MeV. Open circles and solid squares represent the experimental proton and deuteron spectra, respectively. Solid and dashed lines show the results of the corresponding CHIPS model calculation. Statistical errors in the CHIPS results are not shown and can be judged by the point-to-point variations in the lines. The comparison is absolute, using the values of total photonuclear cross section 3.6 mb for Al and 5.4 mb for Ca, as given in Ref. [52].

proton-antiproton annihilation and pion capture on nuclei at rest, because the interaction cross section is not involved. The further development of the model will require a better understanding of the mechanism of the first interaction. However, we believe that even the basic model will be useful in the understanding the nature of multi-hadron fragmentation. Because of the model's features, it is a suitable candidate for the hadron production and hadron cascade parts of the newly developed event generation and detector simulation Monte Carlo computer codes.

30.6 Modeling of real and virtual photon interactions with nuclei below pion production threshold

In the example of the photonuclear reaction discussed in the Appendix D, namely the description of 90° proton and deuteron spectra in $A(\gamma, X)$ reactions at $E_\gamma = 59-65$ MeV, the assumption on the initial Quasmon excitation mechanism was the same. The description of the 90° data was satisfactory, but the generated data showed very little angular dependence, because the velocity of the quasmons produced in the initial state was small, and the fragmentation process was almost isotropic. Experimentally, the angular dependence of secondary protons in photo-nuclear reactions is quite strong even at low energies (see, for example, Ref. [53]). This is a challenging experimental fact which is difficult to explain in any model. It's enough to say that if the angular dependence of secondary protons in the γ^{40}Ca interaction at 60 MeV is analyzed in terms of relativistic boost, then the velocity of the source should reach $0.33c$; hence the mass of the source should be less than pion mass. The main point of this discussion is to show that the quark-exchange mechanism used in the CHIPS model can not only model the clusterization of nucleons in nuclei and hadronization of intranuclear excitations into nuclear fragments, but it can also model complicated mechanisms of the interaction of photons and hadrons in nuclear matter.

In Ref. Appendix D a quark-exchange diagram was defined which helps to keep track of the kinematics of the quark-exchange process (see Fig. 1 in Apendix D). To apply the same diagram to the first interaction of a photon with a nucleus, it is necessary to assume that the quark-exchange process takes place in nuclei continuously, even without any external interaction. Nucleons with high momenta do not leave the nucleus because of the lack of excess energy. The hypothesis of the CHIPS model is that the quark-exchange forces between nucleons [26] continuously create clusters in normal

nuclei. Since a low-energy photon (below the pion production threshold) cannot be absorbed by a free nucleon, other absorption mechanisms involving more than one nucleon have to be used.

The simplest scenario is photon absorption by a quark-parton in the nucleon. At low energies and in vacuum this does not work because there is no corresponding excited baryonic state. But in nuclear matter it is possible to exchange this quark with a neighboring nucleon or a nuclear cluster. The diagram for the process is shown in Fig. 30.14. In this case the photon is absorbed by a quark-parton from the parent cluster PC_1, and then the secondary nucleon or cluster PC_2 absorbs the entire momentum of the quark and photon. The exchange quark-parton q restores the balance of color, producing the final-state hadron F and the residual Quasmon RQ. The process looks like a knockout of a quasi-free nucleon or cluster out of the nucleus. It should be emphasized that in this scenario the CHIPS event generator produces not only "quasi-free" nucleons but "quasi-free" fragments as well. The yield of these quasi-free nucleons or fragments is concentrated in the forward direction.

The second scenario which provides for an angular dependence is the absorption of the photon by a colored fragment (CF_2 in Fig. 30.15). In this scenario, both the primary quark-parton with momentum k and the photon with momentum q_γ are absorbed by a parent cluster (PC_2 in Fig. 30.15), and the recoil quark-parton with momentum q cannot fully compensate the momentum $k + q_\gamma$. As a result the radiation of the secondary fragment in the forward direction becomes more probable.

In both cases the angular dependence is defined by the first act of hadronization. Further fragmentation of the residual quasmon is almost isotropic.

It was shown in Section 30.4 that the energy spectrum of quark partons in a quasmon can be calculated as

$$\frac{dW}{k^* dk^*} \propto \left(1 - \frac{2k^*}{M}\right)^{N-3}, \tag{30.53}$$

where k^* is the energy of the primary quark-parton in the center-of-mass system of the quasmon, M is the mass of the quasmon. The number N of quark-partons in the quasmon can be calculated from the equation

$$< M^2 >= 4 \cdot N \cdot (N-1) \cdot T^2. \tag{30.54}$$

Here T is the temperature of the system.

In the first scenario of the γA interaction (Fig. 30.14), because both interacting particles are massless, we assumed that the cross section for the interaction of a photon with a particular quark-parton is proportional to the

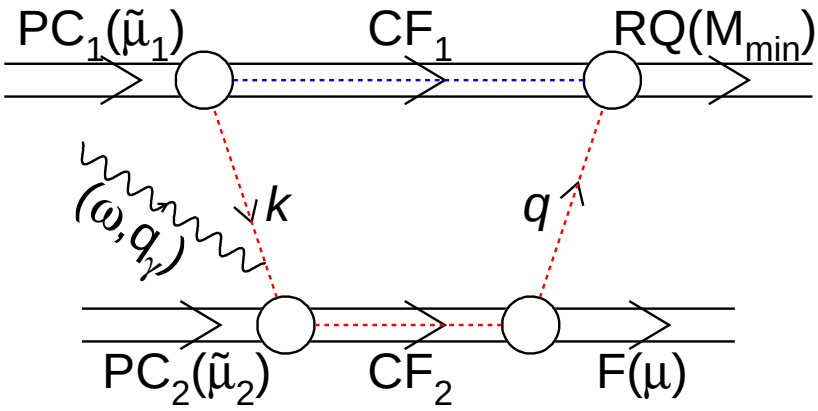

Figure 30.14: Diagram of photon absorption in the quark exchange mechanism. $PC_{1,2}$ stand for parent clusters with bound masses $\tilde{\mu}_{1,2}$, participating in the quark-exchange. $CF_{1,2}$ stand for the colored nuclear fragments in the process of quark exchange. $F(\mu)$ denotes the outgoing hadron with mass μ in the final state. RQ is the residual Quasmon which carries the rest of the excitation energy and momentum. $M_{\rm min}$ characterizes its minimum mass defined by its quark content. Dashed lines indicate colored objects. The photon is absorbed by a quark-parton k from the parent cluster PC_1.

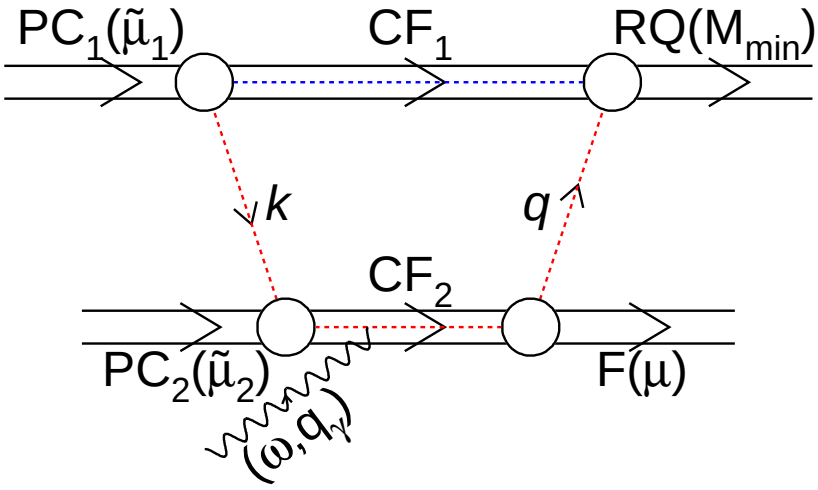

Figure 30.15: Diagram of photon absorption in the quark-exchange mechanism. The notation is the same as in Fig. 30.14. The photon is absorbed by the colored fragment CF_2.

charge of the quark-parton squared, and inversely proportional to the mass of the photon-parton system s, which can be calculated as

$$s = 2\omega k(1 - \cos(\theta_k)). \tag{30.55}$$

Here ω is the energy of the photon, and k is the energy of the quark-parton in the laboratory system (LS):

$$k = k^* \cdot \frac{E_N + p_N \cdot \cos(\theta_k)}{M_N}. \tag{30.56}$$

For a virtual photon, equation (30.55) can be written as

$$s = 2k(\omega - q_\gamma \cdot \cos(\theta_k)), \tag{30.57}$$

where q_γ is the momentum of the virtual photon. In both cases equation (30.53) transforms into

$$\frac{dW}{dk^*} \propto \left(1 - \frac{2k^*}{M}\right)^{N-3}, \tag{30.58}$$

and the angular distribution in $\cos(\theta_k)$ converges to a δ-function. In the case of a real photon $\cos(\theta_k) = 1$, and in the case of a virtual photon $\cos(\theta_k) = \frac{\omega}{q_\gamma}$.

In the second scenario for the photon interaction (Fig. 30.15) we assumed that both the photon and the primary quark-parton, randomized according to Eq. (30.53), enter the parent cluster PC_2, and after that the normal procedure of quark exchange continues, in which the recoiling quark-parton q returns to the first cluster.

An additional parameter in the model is the relative contribution of both mechanisms. As a first approximation we assumed equal probability, but in the future, when more detailed data are obtained, this parameter can be adjusted.

We begin the comparison with the data on proton production in the $^{40}\mathrm{Ca}(\gamma, X)$ reaction at 90° and 59–65 MeV [51], and at 60° and 150° and 60 MeV [54]. We analyzed these data together to compare the angular dependence generated by CHIPS with experimental data. The data are presented as a function of the invariant inclusive cross section $f = \frac{d\sigma}{p_p dE_p}$ depending on the variable $k = \frac{T_p + p_p}{2}$, where T_p and p_p are the kinetic energy and momentum of the secondary proton. As one can see from Fig. 30.16, the angular dependence of the proton yield in photoproduction on ^{40}Ca at 60 MeV is reproduced quite well by the CHIPS event generator.

The second set of measurements that we use for the benchmark comparison deals with the secondary proton yields in $^{12}\mathrm{C}(\gamma, X)$ reactions at 123 and

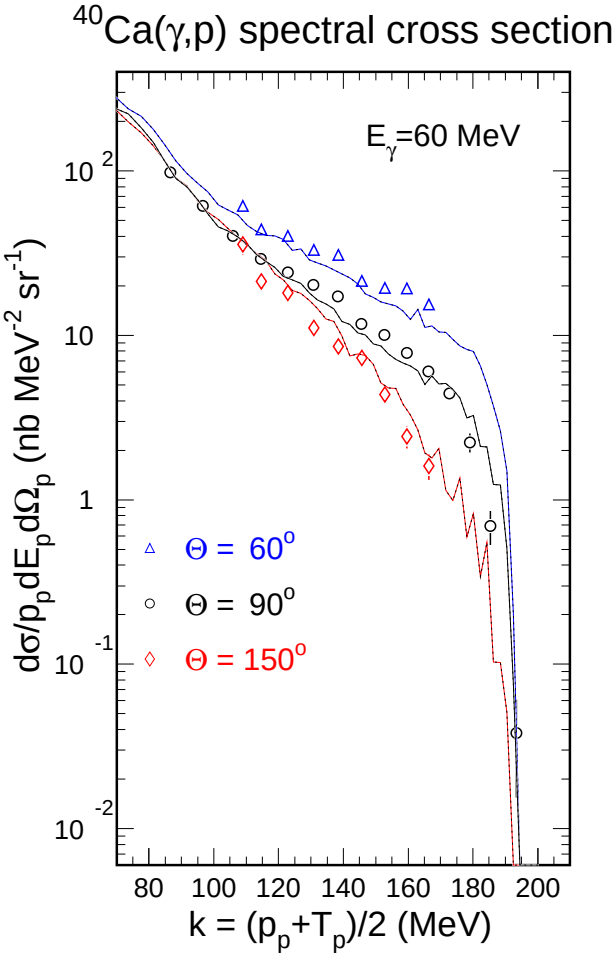

Figure 30.16: Comparison of the CHIPS model results (lines) with the experimental data [51] on proton spectra at 90° in the photonuclear reactions on ^{40}Ca at 59–65 MeV (open circles), and proton spectra at 60° (triangles) and 150° (diamonds). Statistical errors in the CHIPS results are not shown but can be judged by the point-to-point variations in the lines. The comparison is absolute, using the value of the total photonuclear cross section of 5.4 mb for Ca, as given in Ref. [52].

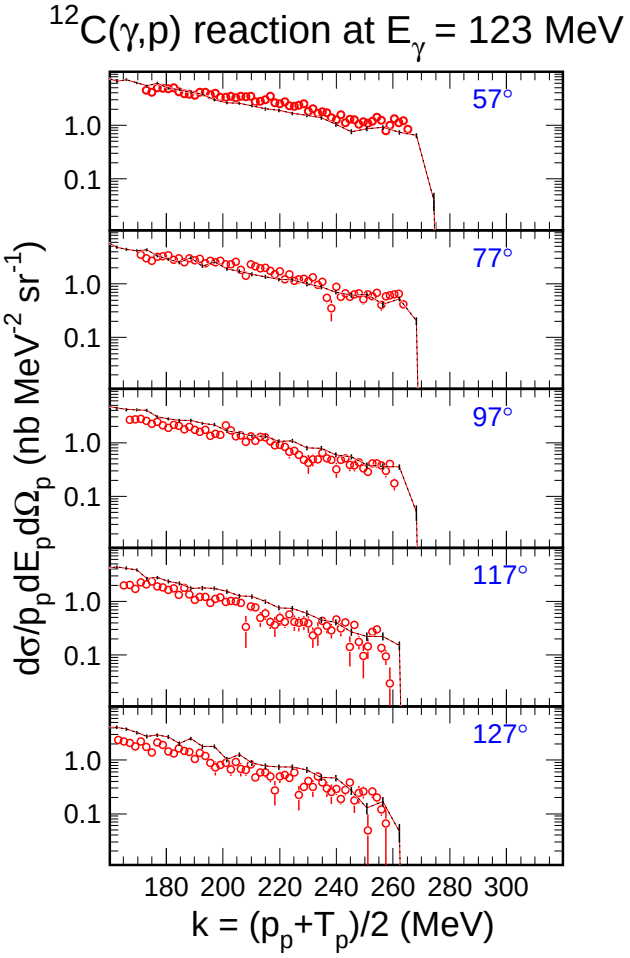

Figure 30.17: Comparison of the CHIPS model results (lines) with the experimental data [55] on proton spectra at 57°, 77°, 97°, 117°, and 127° in the photonuclear reactions on ^{12}C at 123 MeV (open circles). The value of the total photonuclear cross section was set to 1.8 mb.

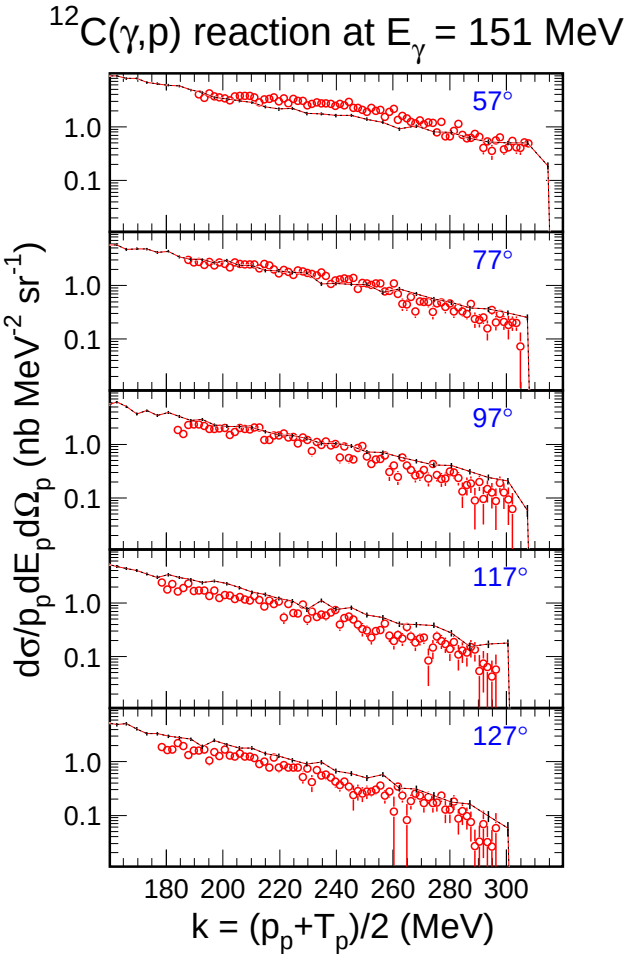

Figure 30.18: Same as in Fig. 30.17, for the photon energy 151 MeV.

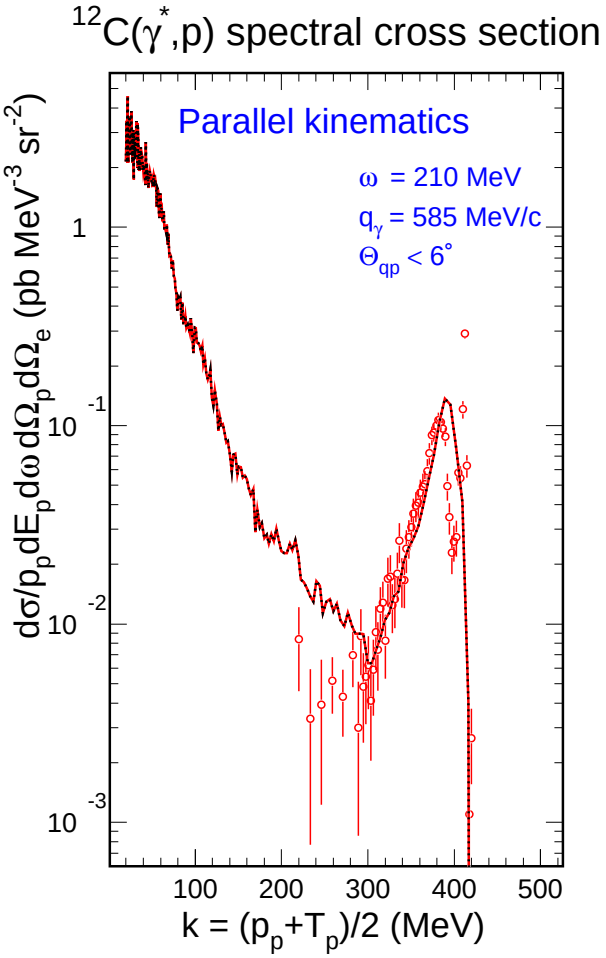

Figure 30.19: Comparison of the CHIPS model results (line) with the experimental data [56] (open circles) on the proton spectrum measured in parallel kinematics in the ^{12}C(e,e′p) reaction at an energy transfer equal to 210 MeV and momentum transfer equal to 585 MeV/c. Statistical errors in the CHIPS result are not shown but can be judged by the point-to-point variations in the line. The relative normalization is arbitrary.

151 MeV [55], which is still below the pion production threshold on a free nucleon. Inclusive spectra of protons have been measured in γ^{12}C reactions at 57°, 77°, 97°, 117°, and 127°. Originally, these data were presented as a function of the missing energy. We present the data in Figs. 30.17 and 30.18 together with CHIPS calculations in the form of the invariant inclusive cross section dependent on k. All parameters of the model such as temperature T and parameters of clusterization for the particular nucleus were the same as in Appendix D, where pion capture spectra were fitted. The agreement between the experimental data and the CHIPS model results is quite remarkable. Both data and calculations show significant strength in the proton yield cross section up to the kinematic limits of the reaction. The angular distribution in the model is not as prominent as in the experimental data, but agrees well qualitatively.

Using the same parameters, we applied the CHIPS event generator to the ^{12}C(e,e′p) reaction measured in Ref.[56]. The proton spectra were measured in parallel kinematics in the interaction of virtual photons with energy $\omega = 210$ MeV and momentum $q_\gamma = 585$ MeV/c. To account for the experimental conditions in the CHIPS event generator, we have selected protons generated in the forward direction with respect to the direction of the virtual photon, with the relative angle $\Theta_{qp} < 6°$. The CHIPS generated distribution and the experimental data are shown in Fig. 30.19 in the form of the invariant inclusive cross section as a function of k. The CHIPS event generator works only with ground states of nuclei so we did not expect any narrow peaks for $^1p_{3/2}$-shell knockout or for other shells. Nevertheless we found that the CHIPS event generator fills in the so-called "$^1s_{1/2}$-shell knockout" region, which is usually artificially smeared by a Lorentzian [57]. In the regular fragmentation scenario the spectrum of protons below $k = 300$ MeV is normal; it falls down to the kinematic limit. The additional yield at $k > 300$ MeV is a reflection of the specific first act of hadronization with the quark exchange kinematics. The slope increase with momentum is approximated well by the model, but it is obvious that the yield close to the kinematic limit of the $2 \to 2$ reaction can only be described in detail if the excited states of the residual nucleus are taken into account.

The angular dependence of the proton yield in low-energy photo-nuclear reactions is described in the CHIPS model and event generator. The most important assumption in the description is the hypothesis of a direct interaction of the photon with an asymptotically free quark in the nucleus, even at low energies. This means that asymptotic freedom of QCD and dispersion sum rules [46] can in some way be generalized for low energies. The knockout of a proton from a nuclear shell or the homogeneous distributions of nuclear evaporation cannot explain significant angular dependences at low energies.

The same mechanism appears to be capable of modeling proton yields in such reactions as the ^{16}C(e,e′p) reaction measured at MIT Bates [56], where it was shown that the region of missing energy above 50 MeV reflects "two-or-more-particle knockout" (or the "continuum" in terms of the shell model). The CHIPS model may help to understand and model such phenomena.

30.7 Chiral invariant phase-space decay in high energy hadron nuclear reactions

Chiral invariant phase-space decay can be used to de-excite an excited hadronic system. This possibility can be exploited to replace the intra-nuclear cascading after a high energy primary interaction takes place. The basic assumption in this is that the energy loss of the high energy hadron in nuclear matter is approximately constant per unit path length (about 1 GeV/fm). This energy is extracted from the soft part of the particle spectrum of the primary interaction, and from particles with formation times that place them within the nuclear boundaries.

Several approaches of transfering this energy into quasmons were studied, and comparisons with energy spectra of particles emitted in the backward hemisphere were made for a range of materials. Best results were achieved with a model that creates one quasmon per particle absorbed in the nucleus.

30.8 Neutrino-nuclear interactions

The simulation of DIS reactions includes reactions with high Q^2. The first approximation of the Q^2-dependent photonuclear cross-sections at high Q^2 was made in [11], where the modified photonuclear cross sections of virtual photons [34] were used. The structure functions of protons and deuterons have been approximated in CHIPS by the sum of non-perturbative multi-peripheral and non-perturbative direct interactions of virtual photons with hadronic partons:

$$F_2(x,Q^2) = [A(Q^2)\cdot x^{-\Delta(Q^2)} + B(Q^2)\cdot x]\cdot(1-x)^{N(Q^2)-2}, \qquad (30.59)$$

where $A(Q^2) = \bar{e^2_S}\cdot D\cdot U$, $B(Q^2) = \bar{e^2_V}\cdot(1-D)\cdot V$, $\bar{e^2}_{V(p)} = \frac{1}{3}$, $\bar{e^2}_{V(d)} = \frac{5}{18}$, $\bar{e^2_S} = \frac{1}{3} - \frac{\frac{1}{3}-\frac{5}{18}}{1+m^2_\phi/Q^2} + \frac{\frac{1}{3}-\frac{5}{18}}{1+m^2_{J/\psi}/Q^2} - \frac{\frac{1}{3}-\frac{19}{63}}{1+m^2_\Upsilon/Q^2}$, $N = 3+\frac{0.5}{\alpha_s(Q^2)}$, $\alpha_s(Q^2) = \frac{4\pi}{\beta_0 ln(1+\frac{Q^2}{\Lambda^2})}$, $\beta_0^{(n_f=3)} = 9$, $\Lambda = 200\ MeV$, $U = \frac{(3\ C(Q^2)+N-3)\cdot\Gamma(N-\Delta)}{N\cdot\Gamma(N-1)\cdot\Gamma(1-\Delta)}$, $V = 3(N-1)$, $D(Q^2) = H\cdot S(Q^2)\left(1-\frac{1}{2}S(Q^2)\frac{\bar{e^2_V}}{\bar{e^2_S}}\right)$, $S = \left(1+\frac{m^2_\rho}{Q^2}\right)^{-\alpha_P(Q^2)}$, $\alpha_P = 1+\Delta(Q^2)$,

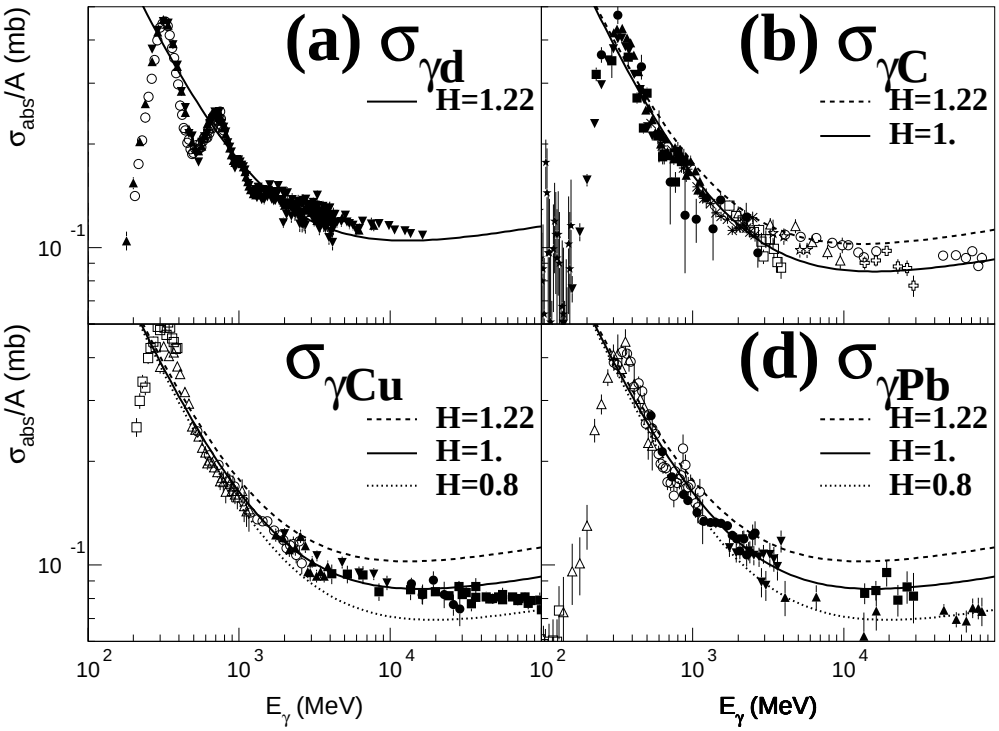

Figure 30.20: Fit of γA cross sections with different H values. Data are from [11].

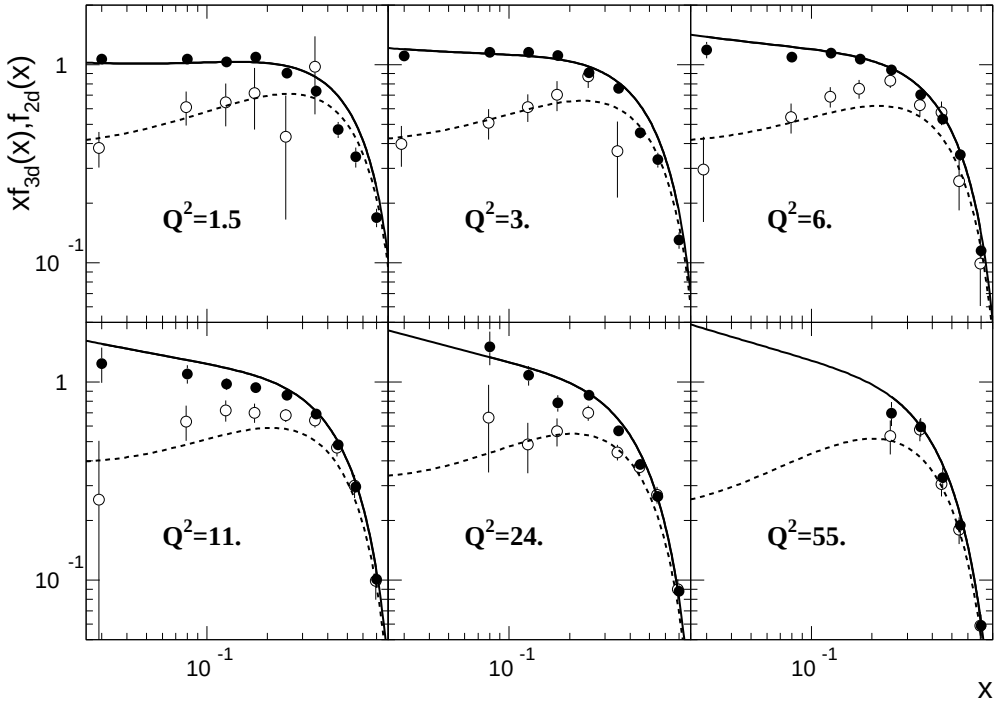

Figure 30.21: Fit of $f_{2d}(x,Q^2)$ (filled circles, solid lines) and $f_{3d}(x,Q^2)$ (open circles, dashed lines) structure functions measured by the WA25 experiment [35].

$\Delta = \frac{1+r}{12.5+2r}$, $r = \left(\frac{Q^2}{1.66}\right)^{1/2}$, $C = \frac{1+f}{g\cdot(1+f/.24)}$, $f = \left(\frac{Q^2}{0.08}\right)^2$, $g = 1 + \frac{Q^2}{21.6}$. The parton distributions are normalized to the unit total momentum fraction.

The photonuclear cross sections are calculated by the eikonal formula:

$$\sigma_\gamma^{tot} = \left[\frac{4\pi\alpha}{Q^2} F_2\left(\frac{Q^2}{2M\nu}, Q^2\right)\right]_{Q^2=0}^{\nu=E}, \tag{30.60}$$

An example of the approximation is shown in Fig. 30.20. One can see that the hadronic resonances are "melted" in nuclear matter and the multi-peripheral part of the cross section (high energy) is shadowed.

The differential cross section of the (ν,μ) reaction was approximated as

$$\frac{yd^2\sigma^{\nu,\bar{\nu}}}{dydQ^2} = \frac{G_F^2 \cdot M_W^4}{4\pi\cdot(Q^2+M_W^2)^2}\left[c_1(y)\cdot f_2(x,Q^2) \pm c_2(y)\cdot x f_3(x,Q^2)\right], \tag{30.61}$$

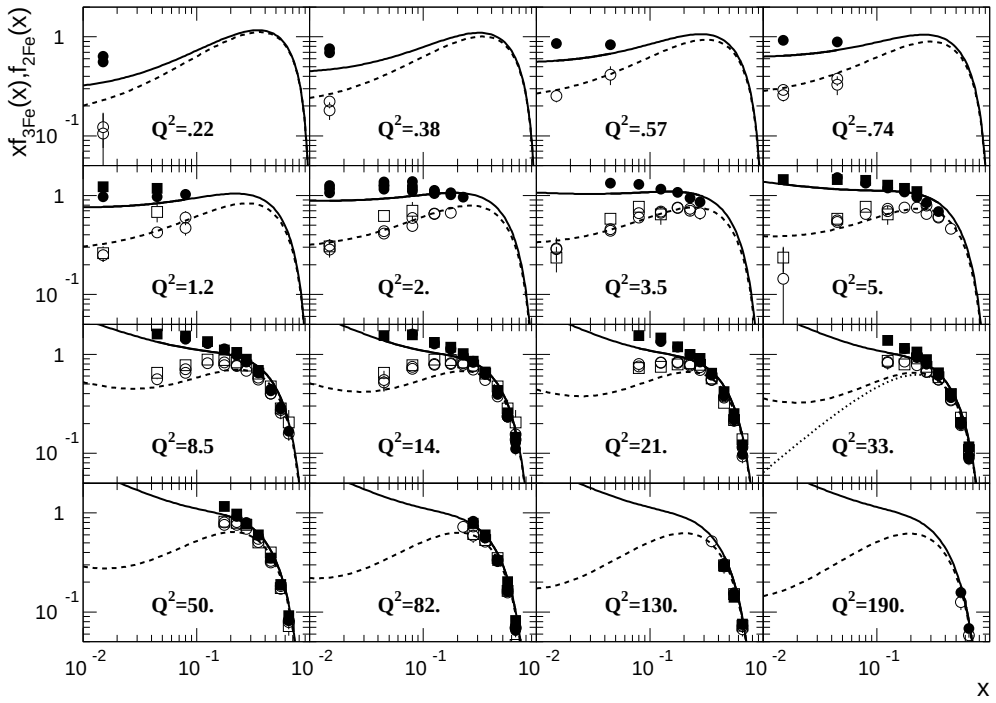

Figure 30.22: Fit of $f_{2Fe}(x,Q^2)$ (filled markers, solid lines) and $f_{3Fe}(x,Q^2)$ (open markers, dashed lines) structure functions measured by the CDHSW [36] (circles) and CCFR [37] (squares) experiments.

where $c_1(y) = 2 - 2y + \frac{y^2}{1+R}$, $R = \frac{\sigma_L}{\sigma_T}$, $c_2(y) = y(2-y)$. As $\bar{e_V^2} = \bar{e_S^2} = 1$ in Eq.30.59, hence $f_2(x,Q^2) = \left[D \cdot U \cdot x^{-\Delta} + (1-D) \cdot V \cdot x\right] \cdot (1-x)^{N-2}$, $xf_3(x,Q^2) = \left[D \cdot U_{f3} \cdot x^{-\Delta} + (1-D) \cdot V \cdot x\right] \cdot (1-x)^{N-2}$, with $D = H \cdot S(Q^2) \cdot \left(1 - \frac{1}{2}S(Q^2)\right)$ and $U_{f3} = \frac{3 \cdot C(Q^2) \cdot \Gamma(N-\Delta)}{N \cdot \Gamma(N-1)\Gamma(1-\Delta)}$. The approximation is compared with data in Fig.30.21 for deuterium [35] and in Fig.30.22 for iron [36, 37]. It must be emphasized that the CHIPS parton distributions are the same as for electromagnetic reactions.

For the (ν,μ) amplitudes one can not apply the optical theorem, To calculate the total cross sections, it is therefore necessary to integrate the differential cross sections first over x and then over Q^2. For the (ν,μ) reactions the differential cross section can be integrated with good accuracy even for low energies because it does not have the $\frac{1}{Q^4}$ factor of the boson propagator. The quasi-elastic part of the total cross-section can be calculated for $W < m_N + m_\pi$. The total (ν,μ) cross-sections are shown in Fig.30.23(a,b).

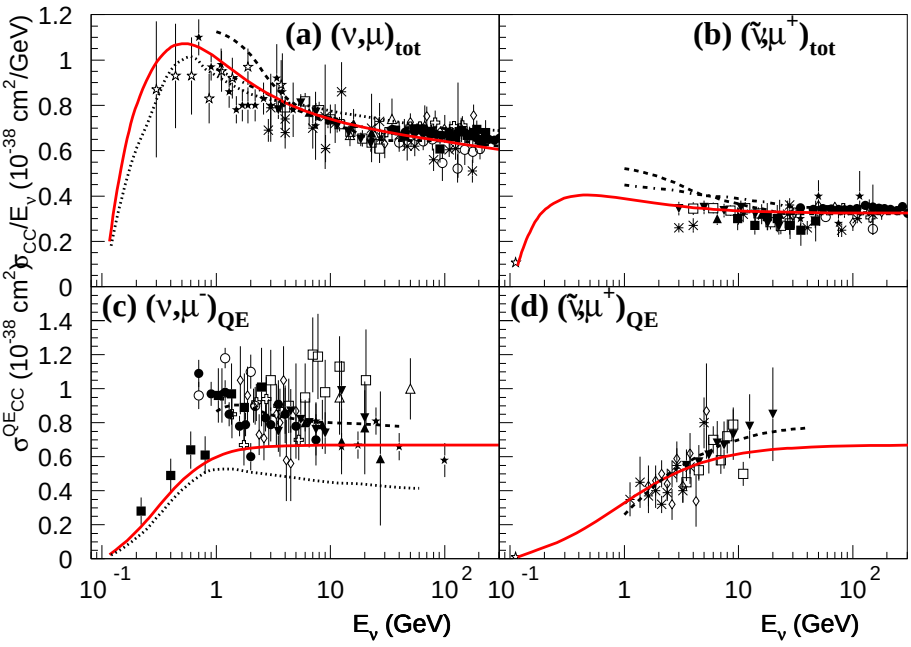

Figure 30.23: Fit of total (a,b) and quasi-elastic (c,d) cross-sections of (ν, μ) reactions (Geant4 database). The solid line is the CHIPS approximation (for other lines see text).

The dashed curve corresponds to the GRV [38] approximation of parton distributions and the dash-dotted curves correspond to the KMRS [39] approximation. Neither approximation fits low energies, because the perturbative calculations give parton distributions only for $Q^2 > 1\ GeV^2$. In [40] an attempt was made to freeze the DIS parton distributions at $Q^2 = 1$ and to use them at low Q^2. The $W < 1.4\ GeV$ part of DIS was replaced by the quasi-elastic and one pion production contributions, calculated on the basis of the low energy models. The results of [40] are shown by the dotted lines. The nonperturbative CHIPS approximation (solid curves) fits both total and quasi-elastic cross sections even at low energies.

The quasi-elastic (ν, μ) cross sections are shown in Fig.30.23(c,d). The CHIPS approximation (solid line) is compared with calculations made in [40] (the dotted line) and the best fit of the $V - A$ theory was made in [41] (the dashed lines). One can see that CHIPS gives reasonable agreement.

The Q^2 spectra for each energy are known as an intermediate result of the calculation of total or quasi-elastic cross sections. For the quasi-elastic interactions ($W < m_N + m_\pi$) one can use $x = 1$ and simulate a binary reaction. In the final state the recoil nucleon has some probability of interacting with the nucleus. If $W > m_N + m_\pi$ the Q^2 value is randomized and therefore the Q^2 dependent coefficients (the number of partons in non-perturbative phase space N, the Pomeron intercept α_P, the fraction of the direct interactions, etc.) can be calculated. Then for fixed energy and Q^2 the neutrino interaction with quark-partons (directly or through the Pomeron ladder) can be randomized and the secondary parton distribution can be calculated. In vacuum or in nuclear matter the secondary partons are creating quasmons [2, 3] which decay to secondary hadrons.

30.9 Conclusion.

For users who would like to improve the interaction part of the CHIPS event generator for their own specific reactions, some advice concerning data presentation is useful.

It is a good idea to use a normalized invariant function $\rho(k)$

$$\rho = \frac{2E \cdot d^3\sigma}{\sigma_{tot} \cdot d^3p} \propto \frac{d\sigma}{\sigma_{tot} \cdot pdE},$$

where σ_{tot} is the total cross section of the reaction. The simple rule, then, is to divide the distribution over the hadron energy E by the momentum and by the reaction cross section. The argument k can be calculated for any outgoing hadron or fragment as

$$k = \frac{E + p - B \cdot m_N}{2},$$

which is the energy of the primary quark-parton. Because the spectrum of the quark-partons is universal for all the secondary hadrons or fragments, the distributions over this parameter have a similar shape for all the secondaries. They should differ only when the kinematic limits are approached or in the evaporation region. This feature is useful for any analysis of experimental data, independent of the CHIPS model.

Some concluding remarks should be made about the parameters of the model. The main parameter, the critical temperature T_c, should not be varied. A large set of data confirms the value **180 MeV** while from the mass spectrum of hadrons it can be found more precisely as 182 MeV. The clusterization parameter is **4.** which is just about $4\pi/3$. If the quark exchange

starts at the mean distance between baryons in the dense part of the nucleus, then the radius of the clusterization sphere is twice the "the radius of the space occupied by the baryon". It gives 8 for the parameter, but the space occupied by the baryon can not be spherical; only cubic subdivision of space is possible so the factor $\pi/6$ appears. But this is a rough estimate, so **4** or even **5** can be tried. The surface parameter fD varies slightly with A, growing from 0 to 0.04. For the present CHIPS version the recommended parameters for low energies are:

A	**T**	**s/u**	**eta**	**noP**	**fN**	**fD**	**Cp**	**rM**	**sA**
Li	180.	0.1	0.3	223	.4	.00	4.	1.0	0.4
Be	180.	0.1	0.3	223	.4	.00	4.	1.0	0.4
C	180.	0.1	0.3	223	.4	.00	4.	1.0	0.4
O	180.	0.1	0.3	223	.4	.02	4.	1.0	0.4
F	180.	0.1	0.3	223	.4	.03	4.	1.0	0.4
Al	180.	0.1	0.3	223	.4	.04	4.	1.0	0.4
Ca	180.	0.1	0.3	223	.4	.04	4.	1.0	0.4
Cu	180.	0.1	0.3	223	.4	.04	4.	1.0	0.4
Ta	180.	0.1	0.3	223	.4	.04	4.	1.0	0.4
U	180.	0.1	0.3	223	.4	.04	4.	1.0	0.4

The vacuum hadronization weight parameter can be bigger for light nuclei and smaller for heavy nuclei, but 1.0 is a good guess. The s/u parameter is not yet tuned, as it demands strange particle production data. A guess is that if there are as many $u\bar{u}$ and $d\bar{d}$ pairs in the reaction as in the $p\bar{p}$ interaction, the parameter can be 0.1. In other cases it is closer to 0.3 as in other event generators. But it is bestnot to touch any parameters for the first experience with the CHIPS event generator. Only the incident momentum, the PDG code of the projectile, and the CHIPS style PDG code of the target need be changed.

30.10 Status of this document

02.12.05 neutrino interactions section and figures added by M.V. Kossov
26.04.03 first four sections re-written by D.H. Wright
01.01.01 created by M.V. Kossov and H.P. Wellisch

Bibliography

[1] B. Andersson, G. Gustafson, G. Ingelman, T. Sjöstrand, Phys. Rep. **97** (1983) 31

[2] P. V. Degtyarenko, M. V. Kossov, and H.P. Wellisch, Chiral invariant phase space event generator, I. Nucleon-antinucleon annihilation at rest, Eur. Phys. J. A 8 (2000) 217.

[3] P. V. Degtyarenko, M. V. Kossov, and H. P. Wellisch, Chiral invariant phase space event generator, II.Nuclear pion capture at rest, Eur. Phys. J. A 9 (2000) 411.

[4] P. V. Degtyarenko, M. V. Kossov, and H. P. Wellisch, Chiral invariant phase space event generator, III Photonuclear reactions below $\Delta(3,3)$ excitation, Eur. Phys. J. A 9, (2000) 421.

[5] M. V. Kossov, Chiral invariant phase space model, I Masses of hadrons, Eur. Phys. J. A 14 (2002) 265.

[6] C.A.Z. Vasconcellos et al., Eur. Phys. J. C **4** (1998) 115; G.A. Miller, A.W. Thomas, S. Theberge, Phys. Lett. B **91** (1980) 192; C.E. de Tar, Phys. Rev. D **24** (1981) 752; M.A.B. Bég, G.T. Garvey, Comments Nucl. Part. Phys. **18** (1988) 1

[7] F. James, *Monte Carlo Phase Space*, CERN 68-15 (1968)

[8] K.G. Wilson, Proc. Fourteenth Scottish Universities Summer School in Physics (1973), eds R. L. Crawford, R. Jennings (Academic Press, New York, 1974)

[9] Monte Carlo particle numbering scheme, in: Particle Data Group, *Review of Particle Physics*, Eur. Phys. J. C **3** (1998) 180

[10] R. Hagedorn, Nuovo Cimento Suppl. **3** (1965) 147

[11] M. V. Kossov, Approximation of photonuclear interaction cross-sections, Eur. Phys. J. A 14 (2002) 377.

[12] S. Giani et al., Geant4: Object Oriented Toolkit for Simulation in HEP, LCB status report CERN/LHCC/98-44, November 1998.

[13] J. P. Wellisch, On hadronic models in GEANT4, Program and Book of Abstracts.International Conference on Advanced Monte Carlo for Radiation Physics, Particle Transport Simulation and Applications, 23-26 October 2000, IST,Lisbon, Portugal, p. 330.

[14] Yu.L. Dokshitzer, V.S. Fadin and V.A. Khoze, Phys. Lett. **115B** (1982) 242L

[15] T. Sjöstrand, Comp. Phys. Comm. **92** (1994) 74

[16] S. Ocubo, Phys. Lett. **5** (1963) 165; G. Zweig, CERN Preprint 8419/TH-412 (1964); I. Iizuka, Progr. Theor. Phys. Suppl. **37** (1966) 21

[17] V.E. Markushin, M.P. Locher, Eur. Phys. J. A **1** (1998) 91

[18] J. Sedlak and V. Simak, Sov. J. Part. Nucl. **19** (1988) 191

[19] C. Amsler, Rev.Mod.Phys. **70** (1998) 1293; C. Amsler and F. Myher, Annu. Rev. Nucl. Part. Sci. **41** (1991) 219

[20] B. Andersson, G. Gustafson, T. Sjöstrand, Nucl. Phys. B **197**(1982) 45; B. Andersson, G. Gustafson, T. Sjöstrand, Physica Scripta **32** (1985) 574

[21] P. Gregory et al., Nucl. Phys. B **102** (1976) 189

[22] M.V. Kossov and L.M. Voronina, Preprint ITEP 165-84, Moscow (1984)

[23] V.I. Efremenko et al., Phys. Rev. C **22** (1980) 700.

[24] S.V Boyarinov et al., Phys. At. Nucl. **56** (1993) 72.

[25] P.V. Degtyarenko et al., Phys. Rev. C **50** (1994) R541

[26] K. Maltman and N. Isgur, Phys. Rev. D **29** (1984) 952.

[27] K. Maltman and N. Isgur, Phys. Rev. D **34** (1986) 1372.

[28] P. Hoodbhoy and R. J. Jaffe, Phys. Rev. D **35** (1987) 113.

[29] N. Isgur, Nucl. Phys. **A497** (1989) 91.

[30] M. V. Kossov, CHIPS: masses of hadrons. (be published).

[31] L. D. Landau, E. M. Lifshitz, "Course of Theoretical Physics" v.4, part 1, "Relativistic Quantum Theory", Pergamon Press, paragraph 96, The method of equivalent photons.

[32] J. Eickmeyer et al. Phys. Rev. Letters **36** (1976) 289-291.

[33] D'Agostini, Hard Scattering Process in High Energy Gamma-Induced Reactions, DESY 94-169, September 1994.

[34] F. W. Brasse et al. Nuclear Physics **B39** (1972) 421-431.

[35] D. Allasia *et al*, Z. Phys C **28**, 321 (1985)

[36] P. Berg *et al*, Z. Phys C **49**, 187 (1991)

[37] E. Oltman *et al*, Z. Phys C **53**, 51 (1992)

[38] M. Glück *et al*, Z. Phys. C **48**, 471 (1990)

[39] J. Kviecinski *et al*, Phys. Rev. D **42**, 3645 (1990)

[40] P. Lipari *et al*, Phys. Rev. Let. **74**, 4384 (1995)

[41] S.V. Belikov *et al*, Z. Phys. A **320**, 625 (1985)

[42] A. Lepretre et al. Nuclear Physics **A390** (1982) 221-239.

[43] P.V. Degtyarenko and M.V. Kossov, Preprint ITEP 11-92, Moscow (1992)

[44] P.V. Degtyarenko et al., Z. Phys. A - Atomic Nuclei, **335** (1990) 231

[45] P.V. Degtyarenko, *Applications of the photonuclear fragmentation model to radiation protection problems*, in: Proceedings of Second Specialist's Meeting on Shielding Aspects of Accelerators, Targets and Irradiation Facilities (SATIF-2), CERN, Geneva, Switzerland, 12-13 October 1995, published by Nuclear Energy Agency, Organization for Economic Co-operation and Development, pages 67 - 91 (1996)

[46] C. Bernard, A. Duncan, J. LoSecco, and S. Weinberg, Phys. Rev. D **12** (1975) 792;

E. Poggio, H. Quinn, and S. Weinberg, Phys. Rev. D **13** (1976) 1958

[47] A. I. Amelin et al., "Energy spectra of charged particles in the reaction of π^- absorption at rest by ^{6,7}Li, ^{9}Be, ^{10,11}B, ^{12}C, ^{28}Si, ^{40}Ca, ^{59}Co, ^{93}Nb, ^{114,117,120,124}Sn, ^{169}Tm, ^{181}Ta and ^{209}Bi nuclei", Moscow Physics and Engineering Institute Preprint No. 034-90, Moscow, 1990.

[48] G. Mechtersheimer et al., Nucl. Phys. **A324** (1979) 379.

[49] C. Cernigoi et al., Nucl. Phys. **A456** (1986) 599.

[50] R. Madey et al., Phys. Rev. C **25** (1982) 3050.

[51] D. Ryckbosch et al., Phys. Rev. C **42** (1990) 444.

[52] J. Ahrens et al., Nucl. Phys. **A446** (1985) 229c.

[53] Jan Ryckebusch et al., Phys. Rev. C **49** (1994) 2704.

[54] C. Van den Abeele; private communication cited in the reference: Jan Ryckebusch et al., Phys. Rev. C **49** (1994) 2704.

[55] P.D. Harty et al. (unpublished); private communication cited in the reference: Jan Ryckebusch et al., Phys. Rev. C **49** (1994) 2704.

[56] L.B. Weinstein et al., Phys. Rev. Lett. **64** (1990) 1646.

[57] J.P. Jeukenne and C. Mahaux, Nucl. Phys. A **394** (1983) 445.

Chapter 31

Bertini Intranuclear Cascade Model in GEANT4

31.1 Introduction

This cascade model is a re-engineered version of the INUCL code and includes the Bertini intra-nuclear cascade model with excitons, a pre-equilibrium model, a nucleus explosion model, a fission model, and an evaporation model. It treats nuclear reactions initiated by long-lived hadrons ($p, n, \pi, K, \Lambda, \Sigma, \Xi, \Omega$) and γs with energies between 0 and 10 GeV. Presented here is an overview of the models and a review of results achieved from simulations and comparisons with experimental data.

The intranuclear cascade model (INC) was was first proposed by Serber in 1947 [19]. He noticed that in particle-nuclear collisions the deBroglie wavelength of the incident particle is comparable (or shorter) than the average intra-nucleon distance. Hence, a description of interactions in terms of particle-particle collisions is justified.

The INC has been used succesfully in Monte Carlo simulations at intermediate energies since Goldberger made the first hand-calculations in 1947 [9]. The first computer simulations were done by Metropolis et al. in 1958 [16]. Standard methods in INC implementations were developed when Bertini published his results in 1968 [3]. An important addition to INC was the exciton model introduced by Griffin in 1966 [10].

The current presentation describes the implementation of the Bertini INC model within the GEANT4 hadronic physics framework [8]. This framework is flexible and allows for the modular implementation of various kinds of hadronic interactions.

31.2 The Geant4 Cascade Model

Inelastic particle-nucleus collisions are characterized by both fast and slow components. The fast ($10^{-23} - 10^{-22}s$) intra-nuclear cascade results in a highly excited nucleus which may decay by fission or pre-equilibrium emission. The slower ($10^{-18} - 10^{-16}s$) compound nucleus phase follows with evaporation. A Boltzmann equation must be solved to treat the collision process in detail.

The intranuclear cascade (INC) model developed by Bertini [3, 4] solves the Boltzmann equation on average. This model has been implemented in several codes such as HETC [1]. Our model, which is based on a re-engineering of the INUCL code [20], includes the Bertini intranuclear cascade model with excitons, a pre-equilibrium model, a simple nucleus explosion model, a fission model, and an evaporation model.

The target nucleus is modeled by up to six concentric shells of constant density as an approximation to the continuously changing density distribution of nuclear matter within nuclei. The cascade begins when an incident particle strikes a nucleon in the target nucleus and produces secondaries. The secondaries may in turn interact with other nucleons or be absorbed. The cascade ends when all particles, which are kinematically able to do so, escape the nucleus. At that point energy conservation is checked. Relativistic kinematics is applied throughout the cascade.

31.2.1 Model Limits

The model is valid for incident $p, n, \pi, K, \Lambda, \Sigma, \Xi, \Omega$ and γs with energies between 0 and 10 GeV. All types of nuclear targets are allowed.

The necessary condition of validity of the INC model is $\lambda_B/v << \tau_c << \Delta t$, where δ_B is the deBroglie wavelenth of the nucleons, v is the average relative velocity between two nucleons and Δt is the time interval between collisions. At energies below $200MeV$, this condition is no longer strictly valid, and a pre-quilibrium model must be invoked. At energies greater than $\approx$ 10 GeV) the INC picture breaks down. This model has been tested against experimental data at incident kinetic energies between 100 MeV and 10 GeV.

31.2.2 Intranuclear Cascade Model

The basic steps of the INC model are summarized as follows:

1. the space point at which the incident particle enters the nucleus is selected uniformly over the projected area of the nucleus,

2. the total particle-particle cross sections and region-depenent nucleon densities are used to select a path length for the projectile,

3. the momentum of the struck nucleon, the type of reaction and the four-momenta of the reaction products are determined, and

4. the exciton model is updated as the cascade proceeds.

5. If the Pauli exclusion principle allows and $E_{particle} > E_{cutoff} = 2$ MeV, step (2) is performed to transport the products.

After the intra-nuclear cascade, the residual excitation energy of the resulting nucleus is used as input for non-equilibrium model.

31.2.3 Nuclear Model

Some of the basic features of the nuclear model are:

- the nucleons are assumed to have a Fermi gas momentum distribution. The Fermi energy is calculated in a local density approximation i.e. the Fermi energy is made radius-dependent with Fermi momentum $p_F(r) = (\frac{3\pi^2\rho(r)}{2})^{\frac{1}{3}}$.

- Nucleon binding energies (BE) are calculated using the mass formula. A parameterization of the nuclear binding energy uses a combination of the Kummel mass formula and experimental data. Also, the asymptotic high temperature mass formula is used if it is impossible to use experimental data.

Initialization

The initialization phase fixes the nuclear radius and momentum according to the Fermi gas model.

If the target is hydrogen (A = 1) a direct particle-particle collision is performed, and no nuclear modeling is required.

If $1 < A < 4$, a nuclear model consisting of one layer with a radius of 8.0 fm is created.

For $4 < A < 11$, the nuclear model is composed of three concentric spheres $i = \{1, 2, 3\}$ with radius

$$r_i(\alpha_i) = \sqrt{C_1^2(1 - \frac{1}{A}) + 6.4}\sqrt{-log(\alpha_i)}$$

.

Here $\alpha_i = \{0.01, 0.3, 0.7\}$ and $C_1 = 3.3836A^{1/3}$.

If $A > 11$, a nuclear model with three concentric spheres is also used. The sphere radius is now defined as

$$r_i(\alpha_i) = C_2 \log(\frac{1 + e^{-\frac{C_1}{C_2}}}{\alpha_i} - 1) + C_1, \tag{31.1}$$

where $C_2 = 1.7234$.

The potential energy V for nucleon N is

$$V_N = \frac{p_F^2}{2m_N} + BE_N(A, Z), \tag{31.2}$$

where p_f is the Fermi momentum and BE is the binding energy.

The momentum distribution in each region follows the Fermi distribution with zero temperature.

$$f(p) = cp^2 \tag{31.3}$$

where

$$\int_0^{p_F} f(p)dp = n_p \mathrm{orn_n} \tag{31.4}$$

where n_p and n_n are the number of protons or neutrons in the region. P_f is the momentum corresponding to the Fermi energy

$$E_f = \frac{p_F^2}{2m_N} = \frac{\hbar^2}{2m_N}(\frac{3\pi^2}{v})^{\frac{2}{3}}, \tag{31.5}$$

which depends on the density n/v of particles, and which is different for each particle and each region.

Pauli Exclusion Principle

The Pauli exclusion principle forbids interactions where the products would be in occupied states. Following the assumption of a completely degenerate Fermi gas, the levels are filled from the lowest level. The minimum energy allowed for the products of a collision correspond to the lowest unfilled level of the system, which is the Fermi energy in the region. So in practice, the Pauli exclusion principle is taken into account by accepting only secondary nucleons which have $E_N > E_f$.

Cross Sections and Kinematics

Path lengths of nucleons in the nucleus are sampled according to the local density and the free $N-N$ cross sections. Angles after the collision are sampled from experimental differential cross sections. Tabulated total reaction cross sections are calculated by Letaw's formulation [14, 15, 17]. For $N-N$ cross sections the parameterizations are based on the experimental energy and isospin dependent data. The parameterization described in [2] is used.

For pions the intra-nuclear cross sections are provided to treat elastic collisions and the following inelastic channels: π^-p $\rightarrow \pi^0$n, π^0p $\rightarrow \pi^+$n, π^0n $\rightarrow \pi^-$p, and π^+n $\rightarrow \pi^0$p. Multiple particle production is also implemented.

The pion absorption channels are π^+nn $\rightarrow$ pn, π^+pn $\rightarrow$ pp, π^0nn $\rightarrow$ nn, π^0pn $\rightarrow$ pn, π^0pp $\rightarrow$ pp, π^-pn $\rightarrow$ nn , and π^-pp $\rightarrow$ pn.

31.2.4 Pre-equilibrium Model

The GEANT4 cascade model implements the exciton model proposed by Griffin [10, 11]. In this model, nucleon states are characterized by the number of excited particles and holes (the excitons). Intra-nuclear cascade collisions give rise to a sequence of states characterized by increasing exciton number, eventually leading to an equilibrated nucleus. For a practical implementation of the exciton model we use parameters from [18], (level densities) and [13] (matrix elements).

In the exciton model the possible selection rules for particle-hole configurations in the source of the cascade are: $\Delta p = 0, \pm 1$ $\Delta h = 0, \pm 1$ $\Delta n = 0, \pm 2$, where p is the number of particles, h is number of holes and $n = p + h$ is the number of excitons.

The cascade pre-equilibrium model uses target excitation data and the exciton configurations for neutrons and protons to produce non-equilibrium evaporation. The angular distribution is isotropic in the rest frame of the exciton system.

Parameterizations of the level density are tabulated as functions of A and Z, and with high temperature behavior (the nuclear binding energy using the smooth liquid high energy formula).

31.2.5 Break-up models

Fermi break-up is allowed only in some extreme cases, i.e. for light nuclei ($A < 12$ and $3(A-Z) < Z < 6$) and $E_{excitation} > 3E_{binding}$. A simple explosion model decays the nucleus into neutrons and protons and decreases exotic evaporation processes.

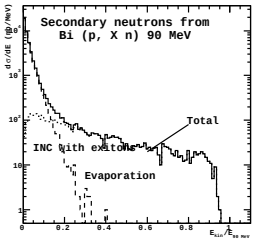

Figure 31.1: Secondary neutrons generated by Bertini INC with exitons and evaporation model.

The fission model is phenomenological, using potential minimization. A binding energy paramerization is used and some features of the fission statistical model are incorporated [7].

31.2.6 Evaporation Model

A statistical theory for particle emission of the excited nucleus remaining after the intra-nuclear cascade was originally developed by Weisskopf [21]. This model assumes complete energy equilibration before particle emission, and re-equilibration of excitation energies between successive evaporations. As a result the angular distribution of emitted particles is isotropic.

The GEANT4 evaporation model for the cascade implementation adapts the often-used computational method developed by Dostrowski [5, 6]. The emission of particles is computed until the excitation energy falls below some specific cutoff. If a light nucleus is highly excited, the Fermi break-up model is executed. Also, fission is performed if that channel is open. The main chain of evaporation is followed until $E_{excitation}$ falls below $\mathrm{E}_{cutoff} = 0.1$ MeV. The evaporation model ends with an emission chain which is followed until $E_{excitation} < E^{\gamma}_{cutoff} = 10^{-15}$ MeV.

An example of Bertini evaporation model in action is shown in Fig. 31.1.

31.3 Interfacing Bertini implementation

Typically Bertini models are used through physics lists, with 'BERT' in their name. User should consult these validated physics model collection to understand the inclusion mechanisms before using directly the actual Bertini cascade interfaces:

G4CascadeInterface *All the Bertini cascade submodels* in integrated fashion, can be used collectively through this interface using method *Apply-*

Yourself. A GEANT4 track (*G4Track*) and a nucleus (*G4Nucleus*) are given as parameters.

G4ElasticCascadeInterface provides an access to elastic hadronic scattering. Particle treated are the same as in case for *G4CascadeInterface* but only elastic scattering is modeled.

G4PreCompoundCascadeInterface provides an interface to INUCL intra nuclear cascade with exitons. Subsequent evaporation phase is *not* modeled.

G4InuclEvaporation provides an interface to INUCL evaporation model. This interface with method *BreakItUp* inputs an exited nuclei *G4Fragment* to model evaporation phase.

31.4 Status of this document

01.12.02 created by Aatos Heikkinen, Nikita Stepanov and Hans-Peter Wellisch
14.06.05 grammar, spelling check and list of pion absorption channels corrected by D.H. Wright
30.05.07 New interfaces documented Aatos Heikkinen

Bibliography

[1] R.G. Alsmiller and F.S. Alsmiller and O.W. Hermann, The high-energy transport code HETC88 and comparisons with experimental data, Nuclear Instruments and Methods in Physics Research A 295, (1990), 337–343,

[2] V.S. Barashenkov and V.D. Toneev, High Energy interactions of particles and nuclei with nuclei (In russian), (1972)

[3] M. P. Guthrie, R. G. Alsmiller and H. W. Bertini, Nucl. Instr. Meth, 66, 1968, 29.

[4] H. W. Bertini and P. Guthrie, Results from Medium-Energy Intranuclear-Cascade Calculation, Nucl. Phys.A169, (1971).

[5] I. Dostrovsky, Z. Zraenkel and G. Friedlander, Monte carlo calculations of high-energy nuclear interactions. III. Application to low-lnergy calculations, Physical Review, 1959, 116, 3, 683-702.

[6] I. Dostrovsky and Z. Fraenkel and P. Rabinowitz, Monte Carlo Calculations of Nuclear Evaporation Processes. V. Emission of Particles Heavier Than ^4He, Physical Review, 1960.

[7] P. Fong, Statistical Theory of Fission, 1969, Gordon and Breach, New York.

[8] Geant4 collaboration, Geant4 general paper (to be published), Nuclear Instruments and Methods A, (2003).

[9] M. Goldberger, The Interaction of High Energy Neutrons and Hevy Nuclei, Phys. Rev. 74, (1948), 1269.

[10] J. J. Griffin, Statistical Model of Intermediate Structure, Physical Review Letters 17, (1966), 478-481.

[11] J. J. Griffin, Statistical Model of Intermediate Structure, Physics Letters 24B, 1 (1967), 5-7.

[12] A. S. Iljonov et al., Intermediate-Energy Nuclear Physics, CRC Press 1994.

[13] C. Kalbach, Exciton Number Dependence of the Griffin Model Two-Body Matrix Element, Z. Physik A 287, (1978), 319-322.

[14] J. R. Letaw et al., The Astrophysical Journal Supplements 51, (1983), 271f.

[15] J. R. Letaw et al., The Astrophysical Journal 414, 1993, 601.

[16] N. Metropolis, R. Bibins, M. Storm, Monte Carlo Calculations on Intranuclear Cascades. I. Low-Energy Studies, Physical Review 110, (1958), 185ff.

[17] S. Pearlstein, Medium-energy nuclear data libraries: a case study, neutron- and proton-induced reactions in ^{5}6Fe, The Astrophysical Journal 346, (1989), 1049-1060.

[18] I. Ribansky et al., Pre-equilibrium decay and the exciton model, Nucl. Phys. A 205, (1973), 545-560.

[19] R. Serber, Nuclear Reactions at High Energies, Phys. Rev. 72, (1947), 1114.

[20] Experimental and Computer Simulations Study of Radionuclide Production in Heavy Materials Irradiated by Intermediate Energy Protons, Yu. E. Titarenko et al., nucl-ex/9908012, (1999).

[21] V. Weisskopf, Statistics and Nuclear Reactions, Physical Review 52, (1937), 295–302.

Chapter 32

The GEANT4 Binary Cascade

32.1 Modeling overview

The Geant4 Binary Cascade is an intranuclear cascade propagating primary and secondary particles in a nucleus. Interactions are between a primary or secondary particle and an individual nucleon of the nucleus, leading to the name Binary Cascade. Cross section data are used to select collisions. Where available, experimental cross sections are used by the simulation. Propagating of particles is the nuclear field is done by numerically solving the equation of motion. The cascade terminates when the average and maximum energy of secondaries is below threshold. The remaining fragment is treated by precompound and de-excitation models documented in the corresponding chapters.

32.1.1 The transport algorithm

For the primary particle an impact parameter is chosen random in a disk outside the nucleus perpendicular to a vector passing through the center of the nucleus coordinate system an being parallel to the momentum direction. Using a straight line trajectory, the distance of closest approach d_i^{min} to each target nucleon i and the corresponding time-of-flight t_i^d is calculated. In this calculation the momentum of the target nucleons is ignored, i.e. the target nucleons do not move. The interaction cross section σ_i with target nucleons is calculated using total inclusive cross-sections described below. For calculation of the cross-section the momenta of the nucleons are taken into account. The primary particle may interact with those target nucleons where the distance of closest approach d_i^{min} is smaller than $d_i^{min} < \sqrt{\frac{\sigma_i}{\pi}}$. These candidate interactions are called collisions, and these collisions are

stored ordered by time-of-flight t_i^d. In the case no collision is found, a new impact parameter is chosen.

The primary particle is tracked the time-step given by the time to the first collision. As long a particle is outside the nucleus, that is a radius of the outermost nucleon plus $3fm$, particles travel along straight line trajectories. Particles entering the nucleus have their energy corrected for Coulomb effects. Inside the nucleus particles are propagated in the scalar nuclear field. The equation of motion in the field is solved for a given time-step using a Runge-Kutta integration method.

At the end of the step, the primary and the nucleon interact suing the scattering term. The resulting secondaries are checked for the Fermi exclusion principle. If any of the two particles has a momentum below Fermi momentum, the interaction is suppressed, and the original primary is tracked to the next collision. In case interaction is allowed, the secondaries are treated like the primary, that is, all possible collisions are calculated like above, with the addition that these new primary particles may be short-lived and may decay. A decay is treated like others collisions, the collision time being the time until the decay of the particle. All secondaries are tracked until they leave the nucleus, or the until the cascade stops.

32.1.2 The description of the target nucleus and fermi motion

The nucleus is constructed from A nucleons and Z protons with nucleon coordinates $\mathbf{r}_i$ and momenta $\mathbf{p}_i$, with $i = 1, 2, ..., A$. We use a common initialization Monte Carlo procedure, which is realized in the most of the high energy nuclear interaction models:

- Nucleon radii r_i are selected randomly in the nucleus rest frame according to nucleon density $\rho(r_i)$. For heavy nuclei with $A > 16$ [2] nucleon density is

$$\rho(r_i) = \frac{\rho_0}{1 + \exp\left[(r_i - R)/a\right]} \tag{32.1}$$

  where

$$\rho_0 \approx \frac{3}{4\pi R^3}(1 + \frac{a^2\pi^2}{R^2})^{-1}. \tag{32.2}$$

  Here $R = r_0 A^{1/3}$ fm and $r_0 = 1.16(1 - 1.16A^{-2/3})$ fm and $a \approx 0.545$ fm. For light nuclei with $A < 17$ nucleon density is given by a harmonic oscillator shell model [3], e. g.

$$\rho(r_i) = (\pi R^2)^{-3/2} \exp\left(-r_i^2/R^2\right), \tag{32.3}$$

where $R^2 = 2/3 < r^2 >= 0.8133A^{2/3}$ fm^2. To take into account nucleon repulsive core it is assumed that internucleon distance $d > 0.8$ fm;

- The nucleus is assumed to be isotropic, i.e. we place each nucleon using a random direction and the previously determined radius r_i.

- The initial momenta of the nucleons p_i are randomly choosen between 0 and $p_F^{max}(r)$, where the maximal momenta of nucleons (in the local Thomas-Fermi approximation [4]) depends from the proton or neutron density ρ according to

$$p_F^{max}(r) = \hbar c(3\pi^2\rho(r))^{1/3} \tag{32.4}$$

- To obtain momentum components, it is assumed that nucleons are distributed isotropic in momentum space; i.e. the momentum direction is chosen at random.

- The nucleus must be centered in momentum space around $\mathbf{0}$, *i. e.* the nucleus must be at rest, i. e. $\sum_i \mathbf{p_i} = \mathbf{0}$; To achieve this, we choose one nucleon to compensate the sum the remaining nucleon momenta $p_rest = \sum_{i=1}^{i=A-1}$. If this sum is larger than maximum momentum $p_F^{max}(r)$, we change the direction of the momentum of a few nucleons. If this does not lead to a possible momentum value, than we repeat the procedure with a different nucleon having a larger maximum momentum $p_F^{max}(r)$. In the rare case this fails as well, we choose new momenta for all nucleons.

  This procedure gives special for hydrogen ^{1}H, where the proton has momentum $p = 0$, and for deuterium ^{2}H, where the momenta of proton and neutron are equal, and in opposite direction.

- We compute energy per nucleon $e = E/A = m_N + B(A,Z)/A$, where m_N is nucleon mass and the nucleus binding energy $B(A,Z)$ is given by the tabulation of [5]: and find the effective mass of each nucleon $m_i^{eff} = \sqrt{(E/A)^2 - p_i^{2\prime}}$.

32.1.3 Optical and phenomenological potentials

The effect of collective nuclear elastic interaction upon primary and secondary particles is approximated by a nuclear potential.

For projectile protons and neutrons this scalar potential is given by the local Fermi momentum $p_F(r)$

$$V(r) = \frac{p_F^2(r)}{2m} \tag{32.5}$$

where m is the mass of the neutron m_n or the mass of proton m_p.

For pions the potential is given by the lowest order optical potential [6]

$$V(r) = \frac{-2\pi(\hbar c)^2 A}{\overline{m}_\pi}(1 + \frac{m_\pi}{M})b_0\rho(r) \tag{32.6}$$

where A is the nuclear mass number, m_π, M are the pion and nucleon mass, $\overline{m}_\pi$ is the reduced pion mass $\overline{m}_\pi = (m_\pi m_N)/(m_\pi + m_N)$, with m_N is the mass of the nucleus, and $\rho(r)$ is the nucleon density distribution. The parameter b_0 is the effective $s-$wave scattering length and is obtained from analysis to pion atomic data to be about $-0.042fm$.

32.1.4 Pauli blocking simulation

The cross sections used in this model are cross sections for free particles. In the nucleus these cross sections are reduced to effective cross sections by Pauli-blocking due to Fermi statistics.

For nucleons created by a collision, ie. an inelastic scattering or from decay, we check that all secondary nucleons occupy a state allowed by Fermi statistics. We assume that the nucleus in its ground state and all states below Fermi energy are occupied. All secondary nucleons therefore must have a momentum p_i above local Fermi momentum $p_F(r)$, i.e.

$$p_i > p_F^{max}(r). \tag{32.7}$$

If any of the nucleons of the collision has a momentum below the local Fermi momentum, then the collision is Pauli blocked. The reaction products are discarded, and the original particles continue the cascade.

32.1.5 The scattering term

The basis of the description of the reactive part of the scattering amplitude are two particle binary collisions (hence binary cascade), resonance production, and decay. Based on the cross-section described later in this paper, collisions will occur when the transverse distance d_t of any projectile target pair becomes smaller than the black disk radium corresponding to the total cross-section σ_t

$$\frac{\sigma_t}{\pi} > d_t^2$$

In case of a collision, all particles will be propagated to the estimated time of the collision, i.e. the time of closest approach, and the collision final state is produced.

32.1.6 Total inclusive cross-sections

Experimental data are used in the calculation of the total, inelastic and elastic cross-section wherever available.

hadron-nucleon scattering

For the case of proton-proton(pp) and proton-neutron(pn) collisions, as well as $\pi^=$ and π^- nucleon collisions, experimental data are readily available as collected by the Particle Data Group (PDG) for both elastic and inelastic collisions. We use a tabulation based on a sub-set of these data for $\sqrt{S}$ below 3 GeV. For higher energies, parametrizations from the CERN-HERA collection are included.

32.1.7 Channel cross-sections

A large fraction of the cross-section in individual channels involving meson nucleon scattering can be modeled as resonance excitation in the s-channel. This kind of interactions show a resonance structure in the energy dependency of the cross-section, and can be modeled using the Breit-Wigner function

$$\sigma_{res}(\sqrt{s}) = \sum_{FS} \frac{2J+1}{(2S_1+1)(2S_2+1)} \frac{\pi}{k^2} \frac{\Gamma_I S \Gamma_F S}{(\sqrt{s}-M_R)^2 + \Gamma/4},$$

Where $S1$ and $S2$ are the spins of the two fusing particles, J is the spin of the resonance, $\sqrt{(}s)$ the energy in the center of mass system, k the momentum of the fusing particles in the center of mass system, $\Gamma_I S$ and $\Gamma)FS$ the partial width of the resonance for the initial and final state respectively. M_R is the nominal mass of the resonance.

The initial states included in the model are pion and kaon nucleon scattering. The product resonances taken into account are the Delta resonances with masses 1232, 1600, 1620, 1700, 1900, 1905, 1910, 1920, 1930, and 1950 MeV, the excited nucleons with masses of 1440, 1520, 1535, 1650, 1675, 1680, 1700, 1710, 1720, 1900, 1990, 2090, 2190, 2220, and 2250 MeV, the Lambda, and its excited states at 1520, 1600, 1670, 1690, 1800, 1810, 1820, 1830, 1890, 2100, and 2110 MeV, and the Sigma and its excited states at 1660, 1670, 1750, 1775, 1915, 1940, and 2030 MeV.

32.1.8 Mass dependent resonance width and partial width

During the cascading, the resonances produced are assigned reall masses, with values distributed according to the production cross-section described above. The concrete (rather than nominal) masses of these resonances may be small compared to the PDG value, and this implies that some channels may not be open for decay. In general it means, that the partial and total width will depend on the concrete mass of the resonance. We are using the UrQMD[13][14] approach for calculating these actual width,

$$\Gamma_{R\to 12}(M) = (1+r)\frac{\Gamma_{R\to 12}(M_R)}{p(M_R)^{(2l+1)}}\frac{M_R}{M}\frac{p(M)^{(2l+1)}}{1+r(p(M)/p(M_R))^{2l}}. \tag{32.8}$$

Here M_R is the nominal mass of the resonance, M the actual mass, p is the momentum in the center of mass system of the particles, L the angular momentum of the final state, and r=0.2.

32.1.9 Resonance production cross-section in the t-channel

In resonance production in the t-channel, single and double resonance excitation in nucleon-nucleon collisions are taken into account. The resonance production cross-sections are as much as possible based on parametrizations of experimental data[15] for proton proton scattering. The basic formula used is motivated from the form of the exclusive production cross-section of the Δ_{1232} in proton proton collisions:

$$\sigma_{AB} = 2\alpha_{AB}\beta_{AB}\frac{\sqrt{s}-\sqrt{s_0}}{(\sqrt{s}-\sqrt{s_0})^2+\beta_{AB}^2}\left(\frac{\sqrt{s0}+\beta_{AB}}{\sqrt{s}}\right)^{\gamma_{AB}}$$

The parameters of the description for the various channels are given in table32.1. For all other channels, the parametrizations were derived from these by adjusting the threshold behavior.

The reminder of the cross-section are derived from these, applying detailed balance. Iso-spin invariance is assumed. The formalism used to apply detailed balance is

$$\sigma(cd\to ab) = \sum_{J,M}\frac{\langle j_c m_c j_d m_d \parallel JM\rangle^2}{\langle j_a m_a j_b m_b \parallel JM\rangle^2}\frac{(2S_a+1)(2S_b+1)}{(2S_c+1)(2S_d+1)}\frac{\langle p_{ab}^2\rangle}{\langle p_{cd}^2\rangle}\sigma(ab\to cd) \tag{32.9}$$

Reaction	α	β	γ
$pp \rightarrow p\Delta_{1232}$	25 mbarn	0.4 GeV	3
$pp \rightarrow \Delta_{1232}\Delta_{1232}$	1.5 mbarn	1 GeV	1
$pp \rightarrow pp^*$	0.55 mbarn	1 GeV	1
$pp \rightarrow p\Delta_*$	0.4 mbarn	1 GeV	1
$pp \rightarrow \Delta_{1232}\Delta^*$	0.35 mbarn	1 GeV	1
$pp \rightarrow \Delta_{1232}N^*$	0.55 mbarn	1 GeV	1

Table 32.1: Values of the parameters of the cross-section formula for the individual channels.

32.1.10 Nucleon Nucleon elastic collisions

Angular distributions for elastic scattering of nucleons are taken as closely as possible from experimental data, i.e. from the result of phase-shift analysis. They are derived from differential cross sections obtained from the SAID database, R. Arndt, 1998.

Final states are derived by sampling from tables of the cumulative distribution function of the centre-of-mass scattering angle, tabulated for a discrete set of lab kinetic energies from 10 MeV to 1200 MeV. The CDF's are tabulated at 1 degree intervals and sampling is done using bi-linear interpolation in energy and CDF values. Coulomb effects are taken into consideration for pp scattering.

32.1.11 Generation of transverse momentum

Angular distributions for final states other than nucleon elastic scattering are calculated analytically, derived from the collision term of the in-medium relativistic Boltzmann-Uehling-Uhlenbeck equation, absed on the nucleon nucleon elastic scattering cross-sections:

$$\sigma_{NN\rightarrow NN}(s,t) = \frac{1}{(2\pi)^2 s}\left(D(s,t) + E(s,t) + (invertedt, u)\right)$$

Here s, t, u are the Mandelstamm variables, $D(s,t)$ is the direct term, and $E(s,t)$ is the exchange term, with

$$D(s,t) = \frac{(g^{\sigma}_{NN})^4(t-4m^{*}2)^2}{2(t-m^2_{\sigma})^2} + \frac{(g^{\omega}_{NN})^4(2s^2+2st+t^2-8m^{*2}s+8m^{*4})}{(t-m^2_{\omega})^2} + \frac{24(g^{\pi}_{NN})^4 m^{*2}t^2}{(t-m^2_{\pi})^2} - \frac{4(g^{\sigma}_{NN}g^{\omega}_{NN})^2(2s+t-4m^{*2})m^{*2}}{(t-m^2_{\sigma})(t-m^2_{\omega})},$$

and

$$E(s,t) = \frac{(g^{\sigma}_{NN})^4\big(t(t+s)+4m^{*2}(s-t)\big)}{8(t-m^2_{\sigma})(u-m^2_{\sigma})} + \frac{(g^{\omega}_{NN})^4(s-2m^{*2})(s-6m^{*2}))}{2(t-m^2_{\omega})(u-m^2_{\omega})} - \frac{6(g^{\pi}_{NN})^4(4m^{*2}-s-t)m^{*4}t}{(t-m^2_{\pi})(u=m_p i^2)} + \frac{3(g^{\sigma}_{NN}g^{\pi}_{NN})^2m^{*2}(4m^{*2}-s-t)(4m^{*2}-t)}{(t-m^2_{\sigma})(u-m^2_{\pi})} + \frac{3(g^{\sigma}_{NN}g^{\pi}_{NN})^2t(t+s)m^{*2}}{2(t-m^2_{\pi})(u-m^2_{\sigma})} + \frac{(g^{\sigma}_{NN}g^{\omega}_{NN})^2t^2-4m^{*2}s-10m^{*2}t+24m^{*4}}{4(t-m^2_{\sigma})(u-m^2_{\omega})} + \frac{(g^{\sigma}_{NN}g^{\omega}_{NN})^2(t+s)^2-2m^{*2}s+2m^{*2}t}{4(t-m^2_{\omega})(u-m^2_{\sigma})} + \frac{3(g^{\omega}_{NN}g^{\pi}_{NN})^2(t+s-4m^{*2})(t+s-2m^{*2})}{(t-m^2_{\omega})(u-m^2_{\pi})} + \frac{3(g^{\omega}_{NN}g^{\pi}_{NN})^2m^{*2}(t^2-2m^{*2}t)}{(t-m^2_{\pi})(u-m^2_{\omega})}. \quad (32.10)$$

(32.11)

Here, in this first release, the in-medium mass was set to the free mass, and the nucleon nucleon coupling constants used were 1.434 for the π, 7.54 for the ω, and 6.9 for the σ. This formula was used for elementary hadron-nucleon differential cross-sections by scaling teh center of mass energy squared accordingly.

Finite size effects were taken into account at the meson nucleon vertex, using a phenomenological form factor (cut-off) at each vertex.

32.1.12 Decay

In the simulation of decay of strong resonances, we use the nominal decay branching ratios from the particle data book. The stochastic mass of a individual resonance created is sampled at creation time from the Breit-Wigner form, under the mass constraints posed by center of mass energy of the scattering, and the mass in the lightest decay channel. The decay width from the particle data book are then adjusted according to equation 32.8, to take the stochastic mass value into account.

All decay channels with nominal branching ratios greater than 1% are simulated.

32.1.13 The escaping particle and coherent effects

When a nucleon other than the incident particle leaves the nucleus, the ground state of the nucleus changes. The energy of the outgoing particle cannot be such that the total mass of the new nucleus would be below its ground state mass. To avoid this, we reduce the energy of an outgoing nucleons by the mass-difference of old and new nucleus.

Furthermore, the momentum of the final exited nucleus derived from energy momentum balance may be such that its mass is below its ground

state mass. In this case, we arbitrarily scale the momenta of all outgoing particles by a factor derived from the mass of the nucleus and the mass of the system of outgoing particles.

32.1.14 Light ion reactions

In simulating light ion reactions, the initial state of the cascade is prepared in the form of two nuclei, as described in the above section on the nuclear model.

The lighter of the collision partners is selected to be the projectile. The nucleons in the projectile are then entered, with position and momenta, into the initial state of the cascade. Note that before the first scattering of an individual nucleon, a projectile nucleon's Fermi-momentum is not taken into account in the tracking inside the target nucleus. The nucleon distribution inside the projectile nucleus is taken to be a representative distribution of its nucleons in configuration space, rather than an initial state in the sense of QMD. The Fermi momentum and the local field are taken into account in the calculation of the collision probabilities and final states of the binary collisions.

32.1.15 Transition to pre-compound modeling

Eventually, the cascade assumptions will break down at low energies, and the state of affairs has to be treated by means of evaporation and pre-equilibrium decay. This transition is not at present studied in depth, and an interesting approach which uses the tracking time, as in the Liege cascade code, remains to be studied in our context.

For this first release, the following algorithm is used to determine when cascading is stopped, and pre-equilibrium decay is called: As long as there are still particles above the kinetic energy threshold (75 MeV), cascading will continue. Otherwise, when the mean kinetic energy of the participants has dropped below a second threshold (15 MeV), the cascading is stopped.

The residual participants, and the nucleus in its current state are then used to define the initial state, i.e. excitation energy, number of excitons, number of holes, and momentum of the exciton system, for pre-equilibrium decay.

In the case of light ion reactions, the projectile excitation is determined from the binary collision participants (P) using the statistical approach towards excitation energy calculation in an adiabatic abrasion process, as de-

scribed in [12]:

$$E_{ex} = \sum_P (E^P_{fermi} - E^P)$$

Given this excitation energy, the projectile fragment is then treated by the evaporation models described previously.

32.1.16 Calculation of excitation energies and residuals

At the end of the cascade, we form a fragment for further treatment in precompound and nuclear de-excitation models ([16]).

These models need information about the nuclear fragment created by the cascade. The fragment is characterized by the number of nucleons in the fragment, the charge of the fragment, the number of holes, the number of all excitons, and the number of charged excitons, and the four momentum of the fragment.

The number of holes is given by the difference of the number of nucleons in the original nucleus and the number of non-excited nucleons left in the fragment. An exciton is a nucleon captured in the fragment at the end of the cascade.

The momentum of the fragment calculated by the difference between the momentum of the primary and the outgoing secondary particles must be split in two components. The first is the momentum acquired by coherent elastic effects, and the second is the momentum of the excitons in the nucleus rest frame. Only the later part is passed to the de-excitation models. Secondaries arising from de-excitation models, including the final nucleus, are transformed back the frame of the moving fragment.

32.2 Comparison with experiments

We add here a set of preliminary results produced with this code, focusing on neutron and pion production. Given that we are still in the process of writing up the paper, we apologize for the at release time still less then publication quality plots.

Bibliography

[1] J. Cugnon, C. Volant, S. Vuillier DAPNIA-SPHN-97-01, Dec 1996. 62pp. Submitted to Nucl.Phys.A,

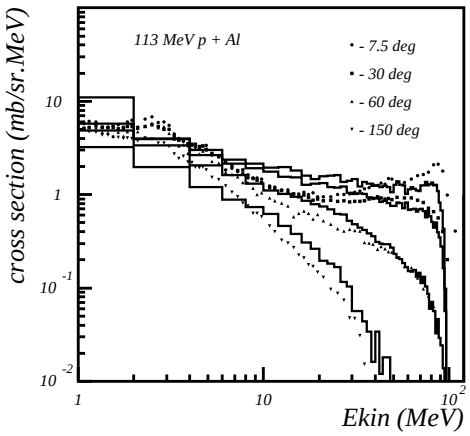

Figure 32.1: Double differential cross-section for neutrons produced in proton scattering off Aluminum. Proton incident energy was 113 MeV.

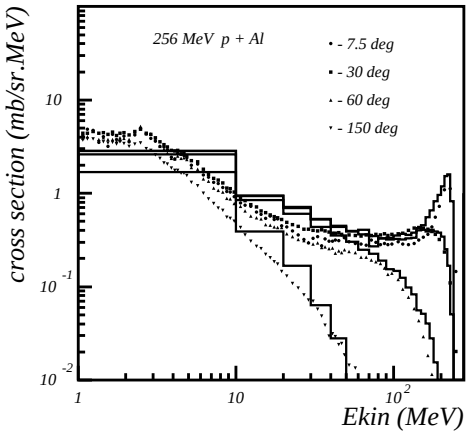

Figure 32.2: Double differential cross-section for neutrons produced in proton scattering off Aluminum. Proton incident energy was 256 MeV. The points are data, the histogram is Binary Cascade prediction.

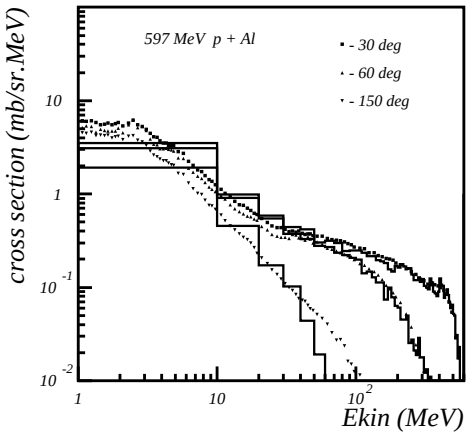

Figure 32.3: Double differential cross-section for neutrons produced in proton scattering off Aluminum. Proton incident energy was 597 MeV. The points are data, the histogram is Binary Cascade prediction.

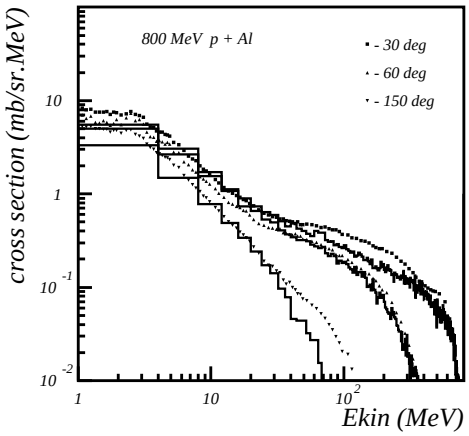

Figure 32.4: Double differential cross-section for neutrons produced in proton scattering off Aluminum. Proton incident energy was 800 MeV. The points are data, the histogram is Binary Cascade prediction.

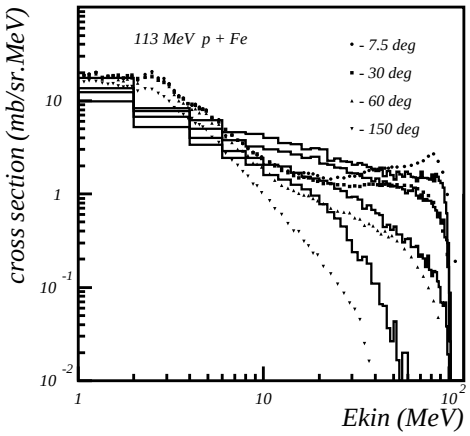

Figure 32.5: Double differential cross-section for neutrons produced in proton scattering off Iron. Proton incident energy was 113 MeV. The points are data, the histogram is Binary Cascade prediction.

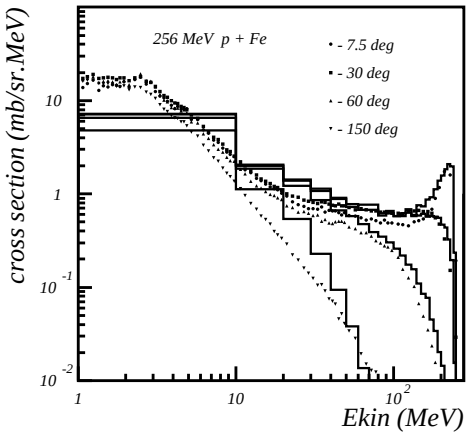

Figure 32.6: Double differential cross-section for neutrons produced in proton scattering off Iron. Proton incident energy was 256 MeV. The points are data, the histogram is Binary Cascade prediction.

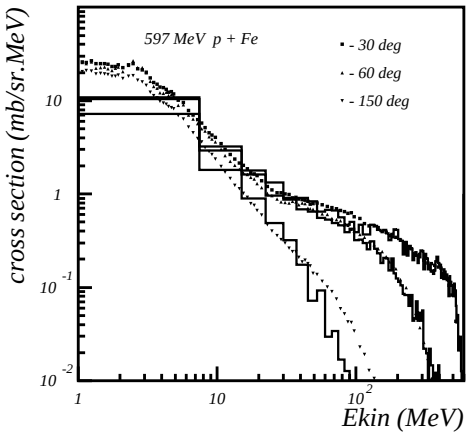

Figure 32.7: Double differential cross-section for neutrons produced in proton scattering off Iron. Proton incident energy was 597 MeV. The points are data, the histogram is Binary Cascade prediction.

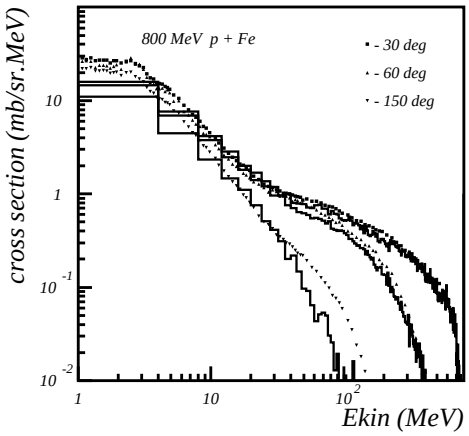

Figure 32.8: Double differential cross-section for neutrons produced in proton scattering off Iron. Proton incident energy was 800 MeV. The points are data, the histogram is Binary Cascade prediction.

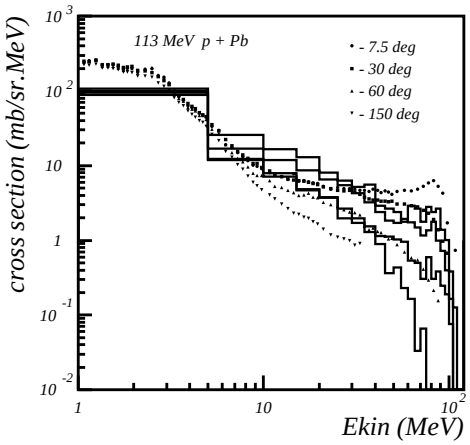

Figure 32.9: Double differential cross-section for neutrons produced in proton scattering off Lead. Proton incident energy was 113 MeV. The points are data, the histogram is Binary Cascade prediction.

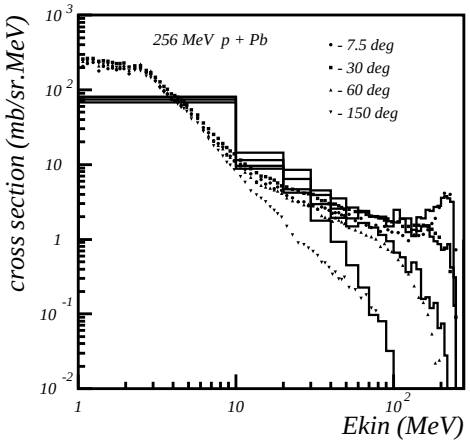

Figure 32.10: Double differential cross-section for neutrons produced in proton scattering off Lead. Proton incident energy was 256 MeV. The points are data, the histogram is Binary Cascade prediction.

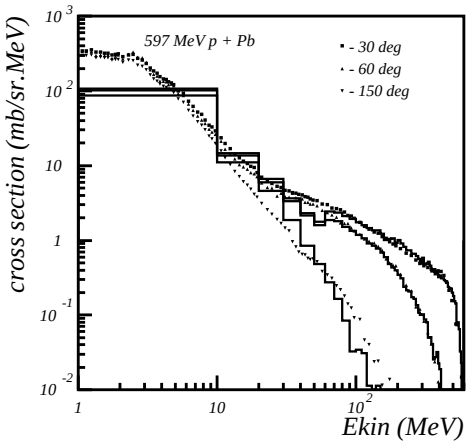

Figure 32.11: Double differential cross-section for neutrons produced in proton scattering off Lead. Proton incident energy was 597 MeV. The points are data, the histogram is Binary Cascade prediction.

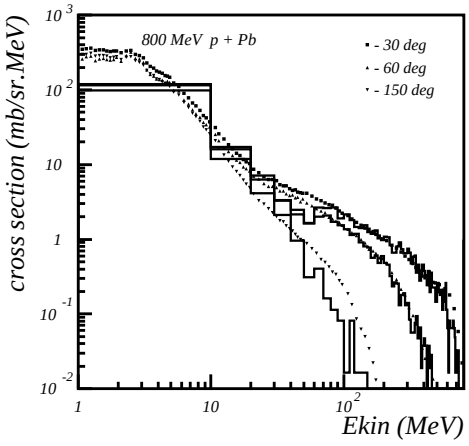

Figure 32.12: Double differential cross-section for neutrons produced in proton scattering off Lead. Proton incident energy was 800 MeV. The points are data, the histogram is Binary Cascade prediction.

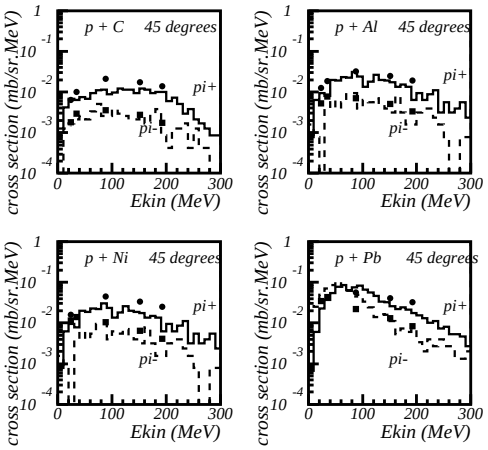

Figure 32.13: Double differential cross-section for pions produced at 45° in proton scattering off various materials. Proton incident energy was 597 MeV in each case. The points are data, the histogram is Binary Cascade prediction.

G. Peter, D. Behrens, C.C. Noack Phys.Rev. C49, 3253, (1994),
Hai-Qiao Wang, Xu Cai, Yong Liu High Energy Phys.Nucl.Phys. 16, 101, (1992),
A.S. Ilinov, A.B. Botvina, E.S. Golubeva, I.A. Pshenichnov, Sov. J. Nucl. Phys. 55, 734, (1992),
and citations therein.

[2] Grypeos M. E., Lalazissis G. A., Massen S. E., Panos C. P., J. Phys. **G17** 1093 (1991).

[3] Elton L. R. B., Nuclear Sizes, Oxford University Press, Oxford, 1961.

[4] DeShalit A., Feshbach H., Theoretical Nuclear Physics, Vol. 1: Nuclear Structure, Wyley, 1974.

[5] reference to be completed

[6] K. Stricker, H. McManus, J. A. Carr Nuclear scattering of low energy pions, Phys. Rev. C **19**, 929, (1979)

[7] M. M. Meier et al., Differential neutron production cross sections and neutron yields from stopping-length targets for 113-MeV protons, Nucl. Scien. Engin. **102**, 310, (1989)

[8] M. M. Meier et al., Differential neutron production cross sections for 256-MeV protons, Nucl. Scien. Engin. **110**, 289, (1992)

[9] W. B. Amian et al., Differential neutron production cross sections for 597-MeV protons, Nucl. Scien. Engin. **115**, 1, (1993)

[10] W. B. Amian et al., Differential neutron production cross sections for 800-MeV protons, Nucl. Scien. Engin. **112**, 78, (1992)

[11] J. F. Crawford et al., Measurement of cross sections and asymmetry parameters for the production of charged pions from various nuclei by 585-MeV protons, Phys. Rev. **C 22**, 1184, (1980)

[12] J. J. Gaimard and K. H. Schmidt, "A Reexamination of the abrasion - ablation model for the description of the nuclear fragmentation reaction," Nucl. Phys. A **531** (1991) 709.

[13] reference to be completed.

[14] reference to be completed

[15] reference to be completed

[16] reference to be completed

Chapter 33

Abrasion-ablation Model

33.1 Introduction

The abrasion model is a simplified macroscopic model for nuclear-nuclear interactions based largely on geometric arguments rather than detailed consideration of nucleon-nucleon collisions. As such the speed of the simulation is found to be faster than models such as G4BinaryCascade, but at the cost of accuracy. The version of the model implemented is interpreted from the so-called abrasion-ablation model described by Wilson *et al* [1],[2] together with an algorithm from Cucinotta to approximate the secondary nucleon energy spectrum [3]. By default, instead of performing an ablation process to simulate the de-excitation of the nuclear pre-fragments, the Geant4 implementation of the abrasion model makes use of existing and more detailed nuclear de-excitation models within Geant4 (G4Evaporation, G4FermiBreakup, G4StatMF) to perform this function (see section 33.5). However, in some cases cross sections for the production of fragments with large ΔA from the pre-abrasion nucleus are more accurately determined using a Geant4 implementation of the ablation model (see section 33.6).
The abrasion interaction is the initial fast process in which the overlap region between the projectile and target nuclei is sheered-off (see figure 33.1) The spectator nucleons in the projectile are assumed to undergo little change in momentum, and likewise for the spectators in the target nucleus. Some of the nucleons in the overlap region do suffer a change in momentum, and are assumed to be part of the original nucleus which then undergoes de-excitation.
Less central impacts give rise to an overlap region in which the nucleons can suffer significant momentum change, and zones in the projectile and target outside of the overlap where the nucleons are considered as spectators to the

initial energetic interaction.
The initial description of the interaction must, however, take into consideration changes in the direction of the projectile and target nuclei due to Coulomb effects, which can then modify the distance of closest approach compared with the initial impact parameter. Such effects can be important for low-energy collisions.

33.2 Initial nuclear dynamics and impact parameter

For low-energy collisions, we must consider the deflection of the nuclei as a result of the Coulomb force (see figure 33.2). Since the dynamics are non-relativistic, the motion is governed by the conservation of energy equation:

$$E_{tot} = \frac{1}{2}\mu\dot{r}^2 + \frac{l^2}{2\mu r^2} + \frac{Z_P Z_T e^2}{r} \tag{33.1}$$

where:

E_{tot} = total energy in the centre of mass frame;
r,$\dot{r}$ = distance between nuclei, and rate of change of distance;
l = angular momentum;
μ = reduced mass of system *i.e.* $m_1 m_2/(m_1 + m_2)$;
e = electric charge (units dependent upon the units for E_{tot} and r);
Z_P, Z_T = charge numbers for the projectile and target nuclei.

The angular momentum is based on the impact parameter between the nuclei when their separation is large, *i.e.*

$$E_{tot} = \frac{1}{2}\frac{l^2}{\mu b^2} \;\Rightarrow\; l^2 = 2E_{tot}\mu b^2 \tag{33.2}$$

At the point of closest approach, $\dot{r}$=0, therefore:

$$\begin{aligned} E_{tot} &= \tfrac{E_{tot}b^2}{r^2} + \tfrac{Z_P Z_T e^2}{r} \\ r^2 &= b^2 + \tfrac{Z_P Z_T e^2}{E_{tot}} r \end{aligned} \tag{33.3}$$

Rearranging this equation results in the expression:

$$b^2 = r(r - r_m) \tag{33.4}$$

where:

$$r_m = \frac{Z_P Z_T e^2}{E_{tot}} \tag{33.5}$$

In the implementation of the abrasion process in Geant4, the square of the far-field impact parameter, b, is sampled uniformly subject to the distance of closest approach, r, being no greater than $r_P + r_T$ (the sum of the projectile and target nuclear radii).

33.3 Abrasion process

In the abrasion process, as implemented by Wilson *et al* [1] it is assumed that the nuclear density for the projectile is constant up to the radius of the projectile (r_P) and zero outside. This is also assumed to be the case for the target nucleus. The amount of nuclear material abraded from the projectile is given by the expression:

$$\Delta_{abr} = FA_P \left[1 - \exp\left(-\frac{C_T}{\lambda}\right)\right] \tag{33.6}$$

where F is the fraction of the projectile in the interaction zone, λ is the nuclear mean-free-path, assumed to be:

$$\lambda = \frac{16.6}{E^{0.26}} \tag{33.7}$$

E is the energy of the projectile in MeV/nucleon and C_T is the chord-length at the position in the target nucleus for which the interaction probability is maximum. For cases where the radius of the target nucleus is greater than that of the projectile (*i.e.* $r_T > r_P$):

$$C_T = \begin{cases} 2\sqrt{r_T^2 - x^2} & : x > 0 \\ 2\sqrt{r_T^2 - r^2} & : x \leq 0 \end{cases} \tag{33.8}$$

where:

$$x = \frac{r_P^2 + r^2 - r_T^2}{2r} \tag{33.9}$$

In the event that $r_P > r_T$ then C_T is:

$$C_T = \begin{cases} 2\sqrt{r_T^2 - x^2} & : x > 0 \\ 2r_T & : x \leq 0 \end{cases} \tag{33.10}$$

where:

$$x = \frac{r_T^2 + r^2 - r_P^2}{2r} \tag{33.11}$$

The projectile and target nuclear radii are given by the expression:

$$
\begin{aligned}
r_P &\approx 1.29\sqrt{r^2_{RMS,P} - 0.84^2} \\
r_T &\approx 1.29\sqrt{r^2_{RMS,T} - 0.84^2}
\end{aligned}
\tag{33.12}
$$

The excitation energy of the nuclear fragment formed by the spectators in the projectile is assumed to be determined by the excess surface area, given by:

$$
\Delta S = 4\pi r_P^2 \left[1 + P - (1 - F)^{2/3}\right] \tag{33.13}
$$

where the functions P and F are given in section 33.7. Wilson *et al* equate this surface area to the excitation to:

$$
E_S = 0.95\Delta S \tag{33.14}
$$

if the collision is peripheral and there is no significant distortion of the nucleus, or

$$
\begin{aligned}
E_S &= 0.95\left\{1 + 5F + \Omega F^3\right\}\Delta S \\
\Omega &= \begin{cases} 0 & : A_P > 16 \\ 1500 & : A_P < 12 \\ 1500 - 320\,(A_P - 12) & : 12 \leq A_P \leq 16 \end{cases}
\end{aligned}
\tag{33.15}
$$

if the impact separation is such that $r << r_P + r_T$. E_S is in MeV provided ΔS is in fm^2.

For the abraded region, Wilson *et al* assume that fragments with a nucleon number of five are unbounded, 90% of fragments with a nucleon number of eight are unbound, and 50% of fragments with a nucleon number of nine are unbound. This was not implemented within the Geant4 version of the abrasion model, and disintegration of the pre-fragment was only simulated by the subsequent de-excitation physics models in the G4DeexcitationHandler (evaporation, *etc.* or G4WilsonAblationModel) since the yields of lighter fragments were already underestimated compared with experiment.

In addition to energy as a result of the distortion of the fragment, some energy is assumed to be gained from transfer of kinetic energy across the boundaries of the nuclei. This is approximated to the average energy transferred to a nucleon per unit intersection pathlength (assumed to be 13 MeV/fm) and the longest chord-length, C_l, and for half of the nucleon-nucleon collisions it is assumed that the excitation energy is:

$$
E^*_X = \begin{cases} 13 \cdot \left[1 + \frac{C_t - 1.5}{3}\right] C_l & : C_t > 1.5\text{fm} \\ 13 \cdot \mathrm{C}_l & : C_t \leq 1.5\text{fm} \end{cases}
\tag{33.16}
$$

where:

$$C_l = \begin{cases} 2\sqrt{r_P^2 + 2rr_T - r^2 - r_T^2} & r > r_T \\ 2r_P & r \leq r_T \end{cases} \tag{33.17}$$

$$C_t = 2\sqrt{r_P^2 - \frac{\left(r_P^2 + r^2 - r_T^2\right)^2}{4r^2}} \tag{33.18}$$

For the remaining events, the projectile energy is assumed to be unchanged. Wilson *et al* assume that the energy required to remove a nucleon is 10MeV, therefore the number of nucleons removed from the projectile by ablation is:

$$\Delta_{abl} = \frac{E_S + E_X}{10} + \Delta_{spc} \tag{33.19}$$

where Δ_{spc} is the number of loosely-bound spectators in the interaction region, given by:

$$\Delta_{spc} = A_P F \exp\left(-\frac{C_T}{\lambda}\right) \tag{33.20}$$

Wilson *et al* appear to assume that for half of the events the excitation energy is transferred into one of the nuclei (projectile or target), otherwise the energy is transferred in to the other (target or projectile respectively). The abrasion process is assumed to occur without preference for the nucleon type, *i.e.* the probability of a proton being abraded from the projectile is proportional to the fraction of protons in the original projectile, therefore:

$$\Delta Z_{abr} = \Delta_{abr} \frac{Z_P}{A_P} \tag{33.21}$$

In order to calculate the charge distribution of the final fragment, Wilson *et al* assume that the products of the interaction lie near to nuclear stability and therefore can be sampled according to the Rudstam equation (see section 33.6). The other obvious condition is that the total charge must remain unchanged.

33.4 Abraded nucleon spectrum

Cucinotta has examined different formulae to represent the secondary protons spectrum from heavy ion collisions [3]. One of the models (which has been implemented to define the final state of the abrasion process) represents the momentum distribution of the secondaries as:

$$\psi(p) \propto \sum_{i=1}^{3} C_i \exp\left(-\frac{p^2}{2p_i^2}\right) + d_0 \frac{\gamma p}{\sinh(\gamma p)} \tag{33.22}$$

where:

$\psi(p)$ = number of secondary protons with momentum p per unit of momentum phase space [c^3/MeV^3];

p = magnitude of the proton momentum in the rest frame of the nucleus from which the particle is projected [MeV/c];

$C1$, $C2$, $C3$ = 1.0, 0.03, and 0.0002;

$p1$, $p2$, $p3$ = $\sqrt{\frac{2}{5}}p_F$, $\sqrt{\frac{6}{5}}p_F$, 500 [MeV/c]

p_F = Momentum of nucleons in the nuclei at the Fermi surface [MeV/c]

d_0 = 0.1

$\frac{1}{\gamma}$ = 90 [MeV/c];

G4WilsonAbrasionModel approximates the momentum distribution for the neutrons to that of the protons, and as mentioned above, the nucleon type sampled is proportional to the fraction of protons or neutrons in the original nucleus.

The angular distribution of the abraded nucleons is assumed to be isotropic in the frame of reference of the nucleus, and therefore those particles from the projectile are Lorentz-boosted according to the initial projectile momentum.

33.5 De-excitation of the projectile and target nuclear pre-fragments by standard Geant4 de-excitation physics

Unless specified otherwise, G4WilsonAbrasionModel will instantiate the following de-excitation models to treat subsequent particle emission of the excited nuclear pre-fragments (from both the projectile and the target):

1 G4Evaporation, which will perform nuclear evaporation of (α-particles, ^{3}He, ^{3}H, ^{2}H, protons and neutrons, in competition with photo-evaporation and nuclear fission (if the nucleus has sufficiently high A).

2 G4FermiBreakUp, for nuclei with $A \leq 12$ and $Z \leq 6$.

3 G4StatMF, for multi-fragmentation of the nucleus (minimum energy for this process set to 5 MeV).

As an alternative to using this de-excitation scheme, the user may provide to the G4WilsonAbrasionModel a pointer to her own de-excitation handler, or invoke instantiation of the ablation model (G4WilsonAblationModel).

33.6 De-excitation of the projectile and target nuclear pre-fragments by nuclear ablation

A nuclear ablation model, based largely on the description provided by Wilson *et al* [1], has been developed to provide a better approximation for the final nuclear fragment from an abrasion interaction. The algorithm implemented in G4WilsonAblationModel uses the same approach for selecting the final-state nucleus as NUCFRG2 and determining the particles evaporated from the pre-fragment in order to achieve that state. However, use is also made of classes in Geant4's evaporation physics to determine the energies of the nuclear fragments produced.
The number of nucleons ablated from the nuclear pre-fragment (whether as nucleons or light nuclear fragments) is determined based on the average binding energy, assumed by Wilson *et al* to be 10 MeV, *i.e.*:

$$A_{abl} = \begin{cases} Int\left(\frac{E_x}{10MeV}\right) & : A_{PF} > Int\left(\frac{E_x}{10MeV}\right) \\ A_{PF} & : otherwise \end{cases} \tag{33.23}$$

Obviously, the nucleon number of the final fragment, A_F, is then determined by the number of remaining nucleons. The proton number of the final nuclear fragment (Z_F) is sampled stochastically using the Rudstam equation:

$$\sigma(A_F, Z_F) \propto \exp\left(-R\left|Z_F - SA_F - TA_F^2\right|^{3/2}\right) \tag{33.24}$$

Here R=11.8/$AF^{0.45}$, S=0.486, and T=3.8·10^{-4}. Once Z_F and A_F have been calculated, the species of the ablated (evaporated) particles are determined again using Wilson's algorithm. The number of α-particles is determined first, on the basis that these have the greatest binding energy:

$$N_\alpha = \begin{cases} Int\left(\frac{Z_{abl}}{2}\right) & : Int\left(\frac{Z_{abl}}{2}\right) < Int\left(\frac{A_{abl}}{4}\right) \\ Int\left(\frac{A_{abl}}{4}\right) & : Int\left(\frac{Z_{abl}}{2}\right) \geq Int\left(\frac{A_{abl}}{4}\right) \end{cases} \tag{33.25}$$

Calculation of the other ablated nuclear/nucleon species is determined in a similar fashion in order of decreasing binding energy per nucleon of the ablated fragment, and subject to conservation of charge and nucleon number. Once the ablated particle species are determined, use is made of the Geant4 evaporation classes to sample the order in which the particles are ejected (from G4AlphaEvaporationProbability, G4He3EvaporationProbability, G4TritonEvaporationProb G4DeuteronEvaporationProbability, G4ProtonEvaporationProbability and G4NeutronEvaporatio

and the energies and momenta of the evaporated particle and the residual nucleus at each two-body decay (using G4AlphaEvaporationChannel, G4He3EvaporationChannel, G4TritonEvaporationChannel, G4DeuteronEvaporationChannel, G4ProtonEvaporationChannel and G4NeutronEvaporationChannel). If at any stage the probability for evaporation of any of the particles selected by the ablation process is zero, the evaporation is forced, but no significant momentum is imparted to the particle/nucleus. Note, however, that any particles ejected from the projectile will be Lorentz boosted depending upon the initial energy per nucleon of the projectile.

33.7 Definition of the functions P and F used in the abrasion model

In the first instance, the form of the functions P and F used in the abrasion model are dependent upon the relative radii of the projectile and target and the distance of closest approach of the nuclear centres. Four radius condtions are treated.

$\underline{r_T > r_P \textbf{ and } r_T - r_P \leq r \leq r_T + r_P}$:

$$P = 0.125\sqrt{\mu\nu}\left(\frac{1}{\mu} - 2\right)\left(\frac{1-\beta}{\nu}\right)^2 - 0.125\left[0.5\sqrt{\mu\nu}\left(\frac{1}{\mu} - 2\right) + 1\right]\left(\frac{1-\beta}{\nu}\right)^3 \tag{33.26}$$

$$F = 0.75\sqrt{\mu\nu}\left(\frac{1-\beta}{\nu}\right)^2 - 0.125\left[3\sqrt{\mu\nu} - 1\right]\left(\frac{1-\beta}{\nu}\right)^3 \tag{33.27}$$

where:

$$\nu = \frac{r_P}{r_P + r_T} \tag{33.28}$$

$$\beta = \frac{r}{r_P + r_T} \tag{33.29}$$

$$\mu = \frac{r_T}{r_P} \tag{33.30}$$

$\underline{r_T > r_P \textbf{ and } r < r_T - r_P}$:

$$P = -1 \tag{33.31}$$

$$F = 1 \tag{33.32}$$

$\underline{r_P > r_T \textbf{ and } r_P - r_T \leq r \leq r_P + r_T}$:

$$P = 0.125\sqrt{\mu\nu}\left(\frac{1}{\mu} - 2\right)\left(\frac{1-\beta}{\nu}\right)^2 \tag{33.33}$$

$$- 0.125\left\{0.5\sqrt{\frac{\nu}{\mu}}\left(\frac{1}{\mu} - 2\right) - \left[\frac{\sqrt{1-\mu^2}}{\nu} - 1\right]\sqrt{\frac{2-\mu}{\mu^5}}\right\}\left(\frac{1-\beta}{\nu}\right)^3$$

$$F = 0.75\sqrt{\mu\nu}\left(\frac{1-\beta}{\nu}\right)^2 \tag{33.34}$$

$$- 0.125\left[3\sqrt{\frac{\nu}{\mu}} - \frac{\left[1-(1-\mu^2)^{3/2}\right]\sqrt{1-(1-\mu)^2}}{\mu^3}\right]\left(\frac{1-\beta}{\nu}\right)^3$$

$\underline{r_P > r_T \textbf{ and } r < r_T - r_P}$:

$$P = \left[\frac{\sqrt{1-\mu^2}}{\nu} - 1\right]\sqrt{1-\left(\frac{\beta}{\nu}\right)^2} \tag{33.35}$$

$$F = \left[1-\left(1-\mu^2\right)^{3/2}\right]\sqrt{1-\left(\frac{\beta}{\nu}\right)^2} \tag{33.36}$$

33.8 Status of this document

18.06.04 created by Peter Truscott

Bibliography

[1] J W Wilson, R K Tripathi, F A Cucinotta, J K Shinn, F F Badavi, S Y Chun, J W Norbury, C J Zeitlin, L Heilbronn, and J Miller, "NUCFRG2: An evaluation of the semiempirical nuclear fragmentation database," NASA Technical Paper 3533, 1995.

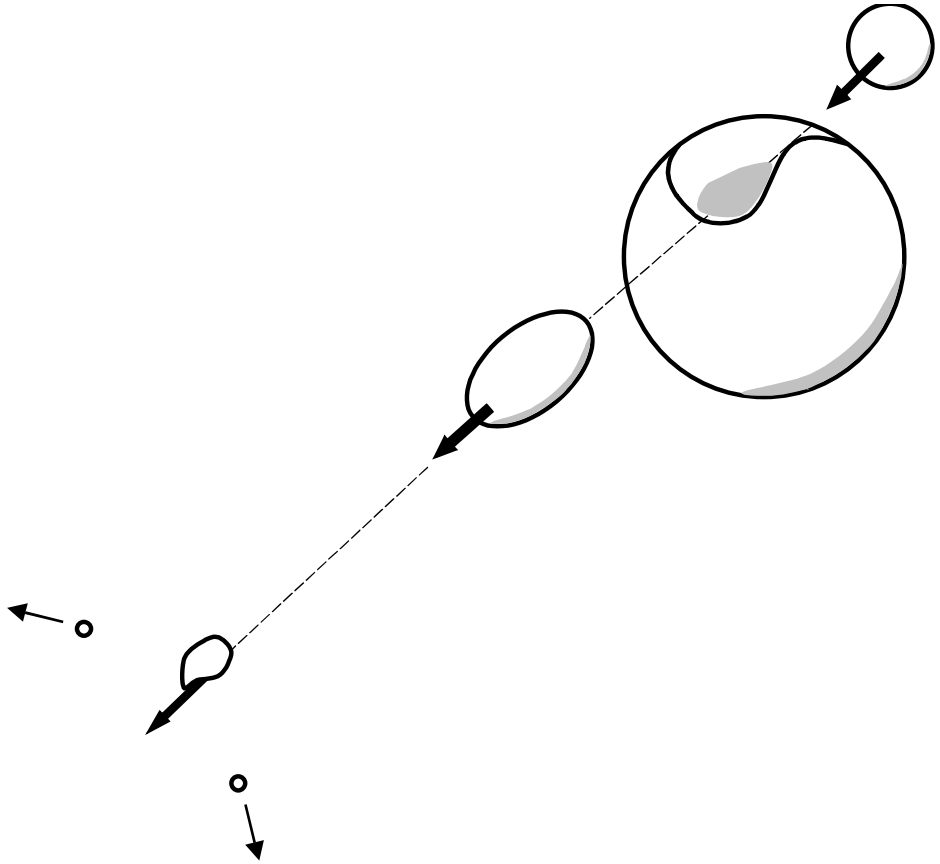

Figure 33.1: In the abrasion process, a fraction of the nucleons in the projectile and target nucleons interact to form a fireball region with a velocity between that of the projectile and the target. The remaining spectator nucleons in the projectile and target are not initially affected (although they do suffer change as a result of longer-term de-excitation).

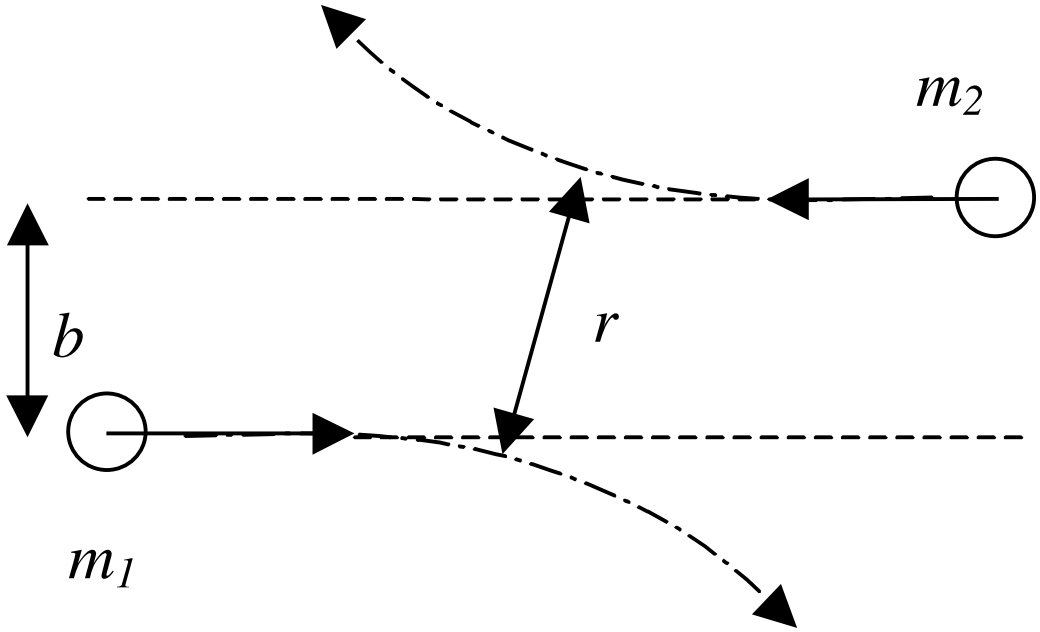

Figure 33.2: Illustration clarifying impact parameter in the far-field (b) and actual impact parameter (r).

[2] Lawrence W Townsend, John W Wilson, Ram K Tripathi, John W Norbury, Francis F Badavi, and Ferdou Khan, "HZEFRG1, An energy-dependent semiempirical nuclear fragmentation model," NASA Technical Paper 3310, 1993.

[3] Francis A Cucinotta, "Multiple-scattering model for inclusive proton production in heavy ion collisions," NASA Technical Paper 3470, 1994.

Chapter 34

Electromagnetic Dissociation Model

34.1 The Model

The relative motion of a projectile nucleus travelling at relativistic speeds with respect to another nucleus can give rise to an increasingly hard spectrum of virtual photons. The excitation energy associated with this energy exchange can result in the liberation of nucleons or heavier nuclei (*i.e.* deuterons, α-particles, *etc.*). The contribution of this source to the total inelastic cross section can be important, especially where the proton number of the nucleus is large. The electromagnetic dissociation (ED) model is implemented in the classes G4EMDissociation, G4EMDissociationCrossSection and G4EMDissociationSpectrum, with the theory taken from Wilson *et al* [1], and Bertulani and Baur [2].
The number of virtual photons $N(E_\gamma, b)$ per unit area and energy interval experienced by the projectile due to the dipole field of the target is given by the expression [2]:

$$N\left(E_\gamma, b\right) = \frac{\alpha Z_T^2}{\pi^2 \beta^2 b^2 E_\gamma} \left\{ x^2 k_1^2(x) + \left(\frac{x^2}{\gamma^2}\right) k_0^2(x) \right\} \tag{34.1}$$

where x is a dimensionless quantity defined as:

$$x = \frac{bE_\gamma}{\gamma\beta\bar{h}c} \tag{34.2}$$

and:

α = fine structure constant

β = ratio of the velocity of the projectile in the laboratory frame to the velocity of light

γ = Lorentz factor for the projectile in the laboratory frame
b = impact parameter
c = speed of light
$\bar{h}$ = quantum constant
E_γ = energy of virtual photon
k_0 and k_1 = zeroth and first order modified Bessel functions of the second kind
Z_T = atomic number of the target nucleus
Integrating Eq. 34.1 over the impact parameter from b_{min} to ∞ produces the virtual photon spectrum for the dipole field of:

$$N_{E1}\left(E_\gamma\right) = \frac{2\alpha Z_T^2}{\pi\beta^2 E_\gamma}\left\{\xi k_0(\xi)k_1(\xi) - \frac{\xi^2\beta^2}{2}\left(k_1^2(\xi) - k_0^2(\xi)\right)\right\} \tag{34.3}$$

where, according to the algorithm implemented by Wilson *et al* in NUCFRG2 [1]:

$$\begin{gathered}\xi = \frac{E_\gamma b_{\min}}{\gamma\beta\hbar c} \\ b_{\min} = (1+x_d)b_c + \frac{\pi\alpha_0}{2\gamma} \\ \alpha_0 = \frac{Z_P Z_T e^2}{\mu\beta^2 c^2} \\ b_c = 1.34\left[A_P^{1/3} + A_T^{1/3} - 0.75\left(A_P^{-1/3} + A_T^{-1/3}\right)\right]\end{gathered} \tag{34.4}$$

and μ is the reduced mass of the projectile/target system, $x_d = 0.25$, and A_P and A_T are the projectile and target nucleon numbers. For the last equation, the units of b_c are fm. Wilson *et al* state that there is an equivalent virtual photon spectrum as a result of the quadrupole field:

$$N_{E2}\left(E_\gamma\right) = \frac{2\alpha Z_T^2}{\pi\beta^4 E_\gamma}\left\{2\left(1-\beta^2\right)k_1^2(\xi) + \xi\left(2-\beta^2\right)^2 k_0(\xi)k_1(\xi) - \frac{\xi^2\beta^4}{2}\left(k_1^2(\xi) - k_0^2(\xi)\right)\right\} \tag{34.5}$$

The cross section for the interaction of the dipole and quadrupole fields is given by:

$$\sigma_{ED} = \int N_{E1}\left(E_\gamma\right)\sigma_{E1}\left(E_\gamma\right)dE_\gamma + \int N_{E2}\left(E_\gamma\right)\sigma_{E2}\left(E_\gamma\right)dE_\gamma \tag{34.6}$$

Wilson *et al* assume that $\sigma_{E1}(E_\gamma)$ and $\sigma_{E2}(E_\gamma)$ are sharply peaked at the giant dipole and quadrupole resonance energies:

$$\begin{aligned} E_{GDR} &= \bar{h}c\left[\frac{m^*c^2R_0^2}{8J}\left(1+u-\frac{1+\varepsilon+3u}{1+\varepsilon+u}\varepsilon\right)\right]^{-\frac{1}{2}} \\ E_{GQR} &= \frac{63}{A_P^{1/3}} \end{aligned} \tag{34.7}$$

so that the terms for N_{E1} and N_{E2} can be taken out of the integrals in Eq. 34.6 and evaluated at the resonances.
In Eq. 34.7:

$$\begin{aligned} u &= \frac{3J}{Q'}A_P^{-1/3} \\ R_0 &= r_0 A_P^{1/3} \end{aligned} \tag{34.8}$$

$\epsilon = 0.0768$, $Q' = 17$MeV, $J = 36.8$MeV, $r_0 = 1.18$fm, and m^* is 7/10 of the nucleon mass (taken as 938.95 MeV/c^2). (The dipole and quadrupole energies are expressed in units of MeV.)
The photonuclear cross sections for the dipole and quadrupole resonances are assumed to be given by:

$$\int \sigma_{E1}\left(E_\gamma\right) dE_\gamma = 60\frac{N_P Z_P}{A_P} \tag{34.9}$$

in units of MeV-mb (N_P being the number of neutrons in the projectile) and:

$$\int \sigma_{E2}\left(E_\gamma\right) \frac{dE_\gamma}{E_\gamma^2} = 0.22 f Z_P A_P^{2/3} \tag{34.10}$$

in units of μb/MeV. In the latter expression, f is given by:

$$f = \begin{cases} 0.9 & A_P > 100 \\ 0.6 & 40 < A_P \leq 100 \\ 0.3 & 40 \leq A_P \end{cases} \tag{34.11}$$

The total cross section for electromagnetic dissociation is therefore given by Eq. 34.6 with the virtual photon spectra for the dipole and quadrupole fields calculated at the resonances:

$$\sigma_{ED} = N_{E1}\left(E_{GDR}\right)\int \sigma_{E1}\left(E_\gamma\right) dE_\gamma + N_{E2}\left(E_{GQR}\right) E_{GQR}^2 \int \frac{\sigma_{E2}\left(E_\gamma\right)}{E_\gamma^2} dE_\gamma \tag{34.12}$$

where the resonance energies are given by Eq. 34.7 and the integrals for the photonuclear cross sections given by Eq. 34.9 and Eq. 34.10.
The selection of proton or neutron emission is made according to the following prescription from Wilson *et al.*

$$\begin{aligned} \sigma_{ED,p} &= \sigma_{ED} \times \left\{ \begin{array}{ll} 0.5 & Z_P < 6 \\ 0.6 & 6 \leq Z_P \leq 8 \\ 0.7 & 8 < Z_P < 14 \\ \min\left[\frac{Z_P}{A_P}, 1.95\exp(-0.075 Z_P)\right] & Z_P \geq 14 \end{array} \right\} \\ \sigma_{ED,n} &= \sigma_{ED} - \sigma_{ED,p} \end{aligned} \tag{34.13}$$

Note that this implementation of ED interactions only treats the ejection of single nucleons from the nucleus, and currently does not allow emission of other light nuclear fragments.

34.2 Status of this document

19.06.04 created by Peter Truscott

Bibliography

[1] J. W. Wilson, R. K. Tripathi, F. A. Cucinotta, J. K. Shinn, F. F. Badavi, S. Y. Chun, J. W. Norbury, C. J. Zeitlin, L. Heilbronn, and J. Miller, "NUCFRG2: An evaluation of the semiempirical nuclear fragmentation database," NASA Technical Paper 3533, 1995.

[2] C. A. Bertulani, and G. Baur, Electromagnetic processes in relativistic heavy ion collisions, Nucl Phys, A458, 725-744, 1986.

Chapter 35

Precompound model.

35.1 Reaction initial state.

The GEANT4 precompound model is considered as an extension of the hadron kinetic model. It gives a possibility to extend the low energy range of the hadron kinetic model for nucleon-nucleus inelastic collision and it provides a "smooth" transition from kinetic stage of reaction described by the hadron kinetic model to the equilibrium stage of reaction described by the equilibrium deexcitation models.

The initial information for calculation of pre-compound nuclear stage consists from the atomic mass number A, charge Z of residual nucleus, its four momentum P_0, excitation energy U and number of excitons n equals the sum of number of particles p (from them p_Z are charged) and number of holes h.

At the preequilibrium stage of reaction, we following the [1] approach, take into account all possible nuclear transition the number of excitons n with $\Delta n = +2, -2, 0$ [1], which defined by transition probabilities. Only emmision of neutrons, protons, deutrons, thritium and helium nuclei are taken into account.

35.2 Simulation of pre-compound reaction

The precompound stage of nuclear reaction is considered until nuclear system is not an equilibrium state. Further emission of nuclear fragments or photons from excited nucleus is simulated using an equilibrium model.

35.2.1 Statistical equilibrium condition

In the state of statistical equilibrium, which is characterized by an eqilibrium number of excitons n_{eq}, all three type of transitions are equiprobable. Thus n_{eq} is fixed by $\omega_{+2}(n_{eq}, U) = \omega_{-2}(n_{eq}, U)$. From this condition we can get

$$n_{eq} = \sqrt{2gU}. \tag{35.1}$$

35.2.2 Level density of excited (n-exciton) states

To obtain Eq. (35.1) it was assumed an equidistant scheme of single-particle levels with the density $g \approx 0.595aA$, where a is the level density parameter, when we have the level density of the n-exciton state as

$$\rho_n(U) = \frac{g(gU)^{n-1}}{p!h!(n-1)!}. \tag{35.2}$$

35.2.3 Transition probabilities

The partial transition probabilities changing the exciton number by Δn is determined by the squared matrix element averaged over allowed transitions $< |M|^2 >$ and the density of final states $\rho_{\Delta n}(n, U)$, which are really accessible in this transition. It can be defined as following:

$$\omega_{\Delta n}(n, U) = \frac{2\pi}{h} < |M|^2 > \rho_{\Delta n}(n, U). \tag{35.3}$$

The density of final states $\rho_{\Delta n}(n, U)$ were derived in paper [2] using the Eq. (35.2) for the level density of the n-exciton state and later corrected for the Pauli principle and indistinguishability of identical excitons in paper [3]:

$$\rho_{\Delta n=+2}(n, U) = \frac{1}{2}g\frac{[gU - F(p+1, h+1)]^2}{n+1}[\frac{gU - F(p+1, h+1)}{gU - F(p, h)}]^{n-1}, \tag{35.4}$$

$$\rho_{\Delta n=0}(n, U) = \frac{1}{2}g\frac{[gU - F(p, h)]}{n}[p(p-1) + 4ph + h(h-1)] \tag{35.5}$$

and

$$\rho_{\Delta n=-2}(n, U) = \frac{1}{2}gph(n-2), \tag{35.6}$$

where $F(p, h) = (p^2 + h^2 + p - h)/4 - h/2$ and it was taken to be equal zero. To avoid calculation of the averaged squared matrix element $< |M|^2 >$ it was assumed [1] that transition probability $\omega_{\Delta n=+2}(n, U)$ is the same as the

probability for quasi-free scattering of a nucleon above the Fermi level on a nucleon of the target nucleus, i. e.

$$\omega_{\Delta n=+2}(n,U) = \frac{< \sigma(v_{rel})v_{rel} >}{V_{int}}. \tag{35.7}$$

In Eq. (35.7) the interaction volume is estimated as $V_{int} = \frac{4}{3}\pi(2r_c + \lambda/2\pi)^3$, with the De Broglie wave length $\lambda/2\pi$ corresponding to the relative velocity $< v_{rel} >= \sqrt{2T_{rel}/m}$, where m is nucleon mass and $r_c = 0.6$ fm.

The averaging in $< \sigma(v_{rel})v_{rel} >$ is further simplified by

$$< \sigma(v_{rel})v_{rel} >=< \sigma(v_{rel}) >< v_{rel} > . \tag{35.8}$$

For $\sigma(v_{rel})$ we take approximation:

$$\sigma(v_{rel}) = 0.5[\sigma_{pp}(v_{rel}) + \sigma_{pn}(v_{rel}]P(T_F/T_{rel}), \tag{35.9}$$

where factor $P(T_F/T_{rel})$ was introduced to take into account the Pauli principle. It is given by

$$P(T_F/T_{rel}) = 1 - \frac{7}{5}\frac{T_F}{T_{rel}} \tag{35.10}$$

for $\frac{T_F}{T_{rel}} \leq 0.5$ and

$$P(T_F/T_{rel}) = 1 - \frac{7}{5}\frac{T_F}{T_{rel}} + \frac{2}{5}\frac{T_F}{T_{rel}}(2 - \frac{T_{rel}}{T_F})^{5/2} \tag{35.11}$$

for $\frac{T_F}{T_{rel}} > 0.5$.

The free-particle proton-proton $\sigma_{pp}(v_{rel})$ and proton-neutron $\sigma_{pn}(v_{rel})$ interaction cross sections are estimated using the equations [4]:

$$\sigma_{pp}(v_{rel}) = \frac{10.63}{v_{rel}^2} - \frac{29.93}{v_{rel}} + 42.9 \tag{35.12}$$

and

$$\sigma_{pn}(v_{rel}) = \frac{34.10}{v_{rel}^2} - \frac{82.2}{v_{rel}} + 82.2, \tag{35.13}$$

where cross sections are given in mbarn.

The mean relative kinetic energy T_{rel} is needed to calculate $< v_{rel} >$ and the factor $P(T_F/T_{rel})$ was computed as $T_{rel} = T_p + T_n$, where mean kinetic energies of projectile nucleons $T_p = T_F + U/n$ and target nucleons $T_N = 3T_F/5$, respecively.

Combining Eqs. (35.3) - (35.7) and assuming that $< |M|^2 >$ are the same for transitions with $\Delta n = 0$ and $\Delta n = \pm 2$ we obtain for another transition probabilities:

$$\omega_{\Delta n=0}(n,U) = \\ = \frac{<\sigma(v_{rel})v_{rel}>}{V_{int}} \frac{n+1}{n} [\frac{gU-F(p,h)}{gU-F(p+1,h+1)}]^{n+1} \frac{p(p-1)+4ph+h(h-1)}{gU-F(p,h)} \tag{35.14}$$

and

$$\omega_{\Delta n=-2}(n,U) = \\ = \frac{<\sigma(v_{rel})v_{rel}>}{V_{int}} [\frac{gU-F(p,h)}{gU-F(p+1,h+1)}]^{n+1} \frac{ph(n+1)(n-2)}{[gU-F(p,h)]^2}. \tag{35.15}$$

35.2.4 Emission probabilities for nucleons

Emission process probability has been choosen similar as in the classical equilibrium Weisskopf-Ewing model [5]. Probability to emit nucleon b in the energy interval $(T_b, T_b + dT_b)$ is given

$$W_b(n,U,T_b) = \sigma_b(T_b) \frac{(2s_b+1)\mu_b}{\pi^2 h^3} R_b(p,h) \frac{\rho_{n-b}(E^*)}{\rho_n(U)} T_b, \tag{35.16}$$

where $\sigma_b(T_b)$ is the inverse (absorption of nucleon b) reaction cross section, s_b and m_b are nucleon spin and reduced mass, the factor $R_b(p,h)$ takes into account the condition for the exciton to be a proton or neutron, $\rho_{n-b}(E^*)$ and $\rho_n(U)$ are level densities of nucleus after and before nucleon emission are defined in the evaporation model, respectively and $E^* = U - Q_b - T_b$ is the excitation energy of nucleus after fragment emission.

35.2.5 Emission probabilities for complex fragments

It was assumed [1] that nucleons inside excited nucleus are able to "condense" forming complex fragment. The "condensation" probability to create fragment consisting from N_b nucleons inside nucleus with A nucleons is given by

$$\gamma_{N_b} = N_b^3 (V_b/V)^{N_b-1} = N_b^3 (N_b/A)^{N_b-1}, \tag{35.17}$$

where V_b and V are fragment b and nucleus volumes, respectively. The last equation was estimated [1] as the overlap integral of (constant inside a volume) wave function of independent nucleons with that of the fragment.

During the prequilibrium stage a "condense" fragment can be emitted. The probability to emit a fragment can be written as [1]

$$W_b(n,U,T_b) = \gamma_{N_b} R_b(p,h) \frac{\rho(N_b,0,T_b+Q_b)}{g_b(T_b)} \sigma_b(T_b) \frac{(2s_b+1)\mu_b}{\pi^2 h^3} \frac{\rho_{n-b}(E^*)}{\rho_n(U)} T_b, \tag{35.18}$$

where

$$g_b(T_b) = \frac{V_b(2s_b+1)(2\mu_b)^{3/2}}{4\pi^2 h^3}(T_b+Q_b)^{1/2} \tag{35.19}$$

is the single-particle density for complex fragment b, which is obtained by assuming that complex fragment moves inside volume V_b in the uniform potential well whose depth is equal to be Q_b, and the factor $R_b(p,h)$ garantees correct isotopic composition of a fragment b.

35.2.6 The total probability

This probability is defined as

$$W_{tot}(n,U) = \sum_{\Delta n=+2,0,-2} \omega_{\Delta n}(n,U) + \sum_{b=1}^{6} W_b(n,U), \tag{35.20}$$

where total emission $W_b(n,U)$ probabilities to emit fragment b can be obtained from Eqs. (35.16) and (35.18) by integration over T_b:

$$W_b(n,U) = \int_{V_b}^{U-Q_b} W_b(n,U,T_b)dT_b. \tag{35.21}$$

35.2.7 Calculation of kinetic energies for emitted particle

The equations (35.16) and (35.18) are used to sample kinetic energies of emitted fragment.

35.2.8 Parameters of residual nucleus.

After fragment emission we update parameter of decaying nucleus:

$$\begin{gathered} A_f = A - A_b; Z_f = Z - Z_b; P_f = P_0 - p_b; \\ E_f^* = \sqrt{E_f^2 - \vec{P}_f^2} - M(A_f, Z_f). \end{gathered} \tag{35.22}$$

Here p_b is the evaporated fragment four momentum.

35.3 Status of this document

00.00.00 created by Vicente Lara

Bibliography

[1] K.K. Gudima, S.G. Mashnik, V.D. Toneev, Nucl. Phys. **A401** 329 (1983).

[2] F. C. Williams, Phys. Lett. **B31** 180 (1970).

[3] I. Ribanský, P. Obložinský, E. Bétaǩ, Nucl. Phys. **A205** 545 (1973).

[4] N. Metropolis *et al.*, Phys. Rev. **100** 185 (1958).

[5] V.E. Weisskopf, D.H. Ewing, Phys. Rev. 57 472 (1940).

Chapter 36

Evaporation Model

36.1 Introduction.

At the end of the pre-equilibrium stage, or a thermalizing process, the residual nucleus is supposed to be left in an equilibrium state, in which the excitation energy E^* is shared by a large number of nucleons. Such an equilibrated compound nucleus is characterized by its mass, charge and excitation energy with no further memory of the steps which led to its formation. If the excitation energy is higher than the separation energy, it can still eject nucleons and light fragments (d, t, ^{3}He, α). These constitute the low energy and most abundant part of the emitted particles in the rest system of the residual nucleus. The emission of particles by an excited compound nucleus has been successfully described by comparing the nucleus with the evaporation of molecules from a fluid [1]. The first statistical theory of compound nuclear decay is due to Weisskopf and Ewing[2].

36.2 Model description.

The Weisskopf treatment is an application of the detailed balance principle that relates the probabilities to go from a state i to another d and viceversa through the density of states in the two systems:

$$P_{i\to d}\rho(i) = P_{d\to i}\rho(d) \tag{36.1}$$

where $P_{d\to i}$ is the probability per unit of time of a nucleus d captures a particle j and form a compound nucleus i which is proportional to the compound nucleus cross section $\sigma_{\rm inv}$. Thus, the probability that a parent nucleus i with an excitation energy E^* emits a particle j in its ground state with kinetic

energy ε is

$$P_j(\varepsilon)\mathrm{d}\varepsilon = g_j\sigma_{\mathrm{inv}}(\varepsilon)\frac{\rho_d(E_{\max}-\varepsilon)}{\rho_i(E^*)}\varepsilon\mathrm{d}\varepsilon \tag{36.2}$$

where $\rho_i(E^*)$ is the level density of the evaporating nucleus, $\rho_d(E_{\max}-\varepsilon)$ that of the daugther (residual) nucleus after emission of a fragment j and $E_{\max}$ is the maximum energy that can be carried by the ejectile. With the spin s_j and the mass m_j of the emitted particle, g_j is expressed as $g_j = (2s_j+1)m_j/\pi^2\hbar^2$.

This formula must be implemented with a suitable form for the level density and inverse reaction cross section. We have followed, like many other implementations, the original work of Dostrovsky *et al.* [3] (which represents the first Monte Carlo code for the evaporation process) with slight modifications. The advantage of the Dostrovsky model is that it leds to a simple expression for equation 36.2 that can be analytically integrated and used for Monte Carlo sampling.

36.2.1 Cross sections for inverse reactions.

The cross section for inverse reaction is expressed by means of empirical equation [3]

$$\sigma_{\mathrm{inv}}(\varepsilon) = \sigma_g\alpha\left(1+\frac{\beta}{\varepsilon}\right) \tag{36.3}$$

where $\sigma_g = \pi R^2$ is the geometric cross section.

In the case of neutrons, $\alpha = 0.76 + 2.2A^{-\frac{1}{3}}$ and $\beta = (2.12A^{-\frac{2}{3}} - 0.050)/\alpha$ MeV. This equation gives a good agreement to those calculated from continuum theory [4] for intermediate nuclei down to $\varepsilon \sim 0.05$ MeV. For lower energies $\sigma_{\mathrm{inv},n}(\varepsilon)$ tends toward infinity, but this causes no difficulty because only the product $\sigma_{\mathrm{inv},n}(\varepsilon)\varepsilon$ enters in equation 36.2. It should be noted, that the inverse cross section needed in 36.2 is that between a neutron of kinetic energy ε and a nucleus in an excited state.

For charged particles (p, d, t, ^{3}He and α), $\alpha = (1 + c_j)$ and $\beta = -V_j$, where c_j is a set of parameters calculated by Shapiro [5] in order to provide a good fit to the continuum theory [4] cross sections and V_j is the Coulomb barrier.

36.2.2 Coulomb barriers.

Coulomb repulsion, as calculated from elementary electrostatics are not directly applicable to the computation of reaction barriers but must be corrected in several ways. The first correction is for the quantum mechanical

phenomenoon of barrier penetration. The proper quantum mechanical expressions for barrier penetration are far too complex to be used if one wishes to retain equation 36.2 in an integrable form. This can be approximately taken into account by multiplying the electrostatic Coulomb barrier by a coefficient k_j designed to reproduce the barrier penetration approximately whose values are tabulated [5].

$$V_j = k_j \frac{Z_j Z_d e^2}{R_c} \tag{36.4}$$

The second correction is for the separation of the centers of the nuclei at contact, R_c. We have computed this separation as $R_c = R_j + R_d$ where $R_{j,d} = r_c A_{j,d}^{1/3}$ and r_c is given [6] by

$$r_c = 2.173 \frac{1 + 0.006103 Z_j Z_d}{1 + 0.009443 Z_j Z_d} \tag{36.5}$$

36.2.3 Level densities.

The simplest and most widely used level density based on the Fermi gas model are those of Weisskopf [7] for a completely degenerate Fermi gas. We use this approach with the corrections for nucleon pairing proposed by Hurwitz and Bethe [8] which takes into account the displacements of the ground state:

$$\rho(E) = C \exp\left(2\sqrt{a(E-\delta)}\right) \tag{36.6}$$

where C is considered as constant and does not need to be specified since only ratios of level densities enter in equation 36.2. δ is the pairing energy correction of the daughter nucleus evaluated by Cook *et al.* [9] and Gilbert and Cameron [10] for those values not evaluated by Cook *et al.*. The level density parameter is calculated according to:

$$a(E, A, Z) = \tilde{a}(A) \left\{ 1 + \frac{\delta}{E}[1 - \exp(-\gamma E)] \right\} \tag{36.7}$$

and the parameters calculated by Iljinov *et al.* [11] and shell corrections of Truran, Cameron and Hilf [12].

36.2.4 Maximum energy available for evaporation.

The maximum energy avilable for the evaporation process (*i.e.* the maximum kinetic energy of the outgoing fragment) is usually computed like $E^* - \delta - Q_j$ where is the separation energy of the fragment j: $Q_j =$

$M_i - M_d - M_j$ and M_i, M_d and M_j are the nclear masses of the compound, residual and evporated nuclei respectively. However, that expression does not consider the recoil energy of the residual nucleus. In order to take into account the recoil energy we use the expression

$$\varepsilon_j^{\max} = \frac{(M_i + E^* - \delta)^2 + M_j^2 - M_d^2}{2(M_i + E^* - \delta)} - M_j \tag{36.8}$$

36.2.5 Total decay width.

The total decay width for evaporation of a fragment j can be obtained by integrating equation 36.2 over kinetic energy

$$\Gamma_j = \hbar \int_{V_j}^{\varepsilon_j^{\max}} P(\varepsilon_j) \mathrm{d}\varepsilon_j \tag{36.9}$$

This integration can be performed analiticaly if we use equation 36.6 for level densities and equation 36.3 for inverse reaction cross section. Thus, the total width is given by

$$\begin{aligned}\Gamma_j = \frac{g_j m_j R_d^2}{2\pi\hbar^2}\frac{\alpha}{a_d^2} \quad \times \quad & \left(\left\{ \left(\beta a_d - \frac{3}{2} \right) + a_d(\varepsilon_j^{\max} - V_j) \right\} \exp\left\{ -\sqrt{a_i(E^* - \delta_i)} \right\} + \right. \\ & \left\{ (2\beta a_d - 3)\sqrt{a_d(\varepsilon_j^{\max} - V_j)} + 2a_d(\varepsilon_j^{\max} - V_j) \right\} \times \\ & \left. \exp\left\{ 2\left[\sqrt{a_d(\varepsilon_j^{\max} - V_j)} - \sqrt{a_i(E^* - \delta_i)} \right] \right\} \right)\end{aligned} \tag{36.10}$$

where $a_d = a(A_d, Z_d, \varepsilon_j^{\max})$ and $a_i = a(A_i, Z_i, E^*)$.

36.3 GEM Model

As an alternative model we have implemented the generalized evaporation model (GEM) by Furihata [13]. This model considers emission of fragments heavier than α particles and uses a more accurate level density function for total decay width instead of the approximation used by Dostrovsky. We use the same set of parameters but for heavy ejectiles the parameters determined by Matsuse *et al.* [14] are used.

Based on the Fermi gas model, the level density function is expressed as

$$\rho(E) = \begin{cases} \frac{\sqrt{\pi}}{12}\frac{e^{2\sqrt{a(E-\delta)}}}{a^{1/4}(E-\delta)^{5/4}} & \text{for} \quad \mathrm{E} \geq \mathrm{E_x} \\ \frac{1}{T}e^{(E-E_0)/T} & \text{for} \quad \mathrm{E} < \mathrm{E_x} \end{cases} \tag{36.11}$$

where $E_x = U_x + \delta$ and $U_x = 150/M_d + 2.5$ (M_d is the mass of the daughter nucleus). Nuclear temperature T is given as $1/T = \sqrt{a/U_x} - 1.5U_x$, and E_0 is defined as $E_0 = E_x - T(\log T - \log a/4 - (5/4)\log U_x + 2\sqrt{aU_x})$.

By substituting equation 36.11 into equation 36.2 and integrating over kinetic energy can be obtained the following expression

$$\Gamma_j = \frac{\sqrt{\pi} g_j \pi R_d^2 \alpha}{12\rho(E^*)} \times \begin{cases} \{I_1(t,t) + (\beta + V) I_0(t)\} & \text{for} \quad \varepsilon_{\mathrm{j}}^{\max} - \mathrm{V_j} < \mathrm{E_x} \\ \{I_1(t,t_x) + I_3(s,s_x)e^s + \\ (\beta + V)(I_0(t_x) + I_2(s,s_x)e^s)\} & \text{for} \quad \varepsilon_{\mathrm{j}}^{\max} - \mathrm{V_j} \geq \mathrm{E_x}. \end{cases} \tag{36.12}$$

$I_0(t)$, $I_1(t,t_x)$, $I_2(s,s_x)$, and $I_3(s,s_x)$ are expressed as:

$$I_0(t) = e^{-E_0/T}(e^t - 1) \tag{36.13}$$

$$I_1(t,t_x) = e^{-E_0/T} T\{(t - t_x + 1)e^{t_x} - t - 1\} \tag{36.14}$$

$$\begin{aligned} I_2(s,s_x) = {} & 2\sqrt{2}\Big\{ s^{-3/2} + 1.5s^{-5/2} + 3.75s^{-7/2} - \\ & (s_x^{-3/2} + 1.5s_x^{-5/2} + 3.75s_x^{-7/2}) \Big\} \end{aligned} \tag{36.15}$$

$$\begin{aligned} I_3(s,s_x) = {} & \frac{1}{2\sqrt{2}} \Bigg[2s^{-1/2} + 4s^{-3/2} + 13.5s^{-5/2} + 60.0s^{-7/2} + \\ & 325.125s^{-9/2} - \Big\{ (s^2 - s_x^2)s_x^{-3/2} + (1.5s^2 + 0.5s_x^2)s_x^{-5/2} + \\ & (3.75s^2 + 0.25s_x^2)s_x^{-7/2} + (12.875s^2 + 0.625s_x^2)s_x^{-9/2} + \\ & (59.0625s^2 + 0.9375s_x^2)s_x^{-11/2} + \\ & (324.8s^2 + 3.28s_x^2)s_x^{-13/2} + \Big\} \Bigg] \end{aligned} \tag{36.16}$$

where $t = (\varepsilon_j^{\max} - V_j)/T$, $t_x = E_x/T$, $s = 2\sqrt{a(\varepsilon_j^{\max} - V_j - \delta_j)}$ and $s_x = 2\sqrt{a(E_x - \delta)}$.

Besides light fragments, 60 nuclides up to ^{28}Mg are considered, not only in their ground states but also in their exited states, are considered. The excited state is assumed to survive if its lifetime $T_{1/2}$ is longer than the decay time, *i. e.*, $T_{1/2}/\ln 2 > \hbar/\Gamma_j^*$, where Γ_j^* is the emission width of the resonance calculated in the same manner as for ground state particle emission. The total emission width of an ejectile j is summed over its ground state and all its excited states which satisfy the above condition.

36.4 Fission probability calculation.

The fission decay channel (only for nuclei with $A > 65$) is taken into account as a competitor for fragment and photon evaporation channels.

36.4.1 The fission total probability.

The fission probability (per unit time) W_{fis} in the Bohr and Wheeler theory of fission [15] is proportional to the level density $\rho_{fis}(T)$ (approximation Eq. (36.6) is used) at the saddle point, i.e.

$$W_{fis} = \frac{1}{2\pi\hbar\rho_{fis}(E^*)} \int_0^{E^*-B_{fis}} \rho_{fis}(E^* - B_{fis} - T)dT = \\ = \frac{1+(C_f-1)\exp(C_f)}{4\pi a_{fis}\exp(2\sqrt{aE^*})}, \tag{36.17}$$

where B_{fis} is the fission barrier height. The value of $C_f = 2\sqrt{a_{fis}(E^* - B_{fis})}$ and a, a_{fis} are the level density parameters of the compound and of the fission saddle point nuclei, respectively.

The value of the level density parameter is large at the saddle point, when excitation energy is given by initial excitation energy minus the fission barrier height, than in the ground state, i. e. $a_{fis} > a$. $a_{fis} = 1.08a$ for $Z < 85$, $a_{fis} = 1.04a$ for $Z \geq 89$ and $a_f = a[1.04 + 0.01(89. - Z)]$ for $85 \leq Z < 89$ is used.

36.4.2 The fission barrier.

The fission barrier is determined as difference between the saddle-point and ground state masses.

We use simple semiphenomenological approach was suggested by Barashenkov and Gereghi [16]. In their approach fission barrier $B_{fis}(A, Z)$ is approximated by

$$B_{fis} = B^0_{fis} + \Delta_g + \Delta_p. \tag{36.18}$$

The fission barrier height $B^0_{fis}(x)$ varies with the fissility parameter $x = Z^2/A$. $B^0_{fis}(x)$ is given by

$$B^0_{fis}(x) = 12.5 + 4.7(33.5 - x)^{0.75} \tag{36.19}$$

for $x \leq 33.5$ and

$$B^0_{fis}(x) = 12.5 - 2.7(x - 33.5)^{2/3} \tag{36.20}$$

for $x > 33.5$. The $\Delta_g = \Delta M(N) + \Delta M(Z)$, where $\Delta M(N)$ and $\Delta M(Z)$ are shell corrections for Cameron's liquid drop mass formula [17] and the pairing energy corrections: $\Delta_p = 1$ for odd-odd nuclei, $\Delta_p = 0$ for odd-even nuclei, $\Delta_p = 0.5$ for even-odd nuclei and $\Delta_p = -0.5$ for even-even nuclei.

36.5 The Total Probability for Photon Evaporation

As the first approximation we assume that dipole $E1$–transitions is the main source of γ–quanta from highly–excited nuclei [11]. The probability to evaporate γ in the energy interval $(\epsilon_\gamma, \epsilon_\gamma + d\epsilon_\gamma)$ per unit of time is given

$$W_\gamma(\epsilon_\gamma) = \frac{1}{\pi^2(\hbar c)^3}\sigma_\gamma(\epsilon_\gamma)\frac{\rho(E^* - \epsilon_\gamma)}{\rho(E^*)}\epsilon_\gamma^2, \tag{36.21}$$

where $\sigma_\gamma(\epsilon_\gamma)$ is the inverse (absorption of γ) reaction cross section, ρ is a nucleus level density is defined by Eq. (36.6).

The photoabsorption reaction cross section is given by the expression

$$\sigma_\gamma(\epsilon_\gamma) = \frac{\sigma_0\epsilon_\gamma^2\Gamma_R^2}{(\epsilon_\gamma^2 - E_{GDP}^2)^2 + \Gamma_R^2\epsilon_\gamma^2}, \tag{36.22}$$

where $\sigma_0 = 2.5A$ mb, $\Gamma_R = 0.3E_{GDP}$ and $E_{GDP} = 40.3A^{-1/5}$ MeV are empirical parameters of the giant dipole resonance [11]. The total radiation probability is

$$W_\gamma = \frac{3}{\pi^2(\hbar c)^3}\int_0^{E^*}\sigma_\gamma(\epsilon_\gamma)\frac{\rho(E^* - \epsilon_\gamma)}{\rho(E^*)}\epsilon_\gamma^2 d\epsilon_\gamma. \tag{36.23}$$

The integration is performed numericaly.

36.5.1 Energy of evaporated photon

The energy of γ-quantum is sampled according to the Eq. (36.21) distribution.

36.6 Discrete photon evaporation

The last step of evaporation cascade consists of evaporation of photons with discrete energies. The competition between photons and fragments as well as giant resonance photons is neglected at this step. We consider the discrete E1, M1 and E2 photon transitions from tabulated isotopes. There are large number of isotopes [18] with the experimentally measured exited level energies, spins, parities and relative transitions probabilities. This information is implemented in the code.

36.7 Internal conversion electron emission

An important conpetitive channel to photon emission is internal conversion. To take this into account, the photon evaporation data-base was entended to include internal conversion coeffficients.

The above constitute the first six columns of data in the photon evaporation files. The new version of the data base adds eleven new columns corresponding to:

7. ratio of internal conversion to gamma-ray emmission probability

8. - 17. internal conversion coefficients for shells K, L1, L2, L3, M1, M2, M3, M4, M5 and N+ respectively. These coefficients are normalised to 1.0

The calculation of the Internal Conversion Coefficients (ICCs) is done by a cubic spline interpolation of tabulalted data for the corresponding transition energy. These ICC tables, which we shall label Band [19], Rösel [20] and Hager-Seltzer [21], are widely used and were provided in electronic format by staff at LBNL. The reliability of these tabulated data has been reviewed in Ref. [22]. From tests carried out on these data we find that the ICCs calculated from all three tables are comparable within a 10% uncertainty, which is better than what experimetal measurements are reported to be able to achive.

The range in atomic number covered by these tables is Band: $1 <= Z <= 80$; Rösel: $30 <= Z <= 104$ and Hager-Seltzer: $3, 6, 10, 14 <= Z <= 103$. For simplicity and taking into account the completeness of the tables, we have used the Band table for $Z <= 80$ and Rösel for $81 <= Z <= 98$.

The Band table provides a higher resolution of the ICC curves used in the interpolation and covers ten multipolarities for all elements up to $Z = 80$, but it only includes ICCs for shells up to M5. In order to calculate the ICC of the N+ shell, the ICCs of all available M shells are added together and the total divided by 3. This is the scheme adopted in the LBNL ICC calculation code when using the Band table. The Rösel table includes ICCs for all shells in every atom and for $Z > 80$ the N+ shell ICC is calculated by adding together the ICCs of all shells above M5. In this table only eight multipolarities have ICCs calculated for.

36.7.1 Multipolarity

The ENSDF data provides information on the multipolarity of the transition. The ICCs included in the photon evaporation data base refer to the multipolarity indicated in the ENSDF file for that transition. Only one type of

mixed mulltipolarity is considered (M1+E2) and whenever the mixing ratio is provided in the ENSDF file, it is used to calculate the ICCs corresponding to the mixed multipolarity according the the formula:

- fraction in $M1 = 1/(1+\delta^2)$
- fraction in $E2 = \delta^2/(1+\delta^2)$

where δ is the mixing ratio.

36.7.2 Binding energy

For the production of an internal conversion electron, the energy of the transition must be at least the binding energy of the shell the electron is being released from. The binding energy corresponding to the various shells in all isotopes used in the ICC calculation has been taken from the Geant4 file G4AtomicShells.hh.

36.7.3 Isotopes

The list of isotopes included in the photon evaporation data base has been extended from $A <= 240$ to $A <= 250$. The highest atomic number included is $Z = 98$ (this ensures that Americium sources can now be simulated).

Bibliography

[1] I. Frenkel. *Sov. Phys.* **9** 533 (1936).

[2] V. E. Weisskopf and D. H. Ewing. *Phys. Rev.* **57** 472 (1940).

[3] I. Dostrovsky, Z. Fraenkel, G. Friedlander. *Phys. Rev.* **116** 683 (1959).

[4] J. Blatt and V. F. Weisskopf, *Theoretical Nuclear Physics* (John Wiley & Sons, Inc., New York, 1952)

[5] M. M. Shapiro. *Phys. Rev.* **90**, 171 (1953).

[6] A. S. Iljinov, M. V. Kazarnovsky and E. Ya. Paryev. *Intermediate–Energy Nuclear Physics* (CRC Press, 1994).

[7] V. F. Weisskopf. *Phys. Rev.* **52**, 295 (1937)

[8] H. Hurwitz and H. A. Bethe. *Phys. Rev.* **81**, (1951)

[9] J.L. Cook, H. Ferguson and A. R. L. Musgrove. *Aust. J. Phys.*, **20**, 477 (1967)

[10] A. Gilbert and A.G.W. Cameron, *Can. J. Phys.*, **43**, 1446 (1965)

[11] A. S. Iljinov, M. V. Mevel *et al.*. *Nucl. Phys.* **A543**, 517 (1992).

[12] J. W. Truran, A. G. W. Cameron, and E. Hilf. *Proc. Int. Conf. on the Properties of Nuclei Far From the Beta-Stability* Leysin, Switzerland, August 31 - September 4, 1970, Vol.1, p. 275

[13] S. Furihata. *Nucl. Instr. and Meth. in Phys. Res.* **B171**, 251 (2000)

[14] T. Matsuse, A. Arima, and S. M. Lee. *Phys. Rev. C* **26**, 2338 (1982)

[15] Bohr N., Wheeler J. W., Phys. Rev., **56** 426 (1939).

[16] Barashenkov V. S., Iljinov A. S., Toneev V. D., Gereghi F. G, Nucl. Phys. **A206** 131 (1973).

[17] Cameron A. G. W. Canad. J. Phys., **35** 1021 (1957), **36** 1040 (1958).

[18] Evaluated Nuclear Structure Data File (ENSDF) - a computer file of evaluated experimental nuclear structure data maintained by the National Nuclear Data Center, Brookhaven National Laboratory (http://www.nndc.bnl.gov/nndc/nudat/).

[19] I.M. Band and M.B. Trzhaskovskaya, Tables of the Gamma-ray Internal Conversion Coefficients for the K, L, M Shells, for 1 <= Z <= 80, Leningrad: Nuclear Physics Institute (1978).

[20] F. Rösel, H.M. Fries, K. Alder and H.C. Pauli, At. Data Nucl. Data Tables 21 (1978).

[21] R.S. Hager and E.C. Seltzer, Nucl. Data A4 (1968).

[22] M. Rysavy and O. Dragoun, On the Reliability of the Theoretical Internal Conversion Coefficients, J. Phys. G: Nucl. Part. Phys., 2000, v.26, N. 12, pp 1859-72.

Chapter 37

Fission model.

37.1 Reaction initial state.

The GEANT4 fission model is capable to predict final excited fragments as result of an excited nucleus symmetric or asymmetric fission. The fission process (only for nuclei with atomic number $A \geq 65$) is considered as a competitor for evaporation process, when nucleus transits from an excited state to the ground state. Here we describe the final state generation. The calculation of the relative probability of fission with respect to the evaporation channels are described in the chapter concerning evaporation.

The initial information for calculation of fission decay consists from the atomic mass number A, charge Z of excited nucleus, its four momentum P_0 and excitation energy U.

37.2 Fission process simulation.

37.2.1 Atomic number distribution of fission products.

As follows from experimental data [1] mass distribution of fission products consists of the symmetric and the asymmetric components:

$$F(A_f) = F_{sym}(A_f) + \omega F_{asym}(A_f), \tag{37.1}$$

where $\omega(U, A, Z)$ defines relative contribution of each component and it depends from excitation energy U and A, Z of fissioning nucleus. It was found in [2] that experimental data can be approximated with a good accuracy, if one take

$$F_{sym}(A_f) = \exp\,[-\frac{(A_f - A_{sym})^2}{2\sigma_{sym}^2}] \tag{37.2}$$

and

$$F_{asym}(A_f) = \exp\left[-\frac{(A_f-A_2)^2}{2\sigma_2^2}\right] + \exp\left[-\frac{A_f-(A-A_2)^2}{2\sigma_2^2}\right]+ \\ +C_{asym}\{\exp\left[-\frac{(A_f-A_1)^2}{2\sigma_1^2}\right] + \exp\left[-\frac{A_f-(A-A_1)^2}{2\sigma_2^2}\right]\}, \tag{37.3}$$

where $A_{sym} = A/2$, A_1 and A_2 are the mean values and σ_{sim}^2, σ_1^2 and σ_2^2 are dispertions of the Gaussians respectively. From an analysis of experimental data [2] the parameter $C_{asym} \approx 0.5$ was defined and the next values for dispersions:

$$\sigma_{sym}^2 = \exp(0.00553U + 2.1386), \tag{37.4}$$

where U in MeV,

$$2\sigma_1 = \sigma_2 = 5.6\ MeV \tag{37.5}$$

for $A \leq 235$ and

$$2\sigma_1 = \sigma_2 = 5.6 + 0.096(A - 235)\ MeV \tag{37.6}$$

for $A > 235$ were found.

The weight $\omega(U, A, Z)$ was approximated as follows

$$\omega = \frac{\omega_a - F_{asym}(A_{sym})}{1 - \omega_a F_{sym}((A_1 + A_2)/2)}. \tag{37.7}$$

The values of ω_a for nuclei with $96 \geq Z \geq 90$ were approximated by

$$\omega_a(U) = \exp(0.538U - 9.9564) \tag{37.8}$$

for $U \leq 16.25$ MeV,

$$\omega_a(U) = \exp(0.09197U - 2.7003) \tag{37.9}$$

for $U > 16.25$ MeV and

$$\omega_a(U) = \exp(0.09197U - 1.08808) \tag{37.10}$$

for $z = 89$. For nuclei with $Z \leq 88$ the authors of [2] constracted the following approximation:

$$\omega_a(U) = \exp[0.3(227 - a)] \exp\{0.09197[U - (B_{fis} - 7.5)] - 1.08808\}, \tag{37.11}$$

where for $A > 227$ and $U < B_{fis} - 7.5$ the corresponding factors occuring in exponential functions vanish.

37.2.2 Charge distribution of fission products.

At given mass of fragment A_f the experimental data [1] on the charge Z_f distribution of fragments are well approximated by Gaussian with dispertion $\sigma_z^2 = 0.36$ and the average $< Z_f >$ is described by expression:

$$< Z_f >= \frac{A_f}{A} Z + \Delta Z, \tag{37.12}$$

when parameter $\Delta Z = -0.45$ for $A_f \geq 134$, $\Delta Z = -0.45(A_f - A/2)/(134 - A/2)$ for $A - 134 < A_f < 134$ and $\Delta Z = 0.45$ for $A \leq A - 134$.

After sampling of fragment atomic masses numbers and fragment charges, we have to check that fragment ground state masses do not exceed initial energy and calculate the maximal fragment kinetic energy

$$T^{max} < U + M(A, Z) - M_1(A_{f1}, Z_{f1}) - M_2(A_{f2}, Z_{f2}), \tag{37.13}$$

where U and $M(A, Z)$ are the excitation energy and mass of initial nucleus, $M_1(A_{f1}, Z_{f1})$, and $M_2(A_{f2}, Z_{f2})$ are masses of the first and second fragment, respectively.

37.2.3 Kinetic energy distribution of fission products.

We use the empiricaly defined [3] dependence of the average kinetic energy $< T_{kin} >$ (in MeV) of fission fragments on the mass and the charge of a fissioning nucleus:

$$< T_{kin} >= 0.1178 Z^2/A^{1/3} + 5.8. \tag{37.14}$$

This energy is distributed differently in cases of symmetric and asymmetric modes of fission. It follows from the analysis of data [2] that in the asymmetric mode, the average kinetic energy of fragments is higher than that in the symmetric one by approximately 12.5 MeV. To approximate the average numbers of kinetic energies $< T_{kin}^{sym}$ and $< T_{kin}^{asym} >$ for the symmetric and asymmetric modes of fission the authors of [2] suggested empirical expressions:

$$< T_{kin}^{sym} >=< T_{kin} > -12.5 W_{asim}, \tag{37.15}$$

$$< T_{kin}^{asym} >=< T_{kin} > +12.5 W_{sim}, \tag{37.16}$$

where

$$W_{sim} = \omega \int F_{sim}(A) dA / \int F(A) dA \tag{37.17}$$

and

$$W_{asim} = \int F_{asim}(A) dA / \int F(A) dA, \tag{37.18}$$

respectively. In the symmetric fission the experimental data for the ratio of the average kinetic energy of fission fragments $< T_{kin}(A_f) >$ to this maximum energy $< T_{kin}^{max} >$ as a function of the mass of a larger fragment A_{max} can be approximated by expressions

$$< T_{kin}(A_f) > / < T_{kin}^{max} >= 1 - k[(A_f - A_{max})/A]^2 \tag{37.19}$$

for $A_{sim} \leq A_f \leq A_{max} + 10$ and

$$< T_{kin}(A_f) > / < T_{kin}^{max} >= 1 - k(10/A)^2 - 2(10/A)k(A_f - A_{max} - 10)/A \tag{37.20}$$

for $A_f > A_{max} + 10$, where $A_{max} = A_{sim}$ and $k = 5.32$ and $A_{max} = 134$ and $k = 23.5$ for symmetric and asymmetric fission respectively. For both modes of fission the distribution over the kinetic energy of fragments T_{kin} is choosen Gaussian with their own average values $< T_{kin}(A_f) >=< T_{kin}^{sym}(A_f) >$ or $< T_{kin}(A_f) >=< T_{kin}^{asym}(A_f) >$ and dispersions σ_{kin}^2 equal 8^2 MeV or 10^2 MeV^2 for symmetrical and asymmetrical modes, respectively.

37.2.4 Calculation of the excitation energy of fission products.

The total excitation energy of fragments U_{frag} can be defined according to equation:

$$U_{frag} = U + M(A, Z) - M_1(A_{f1}, Z_{f1}) - M_2(A_{f2}, Z_{f2}) - T_{kin}, \tag{37.21}$$

where U and $M(A, Z)$ are the excitation energy and mass of initial nucleus, T_{kin} is the fragments kinetic energy, $M_1(A_{f1}, Z_{f1})$, and $M_2(A_{f2}, Z_{f2})$ are masses of the first and second fragment, respectively.

The value of excitation energy of fragment U_f determines the fragment temperature ($T = \sqrt{U_f/a_f}$, where $a_f \sim A_f$ is the parameter of fragment level density). Assuming that after disintegration fragments have the same temperature as initial nucleus than the total excitation energy will be distributed between fragments in proportion to their mass numbers one obtains

$$U_f = U_{frag}\frac{A_f}{A}. \tag{37.22}$$

37.2.5 Excited fragment momenta.

Assuming that fragment kinetic energy $T_f = P_f^2/(2(M(A_f, Z_f + U_f)$ we are able to calculate the absolute value of fragment c.m. momentum

$$P_f = \frac{(M_1(A_{f1}, Z_{f1} + U_{f1})(M_2(A_{f2}, Z_{f2} + U_{f2})}{M_1(A_{f1}, Z_{f1}) + U_{f1} + M_2(A_{f2}, Z_{f2}) + U_{f2}} T_{kin}. \tag{37.23}$$

and its components, assuming fragment isotropical distribution.

Bibliography

[1] Vandenbosch R., Huizenga J. R., Nuclear Fission, Academic Press, New York, 1973.

[2] Adeev G. D. *et al.* Preprint INR 816/93, Moscow, 1993.

[3] Viola V. E., Kwiatkowski K. and Walker M, Phys. Rev. **C31** 1550 (1985).

Chapter 38

Fermi break-up model.

38.1 Fermi break-up simulation for light nuclei.

The GEANT4 Fermi break-up model is capable to predict final states as result of an excited nucleus with atomic number $A < 17$ statistical break-up.

For light nuclei the values of excitation energy per nucleon are often comparable with nucleon binding energy. Thus a light excited nucleus breaks into two or more fragments with branching given by available phase space. To describe a process of nuclear disassembling the so-called Fermi break-up model is used [1], [2], [3]. This statistical approach was first used by Fermi [1] to describe the multiple production in high energy nucleon collision.

38.1.1 Allowed channel.

The channel will be allowed for decay, if the total kinetic energy E_{kin} of all fragments of the given channel at the moment of break-up is positive. This energy can be calculated according to equation:

$$E_{kin} = U + M(A, Z) - E_{Coulomb} - \sum_{b=1}^{n}(m_b + \epsilon_b), \tag{38.1}$$

m_b and ϵ_b are masses and excitation energies of fragments, respectively, $E_{Coulomb}$ is the Coulomb barrier for a given channel. It is approximated by

$$E_{Coulomb} = \frac{3}{5}\frac{e^2}{r_0}(1 + \frac{V}{V_0})^{-1/3}(\frac{Z^2}{A^{1/3}} - \sum_{b=1}^{n}\frac{Z^2}{A_b^{1/3}}), \tag{38.2}$$

where V_0 is the volume of the system corresponding to the normal nuclear matter density and $\kappa = \frac{V}{V_0}$ is a parameter ($\kappa = 1$ is used).

38.1.2 Break-up probability.

The total probability for nucleus to break-up into n componets (nucleons, deutrons, tritons, alphas etc) in the final state is given by

$$W(E,n) = (V/\Omega)^{n-1}\rho_n(E), \tag{38.3}$$

where $\rho_n(E)$ is the density of a number of final states, V is the volume of decaying system and $\Omega = (2\pi\hbar)^3$ is the normalization volume. The density $\rho_n(E)$ can be defined as a product of three factors:

$$\rho_n(E) = M_n(E)S_nG_n. \tag{38.4}$$

The first one is the phase space factor defined as

$$M_n = \int_{-\infty}^{+\infty} ... \int_{-\infty}^{+\infty} \delta(\sum_{b=1}^{n} \mathbf{p_b})\delta(E - \sum_{b=1}^{n} \sqrt{p^2 + m_b^2}) \prod_{b=1}^{n} d^3p_b, \tag{38.5}$$

where $\mathbf{p_b}$ is fragment b momentum. The second one is the spin factor

$$S_n = \prod_{b=1}^{n}(2s_b + 1), \tag{38.6}$$

which gives the number of states with different spin orientations. The last one is the permutation factor

$$G_n = \prod_{j=1}^{k} \frac{1}{n_j!}, \tag{38.7}$$

which takes into account identity of components in final state. n_j is a number of components of j- type particles and k is defined by $n = \sum_{j=1}^{k} n_j$).

In non-relativistic case (Eq. (38.10) the integration in Eq. (38.5) can be evaluated analiticaly (see e. g. [5]). The probability for a nucleus with energy E disassembling into n fragments with masses m_b, where $b = 1, 2, 3, ..., n$ equals

$$W(E_{kin},n) = S_nG_n(\frac{V}{\Omega})^{n-1}(\frac{1}{\sum_{b=1}^{n} m_b} \prod_{b=1}^{n} m_b)^{3/2} \frac{(2\pi)^{3(n-1)/2}}{\Gamma(3(n-1)/2)} E_{kin}^{3n/2-5/2}, \tag{38.8}$$

where $\Gamma(x)$ is the gamma function.

38.1.3 Fermi break-up model parameter.

Thus the Fermi break-up model has only one free parameter V is the volume of decaying system, which can be calculated as follows:

$$V = 4\pi R^3/3 = 4\pi r_0^3 A/3, \tag{38.9}$$

where $r_0 = 1.4$ fm is used.

38.1.4 Fragment characteristics.

We take into account the formation of fragments in their ground and low-lying excited states, which are stable for nucleon emission. However, several unstable fragments with large lifetimes: ^5He, ^5Li, ^8Be, ^9B etc are also considered. Fragment characteristics A_b, Z_b, s_b and ϵ_b are taken from [6].

38.1.5 MC procedure.

The nucleus break-up is described by the Monte Carlo (MC) procedure. We randomly (according to probability Eq. (38.8) and condition Eq. (38.1)) select decay channel. Then for given channel we calculate kinematical quantities of each fragment according to n-body phase space distribution:

$$M_n = \int_{-\infty}^{+\infty} ... \int_{-\infty}^{+\infty} \delta(\sum_{b=1}^{n} \mathbf{p_b}) \delta(\sum_{b=1}^{n} \frac{p_b^2}{2m_b} - E_{kin}) \prod_{b=1}^{n} d^3 p_b. \tag{38.10}$$

The Kopylov's sampling procedure [7] is applied. The angular distributions for emitted fragments are considered to be isotropical.

Bibliography

[1] Fermi E., Prog. Theor. Phys. **5** 1570 (1950).

[2] Kretschmar M. Annual Rev. Nucl. Sci. **11** 1 (1961).

[3] Epherre M., Gradsztajn E., J. Physique **18** 48 (1967).

[4] Cameron A. G. W. Canad. J. Phys., **35** 1021 (1957), **36** 1040 (1958).

[5] Barashenkov V. S., Barbashov B. M., Bubelev E. G. Nuovo Cimento, **7** 117 (1958).

[6] Ajzenberg-Selone F., Nucl. Phys. 1 **360** (1981); **A375** (1982); **392** (1983); **A413** (1984); **A433** (1985).

[7] Kopylov G. I., Principles of resonance kinematics, Moscow, Nauka, 1970 (in Russian).

Chapter 39

Multifragmentation model.

39.1 Multifragmentation process simulation.

The GEANT4 multifragmentation model is capable to predict final states as result of an highly excited nucleus statistical break-up.

The initial information for calculation of multifragmentation stage consists from the atomic mass number A, charge Z of excited nucleus and its excitation energy U. At high excitation energies $U/A > 3$ MeV the multifragmentation mechanism, when nuclear system can eventually breaks down into fragments, becomes the dominant. Later on the excited primary fragments propagate independently in the mutual Coulomb field and undergo de-excitation. Detailed description of multifragmentation mechanism and model can be found in review [1].

39.1.1 Multifragmentation probability.

The probability of a breakup channel b is given by the expression (in the so-called microcanonical approach [1], [2]):

$$W_b(U, A, Z) = \frac{1}{\sum_b \exp[S_b(U, A, Z)]} \exp[S_b(U, A, Z)], \tag{39.1}$$

where $S_b(U, A, Z)$ is the entropy of a multifragment state corresponding to the breakup channel b. The channels $\{b\}$ can be parametrized by set of fragment multiplicities N_{A_f,Z_f} for fragment with atomic number A_f and charge Z_f. All partitions $\{b\}$ should satisfy constraints on the total mass and charge:

$$\sum_f N_{A_f,Z_f} A_f = A \tag{39.2}$$

and

$$\sum_f N_{A_f,Z_f} Z_f = Z. \tag{39.3}$$

It is assumed [2] that thermodynamic equilibrium is established in every channel, which can be characterized by the channel temperature T_b.

The channel temperature T_b is determined by the equation constraining the average energy $E_b(T_b, V)$ associated with partition b:

$$E_b(T_b, V) = U + E_{ground} = U + M(A, Z), \tag{39.4}$$

where V is the system volume, E_{ground} is the ground state (at $T_b = 0$) energy of system and $M(A, Z)$ is the mass of nucleus.

According to the conventional thermodynamical formulae the average energy of a partitition b is expressed through the system free energy F_b as follows

$$E_b(T_b, V) = F_b(T_b, V) + T_b S_b(T_b, V). \tag{39.5}$$

Thus, if free energy F_b of a partition b is known, we can find the channel temperature T_b from Eqs. (39.4) and (39.5), then the entropy $S_b = -dF_b/dT_b$ and hence, decay probability W_b defined by Eq. (39.1) can be calculated.

Calculation of the free energy is based on the use of the liquid-drop description of individual fragments [2]. The free energy of a partition b can be splitted into several terms:

$$F_b(T_b, V) = \sum_f F_f(T_b, V) + E_C(V), \tag{39.6}$$

where $F_f(T_b, V)$ is the average energy of an individual fragment including the volume

$$F_f^V = [-E_0 - T_b^2/\epsilon(A_f)]A_f, \tag{39.7}$$

surface

$$F_f^{Sur} = \beta_0[(T_c^2 - T_b^2)/(T_c^2 + T_b^2)]^{5/4} A_f^{2/3} = \beta(T_b) A_f^{2/3}, \tag{39.8}$$

symmetry

$$F_f^{Sim} = \gamma(A_f - 2Z_f)^2/A_f, \tag{39.9}$$

Coulomb

$$F_f^C = \frac{3}{5}\frac{Z_f^2 e^2}{r_0 A_f^{1/3}}[1 - (1 + \kappa_C)^{-1/3}] \tag{39.10}$$

and translational

$$F_f^t = -T_b \ln (g_f V_f/\lambda_{T_b}^3) + T_b \ln (N_{A_f,Z_f}!)/N_{A_f,Z_f} \tag{39.11}$$

terms and the last term

$$E_C(V) = \frac{3}{5}\frac{Z^2e^2}{R} \tag{39.12}$$

is the Coulomb energy of the uniformly charged sphere with charge Ze and the radius $R = (3V/4\pi)^{1/3} = r_0A^{1/3}(1+\kappa_C)^{1/3}$, where $\kappa_C = 2$ [2].

Parameters $E_0 = 16$ MeV, $\beta_0 = 18$ MeV, $\gamma = 25$ MeV are the coefficients of the Bethe-Weizsacker mass formula at $T_b = 0$. $g_f = (2S_f+1)(2I_f+1)$ is a spin S_f and isospin I_f degeneracy factor for fragment (fragments with $A_f > 1$ are treated as the Boltzmann particles), $\lambda_{T_b} = (2\pi h^2/m_N T_b)^{1/2}$ is the thermal wavelength, m_N is the nucleon mass, $r_0 = 1.17$ fm, $T_c = 18$ MeV is the critical temperature, which corresponds to the liquid-gas phase transition. $\epsilon(A_f) = \epsilon_0[1 + 3/(A_f - 1)]$ is the inverse level density of the mass A_f fragment and $\epsilon_0 = 16$ MeV is considered as a variable model parameter, whose value depends on the fraction of energy transferred to the internal degrees of freedom of fragments [2]. The free volume $V_f = \kappa V = \kappa\frac{4}{3}\pi r_0^4 A$ available to the translational motion of fragment, where $\kappa \approx 1$ and its dependence on the multiplicity of fragments was taken from [2]:

$$\kappa = [1 + \frac{1.44}{r_0A^{1/3}}(M^{1/3} - 1)]^3 - 1. \tag{39.13}$$

For $M = 1$ $\kappa = 0$.

The light fragments with $A_f < 4$, which have no excited states, are considered as elementary particles characterized by the empirical masses M_f, radii R_f, binding energies B_f, spin degeneracy factors g_f of ground states. They contribute to the translation free energy and Coulomb energy.

39.1.2 Direct simulation of the low multiplicity multifragment disintegration

At comparatively low excitation energy (temperature) system will disintegrate into a small number of fragments $M \leq 4$ and number of channel is not huge. For such situation a direct (microcanonical) sorting of all decay channels can be performed. Then, using Eq. (39.1), the average multiplicity value $< M >$ can be found. To check that we really have the situation with the low excitation energy, the obtained value of $< M >$ is examined to obey the inequality $< M > \leq M_0$, where $M_0 = 3.3$ and $M_0 = 2.6$ for $A \sim 100$ and for $A \sim 200$, respectively [2]. If the discussed inequality is fulfilled, then the set of channels under consideration is belived to be able for a correct description of the break up. Then using calculated according Eq. (39.1) probabilities we can randomly select a specific channel with given values of A_f and Z_f.

39.1.3 Fragment multiplicity distribution.

The individual fragment multiplicities N_{A_f,Z_f} in the so-called macrocanonical ensemble [1] are distributed according to the Poisson distribution:

$$P(N_{A_f,Z_f}) = \exp\left(-\omega_{A_f,Z_f}\right)\frac{\omega_{A_f,Z_f}^{N_{A_f,Z_f}}}{N_{A_f,Z_f}!} \tag{39.14}$$

with mean value $< N_{A_f,Z_f} >= \omega_{A_f,Z_f}$ defined as

$$< N_{A_f,Z_f} >= g_f A_f^{3/2}\frac{V_f}{\lambda_{T_b}^3}\exp\left[\frac{1}{T_b}(F_f(T_b,V) - F_f^t(T_b,V) - \mu A_f - \nu Z_f)\right], \tag{39.15}$$

where μ and ν are chemical potentials. The chemical potential are found by substituting Eq. (39.15) into the system of constraints:

$$\sum_f < N_{A_f,Z_f} > A_f = A \tag{39.16}$$

and

$$\sum_f < N_{A_f,Z_f} > Z_f = Z \tag{39.17}$$

and solving it by iteration.

39.1.4 Atomic number distribution of fragments.

Fragment atomic numbers $A_f > 1$ are also distributed according to the Poisson distribution [1] (see Eq. (39.14)) with mean value $< N_{A_f} >$ defined as

$$< N_{A_f} >= A_f^{3/2}\frac{V_f}{\lambda_{T_b}^3}\exp\left[\frac{1}{T_b}(F_f(T_b,V) - F_f^t(T_f,V) - \mu A_f - \nu < Z_f >)\right], \tag{39.18}$$

where calculating the internal free energy $F_f(T_b,V) - F_f^t(T_b,V)$ one has to substitute $Z_f \rightarrow < Z_f >$. The average charge $< Z_f >$ for fragment having atomic number A_f is given by

$$< Z_f(A_f) >= \frac{(4\gamma+\nu)A_f}{8\gamma + 2[1-(1+\kappa)^{-1/3}]A_f^{2/3}}. \tag{39.19}$$

39.1.5 Charge distribution of fragments.

At given mass of fragment $A_f > 1$ the charge Z_f distribution of fragments are described by Gaussian

$$P(Z_f(A_f)) \sim \exp\,[-\frac{(Z_f(A_f) - < Z_f(A_f) >)^2}{2(\sigma_{Z_f}(A_f))^2}] \tag{39.20}$$

with dispertion

$$\sigma_{Z_f(A_f)} = \sqrt{\frac{A_f T_b}{8\gamma + 2[1-(1+\kappa)^{-1/3}]A_f^{2/3}}} \approx \sqrt{\frac{A_f T_b}{8\gamma}}. \tag{39.21}$$

and the average charge $< Z_f(A_f) >$ defined by Eq. (39.17).

39.1.6 Kinetic energy distribution of fragments.

It is assumed [2] that at the instant of the nucleus break-up the kinetic energy of the fragment T^f_{kin} in the rest of nucleus obeys the Boltzmann distribution at given temperature T_b:

$$\frac{dP(T^f_{kin})}{dT^f_{kin}} \sim \sqrt{T^f_{kin}}\exp\,(-T^f_{kin}/T_b). \tag{39.22}$$

Under assumption of thermodynamic equilibrium the fragment have isotropic velocities distribution in the rest frame of nucleus. The total kinetic energy of fragments should be equal $\frac{3}{2}MT_b$, where M is fragment multiplicity, and the total fragment momentum should be equal zero. These conditions are fullfilled by choosing properly the momenta of two last fragments.

The initial conditions for the divergence of the fragment system are determined by random selection of fragment coordinates distributed with equal probabilities over the break-up volume $V_f = \kappa V$. It can be a sphere or prolongated ellipsoid. Then Newton's equations of motion are solved for all fragments in the self-consistent time-dependent Coulomb field [2]. Thus the asymptotic energies of fragments determined as result of this procedure differ from the initial values by the Coulomb repulsion energy.

39.1.7 Calculation of the fragment excitation energies.

The temparature T_b determines the average excitation energy of each fragment:

$$U_f(T_b) = E_f(T_b) - E_f(0) = \frac{T_b^2}{\epsilon_0}A_f + [\beta(T_b) - T_b\frac{d\beta(T_b)}{dT_b} - \beta_0]A_f^{2/3}, \tag{39.23}$$

where $E_f(T_b)$ is the average fragment energy at given temperature T_b and $\beta(T_b)$ is defined in Eq. (39.8). There is no excitation for fragment with $A_f < 4$, for ^4He excitation energy was taken as $U_{^4He} = 4T_b^2/\epsilon_o$.

Bibliography

[1] Bondorf J. P., Botvina A. S., Iljinov A. S., Mishustin I. N., Sneppen K., Phys. Rep. **257** 133 (1995).

[2] Botvina A. S. *et al.*, Nucl. Phys. **A475** 663 (1987).

Chapter 40

INCL++: the Liège Intranuclear Cascade model

40.1 Introduction

There is a renewed interest in the study of spallation reactions. This is largely due to new technological applications, such as Accelerator-Driven Systems, consisting of sub-critical nuclear reactor coupled to a particle accelerator. These applications require optimized targets as spallation sources. This type of problem typically involves a large number of parameters and thus it cannot be solved by trial and error. One has to rely on simulations, which implies that very accurate tools need to be developed and their validity and accuracy need to be assessed.

Above ∼200 MeV incident energy it is necessary to use reliable models due to the prohibitive number of open channels. The most appropriate modeling technique in this energy region is intranuclear cascade (INC) combined with evaporation model. One such pair of models is the Liège cascade model `INCL++` coupled with the `G4ExcitationHandler` statistical de-excitation model. The strategy adopted by the `INCL++` cascade is to improve the quasi-classical treatment of physics without relying on too many free parameters.

This chapter introduces the physics provided by `INCL++` as implemented in Geant4. Table 40.1 summarizes the key features and provides references to detailed descriptions of the physics.

The `INCL++` model is available through dedicated physics lists (see Table 40.1). The `*_HP` variants of the physics lists use the `NeutronHP` model (Chapter 42) for neutron interactions at low energy; the `QGSP_*` and `FTFP_*` variants respectively use the `QGSP` and `FTFP` model at high energy. Figure 40.1

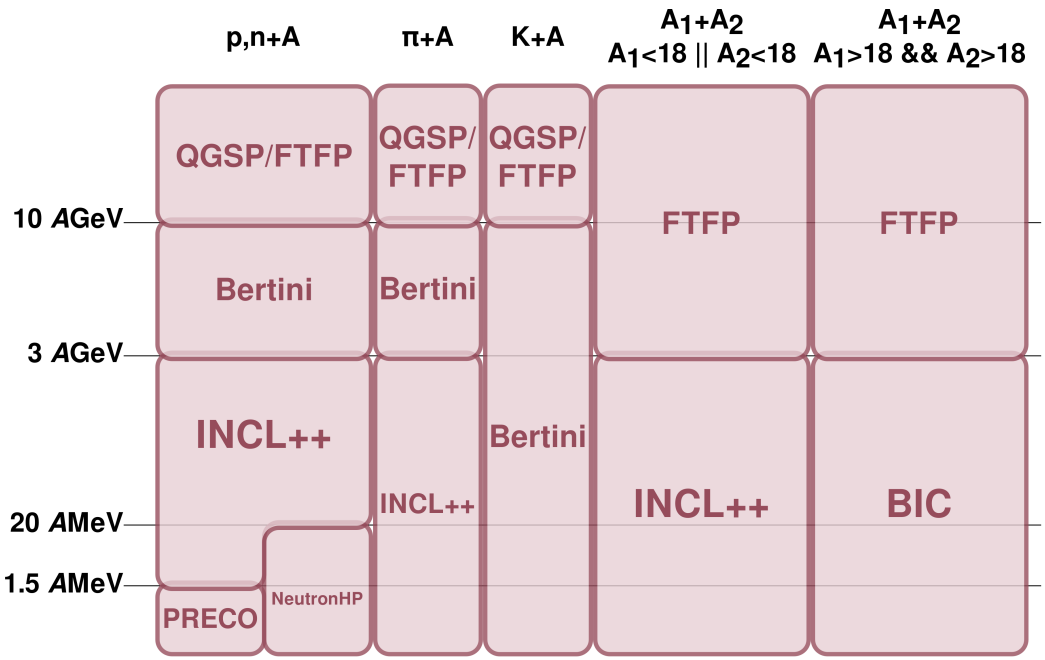

Figure 40.1: Model map for the INCL++-based physics lists. The first two columns represent nucleon- and pion-induced reactions. The third column represents nucleus-nucleus reactions where at least one of the partners is below $A = 18$. The fourth column represents other nucleus-nucleus reactions.

shows a schematic model map of the INCL++-based physics lists.

Finally, the INCL++ model is directly accessible through its interface (G4INCLXXInterface).

40.1.1 Suitable application fields

The INCL++-dedicated physics lists are suitable for the simulation of any system where spallation reactions or light-ion-induced reactions play a dominant role. As examples, we include here a non-exhaustive list of possible application fields:

- Accelerator-Driven Systems (ADS);
- spallation targets;
- radioprotection close to high-energy accelerators;
- radioprotection in space;

- proton or carbon therapy;
- production of beams of exotic nuclei.

40.2 Generalities of the INCL++ cascade

INCL++ is a Monte-Carlo simulation incorporating the aforementioned cascade physics principles. The INCL++ algorithm consists of an initialization stage and the actual data processing stage.

The INCL++ cascade can be used to simulate the collisions between bullet particles and nuclei. The supported bullet particles and the interface classes supporting them are presented in table 40.1.

The momenta and positions of the nucleons inside the nuclei are determined at the beginning of the simulation run by modeling the nucleus as a free Fermi gas in a static potential well with a realistic density. The cascade is modeled by tracking the nucleons and their collisions.

The possible reactions inside the nucleus are

- $NN \rightarrow NN$ (elastic scattering)
- $NN \rightarrow N\Delta$ and $N\Delta \rightarrow NN$
- $\Delta \rightarrow \pi N$ and $\pi N \rightarrow \Delta$

40.2.1 Model limits

The INCL++ model has certain limitations with respect to the bullet particle energy and type, and target-nucleus type. The supported energy range for bullets is 1 MeV–3 GeV. Any target nucleus from deuterium (^{2}H) up is in principle acceptable, but not all areas of the nuclide chart have received equal attention during testing. Heavy nuclei (say above Fe) close to the stability valley have been more thoroughly studied than light or unstable nuclei. The model is anyway expected to accept any existing nucleus as a target.

Light nuclei (from $A = 2$ to $A = 18$ included) can also be used as projectiles. The G4INCLXXInterface class can be used for collisions between nuclei of any mass, but it will internally rely on the Binary Cascade model (see chapter 32) if both reaction partners have $A > 18$. A warning message will be displayed (once) if this happens.

40.3 Physics ingredients

The philosophy of the `INCL++` model is to minimize the number of free parameters, which guarantees the predictive power of the model. All `INCL++` parameters are either taken from known phenomenology (e.g. nuclear radii, elementary cross sections, nucleon potentials) or fixed once and for all (stopping time, cluster-coalescence parameters).

The nucleons are modeled as a free Fermi gas in a static potential well. The radius of the well depends on the nucleon momentum, the r-p correlation being determined by the desired spatial density distribution $\rho_r(r)$ according to the following equation:

$$\rho_p(p)p^2dp = -\frac{d\rho_r(r)}{dr}\frac{r^3}{3}dr, \tag{40.1}$$

where $\rho_p(p)$ is the momentum-space density (a hard-sphere of radius equal to the Fermi momentum).

After the initialization a projectile particle, or bullet, is shot towards the target nucleus. In the following we assume that the projectile is a nucleon or a pion; the special case of composite projectiles will be described in more detail in subsection 40.3.4.

The impact parameter, i.e. the distance between the projectile particle and the center point of the projected nucleus surface is chosen at random. The value of the impact parameter determines the point where the bullet particle will enter the calculation volume. After this the algorithm tracks the nucleons by determining the times at which an event will happen. The possible events are:

- collision
- decay of a delta resonance
- reflection from the nuclear potential well
- transmission through the nuclear potential well

The particles are assumed to propagate along straight-line trajectories. The algorithm calculates the time at which events will happen and propagates the particles directly to their positions at that particular point in time. This means that the length of the time step in simulation is not constant, and that we do not need to perform expensive numerical integration of the particle trajectories.

Particles in the model are labeled either as *participants* (projectile particles and particles that have undergone a collision with a projectile) or *spectators* (target particles that have not undergone any collision). Collisions between spectator particles are neglected.

40.3.1 Emission of composite particles

`INCL++` is able to simulate the emission of composite particles (up to $A = 8$) during the cascade stage. Clusters are formed by coalescence of nucleons; when a nucleon (the *leading* particle) reaches the surface and is about to leave the system, the coalescence algorithm looks for other nucleons that are "sufficiently close" in phase space; if any are found, a candidate cluster is formed. If several clusters are formed, the algorithm selects the least excited one. Penetration of the Coulomb barrier is tested for the candidate cluster, which is emitted if the test is successful; otherwise, normal transmission of the leading nucleon is attempted.

There are at least two peculiarities of `INCL++`'s cluster-coalescence algorithm. First, it acts in *phase space*, while many existing algorithms act in momentum space only. Second, it is *dynamical*, in the sense that it acts on the instantaneous phase-space distribution of nucleons in the system, and not on the distribution of the escaping nucleons.

40.3.2 Cascade stopping time

Stopping time is defined as the point in time when the cascade phase is finished and the excited remnant is passed to evaporation model. In the `INCL++` model the stopping time, t_{stop}, is defined as:

$$t_{\text{stop}} = t_0(A_{\text{target}}/208)^{0.16}. \tag{40.2}$$

Here A_{target} is the target mass number and $t_0 = 70$ fm/c. The intranuclear cascade also stops if no participants are left in the nucleus.

40.3.3 Conservation laws

The `INCL++` model generally guarantees energy and momentum conservation at the keV level, which is compatible with the numerical accuracy of the code. It uses `G4ParticleTable` and `G4IonTable` for the masses of particles and ions, which means that the energy balance is guaranteed to be consistent with radiation transport. However, `INCL++` can occasionally generate an event such that conservation laws cannot be exactly fulfilled; these corner cases typically happen for very light targets.

Baryon number and charge are always conserved.

40.3.4 Initialisation of composite projectiles

In the case of composite projectiles, the projectile nucleons are initialised off their mass shell, to account for their binding in the projectile. The sum of the four-momenta of the projectile nucleons is equal to the nominal four-momentum of the projectile nucleus.

Given a random impact parameter, projectile nucleons are separated in geometrical spectators (those that do not enter the calculation volume) and geometrical participants (those that do). Geometrical participant that traverse the nucleus without undergoing any collision are coalesced with any existing geometrical spectators to form an excited projectile-like pre-fragment. The excitation energy of the pre-fragment is generated by a simple particle-hole model. At the end of the cascade stage, the projectile-like pre-fragment is handed over to `G4ExcitationHandler`.

40.3.5 De-excitation phase

The `INCL++` model simulates only the first part of the nuclear reaction; the de-excitation of the cascade remnant is simulated by default by `G4ExcitationHandler`. As an alternative, the `ABLA V3` model (Chapter 41) can be used instead, by employing the technique described in the Application Developer Guide, section "hadronic interactions".

40.4 Physics performance

`INCL++` (coupled with `G4ExcitationHandler`) provides an accurate modeling tool for spallation studies in the tens of MeV–3 GeV energy range. The `INCL++-ABLA07` [2] model was recognized as one of the best on the market by the IAEA Benchmark of Spallation Models [3] (note however that the `ABLA07` de-excitation model is presenty not available in Geant4).

As a sample of the quality of the model predictions of `INCL++-G4ExcitationHandler` for nucleon-induced reactions, the left panel of Figure 40.2 presents a comparison of double-differential cross sections for pion production in 730-MeV p+Cu, compared with the predictions of the Binary-Cascade model (chapter 32) and with experimental data.

Reactions induced by light-ion projectiles up to $A = 18$ are also treated by the model. The right panel of Figure 40.2 shows double-differential cross sections for neutron production in 290-AMeV ^{12}C+^{12}C. Figure 40.3 shows exci-

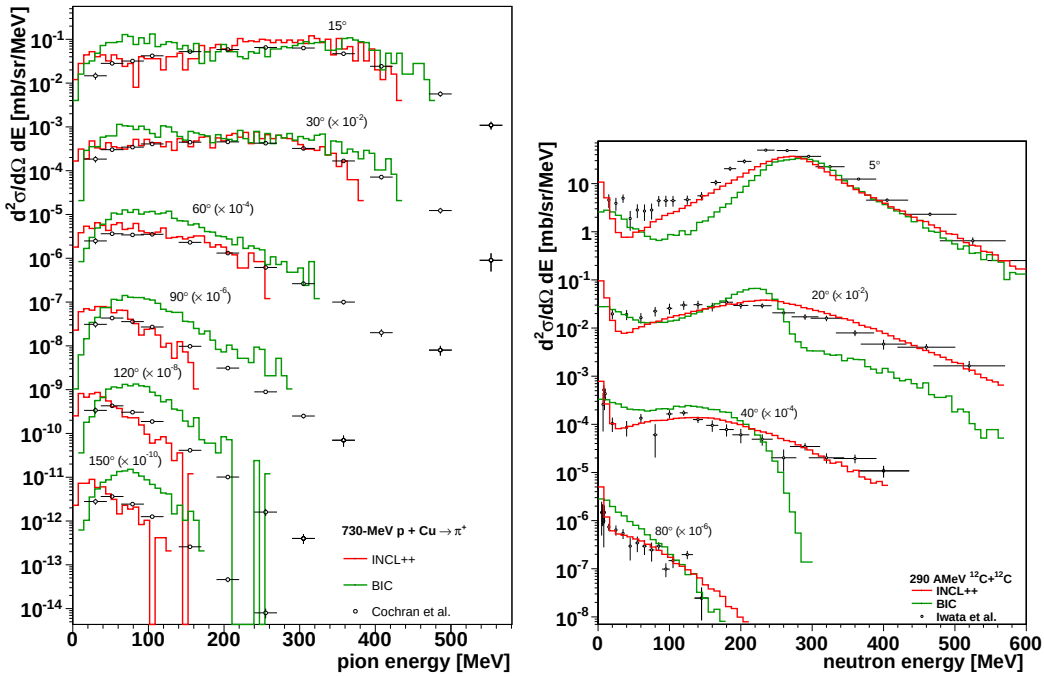

Figure 40.2: Left: double-differential cross sections for the production of charged pions in 730-MeV p+Cu. Right: double-differential cross sections for the production of neutrons in 290-AMeV ^{12}C+^{12}C. Predictions of the `INCL++` and Binary-Cascade models are compared with experimental data from Refs. [4] and [5].

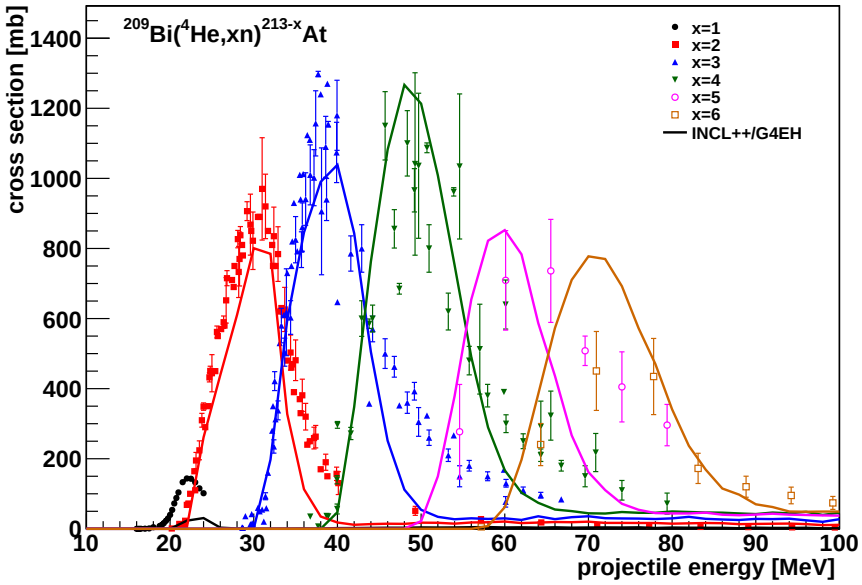

Figure 40.3: Excitation functions for (α, xn) cross sections on ^{209}Bi. The predictions of `INCL++-G4ExcitationHandler` are represented by the solid line and are compared to experimental data [6, 7, 8, 9, 10, 11, 12, 13, 14].

tation curves for ^{209}Bi(α, xn) reactions at very low energy. We stress here that intranuclear-cascade models are supposedly not valid below $\sim$ 150 AMeV. The very good agreement presented in Figure 40.3 is due to the complete-fusion model that smoothly replaces `INCL++` at low energy.

`INCL++` is continuously updated and validated against experimental data.

40.5 Status of this document

28.10.2013: added description of the `INCL++`-based physics lists; general update of the document.

16.11.2012: documentation for `INCL++` added. Written by D. Mancusi (CEA-Saclay, France), based on the legacy `INCL4.2` documentation written by P. Kaitaniemi (Helsinki Institute of Physics, Finland).

Bibliography

[1] A. Boudard et al., `arXiv:1210.3498`, accepted for publication in *Phys. Rev. C* (2012).

[2] A. Kelić, M. V. Ricciardi and K.-H. Schmidt, *Joint ICTP-IAEA Advanced Workshop on Model Codes for Spallation Reactions, Report INDC(NDC)-0530* (2008) 181.

[3] Benchmark of Spallation Models, organized by the IAEA. Web site: `http://www-nds.iaea.org/spallations`.

[4] D. R. F. Cochran et al., *Phys. Rev. D6* (1972) 3085.

[5] Y. Iwata et al., *Phys. Rev. C6* (2001) 054609.

[6] A. Hermanne et al., *Conf. on Nucl. Data for Sci. and Techn., Santa Fe 2004*,

[7] A. R. Barnett et al., *Phys. Rev. C9* (1974) 2010.

[8] E. L. Kelly and E. Segré, *Phys. Rev. 75* (1949) 999.

[9] G. Deconninck and M. Longree, *Ann. Soc. Sci. Brux. 88* (1974) 341.

[10] H. B. Patel, D. J. Shah and N. L. Singh, *Riv. Nuovo Cimento A112* (1999) 1439.

[11] I. A. Rizvi et al., *Appl. Radiat. Isotopes 41* (1990) 215.

[12] J. D. Stickler and K. J. Hofstetter, *Phys. Rev. C9* (1974) 1064.

[13] N. L. Singh, S. Mukherjee and D. R. S. Somayajulu, *Riv. Nuovo Cimento A107* (1994) 1635.

[14] R. M. Lambrecht and S. Mirzadeh, *Appl. Radiat. Isotopes 36* (1985) 443.

Table 40.1: `INCL++` feature summary.

usage	
physics lists	`QGSP_INCLXX`
	`QGSP_INCLXX_HP`
	`FTFP_INCLXX`
	`FTFP_INCLXX_HP`
interfaces	
`G4INCLXXInterface`	nucleon-, pion- and nucleus-nucleus
projectile particles	proton, neutron
	pions (π^+, π^0, π^-)
	deuteron, triton
	^{3}He, α
	light ions (up to $A = 18$)
energy range	1 MeV - 3 GeV
target nuclei	
lightest applicable	deuterium, ^{2}H
heaviest	no limit, tested up to uranium
features	no ad-hoc parameters
	realistic nuclear densities
	Coulomb barrier
	non-uniform time-step
	pion and delta production cross sections
	delta decay
	Pauli blocking
	emission of composite particles ($A \leq 8$)
	complete-fusion model at low energy
	conservation laws satisfied at the keV level
typical CPU time	$0.5 \lesssim$ `INCL++`/Binary Cascade $\lesssim 2$
code size	75 classes, 14k lines
references	Ref. [1] and references therein.

Chapter 41

ABLA V3 evaporation/fission model

The ABLA V3 evaporation model takes excited nucleus parameters, excitation energy, mass number, charge number and nucleus spin, as input. It calculates the probabilities for emitting proton, neutron or alpha particle and also probability for fission to occur. The summary of Geant4 ABLA V3 implementation is represented in Table 41.1.

The probabilities for emission of particle type j are calculated using formula:

$$W_j(N,Z,E) = \frac{\Gamma_j(N,Z,E)}{\sum_k \Gamma_k(N,Z,E)}, \tag{41.1}$$

where Γ_j is emission width for particle j, N is neutron number, Z charge number and E excitation energy. Possible emitted particles are *protons*, *neutrons* and *alphas*. Emission widths are calculated using the following formula:

$$\Gamma_j = \frac{1}{2\pi\rho_c(E)} \frac{4m_j R^2}{\hbar^2} T_j^2 \rho_j(E - S_j - B_j), \tag{41.2}$$

where $\rho_c(E)$ and $\rho_j(E - S_j - B_j)$ are the level densities of the compound nucleus and the exit channel, respectively. B_j is the height of the Coulomb barrier, S_j the separation energy, R is the radius and T_j the temperature of the remnant nucleus after emission and m_j the mass of the emitted particle.

The fission width is calculated from:

$$\Gamma_i = \frac{1}{2\pi\rho_c(E)} T_f \rho_f(E - B_f), \tag{41.3}$$

where $\rho_f(E)$ is the level density of transition states in the fissioning nucleus, B_f the height of the fission barrier and T_f the temperature of the nucleus.

Table 41.1: ABLA V3 (located in the Geant4 directory `source/processes/-hadronic/models/abla`) feature summary.

Requirements	
External data file	G4ABLA3.0 available at Geant4 site
Environment variable for external data	`G4ABLADATA`
Usage	
Physics list	No default physics list, see Section 41.4.
Interfaces	
`G4AblaInterface`	
Supported input	Excited nuclei
Output particles	proton, neutron α fission products residual nuclei
Features	evaporation of proton, neutron and α fission
References	Key reference: [1], see also [2]

41.1 Level densities

Nuclear level densities are calculated using the following formula:

$$a = 0.073A[MeV^{-1}] + 0.095B_s A^{2/3}[MeV^{-2}], \tag{41.4}$$

where A the nucleus mass number and B_s dimensionless surface area of the nucleus.

41.2 Fission

Fission barrier, used to calculate fission width 41.3, is calculated using a semi-empirical model fitting to data obtained from nuclear physics experiments.

41.3 External data file required

ABLA V3 needs specific data files. These files contain ABLA V3 shell corrections and nuclear masses. To enable this data set, the environment variable `G4ABLADATA` needs to be set, and the relevant data should be installed on your machine. You can download them from the Geant4 web site or you can have CMake download them for you during installation. For Geant4 10.0 we use the `G4ABLA3.0` data files.

41.4 How to use ABLA V3

None of the stock physics lists use the ABLA V3 model by default. It should also be understood that ABLA V3 is a nuclear de-excitation model and must be used as a secondary reaction stage; the first, dynamical reaction stage must be simulated using some other model, typically an intranuclear-cascade (INC) model. The coupling of the ABLA V3 to the INCL++ model (Chapter 40) has been somewhat tested and seems to work, but no extensive benchmarking has been realized at the time of writing. Coupling to the Binary-Cascade model (Chapter 32) should in principle be possible, but has never been tested. The technique to realize the coupling is described in the Application Developer Guide.

Finally, please note that the ABLA V3 model is in alpha status. The code may crash and be affected by bugs.

41.5 Status of this document

18.11.20013 ABLA documentation extracted from the old INCL4.2/ABLA chapter. Minor updates to the text.

06.12.2007 Documentation for alpha release added. Pekka Kaitaniemi, HIP (translation); Alain Boudard, CEA (contact person INCL/ABLA); Joseph Cugnon, University of Liège (INCL physics modelling); Karl-Heintz Schmidt, GSI (ABLA); Christelle Schmidt, IPNL (fission code); Aatos Heikkinen, HIP (project coordination)

Bibliography

[1] A.R. Junghans et al *Nuc. Phys. A629* (1998) 635

[2] J. Benlliure et al *Nuc. Phys. A628* (1998) 458

[3] A. Heikkinen et al. *J. Phys.: Conf. Series 119* (2008) 032024

Chapter 42

Low Energy Neutron Interactions

42.1 Introduction

The neutron transport class library described here simulates the interactions of neutrons with kinetic energies from thermal energies up to O(20 MeV). The upper limit is set by the comprehensive evaluated neutron scattering data libraries that the simulation is based on. The result is a set of secondary particles that can be passed on to the tracking sub-system for further geometric tracking within GEANT4.

The interactions of neutrons at low energies are split into four parts in analogy to the other hadronic processes in GEANT4. We consider radiative capture, elastic scattering, fission, and inelastic scattering as separate models. These models comply with the interface for use with the GEANT4 hadronic processes which enables their transparent use within the GEANT4 tool-kit together with all other GEANT4 compliant hadronic shower models.

42.2 Physics and Verification

42.2.1 Inclusive Cross-sections

All cross-section data are taken from the ENDF/B-VI[1] evaluated data library.

All inclusive cross-sections are treated as point-wise cross-sections for reasons of performance. For this purpose, the data from the evaluated data library have been processed, to explicitly include all neutron nuclear resonances in the form of point-like cross-sections rather than in the form of

parametrisations. The resulting data have been transformed into a linearly interpolable format, such that the error due to linear interpolation between adjacent data points is smaller than a few percent.

The inclusive cross-sections comply with the cross-sections data set interface of the GEANT4 hadronic design. They are, when registered with the tool-kit at initialisation, used to select the basic process. In the case of fission and inelastic scattering, point-wise semi-inclusive cross-sections are also used in order to decide on the active channel for an individual interaction. As an example, in the case of fission this could be first, second, third, or forth chance fission.

42.2.2 Elastic Scattering

The final state of elastic scattering is described by sampling the differential scattering cross-sections $\frac{\mathrm{d}\sigma}{\mathrm{d}\Omega}$. Two representations are supported for the normalised differential cross-section for elastic scattering. The first is a tabulation of the differential cross-section, as a function of the cosine of the scattering angle θ and the kinetic energy E of the incoming neutron.

$$\frac{\mathrm{d}\sigma}{\mathrm{d}\Omega} \;=\; \frac{\mathrm{d}\sigma}{\mathrm{d}\Omega}\left(\cos\theta,\; E\right)$$

The tabulations used are normalised by $\sigma/(2\pi)$ so the integral of the differential cross-sections over the scattering angle yields unity.

In the second representation, the normalised cross-section are represented as a series of legendre polynomials $P_l(\cos\theta)$, and the legendre coefficients a_l are tabulated as a function of the incoming energy of the neutron.

$$\frac{2\pi}{\sigma(E)}\frac{\mathrm{d}\sigma}{\mathrm{d}\Omega}\left(\cos\theta,\; E\right) \;=\; \sum_{l=0}^{n_l}\frac{2l+1}{2}a_l(E)P_l(\cos\theta)$$

Describing the details of the sampling procedures is outside the scope of this paper.

An example of the result we show in figure 42.1 for the elastic scattering of 15 MeV neutrons off Uranium a comparison of the simulated angular distribution of the scattered neutrons with evaluated data. The points are the evaluated data, the histogram is the Monte Carlo prediction.

In order to provide full test-coverage for the algorithms, similar tests have been performed for ^{72}Ge, ^{126}Sn, ^{238}U, ^{4}He, and ^{27}Al for a set of neutron kinetic energies. The agreement is very good for all values of scattering angle and neutron energy investigated.

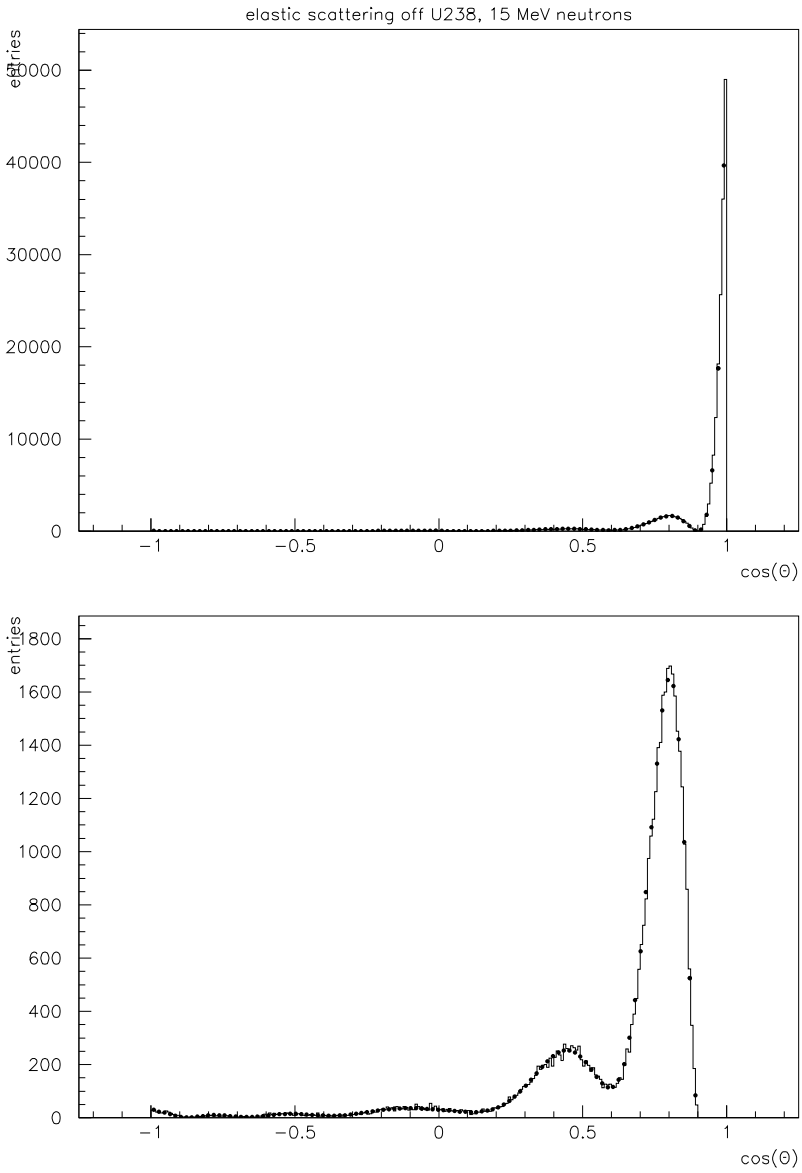

Figure 42.1: Comparison of data and Monte Carlo for the angular distribution of 15 MeV neutrons scattered elastically off Uranium (^{238}U). The points are evaluated data, and the histogram is the Monte Carlo prediction. The lower plot excludes the forward peak, to better show the Frenel structure of the angular distribution of the scattered neutron.

42.2.3 Radiative Capture

The final state of radiative capture is described by either photon multiplicities, or photon production cross-sections, and the discrete and continuous contributions to the photon energy spectra, along with the angular distributions of the emitted photons.

For the description of the photon multiplicity there are two supported data representations. It can either be tabulated as a function of the energy of the incoming neutron for each discrete photon as well as the eventual continuum contribution, or the full transition probability array is known, and used to determine the photon yields. If photon production cross-sections are used, only a tabulated form is supported.

The photon energies E_γ are associated to the multiplicities or the cross-sections for all discrete photon emissions. For the continuum contribution, the normalised emission probability f is broken down into a weighted sum of normalised distributions g.

$$f\left(E \to E_\gamma\right) \;=\; \sum_i p_i(E) g_i(E \to E_\gamma)$$

The weights p_i are tabulated as a function of the energy E of the incoming neutron. For each neutron energy, the distributions g are tabulated as a function of the photon energy. As in the ENDF/B-VI data formats[1], several interpolation laws are used to minimise the amount of data, and optimise the descriptive power. All data are derived from evaluated data libraries.

The techniques used to describe and sample the angular distributions are identical to the case of elastic scattering, with the difference that there is either a tabulation or a set of legendre coefficients for each photon energy and continuum distribution.

As an example of the results is shown in figure42.2 the energy distribution of the emitted photons for the radiative capture of 15 MeV neutrons on Uranium (^{238}U). Similar comparisons for photon yields, energy and angular distributions have been performed for capture on ^{238}U, ^{235}U, ^{23}Na, and ^{14}N for a set of incoming neutron energies. In all cases investigated the agreement between evaluated data and Monte Carlo is very good.

42.2.4 Fission

For neutron induced fission, we take first chance, second chance, third chance and forth chance fission into account.

Neutron yields are tabulated as a function of both the incoming and outgoing neutron energy. The neutron angular distributions are either tabulated,

or represented in terms of an expansion in legendre polynomials, similar to the angular distributions for neutron elastic scattering. In case no data are available on the angular distribution, isotropic emission in the centre of mass system of the collision is assumed.

There are six different possibilities implemented to represent the neu-

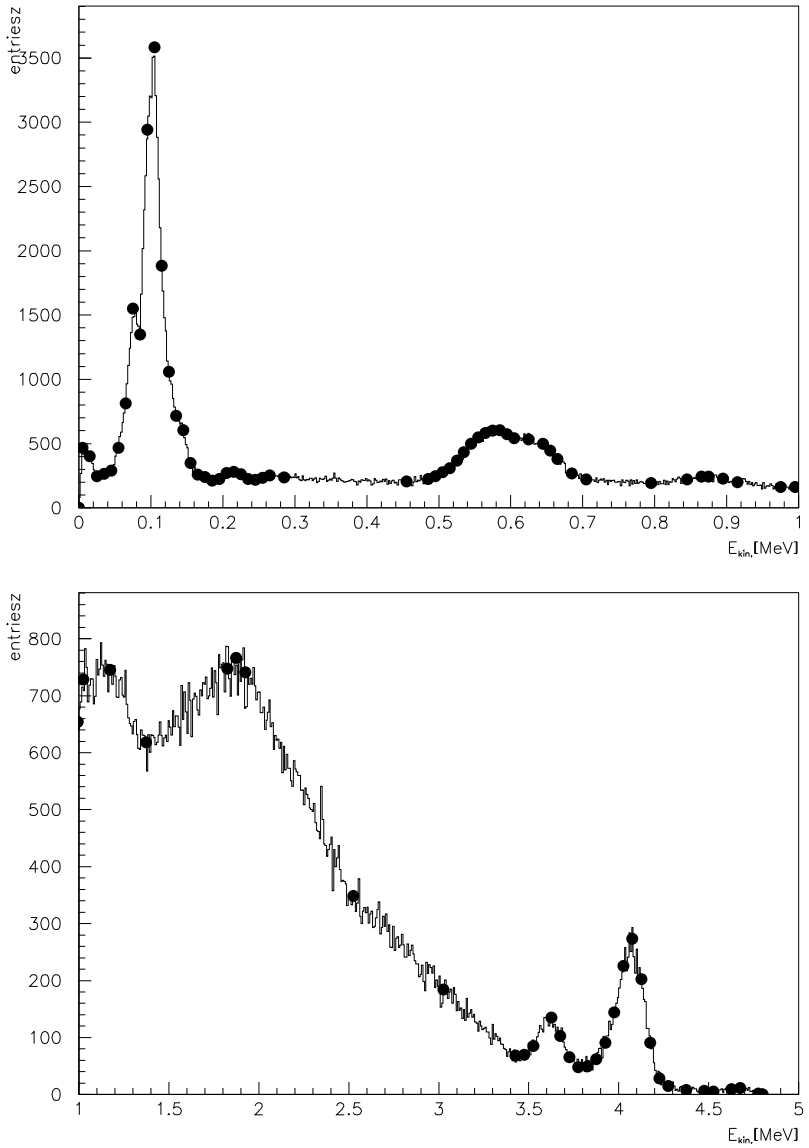

Figure 42.2: Comparison of data and Monte Carlo for photon energy distributions for radiative capture of 15 MeV neutrons on Uranium (^{238}U). The points are evaluated data, the histogram is the Monte Carlo prediction.

tron energy distributions. The energy distribution of the fission neutrons $f(E \to E')$ can be tabulated as a normalised function of the incoming and outgoing neutron energy, again using the ENDF/B-VI interpolation schemes to minimise data volume and maximise precision.

The energy distribution can also be represented as a general evaporation spectrum,

$$f(E \to E') \;=\; f\left(E'/\Theta(E)\right).$$

Here E is the energy of the incoming neutron, E' is the energy of a fission neutron, and $\Theta(E)$ is effective temperature used to characterise the secondary neutron energy distribution. Both the effective temperature and the functional behaviour of the energy distribution are taken from tabulations.

Alternatively energy distribution can be represented as a Maxwell spectrum,

$$f(E \to E') \;\propto\; \sqrt{E'}\mathrm{e}^{E'/\Theta(E)},$$

or a evaporation spectrum

$$f(E \to E') \;\propto\; E'\mathrm{e}^{E'/\Theta(E)}.$$

In both these cases, the temperature is tabulated as a function of the incoming neutron energy.

The last two options are the energy dependent Watt spectrum, and the Madland Nix spectrum. For the energy dependent Watt spectrum, the energy distribution is represented as

$$f(E \to E') \;\propto\; \mathrm{e}^{-E'/a(E)} \sinh\sqrt{b(E)E'}.$$

Here both the parameters a, and b are used from tabulation as function of the incoming neutron energy. In the case of the Madland Nix spectrum, the energy distribution is described as

$$f(E \to E') \;=\; \frac{1}{2}\left[g(E', < K_l >) \;+\; g(E', < K_h >)\right].$$

Here

$$g(E', < K >) \;=\; \frac{1}{3\sqrt{< K > \Theta}}\left[u_2^{3/2}E_1(u_2) - u_1^{3/2}E_1(u_1) + \gamma(3/2, u_2) - \gamma(3/2, u_1)\right],$$

$$u_1(E', < K >) = \frac{(\sqrt{E'} - \sqrt{< K >})^2}{\Theta}, \text{ and}$$

$$u_2(E', < K >) = \frac{(\sqrt{E'} + \sqrt{< K >})^2}{\Theta}.$$

Here K_l is the kinetic energy of light fragments and K_h the kinetic energy of heavy fragments, $E_1(x)$ is the exponential integral, and $\gamma(x)$ is the incomplete gamma function. The mean kinetic energies for light and heavy fragments are assumed to be energy independent. The temperature Θ is tabulated as a function of the kinetic energy of the incoming neutron.

Fission photons are describes in analogy to capture photons, where evaluated data are available. The measured nuclear excitation levels and transition probabilities are used otherwise, if available.

As an example of the results is shown in figure42.3 the energy distribution of the fission neutrons in third chance fission of 15 MeV neutrons on Uranium (^{238}U). This distribution contains two evaporation spectra and one Watt spectrum. Similar comparisons for neutron yields, energy and angular distributions, and well as fission photon yields, energy and angular distributions have been performed for ^{238}U, ^{235}U, ^{234}U, and ^{241}Am for a set of incoming neutron energies. In all cases the agreement between evaluated data and Monte Carlo is very good.

42.2.5 Inelastic Scattering

For inelastic scattering, the currently supported final states are (nA$\rightarrow$) nγs (discrete and continuum), np, nd, nt, n^{3}He, nα, nd2α, nt2α, n2p, n2α, npα, n3α, 2n, 2np, 2nd, 2nα, 2n2α, nX, 3n, 3np, 3nα, 4n, p, pd, pα, 2p d, dα, d2α, dt, t, t2α, ^{3}He, α, 2α, and 3α.

The photon distributions are again described as in the case of radiative capture.

The possibility to describe the angular and energy distributions of the final state particles as in the case of fission is maintained, except that normally only the arbitrary tabulation of secondary energies is applicable.

In addition, we support the possibility to describe the energy angular correlations explicitly, in analogy with the ENDF/B-VI data formats. In this case, the production cross-section for reaction product n can be written as

$$\sigma_n(E, E', \cos(\theta)) \;=\; \sigma(E) Y_n(E) p(E, E', \cos(\theta)).$$

Here $Y_n(E)$ is the product multiplicity, $\sigma(E)$ is the inelastic cross-section, and $p(E, E', \cos(\theta))$ is the distribution probability. Azimuthal symmetry is assumed.

The representations for the distribution probability supported are isotropic emission, discrete two-body kinematics, N-body phase-space distribution, continuum energy-angle distributions, and continuum angle-energy distributions in the laboratory system.

The description of isotropic emission and discrete two-body kinematics is possible without further information. In the case of N-body phase-space distribution, tabulated values for the number of particles being treated by the law, and the total mass of these particles are used. For the continuum energy-angle distributions, several options for representing the angular dependence are available. Apart from the already introduced methods of expansion in terms of legendre polynomials, and tabulation (here in both the incoming neutron energy, and the secondary energy), the Kalbach-Mann systematic is available. In the case of the continuum angle-energy distributions in the laboratory system, only the tabulated form in incoming neutron energy, product energy, and product angle is implemented.

First comparisons for product yields, energy and angular distributions have been performed for a set of incoming neutron energies, but full test cov-

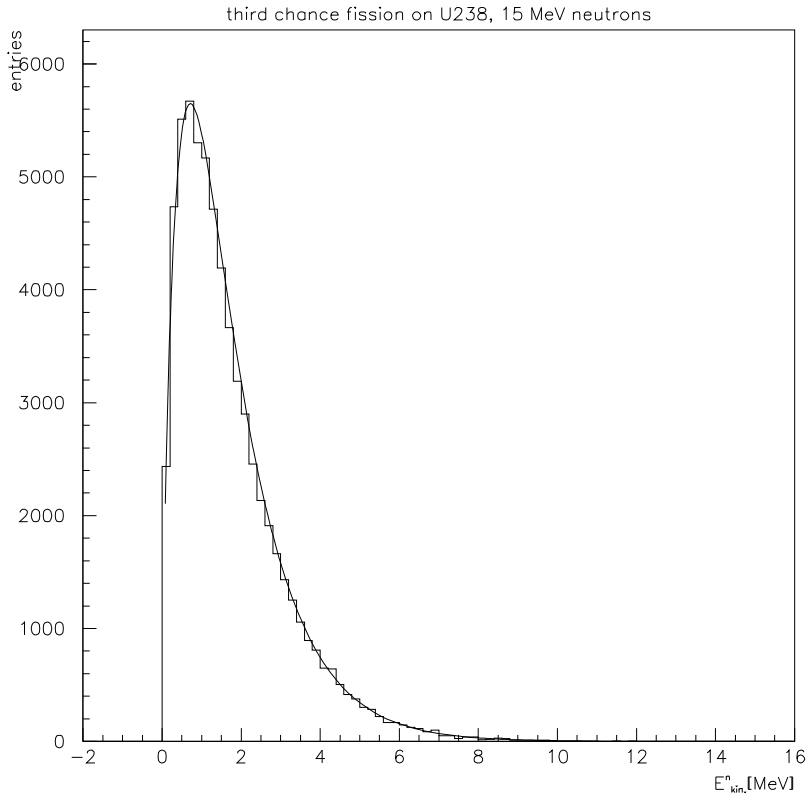

Figure 42.3: Comparison of data and Monte Carlo for fission neutron energy distributions for induced fission by 15 MeV neutrons on Uranium (^{238}U). The curve represents evaluated data and the histogram is the Monte Carlo prediction.

erage is still to be achieved. In all cases currently investigated, the agreement between evaluated data and Monte Carlo is very good.

42.3 High Precision Models and Low Energy Parameterized Models

The high precision neutron models discussed in the previous section depend on an evaluated neutron data library (G4NDL) for cross sections, angular distributions and final state information. However the library is not complete because there are no data for several key elements. In order to use the high precision models, users must develop their detectors using only elements which exist in the library. In order to avoid this difficulty, alternative models were developed which use the high precision models when data are found in the library, but use the low energy parameterized neutron models when data are missing.

The alternative models cover the same types of interaction as the originals, that is elastic and inelastic scattering, capture and fission. Because the low energy parameterized part of the models is independent of G4NDL, results will not be as precise as they would be if the relevant data existed.

42.4 Summary and Important Remark

By the way of abstraction and code reuse we minimised the amount of code to be written and maintained. The concept of container-sampling lead to abstraction and encapsulation of data representation and the corresponding random number generators. The Object Oriented design allows for easy extension of the cross-section base of the system, and the ENDF-B VI data evaluations have already been supplemented with evaluated data on nuclear excitation levels, thus improving the energy spectra of de-excitation photons. Other established data evaluations have been investigated, and extensions based on the JENDL[2], CENDL[4], and Brond[5] data libraries are foreseen for next year.

Followings are important remark of the NeutornHP package. Correlation between final state particles is not included in tabulated data. The method described here does not included necessary correlation or phase space constrains needed to conserver momentum and energy. Such conservation is not guarantee either in single event or averaged over many events.

42.5 Status of this document

00.00.00 created by H.P. Wellisch
08.12.05 section on high precision and low energy parameterized model added by T. Koi
13.12.05 Important Remark added by T. Koi

Bibliography

[1] ENDF/B-VI: Cross Section Evaluation Working Group, *ENDF/B-VI Summary Document*, Report **BNL-NCS-17541 (ENDF-201)** (1991), edited by P.F. Rose, National Nuclear Data Center, Brookhave National Laboratory, Upton, NY, USA.

[2] JENDL-3: T. Nakagawa, et al., *Japanese Evaluated Nuclear Data Library, Version 3, Revision 2,* **J. Nucl. Sci. Technol. 32**, 1259 (1995).

[3] Jef-2: C. Nordborg, M. Salvatores, *Status of the JEF Evaluated Data Library*, **Nuclear Data for Science and Technology**, edited by J. K. Dickens (American Nuclear Society, LaGrange, IL, 1994).

[4] CENDL-2: Chinese Nuclear Data Center, *CENDL-2, The Chinese Evaluated Nuclear Data Library for Neutron Reaction Data*, Report **IAEA-NDS-61**, Rev. 3 (1996), International Atomic Energy Agency, Vienna, Austria.

[5] Brond-2.2: A.I Blokhin et al., *Current status of Russian Nuclear Data Libraries*, **Nuclear Data for Science and Technology**, Volume2, p.695. edited by J. K. Dickens (American Nuclear Society, LaGrange, IL, 1994)

Chapter 43

Radioactive Decay

43.1 The Radioactive Decay Module

G4RadioactiveDecay and associated classes are used to simulate the decay, either in-flight or at rest, of radioactive nuclei by α, β^+, and β^- emission and by electron capture (EC). The simulation model depends on data taken from the Evaluated Nuclear Structure Data File (ENSDF) [1] which provides information on:

- nuclear half-lives,
- nuclear level structure for the parent or daughter nuclide,
- decay branching ratios, and
- the energy of the decay process.

If the daughter of a nuclear decay is an excited isomer, its prompt nuclear de-excitation is treated using the *G4PhotoEvaporation* class [2].

43.2 Alpha Decay

The final state of alpha decay consists of an α and a recoil nucleus with $(Z-2, A-4)$. The two particles are emitted back-to-back in the center of mass with the energy of the α taken from the ENSDF data entry for the decaying isotope.

43.3 Beta Decay

Beta decay is modeled by the emission of a β^- or β^+, an anti-neutrino or neutrino, and a recoil nucleus of either $Z+1$ or $Z-1$. The energy of the β is obtained by sampling either from histogrammed data or from the theoretical three-body phase space spectral shapes. The latter include allowed, first, second and third unique forbidden, and first non-unique forbidden transitions.

The shape of the energy spectrum of the emitted lepton is given by

$$\frac{d^2n}{dEdp_e} = (E_0 - E_e)^2 E_e p_e F(Z, E_e) S(Z, E_0, E_e) \tag{43.1}$$

where, in units of electron mass, E_0 is the endpoint energy of the decay taken from the ENSDF data, E_e and p_e are the emitted electron energy and momentum, Z is the atomic number, F is the Fermi function and S is the shape factor.

The Fermi function F accounts for the effect of the Coulomb barrier on the probability of $\beta^\pm$ emission. Its relativistic form is

$$F(Z, E_e) = 2(1+\gamma)(2p_eR)^{2\gamma-2} e^{\pm\pi\alpha ZE_e/p_e} \frac{|\Gamma(\gamma + i\alpha ZE_e/p_e)|^2}{\Gamma(2\gamma+1)^2} \tag{43.2}$$

where R is the nuclear radius, $\gamma = \sqrt{1-(\alpha Z)^2}$, and α is the fine structure constant. The squared modulus of Γ is computed using approximation B of Wilkinson [3].

The factor S determines whether or not additional corrections are applied to the decay spectrum. When $S = 1$ the decay spectrum takes on the so-called allowed shape which is just the phase space shape modified by the Fermi function. For this type of transition the emitted lepton carries no angular momentum and the nuclear spin and parity do not change. When the emitted lepton carries angular momentum and nuclear size effects are not negligible, the factor S is no longer unity and the transitions are called "forbidden". Corrections are then made to the spectrum shape which take into account the energy dependence of the nuclear matrix element. The form of S used in the spectrum sampling is that of Konopinski [4].

43.4 Electron Capture

Electron capture from the atomic K, L and M shells is simulated by producing a recoil nucleus of $(Z-1, A)$ and an electron-neutrino back-to-back in the center of mass. Since this leaves a vacancy in the electron orbitals, the atomic

relaxation model (ARM) is triggered in order to produce the resulting x-rays and Auger electrons. More information on the ARM can be found in the Electromagnetic section of this manual.

In the electron capture decay mode, internal conversion is also enabled so that atomic electrons may be ejected when interacting with the nucleus.

43.5 Recoil Nucleus Correction

Due to the level of imprecision of the rest-mass energy of the nuclei generated by *G4IonTable::GetNucleusMass*, the mass of the parent nucleus is modified to a minor extent just before performing the two- or three-body decay so that the Q for the transition process equals that identified in the ENSDF data.

43.6 Biasing Methods

By default, sampling of the times of radioactive decay and branching ratios is done according to standard, analogue Monte Carlo modeling. The user may switch on one or more of the following variance reduction schemes, which can provide significant improvement in the modelling efficiency:

1. The decays can be biased to occur more frequently at certain times, for example, corresponding to times when measurements are taken in a real experiment. The statistical weights of the daughter nuclides are reduced according to the probability of survival to the time of the event, t, which is determined from the decay rate. The decay rate of the n^{th} nuclide in a decay chain is given by the recursive formulae:

$$R_n(t) = \sum_{i=1}^{n-1} A_{n:i} f(t, \tau_i) + A_{n:n} f(t, \tau_n) \tag{43.3}$$

where:

$$A_{n:i} = \frac{\tau_i}{\tau_i - \tau_n} A_{n:i} \quad \forall i < n \tag{43.4}$$

$$A_{n:n} = -\sum_{i=1}^{n-1} \frac{\tau_n}{\tau_i - \tau_n} A_{n:i} - y_n \tag{43.5}$$

$$f(t, \tau_i) = \frac{e^{-\frac{t}{\tau_i}}}{\tau_i} \int_{-\inf}^{t} F(t') e^{\frac{t'}{\tau_i}} dt'. \tag{43.6}$$

The values τ_i are the mean life-times for the nuclei, y_i is the yield of the i^{th} nucleus, and $F(t)$ is a function identifying the time profile of the source. The above expression for decay rate is simplified, since it assumes that the i^{th} nucleus undergoes 100% of the decays to the $(i+1)^{th}$ nucleus. Similar expressions which allow for branching and merging of different decay chains can be found in Ref. [5].

A consequence of the form of equations 43.4 and 43.6 is that the user may provide a source time profile so that each decay produced as a result of a simulated source particle incident at time $t = 0$ is convolved over the source time profile to derive the actual decay rate for that source function.

This form of variance reduction is only appropriate if the radionuclei can be considered to be at rest with respect to the geometry when decay occurs.

2. For a given decay mode (α, $\beta^+ + EC$, or β^-) the branching ratios to the daughter nuclide can be sampled with equal probability, so that some low probability branches which may have a disproportionately greater effect on the measurement are sampled with increased probability.

3. Each parent nuclide can be split into a user-defined number of nuclides (of proportionally lower statistical weight) prior to treating decay in order to increase the sampling of the effects of the daughter products.

43.7 Status of this document

created by P. Truscott
21.11.03 bibliography added, minor re-wording by D.H. Wright
20.11.12 discussion of new Fermi function and forbidden decays added by D.H. Wright
20.11.12 sections on alpha and EC decay added by D.H. Wright

Bibliography

[1] J. Tuli, *"Evaluated Nuclear Structure Data File,"* BNL-NCS-51655-Rev87, 1987.

[2] Chapter 25, Geant4 Physics Reference Manual.

[3] D.H. Wilkinson, Nucl. Instr. & Meth. 82, 122 (1970).

[4] E. Konopinski, "The Theory of Beta Radioactivity", Oxford Press (1966).

[5] P.R. Truscott, PhD Thesis, University of London, 1996.

Part V

Gamma- and Lepto-Nuclear Interactions

Chapter 44

Introduction

Gamma-nuclear and lepto-nuclear reactions are handled in Geant4 as hybrid processes which typically require both electromagnetic and hadronic models for their implementation. While neutrino-induced reactions are not currently provided, the Geant4 hadronic framework is general enough to include their future implementation as a hybrid of weak and hadronic models.

The general scheme followed is to factor the full interaction into an electromagnetic (or weak) vertex, in which a virtual particle is generated, and a hadronic vertex in which the virtual particle interacts with a target nucleus. In most cases the hadronic vertex is implemented by an existing Geant4 model which handles the intra-nuclear propagation.

The cross sections for these processes are parameterizations, either directly of data or of theoretical distributions determined from the integration of lepton-nucleon cross sections double differential in energy loss and momentum transfer.

44.1 Status of this document

19.11.12 created by D.H. Wright

Chapter 45

Cross-sections in Photonuclear and Electronuclear Reactions

45.1 Approximation of Photonuclear Cross Sections.

The photonuclear cross sections parameterized in the `G4PhotoNuclearCrossSection` class cover all incident photon energies from the hadron production threshold upward. The parameterization is subdivided into five energy regions, each corresponding to the physical process that dominates it.

- The Giant Dipole Resonance (GDR) region, depending on the nucleus, extends from 10 Mev up to 30 MeV. It usually consists of one large peak, though for some nuclei several peaks appear.
- The "quasi-deuteron" region extends from around 30 MeV up to the pion threshold and is characterized by small cross sections and a broad, low peak.
- The Δ region is characterized by the dominant peak in the cross section which extends from the pion threshold to 450 MeV.
- The Roper resonance region extends from roughly 450 MeV to 1.2 GeV. The cross section in this region is not strictly identified with the real Roper resonance because other processes also occur in this region.
- The Reggeon-Pomeron region extends upward from 1.2 GeV.

In the GEANT4 photonuclear data base there are about 50 nuclei for which the photonuclear absorption cross sections have been measured in the above

energy ranges. For low energies this number could be enlarged, because for heavy nuclei the neutron photoproduction cross section is close to the total photo-absorption cross section. Currently, however, 14 nuclei are used in the parameterization: ^{1}H, ^{2}H, ^{4}He, ^{6}Li, ^{7}Li, ^{9}Be, ^{12}C, ^{16}O, ^{27}Al, ^{40}Ca, Cu, Sn, Pb, and U. The resulting cross section is a function of A and $e = log(E_\gamma)$, where E_γ is the energy of the incident photon. This function is the sum of the components which parameterize each energy region.

The cross section in the GDR region can be described as the sum of two peaks,

$$GDR(e) = th(e, b_1, s_1) \cdot exp(c_1 - p_1 \cdot e) + th(e, b_2, s_2) \cdot exp(c_2 - p_2 \cdot e). \quad (45.1)$$

The exponential parameterizes the falling edge of the resonance which behaves like a power law in E_γ. This behavior is expected from the CHIPS model (Chapter Chapter 30), which includes the nonrelativistic phase space of nucleons to explain evaporation. The function

$$th(e, b, s) = \frac{1}{1 + exp(\frac{b-e}{s})}, \quad (45.2)$$

describes the rising edge of the resonance. It is the nuclear-barrier-reflection function and behaves like a threshold, cutting off the exponential. The exponential powers p_1 and p_2 are

$$\begin{aligned} p_1 = 1, p_2 = 2 \ \text{ for } \quad & A < 4 \\ p_1 = 2, p_2 = 4 \ \text{ for } \quad & 4 \leq A < 8 \\ p_1 = 3, p_2 = 6 \ \text{ for } \quad & 8 \leq A < 12 \\ p_1 = 4, p_2 = 8 \ \text{ for } \quad & A \geq 12. \end{aligned}$$

The A-dependent parameters b_i, c_i and s_i were found for each of the 14 nuclei listed above and interpolated for other nuclei.

The Δ isobar region was parameterized as

$$\Delta(e, d, f, g, r, q) = \frac{d \cdot th(e, f, g)}{1 + r \cdot (e - q)^2}, \quad (45.3)$$

where d is an overall normalization factor. q can be interpreted as the energy of the Δ isobar and r can be interpreted as the inverse of the Δ width. Once again th is the threshold function. The A-dependence of these parameters is as follows:

- $d = 0.41 \cdot A$ (for ^{1}H it is 0.55, for ^{2}H it is 0.88), which means that the Δ yield is proportional to A;
- $f = 5.13 - .00075 \cdot A$. $exp(f)$ shows how the pion threshold depends on A. It is clear that the threshold becomes 140 MeV only for uranium; for lighter nuclei it is higher.
- $g = 0.09$ for $A \geq 7$ and 0.04 for $A < 7$;
- $q = 5.84 - \frac{.09}{1+.003 \cdot A^2}$, which means that the "mass" of the Δ isobar moves to lower energies;
- $r = 11.9 - 1.24 \cdot log(A)$. r is 18.0 for ^{1}H. The inverse width becomes smaller with A, hence the width increases.

The A-dependence of the f, q and r parameters is due to the $\Delta + N \rightarrow N + N$ reaction, which can take place in the nuclear medium below the pion threshold.

The quasi-deuteron contribution was parameterized with the same form as the Δ contribution but without the threshold function:

$$QD(e, v, w, u) = \frac{v}{1 + w \cdot (e - u)^2}. \tag{45.4}$$

For ^{1}H and ^{2}H the quasi-deuteron contribution is almost zero. For these nuclei the third baryonic resonance was used instead, so the parameters for these two nuclei are quite different, but trivial. The parameter values are given below.

- $v = \frac{exp(-1.7 + a \cdot 0.84)}{1 + exp(7 \cdot (2.38 - a))}$, where $a = log(A)$. This shows that the A-dependence in the quasi-deuteron region is stronger than $A^{0.84}$. It is clear from the denominator that this contribution is very small for light nuclei (up to ^{6}Li or ^{7}Li). For ^{1}H it is 0.078 and for ^{2}H it is 0.08, so the delta contribution does not appear to be growing. Its relative contribution disappears with A.
- $u = 3.7$ and $w = 0.4$. The experimental information is not sufficient to determine an A-dependence for these parameters. For both ^{1}H and ^{2}H $u = 6.93$ and $w = 90$, which may indicate contributions from the $\Delta(1600)$ and $\Delta(1620)$.

The transition Roper contribution was parameterized using the same form as the quasi-deuteron contribution:

$$Tr(e, v, w, u) = \frac{v}{1 + w \cdot (e - u)^2}. \quad (45.5)$$

Using $a = log(A)$, the values of the parameters are

- $v = exp(-2. + a \cdot 0.84)$. For ^{1}H it is 0.22 and for ^{2}H it is 0.34.
- $u = 6.46 + a \cdot 0.061$ (for ^{1}H and for ^{2}H it is 6.57), so the "mass" of the Roper moves higher with A.
- $w = 0.1 + a \cdot 1.65$. For ^{1}H it is 20.0 and for ^{2}H it is 15.0).

The Regge-Pomeron contribution was parametrized as follows:

$$RP(e, h) = h \cdot th(7., 0.2) \cdot (0.0116 \cdot exp(e \cdot 0.16) + 0.4 \cdot exp(-e \cdot 0.2)), \quad (45.6)$$

where $h = A \cdot exp(-a \cdot (0.885 + 0.0048 \cdot a))$ and, again, $a = log(A)$. The first exponential in Eq. 45.6 describes the Pomeron contribution while the second describes the Regge contribution.

45.2 Electronuclear Cross Sections and Reactions

Electronuclear reactions are so closely connected with photonuclear reactions that they are sometimes called "photonuclear" because the one-photon exchange mechanism dominates in electronuclear reactions. In this sense electrons can be replaced by a flux of equivalent photons. This is not completely true, because at high energies the Vector Dominance Model (VDM) or diffractive mechanisms are possible, but these types of reactions are beyond the scope of this discussion.

45.3 Common Notation for Different Approaches to Electronuclear Reactions

The Equivalent Photon Approximation (EPA) was proposed by E. Fermi [1] and developed by C. Weizsacker and E. Williams [2] and by L. Landau and E. Lifshitz [3]. The covariant form of the EPA method was developed in Refs. [4] and [5]. When using this method it is necessary to take into account that

real photons are always transversely polarized while virtual photons may be longitudinally polarized. In general the differential cross section of the electronuclear interaction can be written as

$$\frac{d^2\sigma}{dydQ^2} = \frac{\alpha}{\pi Q^2}(S_{TL} \cdot (\sigma_T + \sigma_L) - S_L \cdot \sigma_L), \tag{45.7}$$

where

$$S_{TL} = y\frac{1 - y + \frac{y^2}{2} + \frac{Q^2}{4E^2} - \frac{m_e^2}{Q^2}(y^2 + \frac{Q^2}{E^2})}{y^2 + \frac{Q^2}{E^2}}, \tag{45.8}$$

$$S_L = \frac{y}{2}(1 - \frac{2m_e^2}{Q^2}). \tag{45.9}$$

The differential cross section of the electronuclear scattering can be rewritten as

$$\frac{d^2\sigma_{eA}}{dydQ^2} = \frac{\alpha y}{\pi Q^2}\left(\frac{(1 - \frac{y}{2})^2}{y^2 + \frac{Q^2}{E^2}} + \frac{1}{4} - \frac{m_e^2}{Q^2}\right)\sigma_{\gamma^* A}, \tag{45.10}$$

where $\sigma_{\gamma^* A} = \sigma_{\gamma A}(\nu)$ for small Q^2 and must be approximated as a function of ϵ, ν, and Q^2 for large Q^2. Interactions of longitudinal photons are included in the effective $\sigma_{\gamma^* A}$ cross section through the ϵ factor, but in the present GEANT4 method, the cross section of virtual photons is considered to be ϵ-independent. The electronuclear problem, with respect to the interaction of virtual photons with nuclei, can thus be split in two. At small Q^2 it is possible to use the $\sigma_\gamma(\nu)$ cross section. In the $Q^2 >> m_e^2$ region it is necessary to calculate the effective $\sigma_{\gamma^*}(\epsilon, \nu, Q^2)$ cross section.

Following the EPA notation, the differential cross section of electronuclear scattering can be related to the number of equivalent photons $dn = \frac{d\sigma}{\sigma_{\gamma^*}}$. For $y << 1$ and $Q^2 < 4m_e^2$ the canonical method [6] leads to the simple result

$$\frac{ydn(y)}{dy} = -\frac{2\alpha}{\pi} ln(y). \tag{45.11}$$

In [7] the integration over Q^2 for $\nu^2 >> Q^2_{max} \simeq m_e^2$ leads to

$$\frac{ydn(y)}{dy} = -\frac{\alpha}{\pi}\left(\frac{1 + (1 - y)^2}{2} ln(\frac{y^2}{1 - y}) + (1 - y)\right). \tag{45.12}$$

In the $y << 1$ limit this formula converges to Eq.(45.11). But the correspondence with Eq.(45.11) can be made more explicit if the exact integral

$$\frac{ydn(y)}{dy} = \frac{\alpha}{\pi}\left(\frac{1 + (1 - y)^2}{2} l_1 - (1 - y) l_2 - \frac{(2 - y)^2}{4} l_3\right), \tag{45.13}$$

where $l_1 = ln\left(\frac{Q^2_{max}}{Q^2_{min}}\right)$, $l_2 = 1 - \frac{Q^2_{max}}{Q^2_{min}}$, $l_3 = ln\left(\frac{y^2+Q^2_{max}/E^2}{y^2+Q^2_{min}/E^2}\right)$, $Q^2_{min} = \frac{m_e^2 y^2}{1-y}$, is calculated for

$$Q^2_{max(m_e)} = \frac{4m_e^2}{1-y}. \tag{45.14}$$

The factor $(1-y)$ is used arbitrarily to keep $Q^2_{max(m_e)} > Q^2_{min}$, which can be considered as a boundary between the low and high Q^2 regions. The full transverse photon flux can be calculated as an integral of Eq.(45.13) with the maximum possible upper limit

$$Q^2_{max(max)} = 4E^2(1-y). \tag{45.15}$$

The full transverse photon flux can be approximated by

$$\frac{ydn(y)}{dy} = -\frac{2\alpha}{\pi}\left(\frac{(2-y)^2+y^2}{2}ln(\gamma) - 1\right), \tag{45.16}$$

where $\gamma = \frac{E}{m_e}$. It must be pointed out that neither this approximation nor Eq.(45.13) works at $y \simeq 1$; at this point $Q^2_{max(max)}$ becomes smaller than Q^2_{min}. The formal limit of the method is $y < 1 - \frac{1}{2\gamma}$.

In Fig. 45.1(a,b) the energy distribution for the equivalent photons is shown. The low-Q^2 photon flux with the upper limit defined by Eq.(45.14)) is compared with the full photon flux. The low-Q^2 photon flux is calculated using Eq.(45.11) (dashed lines) and using Eq.(45.13) (dotted lines). The full photon flux is calculated using Eq.(45.16) (the solid lines) and using Eq.(45.13) with the upper limit defined by Eq.(45.15) (dash-dotted lines, which differ from the solid lines only at $\nu \approx E_e$). The conclusion is that in order to calculate either the number of low-Q^2 equivalent photons or the total number of equivalent photons one can use the simple approximations given by Eq.(45.11) and Eq.(45.16), respectively, instead of using Eq.(45.13), which cannot be integrated over y analytically. Comparing the low-Q^2 photon flux and the total photon flux it is possible to show that the low-Q^2 photon flux is about half of the the total. From the interaction point of view the decrease of $\sigma_{\gamma *}$ with increasing Q^2 must be taken into account. The cross section reduction for the virtual photons with large Q^2 is governed by two factors. First, the cross section drops with Q^2 as the squared dipole nucleonic form-factor

$$G^2_D(Q^2) \approx \left(1 + \frac{Q^2}{(843\ MeV)^2}\right)^{-2}. \tag{45.17}$$

Second, all the thresholds of the γA reactions are shifted to higher ν by a factor $\frac{Q^2}{2M}$, which is the difference between the K and ν values. Following the

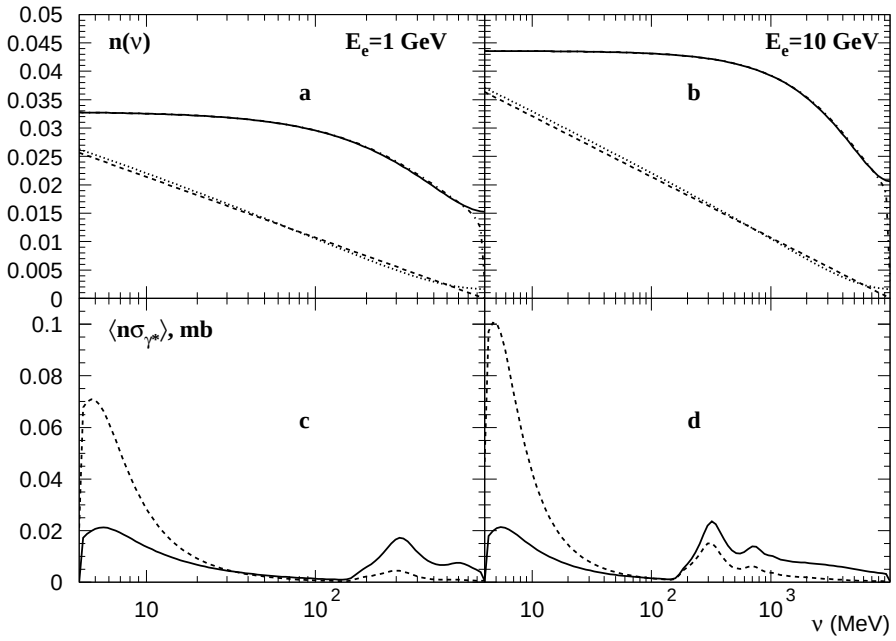

Figure 45.1: Relative contribution of equivalent photons with small Q^2 to the total "photon flux" for (a) 1 GeV electrons and (b) 10 GeV electrons. In figures (c) and (d) the equivalent photon distribution $dn(\nu, Q^2)$ is multiplied by the photonuclear cross section $\sigma_{\gamma^*}(K, Q^2)$ and integrated over Q^2 in two regions: the dashed lines are integrals over the low-Q^2 equivalent photons (under the dashed line in the first two figures), and the solid lines are integrals over the high-Q^2 equivalent photons (above the dashed lines in the first two figures).

method proposed in [8] the σ_{γ^*} at large Q^2 can be approximated as

$$\sigma_{\gamma *} = (1-x)\sigma_{\gamma}(K)G_D^2(Q^2)e^{b(\epsilon,K)\cdot r + c(\epsilon,K)\cdot r^3}, \tag{45.18}$$

where $r = \frac{1}{2}ln(\frac{Q^2+\nu^2}{K^2})$. The ϵ-dependence of the $a(\epsilon,K)$ and $b(\epsilon,K)$ functions is weak, so for simplicity the $b(K)$ and $c(K)$ functions are averaged over ϵ. They can be approximated as

$$b(K) \approx \left(\frac{K}{185\ MeV}\right)^{0.85}, \tag{45.19}$$

and

$$c(K) \approx -\left(\frac{K}{1390\ MeV}\right)^{3}. \tag{45.20}$$

The result of the integration of the photon flux multiplied by the cross section approximated by Eq.(45.18) is shown in Fig. 45.1(c,d). The integrated cross sections are shown separately for the low-Q^2 region ($Q^2 < Q^2_{max(m_e)}$, dashed lines) and for the high-Q^2 region ($Q^2 > Q^2_{max(m_e)}$, solid lines). These functions must be integrated over $ln(\nu)$, so it is clear that because of the Giant Dipole Resonance contribution, the low-Q^2 part covers more than half the total $eA \to hadrons$ cross section. But at $\nu > 200\ MeV$, where the hadron multiplicity increases, the large Q^2 part dominates. In this sense, for a better simulation of the production of hadrons by electrons, it is necessary to simulate the high-Q^2 part as well as the low-Q^2 part.

Taking into account the contribution of high-Q^2 photons it is possible to use Eq.(45.16) with the over-estimated $\sigma_{\gamma^* A} = \sigma_{\gamma A}(\nu)$ cross section. The slightly over-estimated electronuclear cross section is

$$\sigma^*_{eA} = (2ln(\gamma) - 1)\cdot J_1 - \frac{ln(\gamma)}{E_e}\left(2J_2 - \frac{J_3}{E_e}\right). \tag{45.21}$$

where

$$J_1(E_e) = \frac{\alpha}{\pi}\int^{E_e} \sigma_{\gamma A}(\nu) dln(\nu) \tag{45.22}$$

$$J_2(E_e) = \frac{\alpha}{\pi}\int^{E_e} \nu\sigma_{\gamma A}(\nu) dln(\nu), \tag{45.23}$$

and

$$J_3(E_e) = \frac{\alpha}{\pi}\int^{E_e} \nu^2\sigma_{\gamma A}(\nu) dln(\nu). \tag{45.24}$$

The equivalent photon energy $\nu = yE$ can be obtained for a particular random number R from the equation

$$R = \frac{(2ln(\gamma)-1)J_1(\nu) - \frac{ln(\gamma)}{E_e}(2J_2(\nu) - \frac{J_3(\nu)}{E_e})}{(2ln(\gamma)-1)J_1(E_e) - \frac{ln(\gamma)}{E_e}(2J_2(E_e) - \frac{J_3(E_e)}{E_e})}. \tag{45.25}$$

Eq.(45.13) is too complicated for the randomization of Q^2 but there is an easily randomized formula which approximates Eq.(45.13) above the hadronic threshold ($E > 10\ MeV$). It reads

$$\frac{\pi}{\alpha D(y)} \int_{Q^2_{min}}^{Q^2} \frac{ydn(y,Q^2)}{dydQ^2} dQ^2 = -L(y,Q^2) - U(y), \tag{45.26}$$

where

$$D(y) = 1 - y + \frac{y^2}{2}, \tag{45.27}$$

$$L(y,Q^2) = ln\left(F(y) + (e^{P(y)} - 1 + \frac{Q^2}{Q^2_{min}})^{-1}\right), \tag{45.28}$$

and

$$U(y) = P(y) \cdot \left(1 - \frac{Q^2_{min}}{Q^2_{max}}\right), \tag{45.29}$$

with

$$F(y) = \frac{(2-y)(2-2y)}{y^2} \cdot \frac{Q^2_{min}}{Q^2_{max}} \tag{45.30}$$

and

$$P(y) = \frac{1-y}{D(y)}. \tag{45.31}$$

The Q^2 value can then be calculated as

$$\frac{Q^2}{Q^2_{min}} = 1 - e^{P(y)} + \left(e^{R \cdot L(y,Q^2_{max}) - (1-R)\cdot U(y)} - F(y)\right)^{-1}, \tag{45.32}$$

where R is a random number. In Fig. 45.2, Eq.(45.13) (solid curve) is compared to Eq.(45.26) (dashed curve). Because the two curves are almost indistinguishable in the figure, this can be used as an illustration of the Q^2 spectrum of virtual photons, which is the derivative of these curves. An alternative approach is to use Eq.(45.13) for the randomization with a three dimensional table $\frac{ydn}{dy}(Q^2, y, E_e)$.

After the ν and Q^2 values have been found, the value of $\sigma_{\gamma^* A}(\nu, Q^2)$ is calculated using Eq.(45.18). If $R \cdot \sigma_{\gamma A}(\nu) > \sigma_{\gamma^* A}(\nu, Q^2)$, no interaction occurs and the electron keeps going. This "do nothing" process has low probability and cannot shadow other processes.

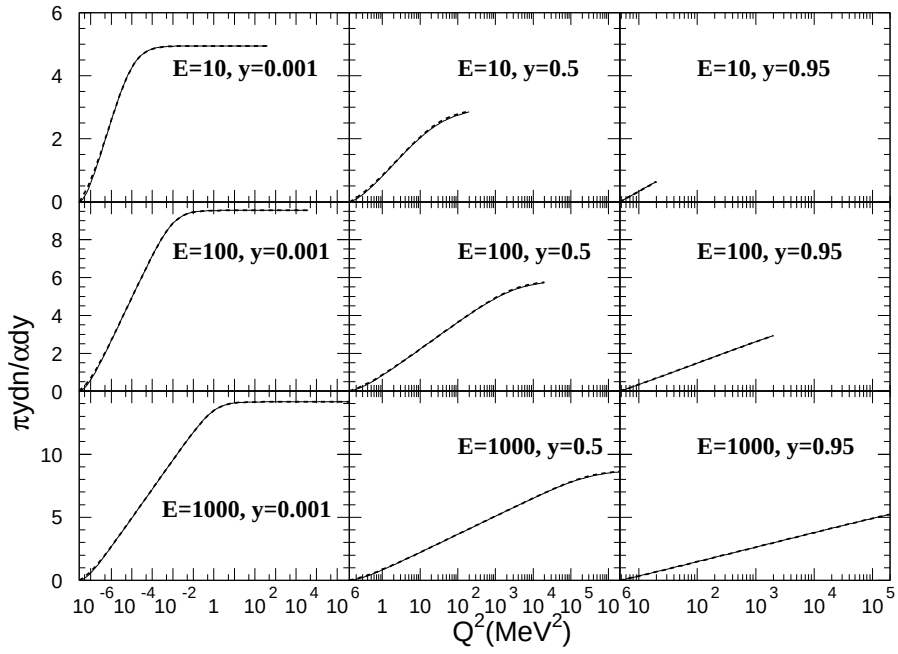

Figure 45.2: Integrals of Q^2 spectra of virtual photons for three energies 10 MeV, 100 MeV, and 1 GeV at $y = 0.001$, $y = 0.5$, and $y = 0.95$. The solid line corresponds to Eq.(45.13) and the dashed line (which almost everywhere coincides with the solid line) corresponds to Eq.(45.13).

45.4 Status of this document

created by H.P. Wellisch and M. Kossov
20.05.02 re-written by D.H. Wright
01.12.02 expanded section on electronuclear cross sections - H.P. Wellisch

Bibliography

[1] E. Fermi, Z. Physik **29**, 315 (1924).

[2] K. F. von Weizsacker, Z. Physik **88**, 612 (1934), E. J. Williams, Phys. Rev. **45**, 729 (1934).

[3] L. D. Landau and E. M. Lifshitz, Soc. Phys. **6**, 244 (1934).

[4] I. Ya. Pomeranchuk and I. M. Shmushkevich, Nucl. Phys. **23**, 1295 (1961).

[5] V. N. Gribov *et al.*, ZhETF **41**, 1834 (1961).

[6] L. D. Landau, E. M. Lifshitz, "Course of Theoretical Physics" v.4, part 1, "Relativistic Quantum Theory", Pergamon Press, p. 351, The method of equivalent photons.

[7] V. M. Budnev *et al.*, Phys. Rep. **15**, 181 (1975).

[8] F. W. Brasse *et al.*, Nucl. Phys. B **110**, 413 (1976).

Chapter 46

Gamma-nuclear Interactions

46.1 Process and Cross Section

Gamma-nuclear reactions in Geant4 are handled by the class *G4PhotoNuclearProcess*. The default cross section class for this process is *G4PhotoNuclearCrossSection*, which was described in detail in the previous chapter.

46.2 Final State Generation

Final state generation proceeds by two different models, one for incident gamma energies of a few GeV and below, and one for high energies. For high energy gammas, the QGSP model is used. Indicent gammas are treated as QCD strings which collide with nucleons in the nucleus, forming more strings which later hadronize to produce secondaries. In this particular model the remnant nucleus is de-excited using the Geant4 precompound and de-excitation sub-models.

At lower incident energies, there are two models to choose from. The Bertini-style cascade (*G4CascadeInterface* interacts the incoming gamma with nucleons using measured partial cross sections to decide the final state multiplicity and particle types. Secondaries produced in this initial interaction are then propagated through the nucleus so that they may react with other nucleons before exiting the nucleus. The remnant nucleus is then de-excited to produce low energy fragments. Details of this model are provided in another chapter in this manual.

An alternate handling of low energy gamma interactions is provided by *G4GammaNuclearReaction*, which uses the Chiral Invariant Phase Space model (CHIPS, Chapter 30). Here the incoming gamma is absorbed into a nucleon or cluster of nucleons within the target nucleus. This forms an

excited bag of partons which later fuse to form final state hadrons. Parton fusion continues until there are none left, at which point the final nuclear evaporation stage is invoked to bring the nucleus to its ground state.

46.3 Status of this document

19.11.12 created by D.H. Wright

Chapter 47

Electro-nuclear Interactions

47.1 Process and Cross Section

Electro-nuclear reactions in Geant4 are handled by the classes *G4ElectronNuclearProcess* and *G4PositronNuclearProcess*. The default cross section class for both these processes is *G4ElectroNuclearCrossSection* which was described in detail in an earlier chapter.

47.2 Final State Generation

Final state generation proceeds in two steps. In the first step the electromagnetic vertex of the electron/positron-nucleus reaction is calculated. Here the virtual photon spectrum is generated by sampling parameterized Q^2 and ν distributions. The equivalent photon method is used to get a real photon from this distribution.

In the second step, the real photon is interacted with the target nucleus at the hadronic vertex, assuming the photon can be treated as a hadron. Photons with energies below 10 GeV can be interacted directly with nucleons in the target nucleus using the measured (γ, p) partial cross sections to decide the final state multiplicity and particle types. This is currently done by the Bertini-style cascade (*G4CascadeInterface*). Photons with energies above 10 GeV are converted to π^0s and then allowed to interact with nucleons using the FTFP model. In this model the hadrons are treated as QCD strings which collide with nucleons in the nucleus, forming more strings which later hadronize to produce secondaries. In this particular model the remnant nucleus is de-excited using the Geant4 precompound and de-excitation submodels.

This two-step process is implemented in the *G4ElectroVDNuclearModel*.

An alternative model is the CHIPS-based *G4ElectroNuclearReaction* (Chapter 30). This model also uses the equivalent photon approximation in which the incoming electron or positron generates a virtual photon at the electromagnetic vertex, and the virtual photon is converted to a real photon before it interacts with the nucleus. The real photon interacts with the hadrons in the target using the CHIPS model in which quasmons (generalized excited hadrons) are produced and then decay into final state hadrons. Electrons and positrons of all energies can be handled by this single model.

47.3 Status of this document

19.11.12 created by D.H. Wright

Chapter 48

Muon-nuclear Interactions

48.1 Process and Cross Section

Muon-nuclear reactions in Geant4 are handled by the class *G4MuonNuclearProcess*. The default cross section class for this process is *G4KokoulinMuonNuclearXS*, the details of which are discussed in section 13.4.

48.2 Final State Generation

Just as for the electro-nuclear models, the final state generation for the muon-nuclear reactions proceeds in two steps. In the first step the electromagnetic vertex of the muon-nucleus reaction is calculated. Here the virtual photon spectrum is generated by sampling parameterized momentum transfer (Q^2) and energy transfer (ν) distributions. In this case the same equations used to generate the process cross section are used to sample Q^2 and ν. The equivalent photon method is then used to get a real photon.

In the second step, the real photon is interacted with the target nucleus at the hadronic vertex, assuming the photon can be treated as a hadron. Photons with energies below 10 GeV can be interacted directly with nucleons in the target nucleus using the measured (γ, p) partial cross sections to decide the final state multiplicity and particle types. This is currently done by the Bertini-style cascade (*G4CascadeInterface*). Photons with energies above 10 GeV are converted to π^0s and then allowed to interact with nucleons using the FTFP model. In this model the hadrons are treated as QCD strings which collide with nucleons in the nucleus, forming more strings which later hadronize to produce secondaries. In this particular model the remnant nucleus is de-excited using the Geant4 precompound and de-excitation sub-models.

This two-step process is implemented in the *G4MuonVDNuclearModel*.

48.3 Status of this document

19.11.12 created by D.H. Wright